Developments and Applications of Modern Airborne Electromagnetic Surveys

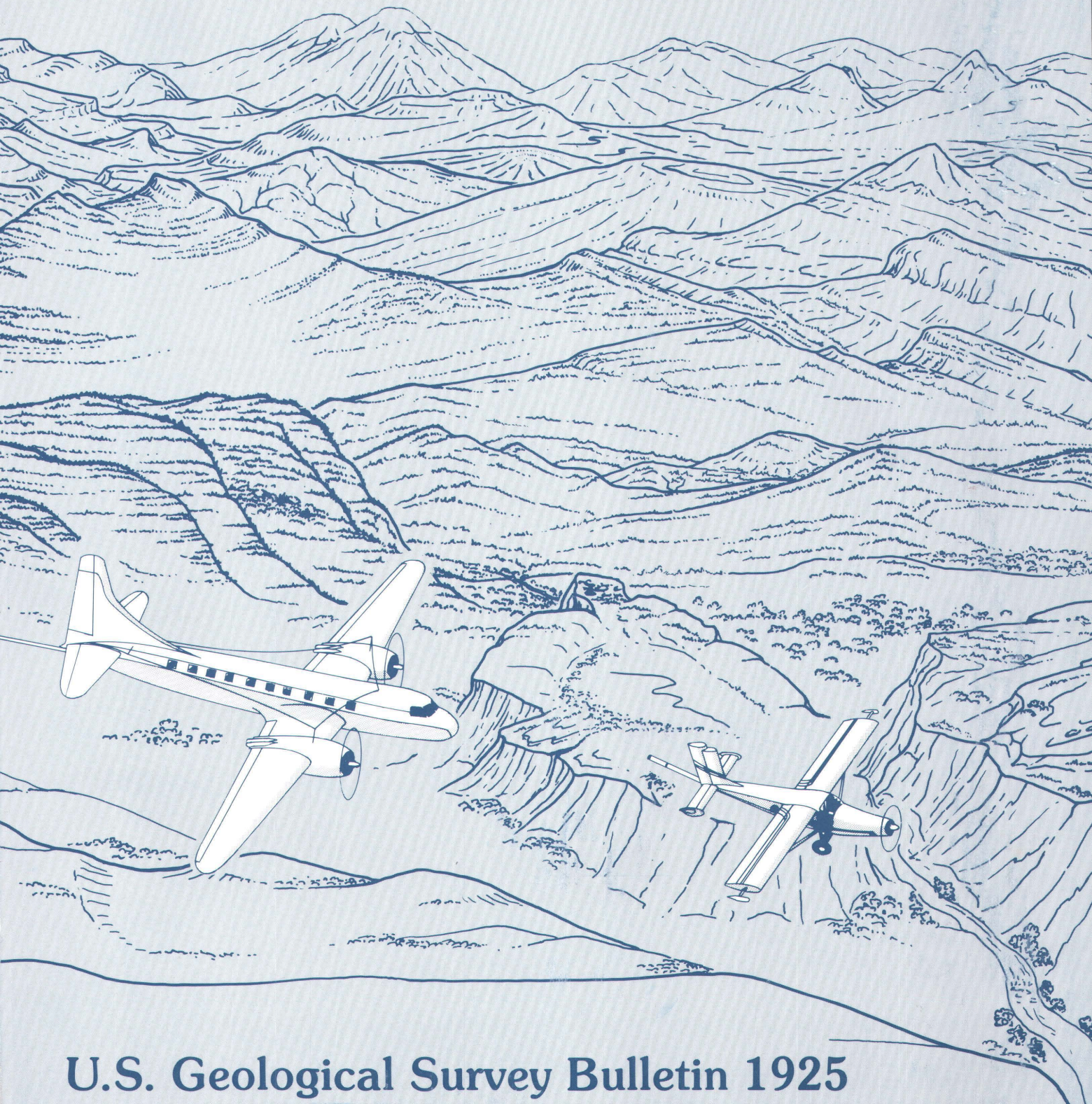

U.S. Geological Survey Bulletin 1925

Front Cover: Past and present U.S. Geological Survey aircraft used for geophysical surveys are depicted flying over terrain typical of the foothills west of Denver, Colorado. The aircraft, in order of age (from left to right), are Beech Model 17, Staggerwing; Douglas DC-3; Convair CV-240; and Fairchild Porter PC 6/C-H2.

Cover design by Art Isom, U.S. Geological Survey.

Developments and Applications of Modern Airborne Electromagnetic Surveys

Edited by DAVID V. FITTERMAN

Proceedings of the U.S. Geological Survey Workshop on Developments and Applications of Modern Airborne Electromagnetic Surveys, October 7-9, 1987

U.S. GEOLOGICAL SURVEY BULLETIN 1925

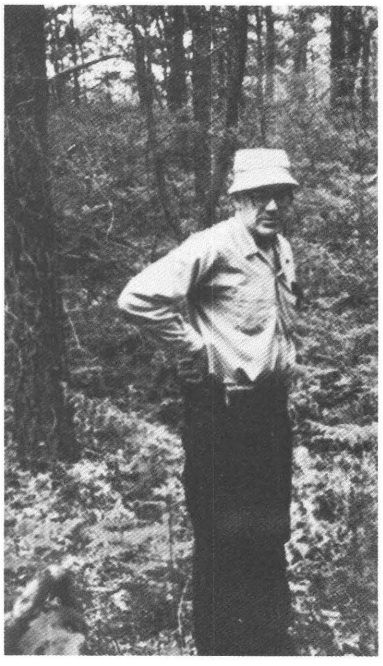

DEDICATION

Frank C. Frischknecht, a geophysicist with the U.S. Geological Survey and a pioneer in the field of airborne geophysics, was killed August 12, 1987, in a helicopter-plane collision near Ketchikan, Alaska.

Frank was born in Bicknell, Utah. He received a Bachelor of Science degree in Electrical Engineering (1950) and a Master of Science degree in Geophysics (1953) from the University of Utah. He continued his education at the University of Colorado, earning a second Master of Science degree in Geophysical Mathematics (1967) and a Doctor of Philosophy (1973) in Electrical Engineering Physics.

Frank's professional career with the U.S. Geological Survey spanned more than 35 years, beginning in 1952 with work on airborne geophysical instrumentation, data compilation, and interpretation problems. From 1955 to 1962, he developed a variety of controlled- and natural-source electromagnetic techniques that were applied to numerous geological problems. In 1962, the U.S. Geological Survey acquired a Convair 240 aircraft and Frank became involved in developing, acquiring, and testing geophysical instrumentation for airborne surveys. Of particular interest to him were a new INPUT electromagnetic system and an automated magnetometer system.

His accumulated experience resulted in the now classic textbook "Electrical Methods in Geophysical Prospecting," published in 1966 in collaboration with George V. Keller. In 1967, Frank published the first computer-generated, layered-earth theoretical electromagnetic sounding curves that became the basis for most early airborne electromagnetic interpretational methods. During this same period, Frank also developed a scale-model electromagnetic test facility that provided data crucial to understanding field observations and testing interpretational methods. His model results are internationally recognized as standards against which numerical results are checked. He developed an airborne very low frequency (VLF) receiver incorporating an electric field reference that enabled it to produce resistivity maps used for geologic mapping. He oversaw initial development and construction of the first airborne power-line receiver, which has since been successfully used to produce resistivity maps with greater depth of exploration that is possible with VLF systems. At the time of his death, Frank had completed and was working on chapters on electromagnetic scale modeling, profiling techniques, VLF, and electromagnetic sounding for the Society of Exploration Geophysicists two-volume series "Electromagnetic Methods in Applied Geophysics."

Frank served as the Chief of the Branch of Electromagnetism and Geomagnetism (1976–1980) and the Branch of Geophysics (1984–1986), during which time he directed expansion of the electromagnetics program and oversaw the modernization of the geomagnetic observatories. Between his tours as Branch Chief he pioneered in the application of traditional geophysical techniques to the many environmental problems associated with locating contamination from land fills and injection wells and mapping abandoned wells. With the Survey's increased involvement in environmental problems, he realized the need for and potential scientific crippling power of quality assurance programs. He played a key role in developing an approach to quality assurance for the Survey that would be scientifically acceptable while meeting regulatory requirements.

Recognized internationally as an authority in geophysics, Frank lectured and conducted field studies in many countries. He was active in the Society of Exploration Geophysicists, serving on several committees and as an Associate Editor of *Geophysics*. In recognition of Frank's scientific achievements he served on the Geologic Division Scientific Advisory Committee and received both the Department of the Interior's Meritorious Service and Distinguished Service Awards.

For all of his professional accomplishments, Frank was a very unassuming person who derived great pleasure from music, ballet, art, hiking, and photography. With a great sense of loss and admiration, this volume is dedicated to him.

DEPARTMENT OF THE INTERIOR
MANUEL LUJAN, JR., Secretary

U.S. GEOLOGICAL SURVEY
Dallas L. Peck, Director

UNITED STATES GOVERNMENT PRINTING OFFICE: 1990

For sale by the
Books and Open-File Reports Section
U.S. Geological Survey
Federal Center
Box 25425
Denver, CO 80225

Library of Congress Cataloging-in-Publication Data

U.S. Geological Survey Workshop on Developments and Applications of Modern Airborne Electromagnetic Surveys (1987 : Golden, Colo.)

Developments and applications of modern airborne electromagnetic surveys : proceedings of the U.S. Geological Survey Workshop on Developments and Applications of Modern Airborne Electromagnetic Surveys, October 7-9, 1987 / edited by David V. Fitterman.
p. cm.—(U.S. Geological Survey bulletin ; 1925)
Includes bibliographical references.
Supt. of Docs. no.: I 19.3:1925
1. Geomagnetism—Congresses. I. Fitterman, David V. II. Title. III. Title: Airborne electromagnetic surveys. IV. Series.
QE75.B9 no. 1925
[QC811]
557.3 s—dc20 90-3332
[538'.7] CIP

CONTENTS

Introduction

By David V. Fitterman[1]

This publication serves as a written record of the U.S. Geological Survey-sponsored workshop on Developments and Applications of Modern Airborne Electromagnetic Surveys held October 7–9, 1987, in Golden, Colorado. The workshop was one of a series sponsored by the U.S. Geological Survey to foster interest in a national airborne geophysical program. Attendees were invited from domestic and foreign government organizations, industry, and academia; more than 60 scientists from 7 countries participated. The meeting consisted of technical presentations detailing the history and state of the art of airborne electromagnetics (AEM), working group discussions on various aspects of data collection, interpretation, and applications, and a panel discussion to summarize the conclusions drawn from the meeting.

In this bulletin are papers from the technical presentations, written summaries of the working group recommendations, and a transcript of the panel discussion. The papers are grouped in five sections. The first section, background and history, describes the involvement of the U.S. Geological Survey in airborne geophysical methods in the past and our plans for the future. Also included are two papers describing the history of early AEM developments and advances during the past decade. These papers set the stage for reports about current technology. The section on interpretation and modeling contains papers on theoretical and real-world studies that show the types of interpretational products being developed today, and consider the geologic models that play havoc with layered-earth interpretations. As computational methods are being developed to handle complicated geometries, further work and advances in computer technology are needed before these models can be used on a routine basis.

The next two sections report on the application of several AEM methods to a diverse spectrum of problems. The section on resource and geological applications contains papers on geological and exploration applications, and the section on environmental and related applications documents some of the more recent uses of AEM methods for ground-water exploration, bathymetry, and ice-thickness determination.

The section on recent hardware developments contains papers describing commercially available airborne geophysical systems, a powerline-energized mapping system being developed by the U.S. Geological Survey, and a remotely piloted aircraft capable of being used as a geophysical platform.

The appendix contains written reports of the five working groups. The working groups were made up of workshop participants who discussed assigned topics in an attempt to reach a consensus on the state of current technology, suggest areas for further research and new applications, and propose recommendations for a national airborne geophysical program. An edited transcript of the panel discussion, the purpose of which was to assess the conclusions of the working groups, is also included.

The workshop was very successful in achieving its goal of bringing together active researchers in the area of airborne electromagnetics to assess the status of modern AEM technology and propose areas for future research. The key next step of acting on these recommendations to produce and utilize AEM systems that are able to answer the many geological, resource, ground-water, and environmental problems we face today rests with the U.S. Geological Survey, its foreign counterparts, industry, and academia. With hard work, perseverance, and funding, we will achieve this goal.

Acknowledgments.—Until the time of his death, the workshop organizing committee was headed by Frank Frischknecht; his efforts in formulating and organizing the workshop contributed to its success. Don Hoover, Bruce Smith, Dal Stanley, and I served on the committee, saw that the workshop ran smoothly, and helped review the workshop articles. Special thanks go to the authors whose articles and working group reports are contained in this volume. The work of Mary Ignelzi, Pamela Ketterer, and Leona Treloar with workshop registration, working group report typing, and preparation of the manuscripts is greatly appreciated.

Manuscript approved for publication, February 19, 1990.

[1]U.S. Geological Survey, Box 25046, MS964, Denver, Colorado 80225.

SECTION 1: BACKGROUND AND HISTORY

National Airborne Geophysics Program

By Thomas G. Hildenbrand[1], Gary L. Raines[2], *and* David V. Fitterman[3]

INTRODUCTION

The U.S. Geological Survey pioneered airborne geophysical exploration (Hanna, in press). In 1943, James R. Balsley, a Survey geophysicist, recognized the potential importance of a magnetic airborne detector (MAD) for geophysical exploration. This device, which was developed by the Navy to detect submarines, utilized a self-orienting fluxgate magnetometer. In 1944, after a few modifications were made to the MAD system, the U.S. Geological Survey flew the first airborne geophysical survey: 10,000 mi of magnetic data were collected over Naval Petroleum Reserve–4 in the northernmost part of Alaska. In the following 44 years, airborne geophysics has evolved into a major component of earth science. Today aircraft are capable of acquiring a wide variety of geophysical data—gravity, magnetic, electromagnetic, radiometric, and visible-infrared-radar multispectral—critical to solving national resource, environmental, and hazards problems.

Historically, the U.S. Geological Survey has conducted or contracted with private industry to conduct airborne geophysical surveys involving the yearly collection of thousands of miles of data (fig. 1). A disturbing trend in the number of line-miles flown has developed, however, during the past 13 years. The Survey has progressively decreased its geophysical data collection effort from 150,000 mi in 1975 to less than 1,000 mi in 1987. This proceedings volume stresses the utility of airborne geophysical data and thus the need for a national airborne geophysical program to systematically acquire geophysical data.

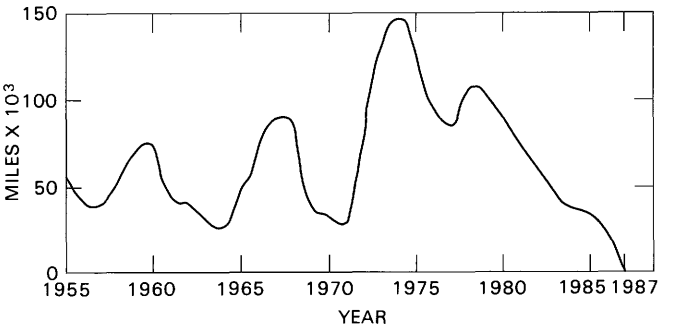

Figure 1. Yearly number of flight-line miles of geophysical surveys flown by the U.S. Geological Survey. Miles flown include airborne radiometric, magnetic, and electromagnetic surveys.

OTHER NATIONAL AIRBORNE GEOPHYSICS PROGRAMS

Canada, Finland, the U.S.S.R., Zimbabwe, Liberia, and Australia have established cost-effective national airborne geophysics programs. For example, Canada has collected more than 6 million line-miles of magnetic data, published more than 9,500 aeromagnetic anomaly maps, and distributed for many years 30,000 aeromagnetic anomaly maps per year (the most requested item of the Geological Survey of Canada). The Canadian aeromagnetic program has been a very successful endeavor that "has led directly or indirectly to the discovery of many ore deposits and its overall cost has been recovered many times over the years through the general economic benefits to the country that results from such discoveries and from taxes that are subsequently paid to the provincial and federal governments" (Hood, in press).

Finland initiated the first national airborne geophysical survey in 1951 (Poikonen, this volume). Electromagnetic, magnetic, and radiometric data were collected at an altitude of 150 m and a flight-line spacing of 400 m. This first phase in Finland's national airborne geophysical survey was completed in 1972 and then was followed by a second phase, a more detailed low-altitude acquisition program. The flight height and line spacing were decreased to 30 m and 200 m, respectively. The

[1]U.S. Geological Survey, 345 Middlefield Road, MS989, Menlo Park, California 94025.

[2]U.S. Geological Survey, c/o MacKay School of Mines, University of Nevada, Reno, Nevada 89557.

[3]U.S. Geological Survey, Box 25046, MS906, Denver, Colorado 80225.

quality and extent of their airborne data are significantly greater than those of U.S. airborne data. For example, the average spacings of airborne magnetic and radiometric surveys in the United States are roughly 5,000 m and 7,000 m, respectively, substantially greater than the 200-m spacing in Finland. Moreover, no large region of uniform airborne electromagnetic (AEM) coverage exists in the United States; available AEM data are collected in small areas associated with local case studies.

The utility of regional-scale airborne electromagnetic data is demonstrated in several of the papers included in this volume. Palacky shows several examples of regional geologic mapping based on AEM data in areas where few outcrops exist. Sinha uses airborne very low frequency (VLF) data to map the locations of regional-scale fracture systems. Poikonen summarizes the use of regional AEM data in Finland for resource exploration. Sengpiel details an outstanding example of the use of helicopter AEM data to search for water resources in the desert regions of Pakistan.

NEED FOR A NATIONAL AIRBORNE GEOPHYSICS PROGRAM

An essential aspect of geologic knowledge includes data on the subsurface obtained either from extrapolation of surface geology or from direct measurement by geophysical methods. Exploitable mineral and groundwater resources occur at depths ranging from tens of centimeters to several hundreds of meters. Petroleum resources generally occur at depths of as much as a few kilometers. Similarly, geologic hazards such as landslides and volcanic eruptions are associated with processes that may occur over an even wider depth range.

High-quality maps, derived from surface geologic observations, are important and necessary for many purposes including extrapolation to subsurface geology. Such extrapolation can be done with adequate accuracy into the near subsurface. Nevertheless, the time has long since passed when surface geologic mapping alone meets most needs. Vast parts of the United States are covered by surficial deposits that prevent observation of the bedrock. Surface exposures of flat-lying rocks in the Midcontinent and elsewhere provide few clues on underlying structures. The optimum approach to geologic investigations is providing the geologist with interpretive geophysical features prior to detailed geologic field mapping, so that he can focus on a viable three-dimensional geologic model.

Most geologic information is obtained from studies of from 1:24,000 to 1:250,000 scale. For investigations at these scales, airborne geophysics provides a more universal approach to subsurface investigations than any other method. There are several reasons for the broad capabilities of airborne methods:

1. Aircraft are suitable and often optimal platforms for acquisition of critical geophysical data, including potential (magnetics and gravity) and electromagnetic fields: the latter range from audio, VLF, and radar frequencies to thermal and near infrared, visible, and gamma-ray spectra. The use of multiple sensors allows acquisition of information on surface and subsurface variations of several rock properties in a single survey.
2. By flying low, the horizontal resolution of aircraft data is more than adequate for mapping at scales as large as 1:5,000. By flying high, images of large swaths can be obtained in a single pass for small-scale mapping. Through the use of multiple sensors, information can be obtained over a continuum of depths from the surface to tens of kilometers.
3. Collection of aircraft data in digital form allows for immediate computer processing, analysis, and display by geographic information systems. The results provide a uniform and consistent data set that can be accessed as often as needed to provide information on new problems or reinterpreted as geologic concepts change.
4. Data can be collected by aircraft over areas that are inaccessible on the ground because of natural reasons, such as rugged topography or hazards, or man-made causes, such as restrictions imposed by private ownership.
5. Airborne geophysics is very cost effective when applied to large areas. Generally, no set of ground-based methods can supply equally useful information at such low unit costs.

The importance of airborne geophysics was recognized in past decades in the relatively large efforts of the U.S. Geological Survey. Twenty or thirty years ago the rate of acquisition of aeromagnetic data far exceeded the capabilities of the U.S. Geological Survey to interpret and fully utilize the data. Now, however, airborne data acquisition is at an all-time low, and available data are inadequate to meet programmatic needs.

Rejuvenation of airborne studies is timely both in terms of the need for subsurface information and the new technological developments that greatly enhance the capabilities of the various methods. Recent improvements in sensors offer order-of-magnitude improvement in resolution (both spectrally and spatially) over the best devices available a few years ago. Improvements in electronic navigation for aircraft from the Global Positioning Satellite System (GPS) soon will be fully operational. Faster computers and better image displays have also increased the capability to interpret geophysical data.

In coordination with governmental agencies, academic institutions, and private industry, the long-term goal of a national airborne geophysics program should be to obtain systematic digital airborne geophysical data for

the United States. Data acquisition should focus on immediate needs of national programs, including mineral and organic fuel assessments, earthquake and volcano hazards, and environmental issues.

REFERENCES CITED

Hanna, W.F., in press, Some historical notes on early magnetic surveying in the U.S. Geological Survey, *in* Proceedings of a Workshop on Geologic Applications of Modern Aeromagnetic Surveys: U.S. Geological Survey Bulletin 1924.

Hood, P.J., in press, Aeromagnetic survey program of Canada, mineral applications, and vertical gradiometry, *in* Proceedings of a Workshop on Geologic Applications of Modern Aeromagnetic Surveys: U.S. Geological Survey Bulletin 1924.

Historical Aspects of Airborne Electromagnetic Development

By Anthony R. Barringer[1]

The pioneering roots of airborne electromagnetic (AEM) system development date to the early 1950's when the International Nickel Company produced the world's first AEM system. This successful system, orginally installed in a wooden aircraft to ease development problems, clearly showed the potential of this exploration technique.

Other developments of the 1950's included the Finnish-derived two-frequency quadrature system, which used a towed bird and provided compensation for metal in the aircraft. It was operated in Canada by Photographic Survey Corporation, a subsidiary of the Hunting Group. The system was quite effective but suffered from noise associated with conductive overburden. Another interesting development during this period was a two-plane Swedish system that used a rotating field and employed two specially positioned lights to aid the pilots in maintaining a farily constant relative aircraft position. The method achieved a high degree of penetration, but conductivity interpretations were difficult.

Another system of the 1950's was the single-engined Otter system, operated by a subsidiary of the Rio Tinto Mining Co., that employed wing-tip coplanar coils and measured in-phase and quadrature components of field. The plane flew at very low altitudes in order to achieve useful penetration and adequate signal-to-noise ratios. The system was eventually licensed to the Canadian Aeroservice Company, later to become Geoterrex Ltd.

One of the most successful systems originally developed in the 1950's was the Texas Gulf Sulphur Inc. helicopter system designed by Varian Associates. This system used coaxial transmitting and receiving coils and a 60-ft-long boom that made the helicopter dangerously unstable; however, it made the spectacular discovery of the Kidd Creek massive sulfide base metal deposit in Ontario that caused all records to be broken on the Toronto Stock Exchange and was followed by a celebrated chain of lawsuits. Unfortunately, the geophysicist operating this system, Peter White, was subsequently killed in the helicopter, and the equipment was never reactivated because of its operational risk.

[1]Barringer Resources Incorporated, 15000 W. 6th Avenue, Suite 300, Golden, Colorado 80401–5047.

At the end of the 1950's, the first model of the induced pulse transient (INPUT) system was constructed under the sponsorship of Selco Exploration, Inc. It flew initially with rather poor signal-to-noise ratios.

During the 1960's, Barringer Research Ltd. made a number of major developmental changes to the INPUT system culminating in the Mark 5 version in 1965. This system initially went to Sweden for LKAB (the Swedish Iron Ore Company) with introductions provided by the airborne geophysical pioneer, Hans Lundberg. It flew the Kiruna iron ore deposit—the largest underground mine in the world—and discovered an anomaly very close to the deposit. The anomaly was not drilled until it was discovered, 8 years later, that copper indicator flowers grew on the anomaly. This floral INPUT anomaly turned out to be a massive sulfide copper orebody that is still in production today.

Shortly after the discovery of the Kiruna anomaly, Selco Exploration Co. Ltd. discovered South Bay Mines in Ontario. This discovery paved the way for the licensing of the INPUT system and its subsequent large-scale usage in many countries.

During the 1960's, a great deal of initial work was carried out on helicopter electromagnetic (HEM) systems that employed towed birds typically 30 ft long. Developmental work by companies such as Dighem Ltd., Aerodat Ltd., Geonics Ltd., Geotech Ltd., Barringer Research Ltd., and others is still continuing. Noise levels in HEM systems have been progressively reduced to the 1-ppm level. The main forte of these helicopter systems, before the current gold exploration boom, was their use in areas where the terrain was too rugged for fixed-wing systems.

Interest grew in very low frequency (VLF) systems that depend on government transmitting stations for their signals. Many geophysical companies introduced equipment to this market. Experiments using both electric and magnetic field components of VLF, LF, and MF transmissions resulted in the system known as E-PHASE. The USGS and the Finnish Geological Survey developed VLF systems that employed both the E- and H-field components. Among the fixed-wing frequency-domain active systems, Vaino Ronka produced a system that towed a winged bird, but little was published on the results.

Digital EM began in the 1970's, and improvements in digital techniques continue to this day. At the end of the 1970's, the INPUT system was upgraded to a digital format called COTRAN (correlation of transients), which differs from INPUT in that it employs the transient EM signal inside the transmitter pulse as well as the signal that follows the pulse.

During the early 1980's, COTRAN development continued as well as work on other digital EM broadband systems. The 1980's have been marked, however, by a severe decline in base metal markets and a drastic reduction in the usage of fixed-wing airborne EM systems. At the same time, increased gold exploration has greatly increased the demand for HEM systems. Detailed, low-altitude mapping of conductivity and magnetic susceptibility trends has become very popular, particularly in Canada, and has proven to be a powerful aid to the geologist and geophysicist in the search for gold, especially in areas where overburden cover is ubiquitous.

Progress continues and I leave it to others to discuss detailed aspects of current and emerging technology.

Airborne Electromagnetics 1978–1988

By A. Becker[1], A.R. Barringer[2], and A.P. Annan[3]

Abstract

In spite of a significant reduction in mineral exploration activity, the recent past has witnessed much technical and scientific advance in the art of airborne electromagnetic surveying. Although some of this progress took the form of significant technical improvement to existing apparatus, a number of radically new prototype systems have also been developed. Virtually all the changes are related to the onboard use of microprocessor-based equipment. This is most apparent in the newest airborne electromagnetic systems where the now common digital data recording is augmented by direct digital data acquisition and real-time processing of the sensor signal. Improved equipment and superior data quality now give a true and practical meaning to the concept of airborne electromagnetic mapping so that the airborne electromagnetic method is no longer restricted to mineral prospecting applications. It can be profitably used in the indirect search for resources or for the resolution of geotechnical, geological, and, to some extent, maritime engineering problems.

These trends are likely to continue into the future where we anticipate the universal acceptance of digital equipment from the sensor onward. It is also easy to envisage generic equipment that may be selected for the task at hand. Two distinct trends will probably emerge. One of these will be defined by a heavy, wide-band, slow-flying laboratory that combines a plurality of sensors linked to a computer and is driven by a high-power, wide-band transmitter. The second trend, in juxtaposition to this concept, is a multiplicity of special-purpose systems designed for small aircraft.

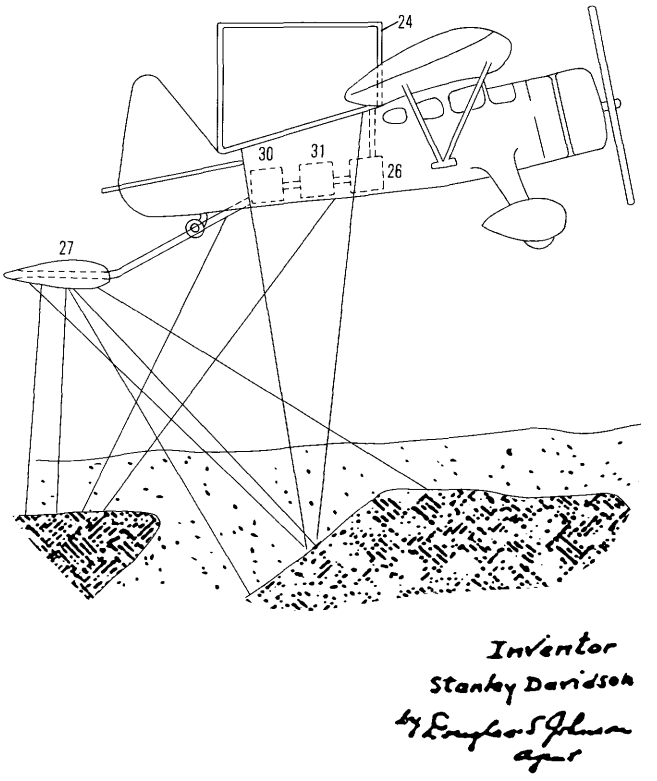

Figure 1. Synoptic diagram showing early AEM system. Transmitter coil (24) is powered by oscillator (26). Towed receiver coil (27) is connected to detector electronics (30, 31). Modified from Davidson (1953).

INTRODUCTION

The 40th anniversary of the filing date, February 13, 1948, of one of the earliest patent applications for a workable airborne electromagnetic (AEM) system for geophysical exploration (fig. 1) (Davidson 1953; Hanula and Longo, 1982, p. 141) is a good time to look again at the subject of AEM instrumentation and to update the record in this field of technology. It has been reviewed periodically (Pemberton, 1962; Ward, 1966, 1970; Becker, 1979), and recently by Collett (1986).

Developments in the methods and apparatus for AEM data acquisition have been intimately related to the mineral exploration industry, which in turn has been well rewarded for its investment in this technology. In fact, each new and successful technological development has resulted in the discovery of a number of economic mineral deposits (Paterson, 1961) that sooner or later were brought to the production stage. Perhaps the best example of this relationship can be seen by examining the record for the INPUT system, which over the last 25 years has led to the discovery of about 25 mines. Over the past decade, however, as advances in the area of AEM data acquisition and processing have been made, it has been shown that AEM can be effectively used in the

[1]Department of Material Science and Mineral Engineering, University of California, Berkeley, California 94720.

[2]Barringer Resources Incorporated, 15000 W. 6th Ave., Suite 300, Golden, Colorado 80401–5047.

[3]A-Cubed Incorporated, 5566 Tomken Road, Mississauga, Ontario L4W 1P4, Canada. Current address: Multiview GeoServices Incorporated, 5566 Tomken Road, Mississauga, Ontario L4W 1P4, Canada.

broader context of geological mapping (Palacky, 1986). Governments in many countries have been prompted to lend their support to AEM instrumentation development because good regional AEM maps not only provide a stimulus to mineral exploration but are also useful in the preparation of geological maps, in the search for water, and the mapping of environmental pollutants.

Continued demand for improvement in data quality has given rise to a new generation of digital AEM equipment, and the current phase of evolution in this area can be readily compared to the digital revolution that took place in the seismic industry 20 years ago. Because of the higher frequencies and bandwidths involved in AEM apparatus, this industry had to await arrival of high-resolution and high-speed digital modules that only became commonly available in the early 1970's. In general, progress has not been smooth; time intervals between major advances irregularly increased as demands for better performance encountered difficult and costly technical barriers. Compared to the original single-frequency equipment, the new apparatus allows data acquisition in a frequency band that spans many decades and yet preserves and even enhances the high signal-to-noise ratio observed with the classical narrow-band apparatus. Thus, we can now expect that the product of an AEM survey will be a geoelectrical section of the ground beneath the flight path rather than a simple indication of an electrical anomaly.

This trend is likely to continue into the future, where, subject to economic and political considerations, we can look forward to much progress in AEM instrumentation as advantage is taken of scientific and technological advances in the allied fields of electronics, signal processing, and data interpretation. Two directions can be envisaged and both will probably be followed. One will lead to the use of large aircraft equipped to carry a complete airborne geophysical laboratory containing broad-band, low-frequency, deep-penetrating AEM equipment and much ancillary equipment such as high-resolution gamma-ray spectrometers, magnetic gradiometers, and possibly even a gravity sensor. The other direction will probably lead to the development of low-cost, special-purpose AEM equipment that can be readily installed on a light fixed-wing aircraft or attached to a small helicopter.

To achieve the objective of reliable geological mapping in all environments, further advances in wide-band data acquisition technology will have to be made with particular emphasis on controlling and (or) monitoring of the flight system configuration. Finally, we note that invention is not always the child of necessity, as indicated by the relationship between AEM developments and the mineral exploration industry, but on occasion can serve as the parent as new uses for the apparatus are found in the solution of geological, hydrological, geotechnical, and environmental problems.

Acknowledgments.—We express public thanks to the many colleagues in the airborne survey industry who contributed to this article. Although the text is based on information believed to be accurate, we take full responsibility for any errors, omissions, or misrepresentations.

HISTORICAL PERSPECTIVE

The roots of successful airborne electromagnetic system development date back to the early 1950's when the International Nickel Company produced the world's first practical airborne EM system (Cartier and others, 1952). This apparatus, which was originally installed in a wooden aircraft to ease development problems, clearly proved the potential of the new exploration technique. Other developments of the 1950's included the Finnish two-frequency quadrature system (Puranen and others, 1960) that used a towed bird and provided compensation for the metal in the aircraft. It was operated in Canada by the Photographic Survey Corporation, a subsidiary of the Hunting Group. This system was quite effective but suffered from noise associated with conductive overburden. Another interesting development of the 1950's was the two-plane Swedish system that used a rotating field (Hedstrom and others, 1956) and employed two specially positioned lights to aid the pilots in maintaining a fairly constant relative aircraft position. It achieved a high degree of penetration, but data interpretation was quite difficult. Here, we must also mention the AEM system developed in the 1970's by V. Ronka of Geonics Limited for the Hudson Bay Mining Company that employed a flying winged bird. Although the system was used in Canada with some success for a number of years, no results were published.

Yet another system of the 1950's was the single-engined Otter system operated by Rio Tinto Mining Company (Snelling and Gribble, 1961). This apparatus employed wing-tip coplanar coils and measured the in-phase and quadrature components of the secondary field. It flew at very low altitudes in order to achieve useful penetration and adequate signal-to-noise ratios. It was eventually licensed to the Canadian Aeroservice Corporation and later to Geoterrex Limited. This type of apparatus was modified by Scintrex Limited and others to allow surveying at three frequencies simultaneously and renamed TRIDEM. It forms the basis of many integrated airborne geophysical installations (Bodger, this volume) now in service in many parts of the world.

Two very successful systems originally developed in the 1950's were the Aero/Newmont and the Texas Gulf Sulphur Incorporated helicopter machines (Pemberton,

1962). In the first of these, the EM system was directly attached fore and aft to the airframe of a Sikorsky S55 helicopter. A noise level of about 1 ppm was achieved in 1956. In the Texas Gulf Sulphur system designed by Varian Associates (Ruddock, 1963), coaxial transmitting and receiving coils were mounted on a separate 60-ft-long boom that when attached to a helicopter made it dangerously unstable. This equipment made the spectacular discovery of the Kidd Creek massive sulfide base metal deposit in Ontario that caused all records to be broken on the Toronto Stock Exchange and was followed by a celebrated chain of lawsuits. Unfortunately, the geophysicist operating this system was subsequently killed in the helicopter, and the equipment was never reactivated because of its operational risks.

The first wide-band time-domain AEM apparatus, the induced pulse transient (INPUT) system, was constructed at the end of the 1950's (Barringer, 1959) but flew initially with rather poor signal-to-noise ratios (Barringer, 1962). During the 1960's, the INPUT system underwent a series of major developmental changes culminating in the Mark V system in 1965. It initially went to Sweden, for LKAB, with introductions provided by the airborne geophysical pioneer, Hans Lundberg. Tests were carried out over the Kiruna iron ore deposit, the largest underground mine in the world, and an anomaly was discovered very close to this deposit. It was not drilled until it was noted, eight years later, that copper indicator flowers grew on the anomaly. This floral INPUT anomaly turned out to be a massive sulfide copper orebody that is still in production today. Shortly after this 1965 discovery, the discovery of South Bay Mines in Ontario by Selco paved the way for licensing of the INPUT system and its subsequent large-scale use.

Further improvements to the INPUT system in the 1970's by Questor Surveys Ltd (Lazenby and Wondergem, 1974, 1975) resulted in the Mark VI system with which most of the Canadian INPUT discoveries were made. This system recently was updated to incorporate a digital receiver (Lazenby and Becker, 1983, 1984). A similar development by Geoterrex and A-Cubed Incorporated resulted in the digital system GEOTEM (Thomson, 1987).

In parallel with this activity in the 1960's, a great deal of initial work was carried out on helicopter EM (HEM) systems in which both elements (transmitter and receiver) were contained in a towed bird that typically was 30 ft long (McLaughlin and others, 1961). Development work by Scintrex Limited, Dighem Surveys and Processing Incorporated, Aerodat Limited, Geotech Limited, Barringer Geoservices, Geonics Limited, and others goes on to this day. The main forte of the helicopter systems, before the current gold exploration boom, was their use in areas where the terrain was too rugged for fixed-wing equipment. During the 1970's, noise levels in the HEM systems were reduced to the 1 ppm level, and today's equipment operates at as many as four frequencies simultaneously using both the horizontal coplanar and vertical coaxial coil configurations.

At the same time, interest was growing in very low frequency (VLF) systems that depend upon government transmitting stations for their signals. Experiments using both electric and magnetic field components of VLF, LF and MF transmissions resulted in the E-PHASE and the RADIOPHASE systems (Barringer and McNeill, 1970). Today, building on the early Barringer Research experience acquired with these systems, many VLF data are gathered on a routine basis using the Herz TOTEM total magnetic field apparatus and on an experimental basis using the USGS five-component system.

Finally, development of digital EM began in the 1970's and continues to this day. At the end of the 1970's the INPUT system was upgraded to a digital format called COTRAN (correlation of transients), which differs substantially from INPUT in that it measures the transient EM signal inside the pulse as well as the signal that follows the pulse. Although such developments were also pursued by others and are reviewed in some detail in the next section, COTRAN is the only wide-band AEM system that records the entire secondary field for which fully developed operational status has been demonstrated (Collett and others, 1983).

PRESENT TRENDS

This decade has witnessed much technical and scientific advance in the methodology and apparatus for AEM surveys. Classical systems have been brought to their probable limits of performance, and radically new prototype systems have entered the experimental phase. Perhaps the most visible change is in the area of helicopter-borne equipment, which has been improved to allow for simultaneous measurements with both the coplanar and coaxial coil configurations at as many as four distinct frequencies in the 100 Hz-50 kHz range (Fraser, 1986). Hood (1985), in his annual instrumentation review, lists no fewer than five such modern HEM systems that are now available under commercial contract or for outright purchase.

Another significant development was the introduction of the "button-on" helicopter INPUT system by Questor Surveys (Becker and Lazenby, 1982). Although a Soviet attempt at this adaptation is on record, it appears to have been unsuccessful. Thus, the North American apparatus can rightly claim to be the world's first time-domain HEM machine that, as shown in figure 2, produces data that not only match fixed-wing results in quality but on occasion surpass them.

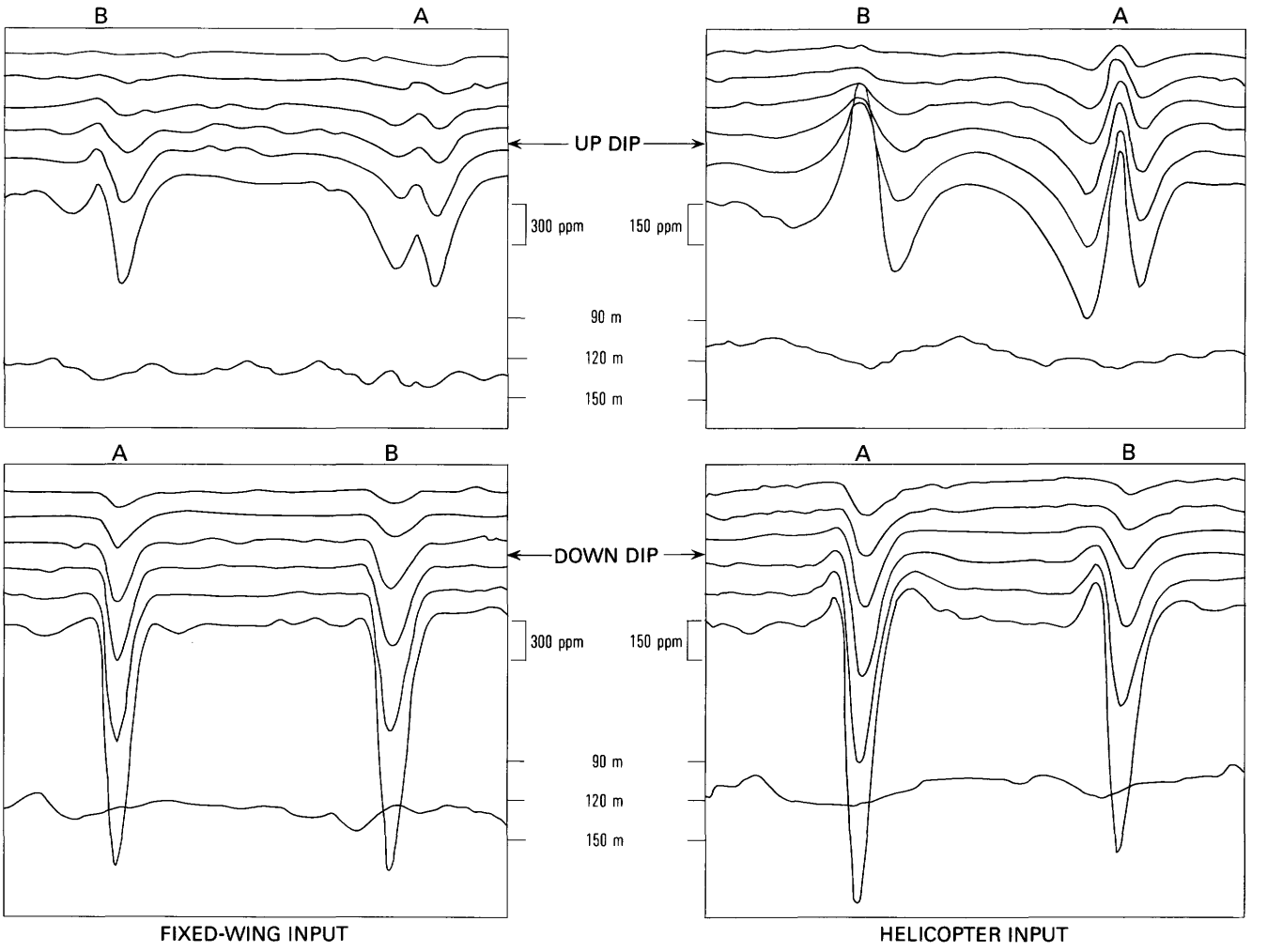

Figure 2. Helicopter and fixed-wing INPUT data over the Cavendish test range. A 2-ms primary pulse width is used for the helicopter system, a 1-ms pulse width for the fixed-wing equipment. A and B identify two conductive zones.

Similar progress has been made on frequency-domain fixed-wing installations that are now common in commercial and government service throughout the world. These are usually designed for a midsized aircraft similar to the DeHavilland Turbo Otter, use coplanar vertical coils on wing-tip mounts, and operate simultaneously at as many as three frequencies. This AEM equipment commonly forms the basis for an integrated geophysical system that includes one or more high-sensitivity magnetometers, a radiometric spectrometer, and ancillary navigation and digital data recording equipment (Peltoniemi, 1986; Bodger, this volume).

The new multicoil, multifrequency equipment, coupled with advances in digital data recording and improved postflight data processing, has resulted in superior data quality that in turn gives a practical meaning to AEM mapping so that this technique is no longer restricted to classical mineral prospecting applications. It can now profitably be used in the indirect search for mineral resources and for the solution of a number of problems in geological, geotechnical, and, to some extent, maritime engineering. Typical DIGHEM data for this type of system are illustrated in figure 3. They indicate the position of the Night Hawk test range deposit and overburden depth and resistivity.

The literature now abounds in examples of AEM resistivity maps related to a wide range of applications. In the last 10 years, if we count the papers presented in this publication, there are no less than 25 published accounts of HEM use for resistivity mapping (Palacky, 1986; Becker, 1988). Significantly 10 of these are related to indirect mineral exploration, 10 to geohydrological and geotechnical work, and the remainder to diverse uses in the search for geothermal resources and in coastal engineering studies. A typical HEM application (Paterson and Reford, 1986) is shown in figure 4, where there appears to be a close relation between the ground resistivity as mapped by HEM and the location of the ground-water supply.

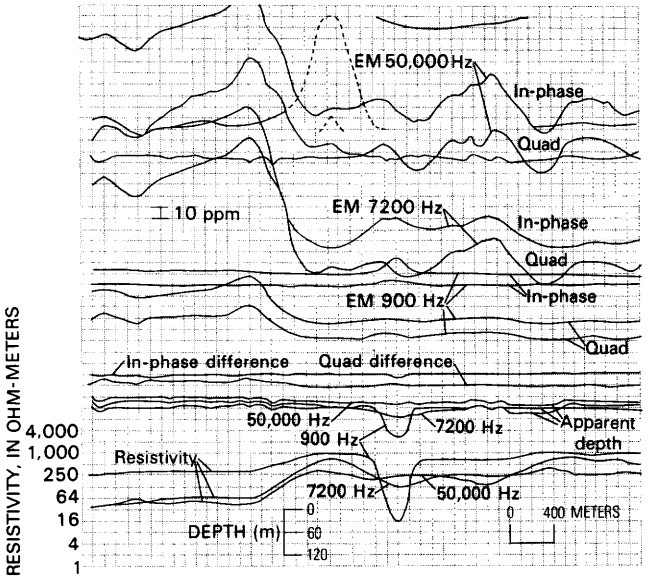

Figure 3. DIGHEM IV data over the Night Hawk test range. In the top half of the figure, EM channels are shown for horizontal coplanar coil pairs at three frequencies and for the vertical coaxial coil pair at 900 Hz. In the bottom half, difference channels, computed apparent depth, and resistivity are shown for all three frequencies. The Night Hawk conductor is indicated by the prominent resistivity anomaly at 900 Hz.

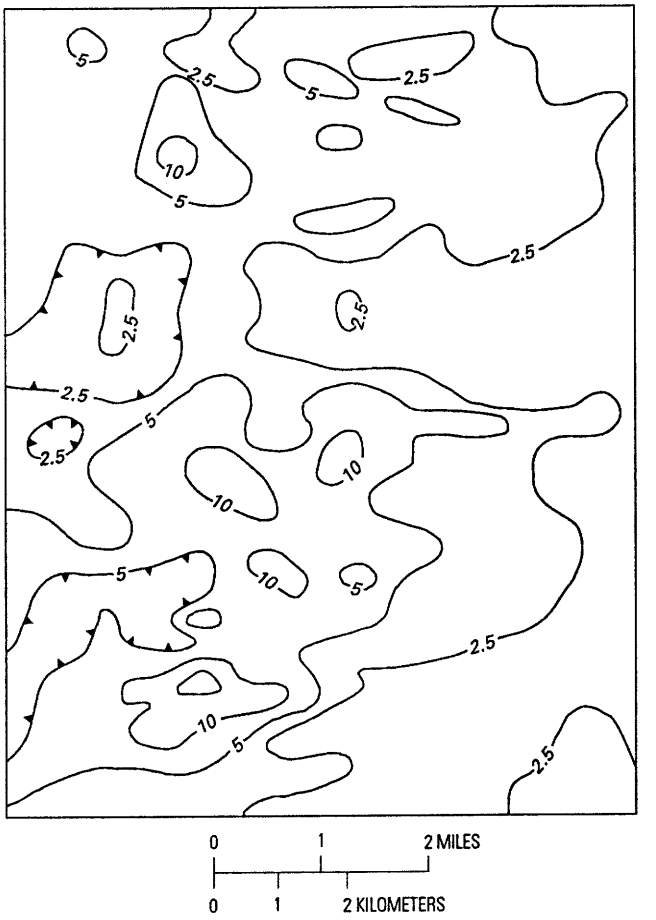

Figure 4. Ground-water survey, western United States, showing contours of conductance (in siemens) of aquifer layer derived from two-channel helicopter EM data.

Although most of airborne resistivity work is now done using frequency-domain HEM equipment, high-quality AEM resistivity maps may also be prepared using the time-domain INPUT system (Becker, 1988). In fact, the first such maps were based on INPUT data. The first qualitative INPUT AEM resistivity map was shown by L.S. Collett in 1963, some 25 years ago, and the first quantitative analysis of such data was presented some 10 years later (Dyck and others, 1974). Since then, at least eight other applications of INPUT to geological mapping, on most of the world's continents, are on record.

In parallel with the amelioration of HEM instrumentation, we have also seen much exciting development in time-domain, fixed-wing, towed-bird systems. Most of this was brought about by the onboard use of microprocessor-based equipment so that the now common digital data recording of an analog signal is enhanced by direct digital data acquisition and inflight processing of the sensor output. All development in this area was done with similar goals in mind. These include increasing the depth of penetration to conductive targets through augmented transmitter power and improved onboard data processing, increasing the operational availability of the system through improved atmospheric rejection capacity and improved compensation of the aircraft signal, and finally improving the ability of the system for high-resolution, deep-penetration airborne resistivity mapping.

Two distinct paths were taken to attain these desired goals. A simple approach (Lazenby and Becker, 1983, 1984; Thomson, 1987) centered on the replacement of the analog receiver in the classical INPUT system with a modern digital detector and the design of a new transmitter loop having spaced turns that lower the power lost in this element. These modifications were accompanied by the installation of a high-power transmitter. The half sine-pulse primary field was retained, but the transmitter loop dipole moment was increased to 4×10^5 A–m^2, or about double that of a conventional INPUT system. This was the path taken by Questor Surveys and Geoterrex, who, by 1985, had operational versions of a high-power digital system. One (Questor Surveys) was installed on a venerable DC–3 machine, whereas the other (Geoterrex GEOTEM) was mounted on a new CASA aircraft.

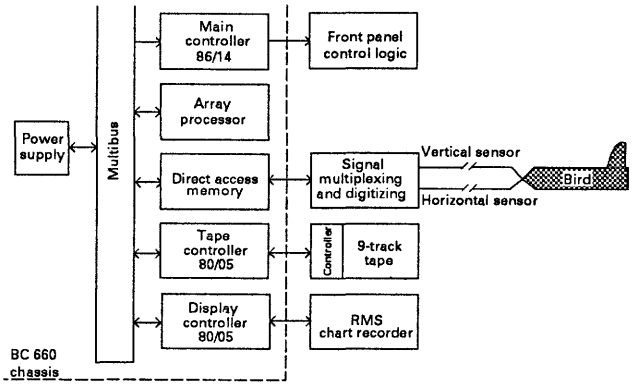

Figure 5. Synoptic diagram showing digital receiver for the INPUT system as designed by Questor Surveys Limited.

The digital receivers in both systems are quite similar; the Questor equipment is shown in figure 5. It serves the following functions:

1. Transmitter triggering.
2. Coherent sampling and a/d conversion of the receiver voltage.
3. Linear digital filtering.
4. Automatic compensation of system (and aircraft) transients.
5. Automatic rejection of atmospherics.
6. Digital recording of acquired data.
7. Inflight, real-time compilation of analog monitor records that confirm proper functioning.

In order to track the received signals, the digitizing module samples them at a rate compatible with an 8-kHz signal bandwidth and has sufficient dynamic range to cover the anticipated 120-db span of the received voltage. The overall subsystem consists of a number of microprocessors controlled by an 8614 unit and linked by a direct-access facility to a common memory. All real-time filtering, compensation, and spike rejection is done by the array processor. The data are then channeled to the 8005 controller units. One of these outputs the survey data to the tape drive, and the other controls the analog monitor data. The digital detector has two channels so that signals from a dual orthogonal coil system can be readily recorded.

The noise-reduction processes described above can be best appreciated with reference to some examples of flight data. Figure 6 shows one such example for a single channel output of the GEOTEM system where the progression is from the raw digital data recorded in flight shown in trace A to the final filtered product shown in the lowest trace labeled D. The principal feature of this illustration is the complete removal of atmospheric spikes without any loss of spatial resolution. This, as shown in trace B, could not be previously done using conventional analog equipment. Figure 7 shows the customary 12-channel presentation of GEOTEM data.

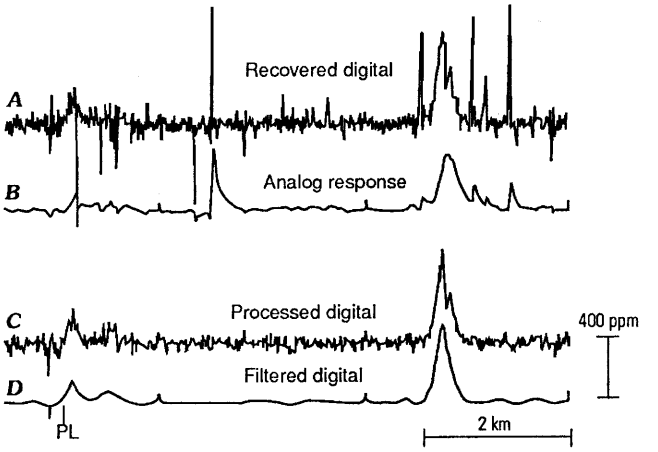

Figure 6. Comparison of analog and digital data for the GEOTEM system. PL denotes a powerline. See text for explanation.

In a similar vein, a 6-channel data set obtained over the Cavendish Test Range in Ontario using the Questor Surveys Limited digital system is shown in figure 8 and demonstrates the system's capacity to compensate for receiver bird motion. This capacity can be evaluated by comparing the upper and lower parts of the illustration; the removal of anomaly A, which is due to system instability, is virtually complete, whereas the small anomaly B observed on previous tests in the area is preserved intact. Finally, it should be noted that because all digital systems basically sample the sensor output every 25–50 μs, many tens of channel outputs can be made available for analysis. The number chosen for the final data presentation, six or twelve, is arbitrary but may be changed as circumstances warrant and may depend on the type of nonstationary multichannel noise-reduction techniques used.

A more ambitious approach to improvements in the state of the art in fixed-wing, towed-bird AEM surveying was initiated by Barringer Geoservices more than 10 years ago when the COTRAN (correlation of transients) system was conceived (Barringer, 1974). In this system, the digital receiver was used to implement

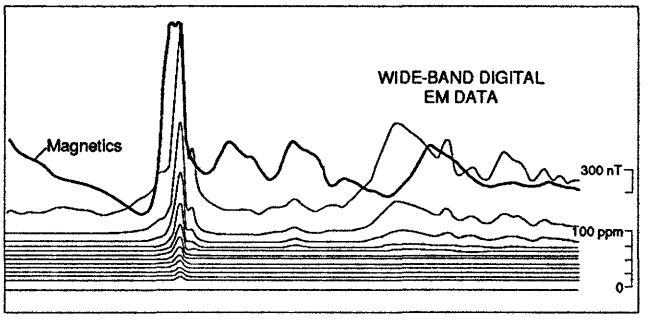

Figure 7. Typical 12-channel GEOTEM data over an anomalous conductor.

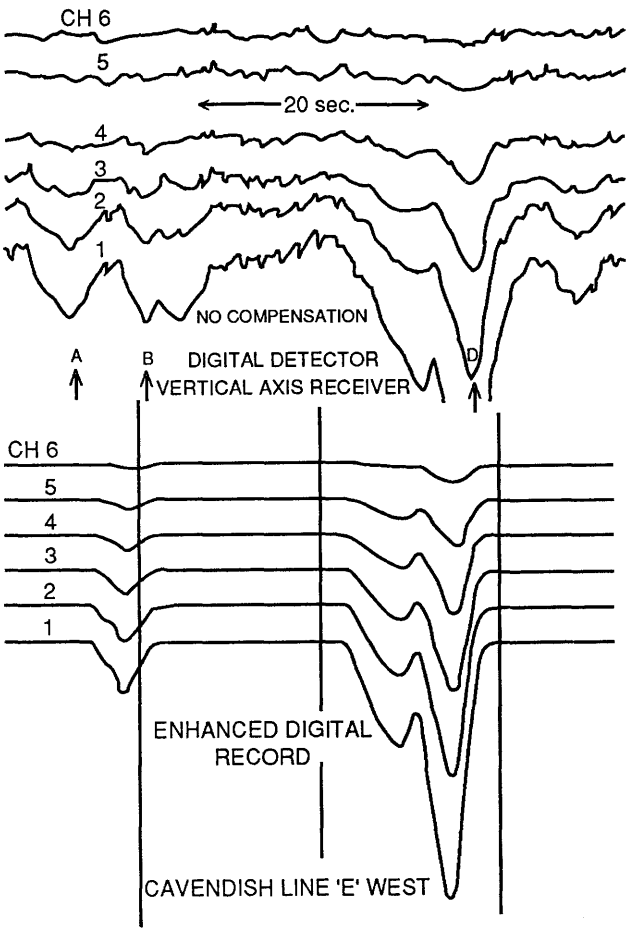

Figure 8. Digital compensation for the INPUT system. Bedrock conductors are located at B and D. Anomaly A is due to system instability and is completely removed.

two new concepts. The first of these is most radical. It was proposed that advantage can be fairly taken of the secondary field signal even during the on time of the primary signal pulse in spite of the relative motion between the sensor located in the bird and the transmitter attached to the aircraft. The COTRAN bird calls for the use of orthogonal receiving coils and a special low-noise design to minimize vibration. The large primary field variations in the observed signal, together with the substantial aircraft eddy current response, are removed by judicious use of the available onboard computing power as well as by postflight secondary processing. The second concept in the COTRAN system is related to flexibility in the transmitted primary field form, which can be varied with the bandwidth required for different applications. The transmitter typically operates at a very low fundamental frequency of 90 Hz—a desirable feature for work in conductive overburden environments. This system was completed in 1980 and was field tested with good results on a Canadian Government survey in the Lake Athabasca area (Collett and others, 1983). Figure 9 shows data acquired on that survey and illustrates the conventional presentation of COTRAN data where the observed signal is decomposed into a number of exponential decays having predetermined time constants. In this case, a continuous, modified square wave of 111-ms duration was used to generate the primary field, and the secondary field was decomposed into a series of exponential step responses whose time constants were preset at 30, 90, 270, 810, and 2,430 μs. One of the principal features of the system is that once the entire signal is recorded, the primary field is removed. Thus, the data may be presented in any form desired in addition to the standard format. One can also choose a conventional time-domain presentation or a multifrequency in-phase and quadrature presentation. Properly acquired and processed wide-band digital data contain much more information than any data acquired heretofore using either analog equipment or its digital equivalent. Figure 10 shows the results from a COTRAN survey of more recent vintage that was carried out in Wisconsin over the Crandon deposit. A standard half-sine INPUT transmitter was employed, and COTRAN algorithms were used to compute the ground response to the entire half-sine waveform. The results are presented in the form of INPUT-style time-domain profiles. The surficial response was removed by eliminating the shortest time constant COTRAN constituents from the data. The INPUT response was also determined by using a conventional digital-processing technique in which only the transient information following the pulse was employed. This allowed a direct and simultaneous comparison to be made between the performance of INPUT and COTRAN under identical conditions. The major improvement in quality obtained by COTRAN is very clear from the records, as is the greatly increased detectability of conductors at altitudes of as much as 1,000 ft above the normal survey clearance of 400 ft. Commercial implementation of the COTRAN system awaits the return of a higher demand for fixed-wing AEM surveys.

Two other research groups embarked, somewhat later, on the same path toward AEM improvements. One of these groups, sponsored by Royal Dutch Shell, developed a towed-bird system driven by a radically new transmitter that produces a continuous high-power primary field in the form of a pseudorandom binary sequence (PRBS). This concept was first used to develop a ground EM system (Duncan and others, 1980) and then was modified for airborne use with the collaboration of Kenting Earth Sciences (Zandee and others, 1985). Its main feature is the almost even distribution of energy throughout the transmitted frequency band, which may be readily altered. In the case of airborne systems, however, the noise distribution introduced by the towed bird is quite different from that seen in ground equipment, and additional strong noise components occur at the low audio frequencies. Presumably the SWEEPEM

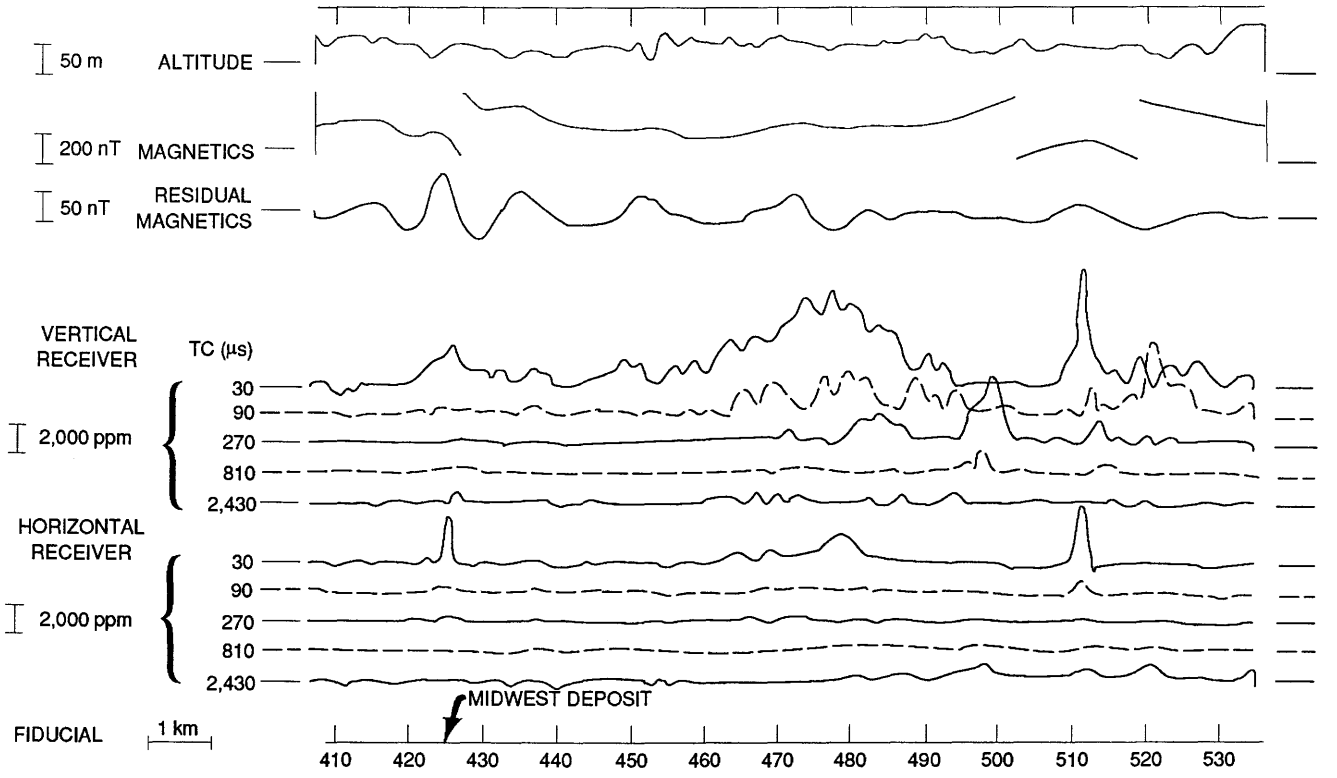

Figure 9. COTRAN field data acquired on a survey in the Athabasca region of Canada. A sharp, short (30 ms) time-constant (TC) response on the horizontal receiver can be clearly associated with the Midwest deposit.

transmitter can be biased toward these lower frequencies for airborne applications. The secondary field is extracted by using a process similar to that used for signal extraction in the VIBROSEIS system of seismic exploration. As in the seismic method, the detected signal is cross-correlated with the transmitter current, and the resulting function is subsequently transformed to obtain the desired multifrequency in-phase and quadrature records. Here again the effects of bird motion must be overcome. As shown in figure 11, this can be done rather successfully, and high data quality can be maintained. As further evidence of the usefulness of these new concepts, we examine digital INPUT results and the in-phase component for the SWEEPEM system output recorded over the Night Hawk test range in Ontario, Canada. Although these two data sets (fig. 12) are quite different, they compare favorably in target detection. To observe the differences inherent to fixed-wing and HEM systems, these results should be compared to those shown in figure 3 for the DIGHEM system.

Another full-wave digital system was developed by A-Cubed Incorporated (Annan, 1986). In this system, a square waveform is used for the transmitted signal so as to favor the low-frequency components of the secondary field, which are most affected by the bird-motion noise and natural magnetic field variations. In developing this system much effort was put into perfecting a smooth high-flying bird in order to improve data quality and facilitate its interpretation because all towed-bird systems require that the bird altitude be either known or properly estimated.

In summary then, it can easily be said that at this time we enjoy an unprecedented range of choices in AEM equipment selection and specification. An HEM survey can be done using a specified coil separation for either a coaxial or a coplanar configuration, or both, and at as many as four simultaneous distinct transmission frequencies, which lie in the audio range. For fixed-wing digital systems, the range of choice is equally broad. These systems differ principally in the spectrum of the transmitted primary field, but differences also exist in onboard and postflight data acquisition and processing methods. All of these processing methods are proprietary and confidential but have been proven capable of extracting a weak geological signal from overwhelming amounts of noise in order to produce useful data for the detection of conductors at subsurface depths of as much as 400 m. These data can also be interpreted to draw reasonably accurate ground-resistivity sections and maps. With the exception of the digital INPUT and the GEOTEM systems, the fixed-wing equipment that embodies the new data acquisition concepts is not available for commercial service because of present economic factors. Nonetheless, the technology for mobilizing such an apparatus has been successfully tested and can be implemented at very short notice.

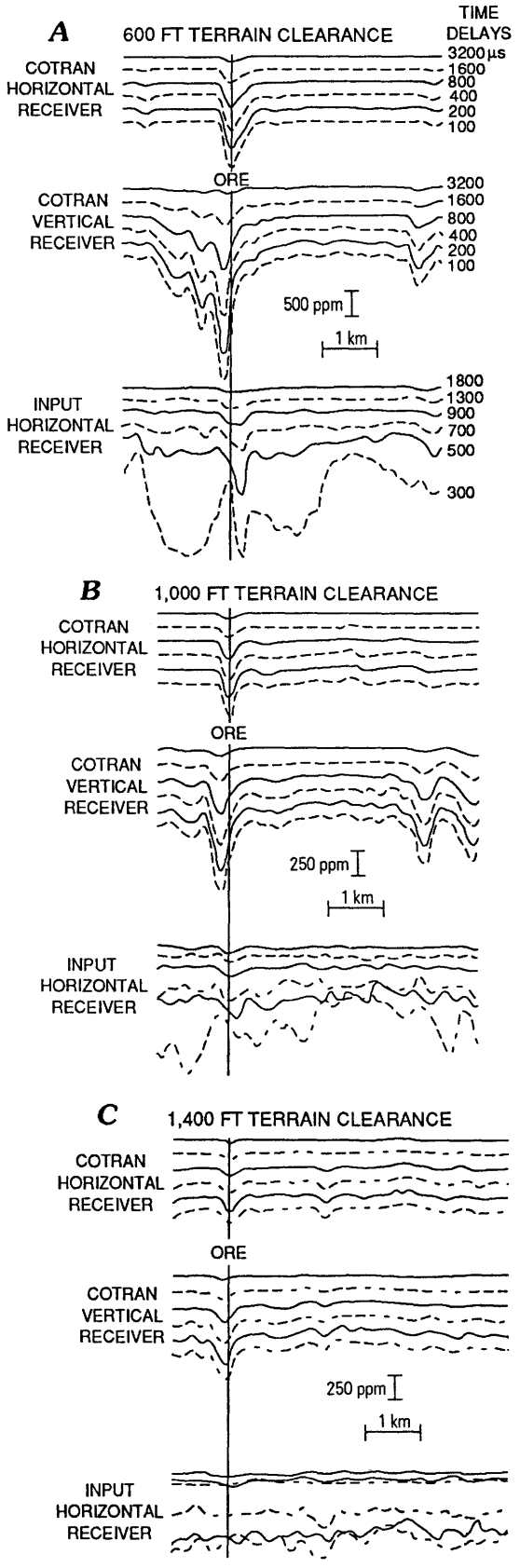

FUTURE OUTLOOK

To say the least, it is dangerous to anticipate the future. We can search in vain for the prediction of the invention of the transistor that led to the $3 digital watch and the $99 home computer. Nonetheless, we stand on fairly safe ground by forecasting a continuation of the trends that we are witnessing today and by drawing on some of the promising work done in the past, which, because of inadequate technology, has not yet been brought to fruition.

Thus, we can see that the use of digital equipment from the sensor onward will probably be accepted universally, and the diagnostic capability of this type of receiver will lead to systematic improvements in system performance. Proper calibration and zero-drift corrections will no longer be a problem. These developments will, in turn, lead to improvements in the quality of airborne resistivity maps and profiles and their universal acceptance for use in a variety of geological problems. As data quality continues to improve, the algorithms used for automated data interpretation will become more sophisticated so that the final product will more closely resemble a geological map.

We can also expect to see a wider acceptance of passive AEM systems such as VLF. Here, too, improvements in equipment and in data acquisition and interpretation methodology will keep pace with other sectors of the industry. The ongoing development in the use of powerline fields for geological mapping in populated areas (Labson, this volume) is a step in this direction. In a similar vein, we will probably see the rebirth of audio frequency magnetics (AFMAG). This airborne and ground method, based on the detection of natural magnetic fluctuations and atmospheric activity, showed excellent promise at its inception some 30 years ago but must wait until proper equipment for the detection and processing of the weak signals is developed. The technology for producing reliable and accurate data for this method is now available and will surely be taken advantage of shortly.

Turning to other matters, it is now relatively easy to envisage generic equipment that may be selected for the task at hand. Two distinct trends will probably emerge. First, large, wide-band, multisystem, slow-flying laboratories will combine a plurality of sensors feeding a VLSI computer and a high-power (30–50 kW), wide-band transmitter with a sophisticated high-sensitivity magnetometer installation and possibly an airborne gravimeter

Figure 10. Comparison of COTRAN and INPUT results over Crandon orebody. COTRAN data are derived from digital signals acquired both during and after transmitted pulse. INPUT data use only information recorded after pulse during transient decay.

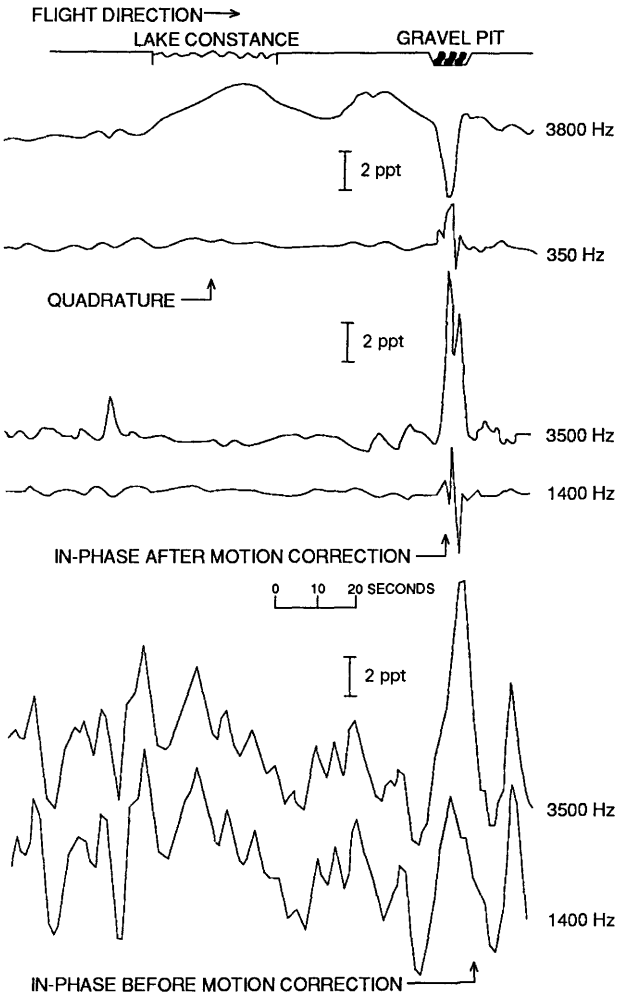

Figure 11. Cancellation of bird-motion effects for the SWEEPEM system, Lake Constance, Ontario.

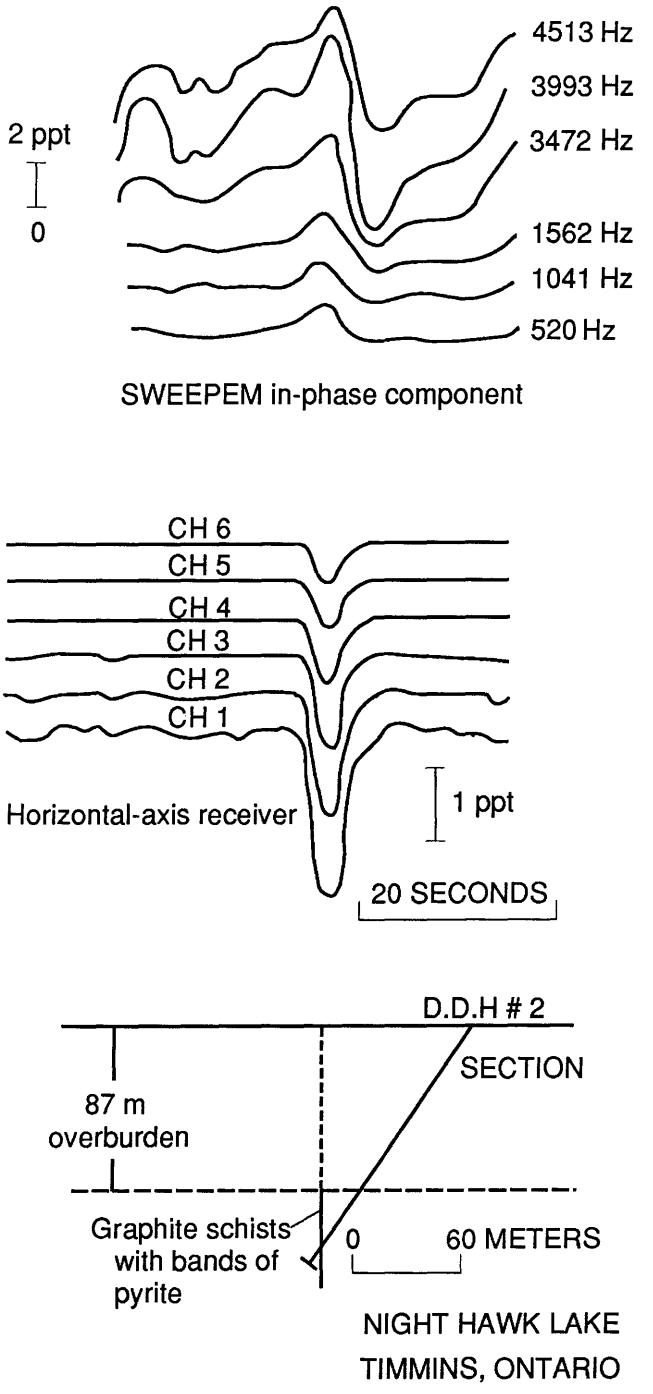

Figure 12. Comparison of multifrequency SWEEPEM data and digital INPUT results over the Night Hawk deposit. Both data sets were acquired at an altitude of about 100 m above ground level.

to gather geological data in areas of very heavy cover with depths to bedrock of the order of 1 km. It is not inconceivable that this equipment will be carried on an airship as the availability of these survey platforms increases. The new high-temperature superconducting materials may also play a role here. Although an ingenious low-frequency superconducting system was built more than 10 years ago (Morrison and others, 1976), the technical difficulties and the high cost of working at liquid-helium temperatures rendered that venture uneconomical at the time.

The other trend that will surely develop is diametrically opposite to the one described above. Modular digital data acquisition design based on a plurality of linked, but separate, dedicated-task microprocessors will result in a multiplicity of special-purpose systems designed to be readily attached to and carried aboard a small aircraft. These systems will be energized by special-purpose transmitters whose waveform and base frequency may be optimized to suit the purpose at hand. The savings in survey costs that can be made in this direction will be so large that it will certainly be pursued. One example of the direction that may be taken was given some 15 years ago by one of the authors (Becker and Sinha, 1972), who demonstrated, with the use of prototype laboratory equipment, that a system whose frequency of operation can be automatically varied in

concert with the overburden resistivity will not only produce a constant-depth resistivity map simply by recording the frequency of operation but will also exhibit a constant sensitivity to a given bedrock target independently of the electrical properties of its geological environment.

REFERENCES CITED

Annan, A.P., 1986, Development of the PROSPECT I airborne electromagnetic system, *in* Palacky, G.J., ed., Airborne resistivity mapping: Geological Survey of Canada Paper 86–22, p. 63–70.

Barringer, A.R., 1959, UK Patent 883465, U.S. Patent 3020471. Application filed February 6, 1962.

_____ 1962, New approach to exploration; the INPUT airborne electrical pulse prospecting system: Mining Congress Journal, v. 48, p. 49–52.

_____ 1974, U.S. Patent 3,852,659, Geophysical prospecting method and apparatus utilizing correlation of received waveforms with stored reference waveforms. Application filed April 9, 1973.

Barringer, A.R., and McNeill, J.D., 1970, The airborne RADIOPHASE system [abs.]: Annual Meeting, 72nd, Toronto, Canada, Program.

Becker, A., 1979, Airborne electromagnetic methods, *in* Hood, P.J., ed., Geophysics and geochemistry in the search for metallic ores: Geological Survey of Canada Economic Geology Report 31, p. 33–43.

_____ 1988, Airborne resistivity mapping: Institute of Electrical and Electronic Engineers, Transactions on Antennas and Propagation, v. 36, no. 4, p. 557–562.

Becker, A., and Lazenby, P.G., 1982, Helicopter INPUT; a new exploration tool [abs.]: European Association of Exploration Geophysicists Annual Meeting, 44th, Cannes, France, Program.

Becker, A., and Sinha, A.K., 1972, A proposal for a new method of AEM mapping [abs.]: Society of Exploration Geophysicists Annual Meeting, 42nd, Anaheim, Calif., Program.

Cartier, W. Wo., McLaughlin, G.H., Robinson, A., and Wise, E.M., 1952, U.S. Patent 2,623,924, System of airborne conductor measurements. Application filed August 11, 1950.

Collett, L.S., 1986, Development of the airborne electromagnetic technique, *in* Palacky, G.J., ed., Airborne resistivity mapping: Geological Survey of Canada Paper 86–22, p. 9–18.

Collett, L.S., Barringer, A.R., and Loveless, A.J., 1983, COTRAN electromagnetic survey of the NEA/1AEA Athabasca test area, *in* Cameron, E.M., ed., Uranium exploration in Athabasca Basin, Saskatchewan, Canada: Geological Survey of Canada Paper 82–11, p. 179–190.

Davidson, S., 1953, U.S. Patent 2,652,530, Electromagnetic induction method and apparatus for locating subterranean electrically conductive bodies. Application filed February 13, 1948.

Duncan, P.M., Hwang, A., Edwards, R.N., Bailey, R.C., and Garland, G.D., 1980, The development and applications of a wide band electromagnetic sounding system using a pseudonoise source: Geophysics v. 45, no. 8, p. 1276–1296.

Dyck, A.V., Becker, A., and Collett, L.S., 1974, Surficial conductivity mapping with the airborne INPUT system: Canadian Institute of Mining and Metallurgy Bulletin, v. 67 (744), p. 104–109.

Fraser, D.C., 1986, Dighem resistivity techniques in airborne electromagnetic mapping, *in* Palacky, G.J., ed., Airborne resistivity mapping: Geological Survey of Canada Paper 86–22, p. 49–54.

Hanula, M.R., and Longo, R.M., eds., 1982, The discoverers—A 50-year history of the Prospectors and Developers Association, some famous prospectors and their discoveries: Toronto, Pitt Publishing, 317 p.

Hedstrom, Erik H.L., and Tegholm, R.V., 1956, Canadian Patent 528,643, Electromagnetic induction method and apparatus for prospecting. Application filed February 3, 1955.

Hood, P., 1985, Mineral exploration—Trends and developments in 1984: Canadian Mining Journal, v. 106, no. 1 p. 14–41.

Lazenby, P.G., and Becker, A., 1983, Redefinition of the INPUT system—Part A–Instrumentation (Grant 003), *in* Pye, E.G., and Barlow, R.B., eds., Exploration technology development program of the Board of Industrial Leadership and Development, summary of research 1981–1983: Ontario Geological Survey Miscellaneous Paper 115, p. 1–9.

_____ 1984, Redefinition of the INPUT system—Part B–Signal processing and field results (Grant 003), *in* Milne, V.G., and Barlow, R.B., eds., Exploration technology development program of the Board of Industrial Leadership and Development, summary of research 1983–1984: Ontario Geological Survey Miscellaneous Paper 120, p. 5–16.

Lazenby, P.G., and Wondergem, H.M., 1974, Canadian Patent 941015, Apparatus for the remote detection of conducting bodies. U.S. Application filed February 12, 1971.

_____ 1975, Canadian Patent 970,471, Apparatus for analyzing transients in a periodic sequence of signals. U.S. Application filed February 26, 1973.

McLaughlin, G.H., Harvey, H.A., Cartier, W.O., and Robinson, W.A., 1961, U.S. Patent 3,015,060, Method and means of prospecting for electrically conducting bodies. Application filed October 15, 1954.

Morrison, H.F., Dolan, W., and Dey, A., 1976, Earth conductivity determinations employing a single superconducting coil: Geophysics, v. 41, p. 1184–1206.

Palacky, G.J., ed., 1986, Airborne resistivity mapping: Geological Survey of Canada Paper 86–22, 195 p.

Paterson, N.R., 1961, Experimental and field data for dual-frequency phase-shift method of airborne electromagnetic prospecting: Geophysics, v. 26, p. 601–617.

Paterson, N.R., and Reford, W.W., 1986, Inversion of airborne electromagnetic data for overburden mapping and groundwater exploration, *in* Palacky, G.J., ed., Airborne resistivity mapping: Geological Survey of Canada Paper 86–22, p. 39–48.

Peltoniemi, M., 1986, Systematic airborne electromagnetic surveys in Finland; an overview, *in* Palacky, G.J., ed., Airborne resistivity mapping: Geological Survey of Canada Paper 86–22, p. 159–168.

Pemberton, R.H., 1962, Airborne electromagnetics in review: Geophysics, v. 27, p. 691–713.

Puranen, M., Kahma, A.A., Ronka, V., 1960, U.S. Patent 2,929,984, Method and apparatus for qualitative electromagnetic surveying. Application filed January 12, 1956.

Ruddock, K.A., 1963, U.S. Patent 3,108,220, Electromagnetic method and apparatus for geophysical prospecting including means for generating an auxiliary flux field to cancel direct coupling between the primary and pick-up coils. Application filed March 3, 1956.

Snelling, E.C., and Gribble, P.D., 1961, U.S. Patent 2,995,699, Geophysical survey apparatus. Application filed August 5, 1955.

Thomson, S., 1987, A new transient EM system—GEOTEM [abs.]: Exploration '87—The Decennial International Conference on Geophysical and Geochemical Exploration for Minerals and Groundwater, September 27–October 1, 1987, Toronto, Program.

Ward, S.H., 1966, The electromagnetic method, *in* Mining geophysics II: Society of Exploration Geophysicists, p. 224–372.

_____ 1970, Airborne electromagnetic methods, *in* Morley, L.W., ed., Mining and groundwater geophysics/1967: Geological Survey of Canada Economic Geology Report 26, p. 81–108.

Zandee, A.P., Best, M.E., and Bremner, T.G.T., 1985, SWEEPEM, a new airborne electromagnetic system [abs.]: Society of Exploration Geophysicists Annual Meeting, 55th, Washington, D.C., p. 236–239.

SECTION 2: INTERPRETATION AND MODELING

Synthetic Modeling and Airborne Electromagnetic Interpretation[1]

By Melvyn E. Best[2]

Abstract

Advances in electromagnetic hardware and computer technology have led to higher quality airborne electromagnetic data. Digital recording has increased the range of options for processing and editing so that data available for interpretation have better signal-to-noise ratios. Digital data of this quality can be used in automated interpretation schemes. In this paper, the concept of *synthetic* modeling is introduced, and data for a synthetic model of shield geology in Canada for the SWEEPEM and TRIDEM airborne systems are generated. Electrical parameters for this data set are computed using a resistivity inversion algorithm for a one-layer overburden earth model. These parameters are compared with those from the synthetic model to investigate the influence of factors such as frequency bandwidth, coil configurations, phase components, and time windows.

INTRODUCTION

In the early days of airborne electromagnetic (AEM) surveys, interpretation consisted of eyeballing anomalous features on analog profiles and plotting these on flight path recovery maps. Geological and geophysical empirical rules of thumb were developed to prioritize the multitude of anomalies found. These subjective methods were successfully used to find a significant number of massive sulfide orebodies in Canada and northern Europe. Pemberton (1962), Paterson (1967), Best (1985), and the references therein provide a review of early AEM systems and interpretation schemes.

From 1960 to the mid-1970's, AEM hardware became more versatile. Shorter signal averaging times, multifrequency transmitters and receivers, time-domain systems, and multicoil configurations were developed (Barringer, 1962; Fraser, 1972; Stemp, 1972). These hardware advances brought about the need for better interpretation methods. Nomograms for free-space dikes and spheres, as well as for multilayer earth models, were developed using analytic and analog modeling (Grant and West, 1965; Keller and Frischknecht, 1966). Time-domain modeling of free-space dikes (Palacky, 1976) provided type curves for the INPUT system. Screening and classifying the large number of anomalies found in a typical survey were still mostly empirical, although more rigorous rules of thumb were being developed.

During the 1970's, two- and three-dimensional numerical modeling programs were developed (Ward and others, 1973; Hohmann, 1975; Lee and others, 1981; Best and others, 1985). Results from numerical modeling, along with field investigations, showed that current channeling and gathering (Spies and Parker, 1983) in conductive terrains could explain the discrepancies between free-space interpretation and the actual geoelectric section obtained from drilling.

In this period, airborne resistivity mapping for surficial geology, bedrock geology in tropical environments, and ground water became more common. Indeed, resistivity mapping began to play an important role in traditional massive sulfide exploration. The resistivity of the near surface was providing an effective method for screening anomalies not associated with bedrock conductors (Fraser, 1978, 1979).

Several new AEM systems have been proposed or developed recently (Barringer, 1976; Zandee and others, 1985; Annan, 1986). These systems use time-domain transmitter pulses and wide-band receivers. Several of them use correlation methods to increase the signal-to-noise ratio. Digital signal processing methods are commonly applied to enhance and extract the earth's response from the signal. The digital data provide interesting opportunities for interpretation. Digital signals can be transformed from time to frequency and vice versa if the bandwidth is sufficiently broad and the digitization interval sufficiently small. Hence, interpretation and display can be carried out in the frequency domain or the time domain, depending on the interpreter's preference and the geological situation.

---

[1]Geological Survey of Canada Contribution 33087.

[2]Geological Survey of Canada, P.O. Box 1006, Dartmouth, Nova Scotia B2Y 4A2, Canada.

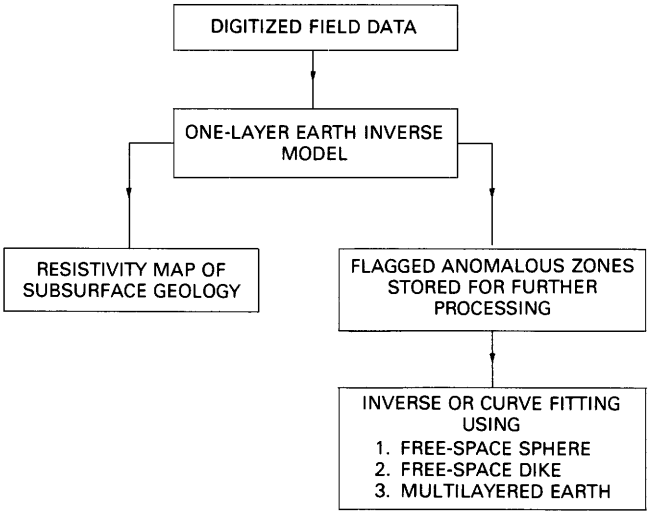

Figure 1. Typical interpretation scheme.

In this paper, interpretation methods utilizing digital data are explored. In particular, a simple approach using nonlinear inversion (Marquardt, 1963; Anderson, 1977) is discussed. Extensions to this method are presented, along with comments on AEM interpretation in the future.

Acknowledgments.—I thank Drs. P.M. Duncan and R.J. Bottomley for their help with the inverse modeling.

INTERPRETATION SCHEME

Figure 1 shows an interpretation scheme for digital AEM data. The input data must be edited and perhaps smoothed (filtered) before commencing interpretation. The objective of the interpretation is to generate a geoelectric model of the earth from the measured data. Depending on the geological situation, the data are fitted to a homogeneous earth or a multilayer earth model by direct comparison to forward solutions (type curves), by parameter estimation from nomograms, or by inversion schemes. Computer accessibility, storage, and costs determine which approach is best. In this paper, frequency-domain data are used to demonstrate an inversion method for a one-layer overburden model. The inversion method uses the Marquardt nonlinear ridge regression inversion algorithm in conjunction with a forward overburden model (Marquardt, 1963; Anderson, 1977).

The best fit at each fiducial provides estimates of the resistivity of the overburden layer and the half-space below and an estimate of the overburden thickness. Profiles and maps can be made for detailed interpretation. In addition, the inversion parameters can flag areas where the overburden model does not fit. These can be sorted in a file for plotting and further interpretation, which could, for example, consist of two- or three-dimensional conductivity modeling.

Table 1. Layering parameters for the geological model shown in figure 2

[The second layer does not exist for fiducials 1000-1083]

Fiducial	Altitude (m)	h (m)	ρ_{OB} (ohm-m)	ρ_E (ohm-m)	d (m)	ρ_2 (ohm-m)
1000	138.8	0	0	2,000		
1004	123.8	0	0	2,000		
1008	131.3	0	0	2,000		
1012	139.5	0	0	2,000		
1016	142.5	0	0	2,000		
1020	139.5	36.0	25.0	350		
1024	152.0	34.0	25.0	350		
1028	165.0	38.0	25.0	350		
1032	161.0	46.0	25.0	350		
1036	135.0	64.0	25.0	350		
1040	123.0	78.0	25.0	350		
1044	123.0	84.0	25.0	350		
1048	117.0	84.0	25.0	350		
1052	123.0	75.0	25.0	350		
1056	129.0	21.0	25.0	350		
1060	114.0	0	0	2,000		
1064	99.0	0	0	2,000		
1068	107.0	0	0	2,000		
1072	113.0	0	0	2,000		
1076	113.0	0	0	2,000		
1080	113.0	0	0	2,000		
1084	114.0	0.1	200	2,000	2.9	200
1088	123.0	0.1	200	2,000	24.0	200
1092	129.0	10.5	10	2,000	27.0	200
1096	129.0	0.1	200	2,000	33.0	200
1100	130.5	0.1	200	2,000	0.1	200

A major objective of an AEM survey is to generate resistivity maps of the subsurface and to screen geologically unfavorable areas from favorable ones. Simple, easy to understand models are needed for the screening and prioritizing steps. More complex modeling can be used for detailed interpretation of the geological areas of interest.

In order to demonstrate these concepts, *synthetic* data were generated for two AEM systems. The systems have different transmitter configurations, coil orientations and separations, and numbers of frequencies but cover a similar frequency bandwidth.

THE GEOLOGICAL MODEL

The geological section shown in figure 2 was used to calculate the synthetic data for testing. Topographic and altitude variations were included to make it realistic. A finite dike (strike length 500 m) and a sphere (radius 100 m) were embedded in an outcropping resistive host rock (2,000 ohm-m). The effects of a variable thickness overburden (25 ohm-m) and a highly conductive overburden were included. The model is two-dimensional except for the three-dimensional dike and sphere located symmetrically about the plane of the section. Table 1 lists

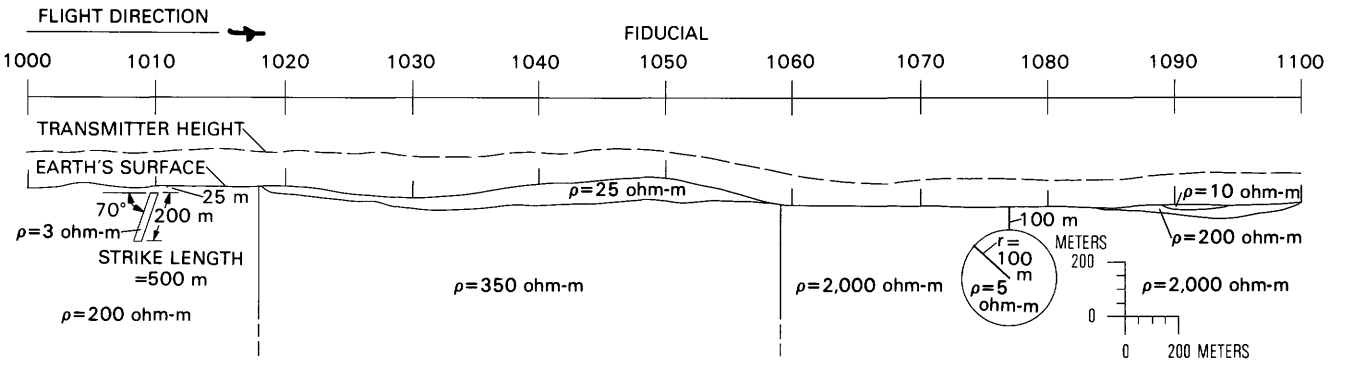

Figure 2. Geological model used to calculate the synthetic data for testing.

the resistivities and layer thicknesses for the model at every fourth fiducial.

In order to generate synthetic data for an AEM system, several assumptions, similar to those of Sinha (1973), were required.

1. The EM response was computed assuming that the earth directly below the midpoint of the AEM system was layered with conductivity and thickness values equal to those at the fiducial (fig. 3). This approximation was used for generating the EM response for a homogeneous earth, a one-layer overburden earth, and a two-layer overburden earth. Because the elevation and topographic changes are gentle, this approximation is quite reasonable except at sharp conductivity boundaries (for example, near fiducials 1019, 1059, 1090, and 1094).

2. The EM responses of the sphere and dike were computed from free-space forward models and added to the homogeneous earth response fiducial by fiducial. The relatively high resistivity of the earth (2,000 ohm-m) is a reasonable approximation to free space, especially at lower frequencies. The 350-ohm-m overburden is distant from the sphere and the dike and therefore does not influence their responses.

3. There were no variations in the transmitter-receiver separation. Variations for the elevation of the transmitter for the SWEEPEM system are given in figure 2 and table 1, whereas the elevation of the TRIDEM transmitter was fixed 60 m above the topography. Under these assumptions, the synthetic data generated for the geological model are not exact. The effects of curved surfaces and sharp vertical conductivity boundaries are not included, and the sphere and dike responses should be computed from numerical three-dimensional modeling. Even using these assumptions, differences between the synthetic data and the actual data for the geological example in figure 2 should be small.

AEM SYSTEMS

Synthetic normalized secondary magnetic field data for the SWEEPEM and TRIDEM AEM systems were generated for the geological model. Figure 4 shows the geometrical configurations of the two systems.

The SWEEPEM system (Best and Bremner, 1985; Zandee and others, 1985) consists of a large horizontal loop (vertical dipole) mounted on a fixed-wing aircraft from which two receivers are towed in a bird. A pseudorandom binary sequence generates the current waveform in the transmitter, and the received signals are cross-correlated with a replica of the transmitted current to produce the earth response. The responses can be generated in time or frequency. For this study, frequencies of 150, 300, 450, 600, 750, 900, 1050, 2100, 3150, 4200, 5250, 6300, and 7350 Hz were considered.

The synthetic in-phase and quadrature responses were computed at each frequency for each fiducial in figure 2; thus, there are 52 data points (13 times 2 components times 2 receiver directions) for each fiducial. Figure 5 shows an example of the in-phase and quadrature responses for the vertical component of the magnetic field at frequencies of 300, 1050, 3150, and 6300 Hz.

The coaxial configuration of the TRIDEM system (Seigel and Pitcher, 1978; Stemp, 1980) consists of a horizontal-dipole transmitter mounted on the nose of the aircraft and a receiver (horizontal component) mounted at the rear. The transmitter simultaneously generates frequencies of 500, 2000, and 8000 Hz, which are detected at the receiver and displayed as in-phase and quadrature responses. The synthetic in-phase and quadrature components were computed at each frequency and each fiducial for the section in figure 2. The transmitter altitude was constant at 60 m above the ground. The 6 data points (3 frequencies times 2 components) for each fiducial are displayed as in-phase and quadrature profiles in figure 6.

EXAMPLES

Examples of resistivity inversion of the synthetic data using the Marquardt algorithm are presented in this section. The discussion focuses on concepts rather than

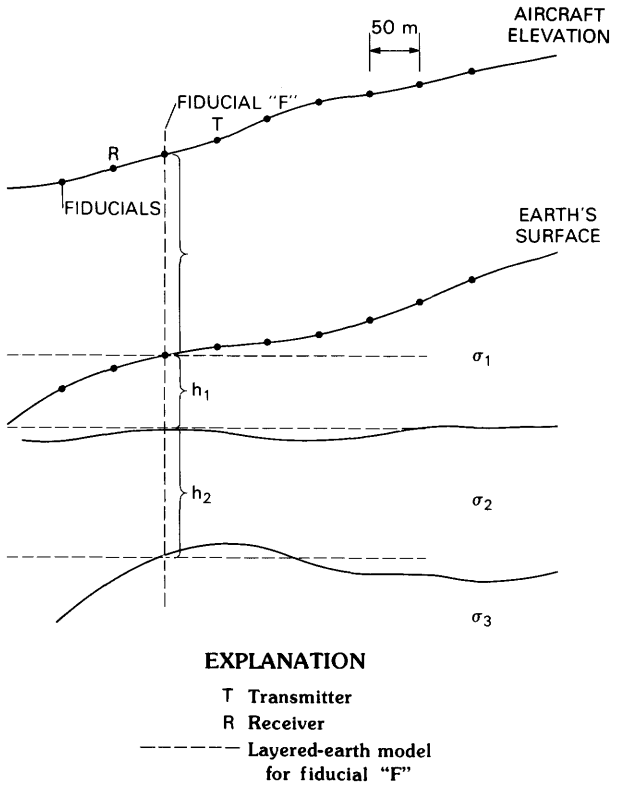

Figure 3. Synthetic modeling assumptions for the layering.

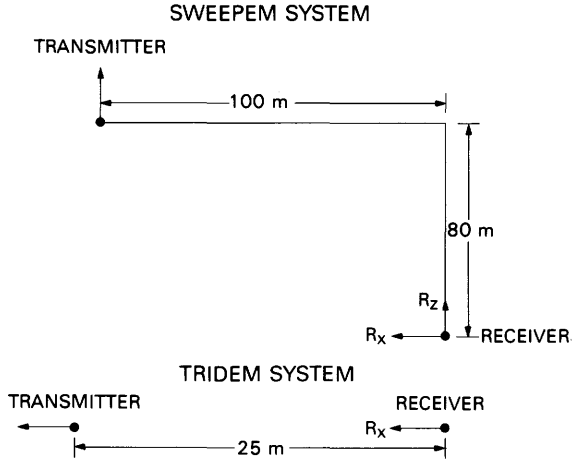

Figure 4. Geometric configurations of the SWEEPEM and TRIDEM AEM systems.

specifics related to the algorithm. Discrepancies between the inversion parameters and the geological model should be expected because of the modeling assumptions discussed earlier.

The data were fit to a one-layer overburden model using the Marquardt algorithm. The best-fit parameters were computed for the one-layer model. Anomalous zones where the fit was poor were flagged. The data associated with the sphere, dike, and surficial conductor

Table 2. SWEEPEM system parameters used for inversion tests
[Magnetic field: B_x, horizontal component; B_z, vertical component; R, real; Q, quadrature; Y, yes; N, no]

Case	Frequency (hertz)	B_x R	B_x Q	B_z R	B_z Q	Fiducials
1	All	Y	Y	Y	Y	All
2	300, 1050, 3150, 6300	Y	Y	Y	Y	Binated[1]
3	All	N	Y	N	Y	Binated[1]
4	All	N	N	Y	Y	Binated[1]

[1]Binated means every second fiducial.

Table 3. Some parameters for the inversion algorithm
[ρ_{OB} and ρ_E are overburden and earth resistivity (in ohm-meters), respectively; h is overburden thickness (in meters)]

A. Minimum and maximum parameter bounds				
	SWEEPEM		TRIDEM	
	Minimum bound	Maximum bound	Minimum bound	Maximum bound
ρ_{OB}	2	1,000	5	188.7
ρ_E	10	10,000	208.3	4,000
h	0.4	400	0.2	200

B. Initial parameter guesses				
	SWEEPEM		TRIDEM	
	Fiducial 1000	Fiducial 1019	Fiducial 1000	Fiducial 1019
ρ_{OB}	300	100	333.3	50
ρ_E	1,000	1,000	1,000	1,000
h	5	25	0.2	25

C. Maximum number of iterations before inversion was stopped		
	SWEEPEM	TRIDEM
Maximum number of iterations	4	5

are quite different from the one-layer model and should appear as flagged anomalous zones. The abrupt changes in the vertical conductivity near fiducials 1019 and 1059 should also appear as flagged zones.

The forward overburden modeling was computed by the fast Hankel transform method of Anderson (1979) with the kernel written in a compact form to reduce computational time. This was coupled to the Marquardt inversion program to form the overburden inverse model.

SWEEPEM

Table 2 lists the four SWEEPEM data sets created for computing resistivity profiles. Case 1 is the complete data set generated for the geological model in figure 2 (52 points per fiducial). Case 2 uses a subset of four frequencies (16 data points per fiducial). Case 3 considers the quadrature component at all frequencies for

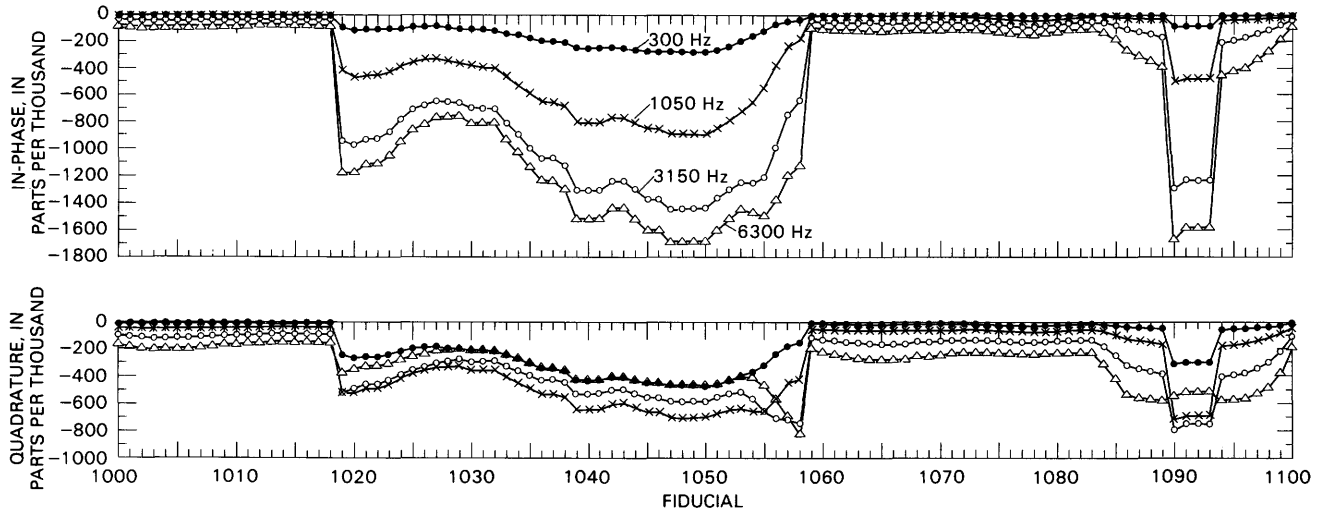

Figure 5. Synthetic in-phase and quadrature SWEEPEM data for the vertical component at 300, 1050, 3150, and 6300 Hz.

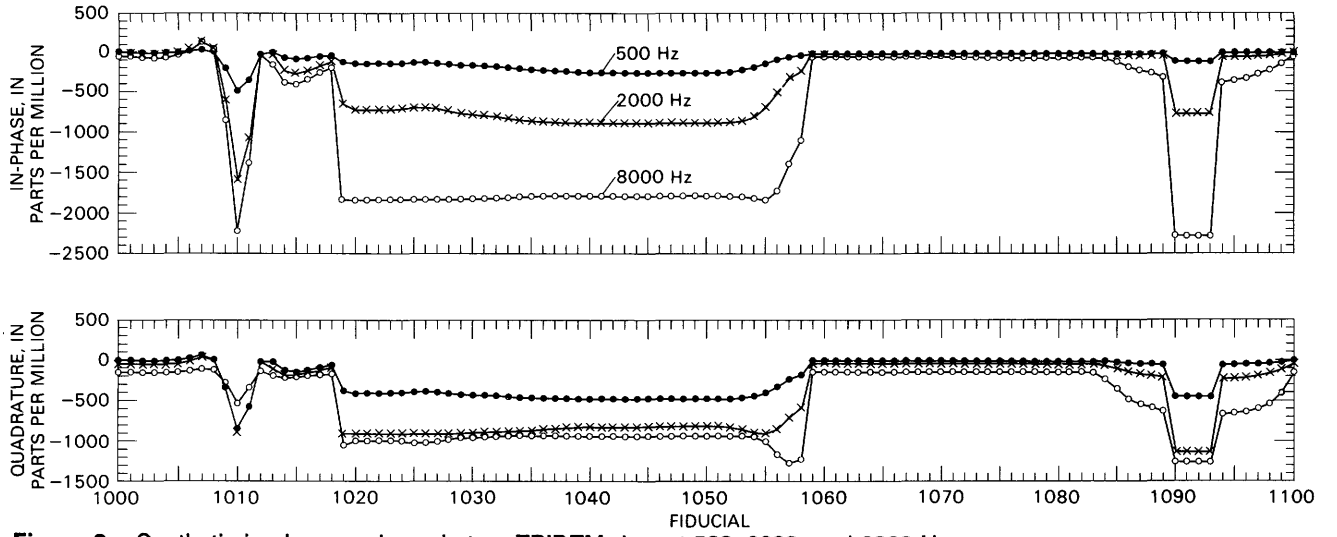

Figure 6. Synthetic in-phase and quadrature TRIDEM data at 500, 2000, and 8000 Hz.

both receiver directions (26 data points per fiducial), and case 4 considers in-phase and quadrature components of the vertical receiver at all frequencies (26 data points per fiducial). Inversions for cases 2–4 are computed at every second fiducial. These four cases test the importance of frequency, receiver component, and phase component on the inversion.

Table 3 lists the minimum and maximum bounds of the three independent variables (overburden resistivity, earth resistivity, and overburden thickness). The transmitter altitude was assumed known, and its value was taken directly from the geological section (fig. 2). After the initial guess at fiducial 1000 (table 3), the initial guess at the next fiducial was given by the best-fit parameter estimates from the previous fiducial. This was continued until the previous estimate was a poor first guess. In this case (for example, fiducial 1019), new initial guesses were made with the process continuing as before. Generally, this provided fast convergence (few iterations) except where the data deviated radically from one fiducial to the next.

An important parameter associated with the inversion algorithm is the standard error of fit, which is a measure of the goodness of the fit and is defined to be the square root of the sum of the residuals squared divided by the number of degrees of freedom. The residuals are the differences between the observed values and the values computed from the forward model. The standard error of fit therefore has the same units as the observed data. The number of degrees of freedom is the number of observations minus the number of unknown parameters. Figure 7 shows profiles of the standard error for the

Table 4. Best-fit parameter values and associated standard errors for a one-layer earth model, SWEEPEM (case 1) and TRIDEM systems

[ρ_{OB} and ρ_E are overburden and earth resistivity, respectively; h is overburden thickness]

	TRIDEM					SWEEPEM (case 1)				
Fiducial	Altitude (meters)	h (meters)	ρ_{OB} (ohm-m)	ρ_E (ohm-m)	Standard error	Altitude (meters)	h (meters)	ρ_{OB} (ohm-m)	ρ_E (ohm-m)	Standard error
1000	60	0.2	188.7	1,973.4	0.51e-5	138.8	0.4	1,000.0	1,991.5	0.47e-3
1004	60	0.2	188.7	1,815.0	0.10e-4	123.8	0.4	1,000.0	2,013.0	0.34e-3
1008	60	0.3	60.2	4,000.0	0.52e-4	131.3	0.4	827.9	2,034.2	0.65e-3
1012	60	0.2	12.7	3,238.8	0.57e-4	139.5	2.4	535.5	2,363.7	0.11e-2
1016	60	0.2	188.7	349.9	0.20e-3	142.5	1.1	1,000.0	2,029.6	0.30e-3
1020	60	36.0	25.0	347.6	0.38e-6	139.5	8.3	14.2	61.5	0.32e-1
1024	60	34.0	25.0	349.5	0.12e-6	152.0	33.9	25.0	342.5	0.33e-3
1028	60	38.0	25.0	348.2	0.13e-6	165.0	38.0	25.0	349.1	0.19e-4
1032	60	45.0	25.0	346.0	0.94e-7	161.0	45.8	25.0	340.6	0.18e-3
1036	60	63.9	25.0	341.0	0.12e-6	135.0	64.0	25.0	348.4	0.25e-4
1040	60	77.8	25.0	336.9	0.15e-6	123.0	77.8	25.0	339.4	0.11e-3
1044	60	83.9	25.0	339.4	0.17e-6	123.0	83.8	25.0	338.9	0.89e-4
1048	60	83.8	25.0	339.2	0.19e-6	117.0	83.8	25.0	338.9	0.10e-3
1052	60	74.8	25.0	338.1	0.18e-6	123.0	74.0	25.0	337.0	0.10e-3
1056	60	21.0	25.1	355.2	0.22e-5	129.0	21.0	25.1	348.1	0.11e-2
1060	60	0.2	188.7	1,973.4	0.51e-5	114.0	0.4	1,000.0	1,990.4	0.77e-3
1064	60	0.2	188.7	1,973.4	0.51e-5	99.0	0.4	1,000.0	1,990.4	0.10e-2
1068	60	0.2	188.7	1,973.4	0.51e-5	107.0	0.4	1,000.0	1,990.4	0.88e-3
1072	60	0.2	188.7	1,980.4	0.46e-5	113.0	0.4	1,000.0	1,990.4	0.26e-2
1076	60	0.2	188.7	1,913.5	0.11e-4	113.0	0.4	1,000.0	1,659.7	0.14e-1
1080	60	0.2	188.7	1,880.7	0.84e-5	113.0	0.4	1,000.0	1,601.8	0.13e-1
1084	60	0.3	25.4	1,947.0	0.15e-5	114.0	3.2	230.8	1,859.0	0.19e-2
1088	60	0.7	13.1	848.9	0.66e-5	123.0	25.1	201.8	2,087.2	0.77e-3
1092	60	10.5	9.6	594.2	0.53e-5	129.0	2.0	2.5	167.5	0.24e-1
1096	60	3.7	54.5	623.5	0.10e-4	129.0	34.4	200.8	2,106.2	0.53e-3
1100	60	0.2	80.6	2,018.3	0.83e-5	130.5	1.0	1,000.0	1,988.7	0.62e-3

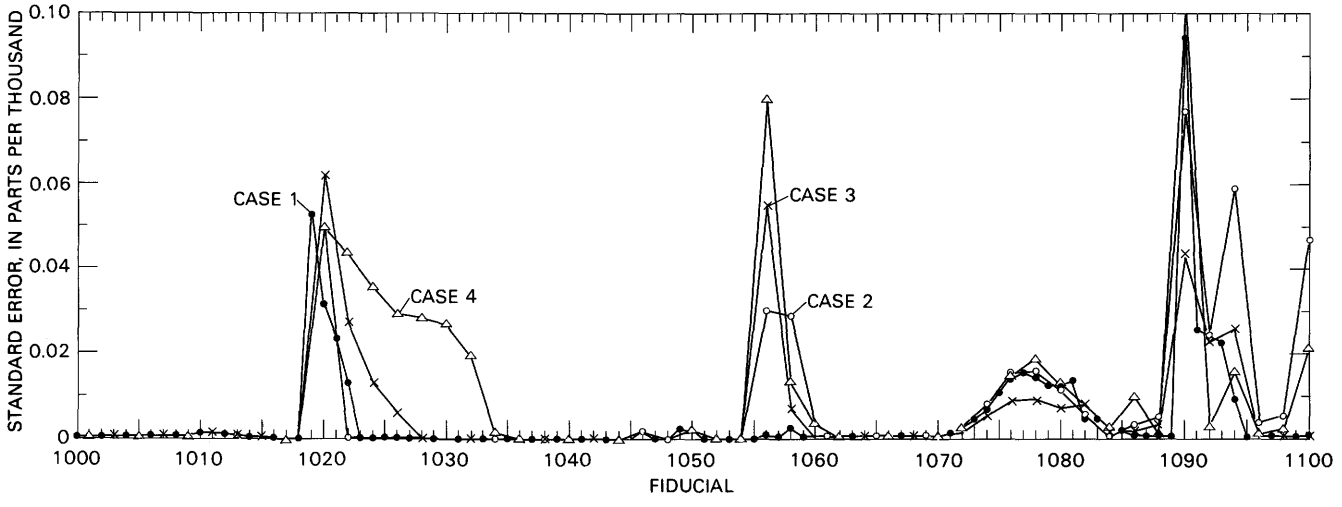

Figure 7. Standard error profiles for the four SWEEPEM cases.

four cases. The standard error increases slightly (that is, the fit is poorer) over the dike (fiducial 1010) and more significantly over the sphere (fiducial 1077) and surficial conductor (between fiducials 1090 and 1100). Note that the standard error also increases at each end of the 25-ohm-m overburden section. The smaller increases within this region near fiducials 1046 and 1050 are due to small variations in altitude and overburden thickness. The standard error flagged the anomalous zones of interest, but other areas were flagged as well. Profiles of the number of iterations required to reach the imposed accuracy criteria, along with the standard error, could

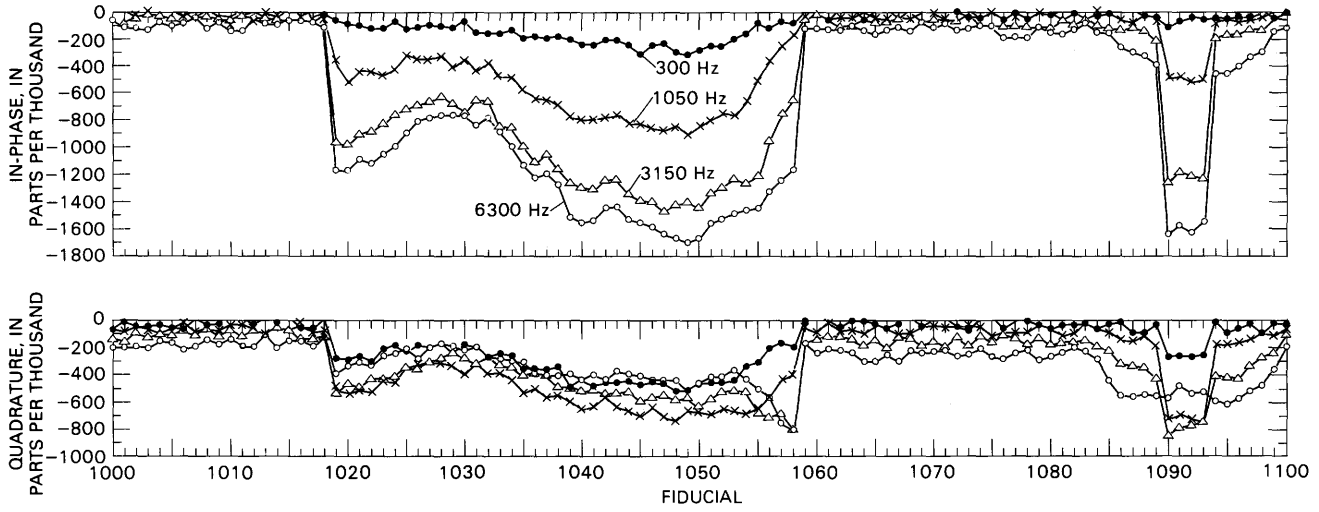

Figure 8. Synthetic in-phase and quadrature SWEEPEM data of figure 5 with random noise (±0.05 normalized secondary fields) added at 300, 1050, 3150, and 6300 Hz.

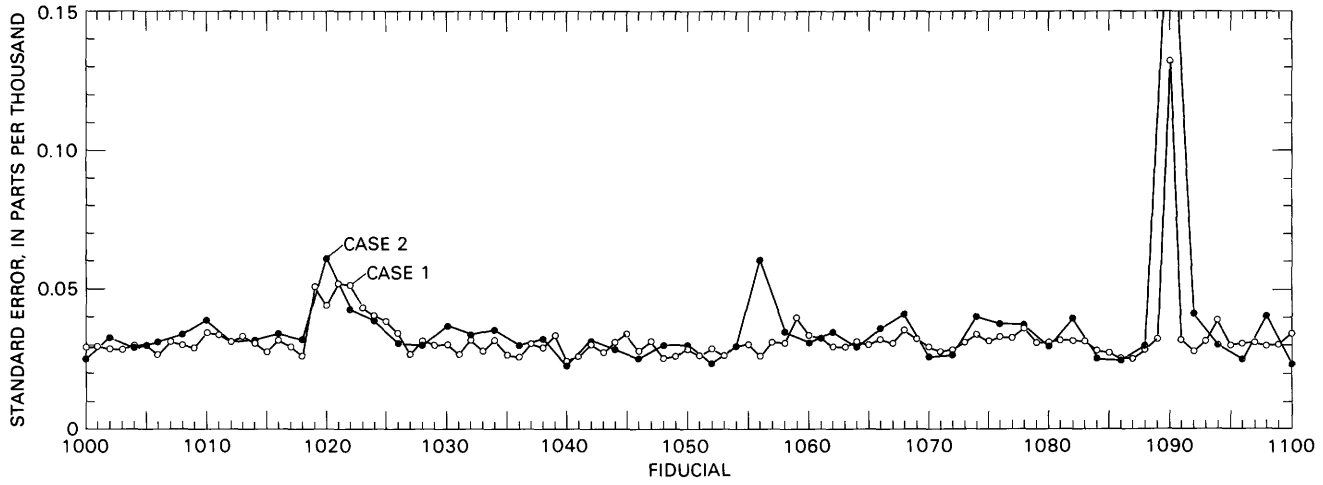

Figure 9. Standard error profiles (cases 1 and 2) for the noisy SWEEPEM data with no weighting.

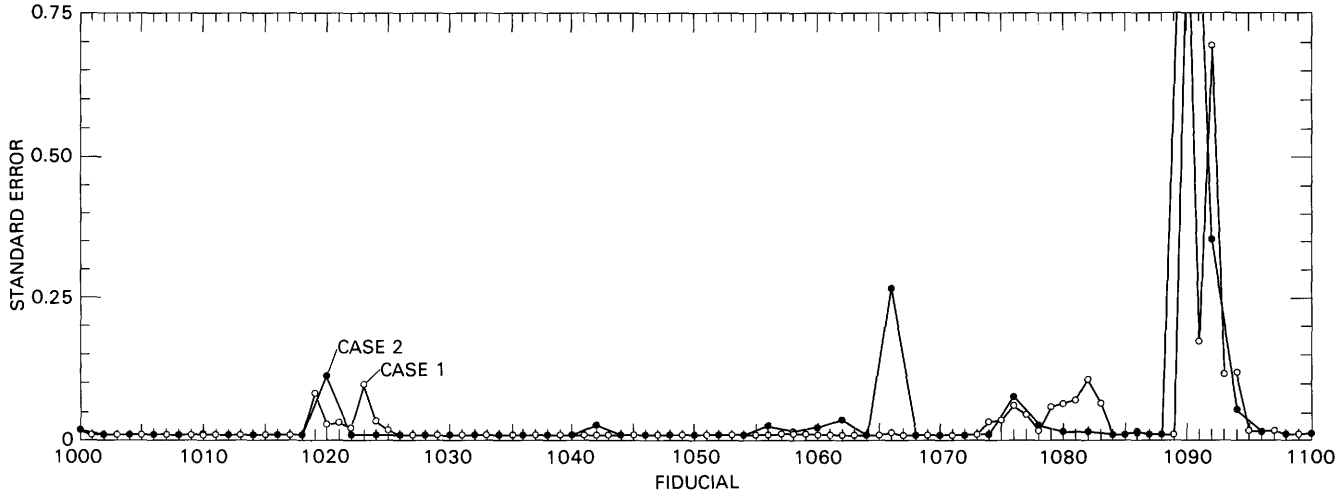

Figure 10. Standard error profiles (cases 1 and 2) for the noisy SWEEPEM data with weighting.

Table 5. Best-fit parameter values and associated standard errors for SWEEPEM system (case 1), with and without weighting

[ρ_{OB} and ρ_E are overburden and earth resistivity, respectively; h is overburden thickness]

		No weighting				Weighting			
Fiducial	Altitude (meters)	h (meters)	ρ_{OB} (ohm-m)	ρ_E (ohm-m)	Standard error	h (meters)	ρ_{OB} (ohm-m)	ρ_E (ohm-m)	Standard error
1000	138.8	16.0	1,000.0	2,029.2	0.029	0.4	419.9	1,702.8	1.8
1004	123.8	1.0	720.2	2,242.4	0.030	0.4	159.4	2,224.7	1.0
1008	131.3	0.4	1,000.0	2,022.7	0.030	0.4	1,000.0	2,003.0	1.0
1012	139.5	0.4	41.6	3,209.8	0.031	1.1	112.4	3,180.0	1.0
1016	142.5	0.4	1,000.0	1,939.8	0.032	0.4	444.6	2,053.2	1.0
1020	139.5	1.2	3.5	51.1	0.044	2.5	7.3	45.6	2.9
1024	152.0	4.0	8.4	67.7	0.040	16.6	24.3	149.3	3.6
1028	165.0	19.0	21.4	79.9	0.032	37.1	24.7	305.2	1.0
1032	161.0	37.8	25.4	142.1	0.032	46.2	24.9	546.6	0.98
1036	135.0	54.4	24.3	132.7	0.026	62.3	24.8	333.1	0.99
1040	123.0	79.1	25.6	1,160.9	0.024	82.5	25.3	824.6	0.94
1044	123.0	90.5	24.9	10,000.0	0.031	82.7	25.0	410.9	1.0
1048	117.0	71.7	25.2	78.3	0.025	79.4	25.0	146.6	1.0
1052	123.0	80.8	25.5	10,000.0	0.029	77.5	25.1	745.1	1.0
1056	129.0	18.7	24.5	269.6	0.026	22.8	26.1	436.6	0.96
1060	114.0	0.4	182.1	1,803.5	0.033	0.4	1,000.0	1,991.9	1.1
1064	99.0	0.4	1,000.0	1,992.4	0.031	0.6	1,000.0	2,002.7	1.0
1068	107.0	0.4	1,000.0	1,940.8	0.035	0.4	1,000.0	1,997.3	1.0
1072	113.0	1.5	405.3	1,965.1	0.028	0.4	1,000.0	1,909.9	1.1
1076	113.0	0.4	1,000.0	1,579.2	0.033	136.2	999.1	506.4	6.2
1080	113.0	0.4	1,000.0	1,643.8	0.031	0.4	1,000.0	1,440.9	6.5
1084	114.0	0.4	33.2	1,868.5	0.028	2.9	275.3	1,692.5	1.0
1088	123.0	0.4	5.6	1,183.5	0.028	29.9	219.0	2,854.3	1.1
1092	129.0	8.8	8.1	1,076.0	0.027	0.4	2.2	24.6	69.
1096	129.0	16.1	125.0	1,305.7	0.030	2.6	31.4	815.6	1.3
1100	130.5	55.5	1,000.0	2,251.0	0.034	0.4	166.4	1,913.3	1.1

perhaps distinguish the various types of anomalous zones.

A better method for flagging anomalous zones of interest is to look directly at the resistivity profiles and maps and relate anomalies to standard error and (or) number of iteration profiles or maps. Table 4 lists the best-fit parameters, along with the standard error, for case 1. The fit is very good except at the fiducials already mentioned. Similar information was generated for the other cases. The importance of the data set (cases 1–4) on the inversion process was studied but will not be discussed in this paper.

Field data have noise from vibrations, sferics, bird motion, and so forth. These effects were investigated by adding 5 percent random noise to the data for cases 1 and 2. An example of adding this random noise to the vertical component (fig. 5) is shown in figure 8. The real noise level should be frequency dependent, instead of constant, and is generally much smaller than 5 percent. Actual noise levels from field tests indicate that noise levels are in the range of a few parts per thousand at low frequencies and perhaps as much as 10–20 ppt at high frequencies. This noisy data set therefore provides an extreme test of the inversion algorithm. Cases 1 and 2 were reinverted using the noisy data. No distinction between areas of layering and areas having anomalous features (dikes, spheres, surficial conductors) can be seen in the standard error profiles (fig. 9).

Figure 10 shows the standard error profiles after reinversion of the noisy data using a weighting function. In this example, the weight of a given data point is equal to the absolute value of the noise added for that point. The larger the noise the less important the corresponding data point is to the fit.

The standard error, when the weights are equal to the estimated accuracy of the data, provides an estimate of the fit in terms of data accuracy. A standard error of approximately one indicates that the fit is as good as the data accuracy. A higher standard error (typically 2–100) indicates that the fit is worse than the accuracy of the data and thus that not all the power in the data is being utilized in the fit (for example, trying to fit a one-layer earth model to a dike response). Note that the standard error is dimensionless when normalized by the weighting.

Table 5 lists the best-fit parameters from the inversion scheme and provides a comparison between

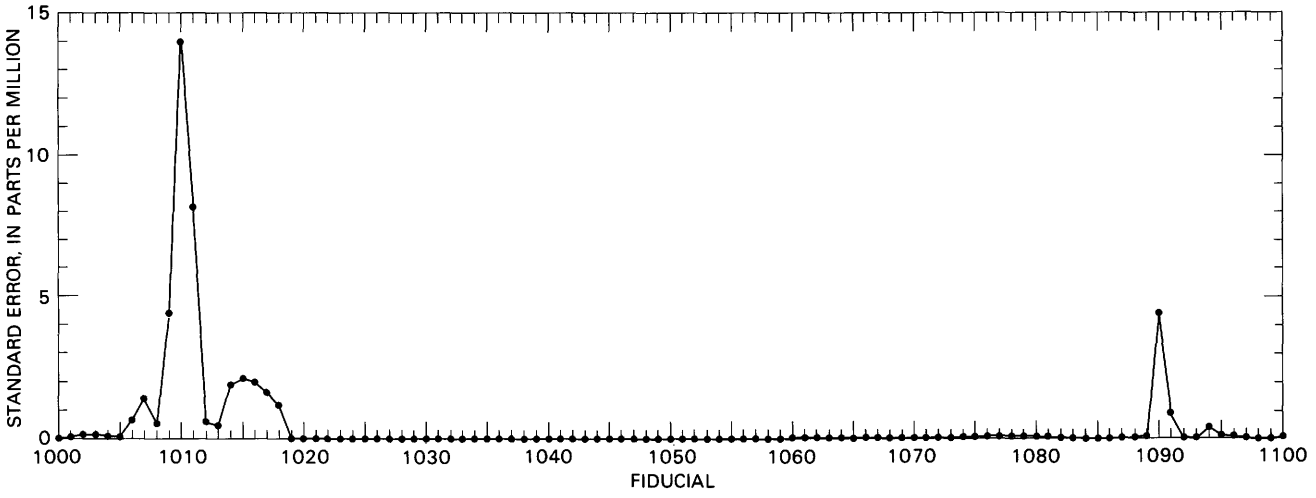

Figure 11. Standard error profile for the TRIDEM system.

weighting and no weighting. Generally, the best-fit parameters are closer to the geological model when weighting is applied.

TRIDEM

Inversion of the TRIDEM and SWEEPEM synthetic data followed similar procedures. The parameter bounds, initial parameter guesses, and other parameter data are given in table 3. Figure 11 shows the standard error profile, and table 4 lists the best-fit parameters and the standard error. The best-fit parameters for the TRIDEM data are not that different from the SWEEPEM estimates, even though there are only six data points per fiducial. Near the dike, the standard error for the TRIDEM data has a larger relative deviation than that associated with the standard error for the SWEEPEM examples shown in figure 7. This was anticipated from direct comparison of the synthetic data in figures 5 and 6.

SUMMARY AND CONCLUSIONS

In this paper, the use of synthetic modeling for testing interpretation algorithms is shown to be effective. Synthetic data, though not a completely accurate representation of actual EM data, do allow concepts to be tested under known conditions. Field data, where the geoelectric structure of the earth is unknown, can then be interpreted with the confidence that the algorithms are working correctly. Incidentally, the need for digital data in automated interpretation is clearly demonstrated by the examples in this paper. Imagine entering the SWEEPEM (or equivalent multicomponent airborne system) data set into a computer file from analog records! The time to carry this out would be months for a typical survey area, and the chances of error would be enormous.

In the future, forward modeling will emphasize the development of faster algorithms and better data storage and retrieval. Faster free-space finite conductor algorithms and multilayer algorithms will be attached to interactive graphics packages on work stations to allow quick comparisons between model and field data. Nomograms will continue to be developed and the parameters stored in a data base for quick retrieval. Fast and accurate interpolation methods for estimating the parameters between stored values are required for these data bases. Numerical modeling algorithms will concentrate on faster computation with data storage, retrieval, and interpolation being more important. Digital data sets, similar to the examples presented in figures 5, 6, and 8, will be stored for inverse modeling or graphical display. Nomograms for two- and three-dimensional models, similar to those developed by Hanneson and West (1984a, b) and Bottomley and others (1984) (see fig. 12), will be developed and the parameter values stored for direct comparison to field data and for inverse modeling to fit field data.

Finally, quicker, more robust resistivity inversion algorithms are required that have better methods for flagging anomalous features. Perhaps multicomponent pattern-recognition techniques and artificial intelligence methods will play a key role in the interpretation methods of the future.

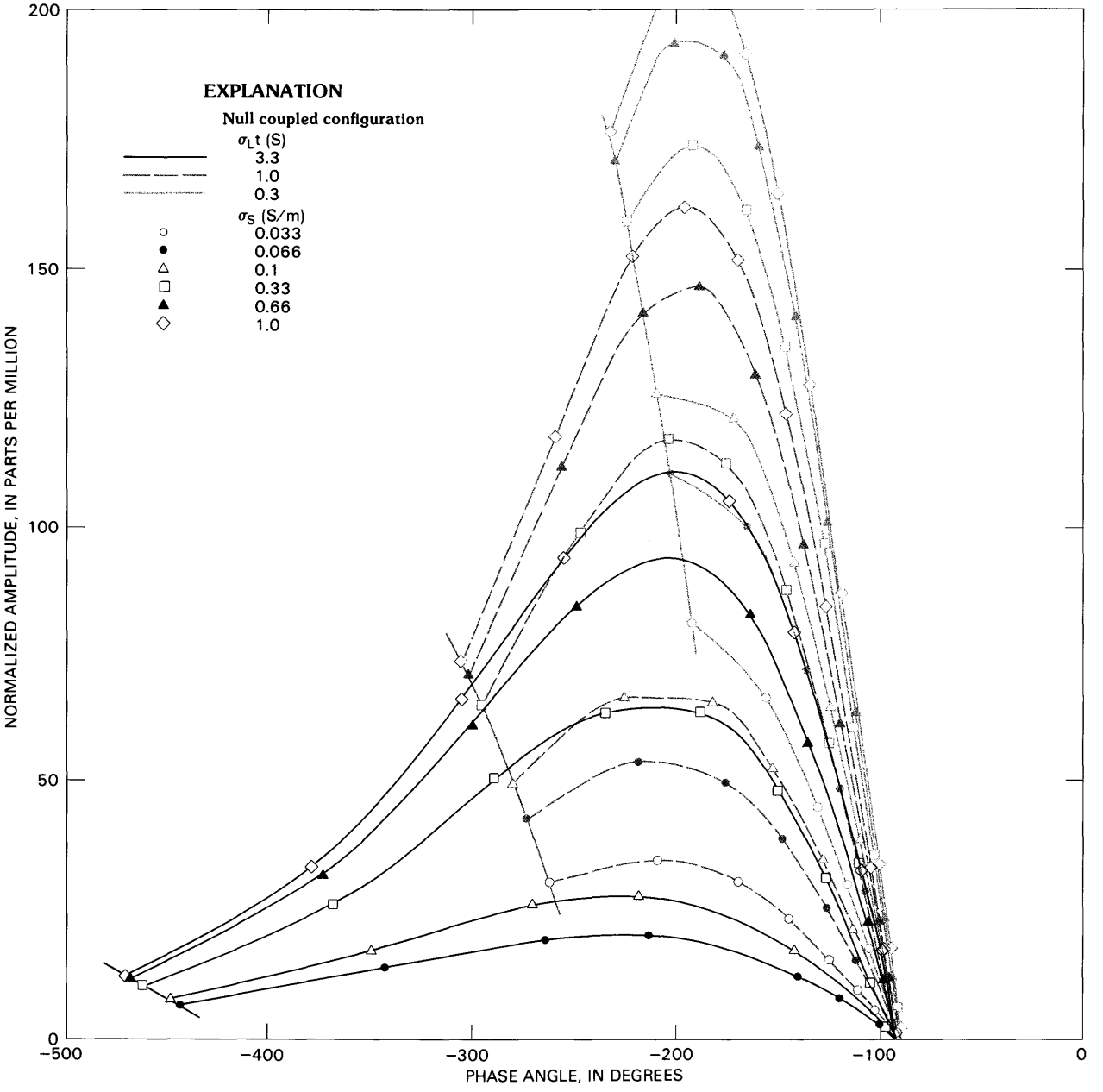

Figure 12. Nomogram for a sphere in a one-layer earth. The values of the conductivity-thickness of the overburden ($\sigma_L t$) and the conductivity of the sphere (σ_S) are given in the figure. Modified from Bottomley and others (1984); other parameters defined in Bottomley and others.

REFERENCES CITED

Anderson, W.L., 1977, Electromagnetic fields about a finite electric wire source: U.S. Geological Survey Open-File Report 74–041, 205 p.

_____ 1979, Numerical integration of related Hankel transform of order 0 and 1 by adaptive digital filtering: Geophysics, v. 44, p. 1287–1305.

Annan, P., 1986, Development of the PROSPECT I airborne electromagnetic system, *in* Palacky, G.J., ed., Airborne resistivity mapping: Geological Survey of Canada Paper 86–22, p. 63–70.

Barringer, A.R., 1962, New approach to exploration—The INPUT electrical pulse prospecting system: Mining Congress Journal, v. 48, p. 49–52.

_____ 1976, U.S. Patent 3,950,695, Geophysical prospecting method utilizing correlation of received waveforms with stored reference waveforms. Application filed April 9, 1973.

Best, M.E., 1985, A systematic approach for evaluating airborne electromagnetic systems: Geophysical Prospecting, v. 33, p. 577–599.

Best, M.E., and Bremner, T.G.T., 1986, The Sweepem airborne electromagnetic system, *in* Palacky, G.J., ed., Airborne resistivity mapping: Geological Survey of Canada Paper 86–22, p. 71–73.

Best, M.E., Duncan, P., Jacobs, F.J., and Scheen, W.L., 1985, Numerical modeling of the electromagnetic response of three-dimensional conductors in a layered earth: Geophysics, v. 50, p. 665–676.

Bottomley, R.J., Duncan, P.M., and Best, M.E., 1984, Interpretation of three-dimensional electromagnetic modeling of conductors in a layered earth: Society of Exploration Geophysicists, International Meeting, 54th, Expanded Abstracts, p. 126–129.

Fraser, D.C., 1972, A new multi-coil aerial electromagnetic prospecting system: Geophysics, v. 37, p. 518–537.

_____ 1978, Resistivity mapping with airborne multi coil electromagnetic system: Geophysics, v. 43, p. 144–172.

_____ 1979, The multi coil II airborne electromagnetic system: Geophysics, v. 44, p. 1367–1394.

Grant, F.S. and West, G.F., 1965, Interpretation theory in applied geophysics: New York, McGraw–Hill, 584 p.

Hanneson, J.E., and West, G.F., 1984a, The horizontal loop electromagnetic response of a thin plate in a conductive earth—Part I, Computation method: Geophysics, v. 49, p. 411–420.

_____ 1984b, The horizontal loop electromagnetic response of a thin plate in a conductive earth—Part II, Computational results and examples: Geophysics, v. 49, p. 421–432.

Hohmann, G.W., 1975, Three-dimensional induced polarization and electrical modeling: Geophysics, v. 40, p. 309–324.

Keller, G.V., and Frischknecht, F.C., 1966, Electrical methods in geophysical prospecting: Oxford, Pergamon Press, 517 p.

Lee, K.H., Pridmore, D.F., and Morrison, H.F., 1981, A hybrid 3–D electromagnetic modeling scheme: Geophysics, v. 46, p. 796–805.

Marquardt, D.W., 1963, An algorithm for least squares estimation of non-linear parameters: Journal of the Society of Industrial and Applied Mathematics, v. 11, p. 431–441.

Palacky, G.J., 1976, Use of decay patterns for the classification of anomalies in time-domain measurements: Geophysics, v. 41, p. 1031–1041.

Paterson, N.R., 1967, Exploration for massive sulfides in the Canadian Shield: Mining and Groundwater Geophysics, Queen's Printer, Ottawa, Canada, p. 275–289.

Pemberton, R., 1962, Airborne electromagnetics in review: Geophysics, v. 27, p. 691–713.

Seigel, H.O., and Pitcher, D.H., 1978, Mapping earth conductivities using a multi-frequency airborne electromagnetic system: Geophysics, v. 43, p. 563–575.

Sinha, A.J., 1973, Comparison of airborne electromagnetic coil systems placed over a multi-layer conducting earth: Geophysics, v. 38, p. 894–919.

Spies, B.R., and Parker, P.D., 1983, Inductive and conductive anomalies in transient electromagnetic exploration: Society of Exploration Geophysicists, International Meeting, 53rd, Expanded Abstracts, p. 626–629.

Stemp, R.W., 1972, Field results from a low level airborne electromagnetic system with a large coil separation: International Geophysical Congress, 24th, Section 9, p. 110–120.

_____ 1980, The Kenting Canso airborne geophysical system: Kenting Earth Sciences Bulletin, February, 1980.

Ward, S.H., Nelson, P.H., and Sill, W.R., 1973, Introduction to special issue on the electrical parameters of rocks: Geophysics, v. 38, p. 1–2.

Zandee, A.P., Best, M.E., and Bremner, T.G.T., 1985, Sweepem, a new airborne electromagnetic system: Society of Exploration Geophysicists, International Meeting, 55th, Expanded Abstracts, p. 236–239.

Layered-Earth Resistivity Mapping

By Douglas C. Fraser[1]

Abstract

Resistivity mapping can augment electromagnetic (EM) anomaly mapping for mining exploration surveys. The advantage of an airborne resistivity contour map as compared to an EM anomaly map is that more information is displayed. An EM anomaly map gives the impression that a number of discrete conductors occur, supposedly separated by nonconductive material, and targets have the appearance of being well defined. The resistivity contour map, however, may show that the picture presented by the EM anomaly map is too simplified. For example, the resistivity map may illustrate that the so-called EM "anomalies" are really part of a wide conductive area. This would obviously cast the EM anomalies in a different light and would probably result in a change in followup exploration decisions. An additional advantage of the resistivity map is that it is free of any prejudices of an interpreter and therefore provides a totally unbiased picture of the survey area.

The use of two or more frequencies provides information on the variation of resistivity with depth. An apparent resistivity map can be produced for each frequency to allow a qualitative interpretation. In addition, two-layer inversion can be performed to quantitatively portray the results in terms of an upper layer and a lower half-space.

Resistivity mapping is applicable wherever a measurable resistivity contrast occurs between different earth materials. Thus it has a wide range of applications including geothermal exploration and shallow-sea bathymetric mapping.

INTRODUCTION

Electromagnetic (EM) anomaly maps are commonly produced by plotting the location of peaks in the EM profile. The EM data at each peak are analyzed using a vertical thin dike model to obtain a conductivity-thickness product (conductance), and the coded conductance is displayed on the EM anomaly map. This procedure is sufficient for mining exploration in areas where conductors dip steeply and are separated by resistive rock and where overburden is absent or fairly resistive.

In areas where conductors are gently dipping or host rocks or overburden are conductive, peaks in the EM profile may reflect decreases in flying height (that is, sensor-source distance) as well as increases in conductivity. The only practical means of separating such EM peaks is to compute some diagnostic model parameter at every data point. These parameters include conductance (using either a vertical or horizontal thin sheet model), or conductivity or its reciprocal resistivity (using a half-space model).

Figure 1*A* illustrates a typical EM anomaly map on which several discrete conductors occur, supposedly separated by nonconductive material. The targets appear to be well defined. The resistivity contour map of figure 1*B* shows however, that the so-called EM anomalies are really part of a wide conductive area. The resistivity map obviously casts the EM anomalies in a different light and would probably result in different followup exploration decisions.

Needless to say, exploration decisions are the key to discovery. The followup of poor targets commonly results from poor or incomplete information. In such cases, funds are spent on nonproductive targets, and the amount available for the exploration of potentially productive targets is reduced. This is one of the reasons why resistivity maps have gained acceptance in the marketplace.

CHOICE OF MODEL PARAMETER

The primary requirements for the choice of an EM model parameter for display on a contour map are that the parameter should be insensitive to changes in flying height and should reflect variations in the conductivity of the earth. For most environments, the half-space yields the most stable model in this regard.

Resistivity contour maps were introduced as a standard product of all DIGHEM helicopter EM surveys in 1975 as an aid for the interpretation of EM data. The resistivity parameter was chosen for display, rather than the intuitively more reasonable conductivity, because of a perceived problem of market acceptance. Few mining clients had ever seen conductivity maps, either airborne or ground, whereas resistivity maps were common byproducts of induced polarization surveys.

[1]Dighem Surveys and Processing Inc., 228 Matheson Blvd East, Mississauga, Ontario L4Z 1X1, Canada.

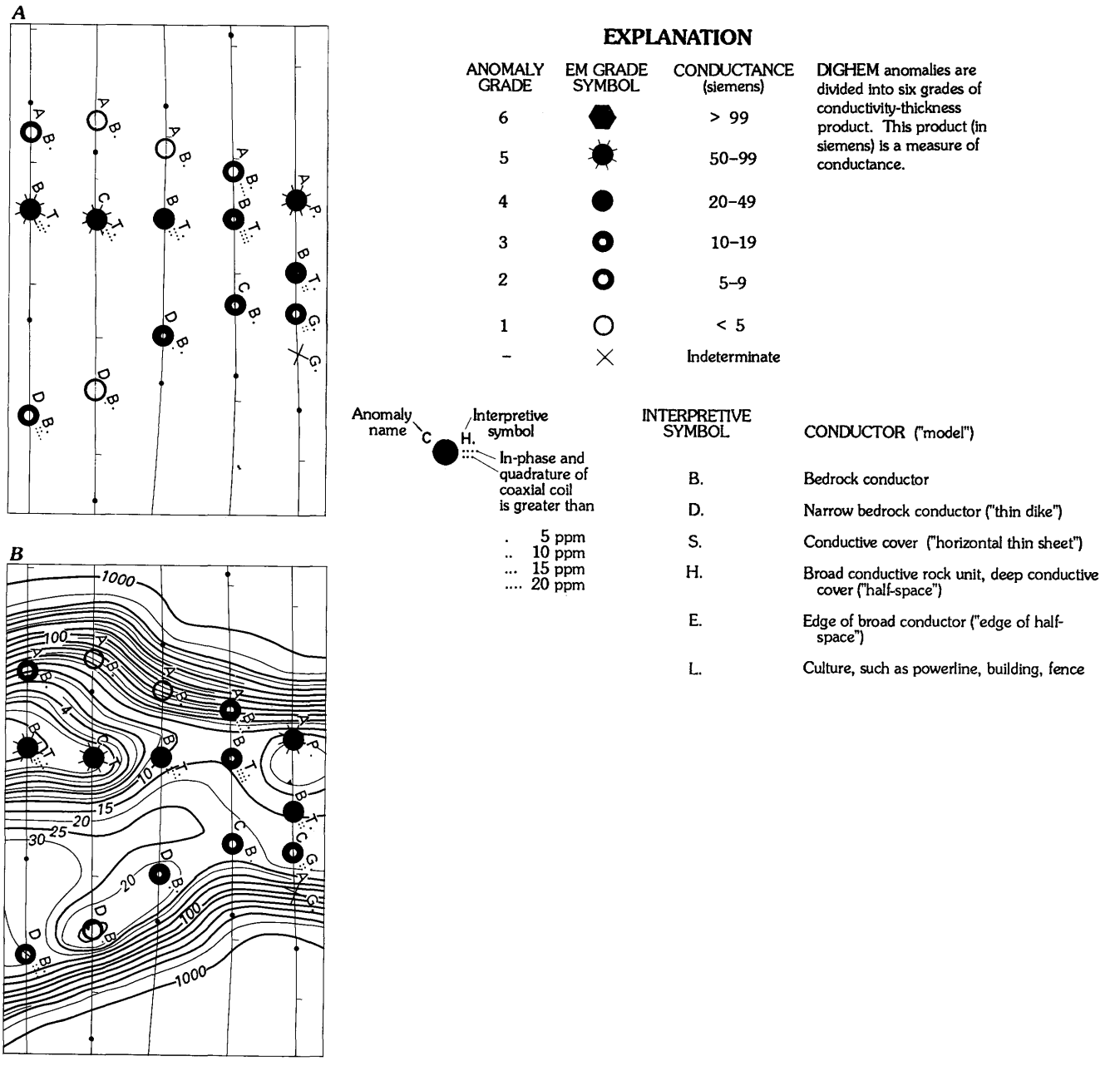

Figure 1. Comparison of EM anomaly and resistivity maps. *A*, EM anomaly map. *B*, Resistivity map (contours in ohm-meters) with EM anomalies superimposed.

It has been argued that conductivity is the more appropriate parameter because the purpose of an EM survey is to detect conductors (Palacky and others, 1986). This, of course, is not necessarily true because the target of a survey (for example, gravel) may be more resistive than the host (for example, clay). The DIGHEM^{IV} system, with frequencies of 900–56,000 Hz, can map resistivities spanning five orders of magnitude; that is, from less than 0.1 ohm-m to more than 10,000 ohm-m. In recent surveys, an 8,000-ohm-m alteration zone was a conductive target in northern Canada and a 500-ohm-m rock unit was a resistive host in the southwestern United States. Clearly, the previous concepts of good conductor, poor conductor, and resistive rock unit are losing their qualitative sense. In the final analysis, it can be argued that the client should rule; in which case, conductivity maps would be generated for hydrologists, resistivity maps for mineral exploration geologists, and so on.

HALF-SPACE MODELS

Figure 2 shows an EM system flying over a uniform conductive earth. For a single frequency, there are three

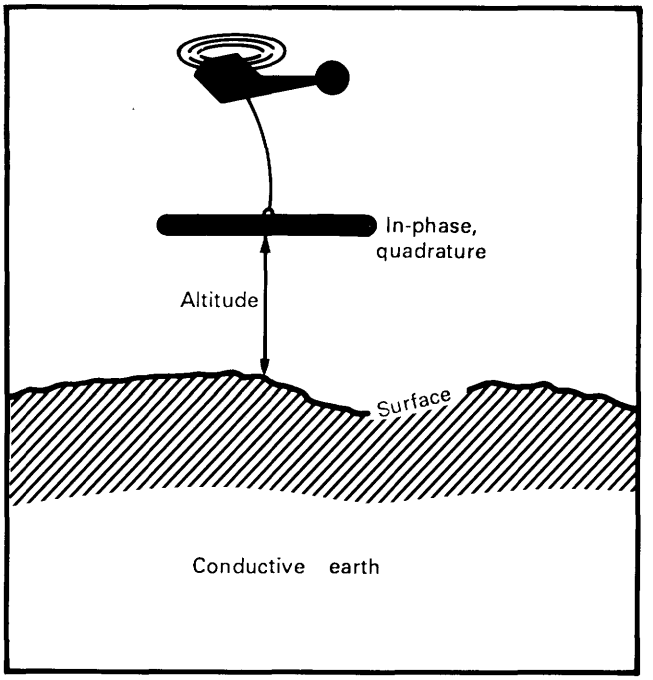

Figure 2. Electromagnetic system flying over a uniform conductive earth. Three measured parameters are obtained from a single frequency survey.

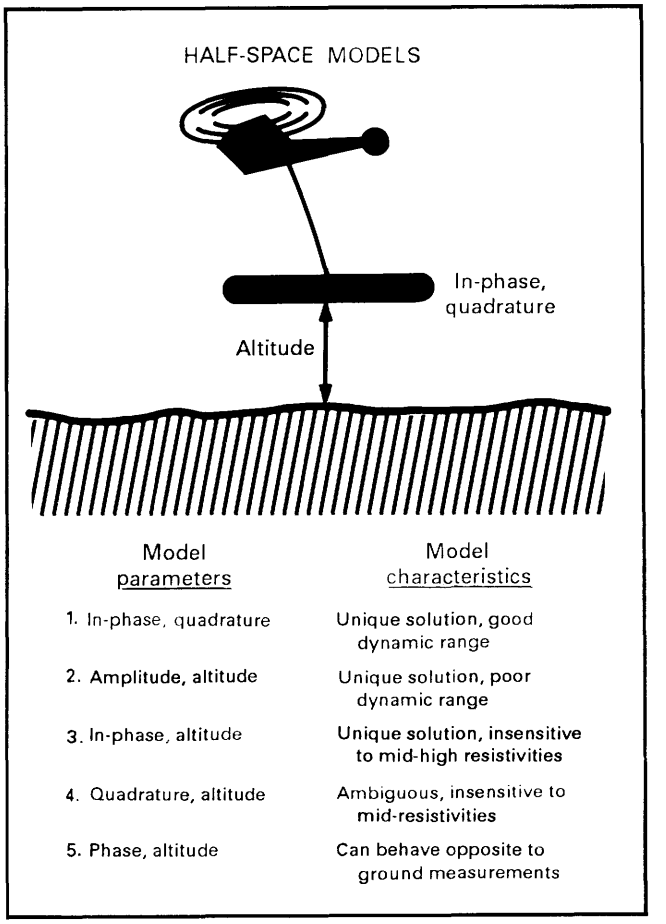

Model parameters	Model characteristics
1. In-phase, quadrature	Unique solution, good dynamic range
2. Amplitude, altitude	Unique solution, poor dynamic range
3. In-phase, altitude	Unique solution, insensitive to mid-high resistivities
4. Quadrature, altitude	Ambiguous, insensitive to mid-resistivities
5. Phase, altitude	Can behave opposite to ground measurements

Figure 3. Five half-space models for the solution of apparent resistivity at a single frequency.

measured variables: in-phase, quadrature, and altitude. Because only two of these variables are needed to compute the half-space resistivity (or apparent resistivity), the half-space resistivity can be computed in a variety of ways.

Five different half-space models applicable for any single frequency are shown in figure 3. These models yield the same resistivity value if a true half-space exists and if trees do not distort the measured altimeter value; however, they yield different resistivity values if the earth is not a half-space or if trees prevent the altimeter from defining the true sensor-source distance. The first model shown in figure 3 has become the model of choice. The five models are briefly reviewed in an example shown in figure 4.

The upper part of figure 4 presents a simple two-layer example with a resistive upper layer. The flying height is 30 m. The parts per million in-phase and quadrature at the 900-Hz frequency for the horizontal coplanar coil-pair are shown. If a ground resistivity expander survey was performed over this section, apparent resistivities of 40–10,000 ohm-m would be obtained. The lower part of figure 4 shows the apparent resistivity values obtained using the five half-space models. Four of the five models yield apparent resistivities within this range.

Half-space model 1 is useful because it provides the true resistivity of the conductive lower layer and the thickness of the resistive upper layer; however, a proper two-layer inversion model is required to obtain the upper layer resistivity. Half-space models 2 through 5 yield zero apparent thickness because the altimeter is used to define the surface of the half space.

Model 4 yields inherently ambiguous results: the same apparent resistivity, 180 ohm-m, would be obtained if the lower layer resistivity was changed from 40 ohm-m to 0.2 ohm-m. Model 5 is peculiar in that the apparent resistivity decreases below 40 ohm-m in proportion to the thickness of the upper resistive layer.

Models 1 through 3 do not display any features that could be considered undesirable. Model 1 is preferred because its dynamic range is greater and because altimeter errors do not distort the resistivity. As a result of studies of this nature, model 1 was proposed (Fraser, 1978) as the standard for half-space inversion. This model is termed the pseudolayer half-space model.

The pseudolayer half-space algorithm is analogous to the interpretive diagram shown in figure 5. This interpretive diagram is similar to those used for the electromagnetic interpretation of a vertical half-plane or other conductor model. The abscissa is the in-phase signal in parts per million, and the ordinate is the

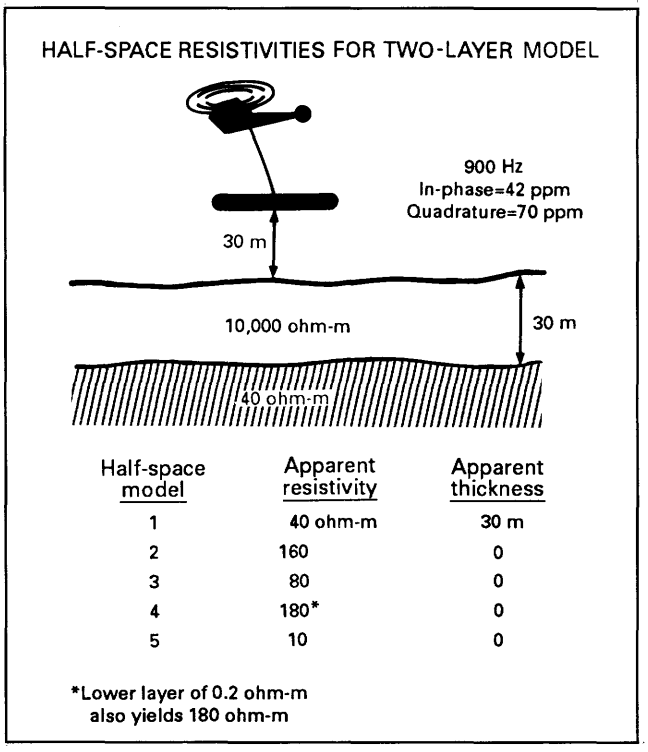

Half-space model	Apparent resistivity	Apparent thickness
1	40 ohm-m	30 m
2	160	0
3	80	0
4	180*	0
5	10	0

*Lower layer of 0.2 ohm-m also yields 180 ohm-m

Figure 4. Half-space resistivities for two-layer model. The upper part shows a two-layer forward case. The lower part shows the inverse solution for apparent resistivity using the five half-space models of figure 3. The apparent thickness is the difference between the computed sensor-source distance and the measured altitude.

corresponding quadrature signal. The two sets of contours yield the resistivity of the conductive earth and the height of the EM bird above the conductive earth. The pseudolayer half-space model actually represents a two-layer case (fig. 6). The resistivity of the upper layer is infinite, and the resistivity of the lower layer is that of the conductive earth or half-space.

In essence, the resistivity is obtained as a function of the in-phase and quadrature channels of the horizontal coils. The distance h from the bird to the conductive earth is obtained as a byproduct of the resistivity calculation. Discrepancies between computed distance h and measured bird altitude a are ascribed to a fictitious, highly resistive upper layer. The pseudolayer half-space model provides resistivities that are altitude independent because altitude does not enter into the resistivity equations. The model is called a pseudolayer half-space because the pseudolayer is merely an artifice to account for discrepancies between measured altitude a and computed distance h. The thickness of the pseudolayer might be a measure of tree height in a dense forest, the thickness of resistive permafrost, or the thickness of a resistive gravel deposit sitting on a clay substratum. A negative thickness for the pseudolayer indicates that a conductive upper layer exists in a two-layer case. The pseudolayer thickness is discussed more fully in Fraser (1978).

Figure 7 presents computed resistivity profiles from a DIGHEM^{III} survey over the Night Hawk test range in Ontario, Canada. The graphite target is buried beneath 90 m of sand (fig. 8). For simplicity, only the EM data from the two coplanar coil-pairs and the altimeter are displayed. Note that on the EM channels the conductor can best be seen on the 900-Hz in-phase. The two lower channels are the apparent resistivity from the pseudolayer half-space model at frequencies of 900 and 7200 Hz.

The apparent resistivities are 16 ohm-m over the conductor for 900 Hz, and 200 ohm-m for 7200 Hz. These resistivity channels show that the 900-Hz frequency penetrates well into the graphite, whereas the 7200-Hz frequency is mainly restricted to the overlying sand.

TWO-LAYER MODEL

Two-layer inversion techniques can be used to separate the response of overburden from that of bedrock. The specialized model shown in figure 9 (Fraser, 1986) may be called the pseudolayer two-layer model. Other models are discussed in Paterson and Reford (1986).

Similar to the previous half-space model, the sensor-source distance h is an unknown. This is desirable because a heavy tree cover will result in the airborne altimeter a understating the sensor-source distance h. Thus, there are four unknowns as shown in figure 9.

Figure 10 presents the same measured data as shown in figure 7 over the Night Hawk conductor. The geologic situation fits a two-layer case reasonably well because the graphite is quite wide. Results of the two-layer resistivity inversion are shown in the lower half of figure 10. The upper limit for the calculation of resistivities is constrained at approximately the numerical value (in hertz) of the highest transmitted frequency. The conductor has a resistivity of 1 ohm-m in highly resistive rocks (constrained at 8,000 ohm-m), and the upper layer of sand has a resistivity of about 300 ohm-m. The computed depth to the conductor is 125 m, as compared to the true value of 90 m as determined by drilling. The overstated depth probably results because the graphite is of insufficient width to fit a two-layer model exactly. Nevertheless, the inversion seems to be reasonably satisfactory in this case in that it yields resistivity values having a greatly increased dynamic range as compared to those computed by using the half-space method (figs. 7, 10).

Figure 11 presents a model study in which a cover layer of 10 ohm-m resistivity overlies a lower layer of 100

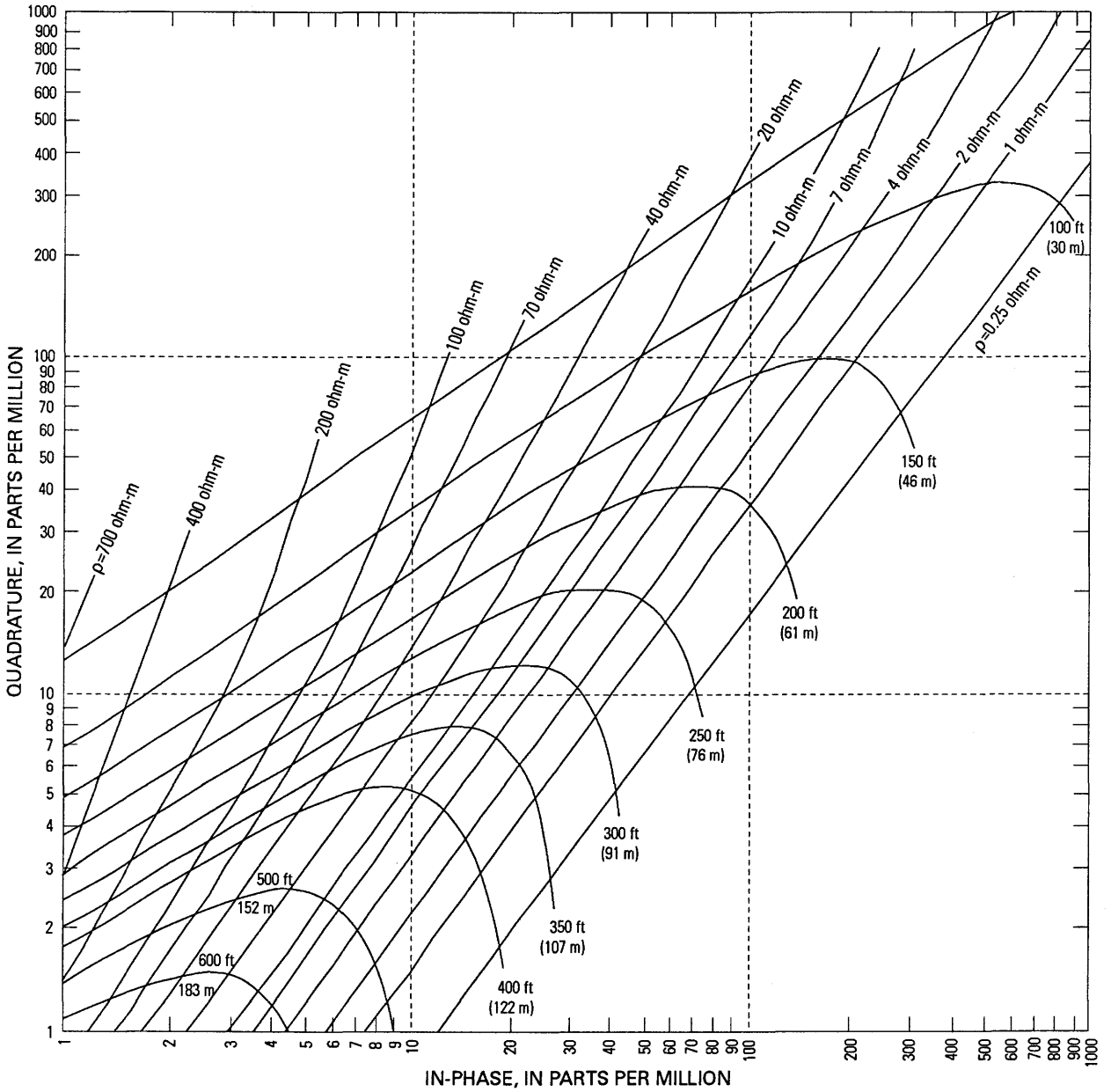

Figure 5. Phasor diagram for the pseudolayer half-space model for an 8-m transmitter-receiver coil separation operating at 900 Hz.

ohm-m. The thickness of the cover is 50 m. A 1-ohm-m target occurs within the lower layer. Figure 12 presents computed EM data for the model of figure 11 to which a few parts per million of noise have been added. Note the variable flying height; the 900- and 7200-Hz EM channels respond mainly to changes in flying height. The target is difficult to detect.

The apparent resistivities are computed using the half-space model. For both frequencies, the apparent resistivities are about 10 ohm-m, which is the true resistivity of the cover. The large variations in EM response are caused mostly by variations in flying height and are eliminated in the apparent resistivity parameters. It is this feature, the elimination of EM anomalies due to flying height variations, that makes the resistivity parameters so essential when flying in conductive environments.

Unfortunately, the 1-ohm-m target is barely visible on the apparent resistivity profiles in this example. The 50 m of 10-ohm-m cover is simply too much for the method, and the target is virtually undetectable. Using the same EM data and the two-layer inversion scheme, some hope emerges.

The results of the two-layer resistivity inversion are shown in the lower half of figure 12. The target is clearly visible and has a lower layer resistivity close to the true

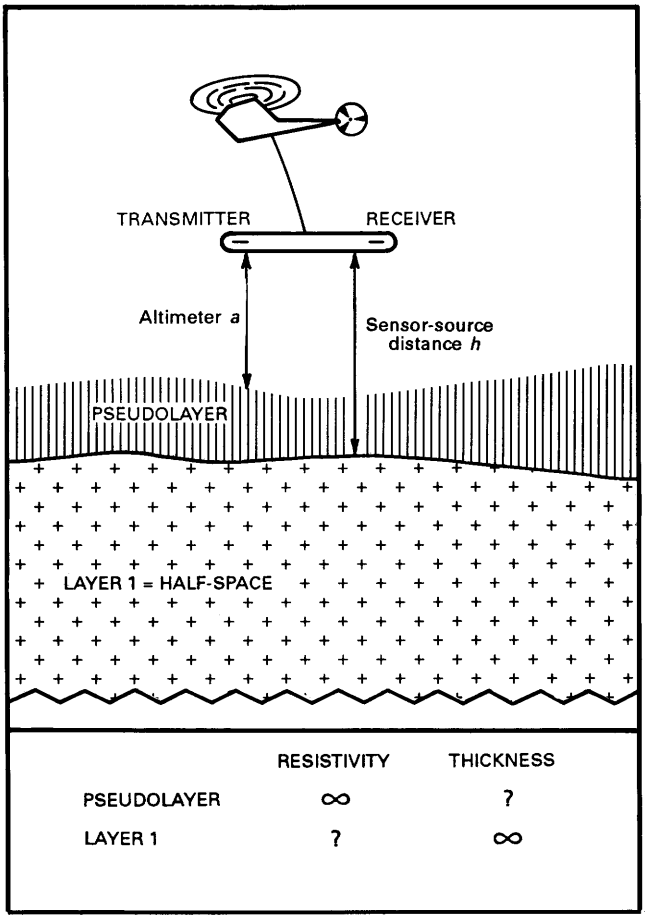

Figure 6. Pseudolayer half-space model employing a fictitious, highly resistive upper layer. This artifice is used to account for discrepancies between the computed sensor-source distance and the measured altitude.

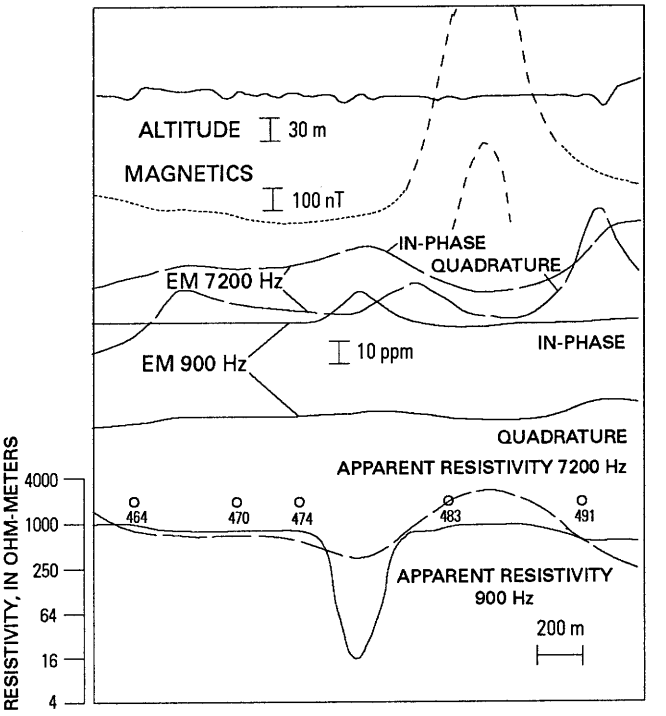

Figure 7. Computed resistivity profiles from a DIGHEM[III] survey over the Night Hawk test range, Ontario, Canada. EM channels from the coplanar coil-pairs are used to compute the apparent resistivity at each frequency. Numbered open circles are fiducials.

value of 1 ohm-m. The upper layer resistivity is shown correctly at 10 ohm-m. The thickness of the upper layer is shown correctly as 50 m over the conductor. The thickness estimate is less reliable over the bedrock of this example.

The two-layer inversion shown in figure 12 seems to be quite satisfactory over the target. Away from the target, spikes in the lower layer resistivity represent an attempt by the model to yield the true resistivity of the bedrock, 100 ohm-m. In this example, the two-layer inversion is unable to recognize the true resistivity of the bedrock except to see that it is more resistive than the cover. In this poorly determined case, it tends to default to 8,000 ohm-m.

Note that there is only one place on the two-layer resistivity profiles of figure 12 where the lower layer (bedrock) is more conductive than the upper layer (cover), and this is the target. Hence, the pseudolayer two-layer model technique identifies the target very well.

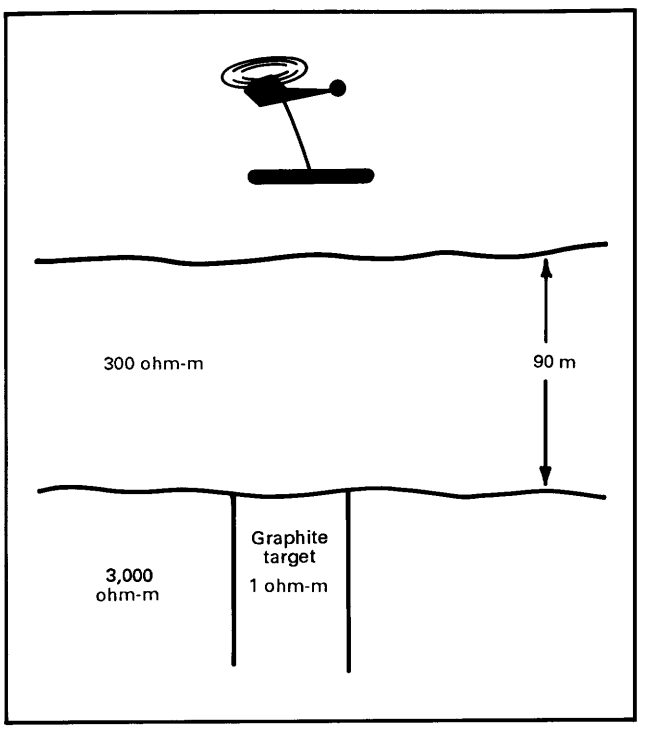

Figure 8. Schematic section through the Night Hawk conductor. The graphite target is almost wide enough (approximately 100 m) to mimic a two-layer case.

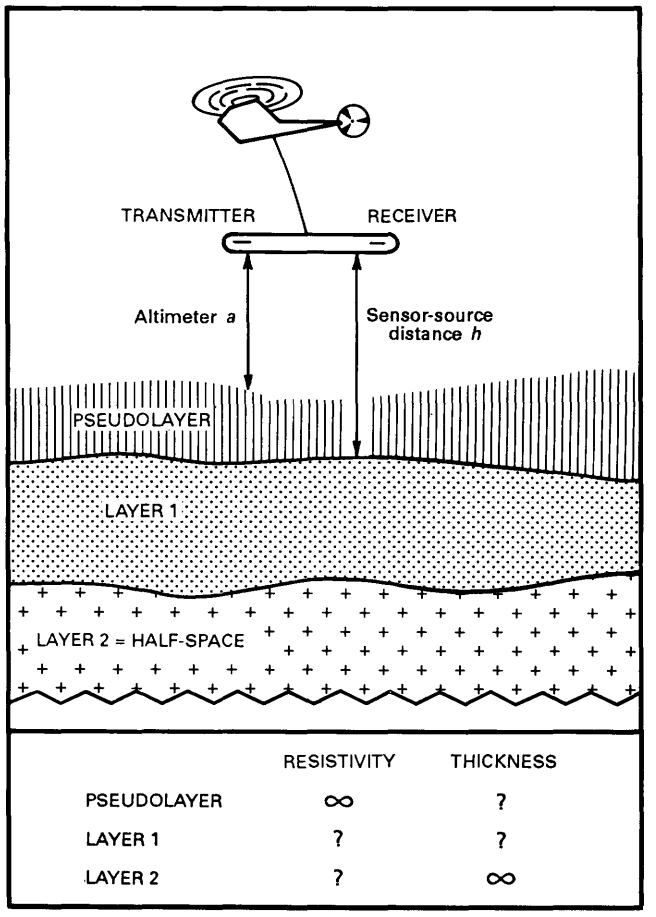

Figure 9. Pseudolayer two-layer model employing a fictitious, highly resistive upper layer to account for discrepancies between the computed sensor-source distance and the measured altitude.

CURRENT TECHNOLOGY

The DIGHEM^{IV} system shown in figure 13 has the highest frequency of the modern class of helicopter EM systems. In the system, there are three horizontal coplanar coil-pairs. A fourth coil-pair, the vertical coaxial, provides a geometric analysis of conductors (Fraser, this volume); however, for resistivity mapping purposes, only the horizontal coplanar coils will be considered.

The frequencies increase from 900 Hz by factors of eight: 900, 7200, and 56,000 Hz. The system can map half-space resistivities from less than 0.1 to greater than 20,000 ohm-m. It also allows more accurate inversions than systems that lack a high-frequency coil-pair.

Figure 14 shows an example of the DIGHEM^{IV} system over the Night Hawk test range. Only the coplanar EM channels are shown. The corresponding half-space resistivities are shown in the lower part of this figure.

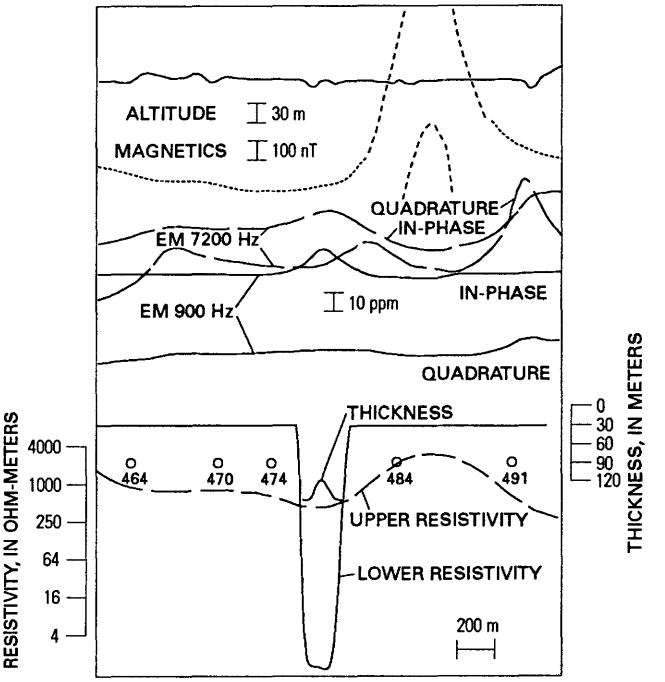

Figure 10. Two-layer inversion of the EM data shown in figure 7 for the Night Hawk section shown in figure 8. Numbered open circles are fiducials.

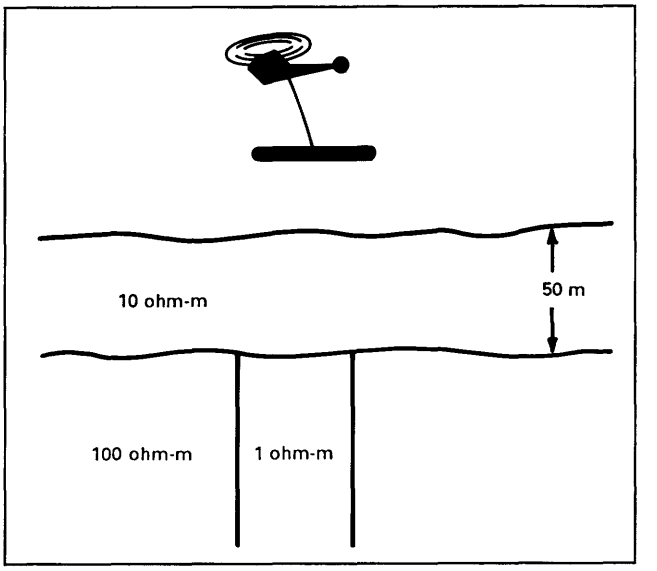

Figure 11. Model of a target (1 ohm-m) covered by a conductive overburden. The target is difficult to detect.

The graphite conductor target is buried beneath 90 m of glacial sand (fig. 8). On the resistivity profiles, the target can be seen most clearly at the lowest frequency of 900 Hz; the target is not seen at all at 56,000 Hz. This is desirable because, ideally, the high-frequency resistivity should define only the cover. Determination of the cover resistivity directly by the high frequency allows better

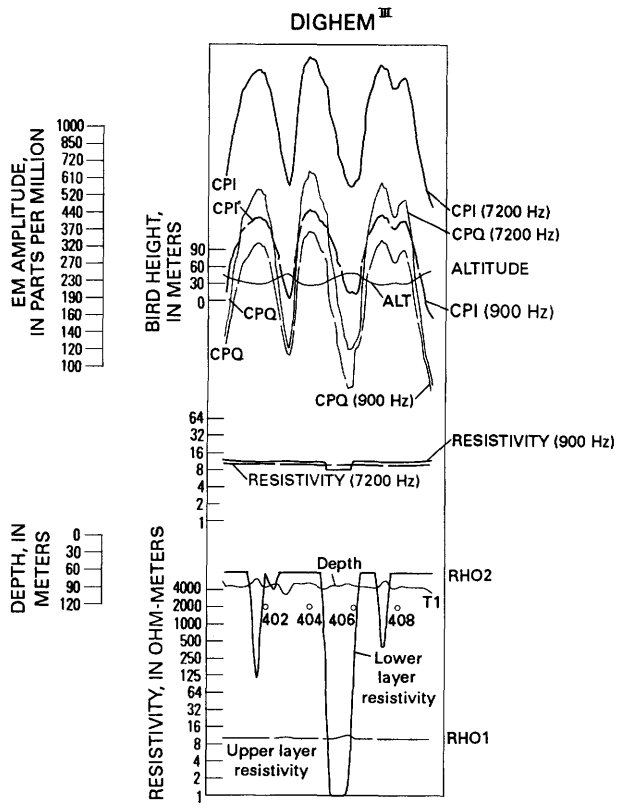

Figure 12. Computed EM data for the model shown in figure 11. In-phase (CPI) and quadrature (CPQ) for coplanar EM channels for 900 and 7200 Hz are shown in the top part of the figure; computed apparent resistivities are shown in the center of the figure; and results of two-layer inversion are shown in the lower part of the figure.

resolution of the upper and lower layer resistivities for a two-layer model and results in better definition of a conductive target under a conductive cover.

CONCLUSIONS

Resistivity mapping using an airborne EM system is accomplished by inverting measured data to yield resistivities according to half-space or layered-earth

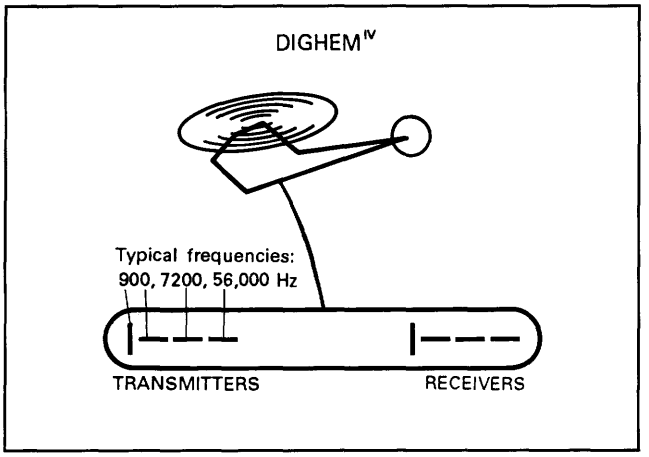

Figure 13. Orientation and frequencies of coil pairs in the DIGHEM^{IV} sensor. Frequencies of the horizontal coplanar coils increase approximately by factors of eight. This frequency spread facilitates determination of resistivity variations with depth.

models. The method eliminates EM anomalies generated by local decreases in flying height and identifies targets otherwise unrecognizable on the EM profiles. Target recognition and thus followup exploration decisions are improved.

REFERENCES CITED

Fraser, D.C., 1978, Resistivity mapping with an airborne multicoil electromagnetic system: Geophysics, v. 43, p. 144–172.

——— 1986, Dighem resistivity techniques in airborne resistivity mapping, *in* Palacky, G.J., ed., Airborne resistivity mapping: Geological Survey of Canada Paper 86–22, p. 49–54.

Palacky, G.J., Annan, A.P., Barlow, R.B., Bazinet, R., Paterson, N.R., and Rathew, A.R., 1986, Panel discussion, *in* Palacky, G.J., ed., Airborne resistivity mapping: Geological Survey of Canada Paper 86–22, p. 181–192.

Paterson, N.R., and Reford, S.W., 1986, Inversion of airborne electromagnetic data for overburden mapping and groundwater exploration, *in* Palacky, G. J., ed., Airborne resistivity mapping: Geological Survey of Canada Paper 86–22, p. 39–48.

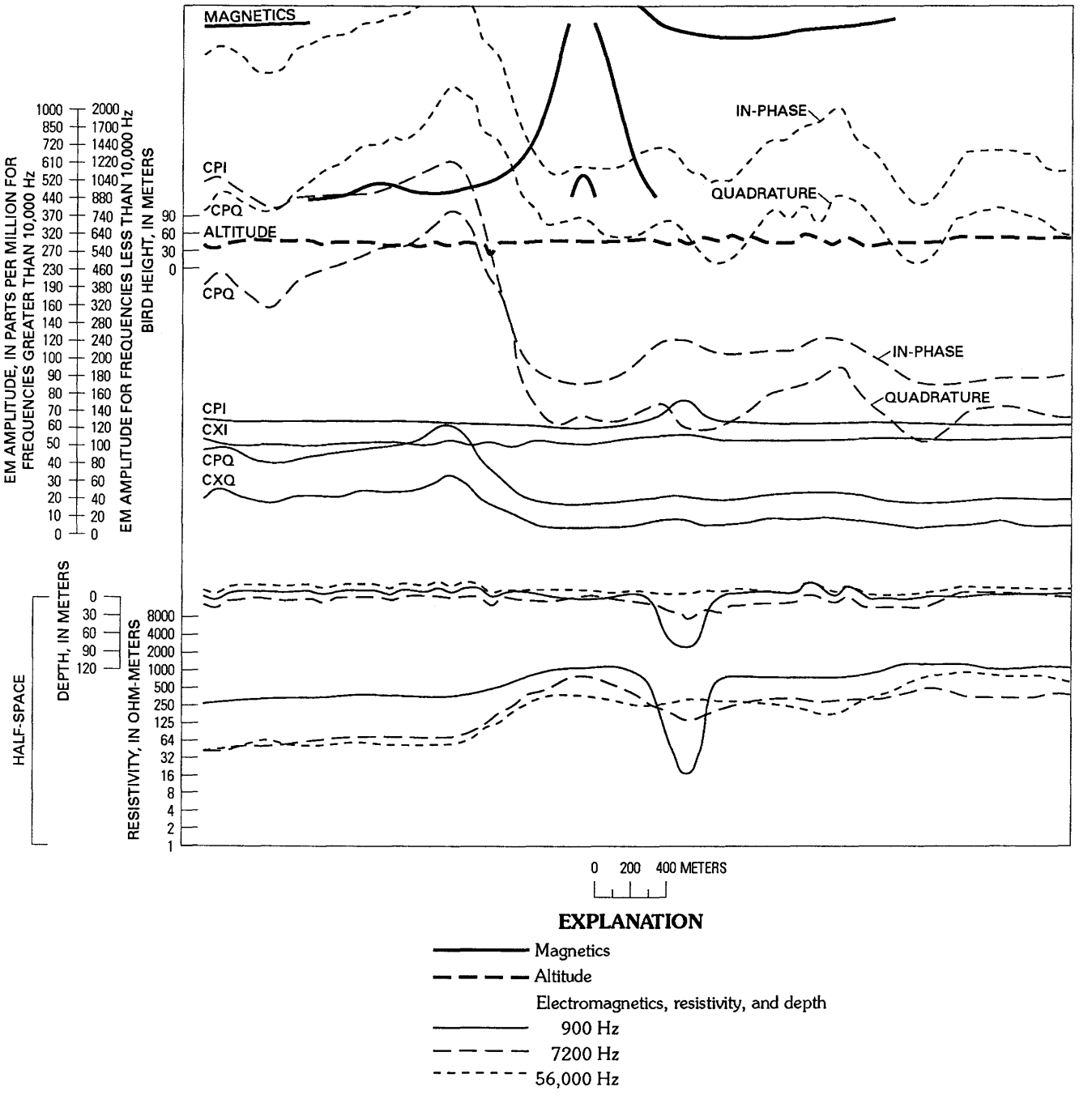

Figure 14. DIGHEM[IV] results over the Night Hawk test range shown in figure 8. CPI, coplanar in-phase; CPQ, coplanar quadrature; CXI, coaxial in-phase; CXQ, coaxial quadrature.

Applications of a New Three-Dimensional Modeling Program to Airborne Electromagnetic Exploration

By Gerald W. Hohmann[1]

Abstract

A versatile three-dimensional numerical modeling program based on an integral equation solution computes the frequency or transient response of one or more three-dimensional bodies in a layered earth. Incorporating divergence-free basis functions allows calculation of accurate results for any conductivity contrast. The basic source is an electric dipole, which can be used to synthesize a loop or a grounded wire source. For airborne electromagnetic computations, the air between the transmitter and the earth is represented by a very high resistivity layer; thus, modifications to the code are minimal. Comparisons with results computed by numerical integration for a layered-earth model show that the airborne electromagnetic results are valid for both horizontal and vertical source loops.

Extensive results for ground configurations illustrate some of the important applications of the program. New insight is provided into the relation between galvanic and vortex responses and into the effect of conductive overburden, particularly when such overburden is in contact with a three-dimensional conductor. The program can simulate large complex bodies, a feature important for airborne work because results for conductors in the earth presently are limited to thin sheets. Surprisingly, small induced polarization responses in surficial conductive patches can profoundly affect short-offset transient responses. Calculations show the advantage of measuring the magnetic field rather than its time derivative in airborne electromagnetic studies where measurements can only be made at early times. Finally, the program has been used to evaluate a rapid one-dimensional inversion technique that possibly could be modified for airborne work.

INTRODUCTION

Three-dimensional model studies can provide much-needed insight for airborne electromagnetic (EM) interpretation, and I will try to illustrate this point by using our computed results for ground EM applications. After a series of improvements over a number of years by myself and several students at the University of Utah, we now have an EM modeling program that computes accurate responses for three-dimensional bodies of arbitrary conductivity contrast in a layered earth. The program is based on an integral equation formulation and is easily modified for airborne simulations. Computation times can be quite high for large or shallow bodies, but the cost is easily justified by the insight produced.

In this paper I briefly discuss the theoretical formulation and the modifications that permit airborne EM simulations. I then review the relationship between vortex and galvanic responses and give several examples from model studies for ground EM that illustrate the kinds of insight that can be produced.

Acknowledgments.—Funding for these model studies was provided by a consortium of companies, including Amoco Production Company, Arco Oil and Gas Company, Chevron Resources, CRA Exploration, and Unocal Corporation. Frank Frischknecht generously provided computer time on the U.S. Geological Survey VAX 11/780 computer for many of the calculations, and Walter Anderson provided valuable programming assistance. In Frank's untimely death we have lost a supporter, a respected colleague, and a good personal friend.

THREE-DIMENSIONAL MODELING TECHNIQUE

At the University of Utah, we have developed two very useful three-dimensional modeling programs for controlled-source EM. The first, based on a time-stepping integral equation solution described by SanFilipo and Hohmann (1985), is for a three-dimensional prism in an otherwise homogeneous earth. SanFilipo and Hohmann introduced the concept of divergence-free basis functions, composed of closed tubes of current, that make possible accurate computations for general three-dimensional bodies at any conductivity contrast. Earlier, Lajoie and West (1976) had identified and solved the problems associated with integral equation solutions for high-contrast three-dimensional plates.

[1]Department of Geology and Geophysics, University of Utah, Salt Lake City, Utah 84112.

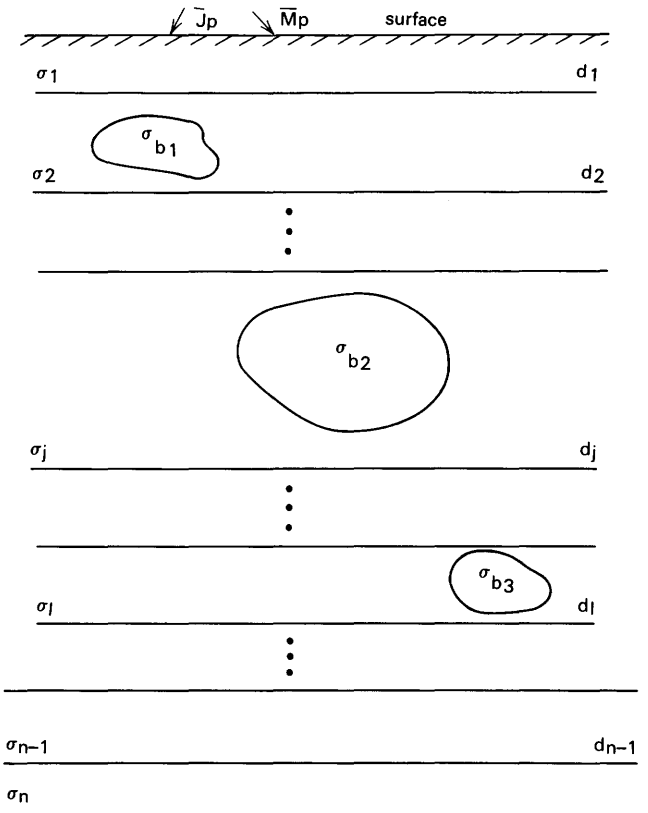

Figure 1. General model for several three-dimensional bodies in an arbitrarily layered earth. $\mathbf{J}_p$ and $\mathbf{M}_p$ *denote* impressed electric and magnetic sources, respectively; σ_i denotes conductivity; d_i is the interface depth.

Our second, more advanced program is based on a frequency-domain formulation that utilizes similar divergence-free basis functions (Newman and Hohmann, 1988). It is more general however, in that it computes responses of multiple three-dimensional bodies in a layered earth. Transient EM (TEM) results are calculated by inverse Fourier transformation using 20–40 frequency-domain values. Figure 1 shows the model configuration; several three-dimensional bodies reside in an arbitrarily layered earth. Here $\mathbf{J}_P$ and $\mathbf{M}_P$ denote impressed electric and magnetic sources, respectively. For the numerical solution, the bodies are taken to be right-rectangular prisms composed of N prismatic cells of constant current and M closed tubes of current flowing normal to the x-, y-, and z-axes.

The basic integral equation describing the problem is

$$\mathbf{E}=\mathbf{E}_p-i\omega\mu_o\mathbf{A}-\nabla V, \tag{1}$$

where the vector potential contribution is given by

$$\mathbf{A}(\mathbf{r})=\int G(\mathbf{r},\mathbf{r}')\,\mathbf{J}_s(\mathbf{r}')dv', \tag{2}$$

and the scalar potential contribution is given by

$$V(\mathbf{r})=-(1/\sigma^*)\int G(\mathbf{r},\mathbf{r}')\nabla\cdot\mathbf{J}_s(\mathbf{r}')dv'. \tag{3}$$

Here $\mathbf{E}$ is the total electric field, $\mathbf{E}_p$ is the primary (half-space) field, $\mathbf{J}_s=(\sigma-\sigma^*)\mathbf{E}$ is the scattering current in the body, and σ^* is the background conductivity. The integral is over the volume of the body. Once the scattering current has been determined, the electric and magnetic fields can be computed at any point.

The problem at high conductivity contrasts can be illustrated by writing equation (1) in operator notation:

$$\mathrm{Z}(\mathbf{J}_s)=\mathbf{E}_p, \tag{4}$$

where the impedance operator Z is composed of three operators; that is,

$$Z(\mathbf{J}_s)=R(\mathbf{J}_s)+L_A(\mathbf{J}_s)+L_V(\mathbf{J}_s). \tag{5}$$

Here R represents the first term in equation (1), L_A represents the vector potential, and L_V represents the scalar potential.

Simply using pulse basis functions alone, meaning that the body is represented by N cells in each of which the scattering current is constant, does not work at conductivity contrasts on the order of 200 or higher because of the disparity in the operators in equation (5). To get an idea of the magnitude of this disparity, we can approximate the operators for a sphere of conductivity $\sigma=1$ S/m and radius $a=10$ m in a 0.001-S/m whole space. Assuming that the scattering current is constant in the sphere, we find that $R\approx 1/\sigma=1$, $L_A\approx\omega\mu_o a^2=0.1$, and $L_V\approx 1/3\sigma^*=300$ for a frequency of 100 Hz. The source of the problem is now apparent: for low background conductivities, information from the induction operator L_A is lost due to the dominance of the galvanic operator L_V, and finer discretization will not help. Fortunately, incorporating divergence-free basis functions composed of M closed tubes of current and utilizing a Galerkin solution solves the problem. The details of this solution were described by Newman and Hohmann (1988).

The basic source in the program is an electric dipole, which can be used to synthesize either a loop or a grounded wire. For airborne EM computations, we simply represent the air between the transmitter and the earth by a very resistive layer, as illustrated in figure 2. Thus, modifications to the code are minimal.

In representing the horizontal loop source, electric dipole contributions are summed around the loop. It is important to ignore grounding terms in order to avoid numerical problems. Because a horizontal magnetic dipole, such as that used in helicopter applications, produces only a transverse electric (TE) field, the

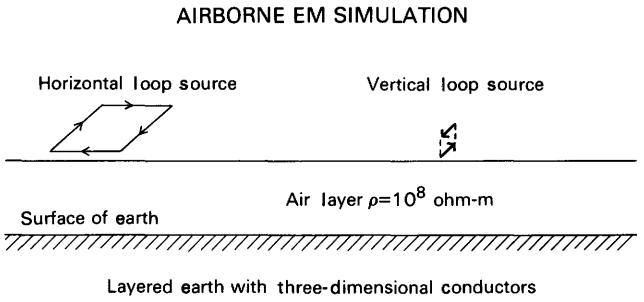

Figure 2. Model for adapting three-dimensional algorithm for airborne electromagnetic computations.

secondary field of such a source can be represented as due to the superposition of two oppositely directed horizontal electric dipoles with only the TE terms included as illustrated in figure 2. The vertical electric dipoles that would represent the other sides of the vertical dipole are excluded because theirs is a transverse magnetic (TM) field.

Initial comparisons with results for a layered earth computed by numerical integration show that our airborne EM results are valid for both horizontal and vertical loops. We have not tried the method for three-dimensional models in airborne applications because we have not yet procured funding for these studies.

VORTEX AND GALVANIC RESPONSES

Probably the most significant advance in electromagnetic methods in the last decade has been the general recognition and documentation of galvanic effects. Electromagnetic responses are a combination of induction due to closed loops of current (vortex currents) and current channeling due to charges on the surfaces of bodies. The former occurs even for a conductor in free-space and hence is dominant in very resistive environments, whereas the latter becomes relatively more important as the resistivity of the host decreases.

However, virtually all interpretation aids for airborne EM are based on numerical or scale model results for thin conductors in free-space. Because galvanic responses can be large even if the resistivity of the earth is as high as 1,000 ohm-m, crucial insight can be gained by studying model results for realistic cases.

Figure 3 illustrates schematically the geometry of vortex currents in a thin plate in free-space. When the current in the transmitting loop is terminated abruptly, currents immediately flow in the conductor as shown in order to preserve the magnetic field. These currents have an associated magnetic field. As time progresses, the currents decay to zero.

On the other hand, if the source loop is on or above a conductive half-space, currents are induced in the half-space when the transmitter current is shut off. These

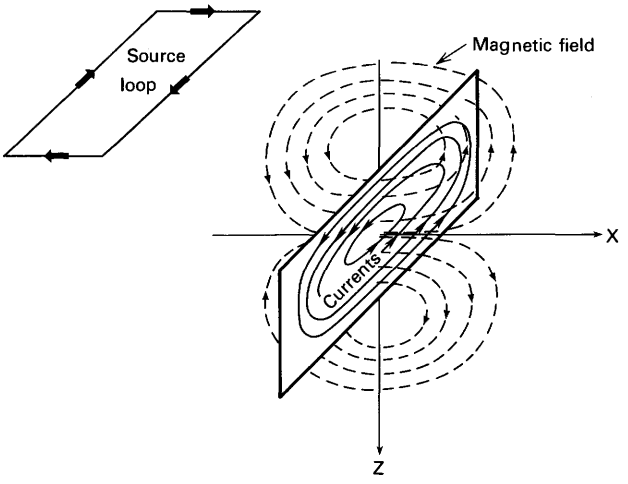

Figure 3. Schematic illustration showing geometry of vortex currents (solid lines) and associated magnetic field (dashed lines).

currents are channeled into a conductor, as shown in figure 4. The result is a magnetic anomaly that is fundamentally different in both geometry and in frequency or transient response. In the time domain, vortex responses decay exponentially, whereas galvanic responses decay according to a power law that is related to the decay of the electric field in the half-space.

EXAMPLES OF GALVANIC EFFECTS

Figure 5 dramatically illustrates the difference between the geometries of galvanic and vortex responses. The anomaly shown is caused by a horizontal conductor, 90 m deep and 400 m in strike length, in a 300-ohm-m earth. The source is a 300 m by 600 m fixed loop to the

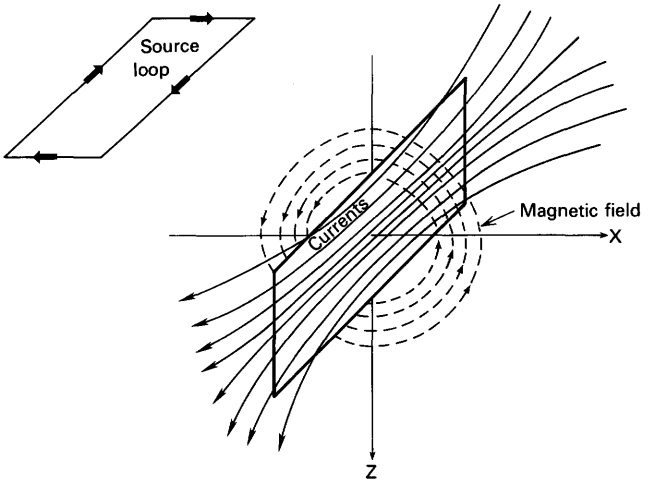

Figure 4. Schematic illustration showing geometry of galvanic currents (solid lines) and associated magnetic field (dashed lines).

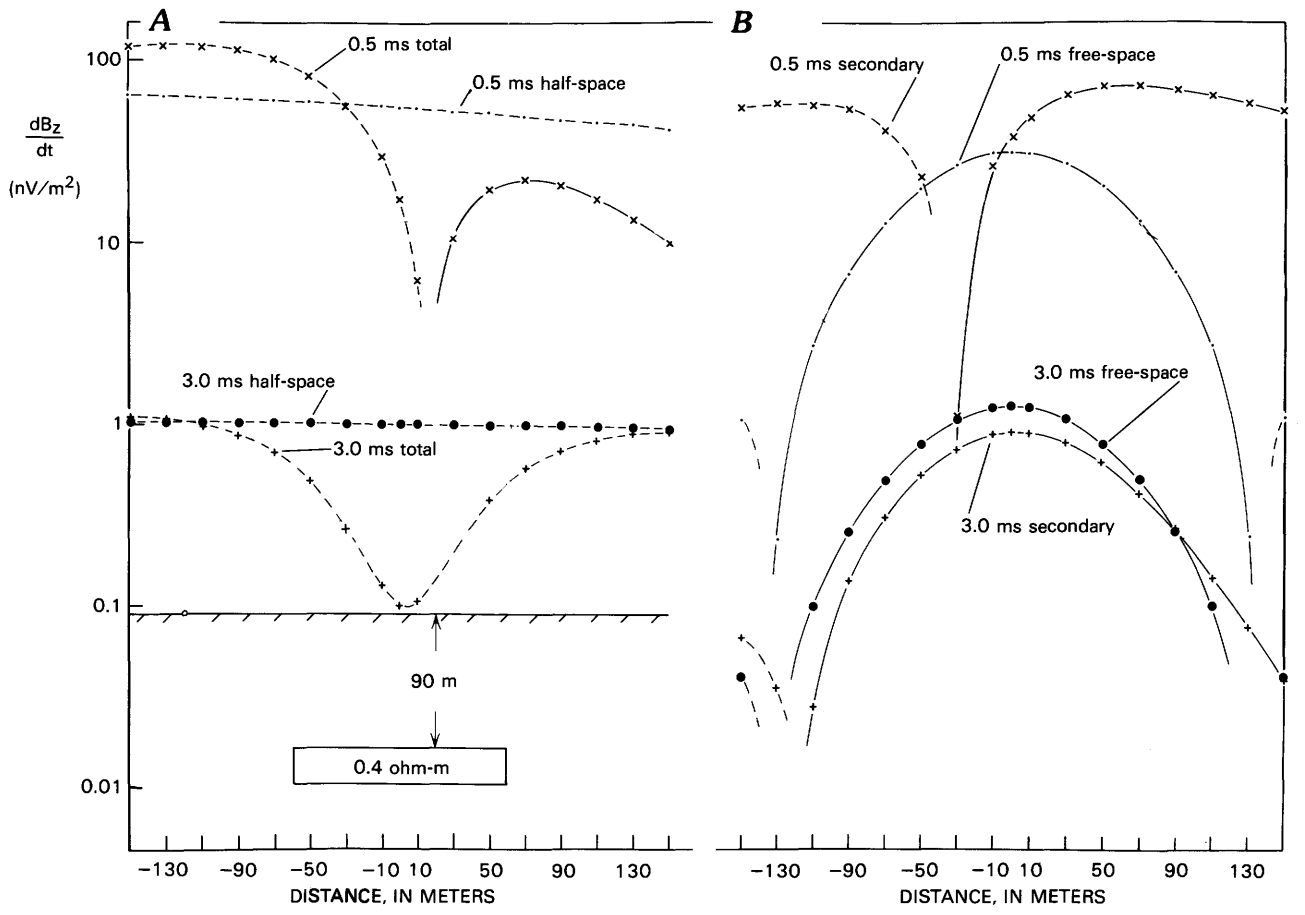

Figure 5. Transient EM profiles for a horizontal conductor with a fixed source. The conductor is 20 m thick and 120 m wide and has a strike length of 400 m. Solid curves denote positive values and dashed curves denote negative values. *A*, Total and half-space fields. *B*, Comparison of secondary fields with those of the same body in free-space. Modified from SanFilipo and others (1985).

left of the body, with its near edge shown by the small circle at the surface of the earth in figure *5A*. Profiles of the time derivative of the vertical magnetic field are shown for two times after the current in the transmitter is shut off.

Galvanic responses for a horizontal body produce crossovers in the vertical magnetic field because the responses are due to channeled currents flowing in one direction. Vortex responses, on the other hand, result in peak anomalies because they are due to closed loops of current flowing horizontally. Typically, galvanic responses dominate at early and late times, and vortex responses are important at intermediate times. Figure *5A* shows a galvanic response at 0.5 ms and a vortex response at 3 ms for a conductor in a 300-ohm-m half-space.

Scattered fields for the same conductor in free-space and in a 300-ohm-m half-space are compared in figure *5B*. The profiles are fundamentally different at 0.5 ms; interpretations based on free-space models would erroneously indicate a vertical conductor. At 3 ms, induction dominates the response of the conductor in the 300-ohm-m half-space, and the profiles are similar to those for a conductor in free-space.

The effect of a conductive host are further illustrated in figure 6, which shows decay curves for the model of figure 5 for five host resistivities, including that of free-space. The time derivative of the vertical magnetic field is shown in figure *6A*, and the time derivative of the horizontal magnetic field is shown in figure *6B*.

Large current channeling effects are apparent at early times for all host resistivities, even 1,000 ohm-m. Host resistivities of 300 ohm-m or higher yield exponential decays at late times, as in the case of a free-space host. For half-space resistivities of 100 ohm-m and 30 ohm-m, however, the response is dominantly galvanic throughout the range and late-time decays conform to power laws. Due to geometric effects, the secondary field at late time may be smaller than the free-space response.

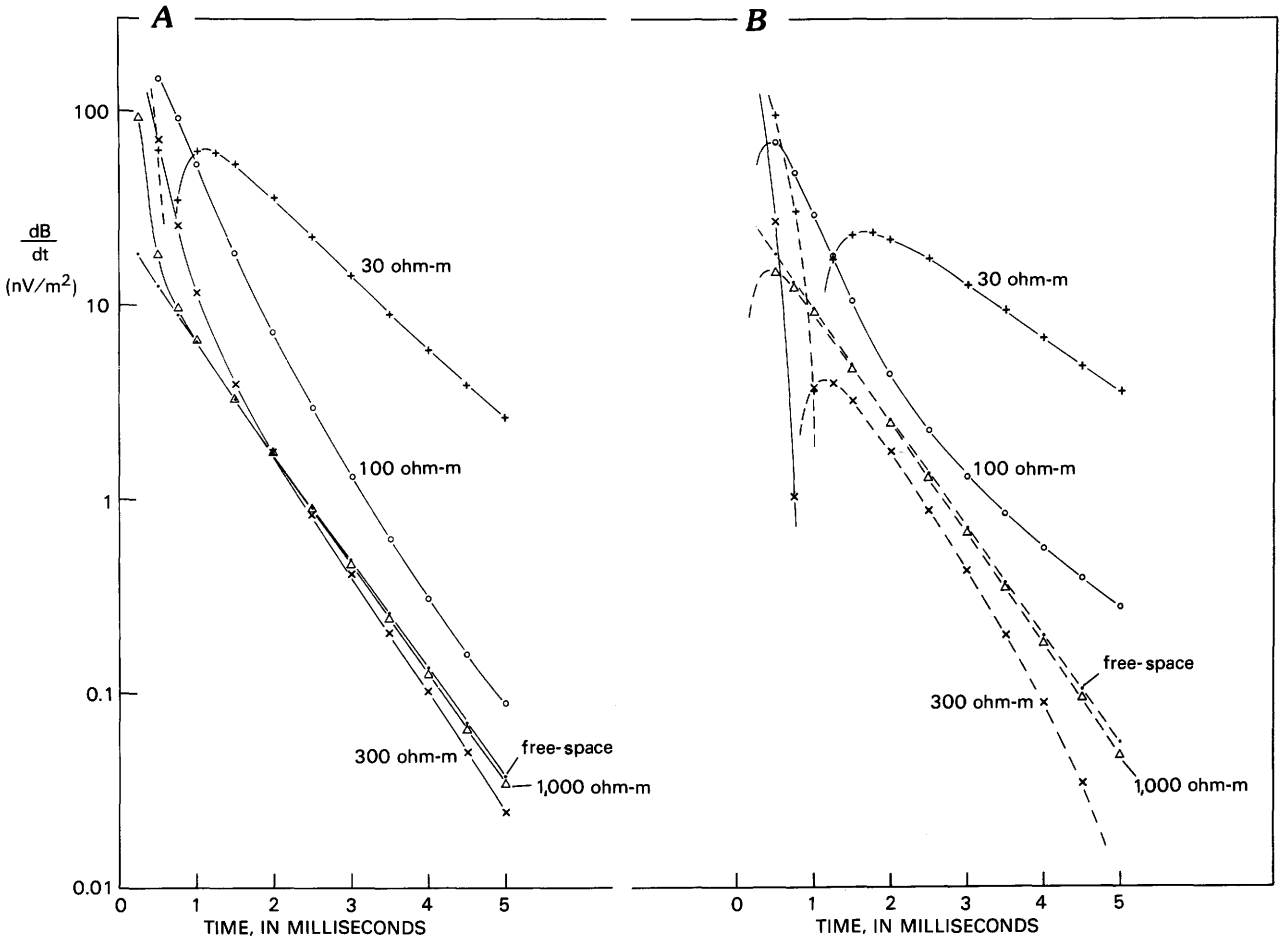

Figure 6. Decay curves at position x=70 m for the model shown in figure 5. *A*, Vertical component. *B*, Horizontal component.

If a buried conductor is in contact with a conductive overburden, currents induced in the overburden are channeled into the conductor and produce a large anomaly if the overburden is not too thick (fig. 7). In figure *7A*, the 10-ohm-m overburden is only 20 m thick and thus is not in contact with the 1-ohm-m conductor at a depth of 40 m. In figure *7B*, the overburden is 40 m thick and thus is in contact with the conductor. Note the large increase in response in figure *7B*, even though the overburden is twice as thick as in figure *7A*.

SIGNAL-TO-GEOLOGIC NOISE RATIOS

Airborne EM surveys commonly are limited by geologic noise, defined as responses of conductors other than those of interest. Eaton and Hohmann (1987) compared signal-to-geologic noise ratios for various ground configurations and for time and frequency domains. As an example with relevance to the airborne case, figure 8 shows the ratio of the response of a vertical tabular conductor to that of its surrounding half-space for a 160 m by 160 m coincident loop configuration. The conductor is a 1-ohm-m prism buried 80 m deep in a 500-ohm-m half-space. It is 80 m wide and has a depth extent of 240 m and strike length of 480 m.

Figures *8A* and *B* show transient impulse and step responses, respectively, plotted in pseudosection form with time increasing downward. The impulse response corresponds to the usual procedure of measuring the time derivative of the magnetic field after the current is shut off, whereas the step response corresponds to measuring the magnetic field. Peak signal-to-noise ratios, defined as the ratio of the target response to the half-space response, are slightly higher for the impulse response. More importantly for airborne applications, however, the peak signal-to-noise ratio occurs earlier for magnetic field measurements—in this case, 3 ms instead of 5 ms. Hence, for transient airborne EM, where measurements can be made only at relatively early times, it probably is advantageous to measure the magnetic field rather than its time derivative, as suggested by Sarma and others (1976).

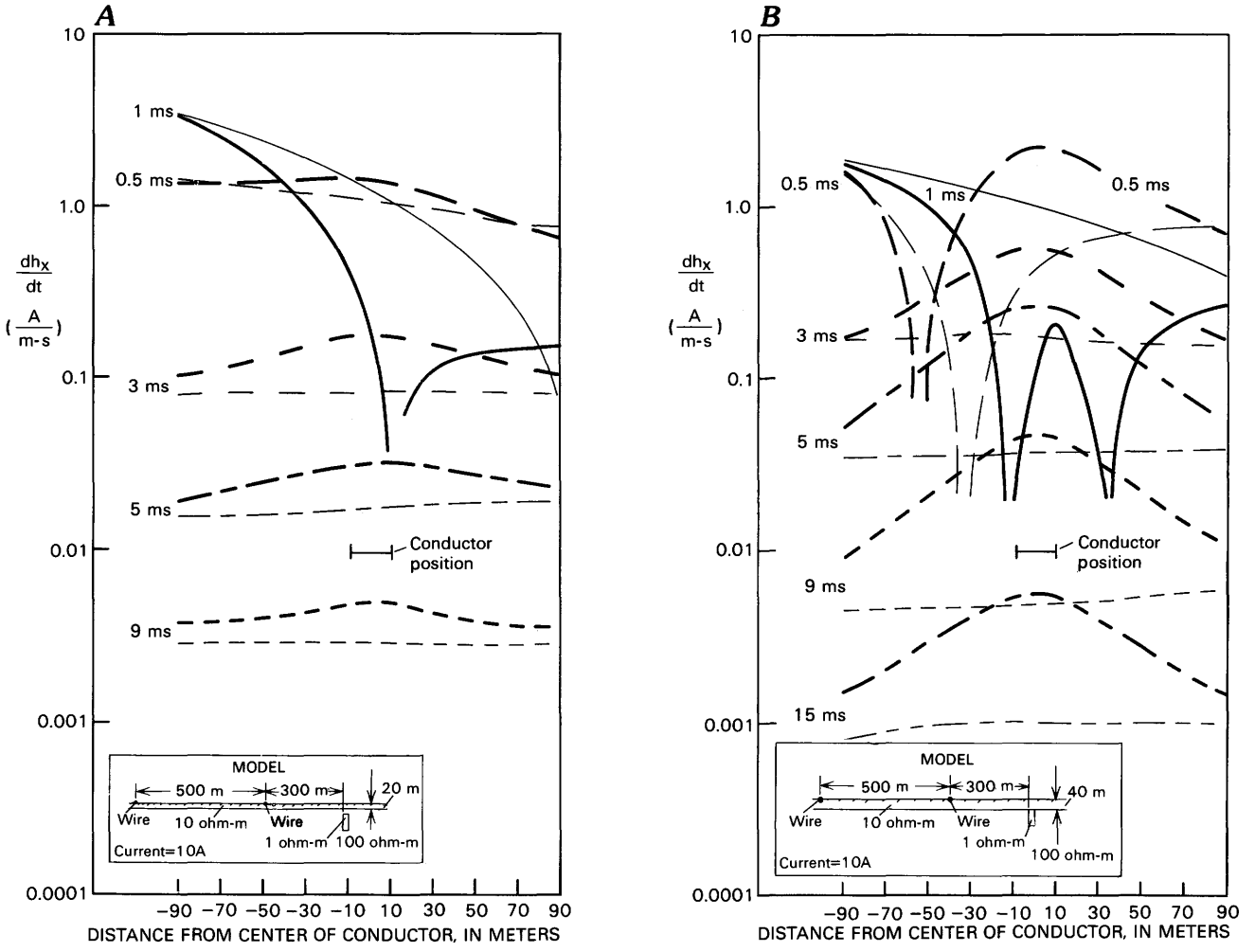

Figure 7. Effect of current channeling from overburden. *A*, Conductor not in contact with overburden. *B*, Conductor in contact with overburden. The thin solid and dashed lines show the half-space response for comparison. Modified from Newman and others (1986).

In-phase and out-of-phase results in the frequency domain are illustrated in figures *8C* and *D*, respectively. The lower signal-to-noise ratios for these results, especially the out-of-phase, demonstrate the advantage of transient measurements for towed-bird systems. Furthermore, the results indicate that in-phase measurements will have much better signal-to-geologic noise characteristics than quadrature measurements for rigid-boom frequency-domain systems.

Figure 9 shows three-dimensional modeling results that explain the sign changes commonly observed in in-loop transient EM surveys. Dashed lines at 1 ms and later indicate negative voltages. These central-loop results were calculated for a 100 m by 100 m transmitting loop moved across a 300 m by 300 m conductive body at the surface of the earth. The body is 50 m thick and has a resistivity of 30 ohm-m; the resistivity of the surrounding earth is 300 ohm-m. The body is polarizable; its induced polarization (IP) response is characterized by the following Cole-Cole parameters: $m = 0.1$, $c = 0.25$, and $\tau = 1$ ms. This Cole-Cole model simulates a realistic clay response having a maximum phase of 10 mrad at 200 Hz and phase angles of 5–7 mrad in the conventional IP range from 0.1 to 1 Hz. Amazingly, this small polarizability causes a sign change beginning at 1 ms.

We computed the response of the same body having no IP response; in that case, there is no anomaly at times later than 1 ms. The early-time positive anomaly due to the increased conductivity is virtually identical to that shown in figure 9 at 0.1 and 0.3 ms. Increasing the resistivity of the body to that of the surrounding half-space but retaining its polarizability results in slightly depressed values at late times and no negative responses. These large IP effects occur only for surficial, polarizable bodies that are conductive as compared to the surrounding earth and only for measurements inside or very close to the transmitting loop. Although it is not clear whether IP effects would be seen in airborne EM

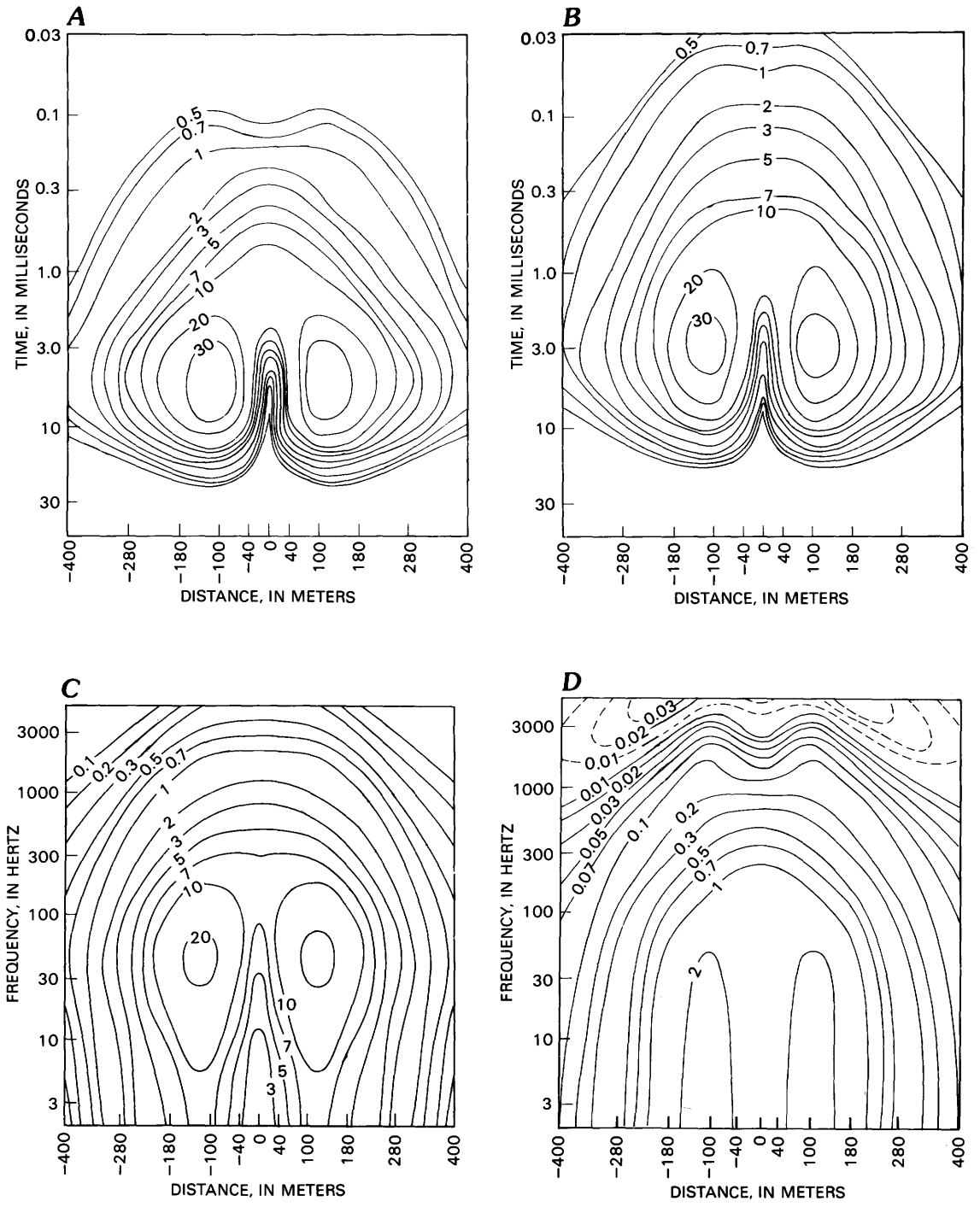

Figure 8. Signal-to-geologic noise ratios for three-dimensional conductor in 500-ohm-m earth. *A*, impulse response; *B*, Step response; *C*, In-phase; *D*, Quadrature, dashed lines are negative values.

measurements, the possibility should be investigated using three-dimensional modeling.

Figure 10 is included for two reasons. First, it illustrates the kind of complex three-dimensional model for which results can be computed using our integral equation algorithm. The model consists of a 50-ohm-m basement overlain by a thick 1,000-ohm-m unit and a thin (50 m) layer of 100-ohm-m overburden. The basement contains an anticlinal feature having a strike length of 3,000 m and relief of 600 m. For this ground application, the model is intended to simulate the case of volcanic flow rocks overlying a potential hydrocarbon trap in the underlying sedimentary rocks. For analyzing airborne resistivity mapping, such a structure might represent a buried bedrock ridge.

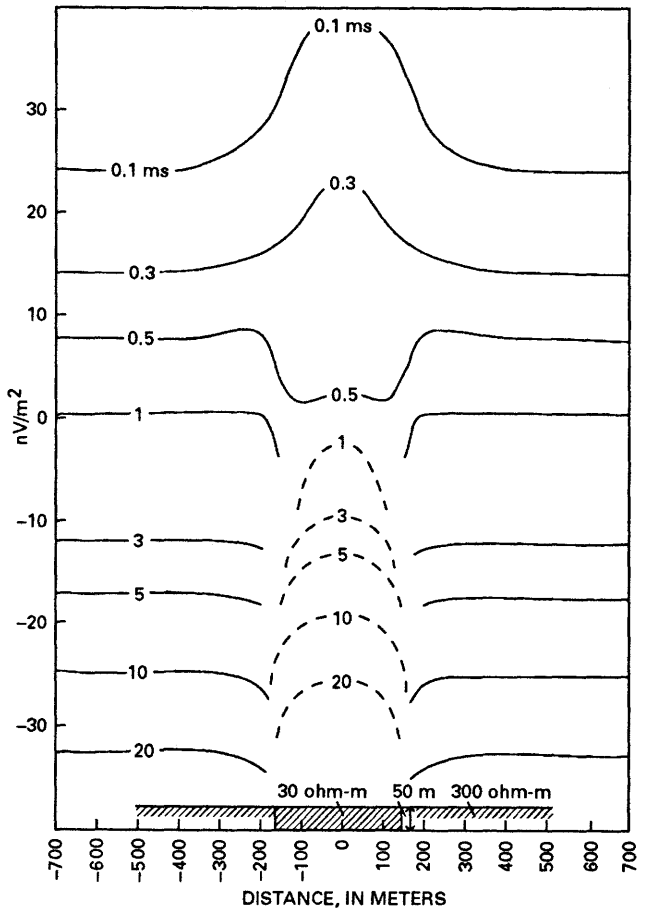

Figure 9. Central loop profiles showing negative values at late times due to surficial, conductive, polarizable body.

Second, figure 10 illustrates results from a rapid inversion technique (Eaton and Hohmann, in press) that may have applications in airborne work. An image of the transmitting loop, which is at the surface of the earth, is assumed to move downward, in free-space, after the current in the loop is shut off. The position of the loop at each time is determined by matching its magnetic field with the measured transient EM response. A continuous resistivity profile with depth then is estimated by using the velocity of the image. In figure 10, these estimated resistivities are contoured for a series of 1 km by 1 km transmitting loop positions along a profile across the center of the structure. The contours show the anticlinal feature, although resolution is poor. Because the inversion procedure is so rapid, it may be possible to adapt it to airborne EM profiling.

CONCLUSIONS

Three-dimensional model studies using an integral equation program valid for any conductivity contrast can provide a great amount of insight for ground electromagnetics. The program is easily adapted to airborne simulations with minimal modifications of the code and could be used to significantly improve interpretation and system design capabilities.

REFERENCES CITED

Eaton, P.A., and Hohmann, G.W., 1987, An evaluation of electromagnetic methods in the presence of geologic noise: Geophysics, v. 52, p. 1106–1126.

_____ in press, A rapid inversion technique for transient electromagnetic soundings: Physics of the Earth and Planetary Interiors.

Lajoie, J.J., and West, G.F., 1976, The electromagnetic response of a conductive inhomogeneity in a layered earth: Geophysics, v. 41, p. 1133–1156.

Newman, G.A., and Hohmann, G.W., 1988, Transient electromagnetic responses of high-contrast prisms in a layered earth: Geophysics, v. 53, p. 691–706.

Newman, G.A., Hohmann, G.W., and Anderson, W.L., 1986, Transient electromagnetic response of a three-dimensional body in a layered earth: Geophysics, v. 51, p. 1608–1627.

SanFilipo, W.A., Eaton, P.A., and Hohmann, G.W., 1985, The effect of a conductive half-space on the transient electromagnetic response of a three-dimensional body: Geophysics, v. 50, p. 1144–1162.

SanFilipo, W.A., and Hohmann, G.W., 1985, Integral equation solution for the transient electromagnetic response of a three-dimensional body in a conductive half-space: Geophysics, v. 50, p. 798–809.

Sarma, D.G., Maru, V.M., and Varadarajan, G., 1976, An improved pulse transient airborne electromagnetic system for locating good conductors: Geophysics, v. 41, p. 287–299.

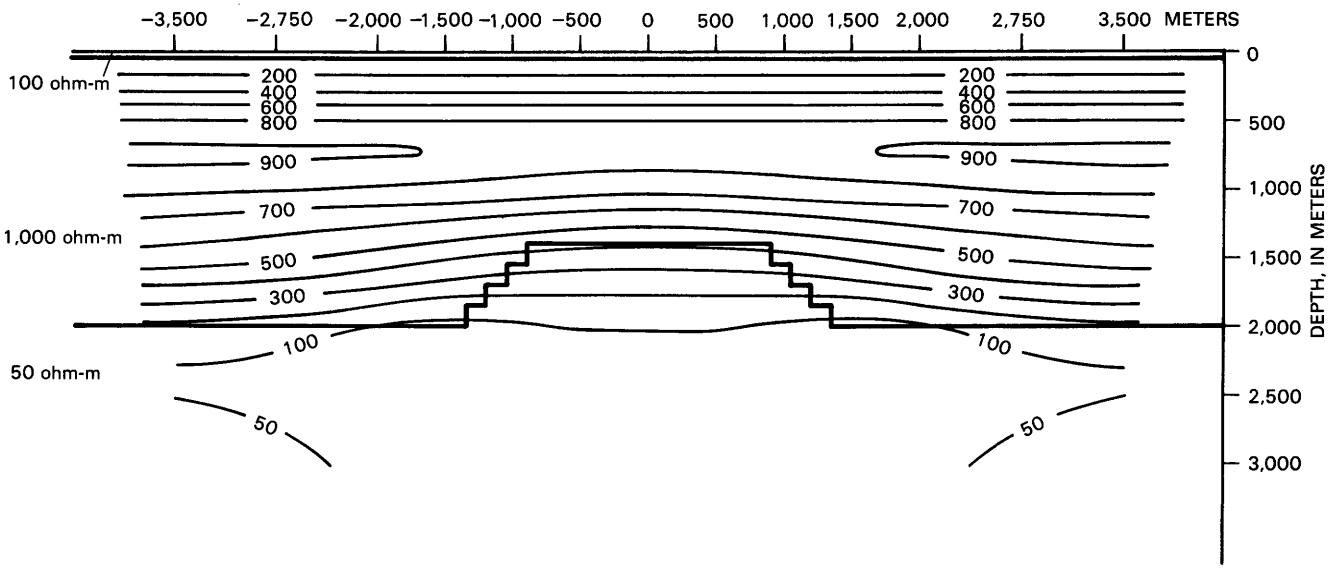

Figure 10. Rapid inversion results for theoretical data over a three-dimensional structural model (thick lines). Contours are in ohm-meters.

Electromagnetic Anomaly Recognition Within Geological and Cultural Noise

By Douglas C. Fraser[1]

Abstract

All airborne electromagnetic (EM) systems work more or less on the same principle and have two objectives when engaged in mineral exploration surveys—to recognize conductors and to categorize their anomalies in some meaningful fashion. Unfortunately, many anomalies that could lead to an ore discovery are masked by undesirable responses. These may be caused by powerlines, fences, and other sources of cultural noise or by geological features.

Some multicoil helicopter EM systems have design features that focus on identification of targets within noisy environments. For example, the positive in-phase response of a conductor can be masked by the negative in-phase response caused by magnetic polarization, or the quadrature response can be masked by the response of conductive overburden. In both of these cases, the response of the target can be obtained by subtracting the scaled-down coplanar response from the coaxial response, assuming both transmitter coils operate at approximately the same frequency.

The response of a desirable target may be distinguishable from large geological and cultural noise responses on the basis of resistivity signatures. A conductive orebody may yield EM signals that are smaller than those from a less conductive, but wide geological formation. In such a situation, the orebody can be well defined because its computed resistivity value will be lower than that of the geological formation.

INTRODUCTION

Electromagnetic (EM) exploration involves the evaluation of a conductor by analyzing its response to transmitted fields of various frequencies or to its time-domain equivalent. Most EM systems employ transmitted fields that are of the same direction (for example, from a vertical dipole). Implicit in such systems is the assumption that the conductivities of the target and the environment are the primary parameters of interest.

A multigeometry method of analysis, introduced by Fraser (1979) for rigidly coupled helicopter EM systems, involves analysis of the response of a conductor to more than one direction of the transmitted field. The transmitted fields have approximately the same frequency because geometry is the only variable in this technique. Analysis of multigeometry data may be more germane than analysis of multifrequency data because the shape of a conductor commonly is more relevant to an exploration program than its conductivity. For example, a poorly conductive orebody and a swamp may have similar conductivities but usually have dramatically different geometries.

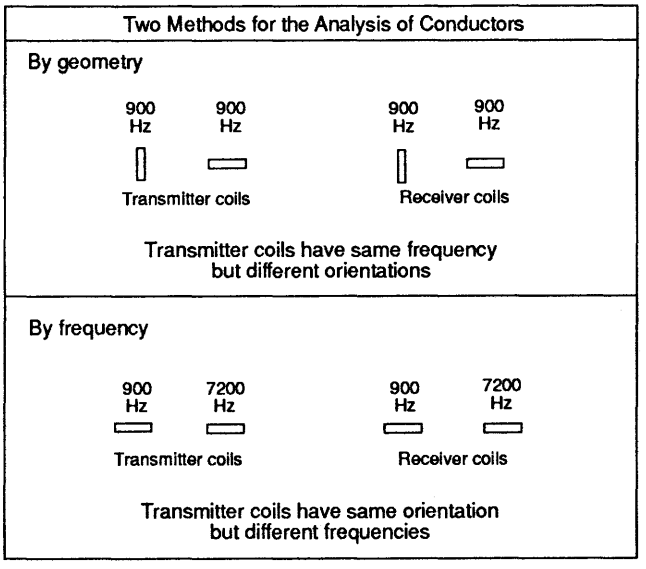

Figure 1. Multigeometry and multifrequency coil orientations in sectional view. The two independent multigeometry EM systems comprise the vertical coaxial and the horizontal coplanar transmitter-receiver coil-pairs.

Figure 1 illustrates transmitter-receiver coil configurations that allow the use of both multigeometry and multifrequency analytic techniques when surveying with modern helicopter EM systems. The frequencies shown are those commonly employed in the DIGHEM[III] system.

This paper demonstrates that the use of a single frequency commonly is all that is required to recognize desirable targets in noisy environments; however, two orthogonal transmitting coils, operating at approximately

[1]Dighem Surveys and Processing Inc., 228 Matheson Blvd. East, Mississauga, Ontario L4Z 1X1, Canada.

this single frequency, generally are required. The examples discussed are restricted to single-frequency multigeometry cases as shown in the upper half of figure 1.

TARGET GEOMETRY

The geometry of the conductor commonly is the most important parameter in the identification of exploration targets. A review of typical EM responses from dikelike targets characteristic of the Canadian Precambrian Shield is presented below, and additional conductor geometries have been described by Fraser (1979).

Figure 2 shows model profiles over a thin vertical dike in free-space. The vertical coaxial anomaly has a peak over the conductor, and the horizontal coplanar anomaly has a double-arch shape. These anomaly shapes are characteristic of a vertical thin conductor. Figure 3 shows model profiles over a thin conductor that dips 65° to the left. The dominance of the left coplanar arch indicates how sensitive the horizontal coplanar coil-pair is to the dip of a conductor. Also note that the vertical coaxial peak correlates with the coplanar trough, a characteristic of thin conductors.

Figure 4 presents DIGHEM^{II} recordings from two flights over steeply dipping thin conductors. For the survey example on the left, the approximately equal size of the coplanar in-phase arches indicates that the conductor is almost vertical. For the survey example on the right, the dominant left coplanar in-phase arch indicates that the conductor dips to the left. For both examples, correlation of the coaxial in-phase peak with the coplanar in-phase trough indicates that the conductors are thin.

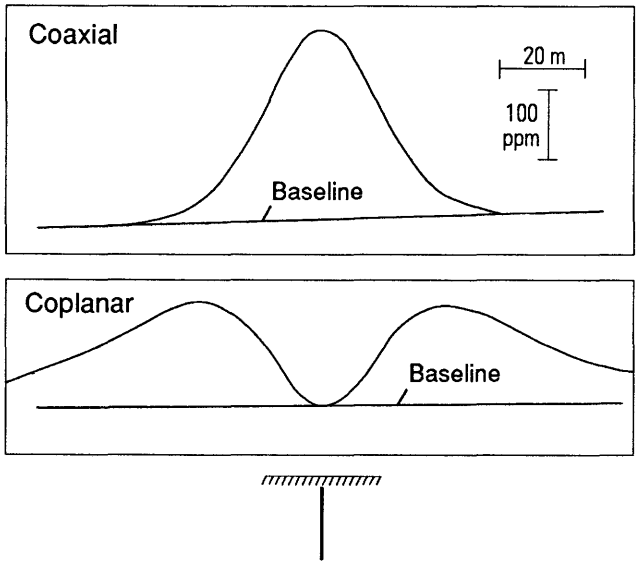

Figure 2. The in-phase anomaly shape for a vertical thin dike is center-peaked for the vertical coaxial coil-pair and is center-zero for the horizontal coplanar coil-pair. Flying height is 32 m. The quadrature anomalies (not shown) have the same shape for this dike model in free-space.

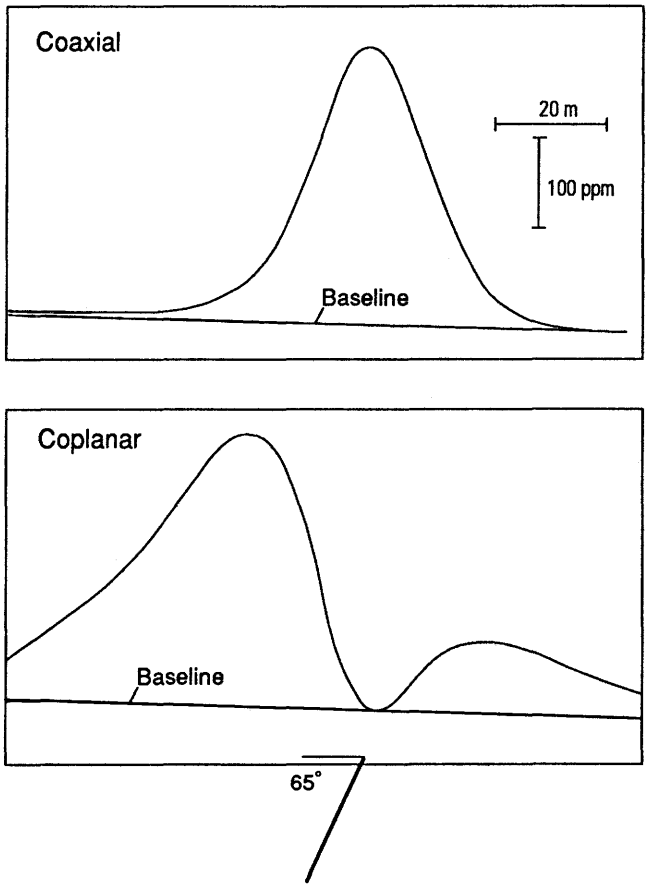

Figure 3. The peak of the vertical coaxial in-phase anomaly coincides with the trough in the horizontal coplanar in-phase anomaly for a dipping thin dike. Flying height is 32 m. The quadrature anomalies have the same shape for this model in free-space.

Figure 5 shows a model profile over a thick vertical conductor. The horizontal coplanar anomaly has a single peak rather than double arches. The thickness of the conductor, only 10 m for a flying height of 32 m, shows how sensitive the horizontal coplanar coil-pair is to the thickness of a conductor.

In a geometric sense, a vertical conductive dike may be classified as thick if its top surface yields a peak in-phase response when the horizontal coplanar transmitter coil passes directly over it (see fig. 5). Conversely, the conductive dike may be classified as thin if its top surface yields no in-phase response when the horizontal coplanar transmitter coil passes over it (see fig. 2). In envisaging the EM coupling involved, it helps to realize that the transmitter-receiver coil separation is small (8 m) relative to the flying height (30–35 m).

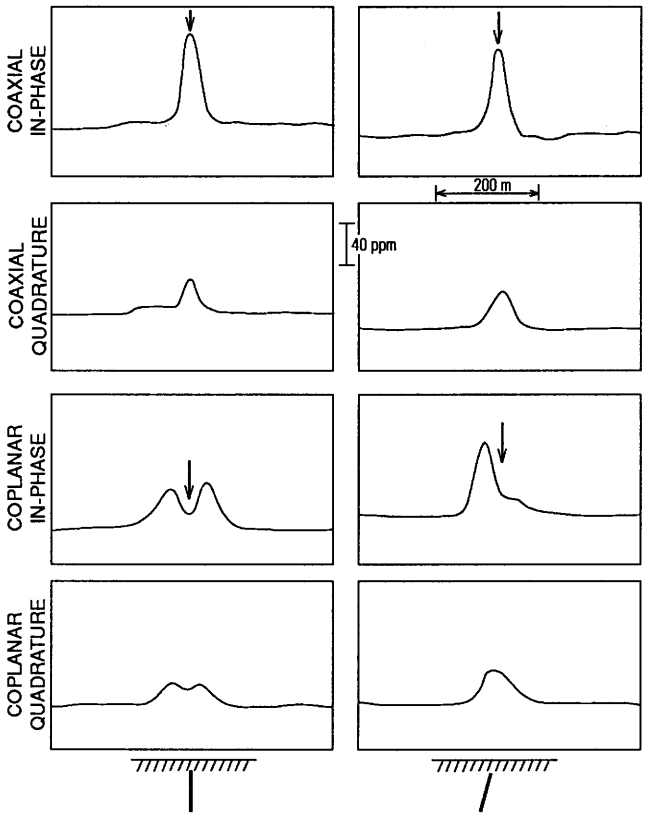

Figure 4. DIGHEM[II] flight record over vertical and left-dipping thin dike conductors. The peak of the coaxial in-phase anomaly coincides with the trough of the coplanar in-phase anomaly. The quadrature anomaly shapes are corrupted by current-gathering quadrature components.

Conductor widths in excess of 10 m typically yield thick anomaly signatures, whereas widths less than 3 m characteristically yield thin signatures.

Figure 6 displays a DIGHEM[II] profile record over a thick conductor yielding the characteristic center-peaked horizontal coplanar anomaly. The ability of multigeometry helicopter EM systems to distinguish between thick and thin conductors is especially important in resistive terrain where strata dip steeply, as in parts of the Canadian Precambrian Shield. In the Canadian Shield, steeply dipping orebodies are generally thicker than 15 m, whereas barren conductors predominantly are thin, commonly less than 2 m thick.

RECOGNIZING TARGETS AMONGST NOISE

The objective of all airborne EM systems, when engaged in mineral exploration surveys, is to recognize conductors and to categorize their anomalies in some meaningful fashion. Anomalies that might lead to an ore discovery commonly are masked by undesirable responses, referred to as "noise," that may be caused by

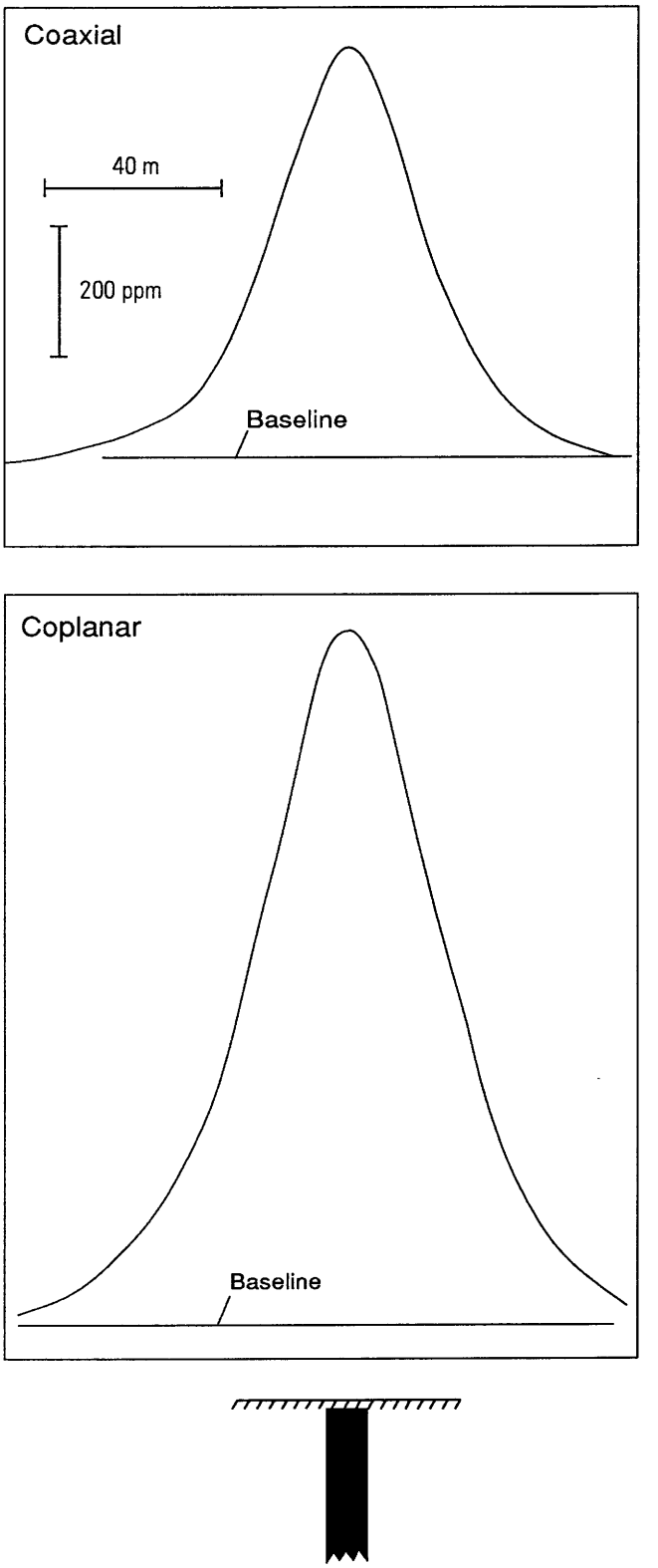

Figure 5. The anomaly shape for a thick vertical dike is center-peaked for both coaxial and coplanar in-phase anomalies. Flying height is 32 m and width of dike is 10 m.

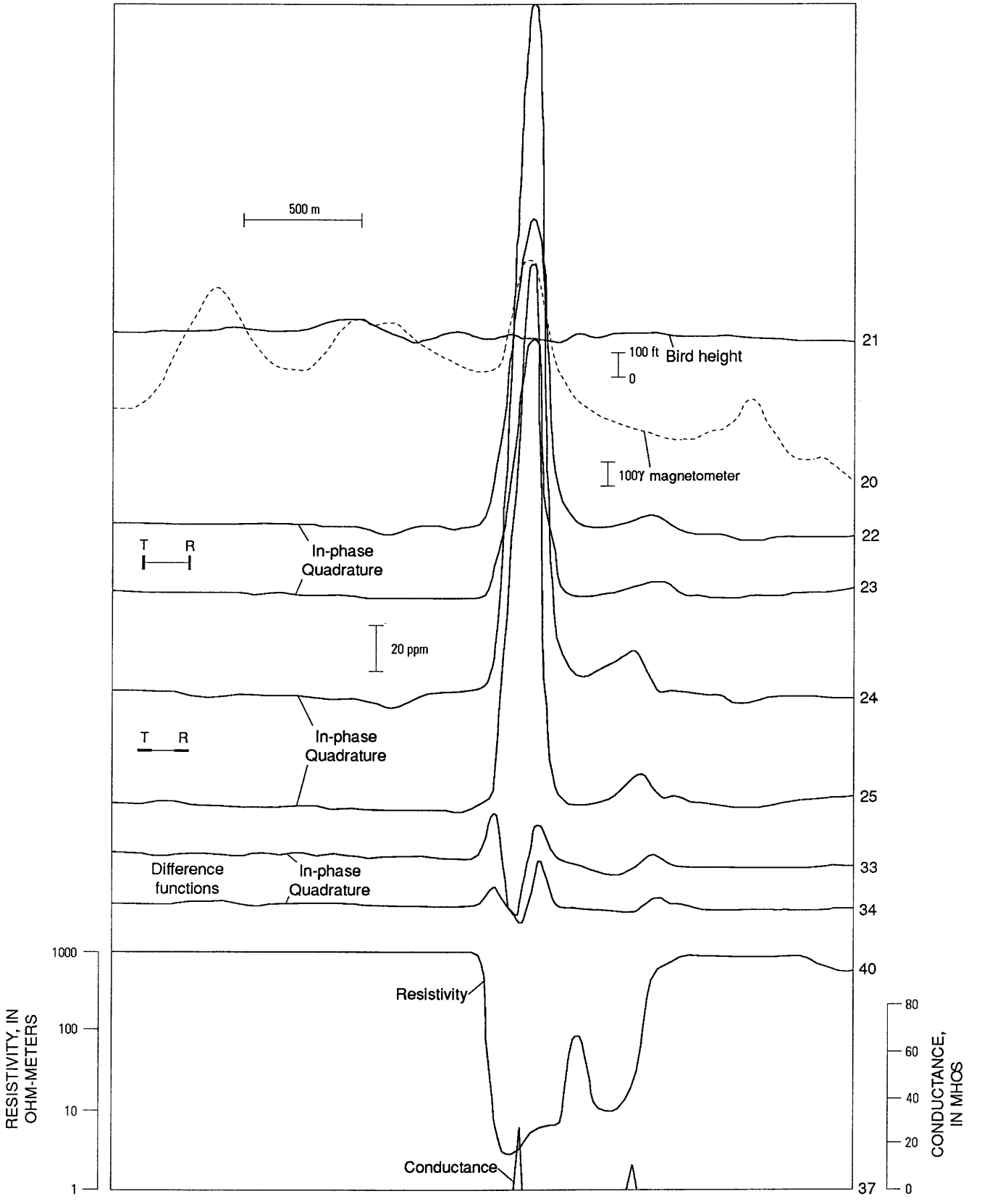

Figure 6. DIGHEM[II] profile record over thick conductor after computer processing. Channels 22 and 23 are from the coaxial coil-pair and 24 and 25 are from the coplanar coil-pair. Bird height refers to the height of the EM bird above the ground.

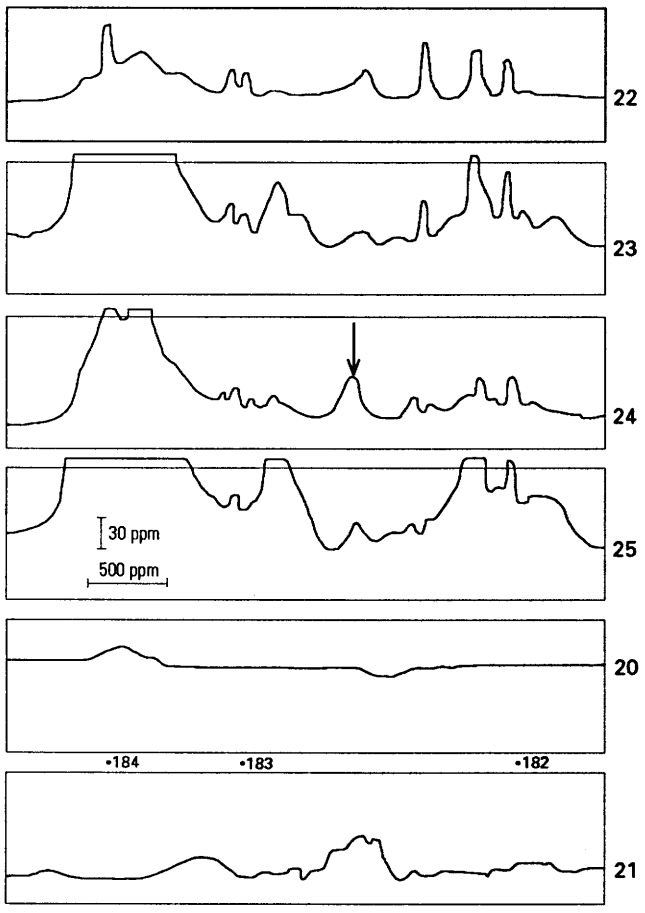

Figure 7. The arrow identifies the Woodlawn massive sulfide orebody on the DIGHEM[II] analog flight record. (Refer to figure 6 for channel identification.) Fiducial numbers (184, 183, 182) are time based.

powerlines, fences, and other cultural sources, or responses by geological sources.

Figure 7 shows a flight record that is dominated by geological and cultural noise from a survey in Australia over the Woodlawn massive sulfide orebody (Fraser, 1981). The huge responses on the left side of the record are due to black shales and are a form of geological noise. The other responses are due to culture sources such as fences, buildings, and so forth.

In figure 7, channels 22 and 23 are the in-phase and quadrature responses of the vertical coaxial coil-pair. Channels 24 and 25 are the in-phase and quadrature responses of the horizontal coplanar coil-pair. A competent geophysicist might well have difficulty selecting the orebody from the other similar responses. The differences between these responses are subtle and difficult for an interpreter to detect when faced with the interpretation of hundreds of kilometers of data in a reasonable amount of time.

Figure 8 shows the same flight line as figure 7 but after computer processing. EM channels 22–25 are the same as before but are plotted at a more sensitive scale. Note channel 40, which identifies the one conductor worthy of attention, the Woodlawn orebody. This channel is the resistivity of the ground (Fraser, 1978a) as calculated from coplanar EM channels 24 and 25. No other anomaly on the resistivity channel yields as low a resistivity as the Woodlawn deposit. Even the conductive shales (which produced the huge EM response of channels 23–25 on the left) are more resistive than the sulfide deposit. The shales have a resistivity of 20 ohm-m and the orebody 6 ohm-m.

Prior to discovery of the Woodlawn deposit, another helicopter EM system had been flown over the area. Because of the very strong response from the shales, the small Woodlawn anomaly was ignored and exploration was concentrated around the shales. The cultural sources were not there at the time of the original survey. This original survey did not lead to the discovery. Woodlawn was discovered a year later in a geochemical program.

This problem of not recognizing a potential target on flight records is a nasty one. It is one thing to obtain an anomaly when the orebody is known and quite another to identify an anomaly as worth following up before the ore deposit has been discovered as will be demonstrated.

Figure 9 shows the DIGHEM[I] response of the New Insco massive sulfide copper deposit near Noranda, Quebec, Canada. Although this clearly is a bona fide anomaly, it was obtained for advertising purposes after the drill had intersected the deposit.

Figure 10 shows the flight line that led to the discovery. The small New Insco anomaly is among much larger anomalies caused by swamps. The flight line passed off the edge of this short deposit, causing the anomaly to be very small. All the anomalies shown here were picked mechanically by the interpreter, who did not recognize that any had value; however, the computer produced a map on which the small New Insco anomaly had the appearance of a strong conductor. Why? Because the computer-drawn map showed that the conductivity-thickness product of the New Insco anomaly was 26 mhos, and the swamp anomalies varied from 1 to 3 mhos. So some people might call this a computer discovery!

Figure 11 shows the discovery line over the Montcalm copper-nickel massive sulfide deposit near Timmins, Ontario (Fraser, 1978b). Prior to the discovery, the area was flown a number of times using other EM systems without any indication of the deposit. The geology is complex, and the area is completely covered with overburden. Earlier surveys were flown subparallel with the strike of the deposit. The discovery survey was also flown parallel with strike. The anomaly of figure 11, although obvious, is quite small.

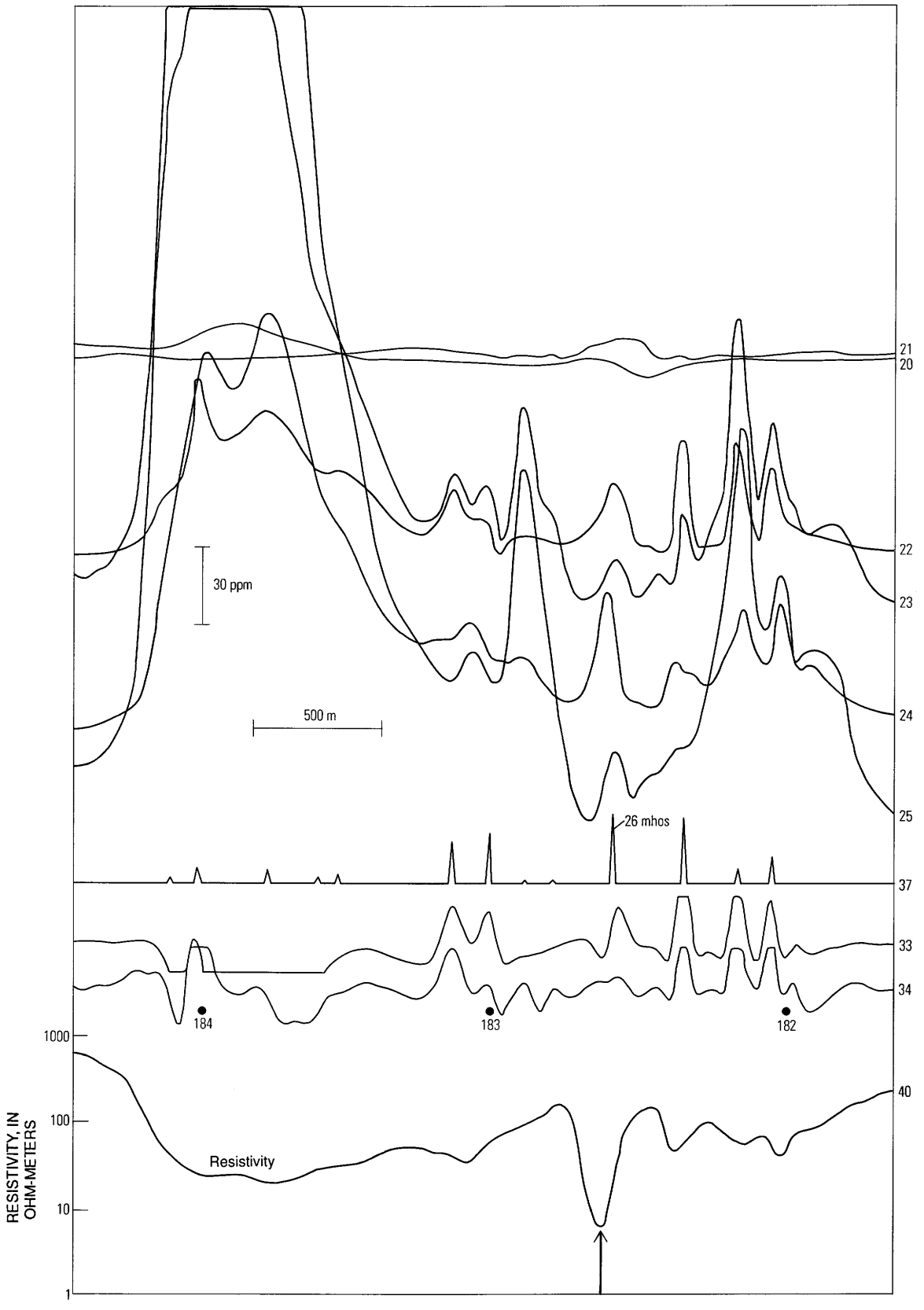

Figure 8. Digitally processed data from the flight line of figure 7. The resistivity channel allows the Woodlawn deposit (arrow) to be identified readily. (Refer to figure 6 for channel identification.) Fiducial numbers (184, 183, 182) are distance based. Resistivity plotted on logarithmic scale.

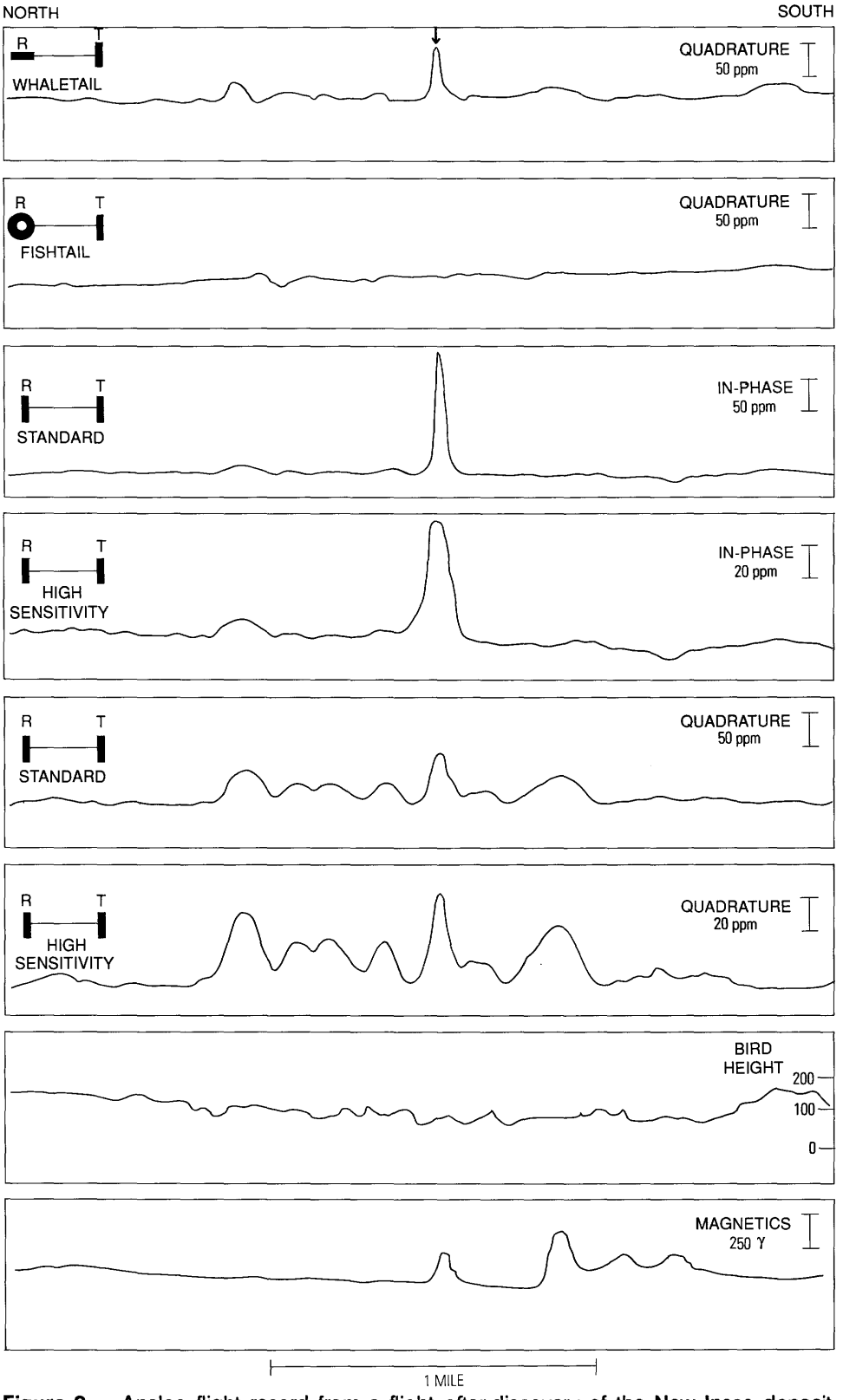

Figure 9. Analog flight record from a flight *after* discovery of the New Insco deposit (arrow) showing a large anomaly.

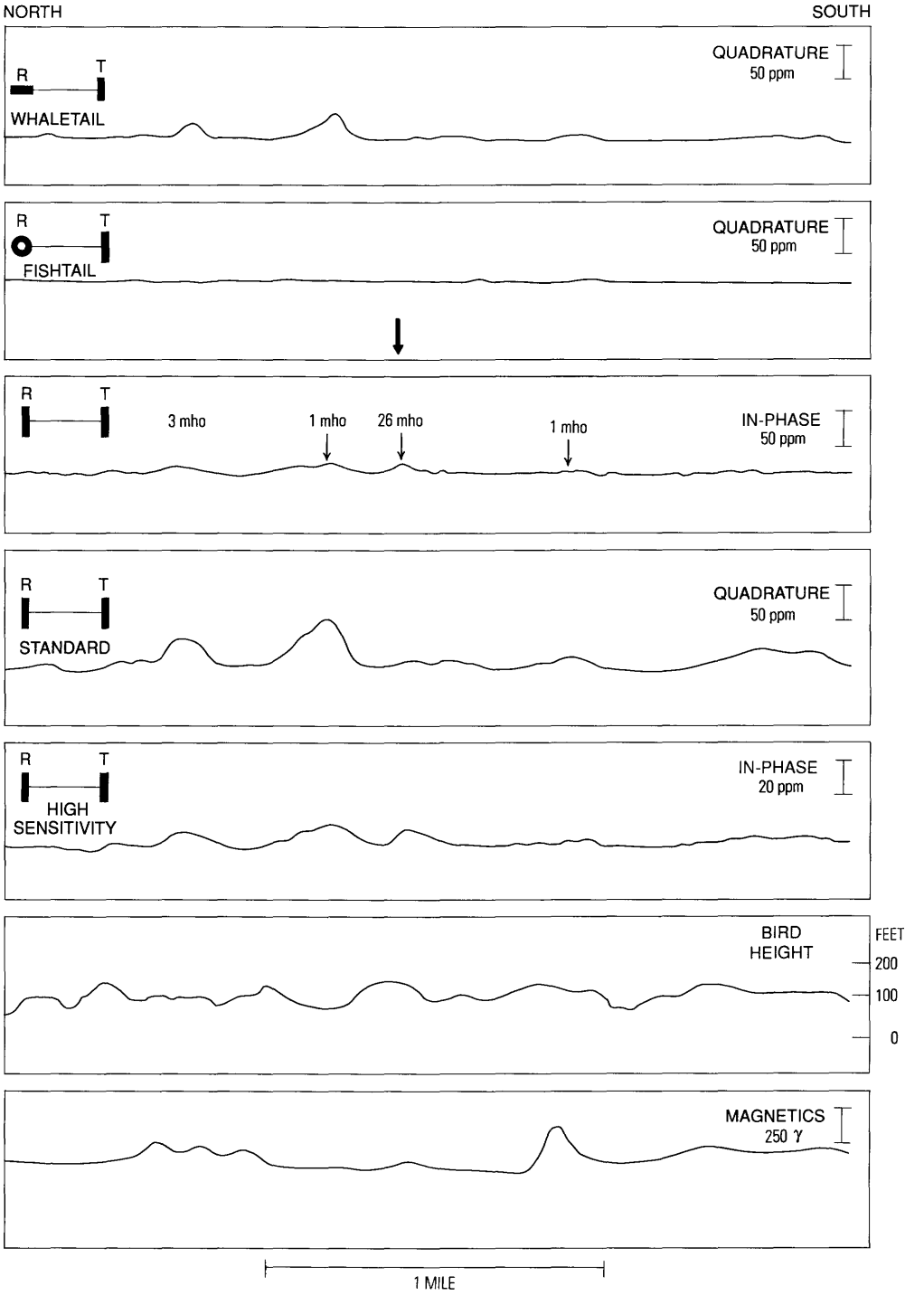

Figure 10. Discovery line over the New Insco deposit. The 26-mho target anomaly (large arrow) is smaller than those generated by nearby swamps.

Figure 12 shows a followup survey to that shown in figure 11. The EM sensor followed very similar paths in both surveys, as shown by the same 9-ppm response on the coaxial in-phase channel. The orebody could have been missed when using the raw data of figure 11, if the interpreter was careless. After computer processing (fig. 12), the target is so evident it could not be overlooked.

These examples of Woodlawn, New Insco, and Montcalm are very different from each other, but they all illustrate that desirable conductors may be difficult to identify on the recorded data channels. Such conductors

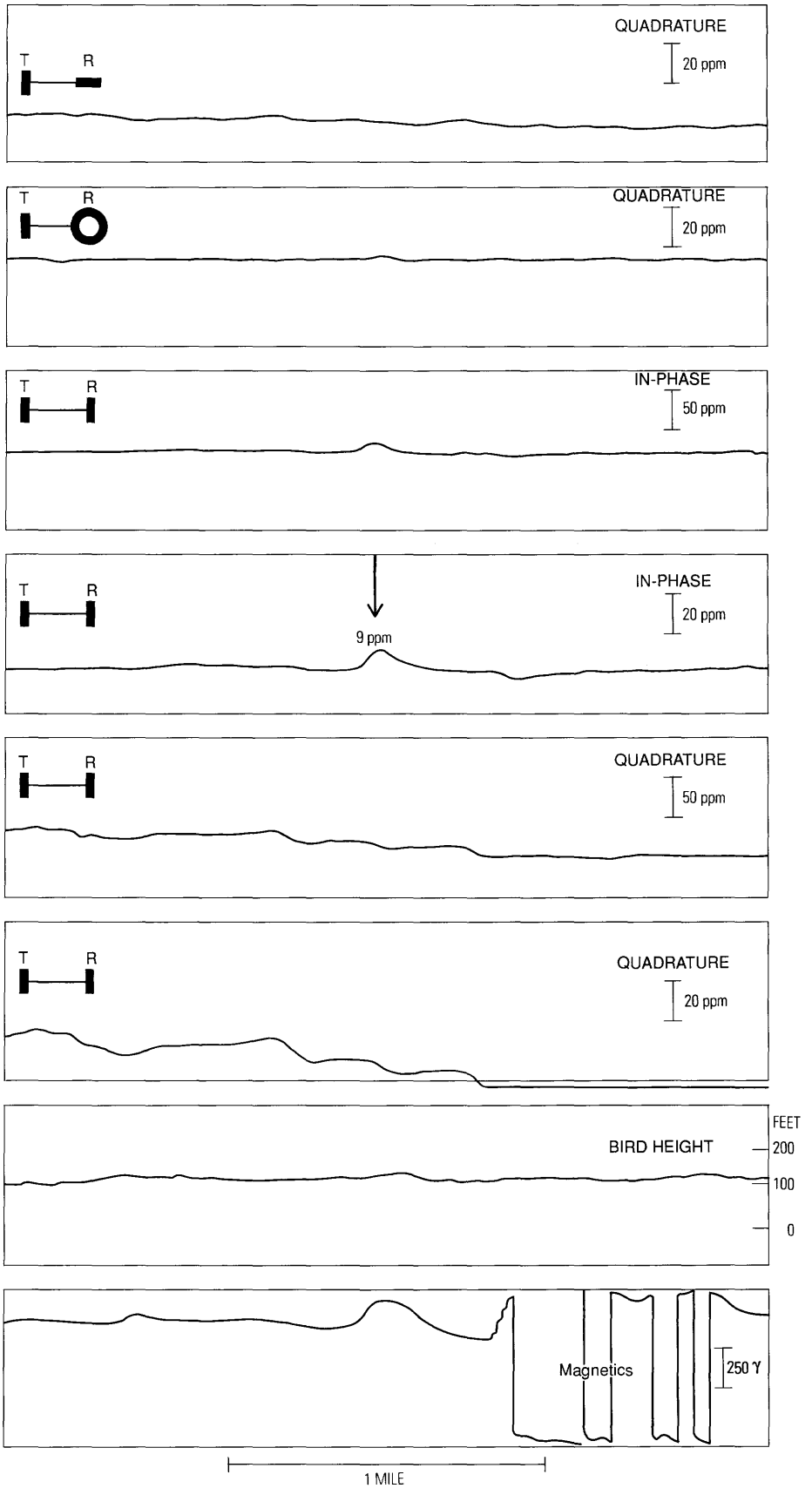

Figure 11. DIGHEM[I] discovery flight over Montcalm orebody (arrow).

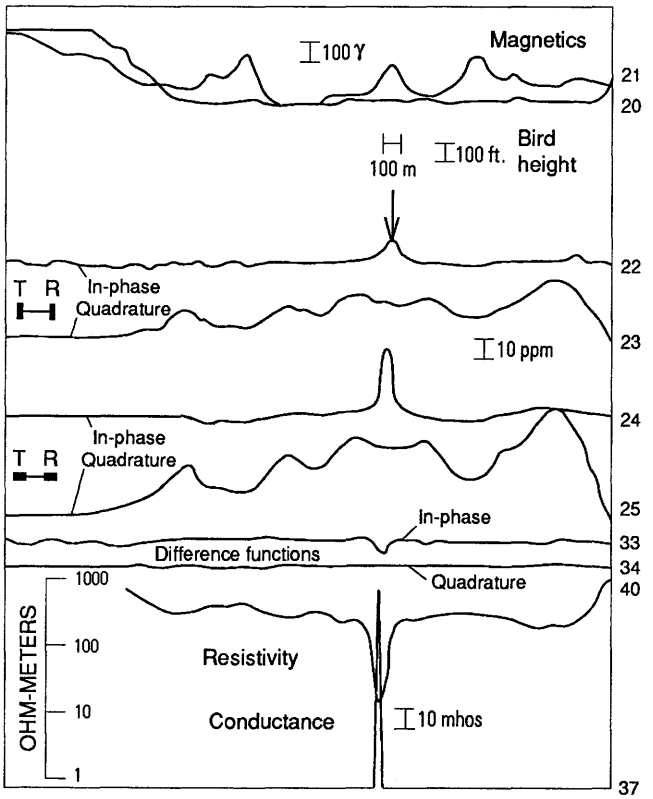

Figure 12. DIGHEM[II] flight line over Montcalm deposit (arrow), with the line parallel with strike and along the same path as the discovery flight line of figure 11.

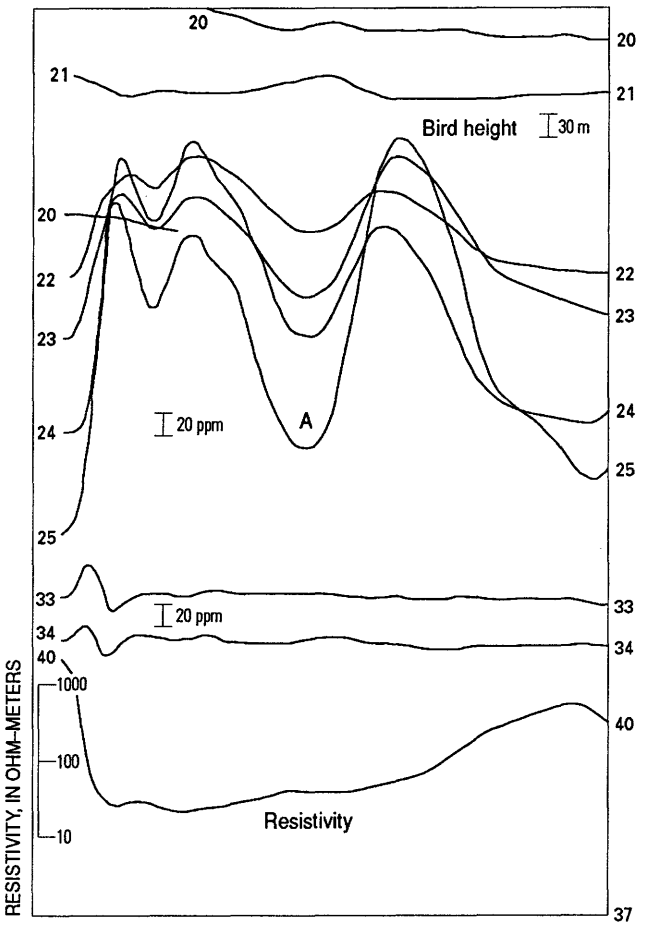

Figure 13. DIGHEM[II] profile over an area of widespread conductivity. The overburden response is suppressed by the EM difference channels 33 and 34. (Refer to figure 6 for channel identification.)

commonly are masked by or lost in the clutter from culture, conductive geology, or conductive overburden. The information required to identify these conductors is commonly hidden in the original responses but can be extracted by using appropriate computer processing techniques.

REDUCTION OF GEOLOGICAL NOISE

Geological noise consists of unwanted geological responses: (1) responses due to unwanted conductive sources and (2) responses due to magnetic polarization sources. Figure 13 shows an example of conductive geological noise. The large in-phase and quadrature EM responses of channels 22–25 reflect variable flying height. The drop in the response at location A reflects an increase in flying height from 30 m to 60 m. The resistivity channel shows that there is no significant resistivity change at location A.

Geological noise yields in-phase and quadrature *coplanar* channels (24, 25) that, respectively, are twice as large as the in-phase and quadrature *coaxial* channels (22, 23). The in-phase difference channel (33) results from subtracting half of the coplanar in-phase response from the coaxial in-phase response. The quadrature difference channel (34) is computed in a similar fashion. This simple but powerful operation eliminates all of the response of horizontal current flow in uniformly layered material. The difference channels therefore tend to eliminate conductive geological noise. On the left side of figure 13, the in-phase and quadrature difference anomalies on channels 33 and 34 define the edge of the conductive clays where granite outcrops. (The frequency in this example is 3600 Hz, whereas for all the other figures it is 900 Hz.)

The second class of geological noise is magnetic polarization response. It consists of only an in-phase component because the magnetic dipoles induced in magnetite alternate in lockstep with the transmitted field. Magnetic polarization yields negative in-phase anomalies as is shown in figure 14. The upper channel 20 is the magnetometer response, which may be compared to the in-phase channels 22 and 24.

Magnetic polarization tends to yield twice the in-phase response on the coplanar coil-pair, as compared to the coaxial. As a result, this noise tends to vanish on

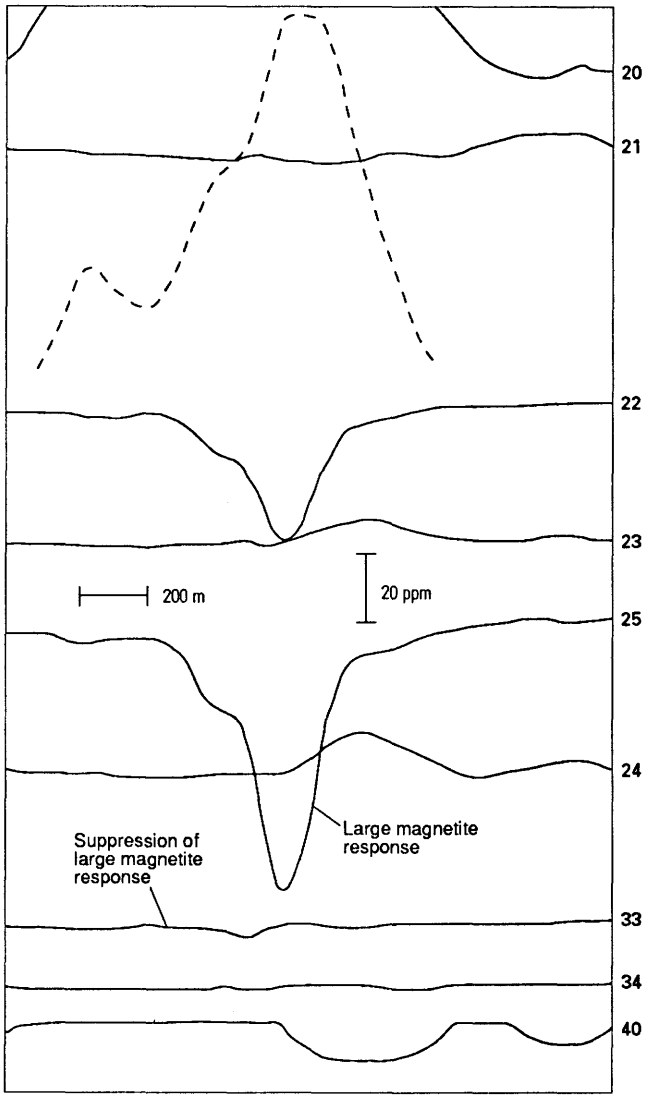

Figure 14. The in-phase difference channel 33 suppresses the in-phase response of large magnetite-containing bodies. (Refer to figure 6 for channel identification.)

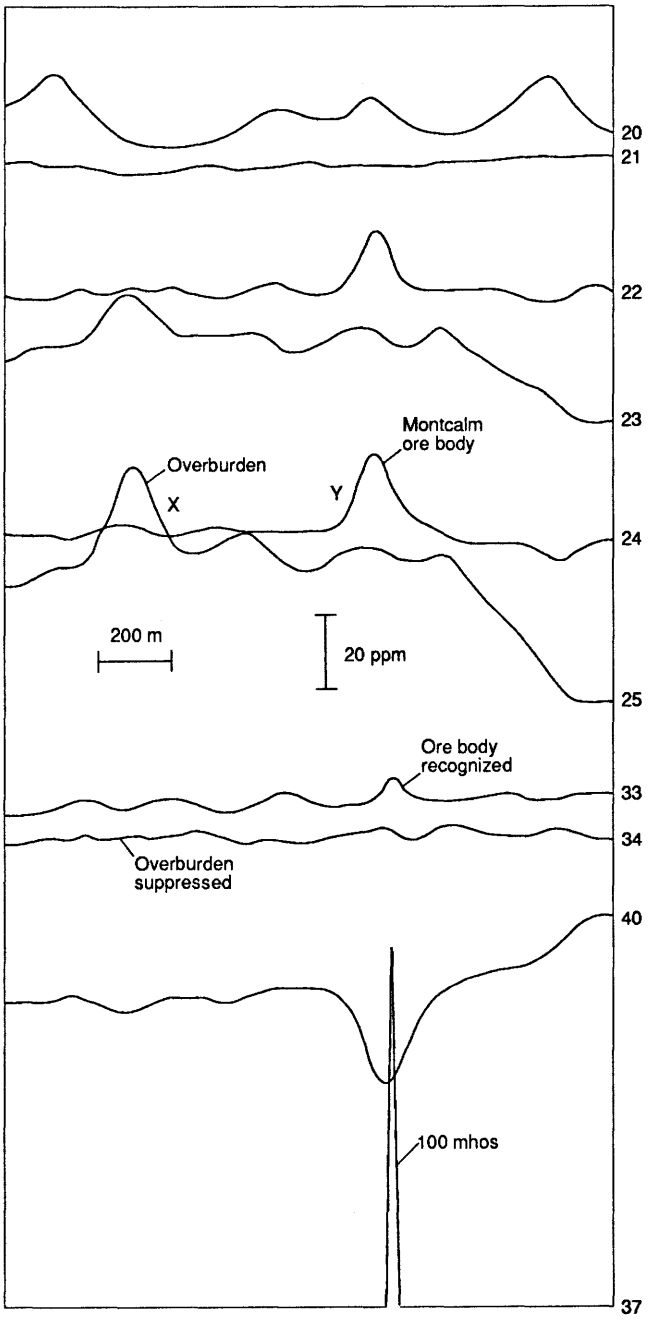

Figure 15. Localized peaks caused by conductive overburden are suppressed by the EM difference channels. (Refer to figure 6 for channel identification.)

the in-phase difference channel. The in-phase and quadrature difference channels therefore tend to be free of geological noise caused by both conductive overburden response and magnetic polarization response. This is only true if both the vertical coaxial and horizontal coplanar coil-pairs are operated at approximately the same frequency.

Figure 15 shows a profile record over two conductors. Conductor X on the left is a swamp and does not give an anomaly on the difference channels. Conductor Y is the Montcalm copper-nickel orebody and gives an anomaly on the difference channels. The ore deposit was selected automatically by computer as shown by the conductance spike of channel 37. It also yields a distinct resistivity low as shown by channel 40.

The circles in figure 16 identify a conductor that cannot be seen on either the vertical coaxial coil-pair or the horizontal coplanar coil-pair. The conductor is masked by a combination of conductive overburden response on the quadrature channels and magnetic polarization response on the in-phase channels. The conductor is identified easily, however, by the difference channels.

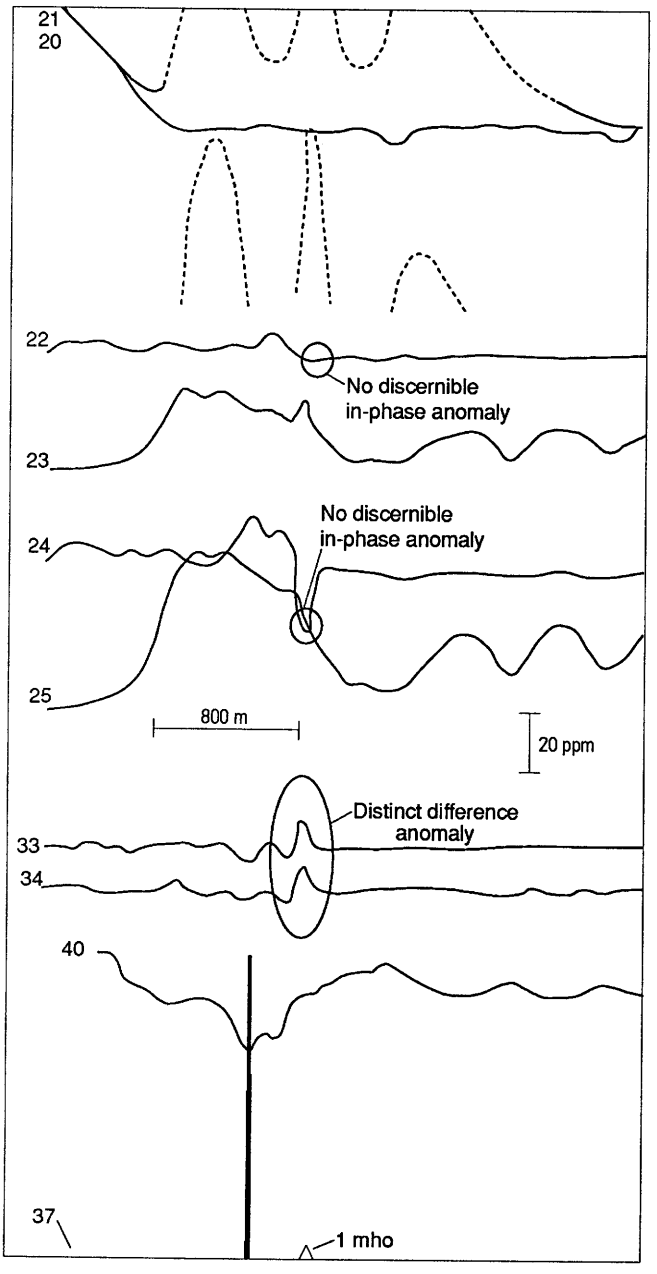

Figure 16. A conductor exists that is hidden by magnetic polarization noise on the in-phase channels 22 and 24 and by conductive overburden noise on the quadrature channels 23 and 25. The conductor can be seen on the in-phase and quadrature difference channels 33 and 34. (Refer to figure 6 for channel identification.)

CONCLUSIONS

A single EM frequency, transmitted on two orthogonal coils, commonly is sufficient to identify conductive targets in noisy environments. The response of the target may be obtained by subtracting the scaled-down coplanar response from the coaxial response, assuming both coil-pairs operate at approximately the same frequency.

Resistivity signatures also may be used to identify targets in a conductive environment. The EM response of the target may be considerably smaller than that of geological noise sources, even if the conductivity of the target is larger. In many cases, the target can be readily identified on the calculated resistivity profile or map.

REFERENCES CITED

Fraser, D.C., 1978a, Resistivity mapping with an airborne multicoil electromagnetic system: Geophysics, v. 43, p. 144–172.

_____ 1978b, Geophysics of the Montcalm Township copper-nickel discovery: Canadian Institute Mining Bulletin, v. 71, no. 789, p. 99–104.

_____ 1979, The multicoil-II airborne electromagnetic system: Geophysics, v. 44, p. 1367–1394.

_____ 1981, Response of the Woodlawn orebody to the DIGHEM–II system, *in* Whiteley, R.J., ed., Geophysical case study of the Woodlawn orebody, New South Wales, Australia: New York, Pergamon Press, p. 137–146.

Theory of the Modified Image Method for Airborne Electromagnetic Data

By Clyde J. Bergeron, Jr.[1], Juliette W. Ioup[1], *and* Gus A. Michel, II[1,2]

Abstract

A modified image method (MIM) can be applied to the inversion of synthetic airborne electromagnetic (AEM) data generated for shallow ocean or sea ice models using a forward Sommerfeld calculation. MIM is used to calculate the response of a two-layered medium to an AEM source. In the MIM model the image plane and surface screening distribution are located one screening length below the free surface of the conducting structure. The screening length is complex and is equal to Q/γ_1, where Q is a two-layer correction factor and γ_1 the first-layer propagation constant. An ad hoc parameter β is introduced into Q to extend the range of agreement between MIM and the exact Sommerfeld theory at the low-frequency end of the AEM spectrum. β is related to a weighted average value of the complex angle of incidence θ of the electromagnetic radiation, and θ in turn is the expansion parameter in the standard Sommerfeld representation of the AEM problem. A complex rescaling factor $(1+F)$ is also introduced that produces a small change in the magnitude and phase of the image source. This effective renormalization of the image field reduces the difference between the image field and the Sommerfeld secondary field for the conducting half-space to less than 1 ppm. The optimum values for both β and F are calculable from the high-frequency synthetic Sommerfeld data by means of an iterative loop in the MIM inversion algorithm. The region of excellent agreement between the complex MIM image field as modified by the β and F function and the Sommerfeld secondary field is within the range of parameters encountered in present-day (or potentially useful) helicopter electromagnetic systems for coastal bathymetry and sea ice thickness measurements, as well as in studies of salt-water intrusion of estuary systems.

INTRODUCTION

A modified image method (MIM) recently introduced by Bergeron (Bergeron and Michel, 1985; Bergeron, 1986; Bergeron, Ioup, and Michel, 1986; Bergeron, Michel, and Ioup, 1986) is used to calculate the response of a two-layered medium to an airborne electromagnetic (AEM) source. In this paper, we discuss the application of MIM to the inversion of synthetic AEM data generated for shallow ocean or sea ice models using a forward Sommerfeld (1909) calculation. The specific problems that the image method described in this paper may be profitably applied to include:

1. The inversion of AEM data gathered by a helicopter electromagnetic system. Such data taken at a minimum of two frequencies over shallow coastal waters can, in the context of a two-layer model shown in figure 1, be rapidly and accurately transformed into the altitude h of the transmitter-receiver pair, the sea electrical conductivity σ_1, the water depth d_1, and the conductivity contrast, or the ratio of the bottom conductivity to that of the sea, σ_2/σ_1. The same type of analysis can be applied to other two-layer conducting structures, such as fresh water over sea water at the mouth of rivers or certain ground-water configurations with fresh water over salt water (Bergeron, 1986).
2. The lateral resolution of AEM surveys in bathymetric applications or underside sea ice roughness determinations (Michel and Bergeron, 1986; Bergeron, Ioup, and Michel, 1986, 1987a, b; Ioup and others, this volume).
3. A straightforward error propagation analysis of the uncertainties in the inverted quantities in terms of system noise, both internal (electronic) and external (bird wobble) (Bergeron, Ioup, and Michel, 1987b).[3]
4. The generation of approximate signal signatures of conducting objects such as sea ice keels, pipelines, mines, or submarines imbedded in the first or second layers (Michel, 1986; Michel and Bergeron, 1986).

In this paper, we restrict ourselves to a demonstration of the speed and accuracy of the MIM inversion algorithm as applied to bathymetric and sea ice AEM surveys.

[1]Department of Physics and Geophysical Research Laboratory, University of New Orleans, New Orleans, Louisiana 70148.

[2]Current address: Naval Oceanographic Office, NAVOCEANO, Stennis Space Center, Mississippi 39522–5001.

[3]We have demonstrated that a significant part of the difference between the measured field and the Sommerfeld field calculated from ground-truth data in a U.S. Navy survey of Cape Cod Bay (Ioup and others, this volume) can be accounted for by bird pendulum motion possibly due to drag forces (Bergeron, Ioup, Michel, 1987c). Almost identical tilt angle versus range plots have been calculated from the high- and low-frequency data using the MIM theory.

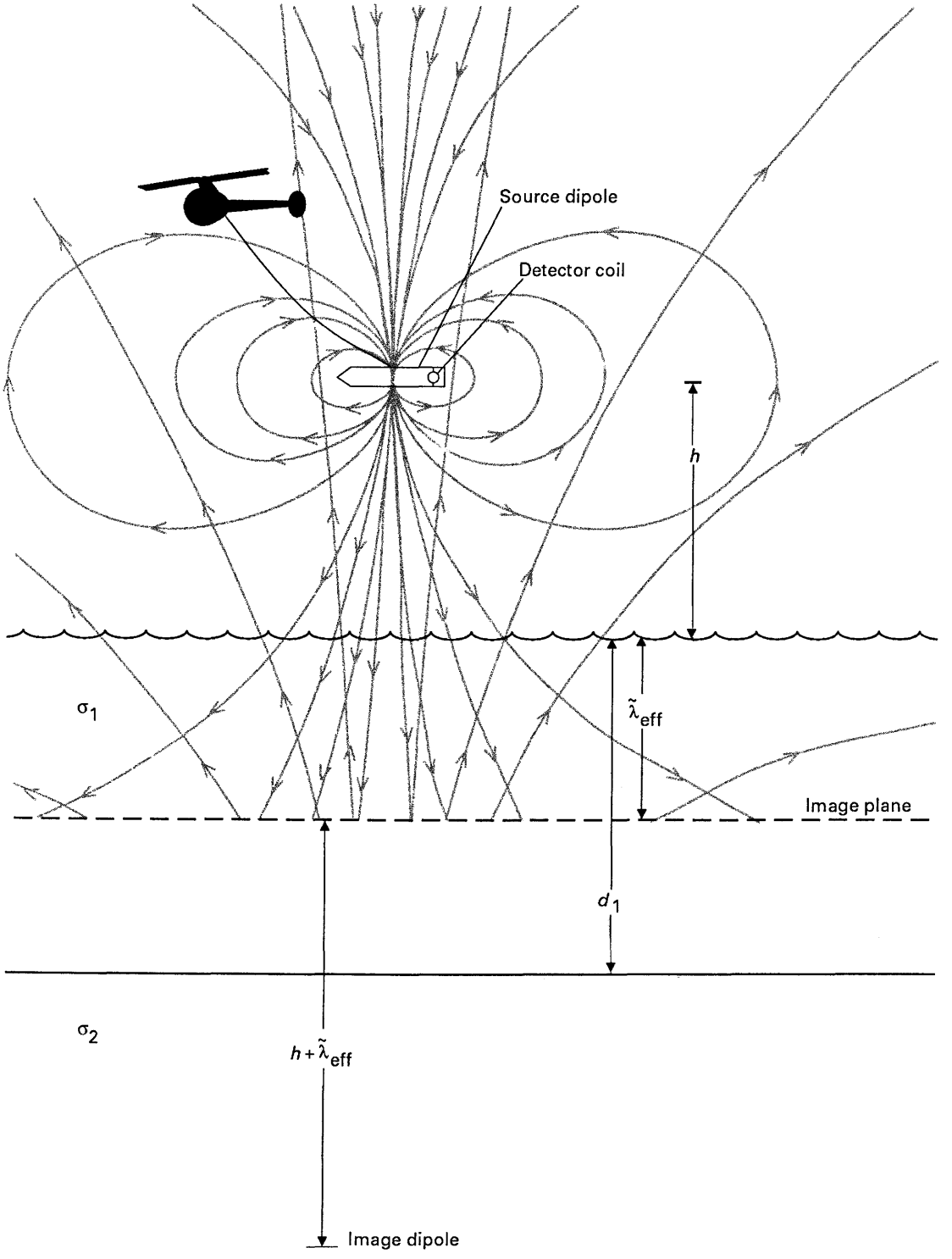

Figure 1. Helicopter-towed bird containing transmitting and receiving coils above the sea (first layer) and sea bottom (second layer). The image and primary fields and the image plane are also shown. The altitude of the bird above the sea is h, the sea depth is d_1, the image plane is located at a depth λ_{eff}, and the conductivities of the sea and sea bottom are σ_1 and σ_2, respectively.

The advantages of the MIM inversion over conventional integral inversion techniques include speed (about 0.01 s per survey point at two frequencies on a mainframe computer and not much slower on a dedicated minicomputer) and accuracy. The intrinsic accuracy of the method has been demonstrated for noise-free synthetic data generated by a forward Sommerfeld calculation using model parameters from actual

AEM surveys (Won and Smits, 1985; Bergeron, Ioup, and Michel, 1987a; Bergeron, Ioup, Michel, and Smits, 1987; Ioup and others, this volume).

In general, the method fails when the conducting structures are at a depth greater than the altitude of the bird. More specifically, the MIM field is not an accurate representation of the secondary field when the effective skin depth is large as compared to the bird altitude.

GENERAL BACKGROUND ON IMAGE METHODOLOGY

The constitutive equations governing the screening response of conducting matter to external electromagnetic fields are the Thomas-Fermi relation for electrostatic fields (Kittel, 1963), London's equation for the superconducting state (Lynton, 1961), and Ohm's Law for the screening of alternating current fields in ohmic conductors (Jackson, 1962). These equations, together with Maxwell's equations, result in a formally identical screening response; that is, the screening charges and (or) currents and their screened fields obey Helmholtz's equation and differ only in their characteristic screening lengths. There is a simple relationship between the three screening lengths when expressed in terms of microscopic electronic parameters (Bergeron, 1986).

Typically, the electrostatic screening length in metals, the Thomas-Fermi length, is of the order of 10^{-10} m. London's penetration depth (10^{-7} m) is the term generally used for the superconducting screening length. The screening length that governs the ohmic response to an alternating current field is usually termed the skin depth. In the present application we define the ohmic response screening length as the reciprocal of the propagation constant for the conducting structure. This definition leads to a complex screening length that is given by $\delta/(1+i)$ for a half-space conductor in which displacement currents are negligible and where δ is the half-space skin depth.

When the source of the external field is at a distance h much greater the primary source below the conductor-vacuum interface at a distance equal to the primary source altitude h above the conducting surface. Thus, the electromagnetic boundary conditions are satisfied at the surface of the conductor. The field of the image source is a very good approximation to the secondary field produced by the screening charges or currents within the interior of the conductor; that is, classical image theory works when $h \gg \lambda$ the relevant screening length. For h greater than but of the order of the screening length, the agreement between the classical image field and the secondary field is poor.

The essential element of the modified image method when $h \simeq \lambda$, where λ is the screening length, is the location of the image plane at a distance of one screening length from the surface into the interior of the conductor, such that at this interior image plane the electromagnetic boundary conditions are satisfied (Bergeron, 1986). The heuristic rationale for this assumption is based on the observation that the weighted average depth of the volume screening distribution, a solution of the Helmholtz equation, is simply one screening length. It has been demonstrated recently (Bergeron, Ioup, Michel, and Smits, 1987) that this general methodology, when applied to the Sommerfeld problem, extends the range of agreement between the secondary field H_S and the field of the image source H_I well into the proximate regime $h \simeq \delta$.

The following analysis includes only the response measured by a coplanar horizontally oriented coil-pair, although the modified image method may be applied to any other transmitter-receiver coil configuration. Figure 1 illustrates the helicopter-towed bird containing transmitting and receiving coils. The free-space image and primary fields are represented by fields produced by static magnetic dipoles, also shown in figure 1. Note that the primary and image sources are located the same complex distance $h + \lambda_{eff}$ from the image plane. This is a valid representation for frequencies utilized in the application discussed here because the free-space wavelength is much greater than the bird altitude, and thus the variation of the field amplitude due to spatial phase change is negligible over distances of the order of h. The spatial phase change is $K_o h$, and $K_o h \ll 1$, where K_o is the free-space propagation constant.

THEORY

When applied to the Sommerfeld problem, the modified image method joins the genre of complex image theory, the first example of which was presented by Wait (1969), based on a suggestion by A.D. Watt. Wait demonstrated that the leading term in an expansion of the Sommerfeld integral corresponds to an image source at a complex depth. Several other investigators have expanded this technique to include both discrete and continuous image distributions (Bannister, 1979; Mahmoud and Metwally, 1981a, b; Metwally and Mahmoud, 1984). Lindell and Alanen (1984) developed an exact image solution that also contains both continuous and discrete distributions of image sources; in effect, they replaced the conventional Sommerfeld representation integral with an integral over the image sources. Lindell and Alanen demonstrated that their method of solution is numerically more tractable than the standard methods of solution of the Sommerfeld integral.

For a layered conducting structure, the effective screening length is given by

$$\lambda_{eff} = Q_m/\gamma_1, \qquad (1)$$

where λ_1 is the complex frequency-dependent propagation constant for the first layer and Q_m is a multilayer correction factor of the form originally developed by Wait (1951) and recently modified by Bergeron (1986). For the case where displacement currents may be neglected,

$$\lambda_1 = (1+i)/\delta_1, \tag{2}$$

where $\delta_1 = (1/\pi\mu_1\sigma_1 f)^{1/2}$ is the first-layer skin depth, σ_1 is the first-layer conductivity, μ_1 is the first-layer magnetic permeability, and f is the frequency of the electromagnetic source. For all layers it is assumed that the magnetic properties are negligible and the magnetic permeability is assumed to be that of free-space.

For a two-layered structure with an infinite second-layer depth, Q is given by

$$Q = \frac{U + \tanh[\gamma_1 d_1]}{1 + U\tanh[\gamma_1 d_1]}, \tag{3}$$

where γ_1 and d_1 are the propagation constant and thickness, respectively, of the first layer,

$$U = [(1-i\beta)/(K-i\beta)]^{1/2}, \tag{4}$$

where K is the conductivity contrast σ_2/σ_1, and σ_1 and σ_2 are the conductivities of the first and second layers; $\beta = \sin^2\theta_r$, where θ_r is the complex angle of refraction related to the angle of incidence θ by Snell's Law. For a distant source for which $K_0 h \gg 1$, the wavefront at the free-space conductor interface approaches that of a plane wave and $0 \leq \theta \leq \pi/2$. Because the index of refraction of a good conductor is much greater than 1, $\theta_R \simeq 0$ and thus $\beta \simeq 0$ and $U \simeq K^{-1/2}$. As pointed out above, the source is "near" ($hK_0 \ll 1$) in AEM applications and is modeled as a dipole. The Hertz potential for the dipole may be expanded in the Sommerfeld representation where the angle of incidence θ is the expansion parameter and goes from 0 to $\pi/2$ and then to $+\infty$ along the imaginary axis (Wait, 1951). Thus $\beta = |\sin^2\theta_r|$ is not zero but rather a function of the expansion parameter θ via Snell's Law.

In the context of the expression for the two-layer function Q, equation (3), we treat β as an adjustable parameter that minimizes the difference between the two-layer Sommerfeld field and the single image at a complex depth field provided by the MIM model. We performed numerical experiments to determine the approximate dependence of the minimizing values of β on the parameters of a two-layer model. The notation that we use was originally introduced by Frischknecht (1967): $A = 2h/\delta_1$, $B = \rho/\delta_1$, and $D = 2d_1/\delta_1$. The A, B, and D are the characteristic lengths of the model scaled to the first-layer skin depth δ_1, where h, ρ, and d_1 are the bird height, coil separation, and first-layer thickness, respectively. The results of these numerical experiments demonstrate the following characteristics of what we call β_{exp}.

1. β_{exp} has a negligible dependence on $K<1$ (bathymetry) and also on B for $A/B = 2h/\rho > 5$.
2. β_{exp} has a weak dependence on D in the range $0 \leq D \leq 4$. This the only range of D that is relevant because for $D>4$, $Q \simeq 1$, and hence the secondary field is that of a conducting half-space—the top layer.
3. $\beta_{exp} \sim 1/A^2$. This implies that for values of the parameter that are relevant to bathymetric or sea ice AEM, $\beta \ll 1$ because $A \geq 5$ at presently attainable low frequencies ($f \geq 50$ Hz). Therefore, for $K>1$ (sea ice or fresh water over salt water), β_{exp} has a negligible effect on U and $U \simeq K^{-1/2}$.

A recently developed approximate theoretical expression for β (Bergeron, Michel, and Ioup, 1986) is of the form

$$\beta_{theo} \sim \tanh^2[(1+i)D/2]/A^2,$$

which is in qualitative agreement with the functional dependence of β_{exp} on the model parameters.

As noted above, when $d_1 > 2\delta_1$, Q approaches its asymptotic value of unity—that is, the perturbation produced by the lower layer on the secondary field approaches a few parts per million of the primary field and is comparable to or smaller than the residual difference between the single image field of MIM and the Sommerfeld field for a conducting half-space limit of the two-layer model. In this limit the β parameter is ineffective. This residual difference thus masks the bottom perturbation, and the MIM inversion of the synthetic Sommerfeld data diverges from the model depth. One possible cause of the residual difference between the single image field and the Sommerfeld field is the neglect of higher order terms in the expansion of the Sommerfeld integral.

In the same spirit with which we introduced the β factor, Michel (1986) showed that a small change in the strength and phase of the image dipole accomplished by a multiplicative complex function $(1+F)$ reduces the residual difference between the half-space MIM and Sommerfeld fields to less than 1 ppm of the primary field; that is, $(1+F_{exp})(H_I/H_P) - (H_S/H_P) < 1$ ppm. The half-space parameters are A and B. F_{exp} has the following properties:

1. It has negligible dependence on B for $A/B > 5$.
2. F is a complex function of A.
3. $|F_{exp}| \sim A^{-2.5} \ll 1$.

Besides the above interpretation of $(1+F)$ as a small change in magnitude and phase of the image source from the exact image of the primary source that is employed in classical image theory, it is possible to think of $(1+F)$ as

accomplishing a renormalization of the image field that transforms it into an almost exact replica of the half-space secondary field. Attempts at arriving at a theoretical form for the $(1+F)$ correction from expansions of the Sommerfeld integral for the secondary field of the half-space have not been fruitful.

INVERSION ALGORITHM

In general, AEM data are gathered at several (at least two) frequencies, one of which may be termed "high," such that $A_{hi}>20$. Therefore, both the β and F factors produce a negligible effect on the image field and may be neglected; that is, $F_{exp}(\text{hi})=\beta_{exp}(\text{hi})\simeq 0$. The high-frequency data are inverted on this assumption to produce values of A_{hi} and B_{hi}, the bird altitude and the skin depth at the high frequency. An additional initial assumption is that at the high frequency the top layer is a conducting half-space ($Q_{hi}\simeq 1$). This latter assumption is tested and corrected for in subsequent iterations of the algorithm. A_{hi} and B_{hi} are rescaled to their low-frequency values, and $\beta_{exp}(\text{lo})$ and $F_{exp}(\text{lo})$ can be calculated. In practice, the initial value for $\beta_{exp}(\text{lo})$ is set to zero. The low-frequency data are then inverted to yield a value for d_1 and K. This value d_1 is used to produce a $\beta_{exp}(\text{lo})$ (remember the dependence on depth of β_{exp} is weak). Also D_{lo} is rescaled to its high-frequency value to determine if $D_{hi}>4$, the criterion for $Q_{hi}\sim 1$. If $D_{hi}<4$, Q_{hi} is calculated and is used in the calculation of new values of A_{hi} and B_{hi} (h and σ_1). The iteration procedure is repeated until the inversion results for h, σ_1, d_1, and K stabilize.

Quantitative details of the inversion algorithm have been reported previously (Bergeron, Michel, and Ioup, 1986; Michel and Bergeron, 1986; Bergeron, Ioup, and Michel, 1987). Nevertheless, we present a brief outline below. The ratio of the vertical components of the quasistatic exact-image dipole field to the primary dipole field may be written as

$$H_I/H_p=(2r^2-1)/(r^2+1)^{5/2}, \tag{5}$$

where

$$r=[A+(1-i)Q]/B. \tag{6}$$

As discussed above,

$$|(H_S/H_P)/(1+F_{exp}(A)-(H_I/H_P)|\leq 1 \text{ ppm}. \tag{7}$$

For the initial pass of the high-frequency data, it is assumed $F_{exp}(\text{hi})=0$ and $Q=1$. Therefore,

$$A_{hi}/B_{hi}=2\,h/\rho=\text{Re}(r)+\text{Im}(r) \tag{8}$$

and

$$1/B_{hi}=\delta_1(\text{hi})/\rho=-\text{Im}(r). \tag{9}$$

We have developed an algebraic inverse relationship of equation (5),

$$r\simeq t^{-1}+at+bt^3+ct^5+dt^7+O(t^9) \tag{10}$$

where $t=(H_S/2H_P)^{1/3}$, and a, b, c, and d are real constants. The values for A_{hi} and B_{hi} are then scaled to the low frequency, and a value for Q_{lo} is extracted from r_{lo} and equation (6). Q_{lo} is next inverted to extract D_{lo} and K. Using the rule for the expansion of a hyperbolic tangent of the sum of two arguments, equation (3) may be transformed into

$$\begin{aligned}&(1+i)d_1/\,\delta_1(\text{lo})\\ &=-(\tfrac{1}{2})\ln[(1-QU+Q-U)/(1-QU-Q+U)].\end{aligned} \tag{11}$$

For a given Q_{lo}, a value for U is determined by the phase condition imposed by the left side of equation (11). As noted above, in the first pass β_{lo} is set equal to zero, thus $U=K^{-1/2}$. d_1 is next determined from equation (11). As described above, recursive iterations are then performed until the output values of the inversion stabilize. In summary, a minimum of four field values (in-phase and quadrature high and low frequencies) are converted by the MIM inversion algorithm to values of the four model parameters, h, β_1, d_1, and K.

CALCULATION OF SYNTHETIC DATA

Synthetic H_S/H_P data were generated from the forward Sommerfeld theory applied to a two-layer mode. The normalized secondary field (H_S/H_P) for the assumed coplanar coiled geometry may be written as (Frischknecht, 1967)

$$H_S/H_P=B^3\,T_0, \tag{12}$$

where

$$T_0=\int_0^\infty R(D,K)\,g^2\exp(-gA)\,J_0(gB)\,dg, \tag{13}$$

$$R(D,K)=$$

$$1-2\,g\left[\frac{(W-V)-(W-V)\exp(-WD)}{(W+g)(W+V)-(W-g)(W-v)\exp(-WD)}\right],$$

$$W=(g^2+2i)^{1/2}, \tag{14}$$

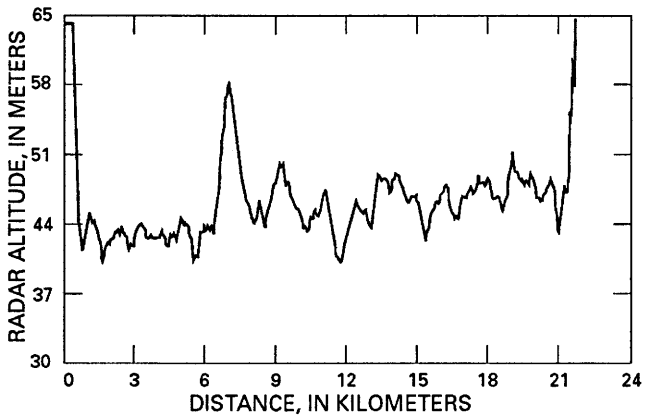

Figure 2. Synthetic bathymetric model for line 5041 of the Cape Cod survey. Water depth in meters and horizontal range in kilometers.

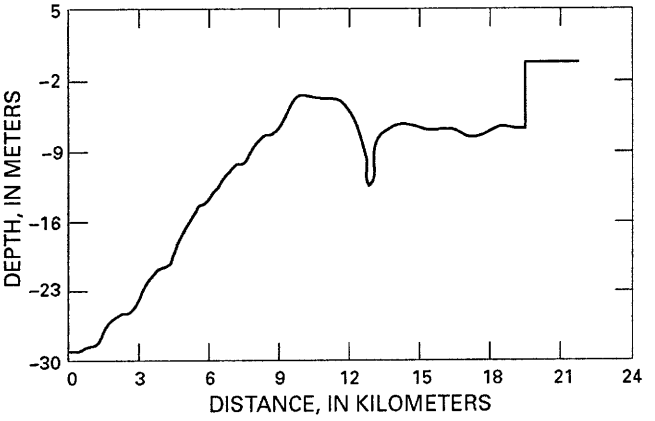

Figure 3. Bird altitude for the bathymetric model of figure 2 obtained from radar altimeter readings along line 5041.

and

$$V=(g^2+2iK)^{1/2}.$$

The T_0 Sommerfeld integral is evaluated numerically for the input values of A, B, D, and K.

BATHYMETRY MODEL AND INVERSION RESULTS

Figures 2 and 3 show the sea depth and bird altitude, respectively, versus range for the bathymetric model. The remaining parameters of the bathymetric model are the sea conductivity and conductivity ratio K; these are assumed to be range independent and were assigned values of 4 S/m and 0.25, respectively. The model data are actual sonar bathymetry and radar altimetry from line 5041 of the Cape Cod survey (Won and Smits, 1985). The MIM inversion of the AEM data of this survey is discussed in Ioup, Bergeron, and Michel (this volume).

Additional parameters of the AEM system that must be assumed are the exciting frequencies, f_{lo} and f_{hi}, and the spacing of the horizontal source and detector coils. For the calculations presented here, the parameters of the DIGHEM helicopter AEM system are assumed: f_{lo} and f_{hi} are 385 Hz and 7.2 kHz for the bathymetry model with a coil separation of 8 m (Fraser, 1979).

The results of the MIM inversion of the synthetic AEM data are shown in figures 4–7. The MIM inversion produces values of the altitude h and the first-layer conductivity σ_1 in excellent agreement with the input values of these parameters, as shown in figures 4 and 5, which show $(h_{inv}-h)/h$ and $(\sigma_{inv}-\sigma)/\sigma$, the fractional difference between the inversion and model values for bird altitude and sea conductivity. A small residual error in σ_1 remains in the shallows of the model as seen in figure 5. A maximum of five iterations was used to correct the initial assumption that $Q_{hi}=1$, which is not valid where $d_1 < \sigma_1(\text{hi})$. The results of the inversion of the low-frequency bathymetric data are presented in figures 6 and 7. Figure 6 shows the fractional difference between the MIM inverted depth and the model depth, and, as can be seen, excellent agreement is obtained. The MIM output for the conductivity contrast K is shown in figure 7. The error is positive ($K_{MIM} > K_{input}$) and is of the order of a few percent over the entire range. In general the conductivity contrast is the least stable of the inverted quantities.

BATHYMETRIC MODEL WITH SYNTHETIC NOISE

If a round-off error of ±1 ppm is introduced into the Sommerfeld data, it propagates into the inversion results for the four output parameters in vastly different

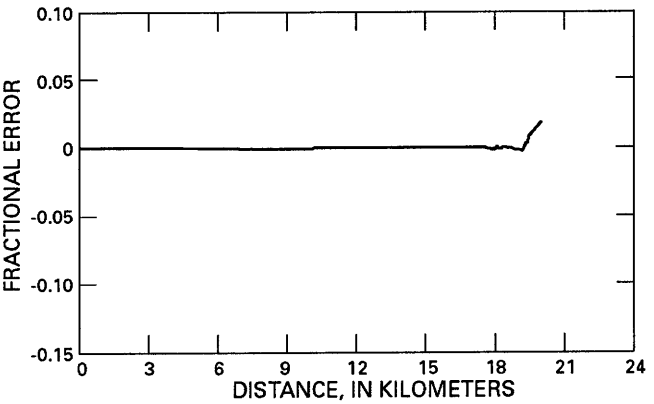

Figure 4. Fractional error for bird altitude (iterative inversion) $(h_{inv}-h)/h$, for the model of figure 3.

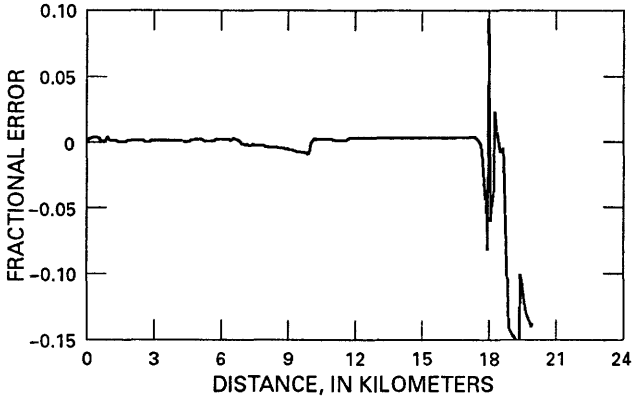

Figure 5. Fractional error for sea conductivity (iterative inversion) $(\sigma_{inv}-\sigma)/\sigma$ for the model of figure 3. The input value for the conductivity is 4 S/m.

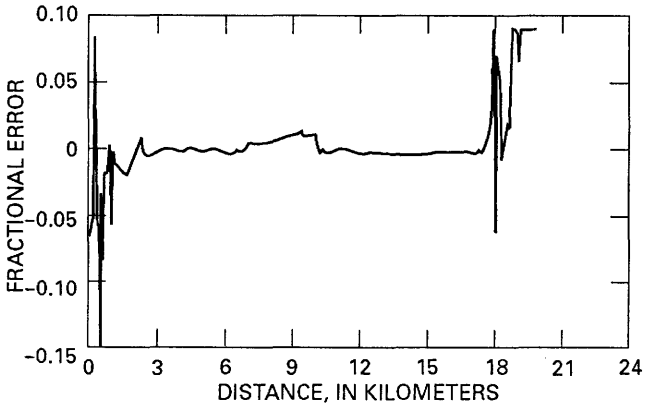

Figure 6. Fractional error between the MIM-inverted depth and the model depth for the model of figure 2.

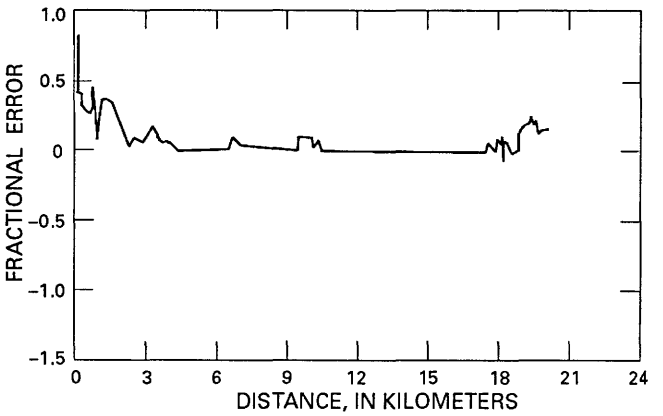

Figure 7. Fractional error in the MIM inversion for the conductivity contrast K for the noisy bathymetry model of figure 2.

fashion. This is illustrated for a linearized bathymetric model in figures 8–11. Figure 8 shows the input bathymetric data (straight lines) and the output of the MIM-inverted depth superposed on the model depth. Figure 9 presents the fractional error introduced into the altitude as a function of range; it is less than 0.1 percent. Figure 10 shows a fractional error introduced into the sea conductivity of about 2–3 percent, and, lastly, figure 11 illustrates the uncertainty in the conductivity contrast K, which varies from a few percent in the shallows to 100 percent at water depths greater than 20 m (about 1.5 skin depths). Thus the inversion of data having noise levels of the order of 1 ppm produces fractional uncertainties in the inversion output that range from 0.1 percent for h to 100 percent for K.

SEA ICE MODEL AND INVERSION RESULTS

A more schematic sea-sea ice model is used in the absence of available AEM survey data of sea ice. This model is illustrated in figure 12, in which a fixed altitude and a slowly varying ice thickness of from 0 to 9 m is assumed. The sea-water conductivity σ_2 is again set at 4 S/m and the ice conductivity σ_1 at 0.04 S/m; thus $K=100$. For the sea-sea ice calculation, f_{lo} and f_{hi} are assumed to be 7.2 kHz and 6.48 MHz. The coil separation distance is again assumed to be 8 m (Fraser, 1979).

The unrealistic high-frequency value of 6.48 MHz assumed for this analysis was chosen so that the same type of inversion algorithm as used for the bathymetry model could be applied here. Ice thickness alone can be calculated from low-frequency AEM data and laser altimeter data, $f_{lo}<1$ kHz. Measurements in this frequency range also result in accurate measures of the under-ice sea conductivity (Bergeron, Ioup, and Michel, 1987b). High-frequency data are required, however, to determine the conductivity of sea ice, which is of interest in many applications (Pounder, 1965; Yakovlev, 1973; Bogorodsky, 1985; Bergeron, Ioup, and Michel, 1987b).

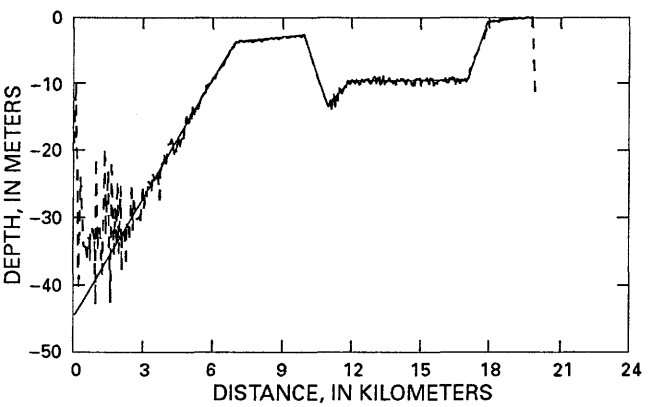

Figure 8. Linearized bathymetric model (solid line) with the MIM depth inversion of synthetic data (dashed line) and a round-off error of ±1 ppm.

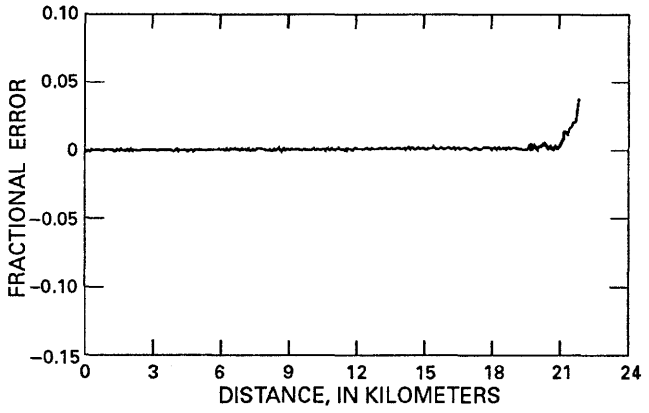

Figure 9. Fractional error in the MIM inversion for the bird altitude for the noisy bathymetry model of figure 8.

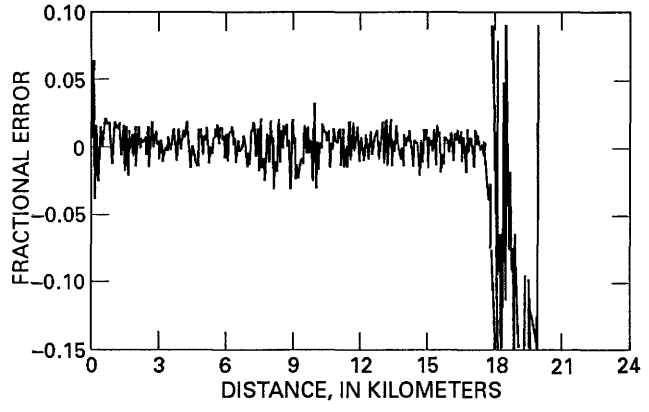

Figure 10. Fractional error in the MIM inversion for the sea conductivity for the noisy bathymetry model of figure 8.

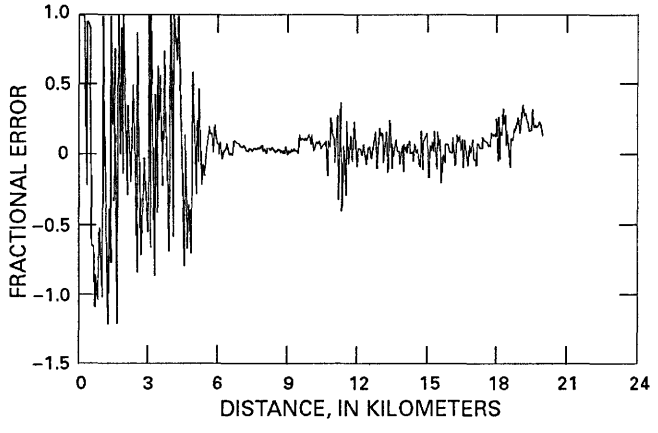

Figure 11. Fractional error in the MIM inversion for the conductivity contrast K for the noisy bathymetry model of figure 8.

MIM inversions of the sea-sea ice synthetic data are shown in figures 13–16. Again the agreement is good except when the thickness of the sea ice is very thin, near the open channel between about 9 and 12 km. In this

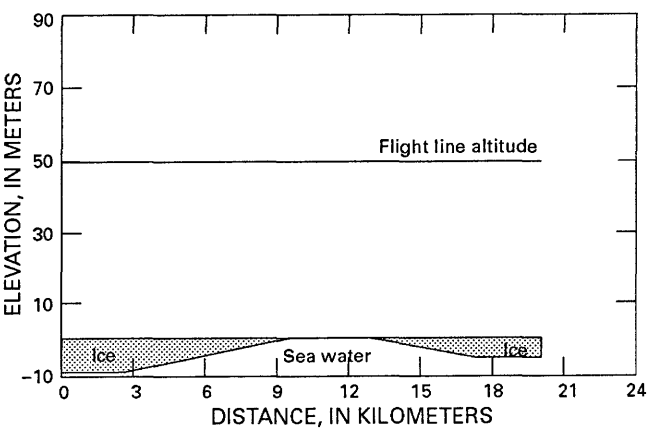

Figure 12. Synthetic sea-sea ice model showing the sea ice thickness and bird flight path, assumed to be a constant for this case.

interval, the inversion algorithm becomes unstable. As can be seen in figure 16, $K_{MIM} \simeq 90$, is 10 percent lower than $K_{input} = 100$. In general, K is the least robust inversion parameter.

CONCLUSIONS

The modified image method produces a fast (0.01 sec per survey point) and accurate inversion of AEM synthetic data generated from two-layer models. System noise levels of 1 ppm for birds with coil spacings of the order of 10 m produce very large uncertainties in the inverted value of the depth and conductivity contrast when the depth is greater than two low-frequency skin depths. In our opinion, *any* inversion scheme will produce results having similar uncertainties from data having comparable noise levels. The inversion of the high-frequency data produces accurate values for

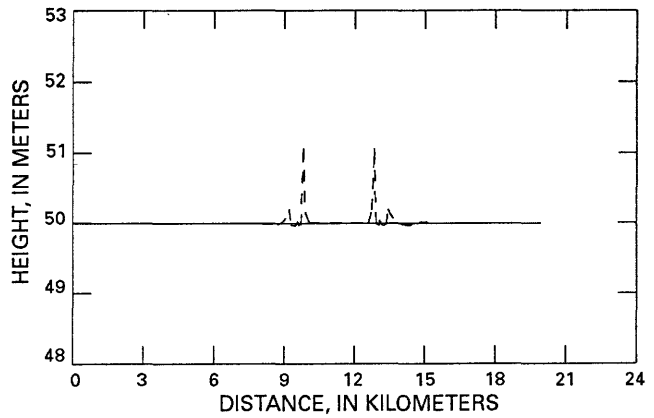

Figure 13. Original constant bird altitude (solid line) for the ice model of figure 12 and the MIM-inverted altitude (dashed line). Deviations in the MIM-inverted altitude occur near the open-water channel in the ice.

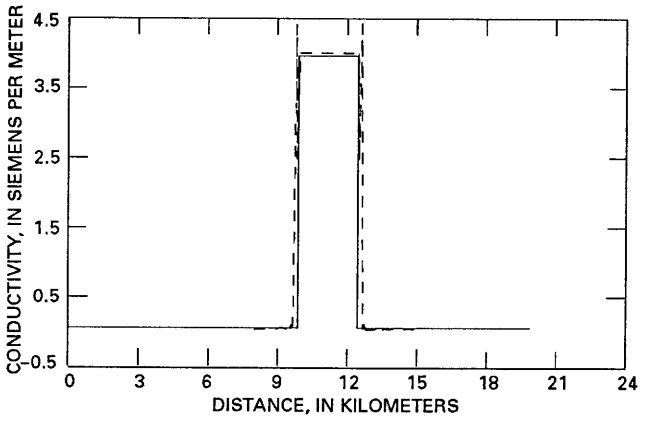

Figure 14. Original conductivity (solid line) and MIM-inverted conductivity (dashed line) of the first layer for the ice model of figure 12. The conductivity of the sea water is 4 S/m, of the ice 0.04 S/m.

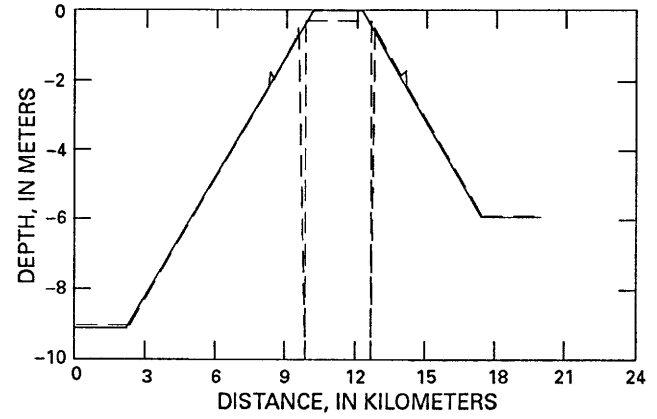

Figure 15. Original ice thickness (solid line) and the MIM-inverted first-layer thickness (dashed line) for the ice model of figure 12.

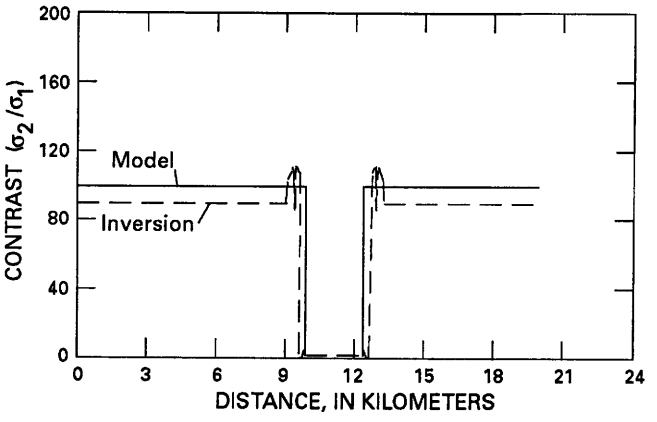

Figure 16. Original conductivity contrast K (solid line) and the MIM-inverted values (dashed line) for the ice model of figure 12.

the bird altitude and sea conductivity. In fact, the MIM altitude determination is more accurate than that of a standard radar altimeter operating at a height of 40–50 m.

MIM inversion results for the sea ice model display comparable accuracy to the bathymetry inversion. Again, the conductivity contrast K is the least stable inversion parameter, and thus the determination of the sea conductivity $\sigma_2 = K\sigma_1$ is relatively poor. But, as pointed out earlier, accurate measures of the under-ice conductivity may be extracted from low-frequency (less than 1 kHz) AEM data.

REFERENCES CITED

Bannister, P.R., 1979, Summary of image theory expressions for the quasistatic fields of antennas at or above the earth's surface: Proceedings, Institute of Electrical and Electronic Engineers, v. 67, p. 1001–1008.

Bergeron, C.J., Jr., 1986, Modified image method; application to the response of layered ohmic conductors to active electromagnetic sources: Journal of Applied Physics, v. 59, p. 3901–3908.

Bergeron, C.J., Jr., Ioup, J.W., and Michel, G.A., II, 1986, Application of MIM to inversion of synthetic AEM bathymetric data: Expanded Abstracts of the 56th Annual International Meeting and Exposition of the Society of Exploration Geophysicists, Houston, p. 49–52.

_____ 1987a, Application of MIM to inversion of synthetic AEM bathymetric data: Geophysics, v. 52, p. 794–801.

_____ 1987b, Lateral resolution of the modified image method for sea ice thickness: Expanded Abstracts of the 57th Annual International Meeting and Exposition of the Society of Exploration Geophysicists, New Orleans, p. 55–58.

_____ 1987c, Bird tilt; reason for calibration of airborne AEM bathymetric data [abs.]: Eos, v. 68, p. 1253.

Bergeron, C.J., Ioup, J.W., Michel, G.A., II, and Smits, Kuno, 1987, Application of the modified image method to experimental data [abs.]: Eos, v. 68, p. 290.

Bergeron, C.J., Jr., and Michel, G.A., II, 1985, Signal limited resolution and bottom feature detectability of AEM coastal survey devices by a modified image method [abs.]: Eos, v. 66, p. 918.

_____ 1986, Modified image method applied to AEM coastal surveys [abs.]: Geophysics, v. 51, p. 1514.

Bergeron, C.J., Jr., Michel, G.A., II, and Ioup, J.W., 1986, Correction factors for the modified image method [abs.]: Eos, v. 67, p. 919.

Bogorodsky, V.V., Bentley, C.R., and Gudmandsen, P.E., 1985, Radioglaciology: Dordrecht, Holland, D. Reidel Publishing Company, 254 p.

Fraser, D.C., 1979, The multicoil II airborne electromagnetic system: Geophysics, v. 44, p. 1367–1394.

Frischknecht, F.C., 1967, Fields about an oscillating magnetic dipole over a two-layer earth, and application to ground and airborne electromagnetic surveys: Quarterly of Colorado School of Mines, v. 62, 326 p.

Jackson, J.D., 1962, Classical electrodynamics: New York, John Wiley and Sons, p. 222–226.

Kittel, C., 1963, Quantum theory of solids: New York, John Wiley and Sons, 559 p.

Lindell, I.V., and Alanen, E., 1984, Exact image theory for the Sommerfeld half-space problem; Part I, Vertical magnetic dipole; Part II, Vertical electric dipole; Part III, General formulation: Institute of Electrical and Electronics Engineers, Transactions, AP32, p. 126–133, 841–847, 1027–1032.

Lynton, E.A., 1961, Superconductivity: London, Methuen, 174 p.

Mahmoud, S.F., and Metwally, A.D., 1981a, New image representation for dipoles near a dissipative earth; 1, Discrete images; Radio Science, v. 16, p. 1271–1275.

_____ 1981b, New image representation for dipoles near a dissipative earth; 2, Discrete plus continuous images: Radio Science, v. 16, p. 1276–1283.

Metwally, A.D., and Mahmoud, S.F., 1984, Mutual coupling between loops on layered earth using images: Institute of Electrical and Electronics Engineers, Transactions, AP32, p. 574–579.

Michel, G.A., II, 1986, Development and application of self-correction methods for MIM inversion of AEM bathymetry data: University of New Orleans, M.S. thesis, 60 p.

Michel, G.A., II, and Bergeron, C.J., Jr., 1986, Signal and diffraction limits on detectability of bottom conductivity contrast features with AEM devices [abs.]: Eos, v. 66, 1271.

Pounder, E.R., 1965, The physics of ice: Oxford, Pergamon Press, 151 p.

Sommerfeld, A.N., 1909, The propagation of waves in wireless telegraphy: Annals Physik, v. 28, p. 665–736.

Wait, J.R., 1951, The magnetic dipole over the horizontally stratified earth: Canadian Journal of Physics, v. 29, p. 577–592.

_____ 1969, Image theory of a quasistatic magnetic dipole over a dissipative half-space: Electronic Letters, v. 5, p. 281–282.

Won, I.J., and Smits, K., 1985, Airborne electromagnetic bathymetry: Naval Ocean Research and Development Activity (NORDA) Report 94, 18 p.

Yakovlev, G.N., ed., 1973, Studies in ice physics and ice engineering [trans. from Russian]: Translations of the Arctic and Antarctic Scientific Research Institute, v. 300, 192 p.

Interpretation of Airborne Electromagnetic Data Using the Modified Image Method

By Juliette W. Ioup[1], Clyde J. Bergeron, Jr.[1], *and* Gus A. Michel, II[1,2]

Abstract

A modified image method (MIM) was used to invert airborne electromagnetic (AEM) data from a 1984 U.S. Navy survey of Cape Cod Bay. High-frequency calibrated data were inverted to give the altitude h of the helicopter-towed AEM bird and the first-layer skin depth δ_1, and hence the first-layer conductivity σ_1. The high-frequency-derived h and δ_1 were employed in calculating the MIM rescaling factor $F(h/\delta_1)$ and the $\beta(h/\delta_1)$ factor, which corrects for the lateral variation of the primary field over the conductive half-space. The effect of these factors on the inversion of the high-frequency data is in general negligible such that the first iteration of the inversion that reflects these factors produces very accurate values of h and σ_1. The low-frequency bottom-probing signals were inverted by means of the MIM algebraic algorithm to give the first-layer thickness d_1 and the ratio of the bottom conductivity to the first-layer conductivity, $K=\sigma_2/\sigma_1$. Results of the MIM inversion of the AEM bathymetry survey of Cape Cod Bay are compared to ground-truth radar altimeter, conductivity, and sonar depth data.

INTRODUCTION

A modified image method (MIM) recently introduced by Bergeron (Bergeron and Michel, 1985, 1986; Bergeron, 1986; Bergeron, Ioup, and Michel, 1986, 1987a, b, this volume; Bergeron, Michel, and Ioup, 1986) was used to invert airborne electromagnetic (AEM) data from a 1984 U.S. Navy survey of Cape Cod Bay (Won and Smits, 1985a, b, 1986a, b; Smits and Won, 1987). The method offers approximate solutions to the Sommerfeld problem (Sommerfeld, 1909); that is, the response of a layered structure of ohmic conductors to an airborne electromagnetic (AEM) source. MIM interpretation of AEM surveys provides computationally fast and accurate measures of bathymetry and sea conductivity (Bergeron, Ioup, Michel, and Smits, 1987).

[1]Department of Physics and Geophysical Research Laboratory, University of New Orleans, New Orleans, Louisiana 70148.

[2]Current address: Naval Oceanographic Office, NAVOCEANO, Stennis Space Center, Mississippi 39522–5001.

The procedure for the inversion of AEM data using the MIM algorithm is described (Bergeron, Ioup, and Michel, 1986, 1987a) in an application of a MIM inversion of Sommerfeld data to a coastal bathymetric model. An iterative procedure developed by Michel (Michel, 1986; Michel and Bergeron, 1986; Bergeron, Ioup, Michel, and Smits, 1987) was utilized to improve the inversion for the case where the high-frequency data is modified by the lower layer; that is, $Q(f_{hi})\neq 1$. More complete details of the MIM theory are described in a paper in this volume by Bergeron, Ioup, and Michel.

Acknowledgment.—The authors wish to acknowledge the gracious cooperation of Kuno Smits, Code 352, Advanced Sensor and Survey Branch, Naval Ocean Research and Development Activity, in providing the Cape Cod data for analysis.

MIM INVERSION OF AEM DATA

Following the notation of Frischknecht (1967), the following parameters are defined:

- h Altitude of source/receiver coils above first layer; that is, bird height above sea water.
- σ_1, σ_2 Electrical conductivities of first and second layers.
- $K=\sigma_2/\sigma_1$ Conductivity contrast between first and second layers.
- x_0 Coil spacing (8 m).
- f_{lo}, f_{hi} Exciting frequencies of source coils ($f_{lo}=385$ Hz, $f_{hi}=7200$ Hz).
- δ_1 Skin depth for first layer (12.8 m and 3 m for two frequencies given above and $\sigma_1=0.5$ S/m).
- d_1 First-layer depth; that is, sea water depth.
- A $2h/\delta_1$.

Inversion of AEM data proceeds as follows. First, the high-frequency data are inverted at each point to obtain a value for the parameter A_{hi}. The low-frequency datum at this point is rescaled by means of a correction factor $F(A_{lo})$ obtained from a comparison of Sommerfeld high-frequency data and measured values. The complex correction factor β, which minimizes the difference between the Sommerfeld and MIM fields in the low-frequency and (or) shallow first-layer regimes, is then employed in the inversion of the low-frequency data. It

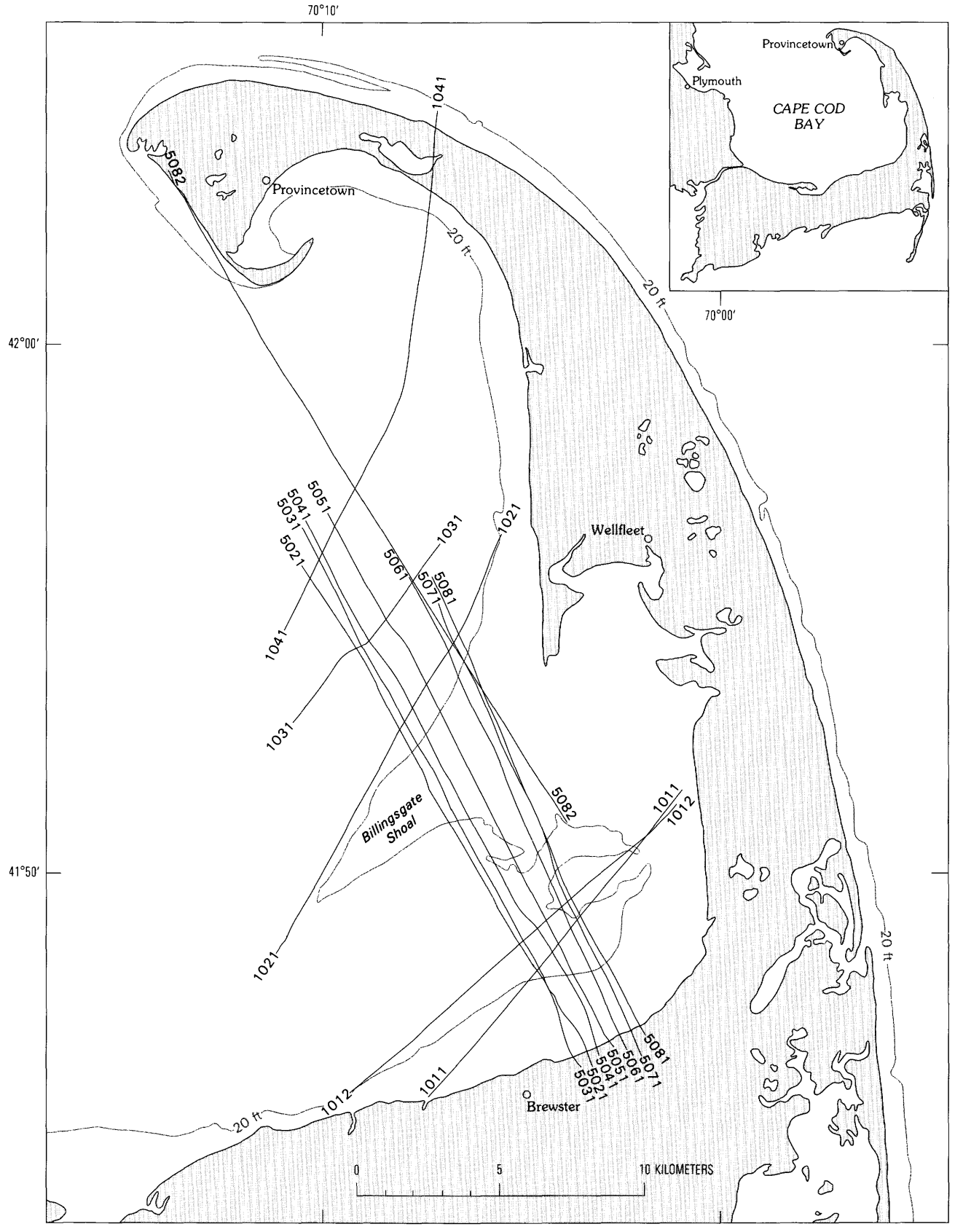

Figure 1. AEM flight lines, Cape Cod Bay. From Won and Smits (1985a).

should be emphasized that the MIM procedure as presented is an unfiltered and unsmoothed inversion. Four data numbers (the in-phase and quadrature fields at the high and low frequencies) are used to calculate four model parameters (the bird altitude, the conductivity of the first layer, the depth of the first layer, and the conductivity contrast between the first and second layers). The results are presented in the figures discussed below.

Figure 1 shows a plan view of Cape Cod Bay, where the data were recorded by DIGHEM for the U.S. Navy during the summer of 1984 (Won and Smits, 1985a, b, 1986a, b; Smits and Won, 1987). An acoustic depth-sounder bathymetric survey of approximately the same area was performed simultaneously to provide ground truth. Eight measurements of water conductivity were also made; measured values are from 4.0 to 4.12 S/m. No ground-truth data were taken of the bottom conductivity.

A commercially available DIGHEM^{III} AEM system was used (Fraser, 1978, 1979, 1981, 1985). It has two horizontal coplanar coil-pairs operating at 385 and 7200 Hz. The coil separation was 8 m. The sampling rate was 1 s, which corresponds to a 50-m sampling interval along the flight lines for typical helicopter speeds. The position of the aircraft was recorded every 5 s, and its location at 1-s intervals was calculated by linear interpolation.

The data were rescaled and phase-shifted using the calibration constants and procedure described by Won and Smits (1985a). A rescaling constant that increased the amplitude on the order of 8 percent and a phase shift of 3°–5° were obtained for each line.

Figures 2–5 show calculations for flight line 5021. The horizontal axis in each figure is the distance in kilometers along the flight line. Figure 2 shows the difference between the values obtained from the MIM inversion for the bird altitude from the high-frequency data and the radar altimeter readings recorded on the bird. Agreement between the altitude calculated by the MIM inversion of the calibrated data and that obtained from radar altimeter readings is excellent; the average bird height is about 50 m and the altitude differences are less than 1 m.

Figure 3 compares first-layer depths obtained from the MIM inversion and from sonar-determined bathymetry. The ground-truth curve was obtained by interpolating measured ground-truth data points to produce the smoother of the two curves shown. Note that the vertical scale is again in meters. The shoal between 7 and 11 km along the line is clearly visible. For depths greater than about two skin depths (here about 26 m), the noise in the data renders an inversion unreliable for any method.

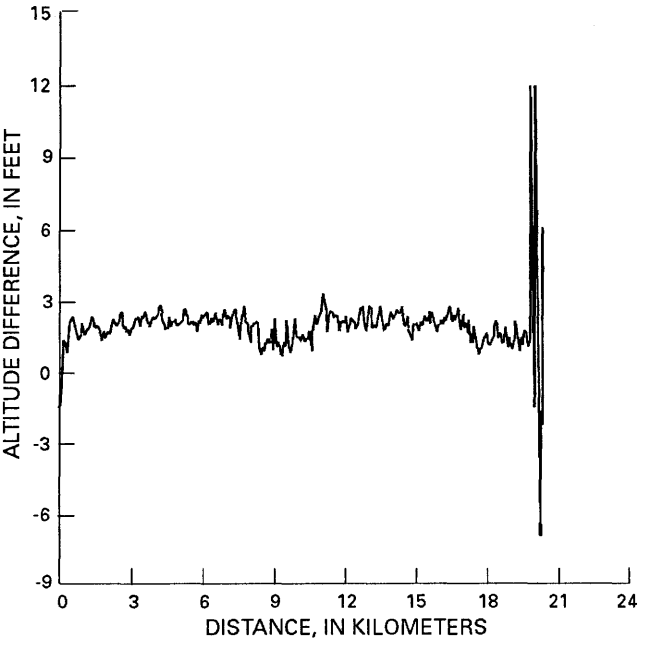

Figure 2. Difference between bird altitude along flight line 5021 obtained from MIM inversion and from radar altimeter readings.

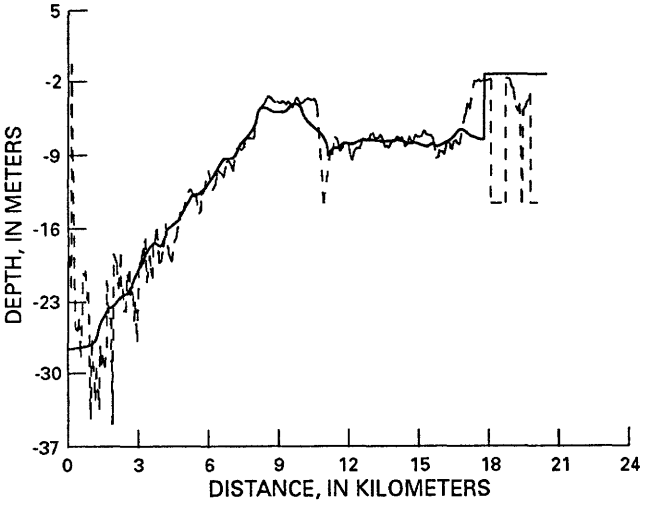

Figure 3. Bathymetry along flight line 5021 obtained from MIM inversion (noisier curve, dashed line), as compared with depth interpolated from sonar measurements (smoother curve, solid line).

The conductivity of the first layer (the sea water) is shown in figure 4 and is close to 4 S/m. At the left side, near zero distance at the beginning of the flight line, the water is very deep, and on the right side, past about 17 km, the water shallows up to the beach. The helicopter altitude was also much greater at the ends of the flight lines (see figure 2). For these two reasons, values at the ends of the flight line are not valid. Conductivities higher than 4 S/m obtained in the relatively shallow water over

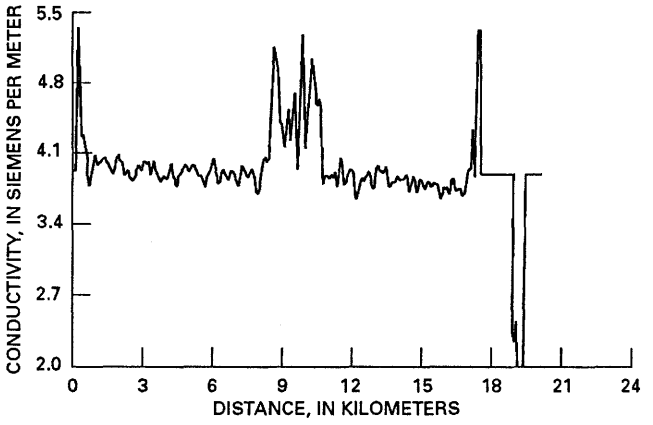

Figure 4. Conductivity of first layer (sea water) along flight line 5021 obtained from MIM inversion.

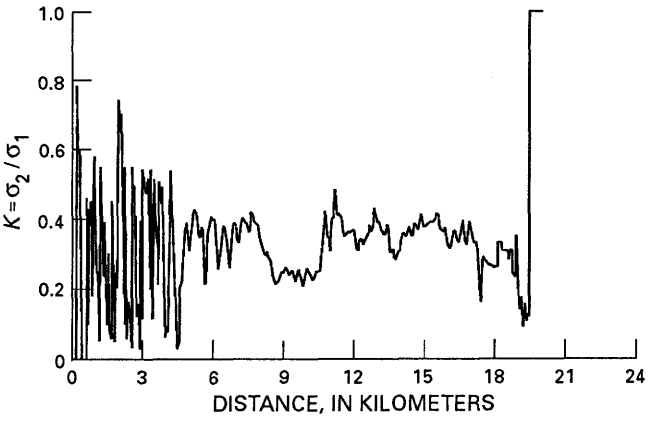

Figure 5. Conductivity contrast K between first and second layers, (that is, between sea water and sea bottom) along flight line 5021 obtained from MIM inversion.

the shoal are possibly the result of a rise in temperature of the water in the first meters of depth on warm windless summer days. An increase of 4 °C in water temperature at a given salinity can result in an increase in conductivity of as much as 10 percent.

Figure 5 shows the conductivity contrast between the first and second layers (that is, the sea water and the sea bottom). Again, values from very deep or very shallow water are not reliable. The sea bottom conductivity is about 1 S/m.

MIM inversions of other flight lines are similar. Some indicate rougher helicopter paths and larger altitude excursions that may have some influence on bird tilt and thus affect the recorded data (Bergeron, Ioup, and Michel, 1987c). Studies underway are attempting to obtain correction/calibration factors for each data value from the bird tilt.

CONCLUSIONS

MIM inversion allows for the rapid and accurate extraction of values for the altitude h of the AEM bird and the conductivity σ_1 of the first layer from the high-frequency data. Using the high-frequency values for h and σ_1 and the low-frequency data, an equally rapid and accurate determination of the first-layer depth d_1 may be accomplished. The total CPU time used on a VAX 8600 was less than 0.01 s per survey point. The low-frequency inversion produces reasonable values for $K<1$; inversion values for $K\gg1$ are generally low by about 10 percent (Bergeron, Ioup, and Michel, 1987b). MIM becomes ineffective at first-layer depths between two and three skin depths (Bergeron, Ioup, and Michel, this volume); however, if the data have an uncertainty of 1 ppm, then any inversion fails at first-layer depths of about two skin depths. The least-stable parameter in the inversion is the conductivity contrast, the second least-stable parameter is depth. They are the most affected by any noise in the data.

AEM data at additional frequencies will allow for a least-squares determination of the model parameters, thereby reducing degradation of the inversion process by system noise. Alternatively, data at more than two frequencies will allow for a more complicated model (more than two layers). For example, a three-layer model might be usefully employed in an analysis of AEM data gathered over a sea ice, shallow sea, and sea bottom system.

REFERENCES CITED

Bergeron, C.J., Jr., 1986, Modified image method—Application to the response of layered ohmic conductors to active electromagnetic sources: Journal of Applied Physics, v. 59, p. 3901–3908.

Bergeron, C.J., Jr., Ioup, J.W., and Michel, G.A., II, 1986, Application of MIM to inversion of synthetic AEM bathymetric data: Annual International Meeting and Exposition of the Society of Exploration Geophysicists, 56th, Houston, Expanded Abstracts, p. 49–52.

_____ 1987a, Application of MIM to inversion of synthetic AEM bathymetric data: Geophysics, v. 52, p. 794–801.

_____ 1987b, Lateral resolution of the modified image method for sea ice thickness: Annual International Meeting and Exposition of the Society of Exploration Geophysicists, 57th, New Orleans, Expanded Abstracts, p. 55–58.

_____ 1987c, Bird tilt: Source of calibration errors in airborne AEM bathymetric data [abs.]: Eos, v. 68, p. 1253.

Bergeron, C.J., Jr., Ioup, J.W., Michel, G.A., II, and Smits, Kuno, 1987, Application of the modified image method to experimental data [abs]: Eos, v. 68, p. 290.

Bergeron, C.J., Jr., and Michel, G.A., II, 1985, Signal limited resolution and bottom feature detectability of AEM coastal survey devices by a modified image method [abs.]: Eos, v. 66, p. 918.

_____ 1986, Modified image method applied to AEM coastal surveys [abs.]: Geophysics, v. 51, p. 1514.

Bergeron, C.J., Jr., Michel, G.A., II, and Ioup, J.W., 1986, Correction factors for the modified image method [abs.]: Eos, v. 67, p. 919.

Fraser, D.C., 1978, Resistivity mapping with an airborne multicoil electromagnetic system: Geophysics, v. 43, p. 144–172.

_____ 1979, The multicoil II airborne electromagnetic system: Geophysics, v. 44, p. 1367–1394.

_____ 1981, Magnetite mapping with a multicoil airborne electromagnetic system: Geophysics, v. 46, p. 1579–1593.

_____ 1985, Airborne electromagnetic bathymetric survey and data analysis, Cape Cod, Massachusetts Area: Naval Ocean Research and Development Activity (NORDA) Final Report, Contract 62306–84–C–0013.

Frischknecht, F.C., 1967, Fields about an oscillating magnetic dipole over a two-layer earth, and application to ground and airborne electromagnetic surveys: Quarterly of Colorado School of Mines, v. 62, 326 p.

Michel, G.A., II, 1986, Development and application of self-correction methods for MIM inversion of AEM bathymetry data: University of New Orleans, M.S. thesis, 60 p.

Michel, G.A., II, and Bergeron, C.J., Jr., 1986, Signal and diffraction limits on detectability of bottom conductivity contrast feature with AEM devices [abs.]: Eos, v. 66, p. 1271.

Smits, K., and Won, I.J., 1987, Airborne electromagnetic bathymetry: Sea Technology, p. 16–22.

Sommerfeld, A.N., 1909, The propagation of waves in wireless telegraphy: Annals Physik, v. 28, p. 665–736.

Won, I.J., and Smits, K., 1985a, Airborne electromagnetic bathymetry: Naval Ocean Research and Development Activity (NORDA) Report 94, 18 p.

_____ 1985b, Airborne electromagnetic measurements of electrical conductivities of seawater and bottom sediments over shallow ocean: Naval Ocean Research and Development Activity (NORDA) Report 95, 19 p.

_____ 1986a, Characterization of shallow ocean sediments using the airborne electromagnetic method: Institute of Electrical and Electronic Engineers, Journal of Oceanic Engineering, OE–11, p. 113–122.

_____ 1986b, Airborne electromagnetic bathymetry: NORDA Review, p. 153–160.

A Novel Approach to Airborne Electromagnetic Data Compilation

By C. Vaughan[1]

Abstract

A novel technique has been developed to rapidly compile and present airborne transient electromagnetic data using an automated algorithm. The method involves fitting a simple pole response to every transient measurement in the survey. The result is a set of initial amplitudes, exponential time constants, and error in fit for every good transient measurement in the survey; noisy transients are rejected. The new parameters may be used to prepare maps of shaded, stacked profiles, where color indicates decay rate and profile amplitude gives anomaly strength. Because decay rate is proportional to apparent conductivity, low and high conductivity responses are distinguished. Two case histories are presented illustrating how the technique may be used both for geological mapping and for discrete target selection in exploration.

INTRODUCTION

Commercially available airborne electromagnetic (AEM) survey systems collect a good deal more information than is usually presented in standard contractor's symbolic interpretations. Among the reasons for this are the overwhelming quantities of digital data collected and the lack of an inexpensive rapid means of compiling the data into a form that is readily understandable to the end user. As an added complication, any means developed must be robust in the presence of all common data deficiencies.

Since 1983, I have participated in a research and development program for wideband digital electromagnetic systems instrumentation and data handling (Vaughan, 1985; Annan, 1986). As part of this program, a novel approach to airborne transient EM data compilation was developed that overcomes many of the difficulties commonly and uncommonly found in AEM data handling. The processing technique, called OUTPUT, is specifically designed to:

1. Extract more information from transient airborne EM data than standard data handling methods,
2. Do this in a highly consistent manner even in the presence of data deficiencies,
3. Present the results in a manner that distills the essential information into a manageable map form while preserving the important geophysical information, and
4. Establish the basis for handling data from wideband multicomponent AEM systems.

The OUTPUT processing technique involves transforming multichannel EM data into an apparent simple pole response. No a priori assumption of target type or geometry is required. No nomograms or models need be available. Each set of transient measurements in the survey is fitted to a single exponential decay in a weighted least-squares sense to yield an initial amplitude, a transient time constant, and a fit quality indicator. Initial amplitude is a measure of the conductor proximity, whereas decay rate provides conductance information. The change of initial amplitude with position along line provides information about target type and orientation that helps to simplify interpretation.

An ideal conductor, such as a well-connected deposit of massive sulfides at shallow depth, is characterized by a strong initial amplitude and a large time-constant value. Conductive overburden responses typically decay quickly (have a small time-constant value) and their initial amplitude is very high because of proximity to the EM system. For areas of continuous conductive cover, the time constant can remain at the same value along the line; however, the initial amplitude may change if the aircraft changes altitude or if the towed receiver bird swings around. On traditional interpretation maps and chart records, this phenomenon generates false anomalies, but because OUTPUT maps key on time constant, they are less affected by such changes. Variations in time constant may occur even when no anomaly peak is observed, such as when surveys are flown subparallel with conductor strike or where bedrock responses are embedded within large surficial responses. These types of targets can be overlooked during standard compilation procedures that place emphasis on anomaly peaks.

[1]A-Cubed Inc., 5566 Tomken Road, Mississauga, Ontario L4W 1P4, Canada. Present address: CGI Controlled Geophysics Inc., 400 Matheson Blvd. East, Suite 31, Mississauga, Ontario L4Z 1N8, Canada.

The OUTPUT transformation method provides a reduction of the parameter space from 6 or 12 channels to 3 estimated parameters and is therefore robust in the presence of noise. Because poor data that cannot be fitted closely are disqualified, the method also serves as a first-pass method of identifying high-quality data that merit more sophisticated treatment.

After a discussion of the procedures involved in the OUTPUT method, two cases of OUTPUT processing will be presented. The cases illustrate how, through processing, airborne EM data can be used to present an expression of the regional geoelectrical structure for geological mapping as well as for pinpointing isolated anomalous targets in mineral exploration.

Acknowledgments.—The author thanks the U.S. Geological Survey for providing an opportunity to present this paper and acknowledges the support of the Canadian National Science and Engineering Research Council through an Industrial Post-Graduate scholarship, Dr. G.F. West, A-Cubed Inc., Controlled Geophysics, and particularly Dr. Peter Annan for his patient support and direction during the course of the research.

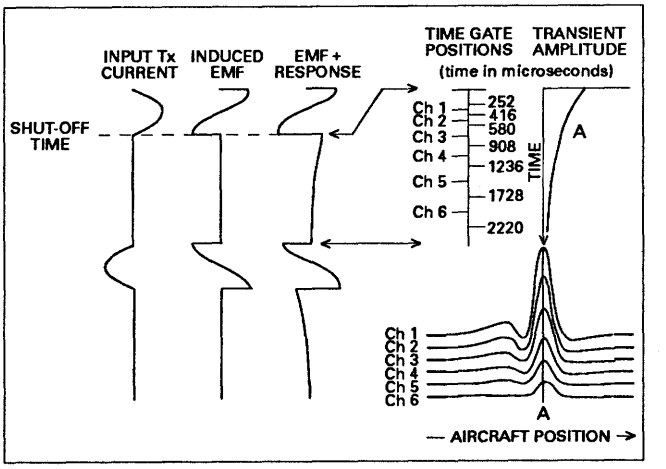

Figure 1. Principles of the INPUT EM system. The transmitter current waveform (Tx) generates a time-varying magnetic field, which induces an electromagnetic field (emf) in the buried conductor and the receiver coil. The eddy currents induced by the emf produce a secondary magnetic field response, which also induces an emf in the receiver. The total measured voltage is the sum of the two emfs. The transient ground response is sampled in six time gates after the transmitter shuts off to produce six channel amplitude profiles as illustrated. These profiles are typical of a vertical thin-sheet model.

BACKGROUND

Figure 1 presents an overview of the operating principles of a typical transient AEM system; in this case, INPUT. A repetitive current waveform of alternating half-sine pulses is transmitted, each followed by a period of off time. The resulting time-varying primary magnetic field induces electromotive eddy currents to flow in the ground, and these in turn produce a secondary field detected by the towed-bird receiver. The total received voltage is a complex waveform. In the presence of a conductor, the waveform exhibits a transient that decays during the transmitter off time. The transient is sampled within a series of time windows and the resulting transient amplitudes are expressed in parts per million of the primary field at the receiver. An anomalous response from a nearby conductor produces the largest response in the earliest channel (channel 1) and a monotonic decrease in amplitude in subsequent channels.

The channels of data are usually plotted in profile form as a function of position and (or) time of the survey aircraft. The shape and strength of the profiles provides important information about the depth, shape, and orientation of the conductor. The rate of decay of the transient is a measure of conductivity and overall size of the body because larger conductors support the flow of larger induced eddy current systems and their transients decay more slowly than those of smaller ones. In the absence of a secondary field, the traces will be characterized by low-amplitude fluctuations due to atmospheric and system noise sources.

During postflight data compilation, peaks of anomalies are selected either manually from the profiles or by using automated algorithms. To permit line-to-line correlation of anomalous responses, the data are best presented in map form. Unfortunately, maps provide a limited parameter space. To overcome this limitation, annotated symbols have come to be the standard means of presenting anomalous responses.

An example of measured INPUT data is shown in figure 2 along with the standard interpretation as provided by the airborne contractor. The anomaly shape is typical of that produced by a finite, vertical platelike conductor. Source geometry information is lost in the interpretation because it is based only on a "Number of Channels" approach wherein the interpreter decides in how many channels the anomaly is visible. In this case, a three-quarters shading indicates that five channels have appreciable amplitude. The strength of the anomaly is provided by plotting the channel 2 amplitude to the lower right of the symbol. The apparent conductivity-thickness product based on a fit to a semi-infinite vertical half-plane nomogram is plotted to the upper right of the symbol. The interpretation is completed by the addition of an identification letter at the upper left and a flag for magnetic association, should there be any, to the lower left.

The number of channels analysis fails to discriminate between high-amplitude, quickly decaying anomalies and lower amplitude, slowly decaying

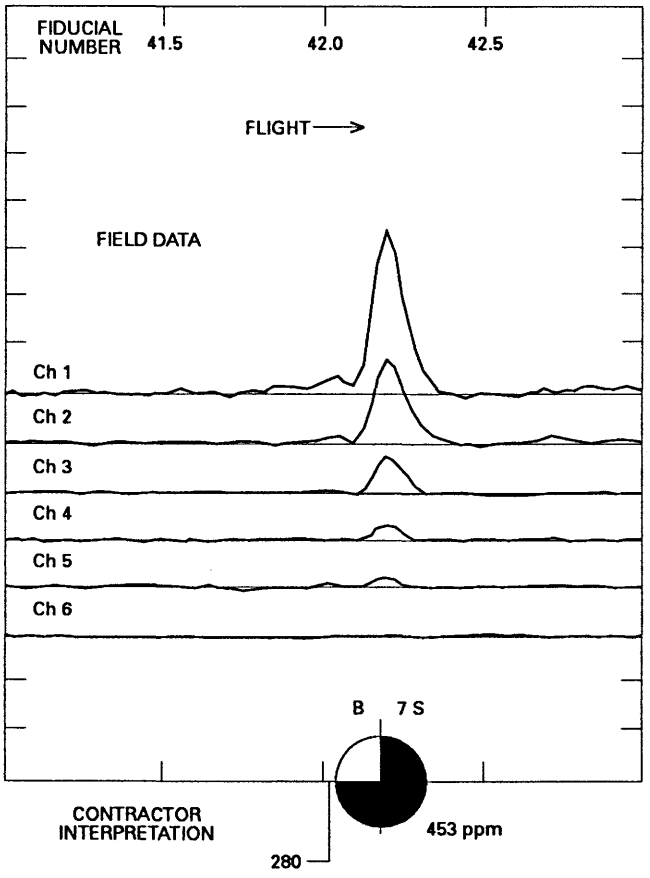

Figure 2. An example of real INPUT data and the standard contractor's interpretation. Note the resemblance to the model profile shown in figure 1. The three-quarters shading of the circle indicates that a five-channel anomaly was detected. The channel 2 amplitude is 453 ppm and the apparent half-plane conductivity-width product 7 S. The value of 280 indicates that there is some magnetic correlation with the EM anomaly, here denoted *B*.

anomalies, both of which may have an identical number of channels of appreciable amplitude. The end user must rely on the provided conductance value and channel 2 amplitude to grade the response. There is no inherent quantitative confidence level in the interpretation because it is so subject to bias. There is also no indication of the goodness of the nomogram fit or indeed if the model is valid.

Anomaly selection carried out by hand requires a trained analyst. Unfortunately, inconsistent results can occur when several individuals interpret parts of the same data set. Recently, automated anomaly-picking procedures have been implemented. Although such procedures are a step in the right direction, the algorithms must be tuned to avoid over- or under-picking. In addition, the technique cannot be used to identify broad changes in conductivity because it stresses discrete targets having peaked response where signal-to-noise ratios are high.

I examined the use of automated algorithms to address the problems just described. Ideally, such an algorithm should be amenable to computer processing using direct methods, it should be generally applicable regardless of target morphology, it should allow poor or noisy data to be disqualified to avoid misinterpretation, and it should be valid for every point in the survey, not just anomalous peaks. The algorithm should handle data deficiencies such as overcompensation, data clipping, and contamination by atmospheric and system noise.

Multichanneled transient data are ideal for least-squares methods because data redundancy can be used to advantage. Two simple models considered were the power law decay and the simple pole. Each model is characterized by two quantities and each is readily applied. Palacky (1972) investigated using each of these models to fit selected peak responses. Both models can be applied to first order, but the single exponential decay of the simple pole is easier to relate to physical processes. The initial amplitude is a function of conductor proximity, shape, and orientation, and the time constant is proportional to conductivity and spatial extent. The latter is true because larger eddy current systems can flow in large conductors and these have large time constants.

The heuristic model for the simple pole is a single-turn loop conductor in free-space (Grant and West, 1965). I call this the generic model because all other confined conductor models can be generated by superposition. For example, complicated responses from thin sheets are modeled by the program PLATE using the superposition of 15 eigencurrent systems, each of which has a characteristic exponential decay. Fitting a simple exponential to real data is equivalent to taking the dominant eddy current system in the conductors nearby.

Fitting the simple pole model to real data results in a reduction of the parameter space by a factor of three or more because the 6 or 12 AEM channels are converted to two estimates: initial amplitude and time constant. A third computed value is the error in fit between the measured and estimated transient. The reduction allows spurious data values to be omitted without seriously affecting the results. Among the common problems handled are clipping of anomaly peaks by instrumentation, spheric spikes, and negative amplitudes due to overcompensation in flight.

Some interpretation schemes use channel ratios to determine decay rates, but these break down if one or both channels used have incorrect or drifting zero-levels. The OUTPUT method uses all available channels to estimate the same parameter to a higher degree of confidence.

The fitting process also results in a partial partitioning of the response into geometry-related factors and electrical factors. For example, response amplitude

is most strongly affected by changes in system geometry and height, whereas time constant is almost invariant. False anomalies produced by rapid changes of system geometry do not show time-constant variations. Conversely, conductors can be identified on the basis of elevated time constant even when amplitude remains fixed, as is the case when flight direction is subparallel with geological strike.

PROCEDURE

Before processing, the entire data set must be properly calibrated and leveled and statistical information about channel noise levels obtained. To do this, a histogram analysis is used.

For each EM channel, a histogram is computed by tabulating the number of occurrences of each amplitude in that channel. Such histograms have a peak at the most frequently occurring amplitude. In data from resistive environments, the peak corresponds to that channel's zero-level. The values resulting from random noise sources are roughly symmetric about the peak. Predominantly positive amplitudes contributed by the anomalous ground response produce a positive skew. Incorrect zero-levels result in a translation of the entire histogram away from zero. By determining the shift amount, a zero-level correction can be obtained.

In figure 3, the solid histograms represent raw data and the outlined histograms the leveled and calibrated data. Channels 1 and 2 have been broadened by the calibration because their gains were initially reduced during recording. Rescaling to unit gain resulted in a factor of four and factor of two increase for channels 1 and 2, respectively. Note the elevated zero-level in channel 3 before leveling. After rescaling, all zero-levels were within 5 ppm of true zero. The individual channel noise levels were estimated from the histogram widths by discounting the ground response and measuring the standard deviation surrounding the peak. The estimated values are more reliable indicators of noise levels than the noise levels based on visual examination of analog charts quoted by the survey companies.

The prepared data are then processed using the OUTPUT program. Every point in the survey consists of a transient measured in a number (usually 6 or 12) of EM channel amplitudes (fig. 4). The simple exponential decay model is matched with each set of channels in the survey using a weighted least-squares method. Noisy channels are weighted less than quiet ones, and if necessary filtering is used to increase signal-to-noise values. Spurious channels are trapped and rejected. Should too many channels be omitted, the entire transient is disqualified and no fit is obtained. In the more resistive parts of a survey area, a large number of channels may have to be rejected because of low signal,

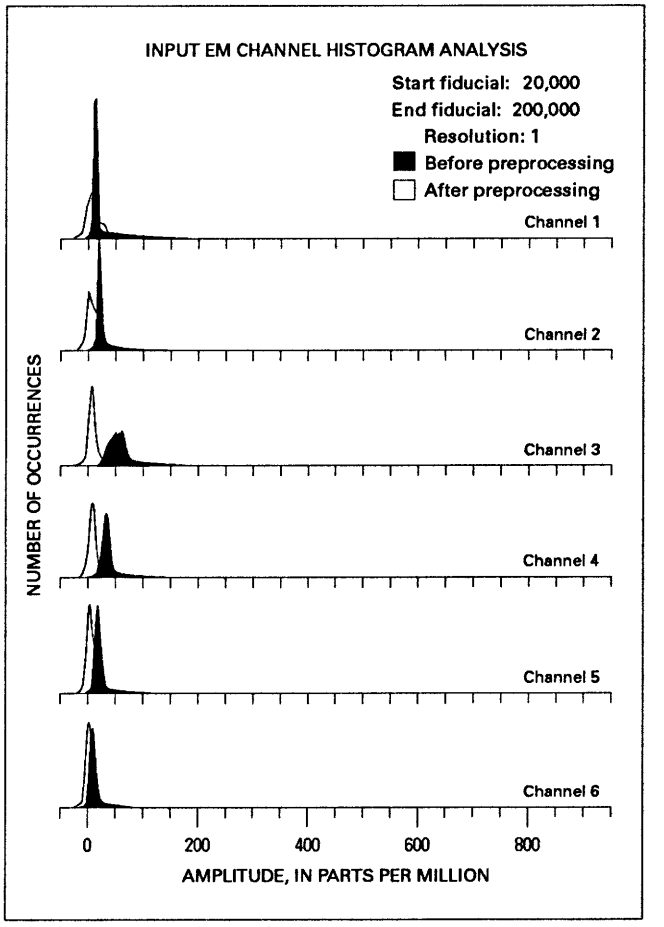

Figure 3. Amplitude-occurrence histograms for each channel in an INPUT EM survey flight before and after preprocessing. Note the zero-level offsets (shifted histogram peaks) from zero, especially in channel 3. After processing, all channel zero-levels were within 5 ppm of 'true' zero.

so the OUTPUT results are frequently blank. Alternatively, a background low time-constant value can be assigned to rejected transients.

The values generated by the OUTPUT program are the initial amplitude (A_0) of the exponential decay in parts per million, the time constant (τ) of the exponential decay in microseconds, and the quality of fit of the decay to the measured channels. The latter is normalized and expressed as a percentage of the transient's energy. The closer the fitted transient matches the measured one, the closer the quality value will be to a maximum of 100 percent.

Figure 5 presents an example of one line of processed survey data in chart form. Six channels of calibrated and leveled EM data are plotted along the bottom of the chart. For clarity, the zero-level of each channel is offset 200 ppm from the previous one. Three types of response are present. At left is a zone of surficial (overburden) response characterized by large-amplitude background response and several minor peaks super-

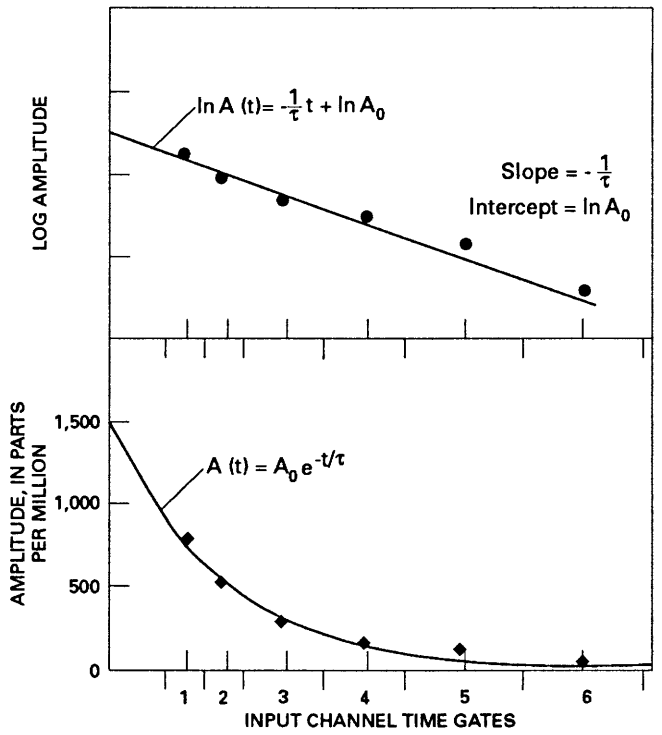

Figure 4. An INPUT transient measurement in original (lower half) and linearized (upper half) forms. The initial amplitude and time constant of a single exponential are obtained from the slope and intercept of the best-fitting straight line. τ, time constant; A_0, initial amplitude in parts per million; t, time.

imposed within it. Note that the late channels have negative amplitudes due to overcompensation during data collection. The central part of the line is a typical response generated by a localized deposit of massive sulfides in the bedrock. The anomaly is narrower and exhibits no overcompensation negatives. Finally, to the extreme right, the low amplitudes of the EM responses indicate that no conductors are present.

Above the EM data are two OUTPUT-generated parameters expressed as pseudochannel 1 and time constant. If channel 1 is the amplitude of the measured transient at a specified time after the primary field shuts off (commonly 300 μs), pseudochannel 1 is defined as the amplitude of the fitted exponential at the same delay time after primary field shut off. For every measured EM channel amplitude, a corresponding pseudochannel amplitude can be produced. The benefit of using the pseudochannel amplitude instead of the estimated initial amplitude is that the pseudochannel value is of a magnitude similar to measured channel data. By extrapolating the fitted model response, a reliable pseudochannel amplitude can generally be computed for very late delay times where the original anomaly amplitudes are far smaller than the noise envelope.

In figure 5, the fitted parameters have zero-values over those parts of the line where data are too noisy or weak to obtain an exponential decay, such as over the resistive zone. Spatial filtering can be used to improve signal-to-noise ratios and obtain some fits in such areas.

The similarity between pseudochannel 1 and calibrated channel 1 indicates that the exponential has fitted the observed data well. The uniformity of the time-constant profile across the zone of surficial response indicates that the electrical properties do not vary significantly, whereas over the massive sulfide response the time-constant values are three to four times larger. The minor peaks superimposed upon the surficial response are not conductors but rather motion-induced false anomalies generated by changes in coupling between the towed receiver and the conductive overburden.

Plan maps are employed to present the processed data in a more useful form. The preferred format is the pseudochannel map of shaded stacked profiles on which profile height represents pseudochannel amplitude and color expresses time constant. On such maps, line-to-line correlation readily reveals conducting structures and color coding allows short time-constant overburden responses to be distinguished from moderate and long time-constant basement conductors.

OUTPUT-processed maps of a INPUT survey in central Canada are shown on plate 1 (diagrams *B–H*) for various delay times. The amplitude of each data point on the maps is colored according to its time-constant value. The shortest time constants are black, the medium time constants are green, and the largest time constants (best conductors) are red. The INPUT survey was also interpreted using traditional symbolic representation of anomalous responses (plate 1, diagram *A*). Total magnetic field data for the survey are also shown (diagram *H*).

A map of a later pseudochannel can be prepared that contains only the better conductors because good conductors have larger time constants and hence take longer to decay away than poorer responses. Alternatively, for geological mapping, earlier pseudochannel maps show overburden distribution, alteration zones, faults, and other weak conductors. The adaptability of the approach is demonstrated in the examples that follow.

EXAMPLES

Two examples of OUTPUT processing demonstrate how the technique can be used. In the first example, a large survey area having numerous anomalous picks was processed to assist in precious metal exploration. The prime targets identified could then be explored using ground geophysical methods and drilling. The second example is part of a regional reconnaissance survey used to promote exploration in the Labrador

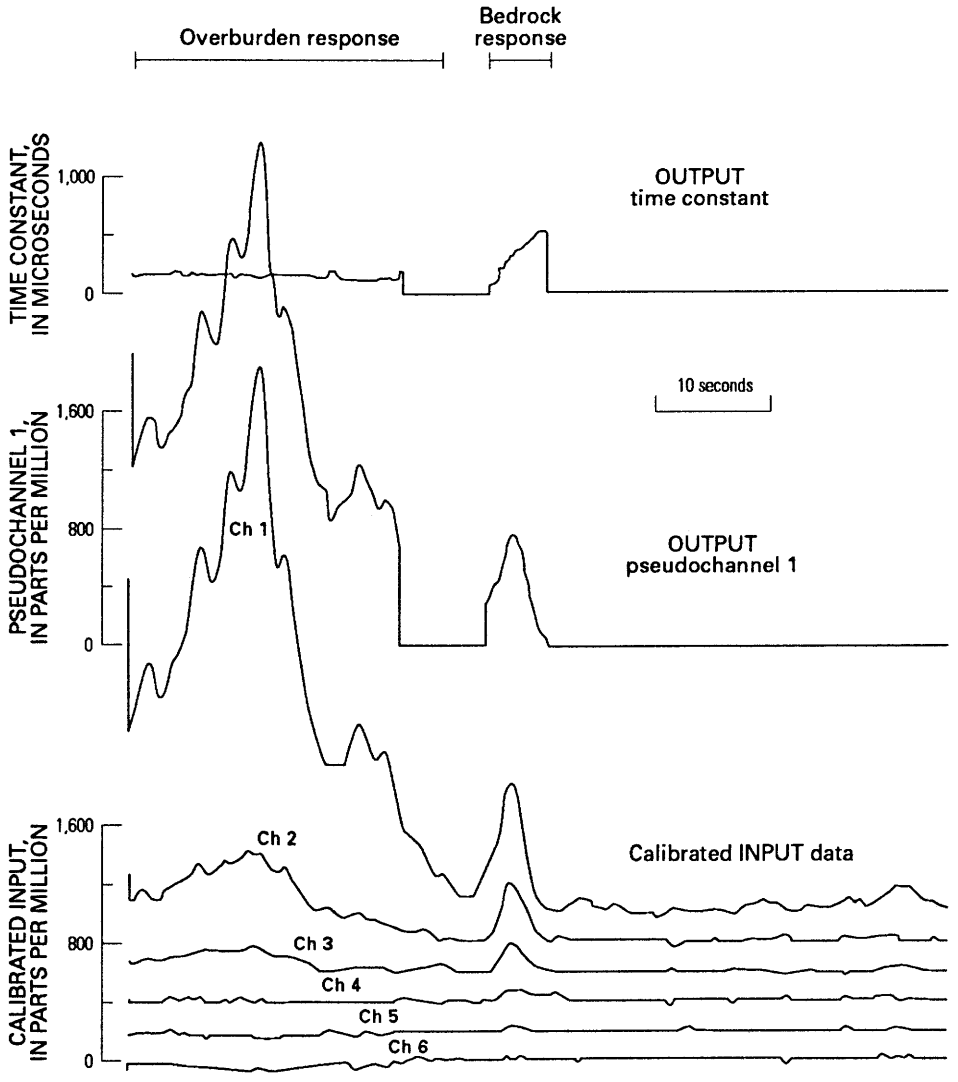

Figure 5. An example of INPUT EM data processed using OUTPUT. The data exhibit three characteristic kinds of response: conductive surficial material, massive sulfides, and resistive terrain. The profiles of pseudochannel 1 and time constant show the results of processing these responses. The surficial conductor data have multiple false anomalies due to variations in the aircraft towed-bird geometry. The uniform time-constant value indicates no changes in electrical properties. The massive sulfides produce both an amplitude peak and a time constant three to four times larger than the surficial material. The resistive terrain data were too weak to obtain any transient fits.

Trough of Quebec, Canada, and demonstrates how geological mapping may be assisted using OUTPUT-processed airborne electromagnetics.

The survey area of the first example is central Canada where shield-type rocks are overlain unconformably by younger Paleozoic rocks and all are covered by overburden. The surface terrain is swampy with numerous lakes. The target mineralization is in the basement rocks at or below the unconformity.

Diagram *A* on plate 1 presents the results of the INPUT survey interpreted in a traditional manner. Each symbol represents a picked anomalous peak. The abundance of intercepts reflects the results of automated anomaly picking. Many of the picks are false anomalies of the kind shown in figure 5. The OUTPUT process was carried out and the data presented in map form.

Diagram *B* on plate 1 is a map of pseudochannel 1. The delay time is 300 μs after primary field shutoff. Three types of electromagnetic responses are revealed: (1) a series of narrow north-trending zones of poor conductivity as indicated by time constants less than 350 μs; (2) a set of linear zones trending northwest that have moderate to high conductivity; and (3) broad areas of low conductivity.

The narrow, north-trending low-conductivity responses correlate with faults within the Paleozoic rocks that have associated conductive alteration products or disseminated mineralization. The broad areas of low conductivity correlate with conductive lake-bottom sediments. The northwest-trending zones of high conductivity correlate with shear zones within the basement rocks. The red areas represent either localized increases in conductivity or an increase in the size of the conductor that allows larger induced eddy current systems to flow.

On maps of later pseudochannels, the poorly conducting responses decay away leaving the best targets (plate 1, diagrams *C–F*). The map of pseudochannel 2 shows a significant reduction in the low-conductivity (black) amplitudes and almost no reduction of the high-conductivity (red and green) amplitudes; the map of pseudochannel 3 shows the same trends. By pseudochannel 4, all amplitudes have diminished significantly and a gain of four times has been applied to boost them. By pseudochannels 5 and 6, the basement targets are clearly visible, free from surficial interference, and a manageable number of high-conductivity zones can be selected for followup. The pattern of anomaly peaks allows estimates of conductor type, orientation, and position to be made. The total magnetic field data presented in shaded stacked profile on diagram *H* of plate 1 show correlation with both basement and Paleozoic structures.

The second example is from the Labrador Trough, in the province of Quebec, Canada, in an area northwest of Retty Lake where platinum has recently been discovered. The southwestern half of the area consists of a sequence of basalt, gabbro, and peridotite and minor pelitic schist, all within a folded structure that trends northwest (plate 2, diagram *A*). The northeastern half consists of basalt and minor peridotite and gabbro but no schist. At the extreme northeastern end of the area, a thrust fault marks the transition to biotite-plagioclase paragneiss. The rocks in the extreme southwestern part of the area are overlain by agglomerate and variegated overburden.

The total magnetic field data are shown in shaded stacked profile on diagram *B* of plate 2. The dominant magnetic responses are produced by the peridotite and agglomerate. Correlation with geology is high, but this is not surprising because regional geologic maps in remote areas commonly are prepared using airborne magnetic surveys. The magnetic response in the northeastern half of the area is low.

The OUTPUT-processed INPUT EM results for pseudochannel 6 (2.28-ms delay time) are presented in diagram *C* of plate 2. All responses fitting better than 80 percent quality are shown.

The electromagnetic responses do not correlate with a particular rock type to the degree that the magnetic responses do. Instead, the responses are influenced by structure such as the noses of folds and the traces of thrust faults. The better conductors correlate with key structural changes, and the poor conductors lie mainly along straight features. The thin, folded gabbro/peridotite beds in the west-central part of the survey area are highly conductive. Notice that OUTPUT results indicate the presence of high conductivity even where flight lines are subparallel with strike.

A number of strong linear features have been mapped in the eastern part of the survey area within the basalt. These probably represent contacts with gabbro and peridotite units not previously mapped. The magnetic data are far less sensitive to these structures. A combination of processed EM and magnetic data thus can assist in regional geological mapping and at the same time indicate potential targets for exploration.

CONCLUSIONS

The OUTPUT computer processing technique described here offers solutions to many of the traditional airborne transient EM data-handling problems. The number of key parameters are reduced, and important geometrical and electrical information is retained over the entire anomalous zone, not just the peak of the anomalous response. Thus the data are useful for both geological mapping and discrete target selection.

The processing can be carried out rapidly and with a minimum of manpower; thus, more time can be spent on interpretation. The OUTPUT method is applicable to cases where flight lines are not normal to strike and to cases where individual channels suffer from clipping or high noise levels. Because well-established rules have been followed to make programs robust in the presence of noise, consistent results are generated. As a byproduct of the computer processing, a quantitative analysis of the data noise levels and quality of estimated parameters is carried out. Finally, the fitted data are stored online in the computer so that the interpreter can prepare maps specifying delay time, quality level, and characteristic anomaly types.

Although OUTPUT processing is an oversimplification in some cases, it facilitates selection of those data that can benefit from more sophisticated analysis. To date, both older archived INPUT EM surveys and new data collected by the GEOTEM transient EM system have been successfully processed using the OUTPUT technique. These data are from a variety of environments including deep-basin uranium deposits and low-conductivity gold prospecting areas. Future developments include algorithms to remove masking overburden

effects and the application of more advanced models. Work is also ongoing to adapt some of these techniques to frequency-domain data.

REFERENCES CITED

Annan, A.P., 1986, The development of the PROSPECT I airborne EM system, *in* Palacky, G.J., ed., Airborne resistivity mapping: Geological Survey of Canada Paper 86–22, p. 63–70.

Grant, F.S., and West, G.F., 1965, Interpretation theory in applied geophysics: New York, McGraw–Hill, 584 p.

Palacky, G.J., 1972, Computer assisted interpretation of multichannel airborne electromagnetic measurements: Research in Applied Geophysics 3, Geophysics Laboratory, University of Toronto, 152 p.

Vaughan, C.J. 1985, Computerized analysis of airborne transient EM data: Society of Exploration Geophysicists, Annual Meeting, 55th, Washington, D.C., Expanded Abstracts of the Technical Program, p. 239–241.

SECTION 3: RESOURCE AND GEOLOGICAL APPLICATIONS

Airborne Electromagnetics, Geological Mapping, and Prospecting for Nontraditional Targets[1]

By G.J. Palacky[2]

Abstract

During the last decade, airborne electromagnetic (AEM) surveying has cut its umbilical cord with prospecting for massive sulfide deposits. It has become apparent that AEM techniques can be successfully used in prospecting for other types of deposits, such as lateritic nickel, bauxite, kimberlite, and uranium. These targets are not as highly conductive as volcanogenic massive sulfides and the main conductive minerals belong to the clay group. The increase in conductivity vis-a-vis fresh rocks is due to in situ chemical weathering that forms conductive saprolite.

The conductivity of saprolite layers produced by selective chemical weathering depends on the lithology of the parent rock. Results of AEM surveys have been successfully used in geological mapping of volcano-sedimentary sequences. An approach consisting of compilation of pseudogeological maps based on AEM data and subsequent field checks of selected features constitutes a viable and cost-effective alternative to traditional mapping, particularly in regions of difficult access and limited outcrop.

Test surveys in northern Ontario demonstrate that AEM surveys can also be used in mapping Quaternary sequences. Identification of clay, till, and sand is feasible, and determining thicknesses of such sediments is promising.

In principle, wide-band or multifrequency AEM surveys can be used for all mentioned applications simultaneously. Combined AEM/magnetic surveys constitute a powerful and cost-effective mapping tool, as recognized in Finland, Sweden, and Quebec where systematic AEM surveys started many years ago.

INTRODUCTION

After World War II, a strong demand for base metals stimulated the development of geophysical techniques capable of speeding up the painfully slow process of traditional prospecting. The combination of airborne magnetic and electromagnetic methods became a powerful exploration tool, initially in North America and subsequently in other parts of the world. Airborne electromagnetic (AEM) technology was developed in Canada in the early 1950's, and most of the massive sulfide discoveries using AEM were made in that country. The market for AEM surveys grew rapidly until 1967, when it stabilized. Worldwide annual production during the peak years was 500,000–600,000 line-km (Palacky, 1986). During that time, 18 systems were operated by Canadian contractors and mining companies who carried out about 80 percent of AEM surveys in the Western world (Collett, 1986). AEM activities began to decline in 1976, and the previously achieved highs were matched only during a brief 3-year period between 1979 and 1981, mostly because of uranium exploration in the Athabasca Basin, Saskatchewan, Canada. With the worldwide drop in the mineral exploration activities in the 1980's, the use of AEM methods has steadily decreased to a low of 158,478 line-km in 1985; 303,210 line-km were surveyed in 1987 (Montgomery, 1986; Senti, 1988). This decline in AEM surveying contrasts with the increase in aeromagnetic surveying, perhaps because airborne magnetics has been perceived as a tool of geological mapping, not of prospecting for ferrous metals, and many countries have acquired complete magnetic coverage of their territories.

Although AEM methods are at least equally suitable for pseudogeological mapping and although in many geological conditions the information extracted from AEM data cannot be obtained using other geophysical methods, AEM methods have not been extensively utilized for these purposes. There are at least three reasons for the limited popularity of AEM methods: (1) lack of familiarity with AEM responses over different geological targets; (2) limited marketing perspective of contractors who identify mining exploration as their sole lucrative market and, until recently, made only lukewarm efforts to develop other applications; and (3) the higher cost of AEM surveys in comparison with total-field magnetic surveys.

All these reasons are intertwined, and remedies can be recommended by addressing them in the listed

[1]Geological Survey of Canada Contribution No. 47388.

[2]Geological Survey of Canada, 601 Booth Street, Ottawa, Ontario K1A 0E8, Canada.

order. Both contractors and potential clients must learn more about AEM responses of various geological targets. This weak link between geology and geophysics has unfortunately escaped the attention of researchers, and unless it becomes well understood AEM methods will continue to have only a limited appeal to geologists. Concepts of resistivity characteristics of geological targets are outlined in Palacky (1988).

Geophysical contractors should have on their staff geoscientists who have a broad vision and good understanding of global markets. One positive trend is the activities of more government organizations in acquiring their own hardware and becoming engaged in systematic AEM coverage. This has been happening in Austria, China, Finland, Germany, India, Norway, Sweden, and the USSR. The pioneering government organization was the Geological Survey of Finland, which started systematic airborne electromagnetic/magnetic coverage of the country in 1954. The program was completed in 1972; in the same year, a more detailed survey including radiometrics was initiated. By the end of 1985, 1,476,000 line-km of combined airborne surveys had been carried out in Finland (Peltoneimi, 1986).

Acknowledgments.—Societé Nationale Elf Aquitaine, Pau, France, and Rio Doc Geologia e Mineração, Rio de Janeiro, Brazil, grated permission to publish results of AEM surveys (Bois-de-Cené and Itapicurú, respectively). AEM surveys in northern Ontario (Val Gagné) were funded under the Mineral Development Agreement between the Governments of Canada and the Province of Ontario. INPUT time-domain AEM surveys (Brazil and France) were carried out by Geoterrex Ltd. of Ottawa, Canada, and helicopter AEM surveys (Ontario) were performed by Aerodat Ltd. of Toronto, Canada. The illustrations were drafted by S.J. Davis and the manuscript typed by M.L. Wilson.

MINERAL EXPLORATION TARGETS

Extensive literature exists describing application of AEM methods in prospecting for volcanogenic massive sulfides. The most up-to-date review is in Nabighian (in press). The "Canadian" prospecting approach was pioneered by the Mattagami Syndicate in the late 1950's (Paterson, 1970). In this approach, a prospective area (greenstone belt) is surveyed using AEM/magnetic methods, anomalies interpreted, and certain targets recommended for ground followup. Depending on the results of the ground geophysical surveys, some conductors are drilled. This approach is fast and cost-effective and has resulted in the discovery of over 50 economic orebodies in Canada. When attempts were made in the 1970's to transplant this exploration sequence to other countries, the approach was not as successful. The lack of success can be traced to the selection of anomalies for followup. The number of bedrock conductors in Canada is relatively small, and in most instances their responses can be clearly separated from those due to Quaternary sediments (mostly clays). In regions where the weathered layer has not been eroded by glaciers, AEM anomalies are associated with most geological formations and visual recognition of bedrock anomalies is very difficult. In order to successfully interpret AEM data, geological input must be greatly increased and conductivity maps must be correlated with geological maps. As a feedback, AEM data can be used to improve geological maps. Most of the pioneering studies in the lithological interpretation of AEM data were made in Brazil (Palacky and Sena, 1979; Palacky, 1981).

By the 1960's attempts had been made to use AEM methods in ground-water exploration (Collett, 1966; Baudoin and others, 1970). This application has grown slowly but steadily and today accounts for 5–10 percent of all AEM surveys (Sengpiel, 1983; Johnson and Seigel, 1986). Mapping of aquifers can be considered a special type of geological mapping.

Kimberlite pipes were perhaps the first nonsulfide mineral targets for which AEM methods were used. Kimberlite, which sometimes hosts diamonds, is an ultramafic igneous rock. Similar to other igneous rocks of this type, it weathers easily and a conductive, clay-rich layer called "yellow ground" forms at the top of the pipe. Magnetic surveys traditionally have been used in exploration for kimberlite, but, as Macnae (1979) demonstrated, many pipes have no magnetic signature. Surveys in various parts of Africa indicate that AEM methods are a more reliable prospecting tool. Figure 1 (Johnson and Seigel, 1986) shows magnetic and conductivity responses of three kimberlite pipes in Tanzania. Although the yellow ground overlying the pipes is conductive (160–320 mS/m), only two pipes are magnetic.

Lateritic nickel orebodies can be detected using AEM surveys because the ore host, a saprolite (one horizon of the weathered layer), is highly conductive. Peric (1981) studied resistivity characteristics of the Musongati deposit in Burundi, which developed by weathering of a dunite massif. The conductivity of the saprolite, as determined by electrical well logging and resistivity soundings, is greater than 150 mS/m. Conductance maps of the area (fig. 2) were compiled from resistivity soundings. Values in excess of 0.4 S delineate a well-developed saprolite layer containing economic grades of nickel. Such concentrations usually occur on slopes. On plateaus, the weathered layer is thick, but because of leaching, the saprolite horizon is thinner. (Details of weathering and additional data from Musongati will be discussed later.) In principle, AEM

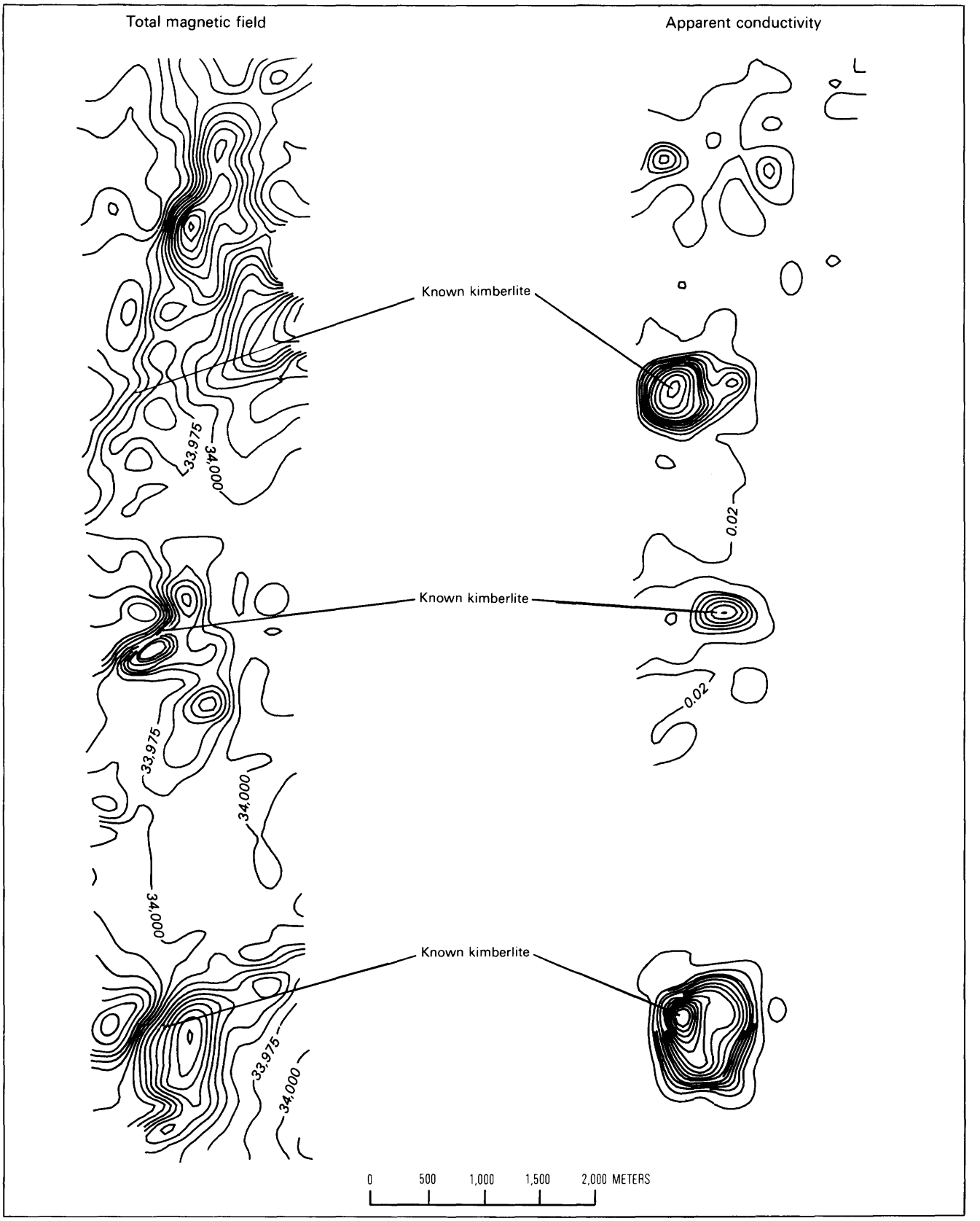

Figure 1. Total magnetic field and apparent conductivity in an area containing three known kimberlite pipes in Tanzania. The conductivity map was compiled using Tridem AEM data. Contour interval 25 nT and 0.02 S/m, respectively. Modified from Johnson and Seigel (1986).

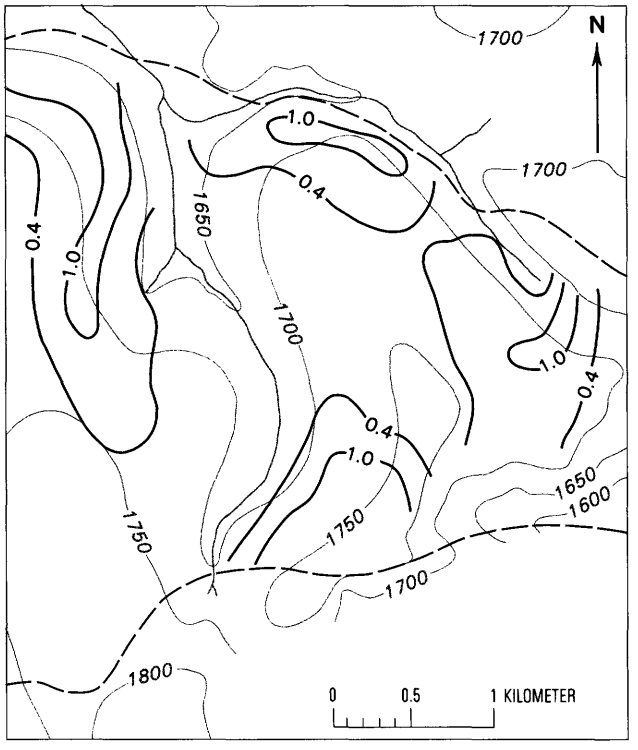

EXPLANATION

—0.4— Conductance—In siemens

—1700— Elevation—In meters

Drainage

Figure 2. Conductance map of the Musongati lateritic nickel deposit. High-grade saprolite was found in areas where conductance exceeds 0.4 S. Modified from Peric (1981).

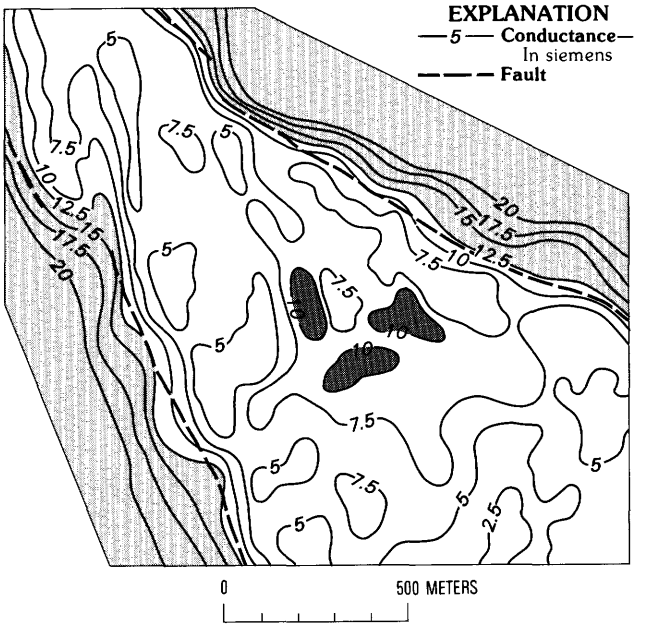

Figure 3. Conductance of Bakonyjákó horst, Hungary. Bauxite accumulations can be detected as conductive areas (black) on the resistive horst. Thick layers of sedimentary rocks on the downthrust side of faults (gray) are highly conductive. Modified from Kilényi and Szabó (1985).

methods can be used for mapping nickel-rich saprolite formed over ultramafic massifs.

Bauxite forms by intense chemical weathering and leaching under tropical conditions. Unlike lateritic nickel, the ore is the leached zone, which is enriched in aluminum oxides and depleted in iron and silica. Although the leached zone is not as conductive as saprolite, it is more conductive than fresh parent rock and EM and resistivity techniques can be used to map accumulations of bauxite. The most extensive use of such techniques in bauxite exploration has been reported in Hungary (Szabadváry, 1987). Figure 3 shows a conductance map of the Bankonyjákó horst north of Lake Balatón. The horst is bounded by subvertical faults, which are accurately outlined by the conductance contours (12.5 S). On the downthrust sides, the thickness of conductive sediments exceeds 300 m. Bauxite targets are anomalies of high conductance (over 10 S) on the horst. The map (from Kilényi and Szabó, 1985) was compiled using the results of resistivity profiling surveys, but similar results could have been obtained using AEM surveys.

In the late 1970's and early 1980's, time-domain AEM surveys were extensively used in the Athabasca Basin, Saskatchewan, Canada, to prospect for unconformity-related uranium deposits. The most spectacular discovery, that of the Cigar Lake deposit, was made using AEM surveys. The deposit, with reserves of 110,000 tons, has the highest grade (12.2 percent U_3O_8) of any uranium orebody in the world. In addition to uranium ore (pitchblende), which formed by replacement of kaolin matrix in the weathered layer, the deposit also contains nickel and cobalt (Ruzicka and LeCheminant, 1986). The discovery made geophysical history because of the depth of the orebody, 415 m, and was possible because of (1) resistive overlying sediments (thin layers of glacial till and sandstone of Devonian age Athabasca Formation, both having conductivities less than 1 mS/m), and (2) the large horizontal extent of conductive regolith, which probably formed by weathering of basement rocks before Athabasca transgression and sedimentation, and the presence of conductive graphitic metapelites in the basement.

Figure 4 summarizes geophysical results for the Cigar Lake area. Magnetic anomalies were detected over Archean granite and the meta-arkose unit of the Aphebian-age Wollastone Group. Conductive regolith is well developed over the metapelitic unit of the same group, parts of which are rich in graphite. Figure 5 shows a geological cross section (*X*–*Y*) that was constructed using drilling results. Resistivity values were interpreted from ground EM and magnetotelluric measurements (Fouques and others, 1986). The significantly larger

extent of the AEM anomaly as compared to that of the graphitic conductors mapped by ground EM surveys (DEEPEM) suggests a significant contribution from the conductive regolith. The orebody itself does not have a higher conductivity than barren regolith, and the EM anomaly can be attributed to a local thickening of the regolith and association with graphitic metapelite. All areas of EM anomaly therefore were systematically drilled in order to discover the orebody.

These four examples have been included to stimulate interest in mineral prospecting for nonsulfide targets. Although the mineral commodities (diamonds, nickel, aluminum, uranium) are very different, EM techniques can be applied in exploration because all of the areas include conductive layers rich in clay minerals.

ELECTRICAL PROPERTIES OF THE WEATHERED LAYER

Weathering is a complex chemical process that results in the decomposition of some primary rock-forming minerals and their substitution by clay minerals. Water-saturated clay minerals make the alteration zone significantly more conductive than the parent rock. Most igneous rocks are resistive when fresh (Angenheister, 1982), and fresh igneous rocks very rarely have conductivities greater than 5 mS/m. Average conductivity values range from 0.15 mS/m for diorite and 0.2 mS/m for granite to 2 mS/m for diabase and gabbro. These conductivity values were determined by in situ measurements; laboratory determinations yield significantly lower values (0.01–0.5 mS/m).

Figure 6 shows weathering profiles for felsic and mafic igneous rocks. A complete weathering profile is composed of the following zones (Butt, 1982):

1. Fresh rock (conductivity generally less than 2 mS/m).
2. Fractured rock, the mineral composition of which is identical to that of fresh rock. Typically, this zone is thicker over felsic rocks.
3. Saprolite, the layer immediately below the water table. The original rock textures are still preserved by stable primary minerals and newly formed secondary

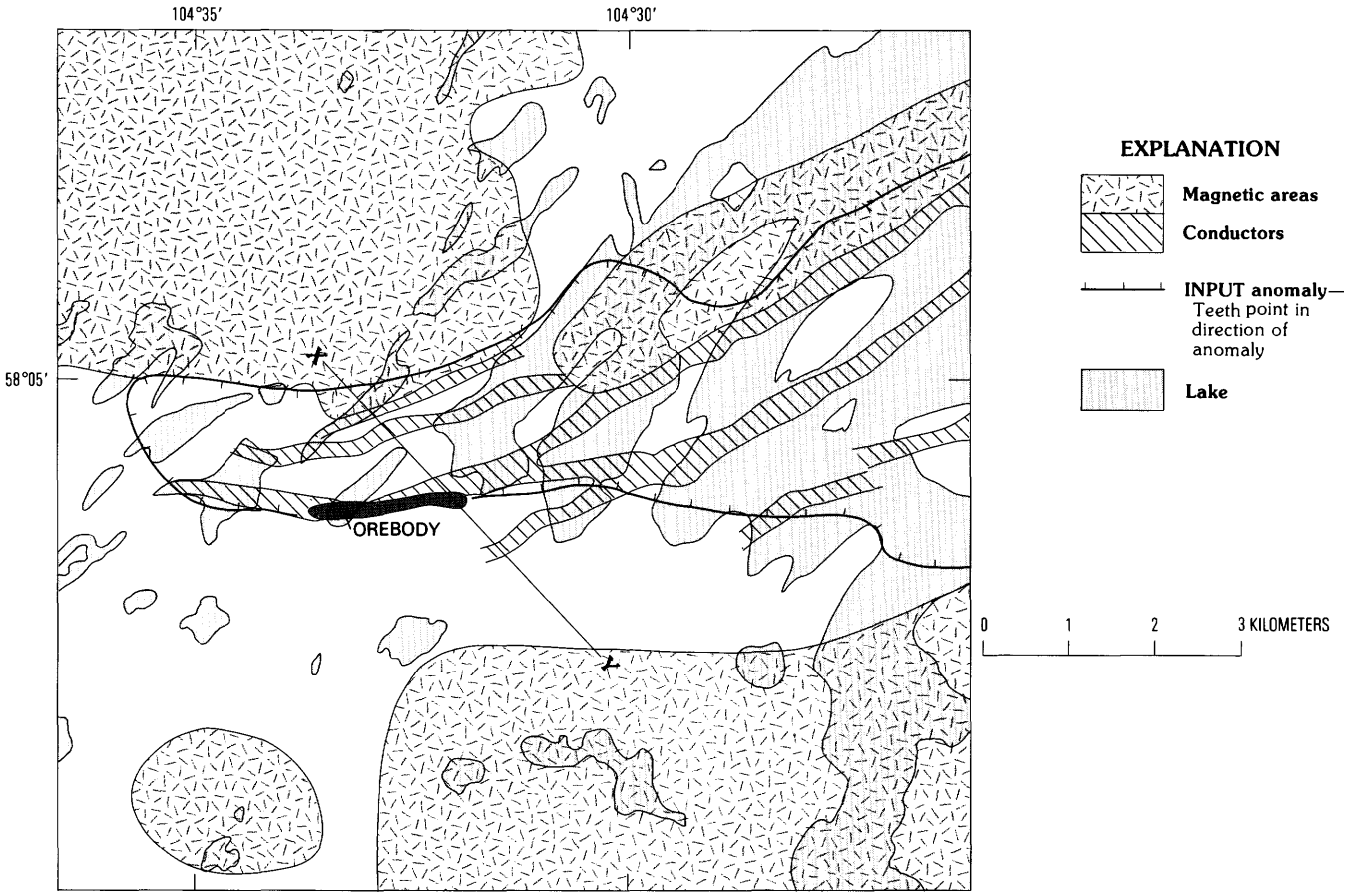

Figure 4. Geophysical responses over the Cigar Lake uranium deposit, Athabasca Basin, Saskatchewan, Canada. Modified from Fouques and others (1986). Geological cross section *X–Y* shown in figure 5.

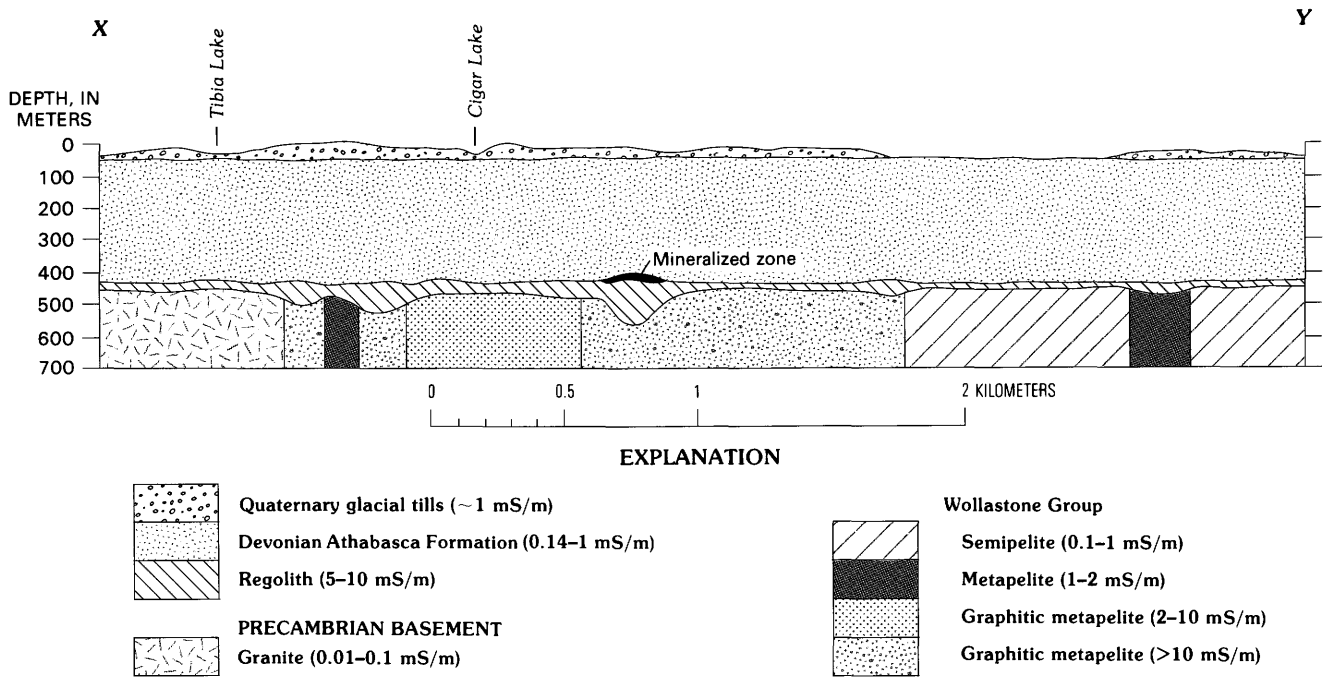

Figure 5. Geological cross section of the Cigar Lake uranium deposit, Saskatchewan, Canada. Conductivities typical of geological formations were obtained by interpretation of ground EM and magnetotelluric data (Fouques and others, 1986). The conductivity of the orebody does not differ from that of the regolith. Line of section *X–Y* shown in figure 4.

clays. Saprolite is the most conductive component of the weathered layer.

4. Leached zone, which develops as a region becomes progressively arid or when it is subjected to a gradual uplift. The resultant lowering of the water table causes leaching of the upper part of the saprolite layer. Depending on local conditions, the saprolite may be completely leached (with a resulting decrease in conductivity of the weathered layer), or the leached zone may be totally absent, or most commonly, an intermediate situation may exist; however, the unleached saprolite layer commonly is thicker than the leached zone.

5. Mottled zone, which develops from saprolite before leaching. Mottling may continue to develop in conditions described above. In the mottled zone, some of the clays that formed during the saprolite-formation stage are replaced by second-generation clay minerals. Mobile constituents are increasingly lost. This zone is only moderately conductive.

6. Ferruginous zone, which is enriched in iron oxide minerals, particularly hematite. Pisolitic concretions form near its transition with the mottled zone. Dehydration of the uppermost ferruginous zone, common in regions with well-defined dry-wet seasons, leads to hardening of the zone and to the formation of duricrust (called "canga" in Brazil and "cuirasse" in West Africa). This zone is highly resistive (conductivity less than 0.5 mS/m).

7. Sand layer, which forms when leaching occurs under acid and oxidizing conditions. It is more common in areas underlain by felsic igneous rocks.

The thickness of the weathered layer depends on many factors including lithology, topography, climate, and tectonic movement. In many regions of Australia, it is more than 100 m thick; elsewhere, it typically is 20–50 m thick. Many investigations concerning the develop-

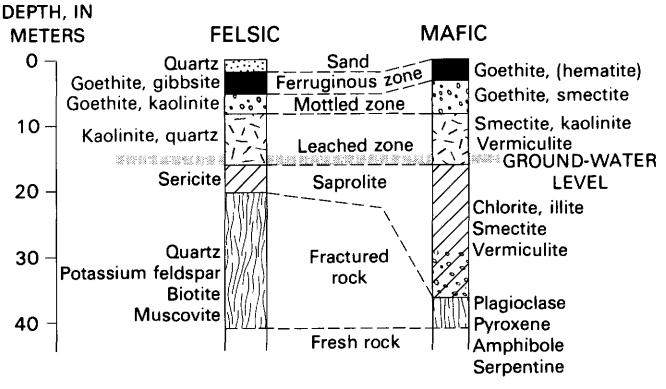

Figure 6. Schematic weathering profiles developed over felsic and mafic igneous rocks. The minerals most common to each horizon are listed on the outside of the columns. Names of the patterned components of the weathered profile are given in the middle column. The depth scale is schematic, and significantly thinner or thicker sequences can be found throughout the world. Modified from Palacky (1987).

ment and properties of the weathered layer have been made in Australia. In this paper, I follow the Australian convention of describing weathered layer components, a convention also adopted by the Geological Survey of Canada. Many European geologists, however, use the term "chloritization zone" rather than saprolite. The term "regolith" is commonly used in Africa and North America for the whole weathering sequence.

It would be wrong to assume that weathered layers are well developed only in tropical regions. Unless removed by erosion, such layers will remain preserved from past geological times when the climate was more conducive to chemical weathering (Zima, 1987). Saprolite is under glacial sediments in parts of Canada and in many deserts of Australia and Africa where present-day climatic conditions favor mechanical rather than chemical weathering. On the other hand, the weathered layer can be thin or even absent in hilly areas in tropical regions that are undergoing rapid tectonic uplift (for example, Jamaica and parts of Thailand).

Electrical properties of the weathered layer depend on the relative importance and mineralogical composition of the saprolite, leached, and mottled zones. Figure 7 shows the results of well logging of two holes drilled in the previously mentioned Musongati peridotite massif in Burundi. The measured resistivity values were converted to conductivity to highlight the conductive saprolite layer. The nickel content is also shown and demonstrates the importance of saprolite as a nickel host rock. Maximum conductivity values of 160 mS/m were obtained in both holes. Both the underlying fresh rock (peridotite) and the overlying mottled zone and duricrust are significantly less conductive (less than 1 mS/m). Comparison of these values with results obtained elsewhere indicates that these values are typical of weathered layers developed over peridotite. Palacky and Kadekaru (1979) analyzed the results of vertical electrical soundings carried out over a peridotite massif near Canabrava, Goiás, Brazil, and came up with a mean conductivity value of 125 mS/m and a standard deviation of 40 mS/m (based on 13 soundings).

As figure 6 illustrates, the mineral composition of saprolite varies according to the lithology of the parent rock. Conductive clay minerals are more abundant in mafic and ultramafic rocks than in felsic igneous rocks; therefore, in situ conductivity measurements can be used to distinguish rock types of different mineral composition. Determinations of saprolite conductivity derived from ground and airborne EM measurements and vertical electrical soundings can be used to compile pseudogeological maps. Conductivities of saprolite formed from granite, andesite, basalt, and peridotite at several locations around the globe are given in figure 8 (Palacky, 1988). The conductivity of granitic saprolite is consistently low (10–25 mS/m). The value listed for

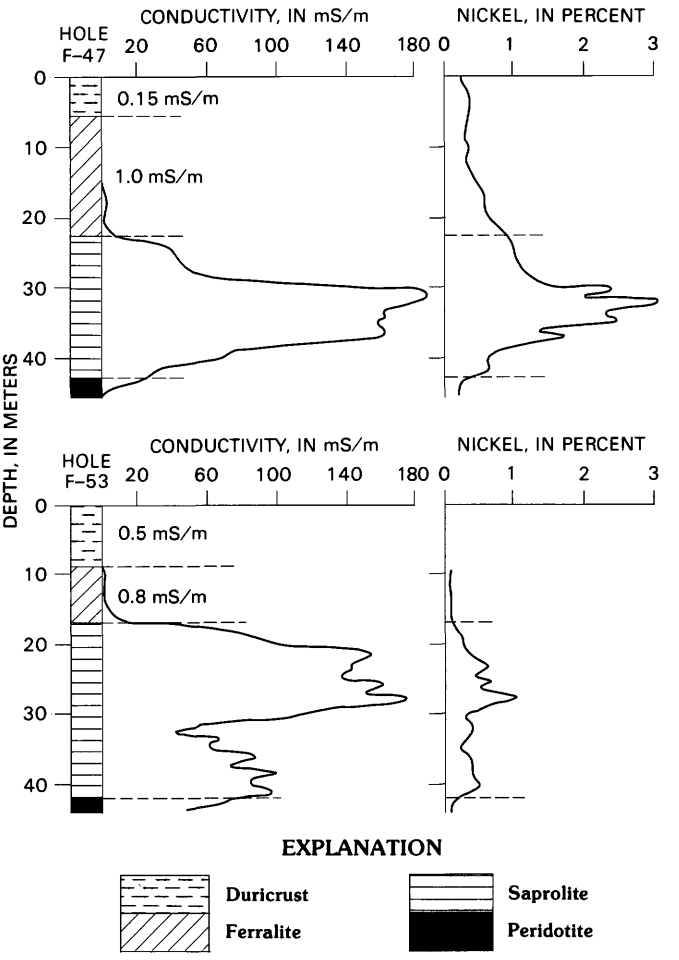

Figure 7. Geological and conductivity logs of the weathered layer developed at the Musongati peridotite massif in Burundi. Conductivity logs were obtained by processing the results of downhole three-electrode resistivity measurements. Nickel content is also shown. Modified from Peric (1981).

Ottawa was determined by well logging of paleosaprolite covered by 60 m of Paleozoic sedimentary rocks. It is significant that saprolite does not lose its distinctive electrical properties after marine transgression, sedimentation, and tectonic uplift. The conductivity of andesitic saprolite in Australia and Brazil is rather low, similar to granite. The conductivity of basaltic saprolite is more variable, from less than 30 mS/m to 200 mS/m; however, one should keep in mind that conductivity is essentially a logarithmic function. Saprolite over peridotite is consistently conductive; average values are greater than 100 mS/m.

In metamorphic areas, saprolite developed over some rock types, notably amphibolite, can be highly conductive. Values of 100 mS/m are typical in West Africa (determinations in Mali and Burkina Faso; see Palacky, 1988). Gneissic saprolite, on the other hand, is fairly resistive (10 mS/m). Significant variations in conductivity have been observed over schistic saprolite in

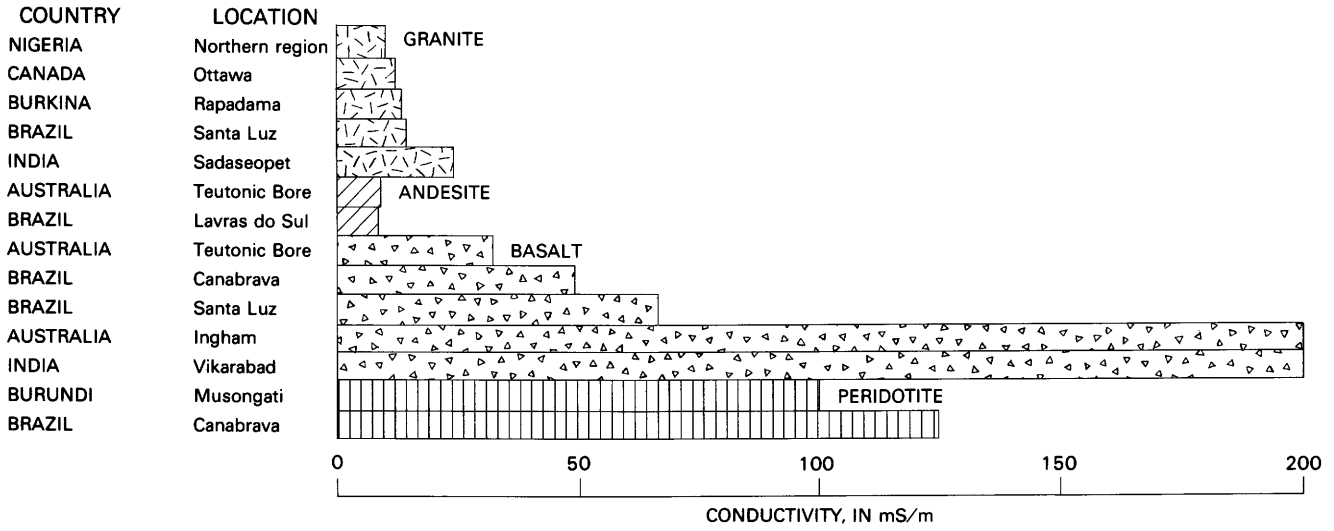

Figure 8. Conductivities of saprolite layers developed over igneous rocks. Conductivity values are based on resistivity soundings, borehole logging, or EM surveys. From tables in Palacky (1987).

different parts of the world (8–50 mS/m), perhaps because schist is a geologically vague term applied to rocks whose texture and chemical composition may significantly differ.

GEOLOGICAL MAPPING USING AEM METHODS

The consistency of saprolite conductivity over certain geological formations leads to the possibility of using EM methods for pseudogeological mapping. The fact that different conductivity patterns exist over granite and volcanosedimentary sequencies was noticed by Makowiecki and others (1965) in Kenya and Tanzania, but because the surveys were conducted for mineral exploration, the matter was not pursued and no recommendations to use AEM methods in geological mapping were made. Time-domain AEM surveys in the Rice Lake greenstone belt, Manitoba, Canada, indicate that distinct AEM anomalies are associated with peridotite dikes (fig. 9) (Dyck and others, 1975). Originally, these anomalies were ascribed to unusually conductive bedrock rather than to conductive saprolite despite the evidence that the AEM response resembled a thick ribbon rather than a vertical dike. At the time of the study, it was believed that saprolite was eroded in the Canadian Shield by glaciation. Recent studies by the Geological Survey of Canada indicate that saprolites buried by Quaternary sediments are quite common in formerly glaciated areas (A. Miller, oral commun., 1987).

AEM surveys can be used to improve the accuracy of geological maps even where detailed mapping has been carried out by traditional means and where it is normally considered accurate and reliable. Figure 10 shows a geological map of an area near Bois-de-Cené, France (30 km south of Nantes) (Bureau de Recherches Géologiques et Minières, 1968). The area is

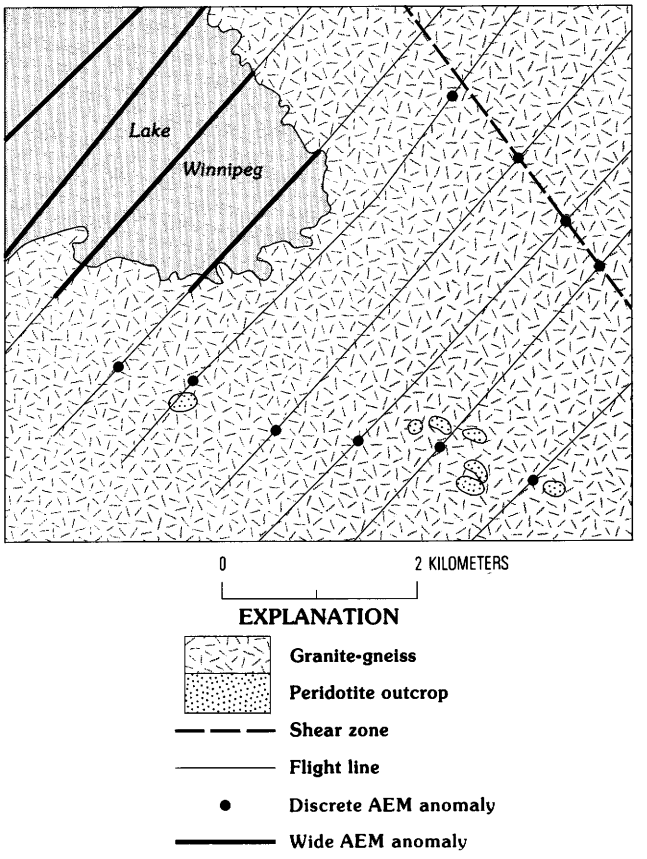

Figure 9. Geology of a part of the Rice Lake greenstone belt, Manitoba, Canada. Flight lines and AEM conductors are also shown. Modified from Dyck and others (1975).

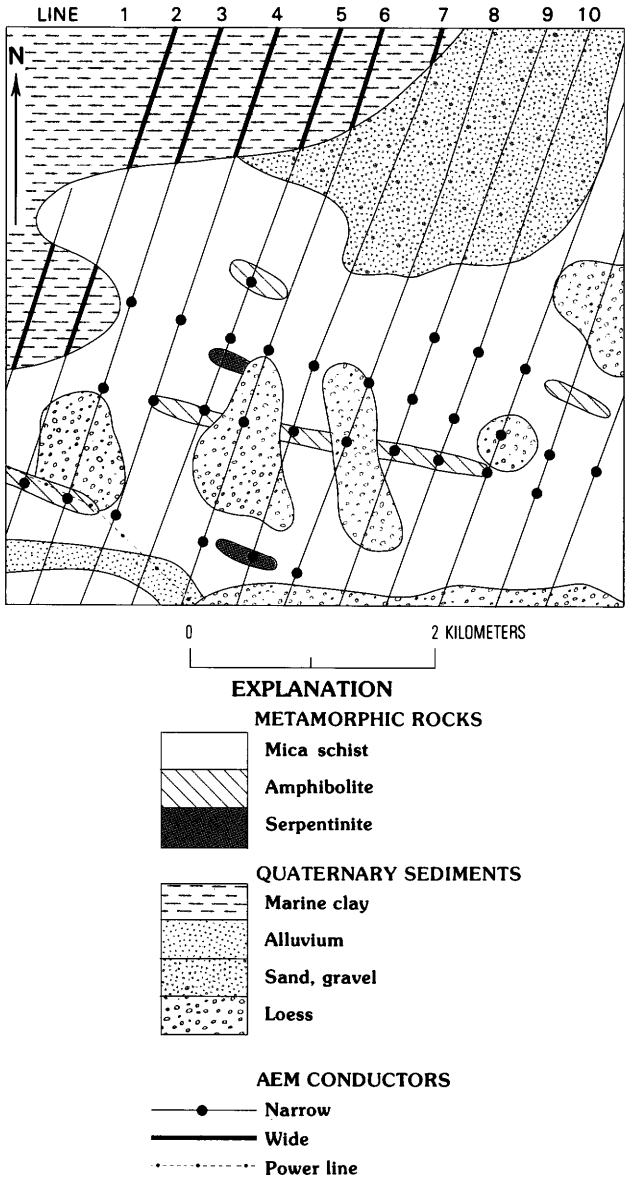

Figure 10. Geology of an area near Bois-de-Cené, France. Ages of metamorphic units are uncertain. Modified from 1:80,000-scale map, sheet 117, Nantes-Île du Pilier (Bureau de Recherches Géologiques et Minières, 1968). Flight lines and AEM conductors are also shown (Palacky, 1987).

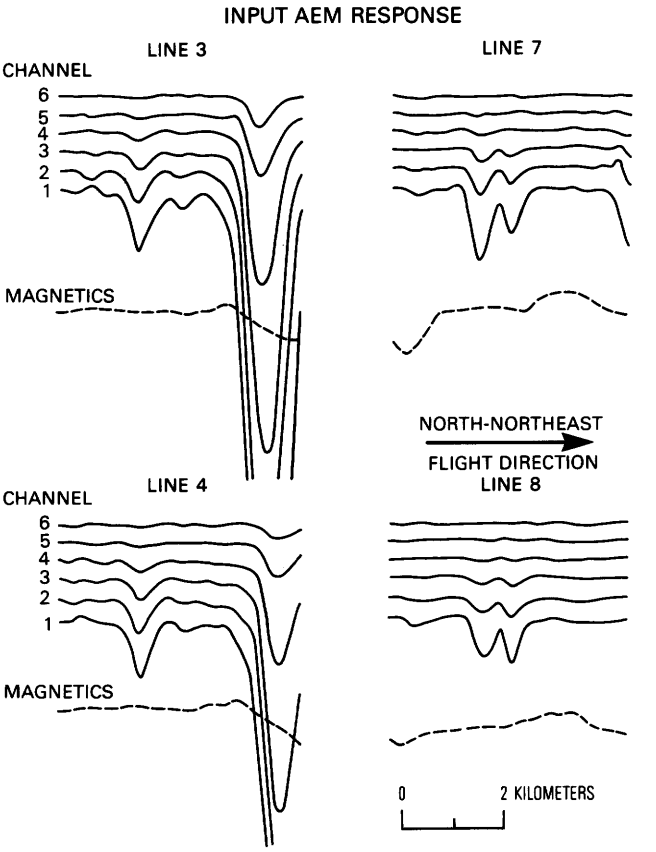

Figure 11. Time-domain AEM data along four lines (3, 4, 7, 8) surveyed in the Bois-de-Cené area, France. Flight lines are shown in figure 9.

underlain by metamorphic rocks: mica schist, amphibolite, and serpentinite dikes. Mapping of crystalline rocks was made difficult by the presence of an extensive Quaternary cover: marine clays in the northwestern corner of the map area and patches of loess, sand and gravel, and alluvia along streams. On the geological map, flight lines are superimposed and AEM anomalies depicted. The time-domain AEM response along selected flight lines is illustrated in figure 11. Strong anomalies are associated with the marine clays (lines 1–7), but other Quaternary sediments are resistive. Medium-amplitude, narrow anomalies are associated with amphibolite and serpentinite dikes, and AEM responses indicate that the dikes are more extensive than mapped. An elongated serpentinite dike was almost missed by mapping; it was noticed only in one spot (fig. 10, line 5, second anomaly from the bottom). Airborne magnetic surveys are believed to be the best tool for mapping of mafic and ultramafic dikes; however, in this instance, no magnetic response is associated with any of the dikes.

The pioneering studies in lithological interpretation of AEM surveys were made in the 1970's in Brazil. Case histories from the Itapicurú greenstone belt in Bahia and from the Rio Grande do Sul shield were published by Palacky (1981). One example from Bahia is given here (figs. 12–14). The Itapicurú greenstone belt extends north-south for a distance of 90 km and is 180 km north-northwest of Salvador, the state capital (latitude 11 °S.). Kishida and Riccio (1980) defined three lithological units in the belt.

1. Metavolcanic mafic unit composed of metabasalt, graphitic schist, iron formation, and intrusive gabbro dikes and sills.

2. Metavolcanic felsic unit composed of acid and intermediate metavolcanic rocks, felsic flow rocks, and volcanic breccias and tuffs.

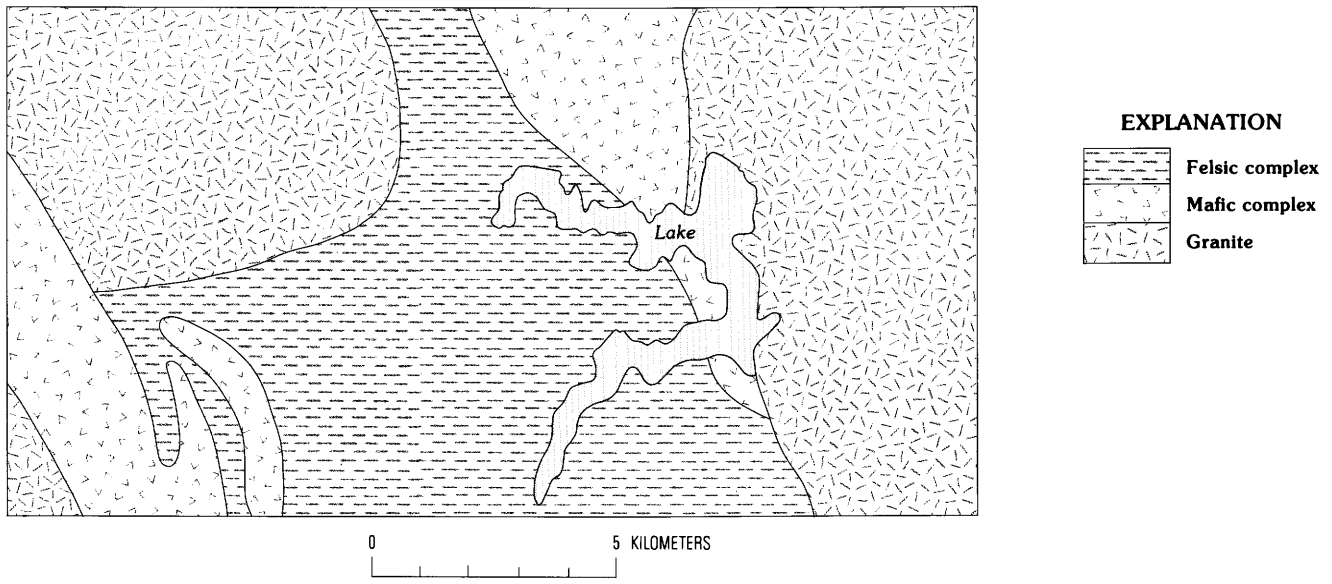

Figure 12. Original geological map of an area in the Itapicurú greenstone belt, Bahia, Brazil, based on aerial photography and ground reconnaissance. Modified from Palacky (1981).

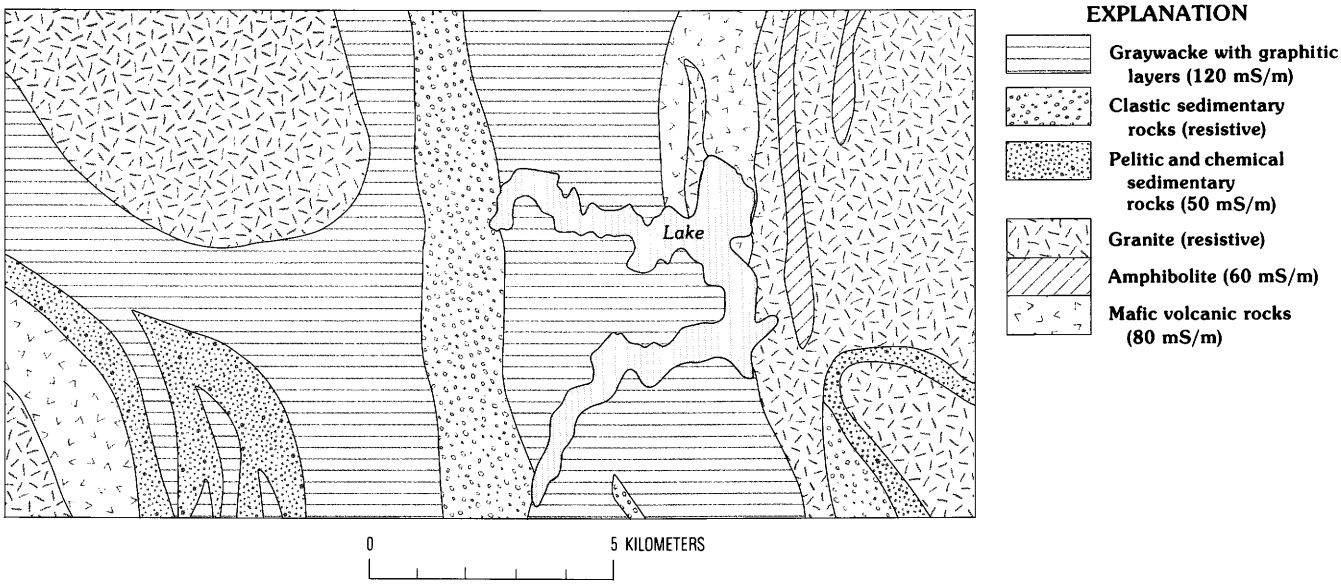

Figure 13. Revised geological map of the area in figure 12 based on interpreted AEM maps and ground checks. Modified from Palacky (1981).

3. Metasedimentary unit consisting of conglomerate, arkose, pelite, and graywacke and frequent graphitic layers. The greenstone belt is almost entirely surrounded by Archean granite gneiss massifs, which are thought to be contemporaneous with the greenstone belt.

Original geological mapping, which was carried out in the initial phases of the mineral exploration project by Rio Doce Geologia e Minerção, was based on aerial photography and ground reconnaissance (mostly recording soil color changes). The almost total absence of outcrops outside the granite gneiss massifs made such an approach difficult and time consuming. Access is limited in roadless areas covered by a dense thorny vegetation (catinga). In the original mapping, only three units were recognized: granite, felsic rocks, and mafic rocks (fig. 12).

Conductivity anomaly patterns are more complex than geological patterns on the original map. For instance, AEM data indicate that resistive areas, which coincide with granite, are much smaller than previously thought (northwestern corner and eastern quarter, fig. 13). Fragments of granite, which do not easily weather, are scattered over a distance of more than 1 km from their source. Neither aerial photography nor magnetic data (fig. 14) indicates the extensive amphibolite

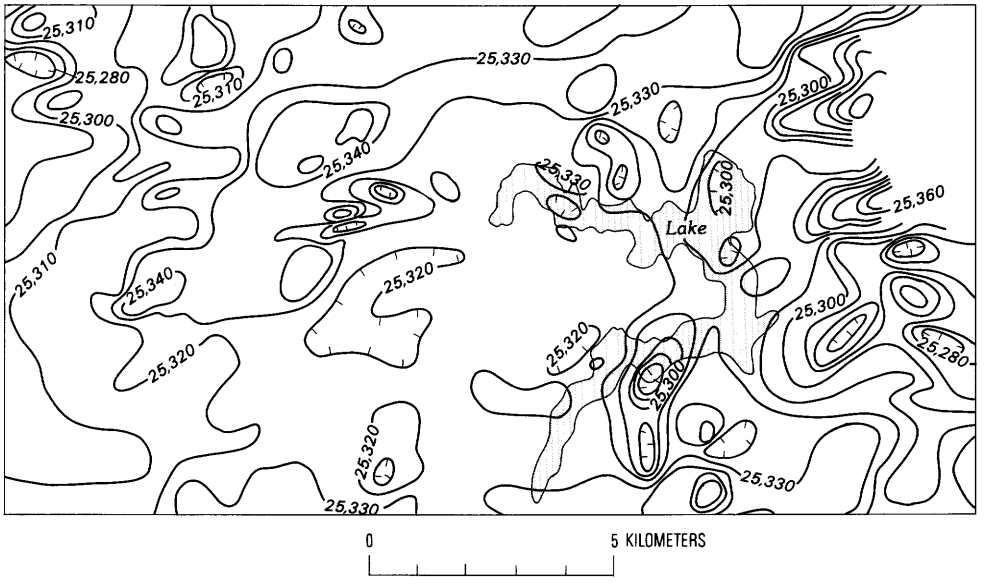

Figure 14. Total magnetic field (contours in nanoteslas) for the area depicted in figures 12 and 13. Line spacing 500 m; mean sensor height 100 m. The magnetic patterns do not reflect lithological changes. Modified from Palacky (1981).

lenses whose existence was verified in the field. Saprolite formed over amphibolite causes AEM anomalies of medium to small amplitude and an average conductivity of 60 mS/m. Mafic volcanic rocks (basalt) were identified on the basis of conductive saprolite (average conductivity 80 mS/m) that causes large-amplitude, wide anomalies. The confirmed extent of volcanic rocks is much smaller than thought previously (southwestern corner, fig. 13). According to their conductivity characteristics, three sedimentary rock types were identified: resistive clastic sedimentary rocks (conglomerate), chemical and pelitic sedimentary rocks (medium to small AEM amplitudes), and graywackes with graphitic layers (large to medium AEM amplitudes, sharp peaks, average conductivity 120 mS/m). Unlike areas of basalt and amphibolite, where the conductor (saprolite) is a product of weathering, areas of sedimentary rocks have sequences of bedrock conductors (graphite, shales).

The magnetic map (fig. 14) shows almost no correlation with the geological map. The magnetic patterns indicate only a less magnetic granite in the eastern part of the area. One should notice the low total magnetic field (slightly more than 25,000 nT). This poor correlation between geological features and magnetic patterns, which is prevalent in the Itapicurú greenstone belt and many other Precambrian areas of Brazil, was the major driving force to develop interpretation of AEM data.

Attempts to use AEM techniques for mapping of lithology and thickness of Quaternary glacial and glaciolacustrine sediments in Canada have been made since the early 1980's (Pitcher and others, 1984). In France, helicopter AEM surveys were used for mapping Quaternary alluvium and the underlying Tertiary strata (Deletie and Lakshmanan, 1986).

The Geological Survey of Canada has been involved in airborne and ground EM surveys designed for mapping Quaternary sediments since 1985. In the first phase of the program, airborne and ground surveys were carried out at the Val Gagné test site, 60 km east of Timmins, Ontario. The test site, the extent of which is 6.4 by 2.6 km, is in the clay belt. Locally, the thickness of clay sediments varies between 10 and 50 m. Thus far, the most accurate information on composition and thickness of Quaternary sediments has been obtained from shallow reflection seismic surveys (Pullan and others, 1987). The results of helicopter AEM surveys were compiled as conductivity and thickness maps derived from various coil configurations and frequencies. A four-frequency EM system was used in the survey (vertical coaxial coil-pairs at 935 and 4600 Hz, horizontal coplanar coil-pairs at 4175 and 32,000 Hz). A conductivity map obtained using the a horizontal coplanar coil-pair at 4175 Hz is shown in figure 15. A thick-horizontal-layer model was used in the conductivity calculations. The average conductivity (20 mS/m) is somewhat lower than values derived from ground EM and resistivity measurements (30 mS/m). A pronounced conductivity low running almost diagonally across the northern half of the test site corresponds to the Black River. Presumably, the clays are less thick underneath the river bed. Generally, the clay cover is thinner north of the Pipestone fault, which runs

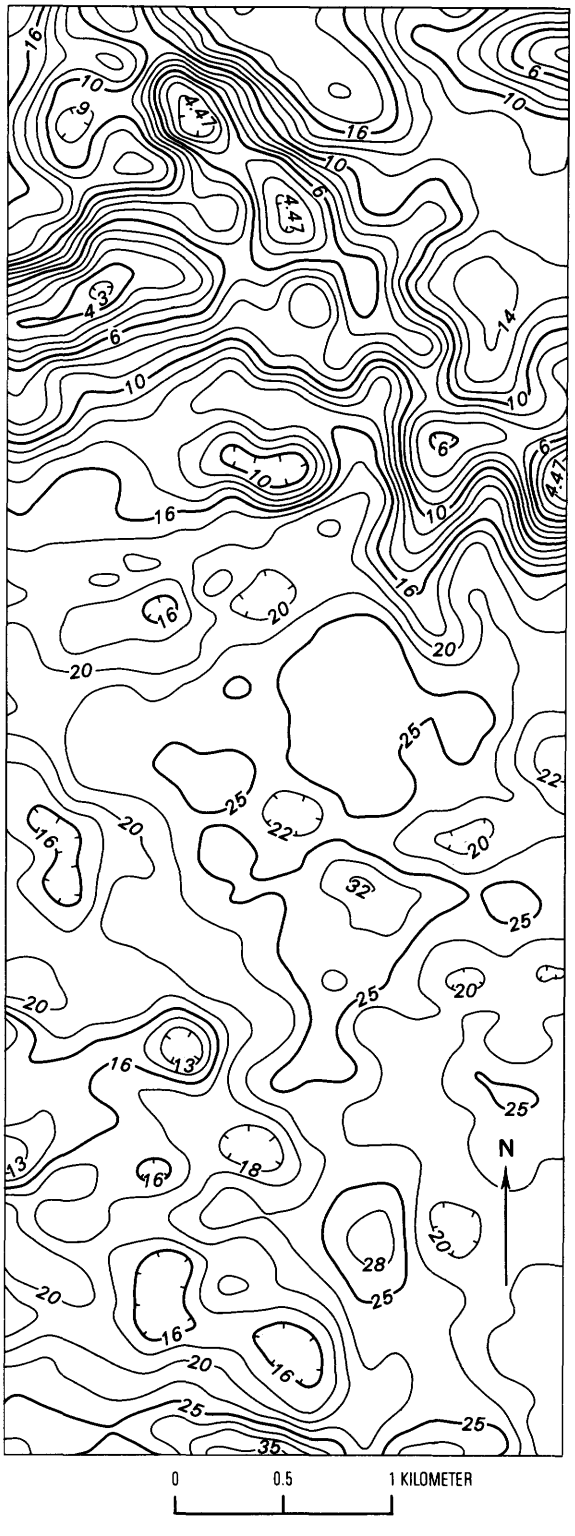

Figure 15. Conductivity (contours in mS/m) of the Val Gagné test site, Ontario, Canada. The map was compiled from horizontal coplanar-coil helicopter AEM data obtained at a frequency of 4175 Hz. Flight-line spacing 100 m; sensor height 30 m.

east-west, 2 km south of the northern border of the area. Other conductivity lows south of the river (minima 3 and 10 mS/m) correspond to bedrock highs whose existence has been confirmed by ground geophysical surveys.

CONCLUSIONS

Modern multifrequency and broad-band AEM systems are capable of more than a simple detection of highly conductive targets such as massive sulfide deposits. Particularly important is a conductor category in which the conductive substance is formed by water-saturated clay minerals. To this category belong weathered layers, lineaments, and clay-rich Quaternary sediments. The conductivity of saprolite, the most conductive component of the weathered layer, depends on the underlying lithology. Hence, results of AEM surveys can be used to identify several rock types, particularly in a volcanic sequence. In given area, saprolite developed over mafic rocks is more conductive than saprolite overlying felsic rocks. Identification of conductive weathered layers aid in prospecting for kimberlite, uranium, nickel, bauxite, and possibly gold. Saprolite-associated gold deposits are known, but no reports of geophysical investigations of electrical properties have been published.

Studies in Canada and France indicate that AEM techniques also are a useful tool for mapping thickness and lithology of Quaternary sediments. The results can indirectly aid mineral exploration programs by identifying narrow valleys suitable for geochemical sampling. The approach is cost-effective as compared with the presently used shallow reflection or refraction seismic surveys.

REFERENCES CITED

Angenheister, G., ed., 1982, Physical properties of rocks: Berlin, Springer Verlag, p. 239–253.

Baudoin, P., Durozoy, G., and Utard, M., 1970, Étude par prospection électromagnétique aérienne d'un contact eau douce-eau salée dans le delta du Rhône [Study of a freshwater-saltwater contact in the Rhône delta using airborne electromagnetic prospecting], *in* Morley, L.W., ed., Mining and groundwater geophysics/1967: Geological Survey of Canada Economic Geology Report 26, p. 626–637.

Bureau de Recherches Géologiques et Minières, 1968, Carte géologique de la France (sheet no. 117, Nantes-Île du Pilier) [2nd ed.]: Scale 1:80,000.

Butt, C.R.M., 1982, History and characteristics of weathering in Australia, *in* Smith, R.E., ed., Geochemical exploration in deeply weathered terrain: Perth, Commonwealth Scientific and Industrial Research Organization, p. 9–18.

Collett, L.S., 1966, Airborne electromagnetic survey over the Winkler aquifer, Manitoba: Geological Survey of Canada Paper 66–2, p. 6–9.

_____ 1986, Development of the airborne electromagnetic technique, *in* Palacky, G.J., ed., Airborne resistivity mapping: Geological Survey of Canada Paper 86–22, p. 9–18.

Deletie, P., and Lakshmanan, J., 1986, Airborne resistivity surveying applied to nuclear power plant site investigation in France, *in* Palacky, G.J., ed., Airborne resistivity mapping: Geological Survey of Canada Paper 86–22, p. 145–152.

Dyck, A.V., Becker, A., and Collett, L.S., 1975, INPUT AEM results from Project Pioneer, Manitoba: Canadian Journal of Earth Sciences, v. 12, p. 971–981.

Fouques, J.P., Fowler, M., Knipping, H.D., and Schiman, K., 1986, Le gisement d'uranium de Cigar Lake; découverte et characteristiques générales [Cigar Lake uranium deposit; discovery and general characteristics]: Canadian Institute of Mining and Metallurgy Bulletin, v. 79, no. 886, p. 70–82.

Johnson, I.M., and Seigel, H.O., 1986, TRIDEM resistivity mapping for natural resources development, *in* Palacky, G.J., ed., Airborne resistivity mapping: Geological Survey of Canada Paper 86–22, p. 125–129.

Kilényi, E., and Szabó, Z., 1985, History and present state of the art of geophysics in Hungary: First Break, v. 3, no. 5, p. 9–23.

Kishida, A., and Riccio, L., 1980, Chemostratigraphy of lava sequences from the Rio Itapicurú Greenstone Belt, Bahia: Precambrian Research, v. 11, p. 161–178.

Macnae, J.C., 1979, Kimberlites and exploration geophysics: Geophysics, v. 44, p. 1395–1416.

Makowiecki, L.Z., King, A.J., and Cratchley, C.R., 1965, A comparison of three airborne electromagnetic methods of mineral prospecting—Results of test surveys in East Africa: Geological Survey of Canada Paper 65–6, p. 63–83.

Montgomery, G.E., 1986, Special report—Geophysical activity in 1985: The Leading Edge of Exploration, v. 5, no. 8, p. 25–48.

Nabighian, M.N., ed., in press, Electromagnetic methods in applied geophysics, v. 2, Applications: Tulsa, Society of Exploration Geophysicists.

Palacky, G.J., 1981, The airborne electromagnetic method as a tool of geological mapping: Geophysical Prospecting, v. 29, p. 60–88.

_____ 1986, Airborne electromagnetics at crossroads, *in* Palacky, G.J., ed., Airborne resistivity mapping: Geological Survey of Canada Paper 86–22, p. 5–8.

_____ 1987, Clay mapping using electromagnetic methods: First Break, v. 5, p. 295–306.

_____ 1988, Resistivity characteristics of geologic targets, *in* Nabighian, M.N., ed., Electromagnetic methods in applied geophysics, v. 1, Theory: Tulsa, Society of Exploration Geophysicists, p. 52–129.

Palacky, G.J., and Kadekaru, K., 1979, Effect of tropical weathering on electrical and electromagnetic measurements: Geophysics, v. 44, p. 69–88.

Palacky, G.J., and Sena, F.O., 1979, Conductor identification in tropical terrains—Case histories from the Itapicurú Greenstone Belt, Bahia, Brazil: Geophysics, v. 44, p. 1941–1962.

Paterson, N.R., 1970, Exploration for massive sulphides in the Canadian Shield, *in* Morley, L.W., ed., Mining and groundwater geophysics 1967: Geological Survey of Canada Economic Geology Report 26, p. 275–289.

Peltoniemi, M., 1986, Systematic airborne electromagnetic surveys in Finland—An overview, *in* Palacky, G.J., ed., Airborne resistivity mapping: Geological Survey of Canada Paper 86–22, p. 159–167.

Peric, M., 1981, Exploration of Burundi nickeliferous laterites by electrical methods: Geophysical Prospecting, v. 29, p. 274–287.

Pitcher, D.M., Barlow, R.B., and McNeill, J.D., 1984, Mapping the overburden in the Black River-Matheson (BRIM) area, District of Cochrane, employing an airborne time-domain system, *in* Wood, J., White, O.L., Barlow, R.B., and Colvine, A.C., eds., Summary of field work and other activities 1984: Ontario Geological Survey Miscellaneous Paper 119, p. 299–307.

Pullan, S.E., Hunter, J.A., Gagné, R.M., and Good, R.L., 1987, Delineation of bedrock topography at Val Gagné, Ontario, Test Site using seismic reflection techniques: Geological Survey of Canada Paper 87–1A, p. 905–912.

Ruzicka, V., and LeCheminant, G.M., 1986, Development in uranium geology in Canada: Geological Survey of Canada Paper 86–1A, p. 531–540.

Sengpiel, K.P., 1983, Resistivity/depth mapping with airborne electromagnetic survey data: Geophysics, v. 48, p. 181–196.

Senti, R.J., 1988, Special report—Geophysical activity in 1987: The Leading Edge of Exploration, v. 7, p. 33–56.

Szabadváry, L., 1987, Bauxite exploration in Hungary: Geophysics, v. 52, p. 1166–1168.

Zima, L. 1987, The interpretation of resistivity soundings over weathered rocks: Geophysical Transactions, v. 32, p. 319–332.

Estimation of Overburden Thickness Using Helicopter Electromagnetic Data

By R.L.S. Hogg[1] and G.A. Boustead[1,2]

Abstract

Helicopter electromagnetic (HEM) data collected for the purpose of detecting conductive mineralization within bedrock can also be used to estimate the thickness of the overburden cover. An inversion method for a horizontal layer of variable conductivity, thickness, and depth that uses the in-phase and quadrature response at two or more frequencies is described. A comparison of drill-hole and airborne survey results from the Casa Berardi region of eastern Canada demonstrates that overburden thickness and basement topography can be reasonably estimated.

INTRODUCTION

Helicopter electromagnetic (HEM) systems have been in operation for about 30 years as an aid to base-metal exploration. The typical system has coaxial and (or) coplanar transmitter/receiver coils at a 7–10 m separation operating at frequencies between 300 and 8000 Hz. In the mid-1970's the idea of calculating apparent resistivity was introduced (Fraser, 1978), and since that time new applications based on horizontally layered conductivity models have been found.

In 1986 Aerodat Limited carried out a 75,000-km helicopter magnetic and very low frequency electromagnetic (VLF-EM) survey in the Casa Berardi region of Quebec, Canada. The area has several gold deposits and is currently the location of intensive exploration activity. The bedrock is typically covered with 10–100 m of glacial overburden, and drilling to sample the basal till is a common gold exploration technique. Aerodat is using the HEM data to estimate the overburden thickness and the basement topography as a guide to drill-site selection. The depth estimation technique was evaluated for a property where data from numerous drill holes are available, and the methodology and results of the evaluation are described in this paper.

[1]Aerodat Limited, 3883 Nashau Drive, Mississauga, Ontario L4V 1R3, Canada.

[2]Current address: Controlled Geophysics, Suite 31, 400 Matheson Boulevard East, Mississauga, Ontario L4Z 1N8, Canada.

METHOD

The basic geological assumption is that the overburden appears as a conductive layer above more resistive bedrock. Ionic conduction in mildly saline solutions and clays can be expected at the base of the overburden. At shallower depths similar conductive horizons may exist interspersed with resistive sands and gravels. The conductivity of these layers may be similar and certainly much higher than that of the underlying bedrock. It is reasonable to assume that multiple, closely spaced layers probably appear to the HEM system as a single thick layer.

The available calculation models are presented in figure 1. The first three models are the simplest and are based on a thin sheet, a layer of uniform and fixed thickness, or a half-space. The depth to the top of the layer and the conductivity σ of the layer are variable. A unique solution for depth H and σ is provided by two measured parameters, typically the in-phase and quadrature response of a given HEM frequency. This is the most common approach to apparent conductivity calculations for HEM data. The depth to the bottom of the conductive layer cannot be determined without fixing the layer conductivity.

In the fourth model (fig. 1), the number of variables is increased from two to three by including the thickness of the layer. Such a model necessarily requires at least three observations. For a two-frequency HEM system, four observations are available and the solution is overdetermined and solvable by least-squares inversion techniques.

Both the two- and three-variable methods are based on a single conductive layer being the primary target. If a relatively resistive layer overlies the conductor, then the presence and thickness of this layer may be revealed if an altimeter is used to monitor the height of the HEM bird above ground surface, as illustrated in figure 2. If the conductive layer is estimated to be at depth H, then the depth to the layer below ground surface can be calculated and the thickness of the overlying resistive layer derived.

A phasor diagram of the HEM response to a conductive layer at various depths and of various thicknesses is presented in figure 3. This particular diagram

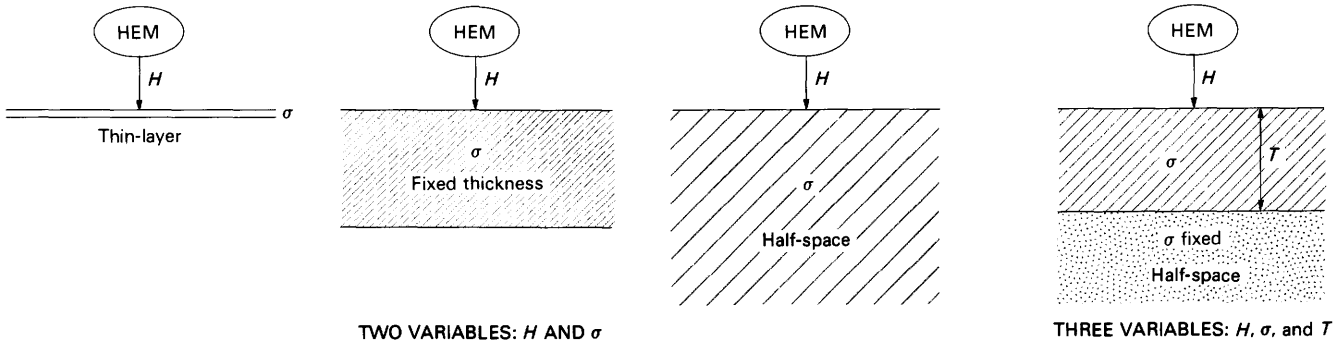

Figure 1. Models for calculation of apparent conductivity. The first three models use a fixed layer thickness of conductivity σ to facilitate the calculation of apparent conductivity. The fourth model adds a thickness variable (T) enabling estimation of true conductivity and thickness. H is depth to top of conductive layer.

is calculated for coaxial coils operated at 5 kHz with a transmitter-receiver coil separation of 7 m. The phasor diagram has been conceptually generalized by indicating $f\sigma T$ as a combined variable where f is the frequency, σ is the layer conductivity, and T the layer thickness.

The lines of constant $f\sigma T$ in figure 3 illustrate that as the depth to the top of the conductive layer increases, the amplitudes of the in-phase and quadrature responses attenuate. Also, as the thickness of the layer increases and the conductance remains constant, the amplitudes of the in-phase and quadrature responses attenuate. By following a line of constant depth and thickness, it is clear that the in-phase component increases more rapidly than the quadrature with increasing $f\sigma T$ until in-phase saturation is reached. At this point, the in-phase increases no further and rapid attenuation of the quadrature response begins.

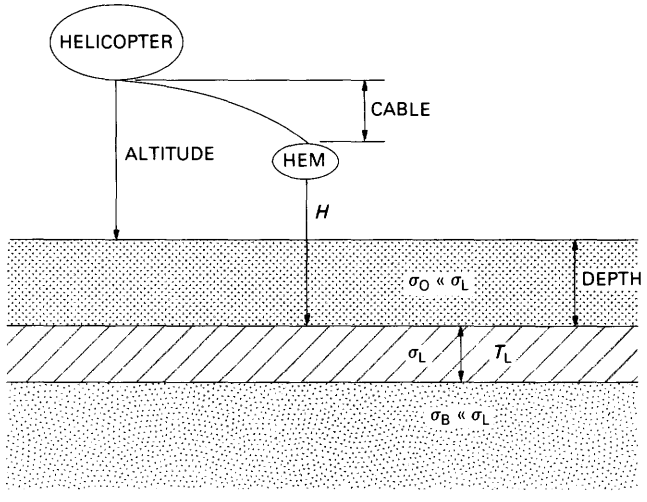

Figure 2. Use of an altimeter to monitor the height (H) of the HEM bird above ground and thus provide the depth to the top of the conductive layer. A resistive cover above the conductor thus becomes an interpreted pseudolayer of known thickness.

Figure 3 also provides insight as to the potential performance of an inversion process. The accuracy of an inversion process is very dependent on the sensitivity of the model to changes in the particular parameters. Assuming multifrequency observations are available, a number of hypothetical responses A–E are indicated in figure 3. Points A, B, and C all are on the logarithmic chart where lines of constant thickness and (or) height are almost parallel. A conductor 30 m deep and 40 m thick and a conductor deeper but thinner will provide almost identical results. For observations only in zones A–C, a mathematical inversion is clearly insensitive in terms of uniquely resolving height and thickness as independent parameters.

This insensitivity is illustrated in alternate fashion in figure 4, which shows typical observed responses, in-phase and quadrature, for the three-frequency HEM system used in a later example and the forward model solution for three different height, resistivity, and thickness combinations. The similarity of the model responses to each other as well as to the observed data is striking.

If observations at D and E (fig. 3) are included, such would not be the case. An observation at E would fix the depth to the top of the layer accurately and consequently the observations at A, B, and C would provide an estimate of thickness. Clearly, the two most valuable observations are a combination of E with A, B, or C. Of these, C is preferred because of its greater signal level.

It is interesting to note that point E corresponds to a $f\sigma T$ value of about 200,000. Considering a layer of conductivity 0.25 S/m, typical of seawater, and a thickness of 20 m, the conductance would be 5 S. The operating frequency required to provide observation E would be 40 kHz. In the case of conducting overburden having a conductivity of about 0.01 S/m, the required operating frequency would be 1.0 MHz. This frequency is far higher than any currently available on HEM systems. Higher frequencies are without question required for better definition of the top of the conductive layer;

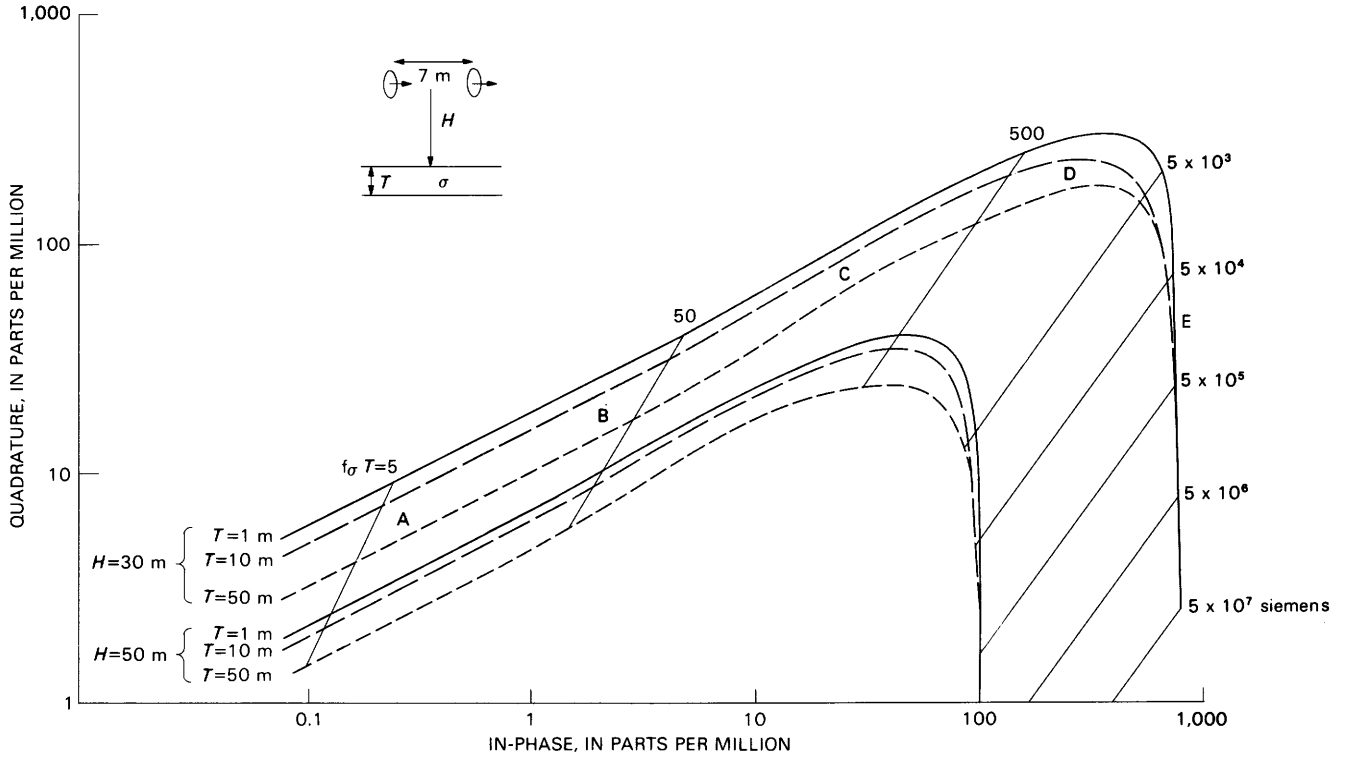

Figure 3. Phasor diagram for a horizontal layer of finite thickness (T) (1, 10, 50 m) at a depth below sensor (H) of 30 and 50 m. f is the frequency. A–E indicate hypothetical responses discussed in text.

		OBSERVED	FIT 1	FIT 2	FIT 3
4175 Hz	COPLANAR Q	257.1 ppm	257.1	257.2	257.2
	COPLANAR IP	119.0 ppm	118.1	118.0	118.1
4600 Hz	COAXIAL Q	68.8 ppm	68.2	68.2	68.1
	COAXIAL IP	30.9 ppm	33.4	33.5	33.8
935 Hz	COAXIAL Q	16.0 ppm	19.6	19.3	18.6
	COAXIAL IP	4.1 ppm	3.9	3.5	2.9
			σ=0.01811 S/m CTP=0.725 S 4.5 m 40.0 m	σ=0.02188 S/m CTP=0.657 S 6.2 m 30.0 m	σ=0.1063 S/m CTP=0.533 S 13.0 m 5.0 m

Figure 4. Response (in parts per million) of a typical three-frequency HEM system showing the non-uniqueness of data interpretation. The conductive layer (crosshatched) has conductivity σ and a conductivity-thickness product CTP. Depth of burial of the conductive layer is represented by the stippled layer. Q is quadrature response; IP is in-phase response.

however, practical or technical limits exist. For example, at frequencies approaching 1 MHz, displacement currents due to the ground's dielectric properties will become significant. Also, geologic environments do not present ideal single-layer cases, and at this high a frequency inhomogeneities in the conductivity profile of the overburden strata will have greater impact on the measured values.

THE INVERSION TECHNIQUE

The overdetermined problem requires an inversion technique that finds an optimum set of N parameters p_j that minimizes the difference between the observation Y_i and the computed forward model response $Y_i = F(p_j)$. The method used is a least-squares technique called eigenvalue decomposition. It is one of many inversion techniques that may be used but is useful because of its method of presenting error estimates of the model parameters. The particular method adopted was used for depth sounding as described by Edwards and others (1981). Briefly, it assumes that for small variation dp_j of the model parameters p_j, the changes of Y_i may be expressed linearly as

$$dY_i = \sum_{j=1}^{N} A_{ij}\, dp_j ,$$

where $A_{ij} = \partial Y_i / \partial P_j$, or, in matrix form,

$$\mathbf{dY} = \mathbf{A}\ \mathbf{dp}. \tag{1}$$

Using a singular value decomposition (SVD) method, the matrix **A** may be rewritten as

$$\mathbf{A} = \mathbf{U}\ \mathbf{L}\ \mathbf{V}^T, \tag{2}$$

where $\mathbf{U}^T\mathbf{U} = \mathbf{I}$, $\mathbf{V}^T\mathbf{V} = \mathbf{I}$, **I** is the identity matrix, and **L** is a diagonal matrix.

Define

$$\mathbf{dY}^* = \mathbf{U}^T\mathbf{dY} \tag{3}$$

and

$$\mathbf{dp}^* = \mathbf{V}^T\ \mathbf{dp}, \tag{4}$$

then

$$\mathbf{dY}^* = \mathbf{L}\ \mathbf{dp}^*. \tag{5}$$

This reconstruction of equation (1) is considerably simpler. The matrix **L** is diagonal, and the diagonal elements L_{ii} are the eigenvalues of **A**. **dp*** and **dY*** are referred to as the eigenparameters and eigendata, respectively.

Edwards and others (1981) illustrated that the error in each eigenparameter can be expressed simply if one first assumes that each datum has an independent standard error estimate e_j of unity. The relationship, expression (3), between the eigendata **dY*** and the original data **dY** is also valid for the errors in the two data types; that is,

$$e_i^* = \sum_{j=1}^{M} U_{ji} e_j .$$

They illustrated that the standard error in p_i associated with a unit standard error in e_i^* is simply $1/L_{ii}$, the reciprocal of the corresponding eigenvalue.

Next, each element $\partial Y_i / \partial p_j$ of matrix **A** is scaled two ways before SVD is undertaken. The element is first divided by e_i, with the effect of rescaling the measurement units of Y_i so that the standard error of each element is unity. This was a requirement of the preceding development of the standard error relationship. Each term is then multiplied by p_j, so that the element is effectively defined as the logarithm of the model parameters rather than the parameters themselves, namely

$$p_j\ \partial Y_i / \partial\ p_j = \partial Y_i / \partial (\log p_j).$$

The benefit of the second scaling operation is that the eigenparameters p_j^* will generally have a more readily understood physical significance in terms of the original model parameters p_j. For example, in this case history the three original parameters p_1, p_2, and p_3 are logarithms of height, thickness, and resistivity.

Typical eigenparameters and associated standard errors encountered during inversion of the test area data are:

	p_1	p_2	p_3	Standard error e^*
p_1^*	0.88	0.36	–0.32	0
p_2^*	–0.48	0.59	–0.65	0
p_3^*	0.05	–0.72	–0.69	2.48

Note that in both p_1^* and p_2^*, the p_2 and p_3 components are of similar amplitude but opposite in sign. Realizing that p_2–p_3 is log (thickness) minus log (resistivity) or log (thickness/resistivity), it is clear that the logarithm of the conductivity-thickness product is a dominant component of both p_1^* and p_2^*. Also noting that the height is the major element of p_1^* and that the standard error of the first two eigenparameters is small, we can deduce that the height parameter and the combined parameter of conductivity times thickness are well determined. The third eigenparameter p_3^* reflects a combined parameter of the reciprocal of resistivity times thickness, which is needed if the initial parameters of layer thickness and resistivity are to be independently resolved. In this particular example, the standard error of p_3 is relatively large and hence we may anticipate a poor estimate of thickness and resistivity as independent parameters; however, a reasonable estimate of height and conductance from p_1^* and p_2^* alone can be made.

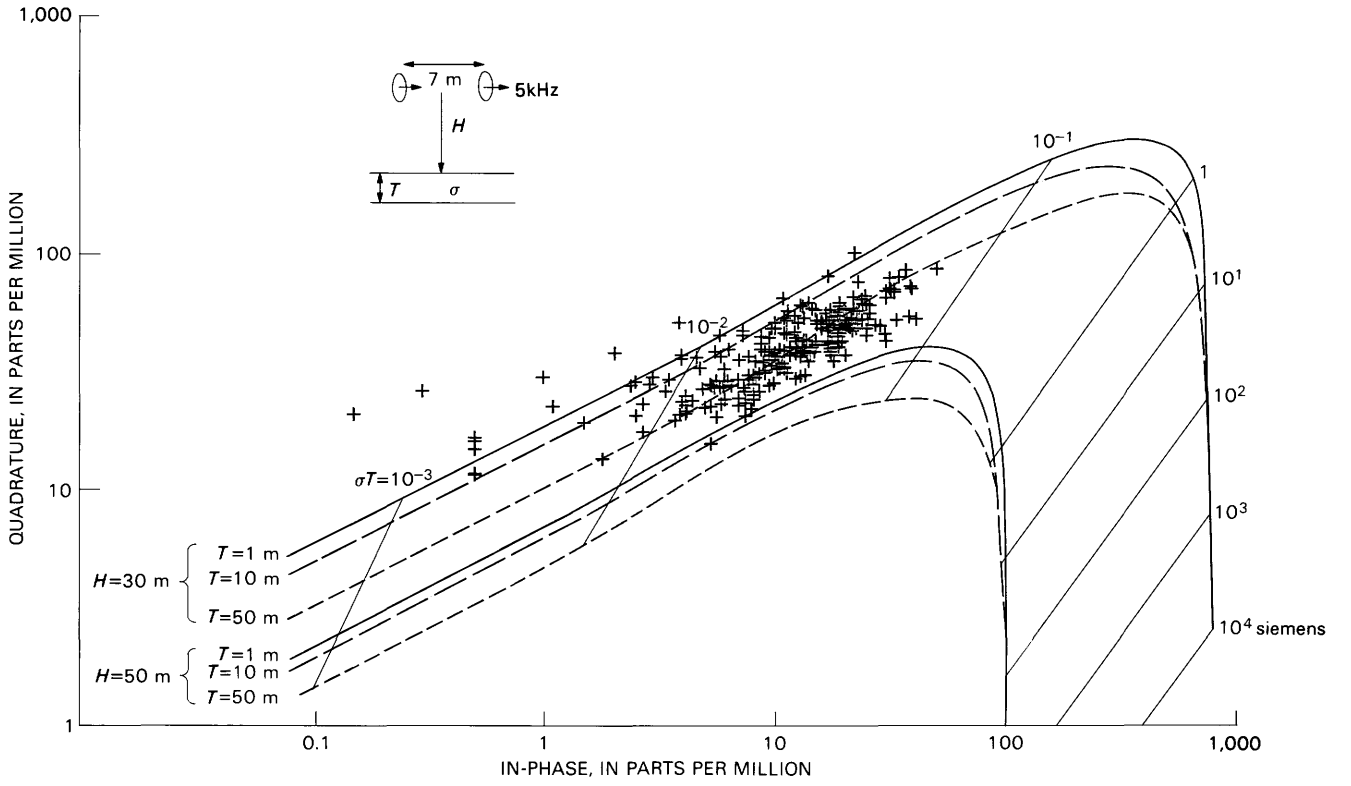

Figure 5. Phasor diagram for a horizontal layer of finite thickness as in figure 3 but populated with the HEM measurements closest to the drill sites of the Casa Berardi test area.

TEST CASE

In the Casa Berardi test area, about 20 km east-west by 5 km north-south, the location and depth for more than 200 overburden drill holes are available. The basement depth can vary by as much as 30–50 m over a 100 m lateral displacement. The HEM system used on the survey had two coaxial pairs operating at 935 and 4600 Hz and one coplanar pair operating at 4175 Hz. The mean flight line spacing was 100 m, and the HEM bird was towed at a terrain clearance of 30 m.

For initial evaluation a limited data set was created. The drill-hole data, points of ground truth, were sorted by location from west to east and the closest airborne measurement assigned to each. This data set was thus treated as a pseudo-flight line with a drill-hole depth at each observation.

A plot of the higher frequency (4600 Hz coaxial) response of this limited data set on the phasor diagram for horizontal layers provides some insight as to how the inversion process may respond (fig. 5). This presentation indicates that in-phase saturation generally is not approached, and therefore resolution of thickness and conductivity as independent parameters is probably limited. It is also clear from the rather concentrated distribution of observations that conductance variations are mostly limited to the range of 0.01–0.1 S. Similarly, the depth H from the bird to the top of the layer is usually less than 50 m.

This limited data set was treated as a pseudo-flight line and the inversion performed; the results are presented in figure 6 in profile form. Each point on the profile is a separate drill-hole location. The depth profile shown is the sum of the calculated depth below surface to the conducting layer and the calculated thickness. The resistivity of the underlying half-space was arbitrarily fixed at 10,000 ohm-m, a reasonable value for fresh metavolcanic and metasedimentary rocks in the area. The data are geographically arranged from west to east and have accidentally, but not unexpectedly, led to some general continuity between adjacent observations. Where the measured in-phase component is negative, interference by nearby magnetic anomalies is the cause and inversion was not attempted.

The top three profiles in figure 6 present the fitted HEM values together with the observed values. A close correlation is evident. This good match is also reflected by the low RMS (root-mean-square) error of fit; however, the fact that the model results fit the observed results well does not confirm that we have good

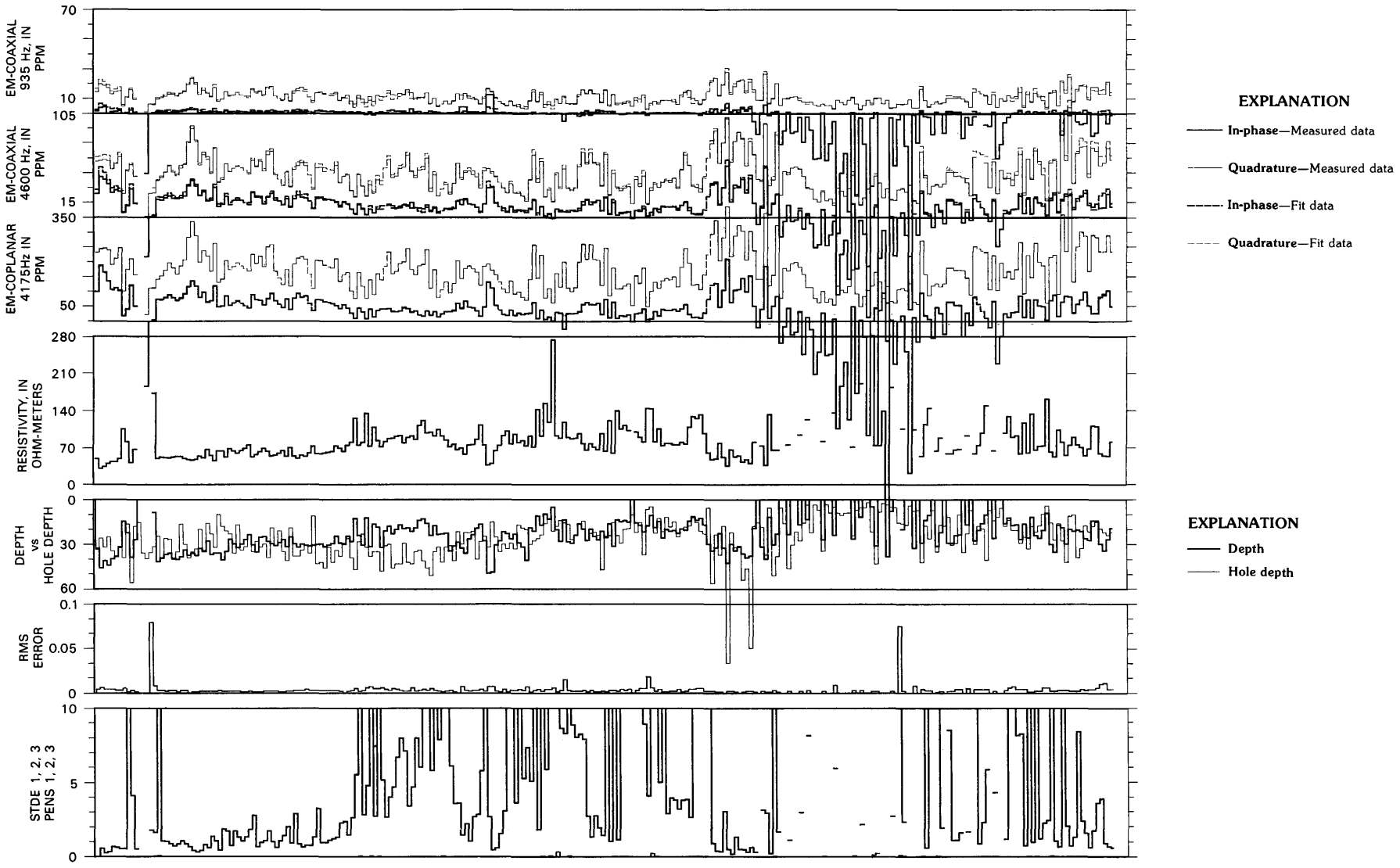

Figure 6. Pseudoprofile for the Casa Berardi study area composed of the HEM measurement closest to each drill-hole location. The data set has been sorted from west to east with each point a separate independent drill-hole site. The upper three profiles present observed and fitted HEM values; the RMS ERROR profile relates to the quality of this fit. The estimated resistivity of the layer and the estimated drill depth to the bottom of the layer are presented. The standard errors STDE of the three eigenparameters are presented on the bottom profile. The first two are consistently near zero and commonly not visible.

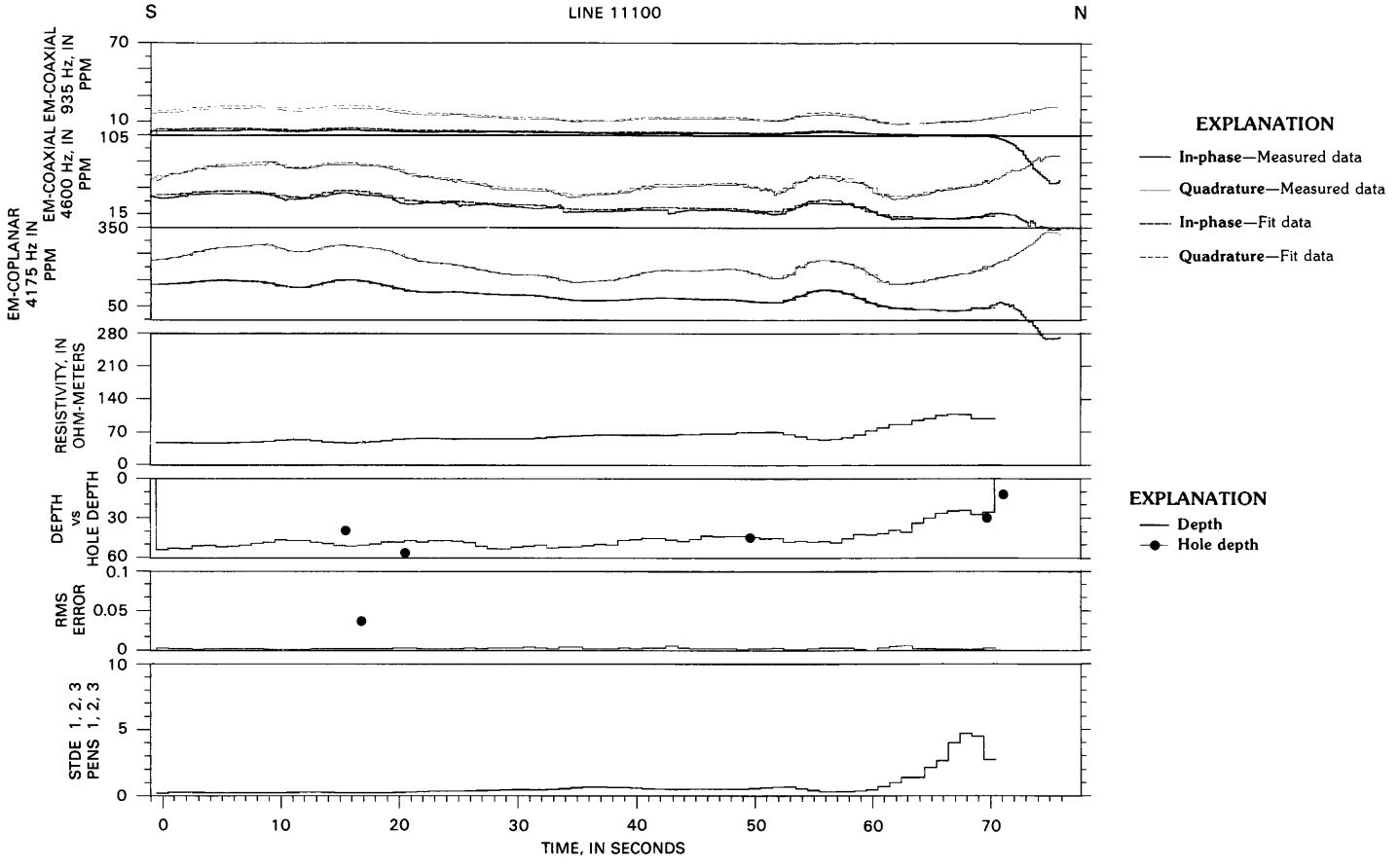

Figure 7. Actual survey profiles at the Casa Berardi study area are shown in the same presentation format as figure 6. Breaks in the profile occur where local magnetic mineralization has made the in-phase response negative and the inversion meaningless. The indicated drill holes may not occur directly under the flight line and their actual relative position is shown in figure 11.

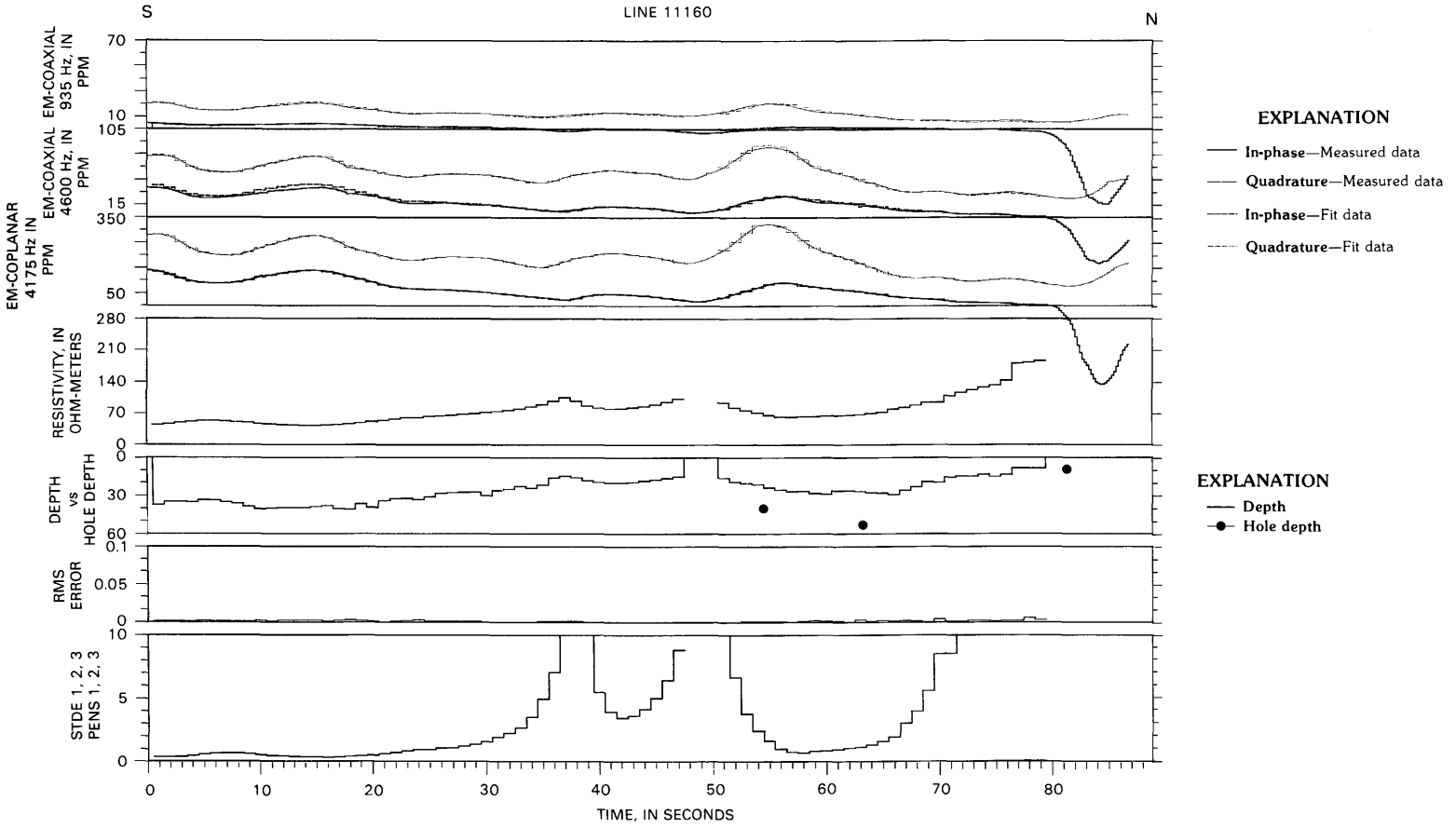

Figure 8. Additional survey profiles, Casa Berardi study area. See figure 7 for description.

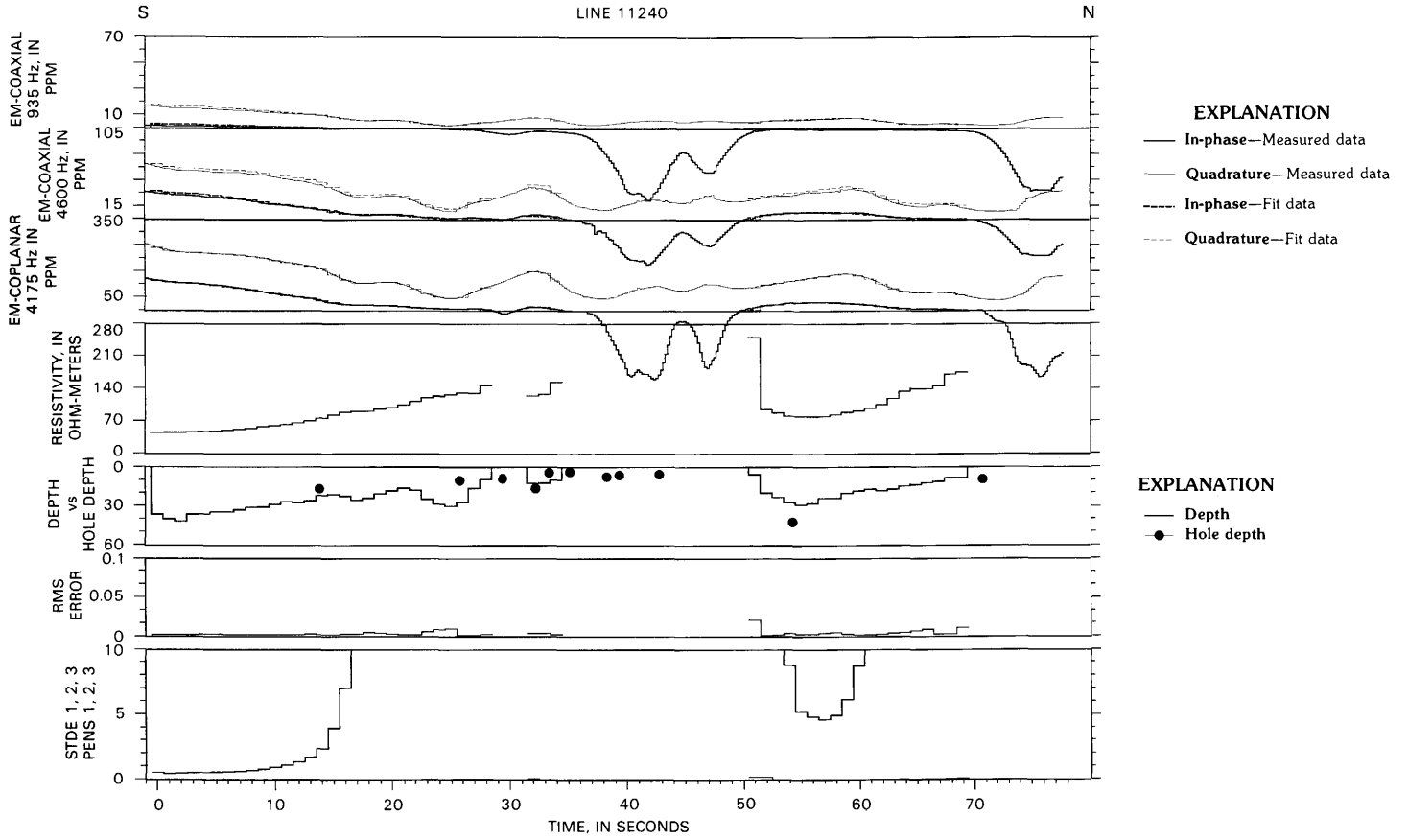

Figure 9. Additional survey profiles, Casa Berardi study area. See figure 7 for description.

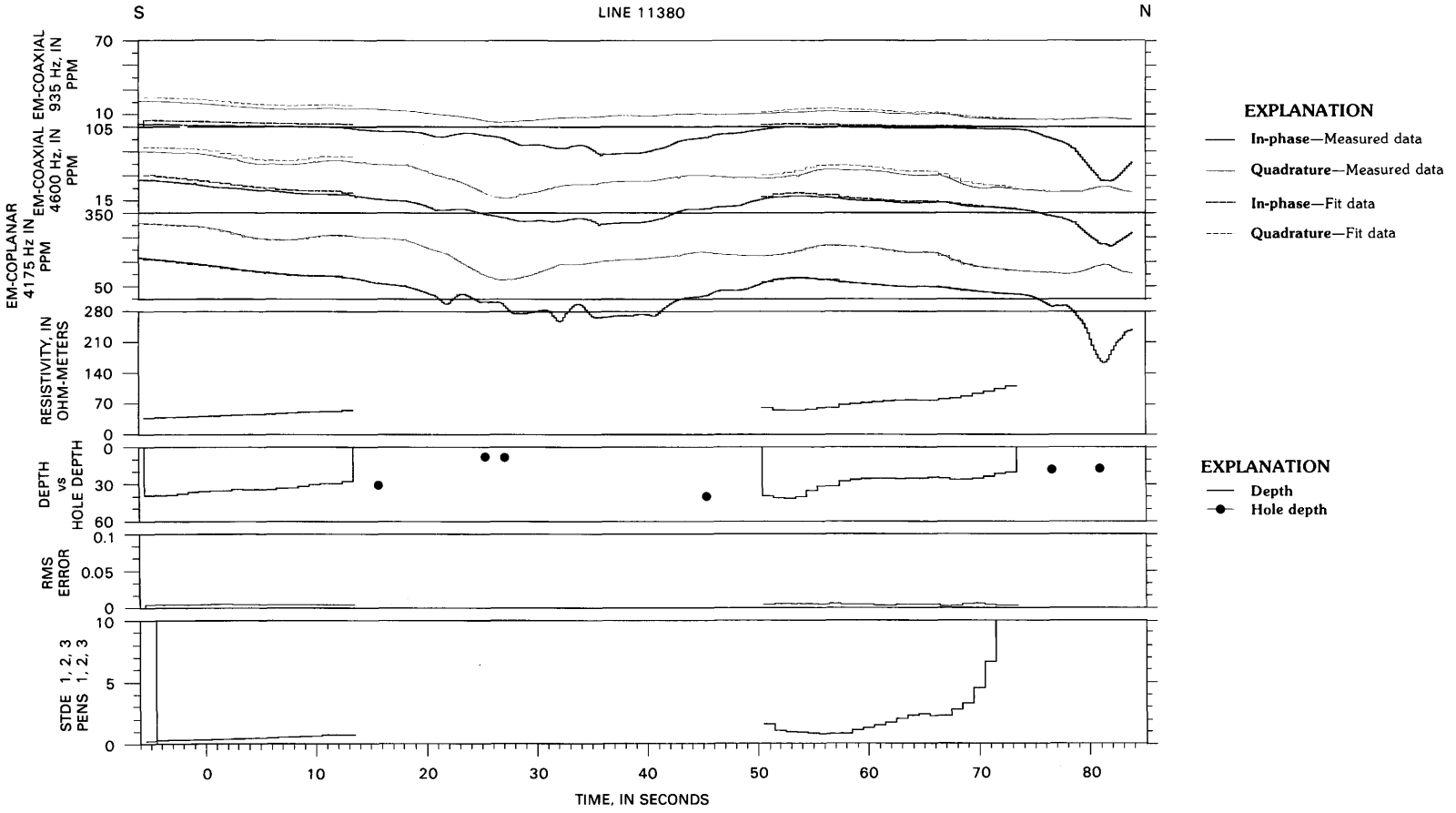

Figure 10. Additional survey profiles, Casa Berardi study area. See figure 7 for description.

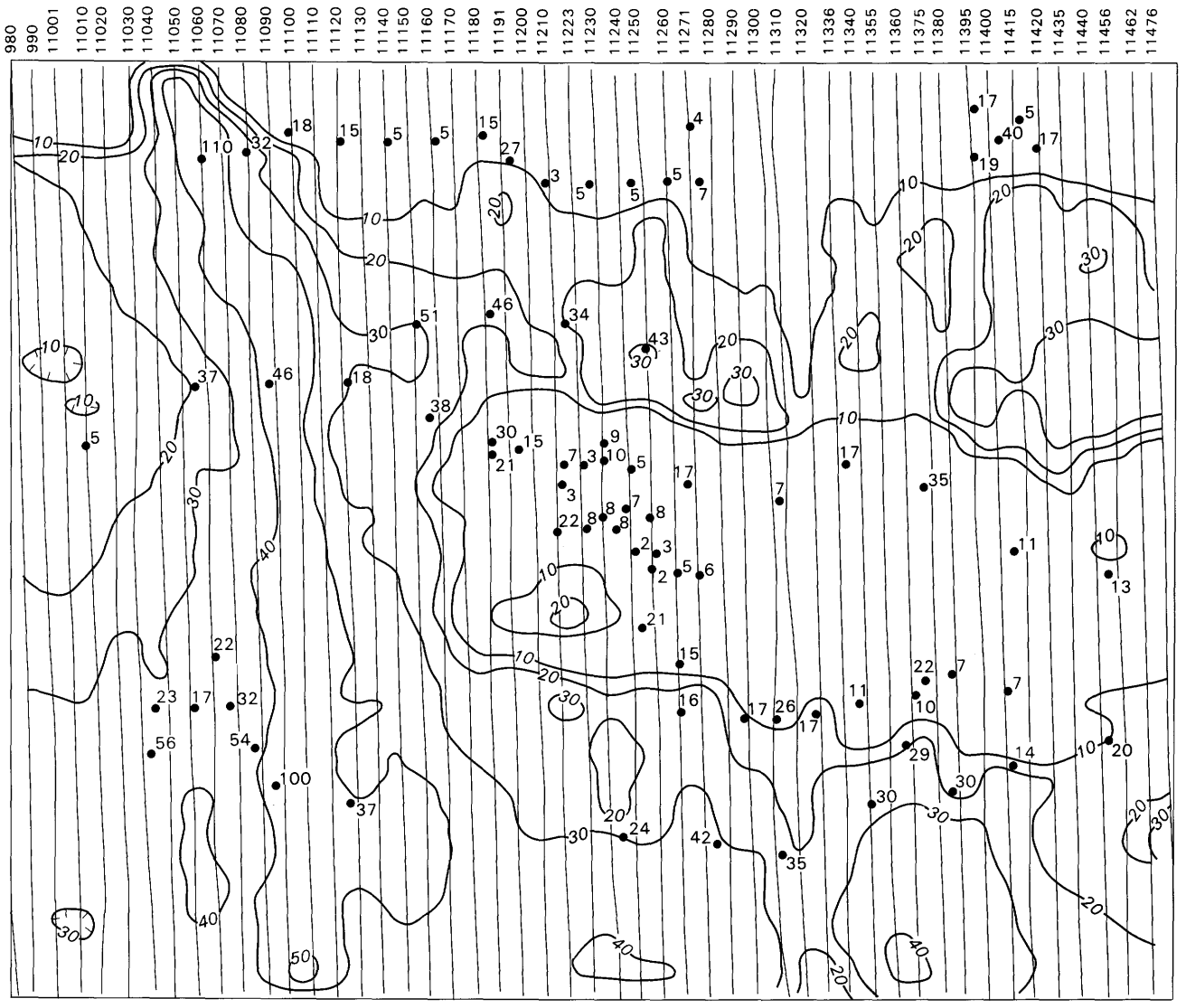

Figure 11. Contours of basement depth (in meters below surface), Casa Berardi study area, based on inversion of the HEM profile data. Drill-hole sites (solid circles) and true depths are indicated. Flight lines are spaced approximately 100 m apart.

parameter estimates. The profiles of the standard error of the three eigenparameters presented at the bottom of the display provide a means of judging the quality of the parameter estimates. The standard errors for eigenparameters 1 and 2 deviate only slightly from zero. The profile visible in the presentation is the error for eigenparameter 3. As noted in the earlier section describing the inversion method, the low error for the first two eigenparameters infers that in this test the height and the conductivity-thickness product are well determined but that conductivity and thickness as independent parameters will only be well determined where the error on the third eigenparameter is low. As anticipated, given the HEM frequencies available in this test, only a small fraction of inversion results presented have a standard error on the third eigenparameter of less than 1.0.

Thus far, we have reviewed only a selected data set for which there is one HEM observation per drill hole. Next, in order to investigate the mapping potential of the method we select a part of the general area having the highest density of drill-hole information. Profiled data across a select group of lines through the test area are shown in figures 7–10. Data displayed include fitted model HEM values and observed HEM values, model resistivity, model depth to the bottom of the conducting layers, measured hole depth to bedrock, and inversion error channels. As in the previous calculations, the inversion was suspended where the in-phase response is negative and clearly altered by nearby magnetic features. Also, the indicated drill-hole results may be as much as 100 m off to the side of the flight line; their position relative to the flight line can be ascertained in figure 11.

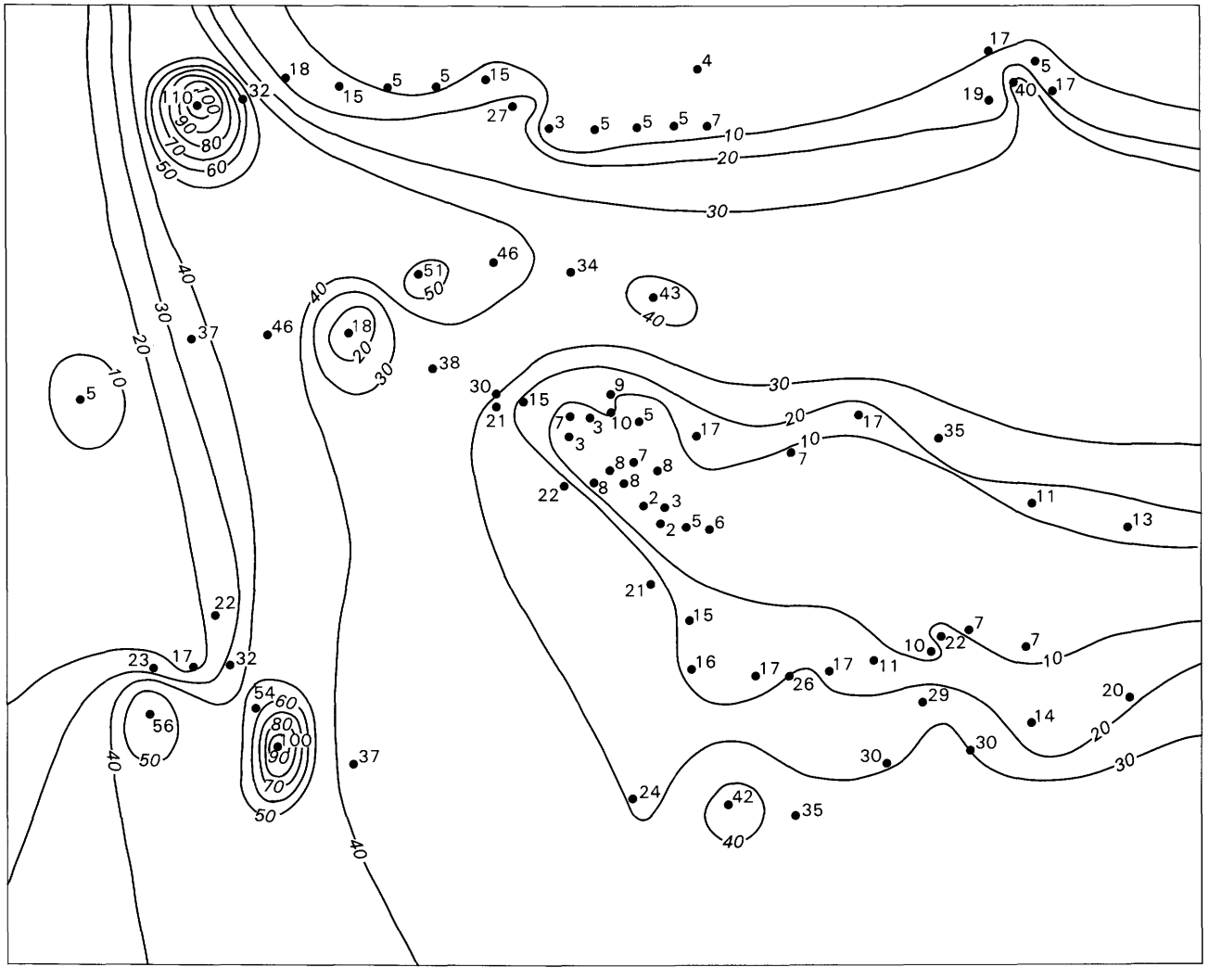

Figure 12. Contours of basement depth (in meters below surface), Casa Berardi study area, based on the drill-hole data alone for the area shown in figure 11. Drill-hole sites (solid circles) and depths are indicated.

Five of the six holes shown in figure 7 are very close to the calculated depths, and the sixth hole at 100 m near a calculated depth of 50 m is quite anomalous. This anomaly may be due to a sharp feature in the bedrock topography as indicated by a 46-m change in drill-hole depth over a lateral distance of about 100 m. An error in the drill-hole depth data is also not out of the question. In figure 8, the hole depths are consistently deeper than the inversion results; however, the form of the calculated profile is consistent with the ground truth. The depths in figure 9 correlate better with the calculated depths where available. The calculated trend of thinning overburden from the south end of the line is supported by the drill-hole depths. The calculated trend of increasing depth toward the center from the north end is also supported. In figure 10 the drill holes fall in zones of negative in-phase response and direct correlation is not possible; however, the calculated depths again correspond with the suggested trend.

Figure 11 presents a contour map of the depth to bedrock as calculated from the inversion data. The circles on the map indicate the drill-hole positions and the associated basement depth in meters below surface. Figure 12 shows a contour map of basement depth based on drill-hole data alone. The data are generally sparse and not evenly distributed, and there is considerable freedom in the position of the contour lines. Certain general trends, however, are well developed for comparison with figure 11. The general trend of a deeper east-west zone on either side of a central shallow area is in agreement with the drill-hole data. Furthermore, the north-south-trending deeper zone to the west and a shallower area near the western margin both are consistent with drilling results. A quantitative comparison of values indicates that for the most part the calculations are very reasonable, and the deviations may be due mostly to local irregularities of the basement surface smaller than the footprint of the HEM system.

CONCLUSIONS

An inversion process for helicopter electromagnetic (HEM) data based on the eigenvalue decomposition technique was applied to a test data set from the Casa Berardi area of Quebec with considerable success. Although the available frequencies of operation were less than optimum and the basement surface was relatively rough, the algorithm was able to make a general estimate of basement topography that is consistent with drill-hole information. New HEM systems having higher operating frequencies will permit this type of inversion to be applied more accurately over a wider range of geological environments. The ability to map from the air the depth, conductivity, and thickness of a conducting geologic horizon has numerous possible geological and geotechnical applications. Positive results from this example offer encouragement for further testing and application of the method.

REFERENCES CITED

Fraser, D.C., 1978, Resistivity mapping with an airborne multicoil electromagnetic system: Geophysics, v. 43, p. 144–172.

_____ 1979, The airborne multicoil II airborne electromagnetic system: Geophysics, v. 44, p. 1367–1394.

Edwards, R.N., Bailey, R.C., and Garland, G.D., 1981, Conductivity anomalies—Lower crust or asthenosphere?: Physics of the Earth and Planetary Interiors, v. 25, p. 263–272.

Application of Airborne Very Low Frequency Electromagnetic Surveys in Geophysical Exploration[1]

By Ajit K. Sinha[2]

Abstract

The airborne very low frequency electromagnetic (VLF–EM) method is increasingly being used in geophysical exploration for detection of sulfide conductors and in reconnaissance geological mapping. Most commonly, it is used with other systems as part of multiparameter airborne surveys. Measured total field VLF–EM data are normally presented in the form of contours where high values indicate the location of conductive anomalies. The vertical quadrature components, which are normally measured with total field anomalies, are presented in profile form, the crossover positions of which indicate the location of conductors.

Airborne VLF surveys at several locations in Canada show the potential of this technique in mineral exploration and geological mapping, especially the mapping of long conductive features such as faults and shear zones in Precambrian bedrock. Current interpretation techniques for airborne VLF data are largely qualitative. More rigorous interpretation is possible if corrections are applied to the raw field data and as response curves for anomalies over conductors of different types become available. The airborne VLF–EM system may also be adapted for airborne resistivity mapping at relatively low cost by adding a horizontal electric field sensor for measuring ground impedance.

INTRODUCTION

The very low frequency electromagnetic (VLF–EM) method of exploration uses signals that are transmitted by several powerful radio transmitters located around the globe for communication with submerged submarines and for directional positioning. Because the method does not require a field portable transmitter, VLF–EM surveys are much less expensive than other EM surveys. The VLF waves, propagating between the Earth's surface and ionosphere, travel long distances without significant attenuation and behave like plane EM waves beyond a few hundred kilometers from the transmitter. The depth penetration of VLF energy into the ground is controlled by its frequency (15–30 kHz) and by ground conductivity. The depth penetrations achievable with VLF sources range from 10 to 200 m in different types of geological materials (Hayles and Sinha, 1986).

The application of ground VLF systems in exploration was pioneered by V. Ronka in the 1960's when he designed the first portable VLF measuring instrument, the Geonics EM–16. Since then, many ground VLF–EM systems have been designed that measure the tilt and ellipticity of the VLF magnetic field as in the case of the EM–16, the ground impedance as in the EM–16R, or the total magnetic field. The early development of the VLF method has been described by Herz (1986).

The airborne VLF–EM survey method was developed as an outgrowth of the ground VLF method with the introduction of the McPhar KEM system in the early 1960's. This system consisted of a pair of crossed coils for measuring the horizontal magnetic field and the tilt angle. The system was relatively simple and did not measure the quadrature component. Geonics Limited developed the EM–18, an airborne version of the EM–16 system. The EM–18 system measured the vertical in-phase and quadrature components of the secondary magnetic field as a percentage of the horizontal magnetic field component. In the late 1960's, Barringer Research Ltd introduced two new systems, RADIOPHASE[3] and E-PHASE[3], both of which relied on the airborne measurement of the VLF fields. The RADIOPHASE method used three orthogonal coils to measure the VLF magnetic fields and a whip antenna to measure the vertical electric field, which served as the phase reference. The E-PHASE method relied on the measurement from an aircraft of the electric wave-tilt using the vertical electric field and the quadrature component of the horizontal electric field. It successfully detected high-resistivity materials such as gravel and sand deposits at several locations (Palacky and Jagodits, 1975).

The concept of using total-field VLF measurements to overcome noise problems arising from aircraft motion resulted in the introduction of a total-field measuring system called Totem 1A by Herz Industries in the 1970's and, later, its two-channel version Totem 2A. In these two systems, the total field is measured by three

---

[1]Geological Survey of Canada Contribution No. 38287.

[2]Mineral Resources Division, Geological Survey of Canada, 601 Booth Street, Ottawa, Ontario K1A 0E8, Canada.

[3]Registered trademarks of Barringer Research Ltd, Toronto.

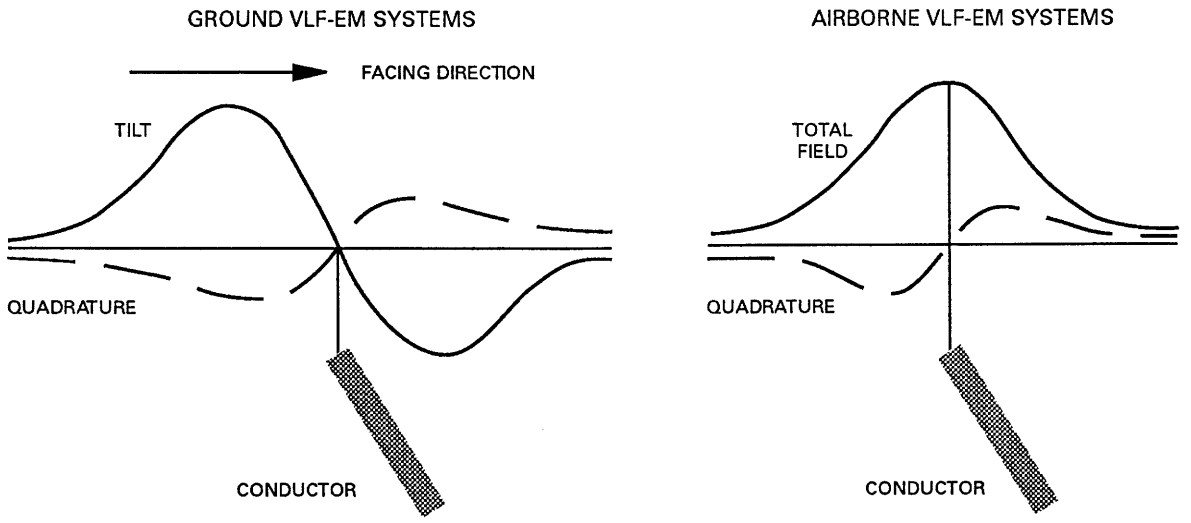

Figure 1. Anomalies over platelike conductors in a resistive host rock obtained using ground and airborne VLF–EM systems.

orthogonal coils and the quadrature component of the vertical magnetic field is measured as a percentage of the total field. Airborne VLF–EM systems are also manufactured by Scintrex Ltd, Toronto, and Sander Geophysics, Ottawa.

Acknowledgments.—I thank Mr. R.B.K. Shives, my colleague at the Geological Survey of Canada (GSC), for providing the data interpretation of the Newfoundland VLF survey. Dr. D.C. Fraser of the Dighem Surveys and Processing Ltd, Toronto, and Westmin Resources, Toronto, provided the data sets from Utik Lake, and Mr. Roger K. Watson of Terraquest Ltd, Toronto, and Goldhunter Exploration Inc., provided the data set at the Irwin and Sandra Townships. Figures 11 and 12 were prepared by Dr. W.J. Scott from the airborne VLF data at Chalk River. The draft illustrations were prepared by Ms. S. Davis, and the manuscript typing was done by Mrs. M. Wilson, both of GSC.

AIRBORNE VLF–EM SYSTEMS

Airborne VLF–EM systems most commonly are flown in conjunction with EM, magnetic, and (or) radiometric surveys using either a fixed-wing aircraft or a helicopter. Although airborne EM or magnetic data are generally processed and interpreted to yield geological models of the ground, VLF data are seldom presented in such fashion. Most commonly, the airborne VLF data are leveled to a common base value, filtered, and presented in contour form for the total field and in profile form for the quadrature component. As a result, airborne VLF interpretation is still largely qualitative and best suited for reconnaissance.

Figure 1 shows the nature of anomalies that might be detected over a platelike conductor in a resistive host rock using ground and airborne VLF systems. In a ground system that measures the tilt angle and vertical quadrature components, the tilt angle will show a crossover-type anomaly over the conductor, with the negative values toward the facing direction. The facing direction is the direction toward which the operator faces while taking the observation. This direction is along the direction of the horizontal primary field and should be the same at all stations in a survey area because the VLF response of a subsurface inhomogeneity is dependent on the facing direction. The quadrature response is also a crossover-type response, but the negative values can be either toward or away from the facing direction. The nature of the quadrature response over a thin tabular conductor can be rather complicated, but factors such as primary field orientation, conductivity contrasts, and depth determine the quadrature response (Sinha, 1985). In an airborne VLF–EM system having total-field measurement capability, the total field is a maximum over the conductor and the vertical quadrature component behaves similarly to that in a ground system.

Figure 2 shows a typical airborne VLF survey record collected in a period of 132 s at a site in central Ontario, Canada. Assuming a nominal speed of 193 km/h for the plane, the survey record represents a length of slightly more than 7 km. The survey was flown using two VLF stations, NAA, at Cutler, Maine (24 kHz), and NSS, at Annapolis, Maryland (21.4 kHz), and has a nominal flight altitude of 100 m as shown by the altimeter trace at the top. The bottom trace shows the total-field magnetic response in nanoteslas in coarse and fine scales. The total-field responses obtained using the two VLF stations

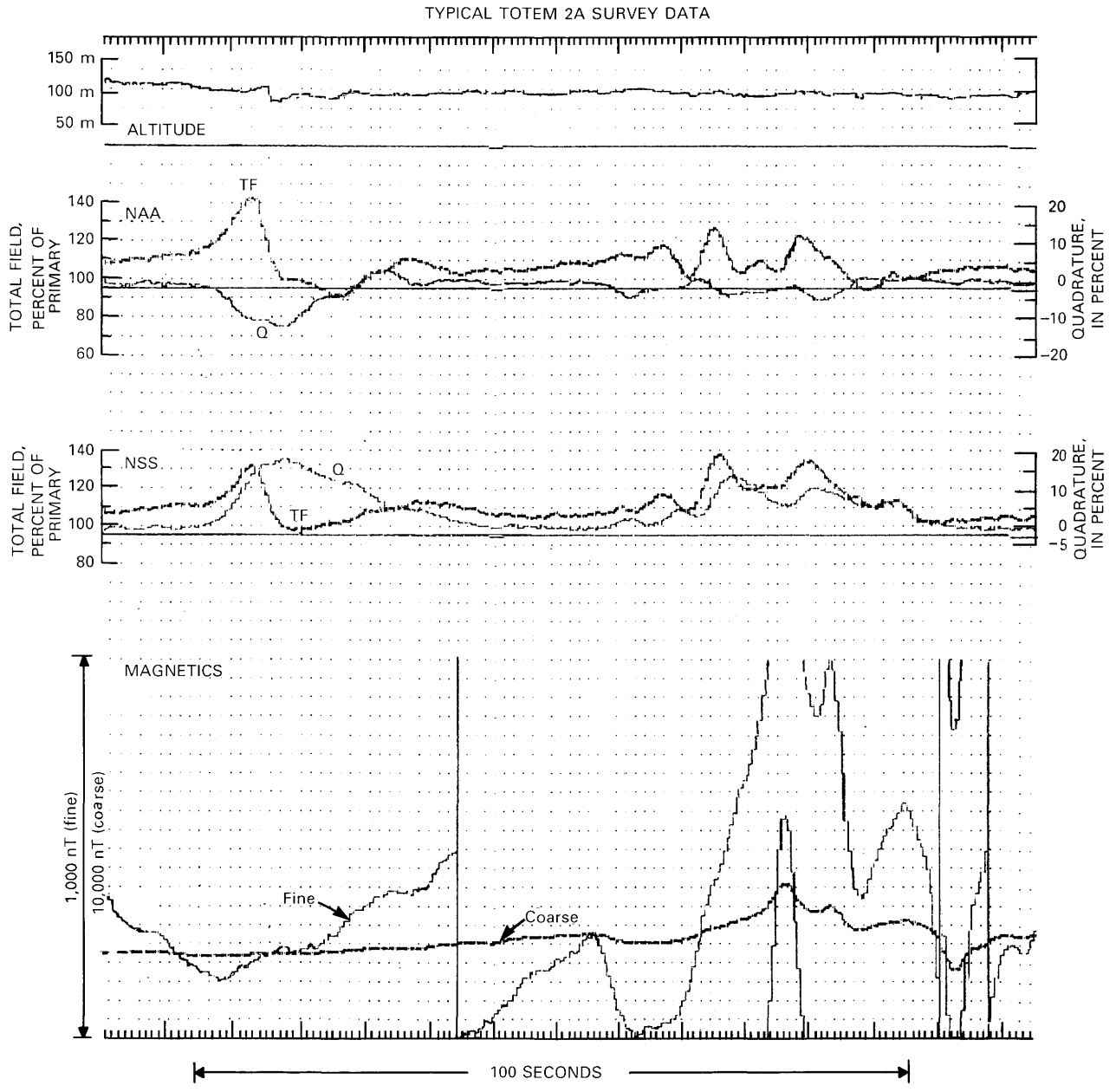

Figure 2. Two-frequency airborne VLF–EM and magnetic survey data from central Ontario using stations NAA and NSS. TF is total field; Q is quadrature.

are quite similar. The data were not compensated for variation of the signals with time and distance from the transmitters. This partly explains the minor discrepancies between the two sets of total-field VLF data. The quadrature responses, on the other hand, are quite different and have reversals at two places. This indicates the sensitivity of the quadrature response to the direction of the incoming VLF field; thus, the quadrature responses may be used to determine the orientation and characteristics of the conductor.

The frequencies used in VLF surveys are comparatively high (15–30 kHz), and the VLF energy can only penetrate the shallow layers of the ground. The depth penetration is 100–200 m in the case of highly resistive ground and only tens of meters in the case of moderately conductive ground (Hayles and Sinha, 1986). Because the primary field for the VLF method behaves like a plane wave, the method is suitable for detection of long but weakly conductive structural features such as faults and shear zones containing water or clay. Current channeling becomes the dominant mechanism for the generation of anomalies in such cases and results in large anomalies over long conductive structures that strike normal to the primary field orientation.

EXAMPLES OF AIRBORNE VLF–EM SURVEYS

Southwest Newfoundland

Airborne VLF–EM data and radiometric and magnetic data for regional mapping purposes were collected by the Geological Survey of Canada in southwest Newfoundland in 1984. The survey was flown with a mean terrain clearance of 125 m and line spacing of 1 km. Survey lines were oriented north-south to provide good coupling with the primary magnetic fields from two U.S. Navy VLF stations, NAA (24 kHz) and NSS (21.4 kHz). Station NAA was used for most of the survey because its signal strength was stronger; however, when that station was not operating, station NSS was used. A Herz Totem 1A system was used to measure the total VLF magnetic field and its vertical quadrature component. The overburden in the survey area was thin and generally resistive, and thus conditions were optimum for VLF measurements.

The locations of VLF conductors were interpreted by using the highs of the total field and the crossover positions of the quadrature values. In general, both measurements indicated identical locations of conductors. Figure 3 shows the locations of VLF conductors in an area, approximately 42 by 42 km, near the southwest coast of Newfoundland. Geologically mapped contacts and fractures and shear zones as determined using photographic lineament studies and surface mapping are also indicated. The agreement between the locations of the VLF conductors and the fractures and lithological contacts is good. The structures trend approximately northeast-southwest in the central part of the area and almost east-west at the northern end. The Chetwynd gold mine in the southeastern corner of the map area is close to the intersection of a VLF conductor and a lithological contact. Some of the mapped lithological contacts do not have a corresponding VLF signature, possibly because there is no significant change of electrical resistivity across the contact. Electrically, the rock mass therefore behaves like a homogeneous medium, although lithologically it may be heterogeneous. This figure shows the ability of airborne VLF surveys to map long linear conductors in areas of thin overburden during the reconnaissance phase of a survey.

Utik Lake, Manitoba

Figure 4 shows filtered, total-field airborne VLF data at Utik Lake, Manitoba, in contour form. The center of the survey grid is at lat 55°15′ N., long 96°7′ W. The survey data were filtered to remove time fluctuations in the transmitter field strength. The filtering also accentuates the short- wave-length response to facilitate recognition of trends in rock strata. The survey area is in a Precambrian greenstone belt where graphitic conductors and iron formations are known to exist. The VLF data were collected by Dighem Surveys and Processing, Inc., using a helicopter, in conjunction with DIGHEM EM and magnetic data (Fraser, 1972). The helicopter was flown with a mean terrain clearance of 30 m and a line separation of 100 m.

The VLF map shows several linear conductors that trend generally east-west. The solid and open circles indicate the locations of strong and weak EM anomalies, which were detected by using the 900-Hz coaxial coil-pairs of the DIGHEM EM system. There is excellent correlation between DIGHEM EM and VLF conductors in the central and southern parts of the map area. The correlation is not bad for the northernmost string of weak EM conductors, but it is poor for a string of weak conductors immediately to the south, possibly because the weak conductors may be too deep to be detected by the VLF method. There are no indications that these EM anomalies are due to cultural noises or power lines. Another possible explanation is that this set of conductors is not interconnected. Because current channeling is responsible for most of the VLF–EM response, discontinuities between the conductors would inhibit the flow of current between them. The DIGHEM EM system would detect the conductors as separate conductors because the induction mechanism responsible for anomaly generation in the DIGHEM system would still work.

Figure 5 shows contours of apparent resistivity for the area obtained from the EM data using the coplanar coil configuration of the DIGHEM system transmitting at 7200 Hz. Fraser (1978) has described the technique for obtaining apparent resistivity maps from DIGHEM data sets. The locations of the low apparent resistivity contours in figure 5 generally coincide with the locations of EM conductors in the central and southern parts of the map and with the locations of weak EM conductors in the northern part of the map. Because the apparent resistivity values are obtained from DIGHEM EM data, which are dependent on the induction mechanism, these zones are shown as low-resistivity areas whether the conductors are interconnected or not. The coincidence of EM conductors and low apparent resistivities tends to reinforce the theory that the southern string of weak conductors in the northern part of the map area either are discontinuous, en echelon-type conductors or are deep. Figure 6 shows the enhanced total-field magnetic map of the area. The magnetic data show good correlation with EM conductors in the central and southern parts of the map area and very poor correlation

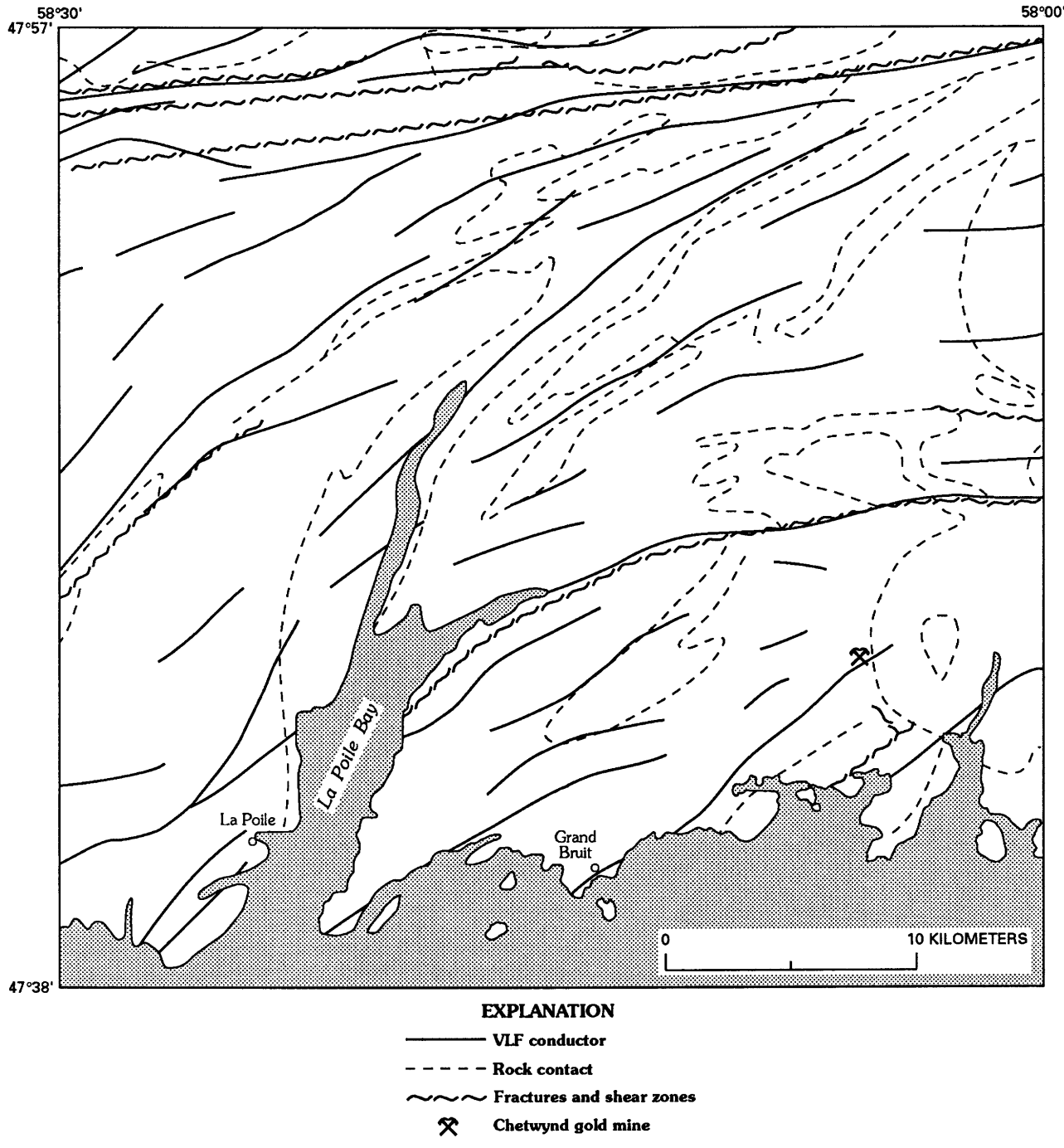

Figure 3. Location of VLF conductors and geologically mapped fractures and shear zones in southwest Newfoundland.

with DIGHEM EM resistivity and VLF anomalies in the northern part of the map. The lack of correlation between magnetic and electrical anomalies reduces the possibility that the northern conductors might contain sulfides.

Irwin and Sandra Townships, Ontario

A combined airborne VLF/magnetic survey was conducted by Terraquest Ltd., Toronto, over the Irwin and Sandra Townships in central Ontario using a fixed-wing aircraft flying at a mean terrain clearance of 100 m and a line spacing of 100 m. The center of the survey area is at lat 49°43′ N., long 87°57′ W. The survey was undertaken for mapping purposes and to look for gold mineralization associated with fractures in the granitic bedrock and with base-metal sulfide deposits. Figure 7 shows the VLF–EM total field in contour form and the vertical quadrature components in profile form. VLF transmitter NAA was used for the survey, which had

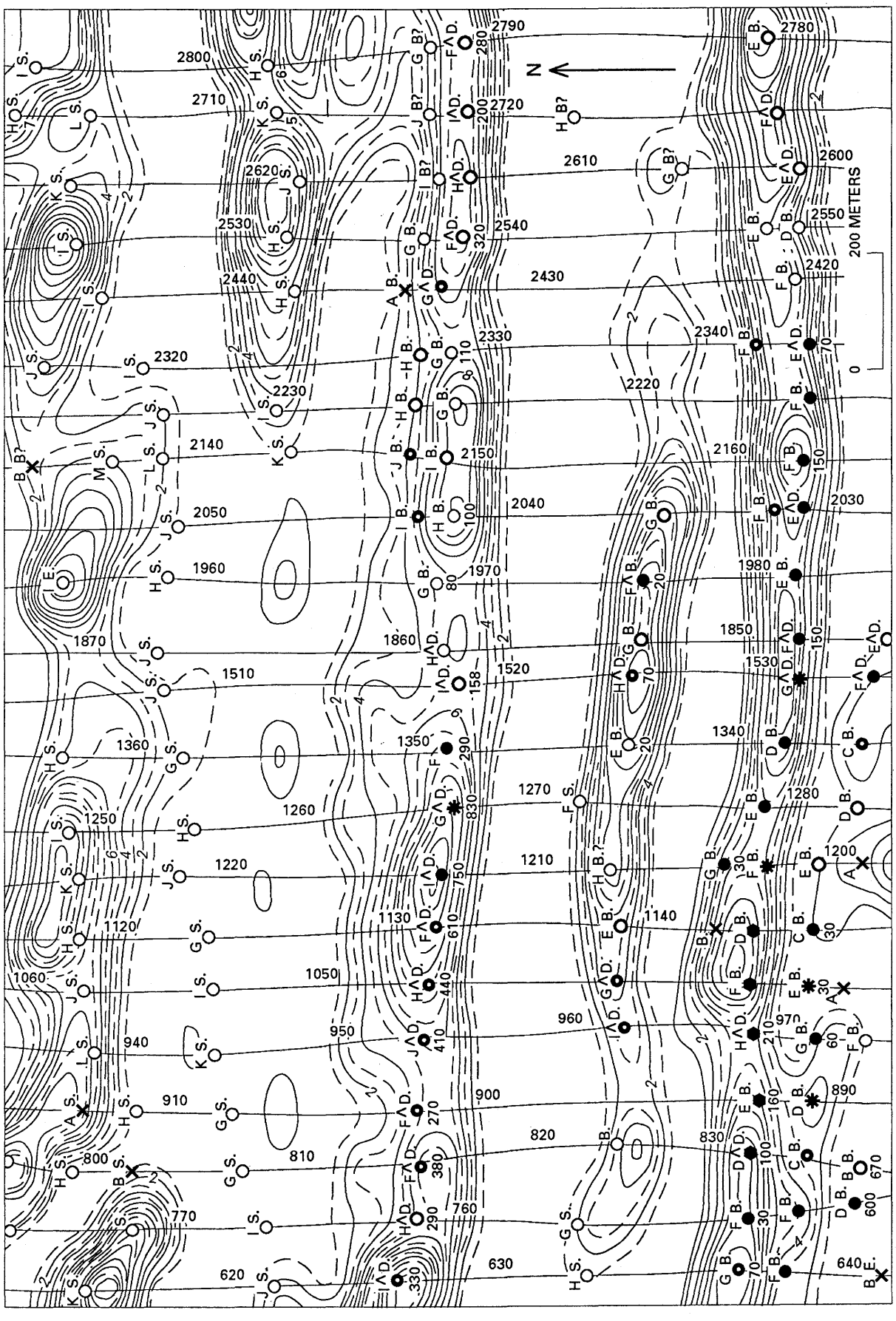

Figure 4 (above and facing page). Filtered total-field VLF data from Utik Lake, Manitoba (lat 55°15′ N., long 96°7′ W.). Contour interval is 1 percent of primary field. The solid and open circles indicate locations of strong and weak anomalies, respectively, as determined using a DIGHEM EM survey. Courtesy of Dighem Surveys and Processing, Inc., and Westmin Resources Ltd.

EXPLANATION

ANOMALY GRADE	EM GRADE SYMBOL	CONDUCTANCE (siemens)
6	●	> 99
5	✱	50–99
4	●	20–49
3	⊙	10–19
2	○	5–9
1	○	< 5
–	×	Indeterminate

DIGHEM anomalies are divided into six grades of conductivity-thickness product. This product (in siemens) is a measure of conductance.

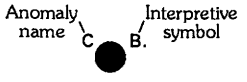

INTERPRETIVE SYMBOL	CONDUCTOR ("model")
B.	Bedrock conductor
D.	Narrow bedrock conductor ("thin dike")
S.	Conductive cover ("horizontal thin sheet")

north-south survey lines. One strong east-west conductor was detected at the northern end of the map area. A somewhat weaker conductor was mapped south of where this conductor intersects the first conductor in the northeastern corner of the map area to form a narrow V. Several conductors of shorter strike length were detected at the southern end of the map area. Vertical quadrature values show some interesting variations. The quadrature profiles are normal (changing from positive to negative as one moves north) over most of the area, with sign reversals at several places. Because the orientation of the primary field was identical on all lines (only NAA was used), the quadrature reversals must be due to the changing nature of the VLF conductors. Hence, this property has the potential for discriminating various types of VLF conductors by comparing the field response to those of a set of computer models. The locations of VLF conductors agree well with a geological map of the area; two long conductors coincide with a major fault and a diorite dike (R.K. Watson, Terraquest Ltd., Toronto, oral commun.).

Chalk River, Ontario

The airborne VLF–EM method has proven useful in the Canadian Nuclear Fuel Waste Management Programme for mapping water-saturated fracture and shear zones at shallow depths in the Canadian Shield. During the initial site selection process for a possible repository for spent nuclear wastes, a large plutonic rock mass with few large fractures was sought because fractures may serve as conduits for the migration of the radionuclides to the biosphere (shallow ground and air).

Chalk River, Ontario, was selected as a test site to study the concept of deep geological burial of nuclear fuel wastes in an unfractured plutonic rock mass. The area is underlain by a large granitic pluton and has a thin veneer of relatively resistive overburden (Dvorak and others, 1989). The area was surveyed using a DIGHEM helicopter system equipped with EM, magnetics, and VLF sensors to study the nature of the top few hundred meters of the granitic bedrock, particularly the fracture occurrences and their pattern over the pluton. The center of the survey area is at lat 46°3′20″ N., long 77°25′30″ W.

VLF fields are directional and thus tend to energize only those conductors that strike more or less parallel with the VLF azimuth (line joining the receiver to the transmitter). At Chalk River, the azimuths for the two VLF stations, NAA and NSS, are almost orthogonal (87° apart) and thus provide a rare example of an area having VLF coverage with orthogonal azimuths. The area was surveyed using a Totem 1A sensor, flying in orthogonal directions (north-south for NAA, east-west for NSS), to examine the effects of flight orientations on the detection of anomalous conductors. The nominal flying altitude was 70 m and line spacing of 100 m.

Figure 8 shows contours of the total-field VLF–EM data obtained using the north-south flight lines (NAA). The mapped conductors show a distinct east-west orientation because east-west trending conductors would have the best coupling with the VLF primary field from NAA. Figure 9 shows contours of the total-field VLF data obtained using east-west flight lines (NSS). In contrast to the previous figure, the mapped conductors trend mostly north-south, trends which of course would couple better with the east-west primary VLF field for NSS. Figures 8 and 9 illustrate the necessity of having at

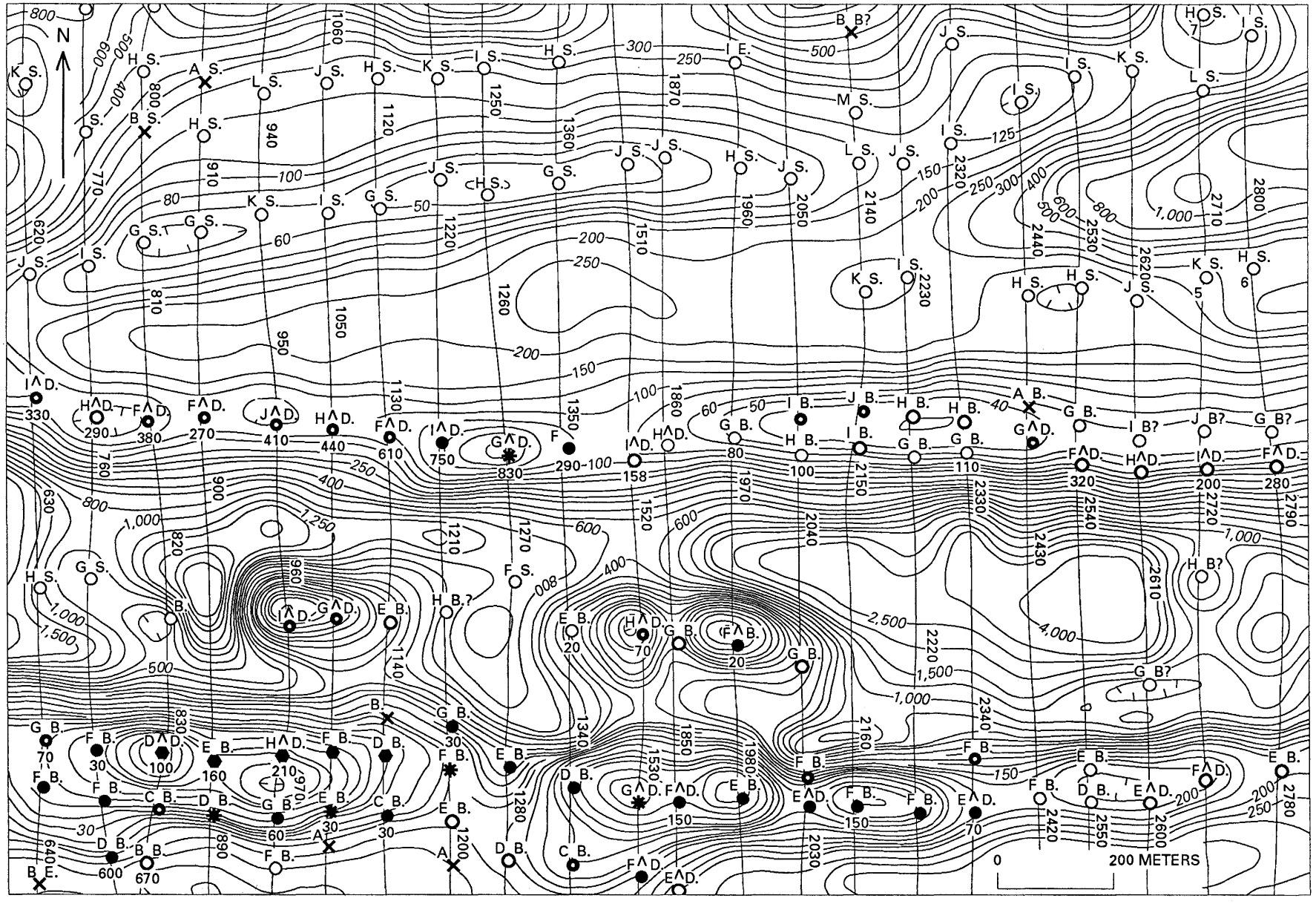

Figure 5. Apparent resistivity, Utik Lake, Manitoba, using the coplanar coil-pairs of the DIGHEM EM system. Contour interval is 50 ohm-m. Explanation as for figure 4. Courtesy of Dighem Surveys and Processing Inc., and Westmin Resources Ltd.

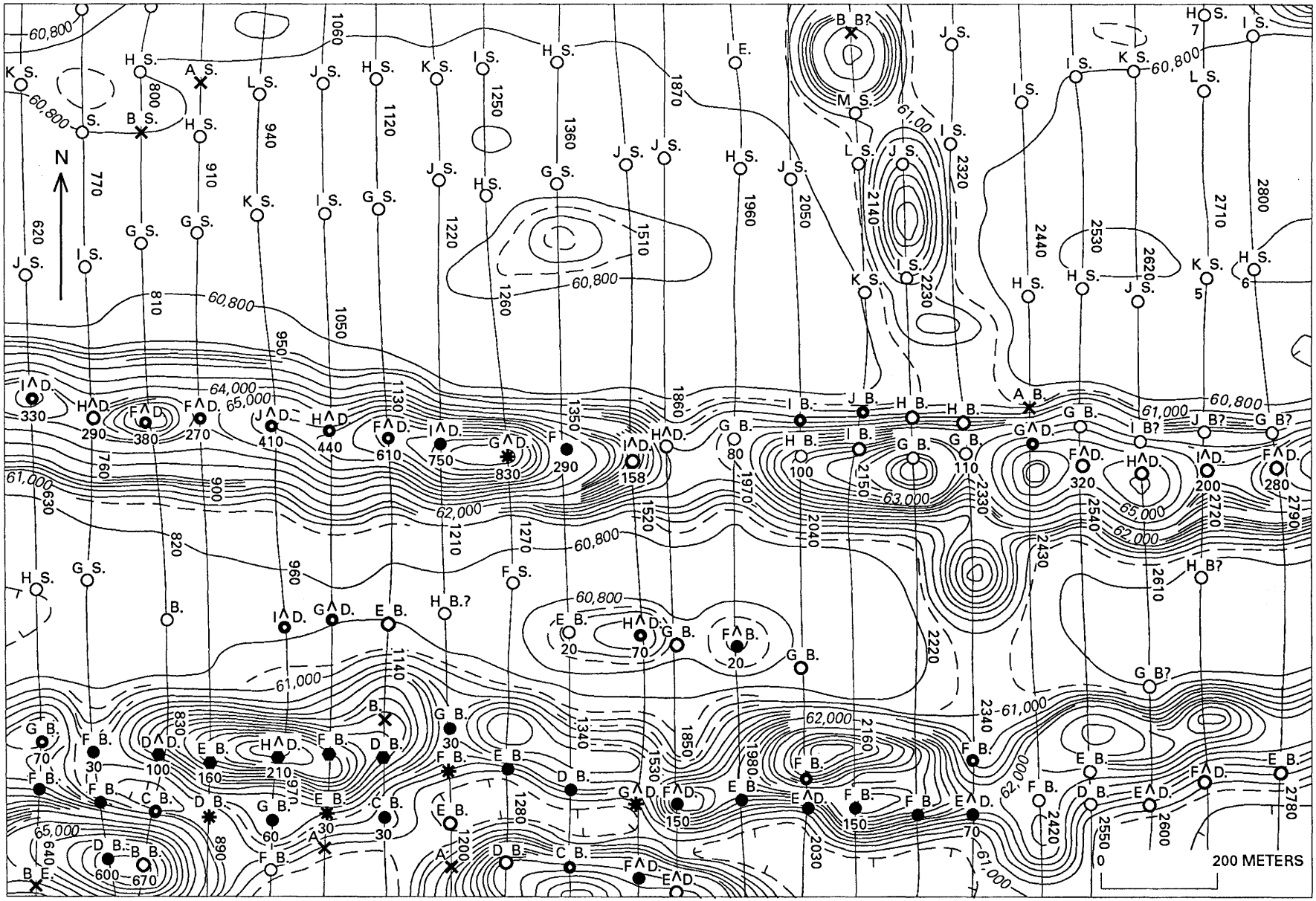

Figure 6. Enhanced magnetic field values, Utik Lake, Manitoba. Contour interval is 150 nT. The map was obtained by filtering the magnetic data and emphasizes near-surface geology. Explanation as for figure 4. Courtesy of Dighem Surveys and Processing, Inc., and Westmin Resources Ltd.

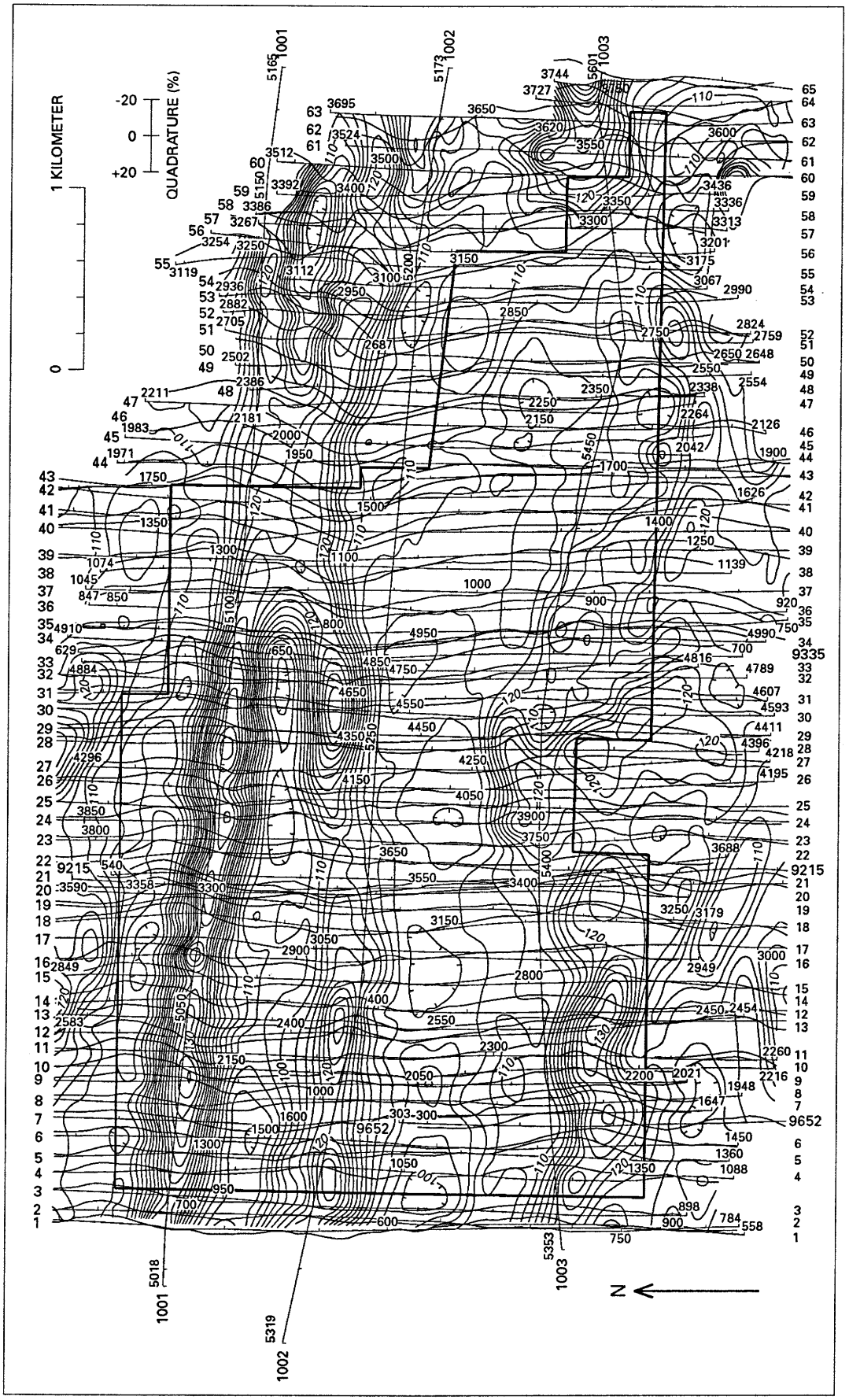

Figure 7. Total field VLF–EM data and vertical quadrature components along profiles at Inwin and Sandra Townships, Ontario (lat 49°43′ N., long 87°57′ W.). Contour interval for total-field values is 2 percent of the primary field. Courtesy of Terraquest Ltd, Toronto, and Goldhunter Exploration Inc.

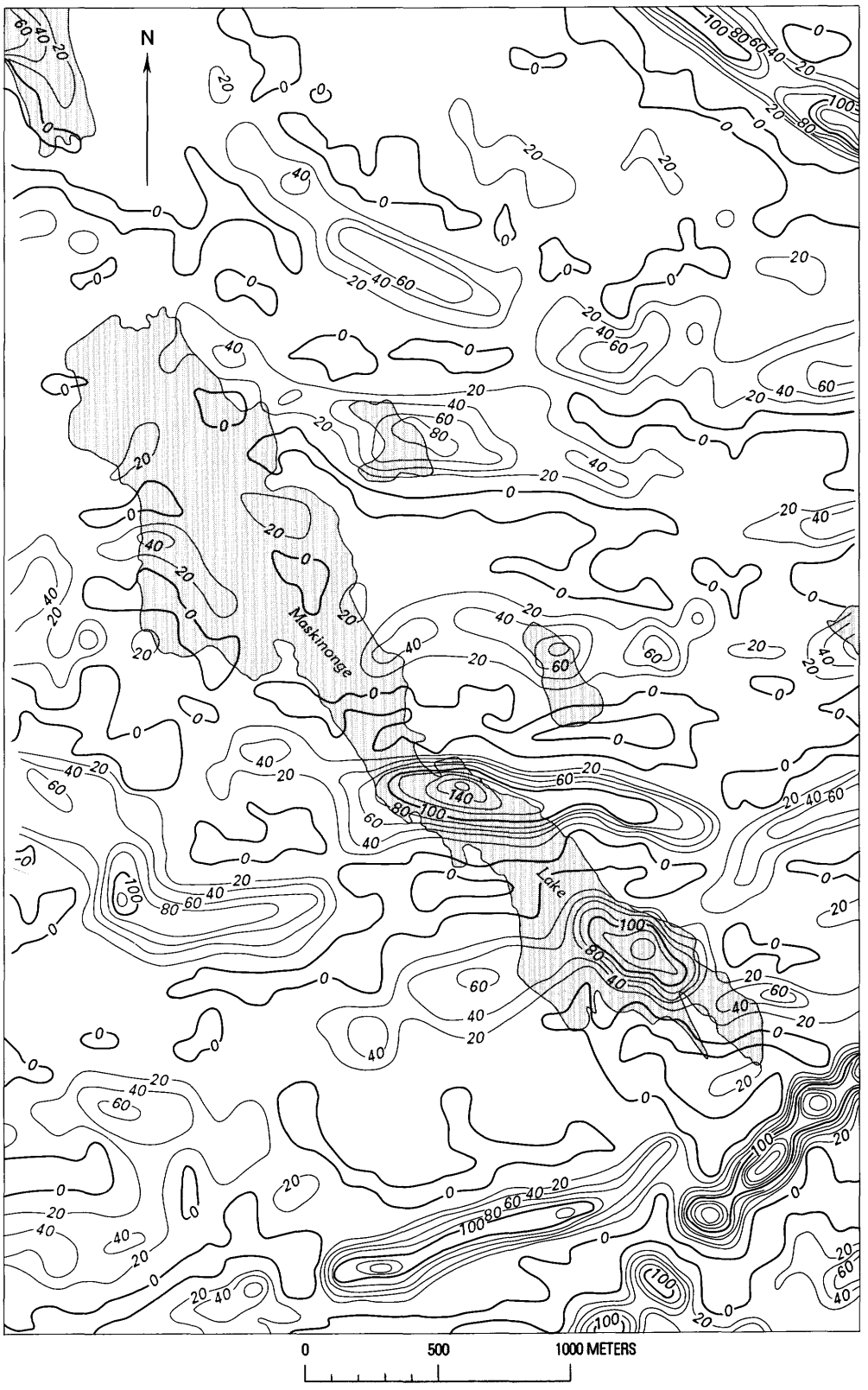

Figure 8. Total-field VLF–EM data obtained from airborne VLF survey at Chalk River, Ontario (lat 46°3′20″ N., long 77°25′30″ W. for the center of the survey area) using station NAA. Contour interval is 2 percent (shown as 20) of the primary field.

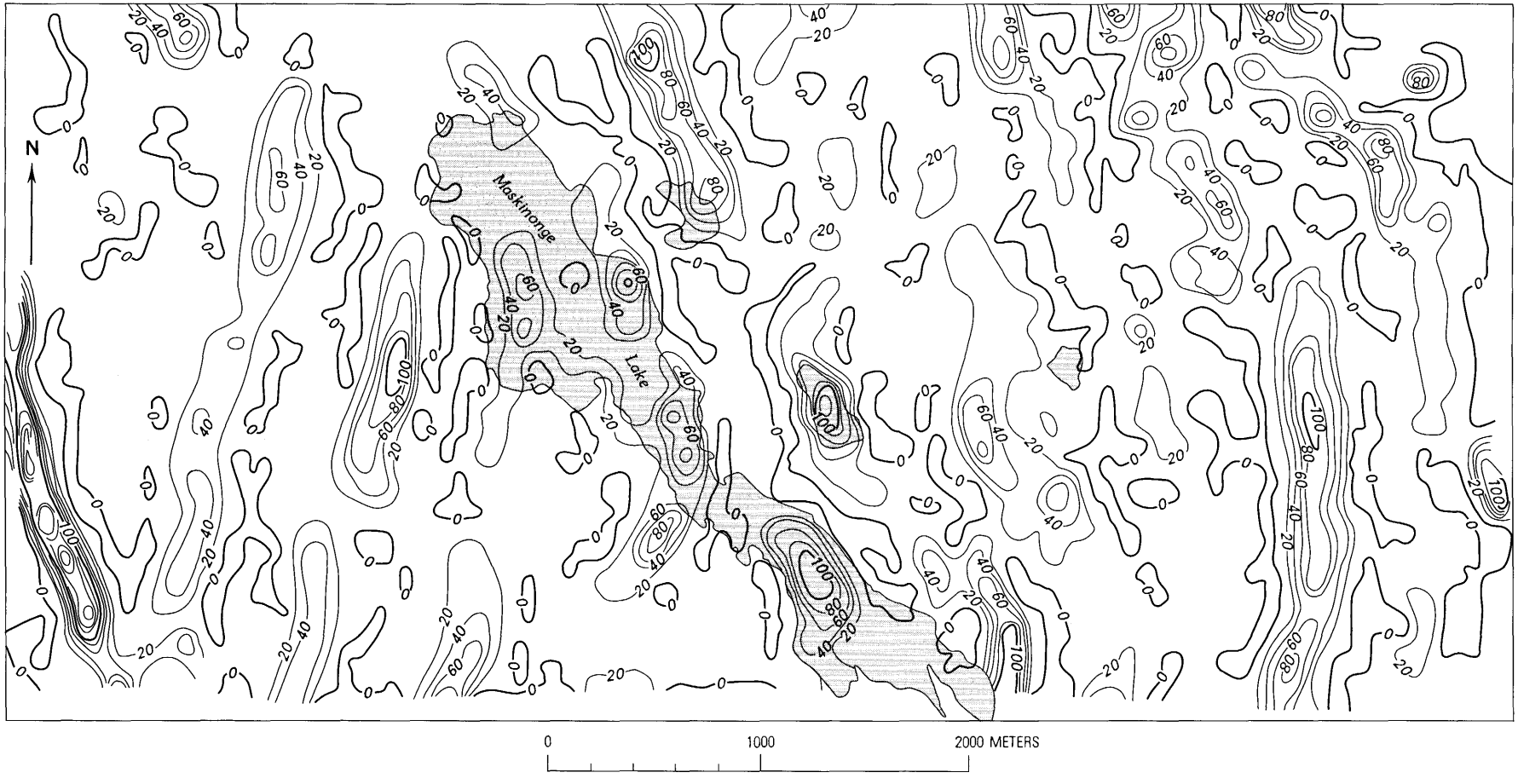

Figure 9. Total-field VLF–EM data obtained from airborne VLF survey at Chalk River, Ontario, using station NSS. Contour interval is 2 percent (shown as 20) of the primary field.

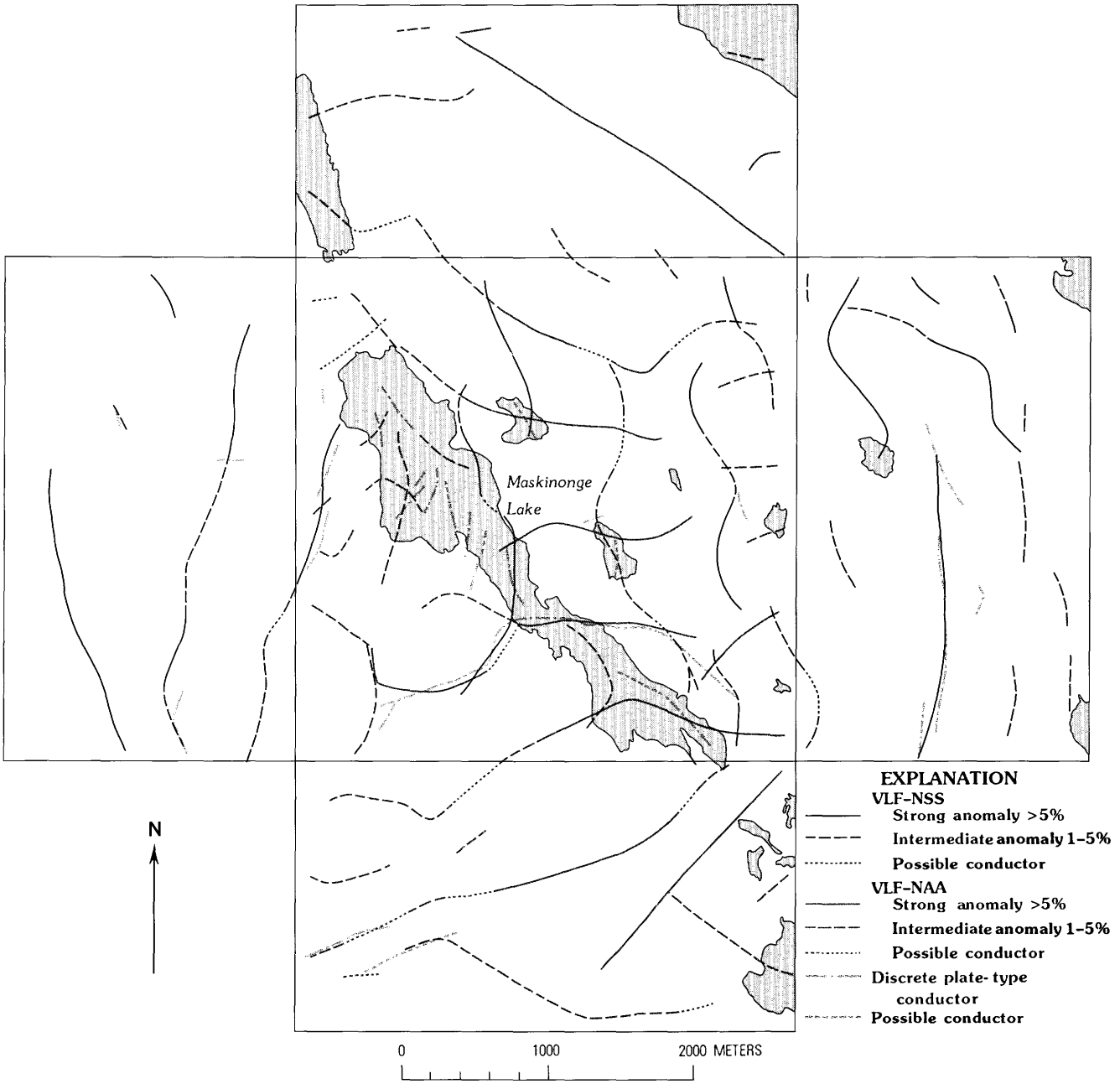

Figure 10. Conductor map for the Chalk River survey area derived from VLF–EM and DIGHEM EM surveys. Modified from Dvorak and others (1989).

least two VLF sources with orthogonal azimuths to map all conductors in an area. Subsequent ground followup surveys (Hayles and Sinha, 1986; Scott, 1989) detected all these airborne VLF–EM conductors. Figure 10 shows the locations of conductor axes as mapped by using both VLF stations. Discrete platelike conductors detected by the DIGHEM EM system are also shown. Although the locations of strong EM conductors commonly coincide with those of VLF conductors, a few discrete EM conductors have no VLF expression, possibly because of their very limited strike lengths that contribute to poor current channeling.

Figures 11 and 12 are histogram plots illustrating the dependence of the detectability of VLF conductors on VLF azimuths by using NAA and NSS data at Chalk River. Figure 11 shows a plot of conductor length versus conductor azimuth for data from NAA only. As expected, most of the long linear conductors have their azimuths close to 90° east-west and a few have azimuths in the 0° or 180° range. On a similar plot of data from NSS (fig. 12) most of the long conductors have azimuths close to 0° or 180° (north-south). These results are similar to those obtained using ground VLF–EM surveys in which VLF sources are placed at different azimuths

(Hayles and Sinha, 1986). The locations of the VLF conductors also agree well with those of dominant fracture sets mapped by Brown and Thivierge (1977).

RECOMMENDATIONS FOR FUTURE DEVELOPMENTS

Present-day airborne VLF–EM systems are relatively simple and provide good qualitative data but rarely are they of a quality that permits quantitative interpretation. The following improvements and additions are recommended to make the systems more effective and data quality more reliable.

1. A totally digital VLF–EM system is needed to make the data more reliable and also independent of the manual control of the gain by the system operator now required to keep the recorded values on scale.

2. The VLF–EM data must be monitored on the ground to remove the effects of changing field strengths with time.

3. The effects on the total VLF–EM field of changes in the altitude of the aircraft and distance and orientation from the transmitter should be investigated and the data suitably compensated for meaningful interpretation.

4. The response of various geological models excited by plane-wave VLF fields should be investigated theoretically and experimentally (using scale models) in order to develop methods of quantitative interpretation of airborne VLF–EM data.

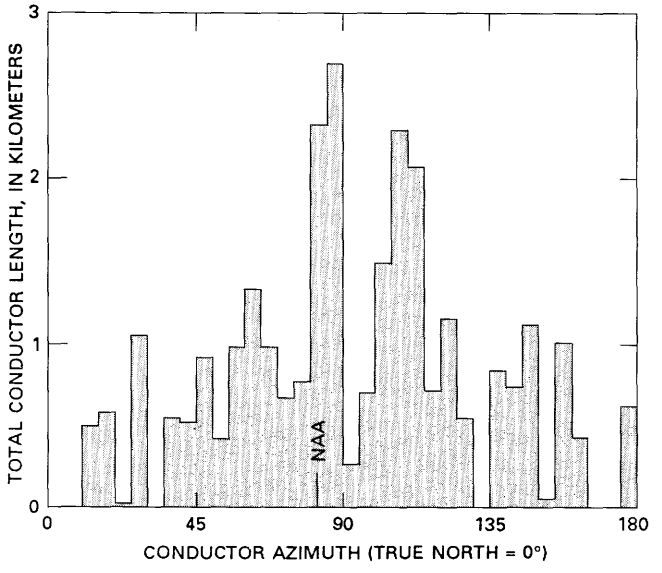

Figure 11. Histogram plot of the distribution of conductor azimuths from airborne VLF data, Chalk River Survey area, using station NAA. Courtesy of W.J. Scott (Geological Survey of Canada, 1989, written commun.).

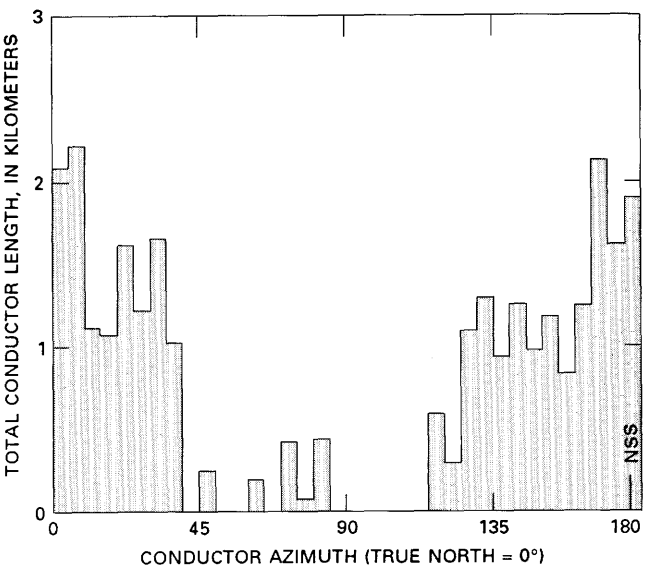

Figure 12. Histogram plot of the distribution of conductor azimuths from airborne VLF data, Chalk River survey area, using station NSS. Courtesy of W.J. Scott (Geological Survey of Canada, 1989, written commun.).

5. The most exciting possibility with airborne VLF–EM is the potential to map the resistivity of the upper layers of the ground at a fraction of the cost of helicopter EM systems. Although the E–PHASE technique (Palacky and Jagodits, 1975) was developed for ground resistivity mapping at VLF and higher frequencies, the method was simplistic in approach and ignored the effects of altitude and displacement currents (Sinha, 1977). As a result, the technique often produced uninterpretable results. By measuring the horizontal components of the electric and orthogonal magnetic field, the ground impedance and hence the resistivity of the ground can be determined from airborne VLF–EM data. The Geological Survey of Canada is studying this possibility, and the Geological Survey of Finland is designing and constructing such a system (Poikonen, this volume). Such a system would make large-scale airborne resistivity mapping a practical proposition because of its cost advantages.

REFERENCES CITED

Brown, P.A., and Thivierge, R.H., 1977, Chalk River—The geological setting: Geological Survey of Canada Internal Report RW/GPH 77–005.

Dvorak, Z., Fraser, D.C., and Sinha, A.K., 1989, DIGHEM^{II} airborne electromagnetic/resistivity/magnetic/VLF survey of the Chalk River Research Area, Ontario, *in* Thomas, M.D., and Dixon, D.F., eds., Geophysical and

related geoscientific studies at Chalk River, Ontario: Atomic Energy of Canada Limited Report.

Fraser, D.C., 1972, A new multicoil aerial electromagnetic prospecting system: Geophysics, v. 37, p. 518–537.

_____ 1978, Resistivity mapping with an airborne multicoil electromagnetic system: Geophysics, v. 43, p. 144–172.

Hayles, J.G., and Sinha, A.K., 1986, A portable local loop transmitter for geological fracture mapping: Geophysical Prospecting, v. 34, p. 873–896.

Herz, A., 1986, Airborne EM instruments operating at VLF and higher frequencies, *in* Palacky, G.J., ed., Airborne resistivity mapping: Geological Survey of Canada Paper 86–22, p. 55–61.

Palacky, G.J., and Jagodits, F.L., 1975, Computer data processing and quantitative interpretation of airborne resistivity surveys: Geophysics, v. 40, p. 818–830.

Scott, W.J., 1989, VLF surveys at Chalk River, *in* Thomas, M.D., and Dixon, D.F., eds., Geophysical and related geoscientific studies at Chalk River, Ontario: Atomic Energy of Canada Limited Report.

Sinha, A.K., 1977, Influence of altitude and displacement currents on plane-wave EM fields: Geophysics, v. 42, p. 77–91.

_____ 1985, Interpretation of ground VLF–EM data in terms of simple models [abs.]: Society of Exploration Geophysicists, Annual International Meeting, 54th, Atlanta, Geophysics, v. 50, p. 273.

Development of Airborne Very Low Frequency Electromagnetic Techniques at the Geological Survey of Finland

By Ari Poikonen[1]

Abstract

The Geological Survey of Finland is responsible for the airborne geophysical survey of Finland. Low-altitude surveys were started in 1972 and are still in progress. The electromagnetic (EM) part of the airborne instrumentation contains fixed-frequency (3113 Hz) wing-tip equipment with a vertical coplanar coil system. This equipment is suitable for the resistivity mapping of areas having resistivities lower than 3,000 ohm-m. The bedrock of Finland is mainly composed of crystalline Precambrian rocks that have resistivities as high as 30,000 ohm-m, and thus supplementary EM equipment was needed. A technique based on measurement of the plane-wave impedance at very low frequencies (VLF) was chosen.

In the first phase of the project, a two-dimensional numerical model based on the network solution was modified so that an inhomogeneous plane wave could be used as primary excitation. This allows simulation of the true VLF primary field; that is, the transversal magnetic plane wave is incident on the ground at an angle close to 90°. The vertical electric field is thus taken into account in modeling. This is of vital importance for determining the attenuation properties of impedance-type measuring parameters in the air and in the modeling of topographic effects.

In the second phase of the project, instrumentation was installed to monitor VLF stations suitable for airborne measurements. The instrumentation can measure the amplitudes of the vertical electric and horizontal magnetic fields and the ratio and phase shift between them.

The third phase, currently in progress, includes the design and construction of airborne instrumentation to measure horizontal components of the magnetic and electric fields using the horizontal magnetic field as phase reference. Measurement of the vertical magnetic field is optional. Much effort has been put into the design of flux-feedback magnetic antennas and selective bandpass filters that use the quadrature amplitude modulation technique.

INTRODUCTION

Systematic airborne geophysical surveys in Finland started with aeromagnetic measurements in 1951, and the first airborne electromagnetic (AEM) system was introduced in 1954. In 1956, the airborne instrumentation was completed with the installation of a gamma-ray scintillometer. Surveys were performed at 150-m altitude with 400-m line spacing and constituted the first phase of the airborne geophysical mapping of Finland, sometimes called the first national airborne geophysical survey. The last airborne measurements in this survey were carried out in 1972. The first phase was immediately followed by more detailed low-altitude surveys that are still in progress. The nominal flight altitude was lowered to 30 m and the line spacing reduced to 200 m. The new airborne instrumentation uses basically the same geophysical sensors as the previous one. The current system has three proton magnetometers that form a horizontal gradiometer. The towed-coil AEM equipment has been replaced by a rigid-coil system, and the volume of the radiometric crystals has been increased to 25 L. According to present plans, this second national airborne geophysical survey will be completed by the end of the present century. A more detailed account of airborne geophysics in Finland has been given by Peltoniemi (1986).

Mineral exploration and geological mapping have been the main applications of the airborne measurements. In recent years, however, there has been a growing demand for various engineering applications such as ground-water prospecting and the mapping of tectonic features in crystalline bedrock for nuclear waste disposal studies. These new applications have placed additional requirements on the existing system.

The bedrock of Finland is mainly composed of crystalline Precambrian rocks having resistivities as high as 30,000 ohm-m. Resistivity mapping of poorly conducting rocks is not possible using traditional low-frequency AEM systems sensitive to good conductors. Existing AEM equipment operates at 3113 Hz and has a vertical coplanar coil system mounted on wing-tips. Because it is not suited to surveys in areas having resistivities higher than 3,000 ohm-m (Oksama, 1987), supplementary EM equipment was needed.

The present report discusses a project set up to assess the potential of very low frequency (VLF) measurements in the mapping of high-resistivity areas (Poikonen, 1985). Calculating apparent resistivity from

[1]Geological Survey of Finland, SF–02150 Espoo, Finland.

such measurements requires knowledge of both the magnetic and electric fields. In the late 1960's and early 1970's, Barringer Research Ltd developed the RADIO-PHASE and E-PHASE systems (Barringer Research Limited, 1970; McNeill and others, 1973), which measure the electric field, and improvements in both systems were made by the U.S. Geological Survey (Frischknecht, 1971).

The project was divided into three phases. The first phase focused on modeling. In the second phase, instrumentation was installed to monitor VLF stations suitable for airborne measurements. The third phase, currently in progress, is devoted to the design and construction of airborne instrumentation.

Acknowledgments.—I thank Mr. Ilkka Suppala and Mr. Matti Oksama for their contribution to the numerical modeling, and Mr. Teemu Koskinen, Mr. Veli Leinonen and Mr. Kalevi Sulkanen for their work in constructing the instrumentation. Finally, I thank Professor Lauri Eskola and Mr. Jouko Vironmaki for their continued interest and support throughout the project.

MODELING

Suitable parameters for determining the apparent resistivity of the ground are the plane-wave impedance Z and the wave tilt W. The former is the ratio of the horizontal electric field E_x to the horizontal magnetic field H_y and the latter is the ratio of the horizontal electric field to the vertical electric field E_z. In practice, however, it is very difficult to measure the horizontal electric field in a moving aircraft. Over ground having resistivities lower than 10,000 ohm-m, the magnitude of E_x is less than 10 percent of that of E_z. When the horizontal antenna is tilted, it receives a projection of E_z that easily exceeds the true horizontal component in magnitude: the more conductive the ground, the smaller the true E_x and therefore the worse the error due to the tilt.

This problem can be overcome by measuring the quadrature component of E_x because the error component is a part of and therefore in phase with H_y, which is used as a phase reference. It makes no difference if E_z is used as a reference because E_z and H_y are in phase over a laterally homogeneous ground. This technique, known as the phase-quadrature method, was utilized in the E-PHASE system. A disadvantage is the lack of phase information, which is of vital importance in the case of layered earth and lateral inhomogeneities.

The pitch and roll of the antenna can be monitored during the flight, and thus the data can be corrected for the leakage of E_z, either in real time by a high-speed processor or by processing after the flight. The potential of these techniques will be assessed during the project.

In the modeling, particular attention was paid to the role of the angle of incidence of the incoming plane wave, attenuation of anomalies with height, and topographic effects.

A two-dimensional numerical model was modified so that we could use an inhomogeneous plane wave—that is, a plane wave having an arbitrary angle of incidence—as primary excitation. This allows simulation of the true VLF primary field, which is in fact the transversal magnetic (TM) plane wave incident on the ground at an angle close to 90°. As a result, the vertical electric field is taken into account in modeling, but only in H-polarization (Poikonen and Suppala, 1989).

In fact, the plane wave with grazing incidence had to be used as a primary excitation to obtain the correct behavior of the apparent resistivity in the air. At other angles of incidence, the increase in apparent resistivity over homogeneous ground with height leads to false results. The vertical electrical field associated with the inhomogeneous plane wave produces charge distributions on horizontal boundaries in the ground; the more resistive the ground, the stronger E_z. The charge distribution at the upper face of a two-dimensional vertical slab results in asymmetry in E_x. This effect is clearly seen in the apparent resistivity anomaly when the resistivity of the ground is 10,000 ohm-m (fig. 1). The results shown in figure 1 also illustrate how the anomaly attenuates with height: at 120 m it has almost disappeared. In H-polarization, anomalies attenuate quite rapidly because they are generated mainly by charges. The electric field of a point charge has a geometrical attenuation inversely proportional to the square of distance. In E-polarization, anomalies are caused mainly by currents. The vector potential and consequently the electric field from the current element have a geometric attenuation that is inversely proportional to distance.

Figure 2 shows a set of various E-polarization anomalies at 120 m above the ground surface. The anomalies can still be easily detected. In fact, in E-polarization the vertical electric field cannot be calculated using a two-dimensional model. Hence, the total fields were first solved by using a homogeneous plane wave as a source, and then the primary field was replaced by an inhomogeneous plane wave corresponding to grazing incidence. Such a technique is justified for two reasons: first, secondary E_z in the air is negligible, and second, the charge distribution at the upper face of the slab affects only E_x (Poikonen and Suppala, 1989).

The topographic effect of a two-dimensional hill structure on apparent resistivity is depicted in figure 3. The effect decreases E_x uphill and increases it downhill as a result of the high contrast in conductivity between the ground and the air at very low frequencies when the total electric field tends to be at right angles to the ground surface. Therefore, on sloping surfaces part of the total field is projected onto the horizontal channel, decreasing E_x uphill and increasing it downhill. This

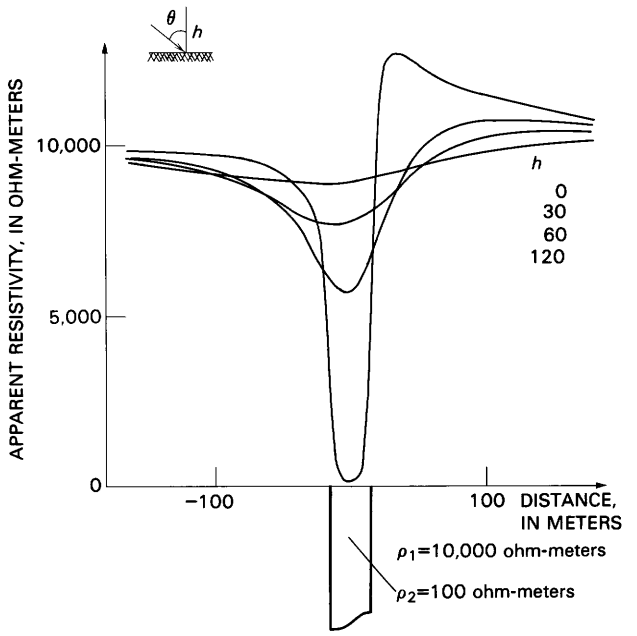

Figure 1. Attenuation of H-polarization apparent resistivity (ρ) with height (h) over a two-dimensional slab. Apparent resistivities are calculated from plane-wave impedances. Frequency 15 kHz; angle of incidence (θ) 90°.

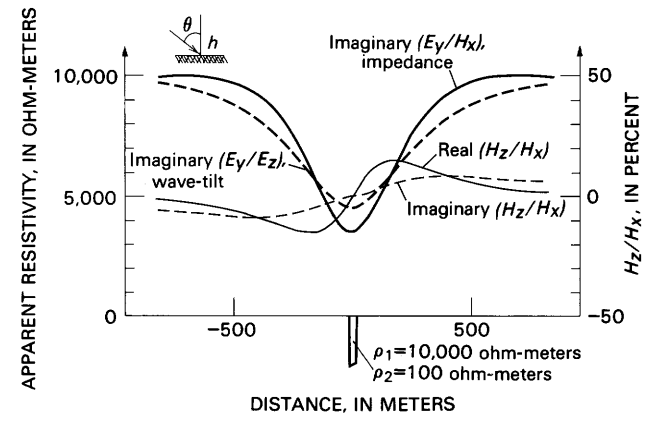

Figure 2. Various VLF apparent resistivity (ρ) anomalies over a two-dimensional slab at an altitude of 120 m for E-polarization. E_y, horizontal electric field; E_z, vertical electric field; H_x, horizontal magnetic field; H_z, vertical magnetic field. Frequency, 15 kHz; angle of incidence (θ) 90°.

effect is basically similar to the tilt effect of the antenna and can be markedly reduced by measuring the quadrature component of E_x as shown in figure 3.

INSTRUMENTATION

The first stage in the design and construction of the instrumentation was to build the monitoring station needed for selecting and identifying suitable VLF

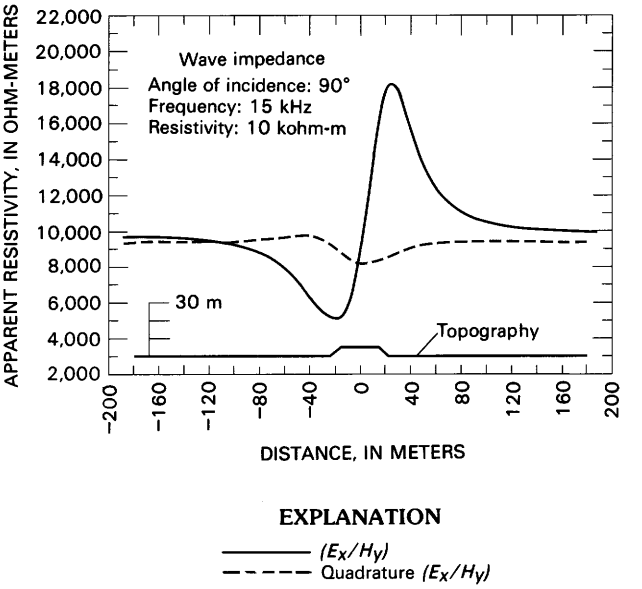

Figure 3. Topographic effect of a hill on apparent resistivity for H-polarization at an altitude of 30 m. E_x, horizontal electric field; H_y, horizontal magnetic field.

stations for airborne measurements and for monitoring changes in field strength during the flights. A block diagram of the monitoring station is shown in figure 4. The vertical electric field is measured using a dipole antenna. The magnetic antenna is a ferrite core loop that measures the horizontal field and can be rotated to find the directions of stations. Both antennas have a flat frequency response in the 10–25 kHz band. Signals from the preamplifiers are fed either to a signal analyzer or to a receiver. The analyzer can be used to give a general view of the stations in the band or to establish the modulation type in a particular transmission. The receiver measures the field strengths of the electric and magnetic fields and the ratio (impedance) and phase shift between them. It can be controlled either manually or by a personal computer that collects and stores the data on floppy disk. Figure 5 shows the results of the station GQD (Rugby) at 19.0 kHz over a 24-hour period. The magnetic field is presented in equivalent electric field units volts per meter assuming a plane-wave relation between the magnetic and electric fields. Field strength is marked by different between day and night propagation. The phase between the magnetic and electric fields and the impedance, however, remain practically constant and very close to their free-space values, indicating that the VLF primary field behaves as a plane wave.

In design of the airborne instrumentation, special attention was paid to the selectivity of the receiver, fast digital selection of available stations, and the noise characteristics and stability of the antennas. The selectivity is acquired using a filter that has a passband wide enough to accommodate modulation and sufficient roll-

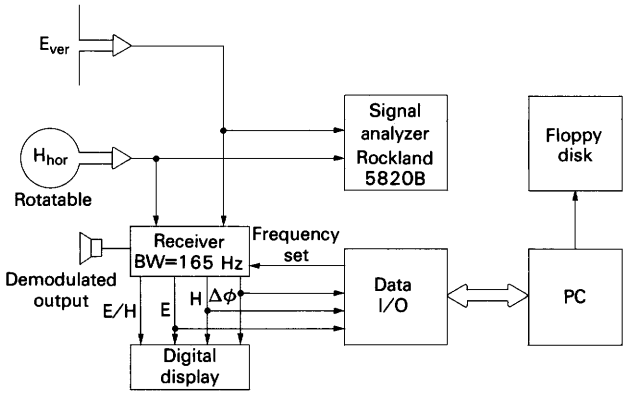

Figure 4. Block diagram of the VLF monitoring station. Frequency range 10–25 kHz.

off outside the passband to reject adjacent stations. These requirements were met most successfully by the 8th-order Butterworth bandpass filter with 160-Hz bandwidth. The frequency response of this filter around 16 kHz is depicted in figure 6. In the VLF band, the stations may occur with a minimum separation of 200 Hz. Even in this extreme case, the filter provides 30-dB rejection against the interfering station.

The realization of this filter requires second-order filter blocks having a quality factor (Q) value of 260. Because in practice this value is too high for active operational-amplifier bandpass filter structures, the filter was realized using the quadrature amplitude modulation (QAM) technique as shown in figure 7. The technique is based on frequency translation, whereby the input signal is first modulated by the desired center frequency and then fed through a low-pass filter. The signal is then remodulated by the same carrier frequency to translate it back to its original band. The quadrature channel is needed to reject image frequencies. The low-pass filter prior to the first mixer stages is used to limit the frequency band. The last low-pass stage removes the clock harmonics and modulation products resulting from the second mixing. The major advantages of the QAM technique are: (1) high-Q elements are not needed because the band limitation is obtained using a low-pass filter; (2) the center frequency of the filter can be set with a clock, thus permitting rapid digital selection of stations; and (3) the channels are synchronous, providing good phase stability. In narrow-band filters, small drifts in center frequency result in large phase shifts.

The antennas in the airborne instrumentation are basically similar to those in the monitoring station. The magnetic antennas are based on the flux-feedback technique (Clerc and others, 1964), which provides good stability. This is particularly important for ferrite core coils because the magnetic properties of ferrite may

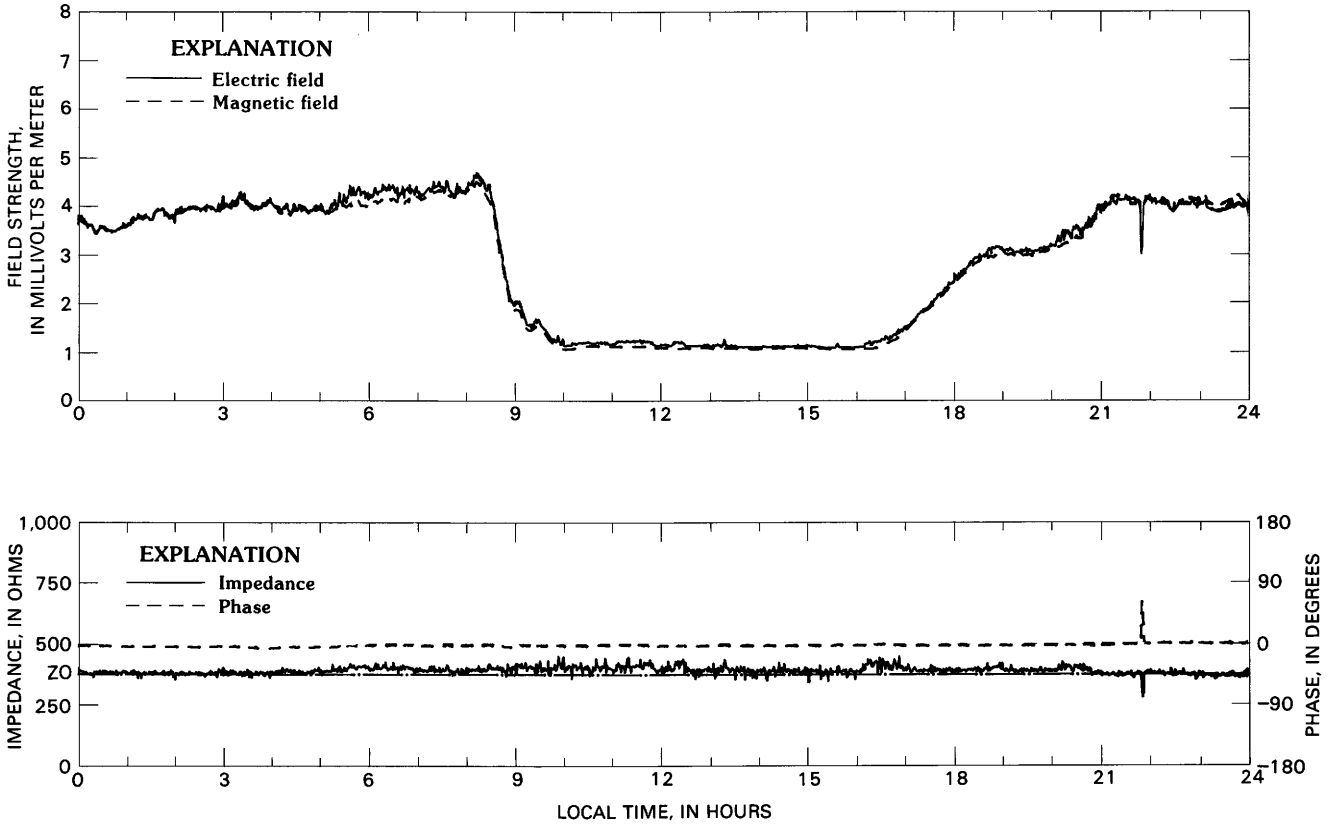

Figure 5. VLF monitoring results of station GQD (Rugby) at 19.0 kHz over a 24-hour period.

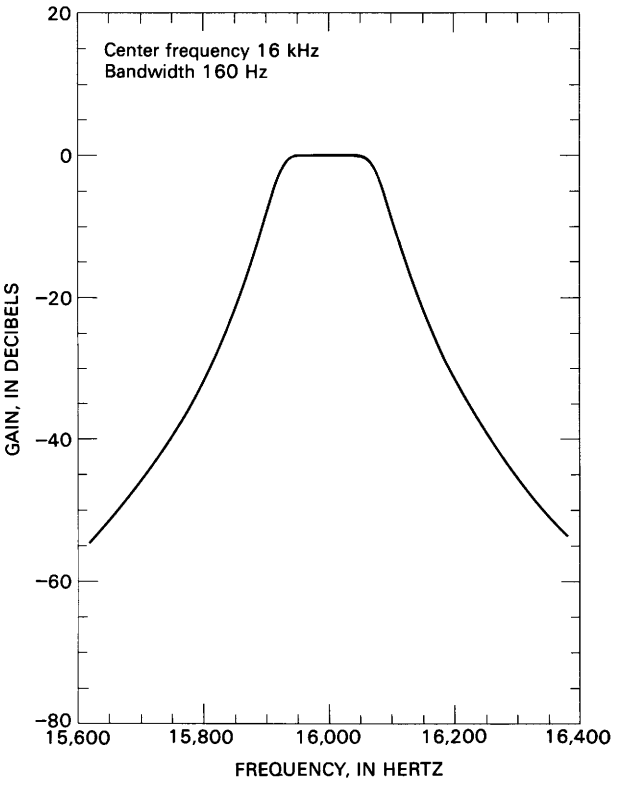

Figure 6. Frequency response of 8th-order Butterworth bandpass filter.

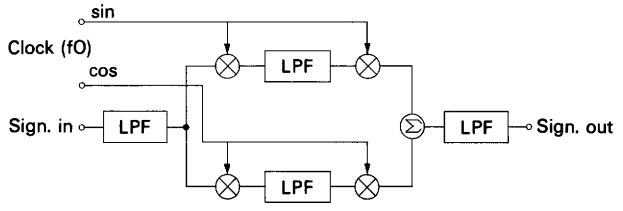

Figure 7. Principle of the quadrature amplitude modulation (QAM) technique for realizing bandpass filter. LPF is low-pass filter.

change considerably with temperature. Figure 8 depicts the theoretical noise characteristics of the magnetic antenna and an ultra-low-noise JFET pair in the input of the preamplifier. The noise is less than 0.5 femtotesla/(Hz)$^{1/2}$ within the whole frequency band. This is far below the atmospheric noise level.

The airborne equipment measures the horizontal components of the magnetic and electric fields using the horizontal magnetic field as a phase reference; measurement of the vertical magnetic field is optional. Handling of data acquisition from the channels by a processor enables processor-controlled orientation of the antennas. When two orthogonal components of the horizontal field are measured and the heading of the aircraft is obtained from the airborne navigation system, the component of the horizontal field can be calculated in any direction.

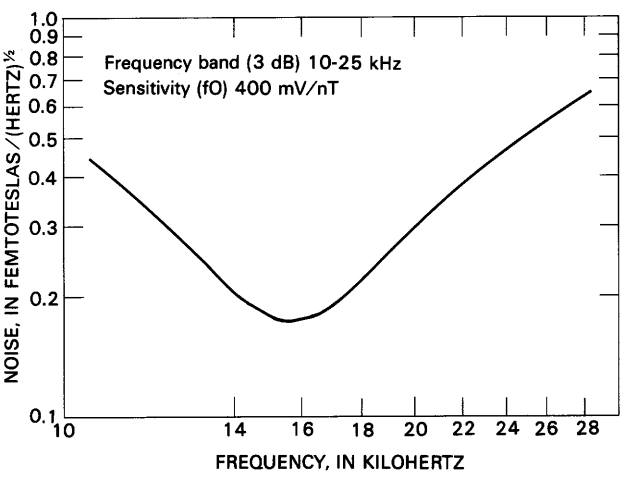

Figure 8. Theoretical noise characteristics of the magnetic antenna.

The final configuration of the airborne instrumentation will be established when enough experience is gained from test measurements.

REFERENCES CITED

Barringer Research Limited, 1970, Radiophase D'Alembert survey: Technical Note TN–2.

Clerc, G., and Gilbert, D., 1964, La contra-réaction de flux appliquée aux bobines à noyau magnétique utilisées pour l'enregistrement des variations rapides du champ magnétique [Flux feedback applied to magnetic coil sensors used to measure rapid magnetic field variations]: Annales Géophysique, v. 20:4, p. 499–502.

Frischknecht, F.C., 1971, Results of some airborne VLF surveys in northern Wisconsin: U.S. Geological Survey Open-File Report 71–115, 32 p.

McNeill, J.D., Jagodits, F.L., and Middleton, R.S., 1973, Theory and application of the E-phase airborne resistivity method [abs.]: Symposium of Exploration Electromagnetic Methods, May 2–4, 1973, University of Toronto.

Oksama, M., 1987, Basic characteristics of AEM system of Geological Survey of Finland: Geological Survey of Finland, Geophysics Department, Report Q 16.2/24.8/87/1.

Peltoniemi, M., 1986, Systematic airborne electromagnetic surveys in Finland—An overview, *in* Palacky, G.J., ed., Airborne resistivity mapping: Geological Survey of Canada Paper 86–22, p. 159–167.

Poikonen, A., 1985, On the applicability of VLF measurements to geological mapping: European Association of Exploration Geophysicists Meeting, 47th, Budapest, Abstracts of Papers, p. 91–92.

Poikonen, A., and Suppala, I., 1989, On modeling airborne VLF measurements: Geophysics, v. 54, p. 1596–1605.

SECTION 4: ENVIRONMENTAL AND RELATED APPLICATIONS

Rapid Reconnaissance Mapping of Freshwater Lenses on Small Oceanic Islands

By Mark Stewart[1]

Abstract

Many small oceanic islands have freshwater lenses that can be used for domestic water supplies or for dry-season augmentation of rainfall catchment systems. These small lenses commonly are irregular in extent and thickness, and some islands have several small, isolated lenses. By making a few reasonable assumptions, the loop-loop electromagnetic profiling method can be used to estimate lens thickness. If it can be assumed that the water table is close to sea level and that the unsaturated and freshwater-saturated geologic units have low bulk conductivities, then the interface depth can be obtained from a three-layer solution. The first layer is the unsaturated zone; its thickness is assumed to be the land surface elevation above sea level. The third layer is the saltwater-saturated zone; it is assumed to be infinitely thick. The layer conductivities are either estimated or obtained from direct-current resistivity soundings. In resistive environments, only the third-layer conductivity has a significant effect on the calculated interface depth. The only remaining unknown thus is the second-layer thickness, which represents the freshwater-saturated zone. The second-layer thickness is very sensitive to the value used for the third-layer conductivity. Matching the electromagnetic-derived interface depth to depths obtained using other geophysical and water-quality methods is necessary, unless relative lens thicknesses are sufficient to meet the survey objectives. Application of this method to field studies of a sandy barrier island and a carbonate key, both in Florida, provides data that correlate well with other available geophysical and water-quality data.

INTRODUCTION

Many small oceanic islands have freshwater lenses. These lenses are necessarily small and sometimes isolated or irregular in shape (Chidley and Lloyd, 1972; Vacher, 1978; Hanson, 1980; Ayers and Vacher, 1986; Kauahikaua, 1987a). Although the lens volume may be small, high recharge rates can create a significant annual ground-water flux. These small lenses can be important sources of domestic drinking water or can provide dry-season augmentation of rainfall catchment systems. Because the lenses and commonly the populations they serve are small, investigations of the potential ground-water resource must use methods that are rapid and relatively inexpensive. Reconnaissance survey methods, which trade some accuracy and precision for speed and convenience of operation and interpretation, are often justified.

The economic constraints imposed by the small size of the lenses mean that only a few monitor or supply wells can be installed. Because the extent and thickness of a small lens are sensitive to local variations in effective recharge or hydraulic conductivity, it can be difficult to determine accurately the lens location and extent using only a few wells. If the basic lens shape and relative variations in thickness can be determined, monitor and withdrawal wells can be better located to effectively and economically assess and manage the resource. The lens extent and variations in thickness also can provide information on the hydrologic and geologic factors that determine lens character.

Electrical geophysical methods can provide very useful, relatively low cost information on the extent and thickness of freshwater lenses. Traditionally, vertical electrical sounding (VES) has been used for this purpose (Swartz, 1937, 1939; Chidley and Lloyd, 1972; Gorhan, 1976; Fretwell and Stewart, 1981; Ayers and Vacher, 1986; Kauahikaua, 1987b). VES can provide good information on the vertical variation of resistivity, it utilizes rugged and low-cost instrumentation, and it can be interpreted with relatively easy to use, microcomputer-based software. Obtaining large numbers of undistorted VES to outline the lens in some detail can be time consuming and difficult. In addition, the large electrode spacings required for complete soundings can be cumbersome if not impossible to achieve in many areas of small, densely vegetated islands. Electromagnetic (EM) soundings, however, have been successfully applied to the problem of island lenses by Kauahikaua (1987a), who

[1]Geology Department, University of South Florida, Tampa, Florida 33620.

used horizontal-loop (slingram) frequency-domain soundings and Schlumberger VES to map a lens on a small carbonate island at Majuro Atoll, Marshall Islands.

EM soundings have several advantages as compared to VES, including comparatively small coil spacings for useful exploration depths and relatively simple and rapid field procedures. Present-day horizontal-loop EM (slingram) systems do require accurately determining instrument zero-levels prior to the survey, which can be done over highly resistive (nonresponsive) crystalline rocks. (Kauahikaua used a site over the thick, unweathered basalts of Hawaii.) In some areas of the world, such as Florida or the Caribbean, a calibration site may be difficult to find or expensive to utilize because the nearest crystalline rock outcrops may be hundreds of kilometers away. In addition, proper interpretation of EM-sounding data requires a higher level of experience and training than interpretation of VES and normally uses longer, mathematically more complicated and sophisticated software for data inversion (Anderson, 1979).

EM terrain conductivity meters (McNeill, 1980a) are widely used for ground-water contamination studies, and many hydrologists are familiar with their basic operation. They operate at three fixed frequencies and coil spacings and are normally used for horizontal profiling. The instruments are relatively inexpensive to purchase or lease, reliable, and easily operated by field technicians. The instruments have preset, stable zero-levels and read directly in conductivity units; they do not have the sounding capabilities of VES or multifrequency, horizontal-loop EM systems. By making a few reasonable assumptions, the EM profiling method can be adapted to the problem of mapping small lenses. This EM procedure is well established (McNeill, 1980a; Stewart, 1982; Fraser, 1984) and, under appropriate conditions, can provide estimates of lens thickness to depths of 30 m below land surface using currently available instrumentation.

EXPLANATION OF METHOD

The electrical skin depth of a homogeneous half-space is defined as

$$\delta = \left(\frac{2}{\sigma\mu_o\omega}\right)^{1/2},$$

where σ is the half-space conductivity, μ_o is the free-space permeability, $\omega = 2\pi f$, and f is the frequency. Skin depth is the depth at which a downward-propagating plane wave has been attenuated to a field strength of $1/e$ compared to its amplitude at the surface. A useful parameter for loop-loop EM methods is the induction number, B, which is defined as (McNeill, 1980a)

$$B = \frac{s}{\delta} = \left(\frac{\sigma\mu_o\omega}{2}\right)^{1/2} s,$$

where s is the transmitter-receiver coil spacing. It can be shown (McNeill, 1980a, Appendix 1) that if $B \ll 1$, then the ratio of the quadrature component of the secondary magnetic field to the free-space strength of the primary magnetic field is:

$$\frac{H_s}{H_p} \cong \frac{i\sigma\omega_o s^2}{4} = \frac{iB^2}{2}, \text{ where } i = \sqrt{-1}.$$

For $B \ll 1$, the intercoil spacing must be much less than the skin depth, so that,

$$\omega \ll \frac{2}{\mu_o \sigma s^2}.$$

The instrument used in this study (Geonics EM–34) is designed so that the condition $B \ll 1$ is approximately satisfied over the operating range of conductivities. This is called operation at "low induction numbers" or the "low induction number approximation." At very low terrain conductivities the instrument response is essentially zero, and at high conductivities the linear relationship between H_s/H_p and σ breaks down and the indicated conductivity deviates substantially from the true half-space conductivity.

Figure 1 (McNeill, 1980b) illustrates the indicated versus true conductivity for the Geonics EM-34 over a homogeneous half-space. The vertical coil (horizontal dipole) configuration maintains an approximately linear response to half-space conductivity at higher conductivities, whereas the horizontal coil (vertical dipole) configuration becomes significantly nonlinear at lower conductivities. For this reason, the horizontal coil configuration is not appropriate for the approximation method described in this paper. The operating range of the instrument is 1–1,000 mS/m, but it can be seen from figure 1 that the linear approximation is an increasingly poorer estimate of true conductivity above 100–200 mS/m for vertical coils and above 60–70 mS/m for horizontal coils.

The EM–34 uses three frequency/coil-spacing pairs, with each pair selected so as to keep $B \ll 1$. The coil spacings are 10, 20, and 40 m, using frequencies of 6400, 1600, and 400 Hz, respectively. It can be seen that maintaining the low induction number approximation places a practical limit on the number of frequency/coil-

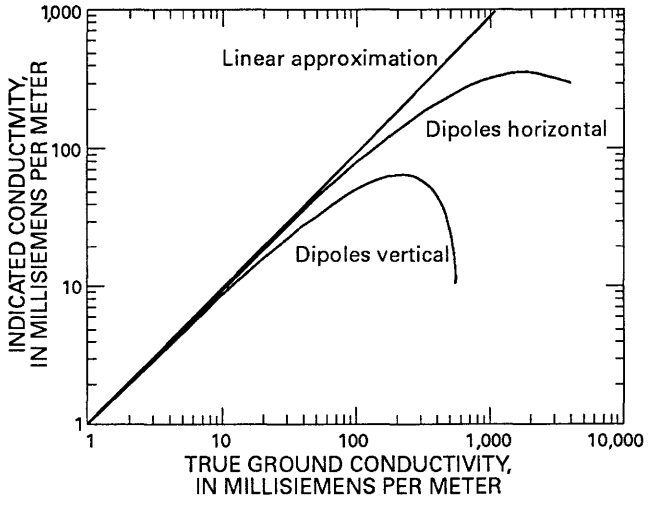

Figure 1. Indicated conductivity versus true half-space conductivity for the Geonics EM–34 terrain conductivity meter.

spacing pairs possible using lightweight, portable instruments. Each frequency/coil-spacing pair has a corresponding effective penetration depth. For the vertical coil (horizontal dipole) configuration, the effective penetration depth is approximately 0.75 times the intercoil spacing. Materials above the effective penetration depth contribute 70 percent of the instrument response measured at the surface (Stewart and Bretnall, 1986). Another consequence of operation at low induction numbers is that there is very little coupling between induced current loops in the ground. Thus within the operating range of terrain conductivities, the effective penetration depths are functions of frequency and coil spacing only and do not change as conductivity varies.

If it can be assumed that the water table is close to sea level and that the geologic units have low bulk conductivities when saturated with freshwater, then the thickness of the freshwater lens can be obtained from the field values of apparent conductivity by using a three-layer solution. The first layer represents the unsaturated zone. Its thickness is assumed to be the elevation of the land surface above sea level. The third layer is the saltwater-saturated zone and is assumed to be infinite in thickness. All layer conductivities are either estimated or obtained from VES data. The only remaining unknown in the three-layer solution is the thickness of the second layer, which represents the freshwater lens (fig. 2). McNeill (1980a) provided a solution for apparent field conductivity for a three-layer case, given the layer conductivities and thicknesses and a specified coil spacing and orientation. This equation is

$$\sigma_a = \sigma_1[1-R(z_1/s)] + \sigma_2[R(z_1/s)-R(z_2/s)] + \sigma_3 R(z_2/s), \quad (1)$$

where σ_a is the apparent or field conductivity, σ_n is the conductivity of layer n, $R(z_n/s)$ is the response function for the nth layer of thickness z_n, and s is the intercoil spacing (McNeill, 1980a, b). The response function, $R(z_n/s)$, incorporates the linear approximation of the low induction number assumption. For vertical coils (horizontal dipoles), the response function is (McNeill, 1980a)

$$R(z_n/s) = [(2z_n/s)^2 + 1]^{1/2} - 2(z_n/s). \quad (2)$$

Solving equation (1) for $R(z_2/s)$ gives,

$$R(z_2/s) = \{\sigma_a - \sigma_1[1-R(z_1/s)] - \sigma_2 R(z_1/s)\}/(\sigma_3-\sigma_2). \quad (3)$$

Let the right-hand term of equation (3) equal C_3; then, using equation (2), another equation for C_3 can be obtained,

$$C_3 = [(2z_2/s)^2 + 1]^{1/2} - 2(z_2/s). \quad (4)$$

Solving for z_2,

$$z_2 = s(1-C_3^2)/(4C_3). \quad (5)$$

The thickness of layer 2, t_2, is found from

$$t_2 = z_2 - z_1 = [s(1-C_3^2)/(4C_3)] - z_1, \quad (6)$$

where C_3 is defined as in equation (4).

If the land surface elevation is unknown or relief is minimal, then the solution can be reduced to a two-layer solution. If the unsaturated and saturated freshwater zones have bulk conductivities less than 10 mS/m, there is little error in combining them into one layer. Now the equation for thickness solves for a single layer thickness z, which is the depth below land surface of the interface, as follows;

$$C_2 = (\sigma_a - \sigma_1)/(\sigma_2 - \sigma_1), \quad (7)$$

$$z = s(1-C_2^2)/(4C_2), \quad (8)$$

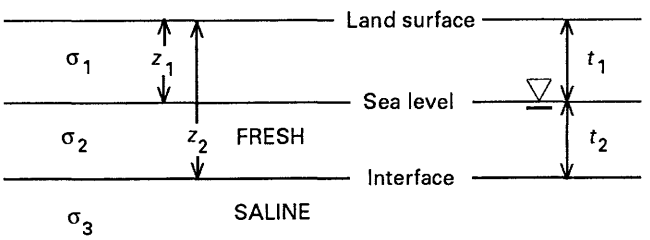

Figure 2. Three-layer case used for interface solution. Layer conductivities indicated by σ_1, σ_2, and σ_3. z_n is depth to bottom of layer n from land surface. t_n is thickness of layer n. ▽ indicates position of water table.

where z is the depth below land surface of the interface, σ_1 is the average conductivity of the unsaturated and freshwater zones, and σ_2 is the conductivity of the saline zone.

This two-layer case is directly analogous to the "buried earth" model used to invert airborne EM surveys. The buried earth model calculates the distance between the EM coils and a buried sheetlike conductor. Subtracting the altitude of the coils gives the "apparent depth" of the interface below land surface (Fraser, 1984). Sengpiel (1982) used this method to map the freshwater lens of a North Sea barrier island. As a result of a combination of low relief and resistive carbonate rocks and soil, Kauahikaua (1987a) was able to use a similar two-layer inversion to interpret his slingram soundings at Majuro Atoll.

SPREADSHEET INTERPRETATION OF DATA

Although equations (4), (6), (7), and (8) can be easily solved using a hand calculator, the calculations quickly become tedious if many measurements are involved. The equations can be incorporated into a FORTRAN or BASIC program, but the most efficient method of solution uses a microcomputer spreadsheet program, such as Microsoft Multiplan or Lotus 1–2-3. Spreadsheets use a grid of rows and columns of cells. If an equation is entered into a cell, it may reference the contents of other, specified cells using either "absolute" or "relative" references. Absolute references always refer to the same cell location in the spreadsheet, whereas relative references maintain the same spatial relationship between the object cell and the reference cell. For example, if an equation in a cell uses the relative values entered in the two cells to the left of the object cell, the equation can be copied down a column of cells and the last equation in the column will still refer to the two cells to its left. This ability to copy equations while maintaining spatial relationships between cells makes spreadsheets very useful tools for repetitive calculations where the data can be entered in columns. On command, the spreadsheet calculates the values of all equations in cells and displays the values in the appropriate cells. Cells containing labels are used to annotate the cells containing equations or data, and absolute references are used to refer to cells containing constants.

For this solution, the layer conductivities and the coil spacing are entered as constants in labeled cells. The profile distance (or station number), station elevation, and field conductivity for each data point are entered into columns. Equations (4) and (5) are entered and copied into adjacent columns using absolute references for layer conductivities and coil spacing and relative cell references for elevation and field conductivity. Recalculating the spreadsheet produces the solution for lens thickness at all stations. The solution is "calibrated" by adjusting the value of σ_3 until the interface position is in good agreement with depths predicted from VES data or from water-quality data from wells. This calibration procedure assumes that the VES or water-quality data provide a reasonable estimate of interface position at discrete points and that the EM data provide an estimate of interface position between calibration points. Most spreadsheet programs have graphing options that allow the effect of modifying the third-layer conductivity to be seen graphically on the screen. This makes the calibration procedure much less tedious.

Table 1. Example of a spreadsheet solution, Flagler Beach

[Sigma-1, sigma-2, and sigma-3 are conductivities of layers 1, 2, and 3, respectively. X is distance (in meters) from high-tide line on the ocean side of lagoon; Elev is elevation (in meters) above mean sea level. Sigma-a is the field conductivity for the 20-m vertical coil spacing. The column labeled C contains cell equations using equation (3) (see text), and the cell equations labeled Z2 and T2 solve equations (5) and (6), respectively. The column labeled 3-PT contains equations that calculate a three-point moving average of the data in column T2]

Sigma-1=5.0 mS/m
Sigma-2=33.0 mS/m
Sigma-3=211.0 mS/m

Coil spacing 20.0 m
Coil orientation vertical

X	Elev	Sigma-a	C	Z2	T2	3-PT
50.00	6.22	110.0	0.54	6.54	-0.32	-0.18
60.00	6.10	110.0	0.53	6.58	-0.48	-0.22
70.00	5.85	118.0	0.58	5.70	0.14	-0.18
80.00	5.41	120.0	0.58	5.60	-0.19	-0.26
90.00	5.00	120.0	0.58	5.71	-0.71	-0.56
100.00	4.96	120.0	0.58	5.72	-0.76	-0.86
110.00	4.88	118.0	0.56	5.98	-1.10	-1.18
120.00	4.71	115.0	0.54	6.39	-1.68	-1.64
130.00	5.04	108.0	0.51	7.18	-2.14	-1.85
140.00	5.36	108.0	0.51	7.07	-1.71	-1.84

FIELD EXAMPLES

The first example is a profile across a narrow (700 m wide), sandy barrier island in the northeastern part of Volusia County on the Atlantic coast of Florida (fig. 3). The maximum elevation on the island is 6.5 m at the primary dune on the ocean side. Most of the island is 3–5 m above mean sea level. The water-table relief is very low, less than 30 cm. EM conductivity readings were taken every 10 m across the island, from the high-tide line on the ocean side to the lagoon, using a 20-m intercoil spacing.

Table 1 shows part of the spreadsheet solution for Flagler Beach. Sigma-1, sigma-2, and sigma-3 are the conductivities of layers 1, 2, and 3, respectively, and sigma-a is the field conductivity for the 20-m vertical coil

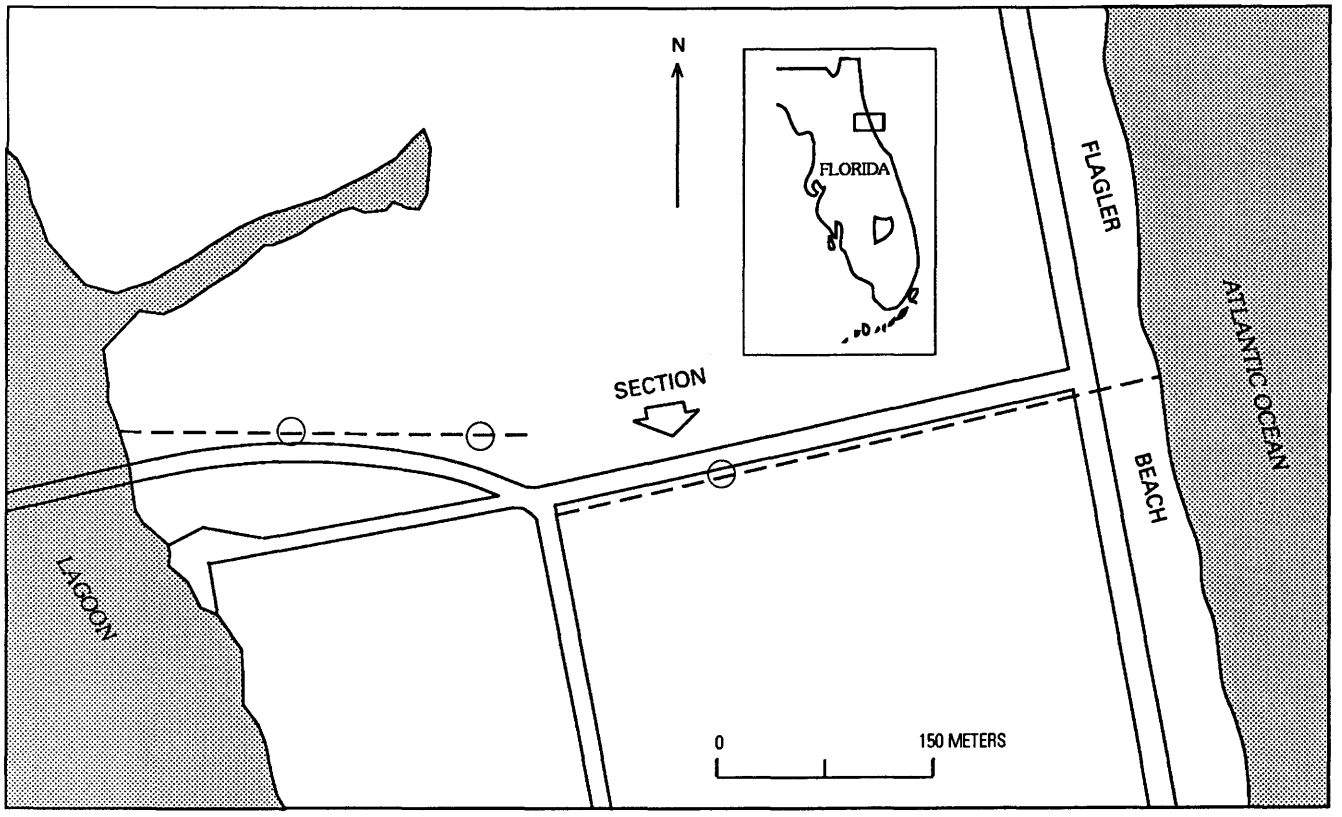

Figure 3. Location of Flagler Beach, Florida, profile. EM profile, dashed line; VES locations, circles.

(horizontal dipole) spacing. The column labeled C contains cell equations using equation (3), and the cell equations in the columns labeled Z2 and T2 solve equations (5) and (6), respectively. The last column on the right contains values for equations that calculate a three-point moving average of the data in column T2. This simple filter is used to reduce the effects of station to station variability in the field data that arise because the interface is assumed to be a relatively smooth surface. Entering a new value for sigma-3 and recalculating produces new values for Z2 and T2. A graph of distance versus elevation and T2 can be produced quickly using a simple set of commands, and thus the effect on the solution of varying any sigma value can be easily seen.

Figure 4 was generated from the spreadsheet solution of table 1. The calculated interface position was calibrated to the interface depths determined from several VES and, to some degree, from chloride-ion data from shallow wells. Again, the calibration process involves varying σ_3 until the EM interface position agrees with the VES solutions. The initial choice of layer conductivities and the range of reasonable σ_3 values are obtained from the VES inversions. Equivalent VES solutions produce values of σ_3 of from 160 to 300 mS/m. It is interesting to compare figure 4 with a simple plot of apparent conductivity versus distance (fig. 5). The approximate interpretation technique described in this report gives a better picture of the lens configuration and appears to reduce topographic effects, probably as a result of using land-surface elevation for first-layer thickness.

The calculated thickness of the freshwater lens is very sensitive to the value of σ_3 used in the three-layer

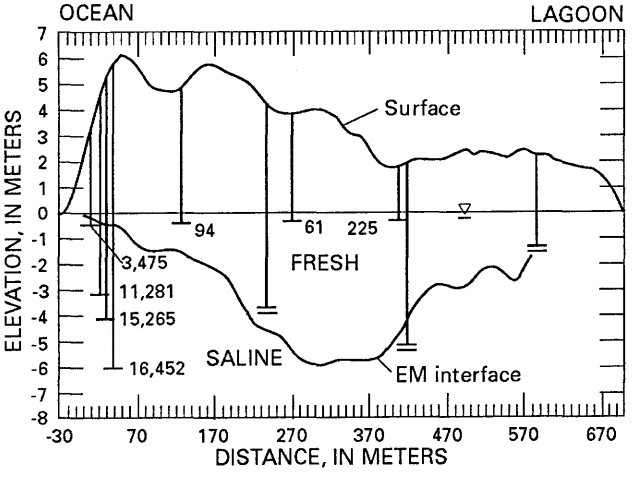

Figure 4. Flagler Beach EM profile (dashed line). Numbers are chloride values in milligrams per liter. VES data (double bar) represent depth to first layer having a resistivity of 10 ohm-m or less. ▽ indicates position of water table. Line of profile shown in figure 3.

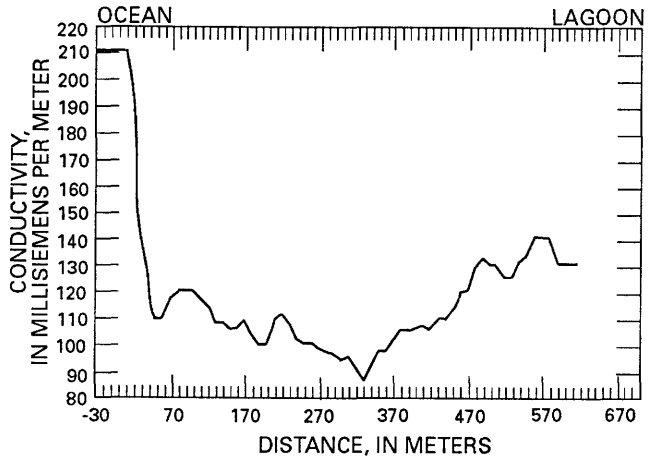

Figure 5. Plot of apparent conductivity versus distance, Flagler Beach profile.

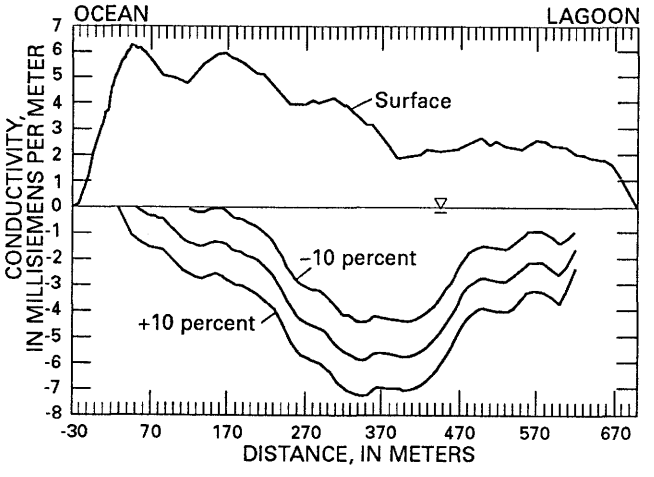

Figure 6. Effect on calculated interface position of varying σ_3 by ± 10 percent, Flagler Beach profile. ▽ indicates position of water table.

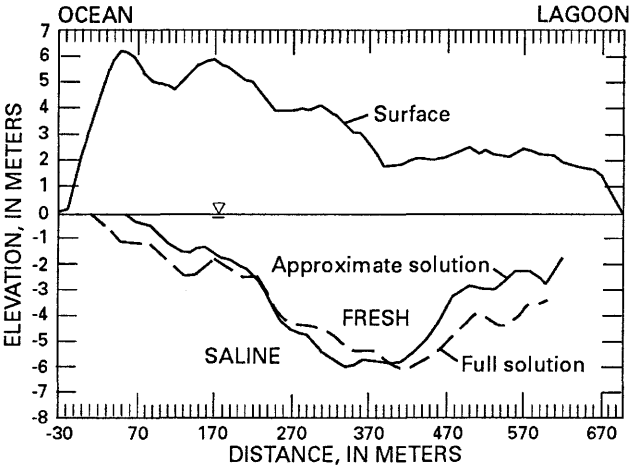

Figure 7. Comparison of approximate (linear) solution of interface depth using low induction number approximation and full (nonlinear) solution using the computer program PCLOOP, Flagler Beach profile. ▽ indicates position of water table.

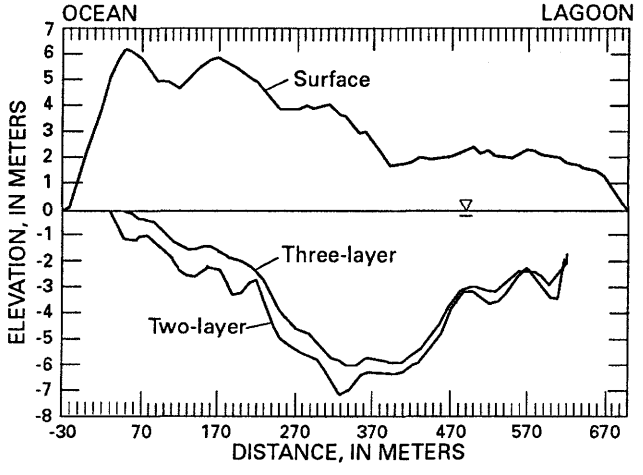

Figure 8. Comparison of calculated interface depths for two-layer and three-layer solutions, Flagler Beach profile. ▽ indicates position of water table.

solution. Figure 6 illustrates calculated sharp-interface positions for the calibrated value of σ_3 of 211 mS/m and for values 10 percent greater or less than the calibrated value (231 and 190 mS/m, respectively). A 10-percent error in estimating the value of σ_3 causes a vertical shift of the interface of about 20 percent of the lens thickness; however, the shape of the lens remains the same as σ_3 varies. This approximation technique probably produces good estimates of lens configuration and relative lens thickness, but absolute values of lens thickness may vary significantly from true thicknesses, depending on how well the calibration procedure determines the appropriate σ_3 value.

Field conductivity values at the Flagler Beach site vary from 80 to 211 mS/m. As discussed earlier, the field value indicated by the meter is a good estimate of true conductivity of a uniform half-space within the range of 1–100 mS/m. Many of the field readings at Flagler Beach exceed 100 mS/m. Because the approximation method used to derive equations (4) and (5) assumes a linear instrument response to changes in true conductivity, the breakdown of the low induction number approximation above 100 mS/m (fig. 1) introduces some error or distortion into the solution when field readings exceed 100 mS/m. Figure 7 illustrates the magnitude of this error for the Flagler Beach profile. The approximate solution uses equations (4) and (5). The full solution uses a program (PCLOOP, Geonics Ltd., 1985) that calculates the instrument response to a given set of layer conductivities and thicknesses using the numerical procedure of Anderson (1979) without resorting to a linear approximation. To use PCLOOP, the value of σ_3 was determined through calibration against the VES and

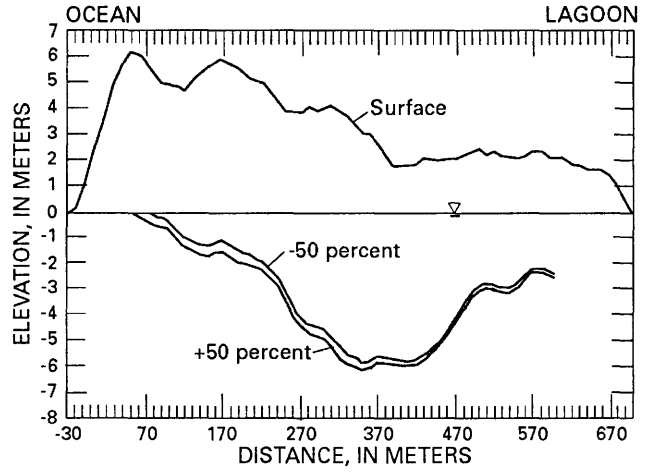

Figure 9. Effect on calculated interface position of varying σ_1 by ±50 percent, Flagler Beach profile. ▽ indicates position of water table.

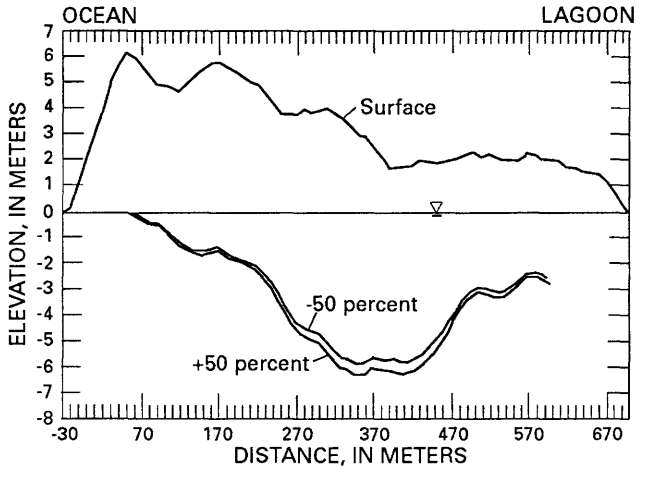

Figure 10. Effect on calculated interface position of varying σ_2 by ±50 percent, Flagler Beach profile. ▽ indicates position of water table.

water-quality data. The second-layer thickness, z_2, was then varied for each field station until the calculated instrument response matched the field conductivity value. The approximate solution varies from the full solution by no more than about 20 percent of the lens thickness, and the deviation is most pronounced at the margins of the lens. The simplicity and economic efficiency of the linear approximation probably outweigh the distortion caused by using the low induction number approximation, at least for the purposes of a reconnaissance survey. Again, the approximate solution provides a good estimate of the configuration and relative lens thickness.

It was stated earlier that if the unsaturated and freshwater-saturated layers have conductivities less than 10 mS/m, then they can be combined into one layer, reducing the problem to a two-layer case. Figure 8

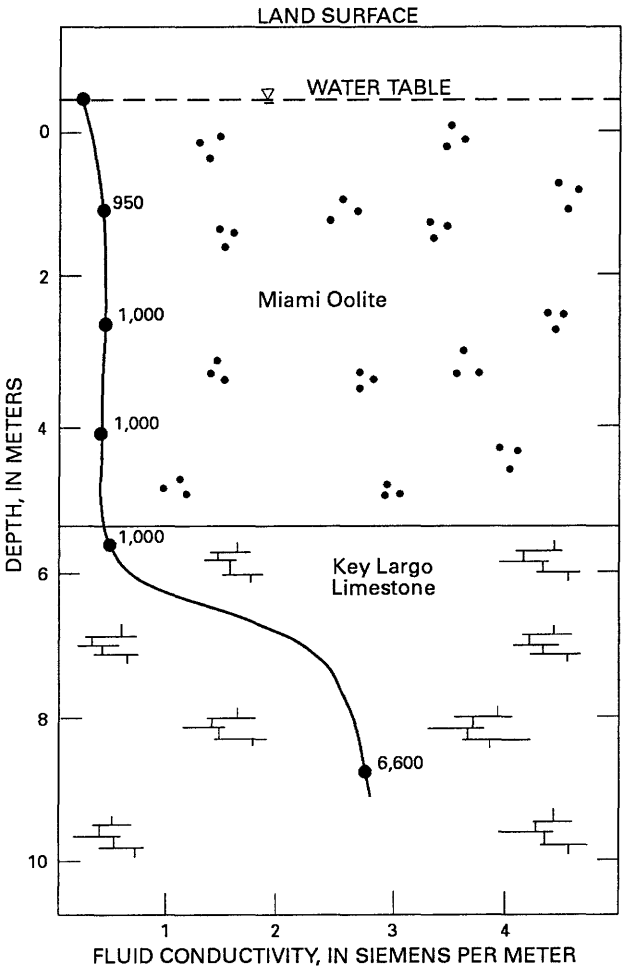

Figure 11. Relationship between the bottom of the freshwater lens and the Miami Oolite-Key Largo Limestone contact, Big Pine Key, Florida. Solid circles indicate chloride-ion concentrations (in milligrams per liter). Modified from Hanson (1980, fig. 7).

compares results for a two-layer solution using equations (7) and (8) and a first-layer conductivity of 10 mS/m with results for the three-layer solution. The variation between the two solutions is small, and the two-layer solution apparently contains more topographic noise. Figures 9 and 10 show the effects of varying the values of σ_1 and σ_2 by 50 percent on the estimated interface position. It can be seen that if the geologic units are resistive when unsaturated or when saturated with freshwater, then only the value of σ_3 has a significant effect on the calculated interface depth.

Another example is from Big Pine Key, Florida, one of the lower Florida Keys. The key is about 9 km long and 2 km wide and has maximum elevations of 1.5–2.5 m. It is formed by an oolite shoal (Pleistocene Miami Oolite) resting on a coral-reef platform (Pleistocene Key Largo Limestone). The Key Largo Limestone is much more permeable than the Miami Oolite (Hanson, 1980). The result of this horizontal layering of a lower per-

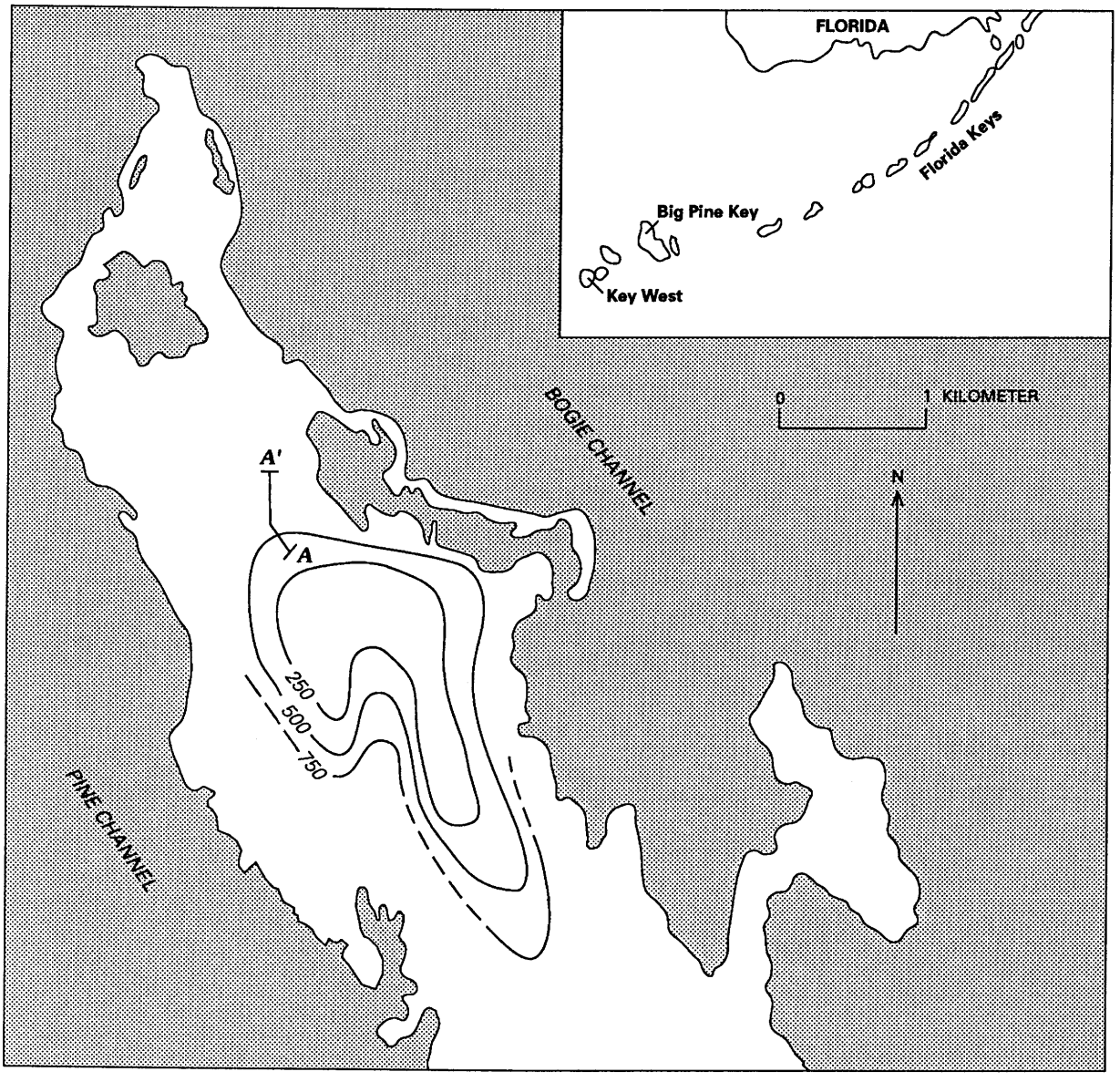

Figure 12. Contours of chloride-ion concentrations (in milligrams per liter) at a depth of 5 m, Big Pine Key, Florida. Line *A–A'* is location of EM–34 profile (fig. 13). Modified from Hanson (1980).

meability unit over a higher permeability unit is a truncation of the lower part of the freshwater lens (Ayers and Vacher, 1986). On Big Pine Key, the Miami–Key Largo contact strongly controls the position of the bottom boundary of the lens, and the transition zone is in the upper part of the Key Largo (fig. 11). A decrease in island width and elevation and a rise in the Miami-Key Largo contact near the middle of Big Pine Key divides the main lens into two fairly distinct smaller lenses. Figure 12 shows the configuration of the northern lens as mapped by Hanson (1980) using water-quality data.

Several kilometers of EM profiling data and several VES were collected on Big Pine Key. The EM readings were spaced 10 m apart, using a 20-m coil separation and vertical coils (horizontal dipoles). The VES data and water-quality and lithologic data from Hanson (1980) were used to calibrate the three-layer EM interface solution. Profile *A–A'* (fig. 13) illustrates part of the EM profile data. The EM data were calibrated by varying σ_3 within the range of 125–200 mS/m obtained from the VES solutions until the bottom of the EM-derived lens matched lens thicknesses predicted from the VES solutions and the water-quality data. The final values chosen for σ_1, σ_2, and σ_3, are 2, 3, and 146 mS/m, respectively. A well near VES 2 (fig. 13) gives a depth of about 7 m below land surface for the Miami-Key Largo contact. Figure 14 compares the approximate (linear response) and full (nonlinear response) solutions for the

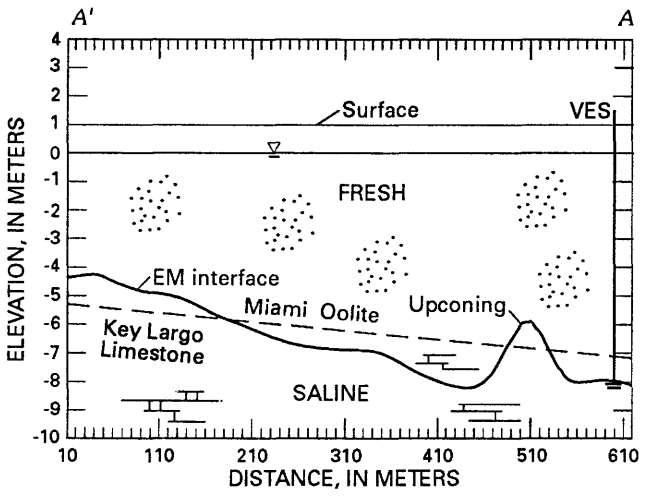

Figure 13. Interface solution for Big Pine Key EM–34 profile. VES interface represents boundary between 241 and 6 ohm-m. Miami-Key Largo contact is from Hanson (1980). ▽ indicates position of water table. Line of profile shown in figure 12.

Big Pine profile. Again, for the purposes of a reconnaissance survey the difference between the two solutions is small, less than 20 percent of the lens thickness, except near the edge of the lens.

The Big Pine profile is part of a larger survey covering much of the island. During calibration of the full set of data, Wightman (1988) noted that the calibrated value of σ_3 varies across the island, with higher values of σ_3 being required where the lens is thinner. This may be due to the increased effect of the saltwater-freshwater transition zone on the sharp interface approximation when the transition zone thickness becomes significant in comparison to the freshwater lens thickness. The implication of this result is that calibrated values of σ_3 should only be extrapolated moderate distances from the calibration site.

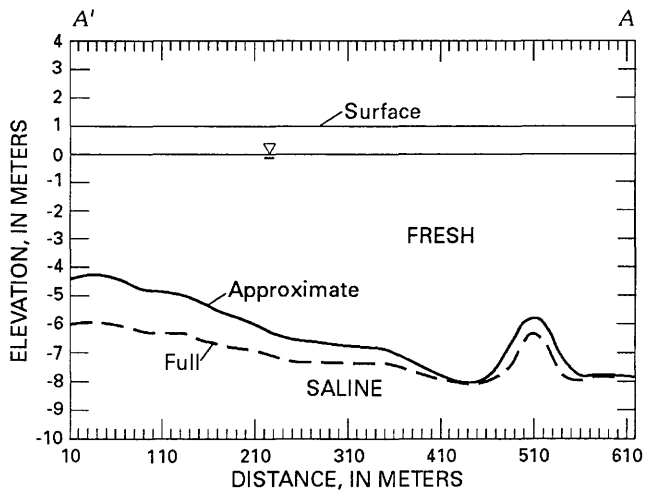

Figure 14. Comparison of approximate (linear) and full (nonlinear) solutions for interface depth, Big Pine Key profile. ▽ indicates position of water table. Line of profile shown in figure 12.

For both field examples, the EM method most likely maps the top of the transition zone. At the foot of the primary dune at Flagler Beach (fig. 4), chloride values are about 3,500 mg/L at the water table. The field conductivity value is 211 mS/m, the value chosen for σ_3 during calibration, and the EM "interface" emerges at the surface. For the Flagler Beach data, the calculated interface position probably corresponds to an isochlor surface of 2,000–4,000 mg/L. These results are similar to the results obtained by Kauahikaua (1987a), who noted that VES tend to place the sharp interface position in the middle of the transition zone, whereas loop-loop EM soundings place the sharp interface near the top of the transition zone. It should be noted that the chloride-ion concentration corresponding to the EM interface will vary, depending principally on the bulk porosity of the rock or soil materials and on the shape and thickness of the transition zone.

SUMMARY

This loop-loop electromagnetic profiling technique has several advantages. First, EM data can be obtained quickly and relatively easily. Second, many small islands and beaches meet the conditions required for successful application:

1. The water table is near sea level.
2. The interface is within 30 m of the land surface.
3. The geologic units are resistive when saturated with freshwater.
4. The rock types (at least along the profile) are relatively homogeneous.

Finally, the EM data can be acquired as profiles or on a grid, to produce either cross sections or a map of lens thickness.

This technique has some limitations. The high-conductivity environment limits the validity of the low induction number approximation used to obtain conductivity from the instrument response (McNeill, 1980a). The procedure yields incorrect values if the interface depth exceeds the exploration depth for the coil spacing used. This limits the depth of investigation to 30 m or less. The EM data must be calibrated against VES or water-quality data because the calculated interface depth is very sensitive to the value of σ_3 used. Where other data are not available for calibration, the calculated interface depths should be used as relative, rather than absolute, values. This procedure probably will not work well where transgressive sedimentary sequences create high-conductivity zones (clay lenses with high-conductivity

waters) within the freshwater zone or in deltaic areas containing clay-rich sediments. It is recommended that this method be used for reconnaissance surveys or as a supplement to other survey methods.

REFERENCES

Anderson, W.L., 1979, Computer program; numerical integration of related Hankel transforms of orders 0 and 1 by adaptive digital filtering: Geophysics: v. 44, no. 7, p. 1287–1305.

Ayers, J., and Vacher, H.L., 1986, Hydrogeology of an atoll island; a conceptual model from a detailed study of a micronesian example: Ground Water, v. 24, no. 2, p. 185–198.

Chidley, T.R.E., and Lloyd, J.W., 1972, A mathematical study of fresh-water lenses: Ground Water, v. 15, no. 3, p. 215–222.

Fraser, D.C., 1984, Airborne mapping of water resources with DIGHEM systems: Dighem Surveys and Processing, Inc., Mississauga, Ontario, 61 p.

Fretwell, J.D., and Stewart, M., 1981, Resistivity study of a coastal karst terrain: Ground Water, v. 19, no. 4, p. 219–223.

Geonics Ltd., 1985, Computer program PCLOOP: Geonics Ltd., Mississauga, Ontario.

Gorhan, H.L., 1976, The determination of the saline/fresh water interface by resistivity soundings: Association of Engineering Geologists Bulletin, v. 13, p. 163.

Hanson, C.F., 1980, Water resources of Big Pine Key, Monroe County, Florida: U.S. Geological Survey Open-File Report 80–447, 36 p.

Kauahikaua, J., 1987a, Description of a fresh-water lens at Laura Island, Majuro Atoll, Republic of the Marshall Islands, using electromagnetic profiling: U.S. Geological Survey Open-File Report 87–582, 32 p.

_____ 1987b, An evaluation of electric geophysical techniques for ground water exploration in Truk, Federated States of Micronesia: U.S. Geological Survey Open-File Report 87–146, 76 p.

McNeill, J.D., 1980a, Electromagnetic terrain conductivity measurement at low induction numbers: Technical Note TN-6, Geonics Ltd., Mississauga, Ontario, 15 p.

_____ 1980b, Interpretation procedures for the EM–34: Technical Note TN-8, Geonics Ltd., Mississauga, Ontario, 18 p.

Sengpiel, K.P., 1982, Resistivity/depth mapping with airborne EM survey data: Bundesanstalt für Geowissenschaften und Rohstoffe, n. 90–885, 24 p.

Stewart, M.T., 1982, Evaluation of electromagnetic methods for rapid mapping of salt-water interfaces in coastal aquifers: Ground Water, v. 20, no. 5, p. 538–545.

Stewart, M.T., and Bretnall, R.E., Jr., 1986, Interpretation of VLF resistivity data for ground-water contamination studies: Ground Water Monitoring Review, v. 6, no. 1, p. 71–75.

Swartz, J.H., 1937, Resistivity studies of some salt-water boundaries in the Hawaiian Islands: American Geophysical Union Transactions, v. 18, p. 387–393.

_____ 1939, Part II—Geophysical investigations in the Hawaiian Islands: American Geophysical Union Transactions, v. 20, p. 292–298.

Vacher, H.L., 1978, Hydrogeology of Bermuda, significance of an across-the-island variation in permeability: Journal of Hydrology, v. 39, p. 207–226.

Wightman, M., 1988, Seasonal variation of fresh-water lens thickness, Big Pine Key, Florida: Tampa, University of South Florida, M.S. thesis, 80 p.

Theoretical and Practical Aspects of Ground-Water Exploration Using Airborne Electromagnetic Techniques

By Klaus-Peter Sengpiel[1]

Abstract

Data for the secondary magnetic field measured by airborne electromagnetic systems having small coil spacing can be used to calculate a centroid depth z^*. This parameter can be combined with the conventional apparent resistivity ρ_a, and the function $\rho_a(z^*)$ approximates the true distribution $\rho(z)$. If this function is only partially known (due to a lack of frequencies), it can be interpolated and extrapolated by a spline function.

The algorithm has been applied to data from a ground-water survey in a desert area. The interpretation yields a reliable picture of the three-dimensional resistivity distribution that makes it possible to locate freshwater lenses within a brackish to saline environment.

INTRODUCTION

In 1987, BGR (Federal Institute for Geosciences and Natural Resources, Hannover, Federal Republic of Germany) began a ground-water survey in desert areas of Pakistan using a three-frequency DIGHEM system of frequencies $f_1 = 32{,}893$ Hz, $f_2 = 3538$ Hz, and $f_3 = 386$ Hz. The survey data were interpreted by using a new inversion technique for dipole induction called the centroid depth algorithm, which has been published in detail (Sengpiel, 1988). A similar inversion technique based on the transfer function c has been introduced for magnetotellurics (MT) by Schmucker (1970a). In the MT case, the observed fields are induced by an almost uniform primary magnetic field characterized by a wavenumber $\lambda = 0$. The dipole field can be represented by a continuous spectrum of wavenumbers. This spectrum can be replaced by a single value $\bar{k} = \bar{\lambda}h$, the effective wavenumber, where $\bar{\lambda}$ is the wavenumber and h is the height above the half-space. Knowledge of the parameter $\bar{k}$ enables us to determine the transfer function and the centroid depth z^* of the in-phase current system in a layered ground. The centroid depth assigns a depth to the apparent resistivity ρ_a for each frequency. The function $\rho_a(z^*)$ yields in many cases a reasonable approximation to the true distribution $\rho(z)$.

Acknowledgements.—I am indebted to my colleagues B. Fluche, H. Rodemann, and B. Roettger for their cooperation in all aspects of the practical application of the above technique, to the helicopter survey crew of BGR headed by H.J. Rehli, and to K. Fielitz and W. Mueller, who did the ground survey.

SECONDARY FIELD Z FROM A DIPOLE SOURCE AT HEIGHT h

For a horizontal coplanar coil system of spacing s, we have the well-known relations

$$Z = s^3 \int_0^\infty R_1 \, \lambda^2 e^{-2\lambda h} J_0(\lambda s) d\lambda \tag{1}$$

and

$$Z = R + iQ, \tag{1a}$$

where R is the in-phase component, Q is the quadrature component, and R_1 is the reflection factor depending on the layer parameters and the frequency. J_0 is the Bessel function of order zero. Mundry's (1984) simplification for $h \geq 3.3\, s$ yields

$$Z = \left(\frac{s}{h}\right)^3 \int_0^\infty R_1 k^2 e^{-2k} dk, \tag{2}$$

where k is a normalized wavenumber,

$$k = \lambda h. \tag{3}$$

There are different inversion procedures yielding the layer parameters from the measured field. For the model of a homogeneous half-space, we obtain its resistivity ρ and the bird height h.

[1]Bundesanstalt für Geowissenschaften und Rohstoffe, Hannover, Federal Republic of Germany.

EFFECTIVE WAVENUMBER FOR DIPOLE INDUCTION

It is permissible to write instead of (2)

$$R=\frac{4}{M}\,\mathrm{Re}\,R_1(k_r)\int_0^\infty k^2e^{-2k}dk=\frac{1}{M}\,\mathrm{Re}\,R_1(k_r), \quad (4)$$

$$Q=\frac{4}{M}\,\mathrm{Im}\,R_1(k_i)\int_0^\infty k^2e^{-2k}dk=\frac{1}{M}\,\mathrm{Im}\,R_1(k_i), \quad (5)$$

where

$$M=4\left(\frac{h}{s}\right)^3 \quad (6)$$

and k_r and k_i are unknown mean values of k.

For a uniform half-space, R_1 has the form

$$R_1(\bar{k})=\frac{v-\bar{k}}{v+\bar{k}}, \quad (7)$$

where

$$v=u+iw=[\bar{k}^2+i2\delta^2]^{1/2}, \quad (8)$$

δ is the distance parameter

$$\delta=h/p, \quad (9)$$

and p is the skin depth for the half-space. Solving for u and w gives

$$u=[(r+\bar{k}^2)/2]^{1/2}, \quad (10a)$$

$$w=[(r-\bar{k}^2)/2]^{1/2}, \quad (10b)$$

where

$$r=[k^4+4\delta^4]^{1/2}, \quad (10c)$$

and $\bar{k}=k_r$ or k_i for R and Q, respectively. From (7) and (8) we get

$$\mathrm{Re}\,R_1=\frac{w^2}{u(k_r+u)}, \quad (11)$$

and

$$\mathrm{Im}\,R_1=\frac{wk_i}{u(k_i+u)}. \quad (12)$$

From (4) and (11) we obtain an equation that yields a simple solution for k_r

$$R\,M=\frac{w^2}{u(k_r+u)}. \quad (13)$$

After some rearrangement, we find

$$k_r=\frac{\delta}{[B(B-1)]^{1/4}}, \quad (14a)$$

where

$$B=1/(1-MR)^2. \quad (14b)$$

MR is a function of δ alone.

For the out-of-phase field, the equation

$$Q\,M=\frac{wk_i}{u(k_i+u)} \quad (15)$$

does not lead to a simple solution for k_i. By numerical integration of (2) we find that

$$k_i^2\ll\delta^2 \quad (16)$$

for all δ of practical interest.

TRANSFER FUNCTION C FOR DIPOLE INDUCTION

From a formula given by Schmucker (1970b), it can be established that the above parameter v (for arbitrary k) is related to a spectral component $C(k, \delta)$ of the transfer function simply by

$$C(k,\delta)=\frac{1}{v(k,\delta)}. \quad (17)$$

If we use the mean value of k_r or k_i for k and split $C=C(k)$ into its real and imaginary parts, we obtain

$$\mathrm{Re}\,C=\frac{u(k_r)}{r(k_r)}, \quad (18)$$

$$\mathrm{Im}\,C=-\frac{w(k_i)}{r(k_i)}\simeq-\frac{1}{2\delta}. \quad (19)$$

Since k_r is a function of δ alone, Re C is also a function of δ.

Re C and Im C are shown in figure 1 and compared with Re C_0 and Im C_0 for a uniform source field ($k=0$). In the latter case,

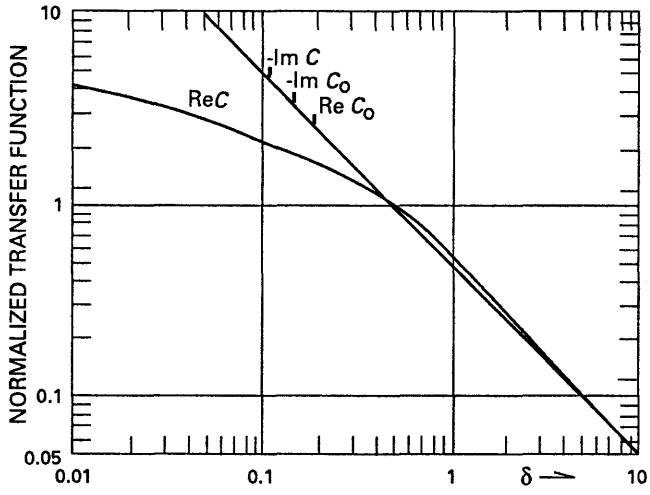

Figure 1. Real (Re) and imaginary (Im) parts of the normalized transfer function C for dipole induction and C_0 for induction by a uniform field, both as a function of $\delta = h/p$. h is height above half-space; p is skin depth of half-space.

$$\text{Re } C_0 = -\text{Im } C_0 = \frac{1}{2\delta} = \frac{1}{h}\frac{p}{2}, \tag{20}$$

or

$$\text{Re } c_0 = h \text{ Re } C_0 = \frac{p}{2},$$

where c_0 is a length. Weidelt (1972) has shown that Re c_0 is the centroid depth (z^*) of the in-phase current system induced by a uniform primary field.

We now define

$$z_H^* = \text{Re } c = h \text{ Re } C \tag{22}$$

as the centroid depth z_H^* for dipole induction in a homogeneous half-space. From figure 1, we learn that Re $C <$ Re C_0 for small values of δ; that is, for high resistivities. For this case, the centroid depth is essentially controlled by the geometric attenuation instead of the conventional skin effect.

It is remarkable that the imaginary parts of the transfer function for dipole and uniform induction are virtually the same:

$$\text{Im } c \simeq \text{Im } c_0 = -\frac{p}{2}. \tag{23}$$

Schmucker uses Im c_0 to calculate the ambient resistivity ρ_0^* at depth z_0^*. We determine the half-space resistivity ρ^* directly from R and Q using the Mundry (1984) or Fraser (1978) inversion.

THE FUNCTION ρ_a (z^*) FOR DIPOLE INDUCTION OVER A LAYERED HALF-SPACE

In the case of a layered ground, the Mundry inversion yields the resistivity ρ_a of the equivalent half-space and the distance D_a of the EM bird to the surface of the equivalent half-space, as shown in figure 2. For this general case, we define the centroid depth as

$$z^* = D_a - h + D_a \text{ Re } C, \tag{24}$$

where $D_a - h$ is the apparent depth of the half-space and D_a Re C is the centroid depth z_H^* for the equivalent half-space.

To calculate k_r, we must replace δ by δ_a

$$\delta_a = D_a/p_a, \tag{25}$$

$$p_a = 503.3\sqrt{\rho_a/f}, \tag{26}$$

(p_a in meters, ρ_a in ohm-meters, f in hertz), and M by M_a

$$M_a = 4\left(\frac{D_a}{s}\right)^3. \tag{27}$$

Schmucker's ambient resistivity ρ^* at depth z^* is simply

$$\rho^* = \rho_a. \tag{28}$$

We are now in a position to calculate the corresponding values $\rho_a(f)$ and $z^*(f)$ for each frequency.

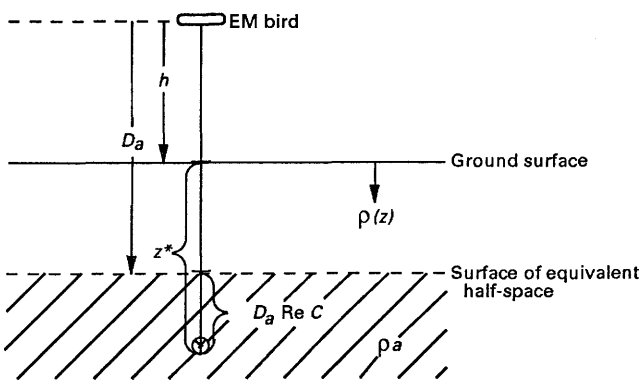

Figure 2. Illustration of equation (24). For a layered ground, the centroid depth $z_H^* = D_a$ Re C corresponds to the surface of the equivalent half-space. z^* is the centroid depth with respect to the ground surface.

MODEL CALCULATIONS

Model calculations show how the step function $\rho(z)$ for a layered half-space is approximated by the $\rho_a(z^*)$ function. Results of a number of model calculations have already been published (Sengpiel, 1986a, b). I add here two more examples (figs. 3, 4) based on the $\rho(z)$ function as derived from Schlumberger resistivity soundings in a survey area in Pakistan. In both cases, the $\rho_a(z^*)$ function is calculated for frequencies between 30 and 40,000 Hz. In figure 3, the resistivities of the layers decrease with depth. Below 20 m (the depth of the water table), the resistivity is controlled by the salinity of the ground water. From borehole logs, we know that the formation resistivity changes smoothly with depth throughout this survey area instead of in steps as in the function $\rho(z)$ as derived from the geoelectric data. Thus, the approximation of $\rho(z)$ in figure 3 by the $\rho_a(z^*)$ curve is even better than it looks. In the unfavorable case of figure 4, where the freshwater formation ($\rho = 35$ ohm-m) is covered by a thick conducting layer ($\rho = 10$ ohm-m) and underlain by a saltwater substratum ($\rho = 2$-ohm-m) at a depth of 149 m, the approximation by the $\rho_a(z^*)$ function is rather poor. Nevertheless, this function qualitatively shows the presence of a three-layer half-space where $\rho_1 < \rho_2 > \rho_3$.

With our three-frequency system we obtain only three points on the $\rho_a(z^*)$ is curve indicated in figures 3 and 4 by the frequencies 386, 3538, and 32,893 Hz. Because the function $\rho_a(z^*)$ is always a smooth curve, it appeared plausible to interpolate and extrapolate it using a cubic spline function through the above three points. It can be concluded from both figures that the interpolation is quite close to the $\rho_a(z^*)$ curve itself, whereas a limit

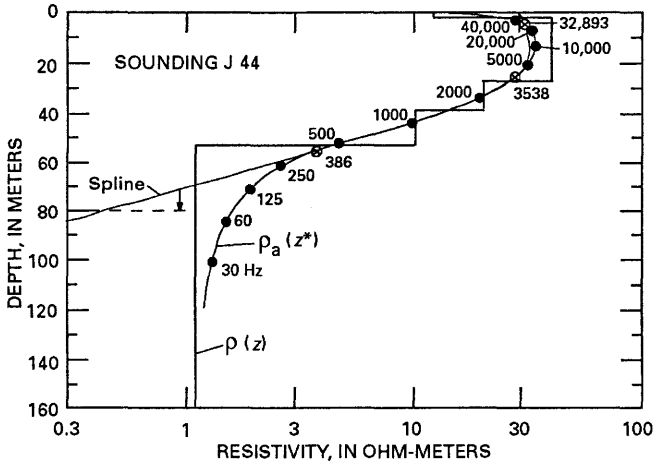

Figure 3. Resistivity-depth plot of the layer model $\rho(z)$, its approximation by the $\rho_a(z^*)$ function for frequencies between 30 and 40,000 Hz, and a spline interpolation through three points (circled x's) on the $\rho_a(z^*)$ curve. These points are obtained from the operating frequencies. Horizontal dashed line indicates limiting depth z^* (max).

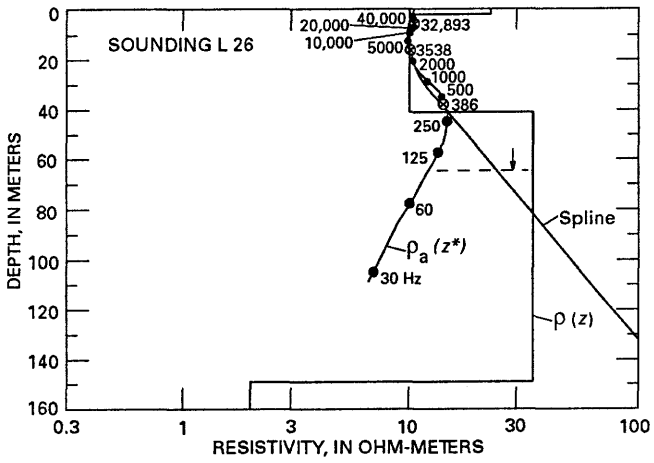

Figure 4. Resistivity-depth plot as in figure 3, but based on a unfavorable model $\rho(z)$. Horizontal dashed line indicates limiting depth z^* (max).

must be set for downward extrapolation beyond the largest z^* value. This limiting depth $z^*(\max)$ was chosen to be

$$z^*(\max) = z^*(f = 386 \text{ Hz}) + 25 \text{ m}.$$

This value is indicated in figures 3 and 4 by a horizontal dashed line and in the resistivity sections of plate 3 by a thick black line. It is obvious from figures 3 and 4 that a few more frequencies, yielding additional points on the $\rho_a(z^*)$ curve, would be sufficient to closely represent the complete $\rho_a(z^*)$ curve by the spline function.

PROCESSING OF SURVEY DATA

Although the calculation of the centroid depth z^* has proven to yield stable results, a correct $\rho_a(z^*)$ function can be obtained only after the survey data are properly adjusted for zero-levels and calibration. On highly conducting ground, which commonly is encountered in arid regions, calibration and phase adjustment of the EM system are considerably complicated by strong secondary fields. To be on the safe side, we compared our survey data with calculated data based on the interpreted models of Schlumberger soundings at 30 sites (Fielitz, 1987). Although the low-frequency EM amplitudes probably are correctly calibrated, the high-frequency amplitudes were too small based on comparisons with the Schlumberger soundings. Accordingly, the high-frequency amplitudes were multiplied by a factor of two to obtain agreement with the Schlumberger soundings. The reasons for the incorrect calibration are not yet fully understood.

We have processed data from the first 2,000 line-km of the abovementioned ground-water survey in a desert area of central Pakistan. The area is rather flat, and the water table is at an almost constant depth of 20 m. The ground water is mainly saline or brackish. The presence of freshwater aquifers in the survey area was already established by a geoelectric and hydrogeologic reconnaissance survey (Fielitz, 1987).

The airborne data were sampled every 0.5 s corresponding to a horizontal distance of about 20 m. Interpolated and extrapolated ρ_a values were calculated for depth intervals of 2 m between 0 and 128 m. These data were stored together with the corresponding UTM coordinates and other information for compilation and display.

REPRESENTATION OF AEM SURVEY RESULTS

An initial picture of the vertical resistivity distribution along a flight line is provided by a printer plot (not shown here) that permits an early check of the results. In the final presentation, the interpolated resistivity values are color coded, with red representing $\rho_a < 7$ ohm-m (saltwater) and blue $\rho_a > 18$ ohm-m (freshwater). Intermediate resistivities are represented by yellow and green and correspond to brackish water. We produce resistivity sections along flight lines and resistivity maps for selected depths.

Plate 3 shows resistivity sections for areas containing small and large quantities of fresh ground water, in a brackish to saline environment. Note the large vertical exaggeration (50:1). It should be further mentioned that there are about 50 vertical columns of resistivity data per line-kilometer, each calculated and plotted independently of the neighboring columns. The horizontal width of the colored columns is proportional to the flight speed, granting complete coverage of the section. The thick black line indicates the depth $z^*(\max)$; the resistivities below it were obtained by extrapolating too far and therefore are not reliable.

It is clear that the availability of interpolated resistivity data at a depth interval of 2 m makes it easy to produce resistivity maps for a specified constant depth z. Examples of such maps for $z = 30$ m and $z = 10$ m are shown on plate 3. The flight lines (black) are north-south and have a nominal spacing of 400 m. The four tielines (east-west) can be used to adjust the survey data to the level of the crossovers; however, the two examples show unadjusted data. The locations of significant minimum and maximum ρ_a values along the flight lines are given in ohm-meters. The map for $z = 10$ m represents the irregular resistivity pattern in the dry top layer consisting of fine-grained sand, silt, and clay. At $z = 30$ m, the resistivity is controlled by the salinity of the ground water. As established from a large number of Schlumberger soundings and from hydrogeological investigations of dug wells and drill holes in this area, ρ_a values between 18 and 100 ohm-m can be attributed to freshwater formations. The AEM survey will be continued, as well as the hydrogeological assessment of the quantity, quality, and origin of the freshwater body.

CONCLUSIONS

The centroid depth algorithm is easy to implement using a computer and can be used to invert large amounts of multifrequency data economically. An initial model or knowledge of the number of ground layers is not required. The method has two shortcomings: (1) thin, resistive layers intercalated between more conducting ones are not shown by the $\rho_a(z^*)$ function, and (2) conducting top layers reduce the range of depth information. Such effects are common to all EM methods. Due to the smooth nature of the $\rho_a(z^*)$ curve, the curve can be reasonably represented by a spline function through N known curve points, where N equals the number of operating frequencies. The first application of this interpretation technique to data from a three-frequency AEM ground-water survey provided an approximate three-dimensional resistivity pattern of the ground down to depths of 100 m. Based on this information, a large freshwater body was located within the unconsolidated sediments of a desert area and clearly distinguished from its brackish to saline environment.

REFERENCES CITED

Fielitz, K., 1987, Geoelectrical investigations for ground water exploration in desert areas of Pakistan: Unpublished report, Bundesanstalt für Geowissenschaften und Rohstoffe archives, no. 101 714.

Fraser, D.C., 1978, Resistivity mapping with an airborne multicoil electromagnetic system: Geophysics, v. 43, p. 144–172.

Mundry, E., 1984, On the interpretation of airborne electromagnetic data for the two-layer case: Geophysical Prospecting, v. 32, p. 336–346.

Schmucker, U., 1970a, Anomalies of geomagnetic variations in the southwestern United States: University of California, Bulletin of the Scripps Institution of Oceanography, v. 13, 165 p.

_____ 1970b, An introduction to induction anomalies: Journal of Geomagnetism and Geoelectricity, v. 22, p. 9–33.

Sengpiel, K.P., 1986a, Groundwater prospecting by multifrequency airborne EM techniques, *in* Palacky, G.J., ed., Airborne resistivity mapping: Geological Survey of Canada Paper 86–22, p. 131–128.

——— 1986b, New possibilities for groundwater exploration using airborne electromagnetics: Salt Water Intrusion Meeting, 9th, Delft University of Technology, Proceedings, p. 671–683.

——— 1988, Approximate inversion of airborne electromagnetic data from a multi-layered ground: Geophysical Prospecting, v. 36, no. 4, p. 446–459.

Weidelt, P., 1972, The inverse problem of geomagnetic induction: Zeitschrift für Geophysik, v. 38, p. 257–289.

Airborne Electromagnetic Bathymetry

By I.J. Won[1] and K. Smits[2]

Abstract

An experimental airborne electromagnetic (AEM) survey was carried out in the Cape Cod Bay area to investigate the potential of extracting bathymetric information over a shallow ocean. A commercially available DIGHEM[III] AEM system without any significant modification was used for the survey. The helicopterborne system operated at 385 and 7200 Hz, both in horizontal coplanar configurations. A concurrent ground-truth survey included extensive acoustic profiles and spot water conductivity measurements.

Because of the lack of knowledge about the absolute system calibration, a postsurvey calibration was made for each flight line using a small portion of AEM data to derive the zero-level signal, amplitude, and phase calibration factors for each coil-pair. The interpreted bathymetric profiles show excellent agreement with corresponding acoustic depth profiles for as much as one skin depth (possibly more) of the source frequency. With further improvements in hardware and software, the bathymetric penetration perhaps can be extended beyond one skin depth. AEM data can be used to produce conductivity profiles of both seawater and bottom sediments that may find potential applications in various offshore geotechnical engineering works.

INTRODUCTION

Naval Ocean Research and Development Activity (NORDA) has been investigating a possible application of the airborne electromagnetic (AEM) method to bathymetric charting in a shallow ocean. A rapid and cost-effective airborne bathymetric method is needed to supplement or even replace traditional shipborne acoustic sounding methods, which are time-consuming and often not suited to shallow coastal areas. Periodic and repetitive bathymetric mapping of heavily trafficked shallow-ocean regions is necessary for monitoring bottom-sediment movements and ship-lane maintenance and for a variety of geotechnical operations and routine charting.

[1]Geophex, Ltd., 605 Mercury Street, Raleigh, North Carolina 27603.

[2]Naval Ocean Research and Development Activity (NORDA), NSTL, Mississippi 39529.

The frequency-domain AEM method has been routinely used for mapping surface resistivity to explore mineral, ground-water, and aggregate resources. In this report, we present results of an experiment designed to test the theory, hardware, and interpretation techniques of a frequency-domain AEM method for bathymetric application.

THE AEM SYSTEM AND ITS OPERATION

The basic principle of the frequency-domain AEM system involves the measurement of change in mutual impedance between a pair of coils moving over the earth. The separation between the two coils is typically 6–8 m. The transmitter coil sets up a sinusoidally varying primary field that induces a system of currents in the conductive earth below. This induced current in turn generates a secondary magnetic field that is measured.

When the two coils are maximum coupled (that is, are in a mutually coplanar or coaxial configuration), the primary transmitted field at the receiver coil is very large compared to the secondary field. It is desirable, therefore, to remove this large field, mainly to reduce the dynamic range required of the receiver circuits. Most existing AEM systems accomplish this by using a third coil, commonly called the bucking coil, placed halfway between the transmitter and receiver coils in a maximum-coupled configuration. The dipole moment (the product of the number of turns and cross-sectional area) of the bucking coil is such that the induced voltage from the primary field is equal to that of the receiver coil. The bucking coil and the receiver coil are wired in opposing or bucking polarities. Consequently, the primary field strength at the preamplifier input is significantly reduced. The remaining signal of the primary field is further nulled out electronically in the receiving circuits.

The dipole moment of this bucking coil is approximately one-eighth that of the receiver coil because the bucking coil is placed at halfway and the primary field decreases as the cube of distance. Because the secondary field generated by the earth below is seen by both the bucking and receiver coils, the received secondary field signal is seven-eighths that of the true secondary field signal. The true secondary field is obtained by calibrating the display and recording devices.

The secondary field detected by the receiver coil is split into in-phase and quadrature (out-of-phase) components, which customarily are measured in parts per million relative to the primary field amplitude. This complex quantity is called the mutual coupling ratio and is the basis for the inversion process.

TEST SURVEY OVER CAPE COD BAY

The test survey area and the AEM flight lines are shown in figure 1. All flights and ground-truth surveys were performed during a 3-day period in June 1984. The AEM system used was a commercially available DIGHEM^{III} system described by Fraser (1978, 1979, 1981). It was equipped with two horizontal coplanar coil-pairs operating at 385 and 7200 Hz. Both pairs had an 8-m coil separation. An additional coaxial coil pair operating at 900 Hz was deactivated because of an electronic malfunction.

The sensor platform, or bird, was towed by a Sikorsky S58T twin-engine helicopter using a 30-m cable and maintained an average altitude range of 40-50 m above the sea surface. The aircraft altitude was measured by a radar altimeter (Sperry Model 220) mounted on the aircraft that had a manufacturer-specified accuracy of 5 percent. A total of about 200 line-km of AEM data consisting of 13 profiles was obtained in three sorties in less than 7 hours. The sampling rate was 1 s, corresponding to about 50 m along the ground track (ground speed of about 3 km/min). The maximum water depth in the survey area is about 40 m according to the bathymetric chart (NOAA Chart 13,246).

The flight plan included data collection before and after each profile at an altitude of about 270 m in order to calibrate the zero-level of the receiver coils. In addition, three short calibration flights were made in an area about 15 km east of the Cape, where the bathymetric chart indicates water depths in excess of 60 m. These data were intended to be used to determine the absolute calibration constants for amplitude and phase of each coil-pair on an assumption that the water body below is a uniform conductive half-space. It turned out, however, that this calibration method was not sufficiently accurate for the bathymetric processing. As discussed below, both zero-level signal and amplitude/phase-calibration constants were derived using a small data segment from each flight.

Figure 2 shows a raw AEM data profile and corresponding radar altimeter profile along line 5021 (see fig. 1 for location). Clearly, the AEM data are overwhelmingly correlatable with variations in altitude. A very crude indication of water depth may be observed from the ratio of the quadrature component to the in-phase component of the 385-Hz data. The ratio increases with a decreasing water depth, but unfortunately this relationship is highly nonlinear.

There is no easy way to estimate either measurement or instrument error from such a profile. Examination of short record sections indicates an estimated root-mean-square error of generally less than 5 ppm.

Even though the aircraft altitude is maintained mostly within a 10-m range (between 40 and 50 m), the corresponding variations of the AEM responses amount to more than 500 ppm. Because of the high conductivity of the sea water, errors induced by inaccurate altimetry pose a critical problem. At a bird altitude of 45 m and water depth of 10 m, a 1-percent altitude change produces amplitude differences of 22 ppm at 385 Hz and 33 ppm at 7200 Hz, whereas a 1-m change of water depth produces amplitude differences of only 10 ppm at 385 Hz and 0 ppm at 7200 Hz.

It soon became evident that because the radar altimeter employed has a specified accuracy of 5 percent, the radar altitude could not be used for the bathymetric processing. Instead, a new algorithm was developed to use the 7200-Hz response to derive the flight altitude for use in the inversion process. The altitudes thus derived show fairly random zero-biased root-mean-square differences (with respect to the radar altitudes) amounting to about 2–3 percent.

A Del Norte navigation system supported by three ground transponders was originally planned for the survey. Because of poor signal reception, a Loran-C system was installed on site with a makeshift arrangement of a printer that produced coordinates at 5-s intervals. These coordinates were later interpolated to produce 1-s-interval coordinate data corresponding to the AEM data.

A ground-truth bathymetric survey was carried out concurrently with the AEM flights using an acoustic depth sounder. A total of about 120 line-km of depth profiles was obtained, which covered about three-fifths of the AEM flight area. Unfortunately, due to practical reasons, the flight lines and the ship track did not coincide and were commonly more than 500 m apart. Therefore, the best available ground truth still reflects another interpolated approximation. Unless the bottom topography fluctuates rapidly, the ground truth is considered to be accurate within 1–2 m.

Water conductivity was measured at eight locations along the ship track at a depth of 3 m. The water conductivity is between 4.0 and 4.12 S/m. Although these values may be fairly representative for deep water, there are considerable uncertainties for very shallow water (<3 m) because water temperatures may rise significantly during the day (particularly during sunny days in June, as in this survey). A mere 4 °C difference in the water temperature at a given salinity can result in as

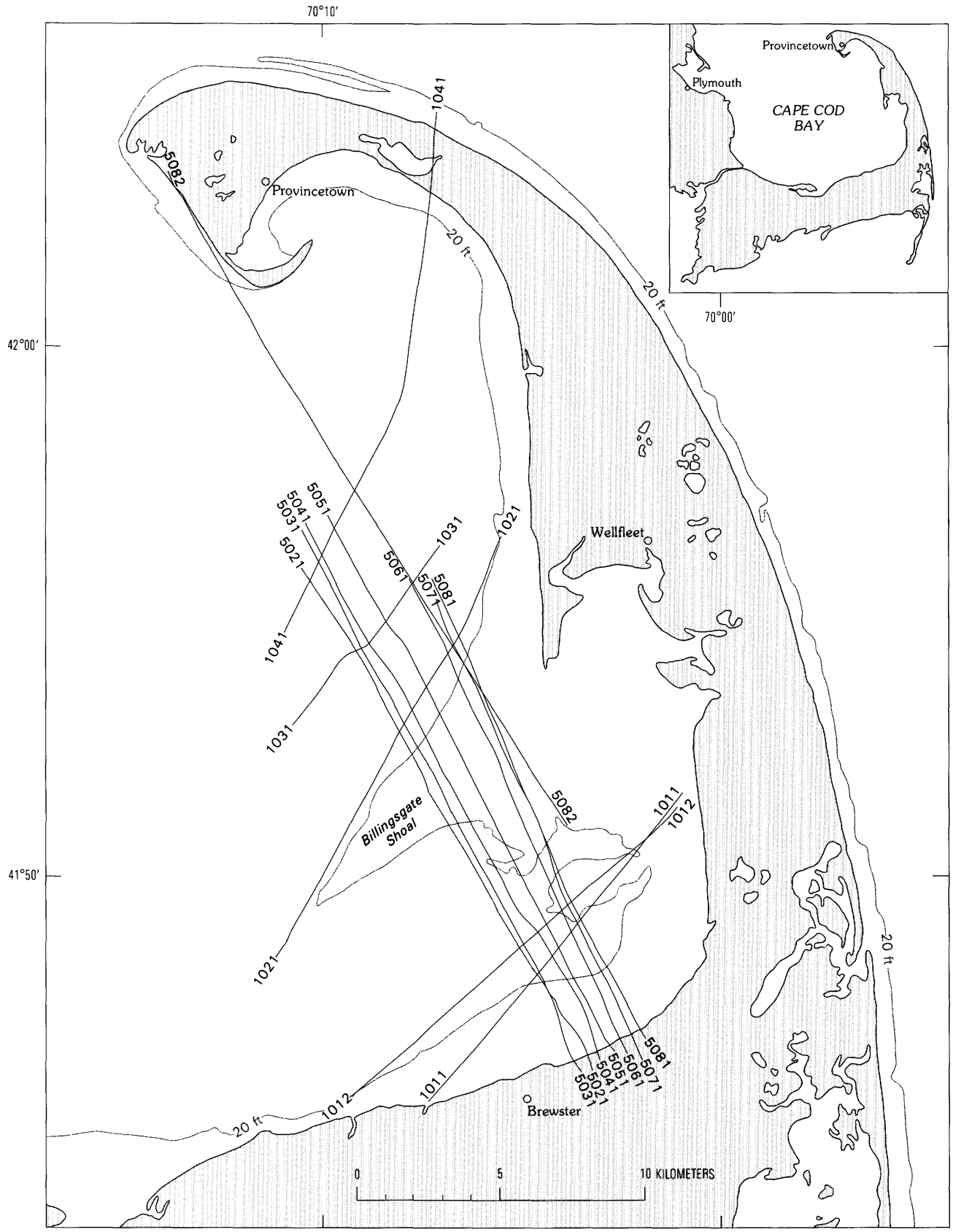

Figure 1. Cape Cod Bay test area and AEM flight lines. Line numbers are shown at the ends of each line.

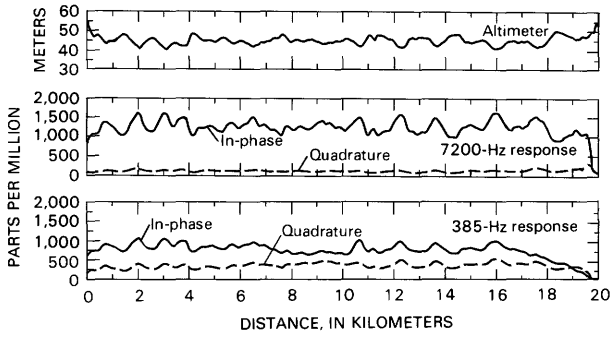

Figure 2. Raw AEM and radar altimeter profiles along flight line 5021.

much as a 10 percent change in water conductivity. Unfortunately, no ground-truth measurements were made during the survey to confirm this possibility.

INTERPRETATION

The high conductivity of seawater (3–5 S/m, depending on salinity and temperature and no freshwater inlets) severely restricts penetration of EM waves. Bathymetric range and resolution are primarily governed by the source frequency and coil spacing. Figure 3 shows the skin depths as a function of frequency for water conductivities of 2, 3, 4, and 5 S/m.

For the employed frequencies of 385 and 7200 Hz and seawater having a conductivity of 4 S/m, we expect skin depths of 12.8 and 3.0 m, respectively. From figure 3, the source frequency obviously should be less than 100 Hz to achieve a depth range of 50 m or more.

Fundamental equations for the magnetic field generated by a vertical magnetic dipole at or above the surface of a layered earth are given by Kozulin (1963) and Frischknecht (1967). The mutual coupling ratio for a horizontal coplanar configuration used for the present frequency-domain AEM system is defined as the ratio of the total magnetic field (H_z) to the primary field (H_z^P):

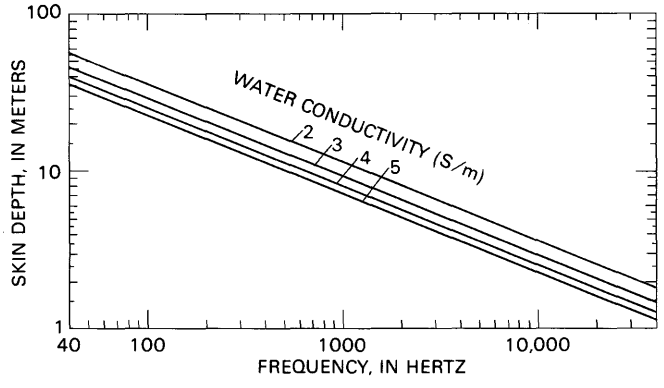

Figure 3. Skin depth as a function of frequency for seawater having conductivity of 2–5 S/m.

$$H_z/H_z^P = 1 - a^3 \int_0^\infty \lambda^2 R(\lambda, d, \sigma_1, \sigma_2, h, f)\, J_0(\lambda a)\, d\lambda. \quad (1)$$

The kernel function R corresponding to a two-layer earth whose geometry is shown on figure 4 can be expressed as

$$R = \frac{V_{0,1} + V_{1,2}\, e^{-2V_1 d}}{1 + V_{0,1} V_{1,2}\, e^{-2V_1 d}} e^{-2\lambda h} \quad (2)$$

where

$$V_{0,1} = (V_0 - V_1)/(V_0 + V_1),$$

$$V_{1,2} = (V_1 - V_2)/(V_1 + V_2),$$

$$V_0 = \lambda,$$

$$V_1 = \sqrt{\lambda^2 + i2\pi\mu_0\sigma_1 f},$$

and

$$V_2 = \sqrt{\lambda^2 + i2\pi\mu_0\sigma_2 f}.$$

In the above expressions

- f transmitter frequency (hertz),
- h bird altitude (meters),
- a coil separation (meters),
- d water depth (meters),
- σ_1 water conductivity (siemens per meter),
- σ_2 sediment conductivity (siemens per meters),
- μ_0 magnetic permeability of free-space (henrys per meter),
- λ variable of integration, and
- J_0 the zeroth-order Bessel function.

The integral in equation (1) can be evaluated by the linear digital filter method (Koefoed and others, 1972). We used the filter coefficients published by Anderson (1979b) for the Hankel transform integral.

The first term in equation (1) represents the primary field and is customarily bucked out during measurements, and only the second term, which represents the ocean response, is recorded (in parts per million). Figure 5 shows computed in-phase and quadrature frequency responses for various water depths.

The responses over an ocean are extremely high as compared with a normal land survey due to the highly conductive seawater. The response is exceedingly sensitive to bird altitude. The in-phase response increases with the source frequency, whereas the quadrature response peaks approximately at a frequency at which the water depth equals the corresponding skin depth. This has been explained theoretically by Won (1980).

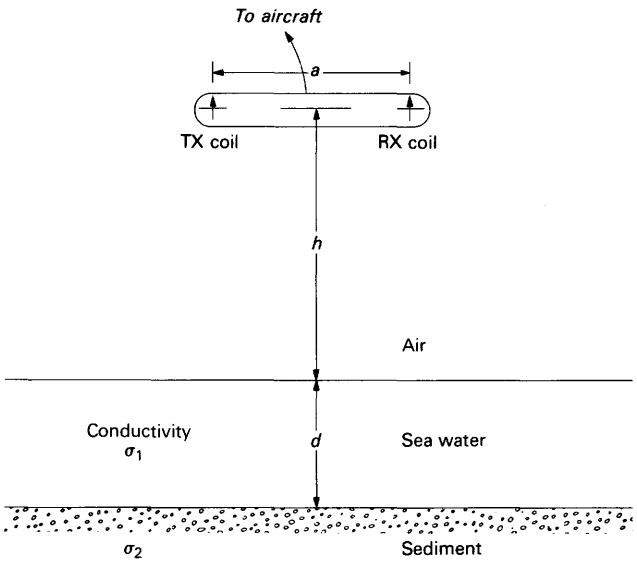

Figure 4. AEM bathymetric model used for inversion. Unknowns are water depth (d), conductivities of seawater (σ_1) and bottom sediment (σ_2), and the bird altitude (h).

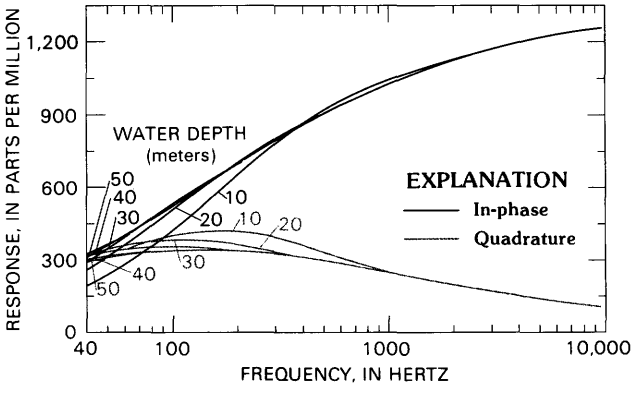

Figure 5. AEM bathymetric responses for water depths of 10, 20, 30, 40, and 50 m. The bird altitude is assumed to be 45 m, the coil separation 8 m, the water conductivity 4 S/m, and the sediment conductivity 1 S/m.

We are concerned with the differential changes in the response for varying bathymetric depth, and figure 6 shows the differences of the responses with respect to an infinitely deep ocean having the same (4 S/m) conductivity. Notice that the total change corresponding to a water depth change from 10 to 50 m amounts to about 100 ppm. In general, this response increases proportionally to the inverse cube of the bird altitude. It is obvious, therefore, that the recording device needs to have a much larger dynamic range than recorders used for land surveys.

Various inversion techniques are presently available to solve the unknown parameters in equation (1). These include several variations of the least-squares method, including the Marquardt algorithm (Marquardt, 1963; Anderson, 1979a) and methods based on

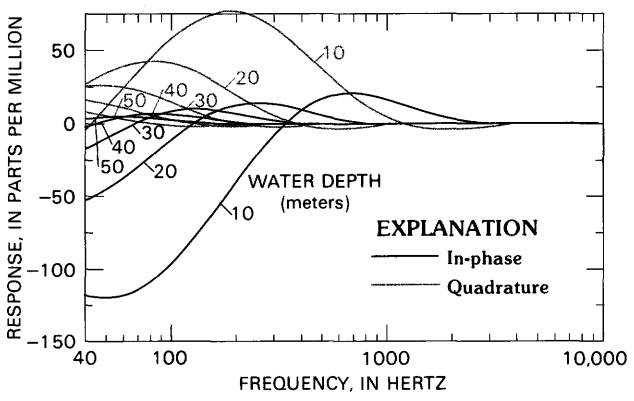

Figure 6. AEM bathymetric response for water depths of 10, 20, 30, 40, and 50 m relative to infinitely deep water. The bird altitude is assumed to be 45 m, the coil separation 8 m, the water conductivity 4 S/m, and the sediment conductivity 1 S/m.

generalized inverse theory (Backus and Gilbert, 1967; Fullagar and Oldenburg, 1984; Son, 1985).

The Cape Cod test data were initially interpreted using a multilayer least-squares algorithm developed by Anderson (1979a). Subsequently, the data were reprocessed using a different Marquardt least-squares algorithm, subroutine ZXSSQ in the IMSL Library package (IMSL, Inc., Houston). The inverted bathymetry in both cases agrees in a gross sense with known bathymetry, but shows considerable static and long wavelength errors that commonly exceed 5–10 m. Further careful inspection of the least-squares inversion results leads us to the following conclusions.

1. Computer inversion time is unacceptably long: One-point inversion of the two-frequency data consumes from 5 s to 1 min on a VAX 11/780 computer, even when the water depth is the only sought parameter and all other parameters are prescribed and fixed.

2. AEM response is too sensitive to the bird altitude to accept the specified 5-percent accuracy of the radar altimeter used for the survey. (At 385 Hz, for example, a 5-percent altitude change at a 10 m water depth causes a difference of 108 ppm; a 1 m depth change at the same 10 m depth causes a difference of only 10 ppm).

3. Both water and sediment conductivities must be allowed to vary, albeit in constrained ranges, in order for the resultant water depths to agree reasonably with ground-truth data.

From the above considerations, it is obvious that the traditional least-squares approach is not suitable for the present problem. At each data location, we have four measured quantities: in-phase and quadrature components at two frequencies. From these data, we must determine four parameters: water depth, water conductivity, sediment conductivity, and bird altitude.

Because of so many unknowns relative to the knowns, the least-squares method is unstable and not reliable.

The AEM bathymetric profiles reported here are derived from yet another method: analytic solutions of simultaneous nonlinear equations. From four measured quantities at each data location, we derive exact solutions of four parameters: water depth, water conductivity, sediment conductivity, and bird altitude. The method does not always produce a set of unique solutions for the problem. When unconstrained, the solutions are exact (because the number of knowns and unknowns is the same) and there are zero residuals, regardless of data error. Severe data error may produce physically unacceptable solutions such as negative depth or conductivities. Although least-squares methods (in which the number of knowns is usually much greater than the number of unknowns) may produce a stable solution set (even though its root-mean-square error may be high) from a noisy data set, the present analytic approach is understandably sensitive to data error.

An inversion algorithm using a modified Newton-Raphson method (see, for example, Fröberg, 1969) is applied to the data in two steps. At each step, we solve two equations for two unknowns. First, we derive the sensor altitude and water conductivity from the 7200-Hz data and then water depth and sediment conductivity from the 385-Hz data. This two-step approach stabilizes the solution by decoupling water conductivity and water depth, even when the ocean looks like a thin sheet (for which only the conductivity-depth product may normally be resolvable).

Inversion time for deriving all four parameters amounts to 0.5–2 s on a VAX 11/780 computer. The analytic method, as in the least-squares method, also requires initial guesses and, to ensure physically acceptable solutions, reasonable solution constraints. The constraints used for the final processing of the Cape Cod data are:

1. Water conductivity (σ_1) 3–5 S/m,
2. Sediment conductivity (σ_2) 0.01–2 S/m,
3. Water depth (d) 0–50 m, and
4. Bird altitude (h) positive.

Measurements of water conductivity at a depth of 3 m at eight locations are from 4.0 to 4.12 S/m. Although no bottom sediment conductivity data are available, an extensive in situ study by Hulbert and others (1982) off the Florida coast shows conductivities of 0.4–1.4 S/m within the first 5 m depth that decrease only slightly with increasing depth of burial.

The inversion process is initiated as follows. For the very first point, we prescribe starting values of $\sigma_1 = 4$ S/m, $\sigma_2 = 1$ S/m, d as read from the hydrographic chart, and h as indicated by the radar altimeter. Once the process starts, the solution set at the present location is prescribed as the initial parameters for the next location. Thus, after the first data point of a profile, the interpretation becomes completely autonomous.

We present only the bathymetric results. Other parameters will be presented in a separate report. It should be noted, however, that (1) the derived electromagnetic altitude is well within ±1 m of the radar altitude (less than the manufacturer-specified 5 percent error), (2) water conductivity is generally 4±0.2 S/m, except for very shallow water regions, and (3) bottom-sediment conductivity is from 0.5 to 1.5 S/m in most profiles.

DATA CALIBRATION

From the beginning we realized that using an existing commercial frequency-domain AEM system designed for land surveys posed a serious problem in establishing the zero-level signal and gain- and phase-calibration factors. Exploration geophysicists usually pay more attention to relative anomalies than to their absolute values. In the AEM bathymetric survey, we face the challenge of determining absolute values.

An initial attempt to use a set of uniform calibrations (derived from the deep ocean data) for the entire survey data produced unsatisfactory results. Although the AEM bathymetry approximately followed known depth profiles, it manifested significant static bias and long wavelength errors commonly amounting to 5–10 m.

For the Cape Cod test data, we experimented with three calibration techniques: zero-level calibration, amplitude/phase calibration, and zero-level/amplitude/phase calibration. Of these, the last was superior to others in inversion results and was adopted for the final processing.

Calibration factors for selected profiles are listed in table 1. Amplitude correction factors are from 0 to 7 percent, phase correction factors from 2° to 5° and zero-level correction factors from –28 to –2 ppm. The calibration constants were derived as follows. In order to standardize the process, we chose an arbitrary 50-data point profile segment (about 2.4 km long) over a relatively flat and deep ocean for which the average water depth was known. For each data point, we then prescribed $\sigma_1 = 4$ S/m, $\sigma_2 = 1$ S/m, and h = radar altitude. The last is the only parameter that varies for each data point. Using these prescribed parameters, we subjected the 50-point data set segment to the Marquardt least-squares inversion to derive the best-fit amplitude, phase, and zero-level values. Because of the large data set, the inversion produces very stable calibration factors. These calibration factors are applied to each raw data profile before the final inversion process. It should be pointed out that this known-depth-point calibration method also

Table 1. Cape Cod AEM data calibration constants
[Phase in degrees; zero-level in parts per million]

	385 Hz				7200 Hz			
			Zero-level				Zero-level	
Line	Amplitude	Phase	In-phase	Quadrature	Amplitude	Phase	In-phase	Quadrature
5021	1.063	2.56	0	-17.1	1.089	2.91	0	-12.7
5031	1.028	3.68	0	-2.4	1.056	4.30	0	-13.3
5041	1.072	5.20	0	-27.5	1.099	4.90	0	-27.7
5051	1.025	3.49	0	-5.0	1.054	4.30	0	-17.3
1021	1.040	-0.61	0	38.6	1.078	2.77	0	-14.0
5082	0.996	2.54	0	-4.3	1.036	2.39	0	-3.3

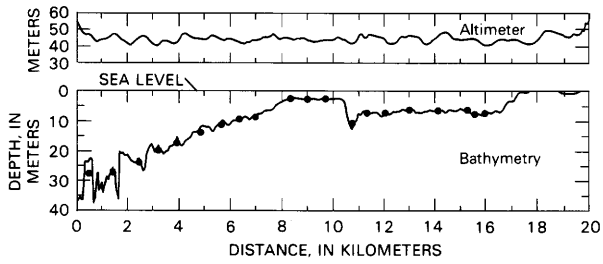

Figure 7. AEM bathymetric and radar altimeter profiles for line 5021. The solid line represents water depths inferred from AEM bathymetry, and the solid circles represent depths obtained using a shipborne acoustic profiler. Depths are computed at approximately 50 m intervals.

compensates for tidal fluctuation, which amounted to a maximum height of 2.8 m during the 7-hour flight period.

Obviously, such an empirical calibration technique is not as desirable as a fully automatic procedure, and future production AEM bathymetry systems must have automatic electronic calibration capability. It should be noted, however, that the data used for the calibration comprise only a fractional segment (about 10 percent of a given profile); thus, most of the profile is not directly influenced by the scheme.

RESULTS

Figure 7 shows interpreted AEM bathymetry for line 5021 (fig. 1). The agreement between AEM and acoustic depths is excellent to a water depth corresponding to about one skin depth (12.8 m) of the 385-Hz signal. In fact, the agreement to this depth is well within the interpolation accuracy of ground-truth data. For water depths greater than the skin depth, progressively degrading resolution results in oscillatory bathymetric profiles. Such oscillatory behaviors over deep water are common to all AEM bathymetric profiles obtained in the Cape Cod Bay survey, exhibit more or less the same rate of degradation with depth, correlate somewhat with variations in the aircraft altitude, and probably are random Gaussian error (not rigorously determined).

In essence, the oscillatory behavior is a direct result of the decreasing signal-to-noise ratio with respect to the altitude uncertainty. At a depth of 20 m, for instance, the maximum theoretical 385-Hz response (as compared with that for infinitely deep water) is expected to be about 10 ppm (fig. 6), whereas a mere 0.2-m error in altitude results in the same amount of difference in response. Because the bathymetric errors probably are random, yet correlate with aircraft altitude, we tentatively conclude that the error sources are related to altimeter resolution and to bird attitude uncertainties such as pitching and rolling associated with aircraft altitude variations. The bird attitude can be monitored in the future using inclinometers whose output can be incorporated into the interpretation (Son, 1985).

The oscillatory behavior can sometimes be suppressed by using a least-squares inversion method if a sufficient number of redundant measurements is available. The resultant solutions in this case carry large root-mean-square errors yet may give a deceptively smooth solution profile. (Errors never die; they simply become hidden in the process.) The present analytic inversion method produces zero-residual solutions that fit the observed data regardless of the measurement errors. Although the two approaches are equivalent in the sense of error budgeting, the analytic inversion method probably is superior in field logistics and computational speed.

Figure 8 shows interpretive error profiles for line 5021. The differences between the radar altitude and the electromagnetic altitude derived from the 7200-Hz record are mostly less than 1 m, except toward the shoreline where water becomes very shallow and the interpretative model for the AEM data fails. Although the differences appear to be random, they are fairly correlatable with altitude changes. It is understandable that when the aircraft altitude changes, the air speed generally also changes. Changes in air speed result in changes in the towing angle, which, in turn, produce a relative motion between the aircraft (on which the

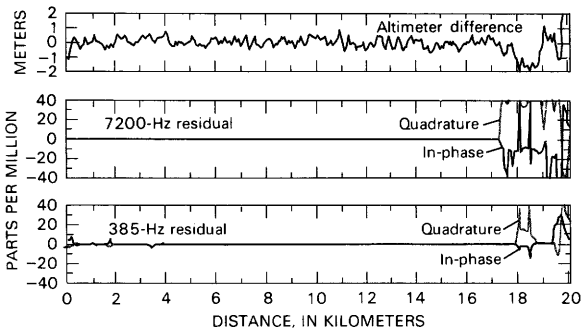

Figure 8. Interpretative error profiles for line 5021. Top graph shows difference between radar altitude and electromagnetic altitude deduced from 7200-Hz data. Lower two graphs show differences between measured and computed EM responses for 7200- and 385-Hz records.

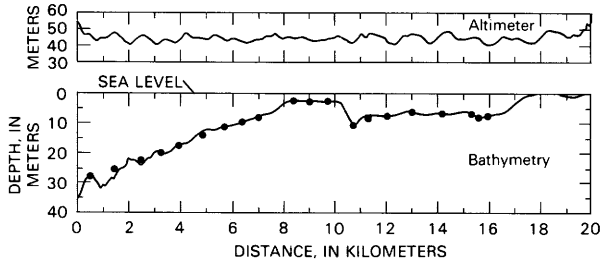

Figure 9. AEM bathymetric profile for line 5021 after filtering with 11-point running average filter. This filter was also applied to data shown in figures 10–14. Solid circles represent acoustic depths.

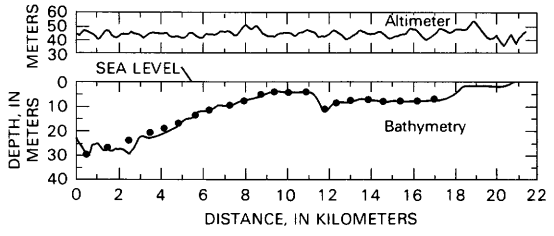

Figure 10. Filtered AEM bathymetry profile for line 5031. Solid circles represent acoustic depths.

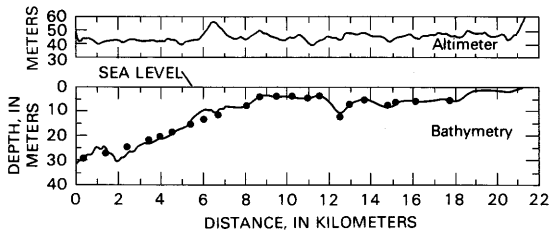

Figure 11. Filtered AEM bathymetry profile for line 5041. Solid circles represent acoustic depths.

altimeter is mounted) and the bird. This relative motion probably is responsible for altimetry differences, and

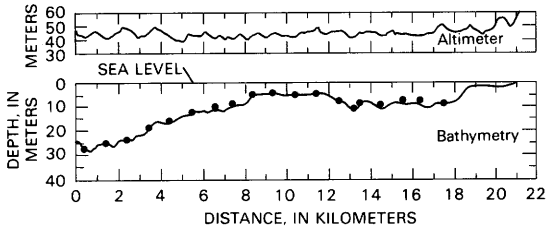

Figure 12. Filtered AEM bathymetry profile for line 5051. Solid circles represent acoustic depths.

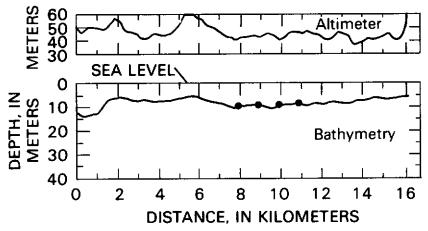

Figure 13. Filtered AEM bathymetry profile for line 1021. Solid circles represent acoustic depths.

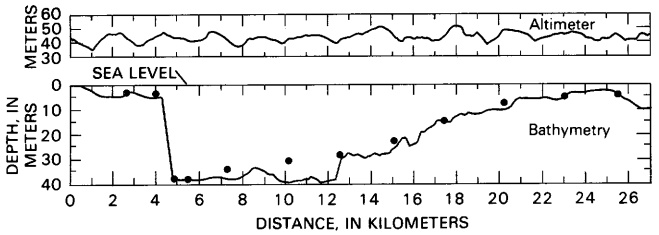

Figure 14. Filtered AEM bathymetry profile for line 5082. Solid circles represent water depths read from bathymetric chart (NOAA chart 13,246).

mounting the altimeter on the bird may help to resolve this problem.

If we assume that the oscillatory behavior of the AEM bathymetry (fig. 7) is of a random nature, we are justified in smoothing the interpreted bathymetric profile by low-pass filtering. To this end, we applied a simple, equal-weight, 11-point running average filter to line 5021 (fig. 9). Figures 10–14 show additional AEM bathymetric profiles produced using same procedure. All other profiles shown in figure 1 have more or less the same bathymetric qualities, and the same 11-point filter has been applied to all profiles. For line 5082 (fig. 14), for which the ground-truth survey was not performed, we show water depths as read from the bathymetric chart. The maximum depth along this profile is about 40 m where the AEM bathymetry agrees with the chart value. This implies that the AEM depth range can be almost three times the skin depth of the lowest frequency.

A composite of seven AEM profiles is shown in figure 15. Striking details of the sea-bottom morphology

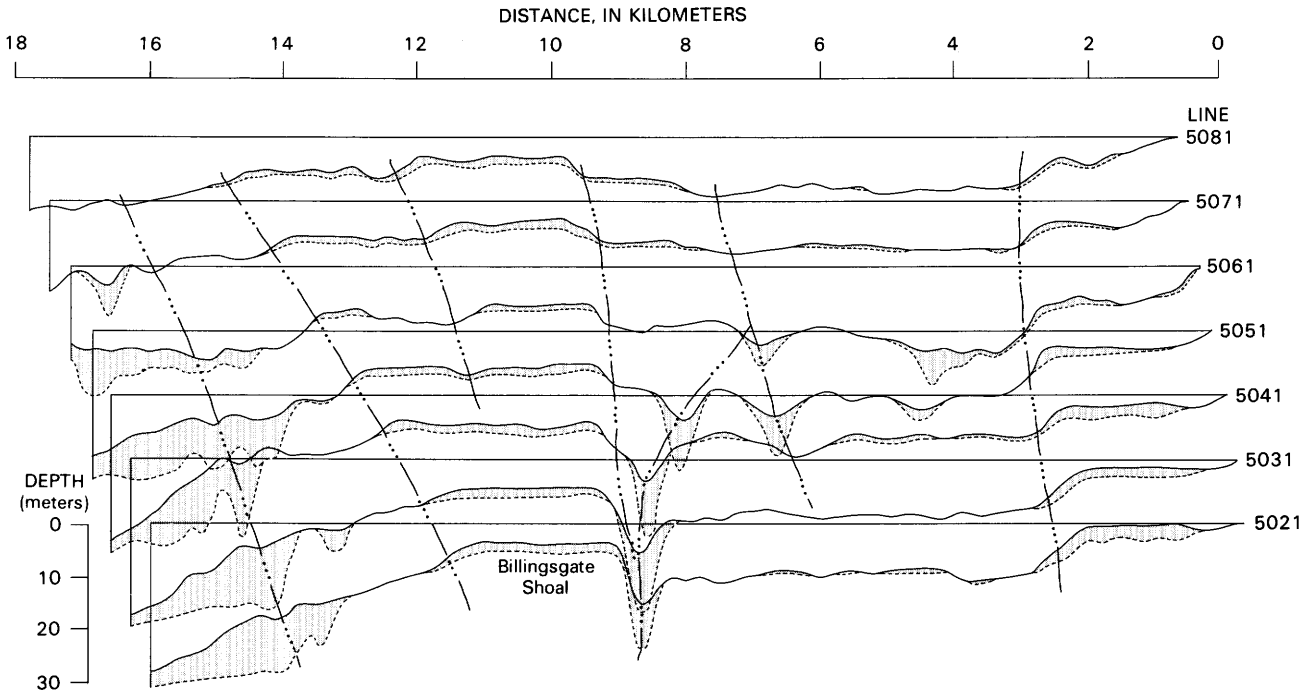

Figure 15. Composite of seven AEM bathymetry profiles for the Cape Cod Bay. Shaded sections represent thicknesses of unconsolidated sediments as inferred from AEM bottom-conductivity data.

including subtle trends and developments of slopes, trenches, and shoals can be observed. The fact that each profile is independently derived and yet shows remarkable correlations with neighboring profiles gives further confidence to the AEM results.

CONCLUSIONS

From our experience with the Cape Cod AEM bathymetry experiment, we summarize some of the error sources that degrade the bathymetric resolution:

1. Calibration errors in amplitude, phase and zero-level.
2. Error in the interpretive ocean model, particularly assuming a vertically homogeneous bottom-sediment layer.
3. Altimeter error.
4. Measurement error due to pitching and rolling of the bird (negligible to as much as 10° if the bird altitude is 50 m or higher).
5. Ground-truth interpolation error due to non-coincidence of tracks by boat and aircraft.
6. Electronic measurement noise.

Errors from most of the above sources can be reduced through improvements in equipment and interpretation software.

It is envisioned that with additional research and development efforts, the AEM method can be used to produce accurate bathymetric charts over shallow oceans perhaps as deep as 100 m. Compared with traditional acoustic sounding techniques, the AEM method provides an order-of-magnitude faster survey speed at reduced cost and thereby yields a synoptic knowledge of ocean-bottom topography. With improved interpretational schemes, real-time data processing may be possible.

In addition, the method has potential application for remote measurement of electrical conductivities of ocean water and bottom sediments. Bottom-sediment conductivity, in particular, is closely related to certain mechanical characteristics such as hardness, porosity, density, and perhaps sediment types that carry broad geotechnical implications for many offshore activities.

REFERENCES CITED

Anderson, W.L., 1979a, Program MARQLOOPS; Marquardt inversion of loop-loop frequency soundings: U.S. Geological Survey Open-File Report 79–240, 75 p.

———1979b, Numerical integration of related Hankel transforms of order 0 and 1 by adaptive digital filtering: Geophysics, v. 44, p. 1245–1265.

Backus, G.E., and Gilbert, F., 1967, Numerical application of a formalism for geophysical inverse problem: Geophysical Journal of the Royal Astronomical Society, v. 13, p. 247–276.

Fraser, D.C., 1978, Resistivity mapping with an airborne multicoil electromagnetic system: Geophysics, v. 43, p. 144–172.

_____ 1979, The Multicoil II airborne electromagnetic system: Geophysics, v. 44, p. 1367–1394.

_____ 1981, Magnetic mapping with a multicoil airborne electromagnetic system: Geophysics, v. 46, p. 1579–1593.

Frischknecht, F.C., 1967, Field about an oscillating magnetic dipole over a two-layer earth and application to ground and airborne electromagnetic surveys: Quarterly of the Colorado School of Mines, v. 62, no. 1, 370 p.

Fröberg, C.E., 1969, Introduction to numerical analysis (2nd ed.): Reading, Mass., Addison-Wesley, 433 p.

Fullagar, P.K., and Oldenburg, D.W., 1984, Inversion of horizontal loop electromagnetic frequency soundings: Geophysics, v. 49, no. 2, p. 150–164.

Hulbert, M.H., Lambert, D.N., Bennett, R.H., Freeland, G.L., Burns, J.T., Sawyer, W.B., and Field, F., 1982, In-situ electrical resistivity measurement of calcareous sediments: American Society for Testing and Materials, Special Publication STP777, p. 414–428.

Koefoed, O., Ghosh, D.P., and Polman, G.J., 1972, Computation of type curves for electromagnetic depth sounding with a horizontal transmitting coil by means of a digital linear filter: Geophysical Prospecting, v. 20, p. 406–420.

Kozulin, Y.N., 1963, A reflection method for computing the electromagnetic field above horizontal lamellar structures: Izvestiya, Academy of Sciences USSR, Geophysics Series (English ed.), no. 3, p. 267–273.

Marquardt, D.W., 1963, An algorithm for least-squares estimation of non-linear parameters: Journal of the Society of Industrial and Applied Mathematics, v. 11, p. 431–441.

Son, K.H., 1985, Interpretation of electromagnetic dipole-dipole frequency sounding data over a horizontally stratified earth: Raleigh, North Carolina State University, Ph.D. thesis, 180 p.

Won, I.J., 1980, A wideband electromagnetic exploration method—Some theoretical and experimental results: Geophysics, v. 45, p. 928–940.

Airborne Electromagnetic Measurement of Sea Ice Thickness and Sub-Ice Bathymetry

By Austin Kovacs[1] *and* Nicholas C. Valleau[2]

Abstract

A pilot study was made in May 1985 in the area of Prudhoe Bay, Alaska, to determine the feasibility of using an airborne electromagnetic (AEM) sounding system for profiling sea ice thickness and the sub-ice water depth and conductivity. The multifrequency AEM sounding system consisted of control and recording electronics and an antenna. The electronics module was installed in a helicopter, and the 7-m-long tubular antenna was towed beneath a helicopter at about 35 m above the ice surface. The profiling results indicate that both first- and second-year sea ice can be profiled, but resolution decreases if the ice is rough. This decrease is associated with the large AEM-system-induced surficial current area (footprint) over which the integrated sounding measurement is made. This large footprint effectively smooths out the sea ice relief. Sub-ice water depth and seawater conductivity were also determined. The results of the feasibility study are highly encouraging and further system development is warranted.

INTRODUCTION

An airborne electromagnetic (AEM) system was used for the first time in May 1985 for estimating sea ice thickness, water conductivity, and water depth from about 1 to 20 m under the ice cover. The AEM system used was a geophysical exploration device typically used for detecting highly conductive mineral deposits. The concept of using this technology for measuring coastal bathymetry was recently reviewed by Morrison and Becker (1982); its use for determining sea ice thickness was reviewed by Becker and others (1983). The feasibility of using AEM techniques for measuring sea ice thickness perhaps originated in 1968 (Geoscience) but was not pursued beyond an analytical verification.

The AEM system used in our field study had four pairs of coils (transmit Tx and receive Rx) that allowed simultaneous operation at nominal frequencies of 530, 930, 4158, and 16,290 Hz. A fifth frequency of 32,020 Hz was also evaluated by replacing the 16,290-Hz coils. The transmit-receive coils were separated about 6.5 m inside a Kevlar tube (bird) 7.5 m long and 0.5 m in diameter. The bird weighed about 200 kg and typically was flown about 35 m above the ice surface (fig. 1).

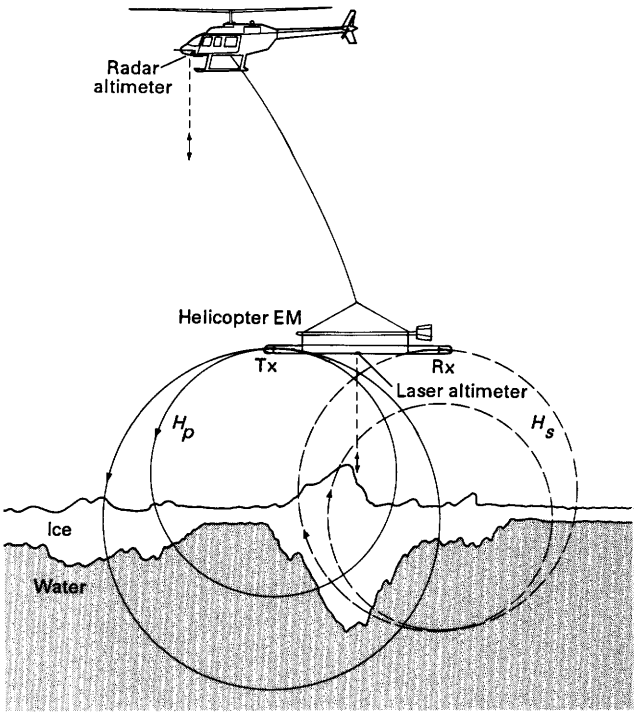

Figure 1. Helicopter-borne AEM system. The transmitter coil Tx creates a primary magnetic field H_p, which induces eddy currents in a conductive medium. The resultant secondary magnetic field H_s is detected by the receiver coil Rx.

In principle, the transmit coil produces a primary magnetic field H_p that induces a secondary magnetic field H_s in a nearby conductive medium (for example, seawater). The resulting primary and secondary magnetic fields are sensed by the receiver coils (fig. 2). The distance to and the conductivity of the conductive medium affect the Tx-Rx mutual coupling ratio H_s/H_p. Through the use of bucking coils and the system electronics, the primary field at the receiver is canceled out, and highly precise measurements of the in-phase (IP) and quadrature (Q) components of the secondary magnetic field relative to the primary field (in parts per

[1]U.S. Army Cold Regions Research and Engineering Laboratory, 72 Lyme Road, Hanover, New Hampshire 03755.

[2] Dighem Surveys and Processing, Inc., 228 Matheson Blvd. East, Mississauga, Ontario L4Z 1X1, Canada.

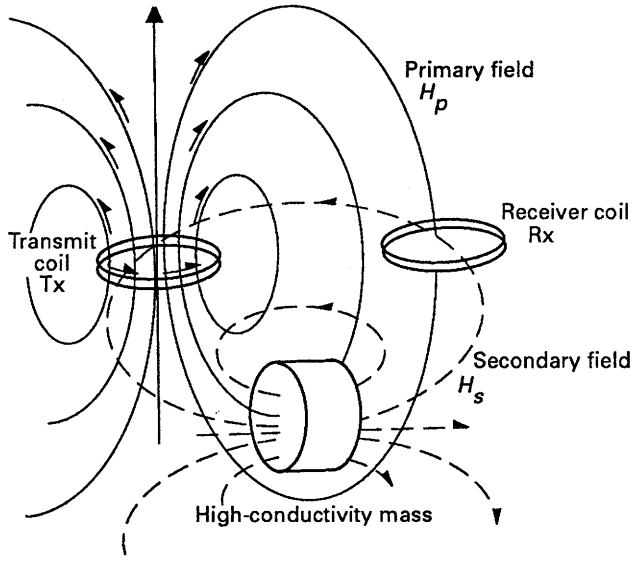

Figure 2. Magnetic fields associated with AEM sensing using a horizontal coplanar (whale tail) coil arrangement. Other possible coil arrangements include vertical coplanar and vertical coaxial coils.

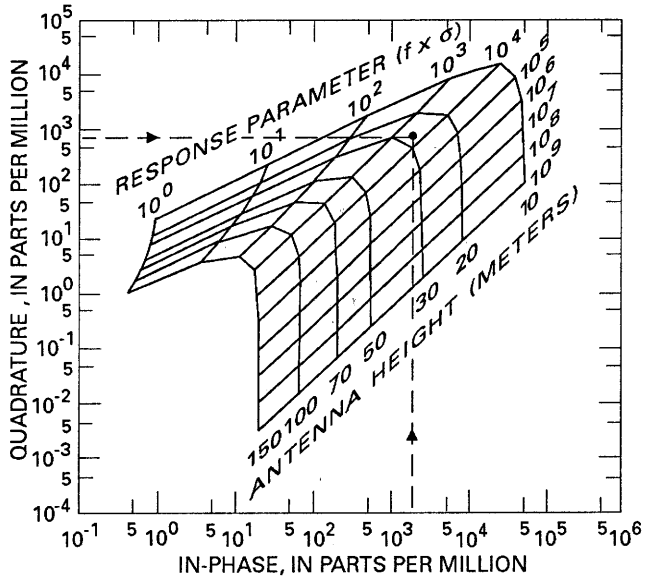

Figure 3. Argand diagram used for determining AEM system bird elevation above a high-conductivity layer and apparent conductivity (σ) of the layer. The diagram models the response of a horizontal coplanar coil pair, separated about 6.5 m, above a half-space.

million) are made and recorded. With the aid of an Argand diagram, formulated on the basis of a given Tx and Rx coil spacing and orientation, the apparent conductivity and height of the bird above the conductive surface can be estimated. An example of an Argand diagram is given in figure 3. If IP is 2,000 ppm and Q is 850 ppm, then the intercept of the related lines on the diagram indicates the bird is about 26 m above the conductor, or in our case the seawater, and the response parameter is 5,000. In addition, if the coil was operating at a frequency of 2000 Hz, then the conductivity of the seawater is 2.5 S/m (5,000÷2,000 = 2.5). Through appropriate multilayer analyses, the Argand diagram estimates can be refined and extended by nonlinear regression techniques to provide improved estimates of the properties of the ice, water, and seabed.

Because sea ice is relatively resistive and therefore transparent at the AEM system's low frequencies, the system senses the conductive seawater and determines the distance from the bird to the sea surface. A laser built into the bird measures the distance from the bird to the ice surface. Subtracting this distance from that determined by the AEM system to the seawater surface gives the apparent ice thickness, or the snow and ice thickness where a snow cover exists.

Sea ice electromagnetic, optic, acoustic, and mechanical properties are controlled to a large extent by ice temperature and the volume of the small vertical elongated inclusions of saline liquid (brine) that are trapped within the sea ice during the growth process (Kovacs and others, 1987). With the use of higher AEM system operating frequencies and appropriate algorithms, we hope to determine the apparent conductivity of the sea ice as well. Then, in principle, through the use of data such as those given in figure 4, the average brine volume of the ice can be estimated. From data such as those in figure 5, an assessment of the mechanical properties of the ice sheet can be made. This assessment can then be used to determine the load capacity of an ice sheet for aircraft landings or vehicle traffic.

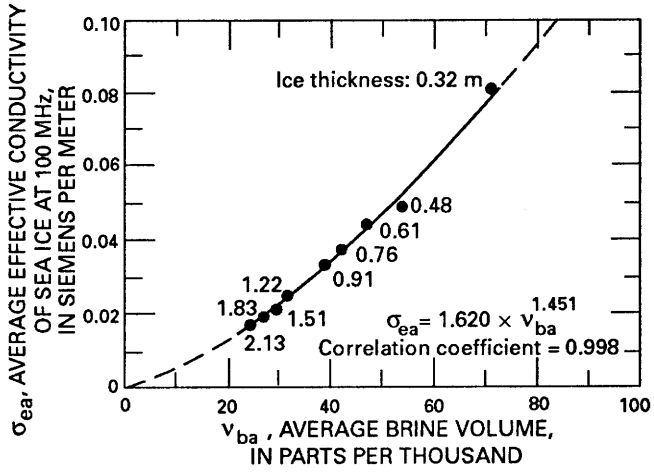

Figure 4. Average effective conductivity of model sea ice at 100 MHz versus average ice sheet brine volume with ice sheet thickness as a parameter. Modified from Kovacs and others (1987).

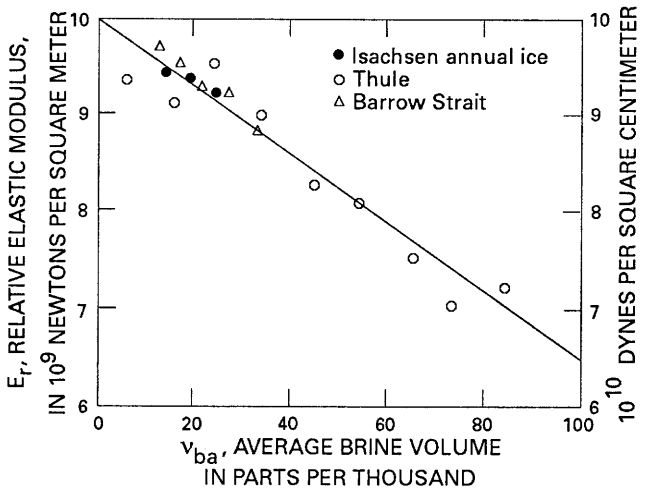

Figure 5. Relative elastic modulus of small sea ice test samples versus average brine volume. Modified from Cox and Weeks (1985).

Acknowledgments.—Funding for this study was provided by the U.S. Department of Navy, Naval Ocean Research and Development Activity, (NORDA) contract N6845286MP60003, program element 63704. The authors acknowledge the field assistance provided by Quincy Robe of the U.S. Coast Guard Research and Development Center, Groton, Conn.; Brian M. Bennett of the Cold Regions Research and Engineering Laboratory; and Chester F. Bassani and Victor R. Cole of Geotech Ltd. The helpful comments of Scott J. Holladay, consultant, Toronto, Canada, and Alex Becker, University of California at Berkeley, are also acknowledged.

FIELD RESULTS

Field trials conducted in 1985 in the Prudhoe Bay area of Alaska included flights over first-year and multiyear sea ice and a large, grounded multiyear rubble formation. Calibration of the AEM system was done by flying the bird at a known height (as determined by the laser altimeter) over deep open water and adjusting system response to agree with the response that should be received from this conductive body. An example of an AEM profile over a snowfree, relatively uniform, 0.75-m-thick refrozen lead is shown in figure 6. The variation in thickness seen in the profile for the ice is believed to be due in part to system noise, the ~10-cm accuracy of the laser profilometer, and bird orientation variations related to some swinging of the bird at the end of the 30-m-long tow cable. Although the latter could not be fully accounted for in the bird pendulum potentiometer pitch and roll data, the AEM data gave an average thickness for the lead ice of 0.80 m, an extremely encouraging result. An improved vertical accelerometer and pitch and roll sensor package, reduction of system noise, and a more accurate laser profilometer should further improve these results. The average seawater conductivity σ_w was determined to be 3.0 S/m, or about 0.4 S/m higher than the measured value. Note that the water depth under the ice was also profiled. Because we did not anticipate this determination being made at this site, no direct sounding verification was made.

AEM system profiles were made over a multiyear pressure ridge and adjoining low-lying ice. The AEM bird was flown down a 250-m-long track established on the ice. This track consisted of three parallel lines spaced 11.5 m apart. Snow and ice thicknesses along each line were determined by drill-hole measurements and are shown in profiles in figure 7. The profiles show, as expected, that ice thicknesses vary between the profiles at each station location. The snow and ice was thickest at the ridge location. The average snow and ice thicknesses as determined by drill-hole measurement for each profile were 3.56, 3.58 and 3.74 m, for an overall average ice thickness of 3.62 m.

Two ice-thickness profiles obtained using the AEM system are given in figure 8. There are significant relief differences between the two profiles, and neither profile clearly shows the thicker ridge ice. Three profiles were made using the 32-kHz coil in the bird and two using the 16-kHz coil. The 32-kHz profiles gave average ice thicknesses of 4.06, 3.18 and 3.52 m, for an overall average ice thickness of 3.59 m. The 16-kHz profiles gave average ice thicknesses of 3.13 and 3.54 m, for an overall average of 3.3 m. Because there is substantial variation in ice thickness along each of the drill-hole-measured profiles and because the AEM bird wandered along the flight track, a good correlation between the AEM ice profiles and the drill-hole-measured ice thicknesses

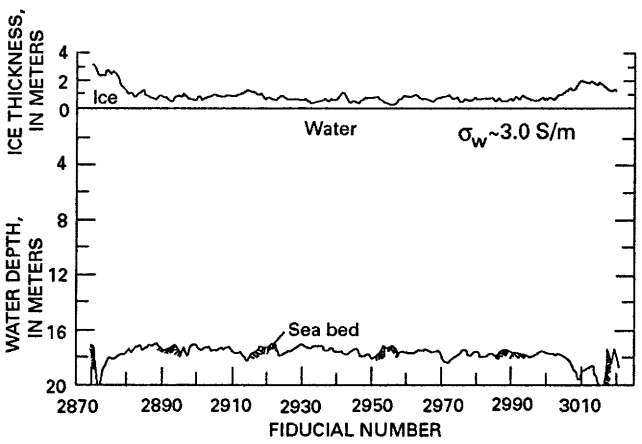

Figure 6. Profile resulting from AEM sounding over 0.75-m-thick lead ice that extends between about fiducials 2890 and 3000. Complete profile is about 4 km long. Water depth shown is that below the bottom of the sea ice.

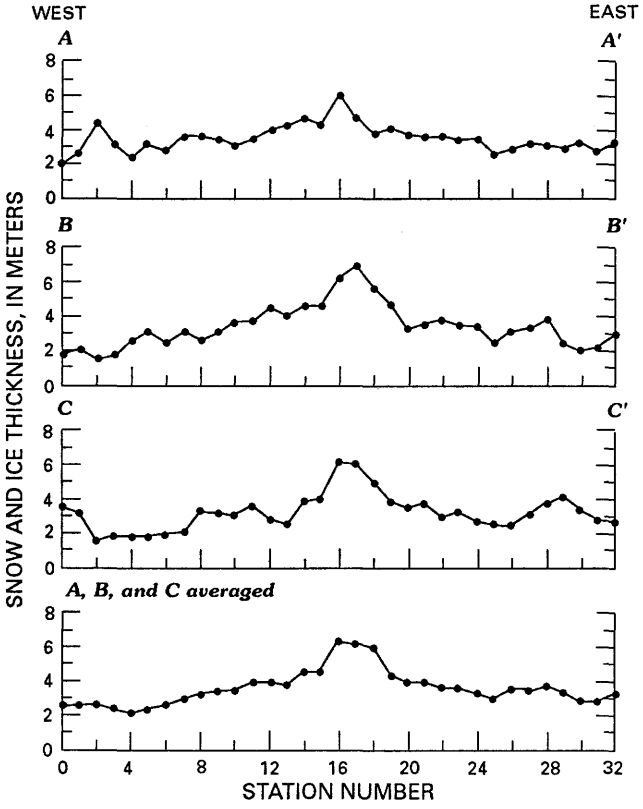

Figure 7. Drill-hole-measured snow and multiyear ice thicknesses along three 250-m-long parallel lines spaced 11.5 m apart. Drill-hole measurements were made at 7.5-m intervals along each line. The three lines form the track or flight corridor down which the AEM system antenna was flown.

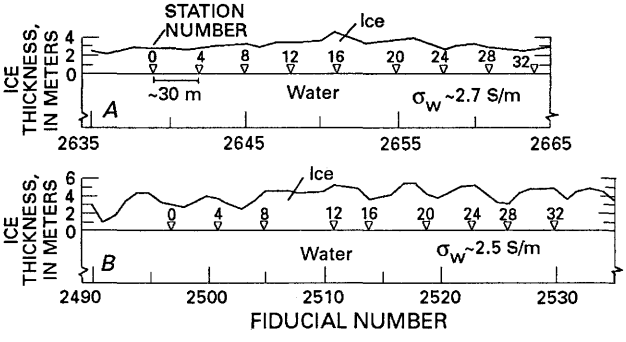

Figure 8. Two AEM profiles along a track established on multiyear sea ice. Distance from first inverted triangle station marker to last is 250 m. Station numbers correspond to those shown in figure 7.

cannot be expected. The average of all drill-hole-measured snow and ice thicknesses along the track, however, is 3.6 m, the same as that for the combined AEM data.

The AEM data do not show the thick ridge ice because of the size of the AEM sounding footprint and, therefore, the area over which the water surface was

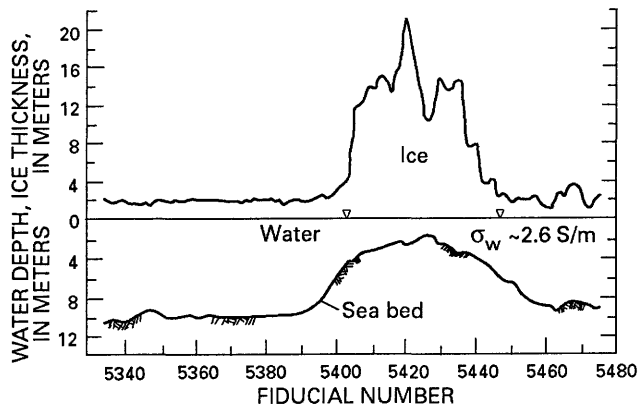

Figure 9. AEM profile over first-year sea ice and a large, grounded multiyear rubble formation. The distance between the inverted triangle markers is about 0.66 km.

integrated into each AEM distance determination. Our preliminary assessment indicates that the AEM system footprint diameter is about 1.3 bird heights, and therefore the AEM-determined distance to the ice-water interface is an averaged one related to a relatively large area of depressed seawater relief caused by the undulating ice bottom topography. This averaging effect smooths out variations in the ice roughness, as in profile *A* in figure 8, but does not explain the odd variations in ice thickness along profile *B*. The pitch and roll data do not indicate that bird motion was responsible for the variations in profile *B*.

A profile over first-year sea ice and a large, grounded multiyear rubble formation is shown in figure 9. This formation formed on a shoal in the fall of 1983, survived the summer breakup and melt season, and was still grounded in place at the time of our May 1985 survey. The shoal on which the formation rested was about 8 m below the sea surface, as indicated by bathymetry charts of the site. The AEM profile indicates that 1.5–3 m of water existed under the ice rubble. Because the ice formation was firmly grounded, no water should be shown above the shoal. The cause of this ambiguity is believed to be unfrozen seawater within the submerged ice keel block structure and (or) the seawater off to the side of the ice keel being sensed by the AEM system. The thickest ice is indicated to be about 22 m thick, a reasonable thickness based on ice surface-elevation measurements and the apparent shoal depth. The average thickness of the snow-covered first-year sea ice to the left of the feature is about 1.75 m thick, and the sea bottom is about 10 m deep at fiducial 5390. Drill-hole measurements indicate a very similar snow and ice thickness, but the measured water depth is about 1.5 m greater. The average AEM-determined seawater conductivity is 2.6 S/m, in agreement with measured values.

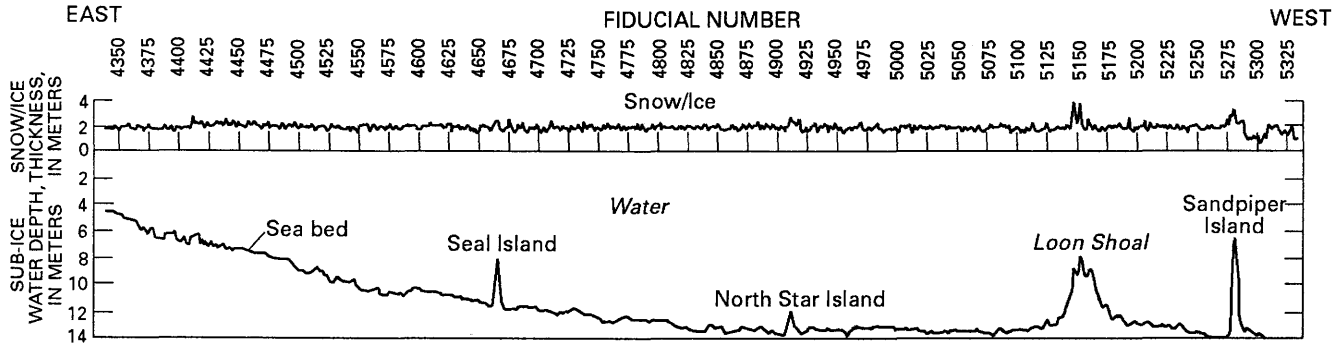

Figure 10. AEM profile results obtained from flight 6L7 over fast ice west of Prudhoe Bay, Alaska.

Flight line 6L7 was flown in a northwesterly direction along the north side of manmade gravel islands Seal, Sandpiper, and North Star and across Loon Shoal. The AEM snow-ice thickness and sub-ice water depth along the flight line are shown in figure 10. The snow-ice thickness varies but averages 1.89 m. The average drill-hole-measured snow-ice thickness is 1.74 m.

The apparent shoaling of the seabed at the islands is due to the AEM system sensing the submerged slope of these islands. Our assessment of the AEM-determined under-ice water depth indicates that the AEM data overestimates the water depth but by less than 10 percent.

The AEM system is undergoing further instrumentation development, and further analytical refinement is in progress to tailor the system to airborne measurement of sea ice thickness. The system currently is capable of penetrating sea ice of varying thickness and providing the relative thickness of the ice without being affected, as impulse radar is, by the in situ conductivity of the ice. The large footprint of the AEM system, however, may not allow relative variations in ice cover relief, such as small pressure ridges and leads, to be distinguished in the ice profile.

CONCLUDING REMARKS

The airborne electromagnetic survey system discussed has an advantage over high-frequency (50–1,000 MHz) sounding devices such as impulse radar (Kovacs and Morey, 1980, 1986; Kovacs and others, 1987) in that it is not adversely affected by the conductivity of the sea ice. The AEM system basically measures the distance to and roughness of the sea surface as created by ice bottom relief. AEM sounding is limited by the system's large footprint, which has the effect of smoothing local variations in ice thickness. Thus, although the system appears to offer a method for determining the relative thickness of an ice floe, it cannot provide high-resolution site-specific ice thickness information. Potential advantage of the AEM system is that it may be able to determine the apparent conductivity of the ice sheet; thus the average brine volume of the ice sheet (fig. 5) can be assessed and an estimate of ice sheet strength can be made.

REFERENCES

Becker, A., Morrison, H., and Smits, K., 1983, Analysis of airborne electromagnetic systems for mapping thickness of sea ice: Naval Ocean Research and Development Activity, NORDA Technical Note 216, 34 p.

Cox, G.F.N., and Weeks, W.F., 1985, On the profile properties of undeformed first year sea ice: Unpublished report prepared for the David Taylor Ship R & D Center, U.S. Army, Corps of Engineers, Cold Regions Research and Engineering Laboratory, Hanover, N. Hamp.

Geoscience, 1968, Proposal for a feasibility study of an airborne technique for measuring sea ice thickness: Proposal submitted to U.S. Navy Oceanographic Office, Washington, D.C., by Geoscience Incorporated, Cambridge, Mass.

Kovacs, A., and Morey, R.M., 1980, Investigation of sea ice anisotropy, electromagnetic properties, strength, and under-ice current orientation: U.S. Army, Corps of Engineers, Cold Regions Research and Engineering Laboratory, CRREL Report 80–20, 18 p.

——— 1986, Electromagnetic measurements of multi-year sea ice using impulse radar: Cold Regions Science and Technology, v. 12, p. 67–93.

Kovacs, A., Morey, R.M., and Cox, G.F.N., 1987, Modeling the electromagnetic properties of sea ice, part I: Cold Regions Science and Technology, v. 14, p. 207–235.

Morrison, H.F., and Becker, A., 1982, Analysis of airborne electromagnetic systems for mapping depth of seawater: Engineering Geoscience Report, University of California at Berkeley, 56 p.

Airborne Radar Sounding in Temperate and Polar Ice

By David L. Wright[1], Steven M. Hodge[2], *and* Raymond D. Watts[3]

Abstract

The first successful airborne radar ice soundings of Columbia Glacier, Alaska, were performed by the U.S. Geological Survey (USGS) in 1978. A key to success was the recognition that in temperate ice (ice at the pressure melting point throughout) the greater wave propagation losses, as compared to propagation losses in colder ice, are due mostly to scattering by water-filled cavities in the ice. It was also recognized that an effective means to increase radar penetration of temperate ice is to reduce scattering losses by lowering the operating frequency in order to make the wavelength in the ice long as compared to the average dimension of the scatterers. An impulse radar system that operates at a center frequency of about 1.5 MHz was designed and built to sound temperate ice because an impulse radar system ideally radiates only a single cycle of a sine wave for each transmitter pulser firing, thus preserving the highest possible resolution consistent with the reduced radiated frequency. The system was installed in a small single-engine aircraft and profiled bottom topography in ice as thick as 550 m without data processing. The bottom profiles aided glacier dynamics modeling that resulted in the prediction of the instability of the Columbia Glacier that began in the early 1980's and continues to the present time.

In 1987 the USGS recorded more than 6,000 km of radar ice sounding profiles on a 150 by 150 km grid centered on the summit of the Greenland ice sheet using an LC–130 aircraft belonging to the National Science Foundation (NSF), a radar system designed and built by the Technical University of Denmark (TUD), and a new high-speed digital data acquisition and averaging system designed and built by the USGS. The data-averaging system added 512 waveforms during the time the aircraft moved 15 m at a speed of 445 km/hr. The addition of 512 waveforms improved the signal-to-noise ratio by about 13.5 dB for uncorrelated noise. The TUD radar was operated at 60 MHz with a pulse length of 250 ns and obtained bottom returns through more than 3,000 m of the polar ice in the central part of the Greenland ice sheet. The data are being used to produce a map of the bottom topography that will aid in siting an NSF-sponsored scientific corehole through the Greenland ice sheet.

[1]U.S. Geological Survey, MS964, Box 25046, Federal Center, Denver, Colorado 80225.

[2]U.S. Geological Survey, University of Puget Sound, Tacoma, Washington 98416.

[3]U.S. Geological Survey, MS521, National Center, Reston, Virginia 22092.

INTRODUCTION

Airborne ice sounding has been successfully carried out in both temperate and polar ice by the U.S. Geological Survey (USGS). Temperate ice is defined as ice that is at the pressure melting point from surface to base, and it differs from cold ice in that the effective attenuation for the propagation of electromagnetic waves is higher in temperate ice than in cold ice. The increase in effective attenuation is partly the result of the increase in ohmic losses for warm ice but, more importantly, the result of increased scattering losses due to water-filled cavities embedded in temperate ice (Watts and England, 1976). In order to minimize the increased losses, much lower frequency radar systems have been employed. Decreasing the frequency to a few megahertz results in wavelengths that are long as compared to the typical dimensions of the water-filled cavities; thus the relative scattering cross section is reduced. The type of radar and the antennas used for a radar system operating at a few megahertz are significantly different from radars developed for sounding cold polar ice where higher frequencies are generally used. In 1978 the USGS designed, built, and used an impulse radar system for temperate ice as part of the Columbia Glacier project (Watts and Wright, 1981).

Polar ice may be more than 3,000 m thick but typically has a lower rate of attenuation than temperate ice, although exceptions can occur due to deformational heating and heat transport from the underlying rocks. For polar ice sounding, frequencies of tens or hundreds of megahertz typically are used. In 1987 the USGS conducted an airborne radar study of part of the Greenland ice sheet using a 60-MHz radar system designed and built by the Technical University of Denmark (TUD) (Skou and Sondergaard, 1976). Results of this study will be used to help situate a new scientific corehole through the Greenland ice sheet.

Acknowledgments.—We thank the VXE–6 squadron of the United States Navy for making it possible to complete the required ice sounding in a limited time by their safe and efficient operation of the LC–130 aircraft. We also thank N. Skou and E. Lintz Christensen of the Electromagnetics Institute of the Technical University of Denmark for installation and reliable operation of the TUD radar system. This report is based, in part upon activities supported by the National Science

Foundation under Agreement DPP–8518618. Any opinions, findings, and conclusions or recommendations expressed in this publication are those of the authors and do not necessarily reflect those of the National Science Foundation.

COLUMBIA GLACIER

Columbia Glacier, an iceberg-calving valley glacier, terminates in Prince William Sound near Valdez, Alaska, the southern terminus of the Trans-Alaska oil pipeline that carries oil from Prudhoe Bay in northern Alaska. Some of the icebergs calved by the Columbia Glacier drift into the narrow shipping channel used by oil tankers that transport oil from Valdez. Austin Post (1975) of the USGS observed that most of the valley glaciers that terminated in the ocean along the Canadian and Alaskan west coast had gone into a rapid retreat phase during the last 50 years and that the recession was accompanied by the discharge of significantly more ice. He questioned whether the Columbia Glacier might be poised to do the same, with potentially serious consequences for the shipment of Alaskan oil because of increased iceberg discharge into Prince William Sound. An intensive study of the Columbia Glacier was initiated in order to answer that question. As part of the multifaceted study, numerical modeling was employed as a predictive technique (Sikonia, 1982), and knowledge of the bottom topography was required as data for the modeling; however, because most of the lower part of the Columbia Glacier is severely crevassed, airborne radar sounding was the only feasible means of obtaining the required data.

An impulse radar system was designed, built, and installed in the USGS Fairchild Porter, a single-engine turboprop aircraft shown schematically in figure 1. The 100-m-long, resistively loaded dipole antennas were deployed and retrieved through the wingtips by hand-operated winches. The antennas were held almost level in flight by plastic funnels that served as drogues. The transmitter was a free-running, avalanche transistor pulser. The receiver included a time-varying gain amplifier to partially compensate for geometric "spreading loss" and attenuation in the ice. The amplified received signal was displayed on a sampling oscilloscope, and output from the oscilloscope was recorded on magnetic tape using an analog instrumentation tape recorder. Both the recorded radar data and the oscilloscope horizontal sweep voltage output were recorded.

Profiles were reconstructed by playing back the tapes in the following manner. The radar data modulated the storage oscilloscope beam intensity; the recorded horizontal sweep voltage controlled the vertical position of the beam; and an auxiliary slow-ramp generator controlled the horizontal position of the beam. The storage oscilloscope screen was photographed, but because each photograph contains only a segment of a profile, several sequential photographs were necessary to reconstruct a profile.

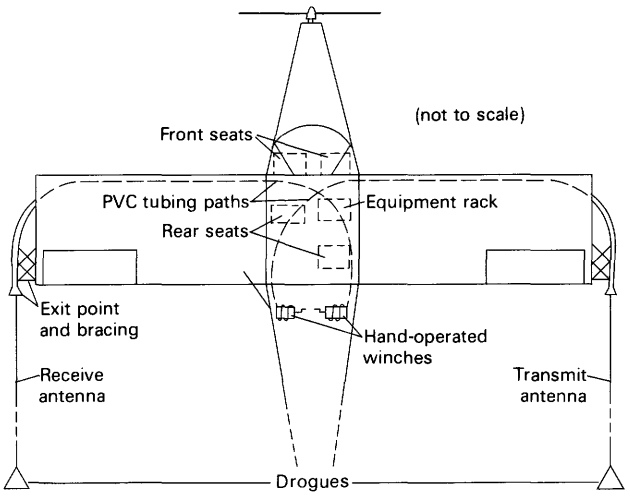

Figure 1. Schematic representation of the USGS Fairchild Porter aircraft used for the Columbia Glacier survey. Antenna deployment and retrieval system are shown.

Digitization of the data had to be done later as a separate step. An example of a digitized profile is shown in figure 2 and illustrates both the potential of the radar survey technique and some of the problems encountered. The maximum depth on this particular profile is about 410 m. In valley glaciers, returns from the sides may arrive during the same time period as returns from the surface or bottom, sometimes making identification of the surface and bottom returns difficult. Antenna ringing was a second difficulty and was brought on, in part, by the need to lengthen the antennas even more than had been anticipated in order to get sufficient penetration of the ice. The lengthening was done quickly in the field by simply adding center sections of wire that contained no resistive loading, but the resulting antennas were not optimally loaded. Despite this drawback, the airborne radar system used on the Columbia Glacier project profiled ice as deep as 550 m and was used to help produce a map of the bed topography of Columbia Glacier (Brown and others, 1986).

Some of the records were later digitally processed in order to improve the image quality. An example of digital processing is shown in figure 3; the example was derived from the same data as figure 2, but deconvolution and filtering were applied to the data to compress the waveform and concentrate the energy into a narrower time window. A benefit is that both the surface and bottom returns are sharpened.

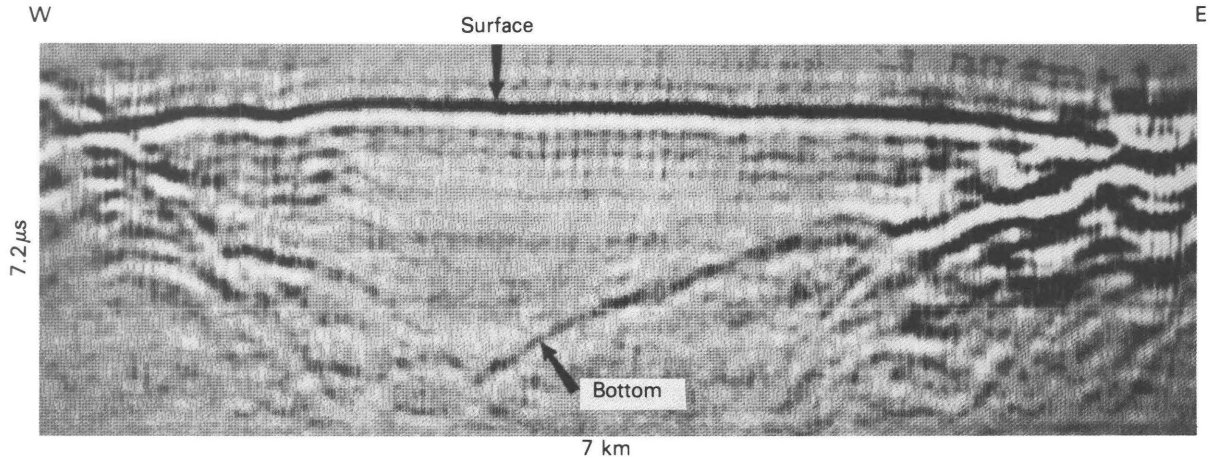

Figure 2. Reconstructed airborne radar profile across the lower part of Columbia Glacier, Alaska. The data were played back from the original analog magnetic tapes and digitized. Reflections from the valley walls are seen at the left and right. The maximum ice depth on this profile, assuming an average propagation velocity of 1.67×10^8 m/s, is 410 m. Vertical exaggeration is about 4.1.

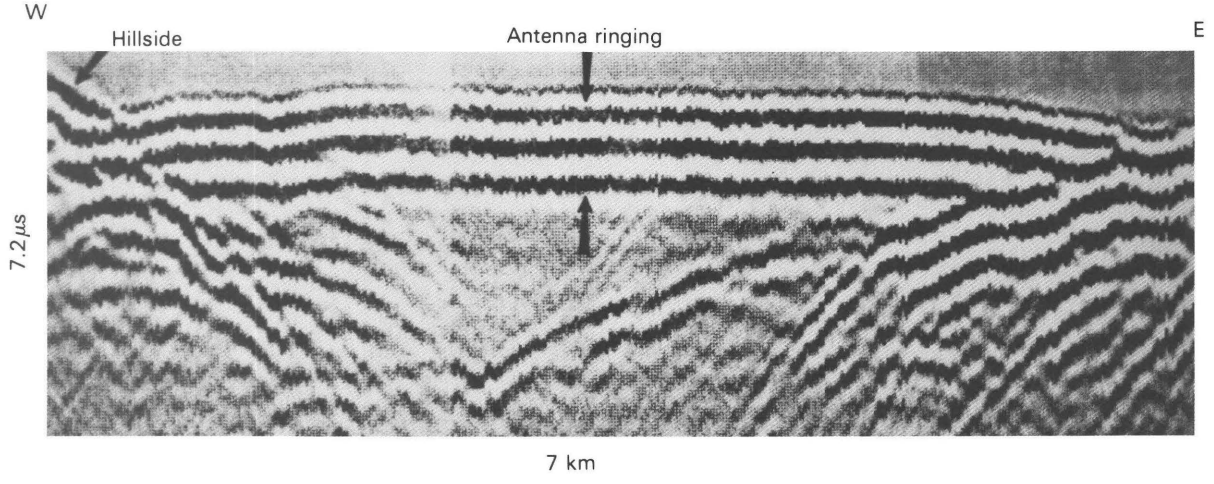

Figure 3. Processed airborne radar profile of figure 2 after deconvolution and filtering operations were applied to compress the long waveform. The digital processing has the effect of concentrating the electromagnetic energy into a narrower time window, thus sharpening the image.

GREENLAND ICE SHEET

Increasing concern about possible anthropomorphically induced climatic changes prompted development of a major polar ice-core drilling program in Greenland by the National Science Foundation (NSF). The primary objective of the program is to obtain a new well-dated continuous ice core from the surface to the base of the ice sheet and to apply the many new analytical techniques that have been perfected since the last ice core was obtained from the Greenland ice sheet (National Science Foundation, 1987). Cores from a polar ice sheet can be used to extract a wide range of detailed paleoclimatic data. In central Greenland, the ice sheet may contain a continuous time record from the present to as much as several hundred thousand years ago at its base, and it should be possible to make measurements having annual time resolution as far back as 10,000 years ago.

The new corehole needs to be drilled in a region where the ice flow is as simple as possible to permit reliable dating and interpretation of the ice core. Because the complexity of ice flow at depth depends to a large degree on the bedrock topography, detailed radar soundings are an essential first step in the selection of an optimum drill site.

In 1987, the USGS carried out an airborne radar survey of a grid centered on the summit of the Greenland ice sheet. The primary objective of the survey was to map the bedrock topography in the general area of the proposed new corehole. The choice of the grid size, 150 by 150 km, was based on having an area large enough to encompass all possible drill sites based on a variety of

criteria (for example, snow accumulation rates); the choice of the grid spacing, 12.5 km, was based on ice-flow considerations (about three to four times the ice thickness).

Survey data were acquired using a new high-speed digital data acquisition system (Wright and others, 1989). In an attempt to maximize the signal-to-noise ratio, summation averaging was employed. For uncorrelated noise and using a coherent (phase preserving) radar system, the improvement in signal-to-noise power ratio is proportional to the number of signals averaged. For a 30-dB improvement in signal-to-noise ratio, 1,000 waveforms must be added. Because the TUD radar system does not preserve phase information, the improvement in signal-to-noise ratio for 1,000 waveforms added would be about 15 dB (Schwartz and Shaw, 1975). There are practical limits to waveform addition, the primary one being the time required to add waveforms, particularly in profiling or borehole-logging operations in which it is desired or necessary to acquire spatially dense data without stopping. Time is especially limiting in airborne profiling because of the high flight speeds involved. For this reason we developed a new data acquisition system (DAS) in an effort to take full advantage of recent technological advances in fast waveform digitizers and high-speed memory chips.

The DAS as shown in figure 4 was used in Greenland with an IBM PC/AT computer equipped with a Professional Graphics Controller (PGC). The mass storage unit used was a Cipher M891 9-track tape drive with cache memory. The tape controller was built by Overland Data. Although 9-track digital tape is not the most compact medium available for data storage and cannot be used at extreme temperatures, it was selected to provide for maximum data transportability from computer system to computer system and to enable storage in an easily archived format. The tape drive is also faster than some tape cartridges, although not as fast as Winchester disks. The measured maximum sustained data transfer rate to the tape drive was 150 kbytes/s. No failures of the tape system were experienced during the Greenland project.

The LC–130 Hercules turboprop aircraft (fig. 5) used for the survey was operated for NSF by the VXE–6 squadron of the U.S. Navy. It was specially modified with coaxial cables running through the wing to hard mounting points for the radar antennas. Part of the 60-MHz four-antenna array may be seen under the wing. The TUD radar system has been very successful in sounding deep polar ice.

During operation, data from the TUD radar were digitized and displayed in real time on the IBM PC/AT computer screen (fig. 6). The Compaq computer on the upper shelf was interfaced to the aircraft inertial navigation system (INS) through a navigational data acquisition system designed and built by engineers at the University of Washington (Terry and Radke, 1986). Because the new radar DAS was untried in the field, there were three additional backup data acquisition systems. The first was a Honeywell Visicorder and camera for continuous photographic copy. That unit was in continuous operation and was in the rack to the lower right of the computers. When the data from both the magnetic tapes and the Visicorder are fully analyzed, comparisons can be made. The TUD radar was also equipped with film-strip recorders. A sampling oscilloscope and an analog instrumentation tape recorder, mounted on the shelf to the right of the Compaq computer, comprised the final backup system. The last system was used as the primary data acquisition system in the first airborne radar sounding of the Columbia Glacier, Alaska, in 1978 but was not needed in Greenland. The Columbia Glacier recording system could not provide data averaging because it used signal sampling and was therefore two to three orders of magnitude slower than the new system.

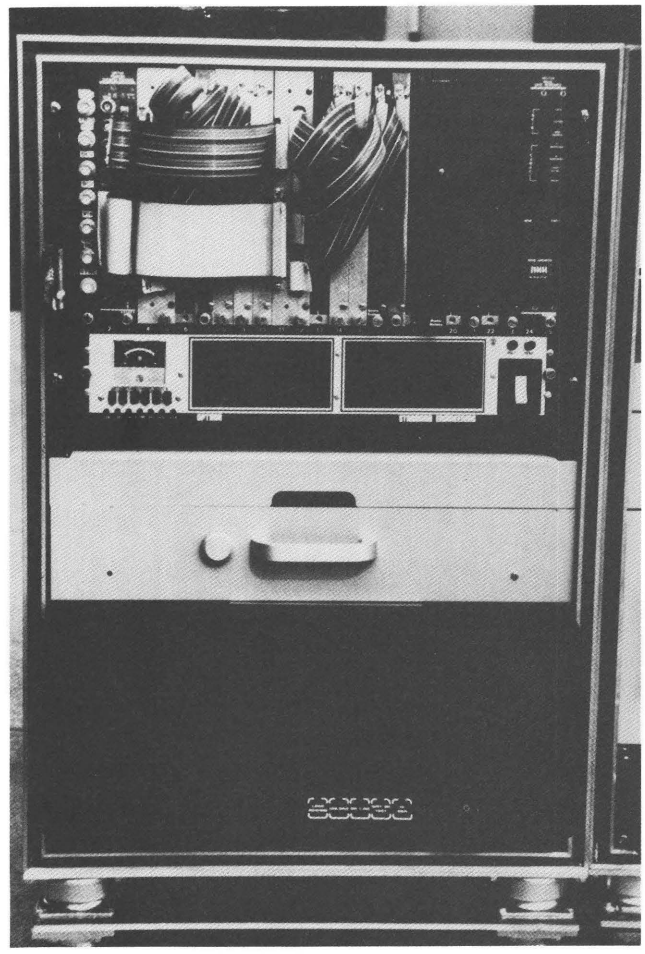

Figure 4. Data acquisition system for the Greenland survey in a 25-slot crate in the upper part of the equipment rack. The tape drive is visible in the lower part of the rack.

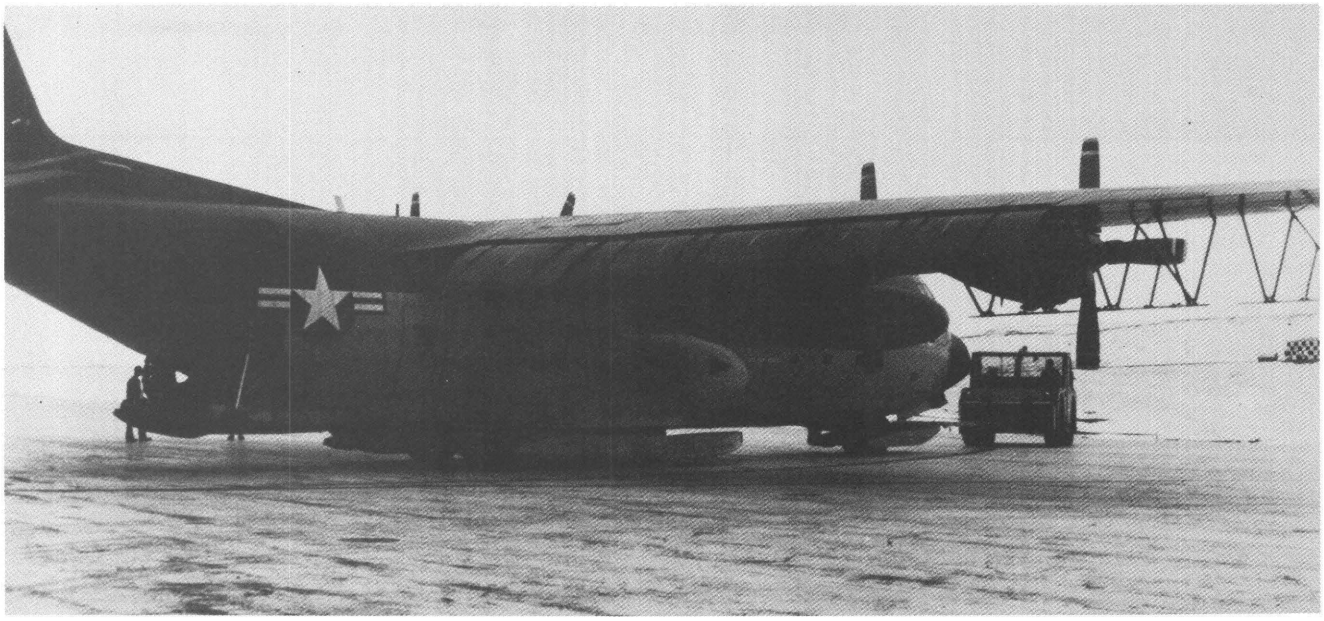

Figure 5. LC–130 Hercules turboprop aircraft operated for NSF by the U.S. Navy. Aircraft is equipped with skis for operations on ice and has special hard mounting points on wing for mounting antennas seen under wing.

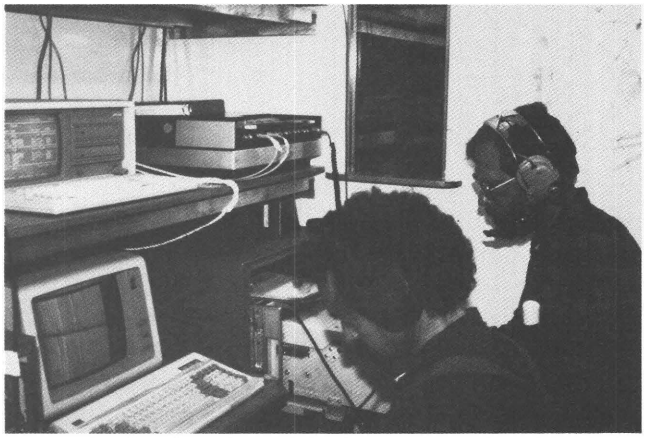

Figure 6. Data from TUD radar were digitized and displayed in real time on IBM PC/AT screen (lower screen). System was operated inside a specially designed electromagnetically shielded hut to avoid possible interference with radar receiver. Upper (Compaq) screen displays navigation data, which are synchronized with radar data recorded on magnetic tape. A Honeywell Visicorder is in right-hand rack, and a back-up instrumentation tape recorder is on shelf to right of Compaq computer. DAS and tape drive shown in figure 4 are in a rack just off left-hand side of photograph.

Fortunately, the new DAS proved to be quite reliable. Initial difficulties with intermittently garbled data disappeared when a general-purpose interface-bus (GPIB) cable was replaced by a shorter one. The first cable was longer than allowed by the IEEE–488 standard for the GPIB and apparently caused problems with the high-speed direct memory access (DMA) data transfers from the DAS to the National Instruments GPIB board in the IBM PC/AT.

The instrumentation was housed in a hut that was designed for use on the surface of the Antarctic ice sheet. The hut is completely electromagnetically shielded and was used in the aircraft because of concern that the digital electronics might radiate enough radio-frequency energy to affect the sensitive TUD radar receiver. In practice, however, the receiver was not detectably affected by the operation of our systems. This proved to be merciful to the DAS operators because the heat produced by our equipment made it very uncomfortable to operate with the door closed despite the presence of two vigorous ventilating fans. The hut's thermal characteristics will be better appreciated in Antarctica.

The location of the survey grid is shown in figure 7. The grid was centered at lat 72°17′38.266″ N., long 37°55′18.483″ W., at the summit of the Greenland ice sheet. The altitude of the ice surface at that point is 3,260 m, and the thickness of the ice is about 3,000 m. The aircraft was flown each day from Thule Air Base to the grid. There was usually enough time on station to fly four to six of the 150-km grid lines on each mission.

The center of the grid was occupied at the time of our survey flights by a field party led by Dr. John Bolzan of the Ohio State University. The presence of the field party was important because it provided us with accurate positioning for calibration of the aircraft instrument navigation system (INS) that became the primary

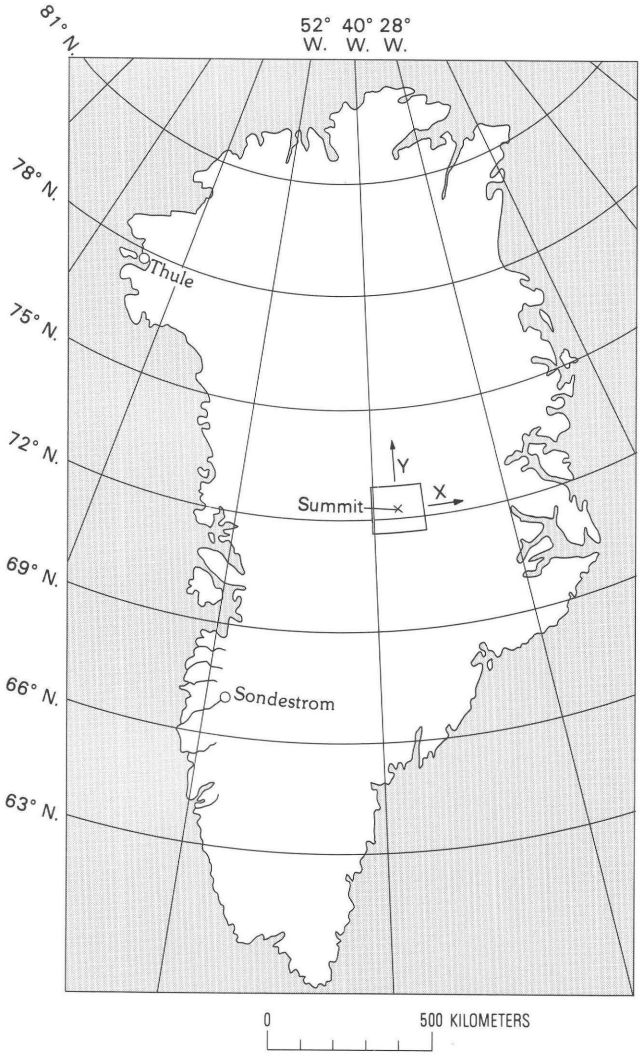

Figure 7. Location of 150 by 150 km survey grid in central Greenland. Center of grid is at summit of Greenland ice sheet at lat 72°17′38.266″ N., long 37°55′18.483″ W., where altitude at the ice surface is 3,260 m. Corners of the grid are as follows:

Northwest corner (X = −75 km, Y = +75 km)
lat 72°57′12″ N., long 40°12′48″ W.;
Northeast corner (X = +75 km, Y = +75 km)
lat 72°57′12″ N., long 35°37′49″ W.;
Southeast corner (X = +75 km, Y = −75 km)
lat 71°36′36″ N., long 35°47′33″ W.;
Southwest corner (X = −75 km, Y = −75 km)
lat 71°36′36″ N., long 40°03′04″ W.

Data also were generally obtained in a 15-km-wide border zone outside main grid.

navigation system. The INS was supposed to be a backup to a Global Positioning System (GPS), but for reasons that are still not clear, it was impossible to lock onto the satellites with the GPS receiver aboard the aircraft, and even a ground-based GPS receiver at Thule Air Base had difficulty achieving a lock on the satellites. This was unexpected because tests using the same system in Greenland during the previous year and at Point Mugu, California, only one month earlier were completely successful. After every two or three flight lines, a pass was made over the base camp to reset the INS to known coordinates. The INS drift between resets was in most cases less than 2 km, so the grid was flown with acceptable navigational control despite the failure of the GPS navigation.

During profiling operations, the data were displayed in raster fashion with signal magnitude converted to a color scale of 256 displayable colors and a screen resolution of 640 by 480 picture elements (pixels). Each waveform was displayed on the horizontal (640 pixels) axis of the screen. The DAS operator could select which points to display by selecting the starting point, number of points to be displayed, and number of points to skip, if any. Six alternative color tables are included in the software, and these can be toggled cyclically without interfering with data acquisition or display. It was found, as expected, that some color tables are significantly better than others in terms of the human eye's ability to discern small differences; however, the best color table for the eye does not necessarily produce the best black-and-white photographic reproduction of the color display. Each data word (digitized sample point) sent from the DAS to the computer is 24 bits. The software is written so that any 8, not necessarily consecutive, of the 24 bits can be displayed.

A significant factor in airborne applications, especially when high spatial data density is desired, is the total system cycle time. The cycle time is a function not only of the DAS parameters such as points per waveform and number of waveforms added but also of the repetition rate of the radar and, especially for small numbers of added waveforms, the time it takes for the computer to read, process, display, and write the data to tape. The number of waveforms added before output to the computer was sometimes varied, but all of the examples shown here use 512 waveforms. The TUD radar was operated for these survey flights with a 12.5-kHz repetition rate. One full screen is 480 lines, and it took about 60 s to fill the screen when adding 512 waveforms. The flight speed averaged about 445 km/hr (240 knots) or 124 m/s. One full screen thus displayed about a 7-km segment of profile, and the along-track density of recorded data was one record every 15 m. During the Greenland profiling each waveform was digitized using 2,048 points at a 40-ns digitizing interval, and thus each record was about 82 μs long, sufficient to record the bottom return at the deepest part of the Greenland ice sheet. The 62 μs required to add 2,048 points in the DAS, plus the 82-μs digitizing window, resulted in a 144-μs period that was longer than the 80-μs period of the 12.5-kHz repetition frequency at which the TUD radar was operated; therefore, every second waveform was captured, giving an effective repetition

frequency of 6.25 kHz. At this rate, and when adding 512 waveforms before dumping the data to the computer, the DAS could have been read at a rate as high as 12.2 times per second; however, the actual rate was about 8 times per second. The difference is due to the fact that the average time required for the computer to read, process, display, and write to tape slightly exceeded the time it took for the DAS to make the data available; therefore, the DAS sometimes had to wait for short periods for the computer to finish its tasks. Most of this excess time was probably involved in the PGC graphics operations. The transfer of data from the DAS to the computer took approximately 12 ms, and the write-to-tape was executed asynchronously, requiring only a few milliseconds to initiate. Five records were accumulated in the tape drive buffer before being written to tape. The actual "write" took about 200 ms to complete. The IBM PC/AT was running at an 8-MHz clock rate, and the software was written entirely in assembly language to achieve maximum speed.

Figure 8 is a black-and-white photographic reproduction of the color screen as it appeared on a segment of a north-south flight-survey line over the base camp. Two metal aircraft cargo pallets set up "A-frame" fashion provided an excellent radar reflector that produced the diagonal stripe (marked by the diagonal arrow). The tip of the arrow near the top of the figure is at the top of the lower of two bright horizontal bands and corresponds to the location of the return from the ice surface; the two bands are caused by receiver saturation. The top saturation band is a residual effect from the transmitter pulse that is present just after the receiver is turned on. The thin dark band between the two bright bands indicates recovery from saturation. The second bright band is due to saturation caused by the strong return from the ice surface. The saturation is the reason that the diagonal return from the pallets does not persist to the surface. The tip of the top arrow also indicates the base camp location. The flight altitude above the ice surface was typically 150–300 m. Because the flight lines were flown at a constant pressure altitude, height above the ice varied for different locations on the grid.

The navigational data were synchronized with the magnetic tape radar data, so that precise geographic locations can be recovered for all of the survey lines after they are fully processed, but the return from the pallets combined with the time calibration marker, faintly visible along the left-hand edge of the figure, provide an alternative means of approximately calibrating the horizontal dimension of figure 8. The marks on the time calibration are at 2-μs intervals. Because the pallet reflection was propagating in air, the propagation velocity was 3×10^8 m/s; therefore, the total width of figure 8 represents approximately 6.4 km. The return from the sub-ice bedrock surface is indicated by the vertical arrow near the bottom of figure 8. Again using the time calibration and assuming an average velocity in the ice of 1.67×10^8 m/s, the thickness of ice at the base camp is calculated to be 3,000 m. It should be noted that small errors exist in the measurements because of curvature in the screen. More accurate measurements will be made as part of the full data reduction process.

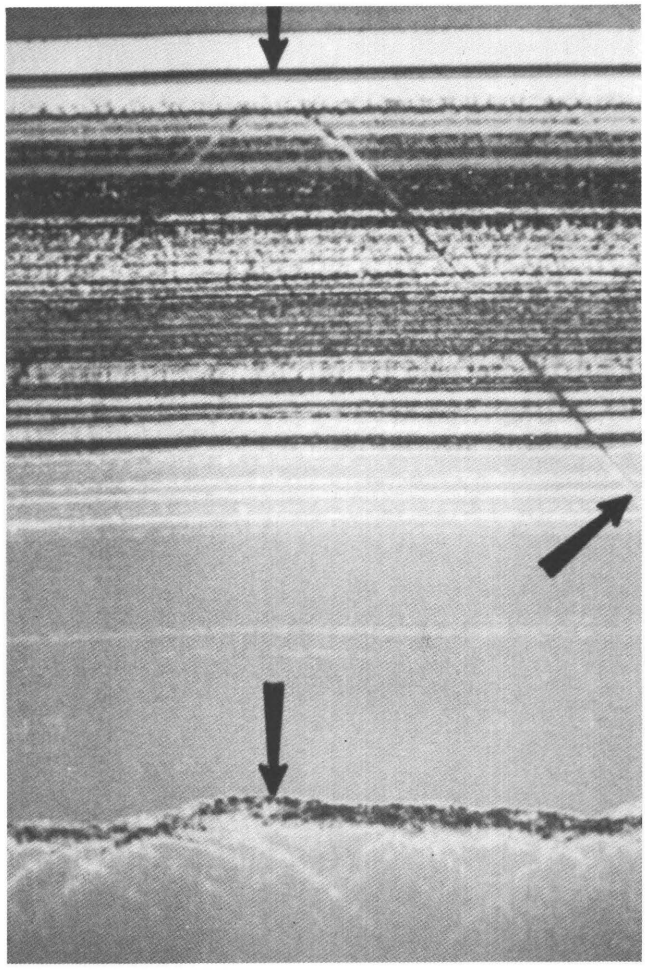

Figure 8. During profiling screen displays a rasterized color scale. Black-and-white photographic reproductions of color screen result in loss of some detail. This image shows a 6.4-km-long segment of a north-south line through centerline of grid (fig. 7). Top arrow locates surface return and also location of base camp set up at center of grid. Diagonal arrow indicates reflection from metal aircraft cargo pallets that were set up "A-frame" style. Bottom arrow indicates reflection from base of ice sheet. At this point, Greenland ice sheet is 3,000 m thick. Sub-ice terrain is not completely flat at this location.

The horizontal stripes below the receiver saturation bands are a common feature of radar sounding of polar ice sheets. This internal layering is postulated to be due to slight increases in the acidity and hence the electrical conductivity of the ice during periods of increased volcanic activity (Hammer, 1980; Millar, 1981;

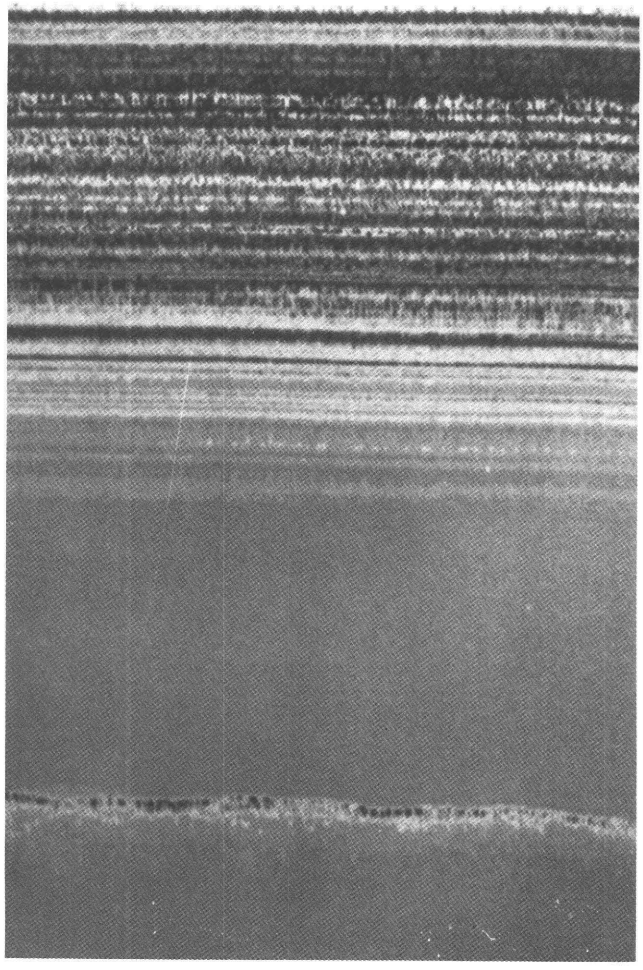

Figure 9. This profile segment is part of a north-south flight line 12.5 km west of centerline of grid. Sub-ice topography is relatively flat. Internal layering is not visible in deeper parts of this region.

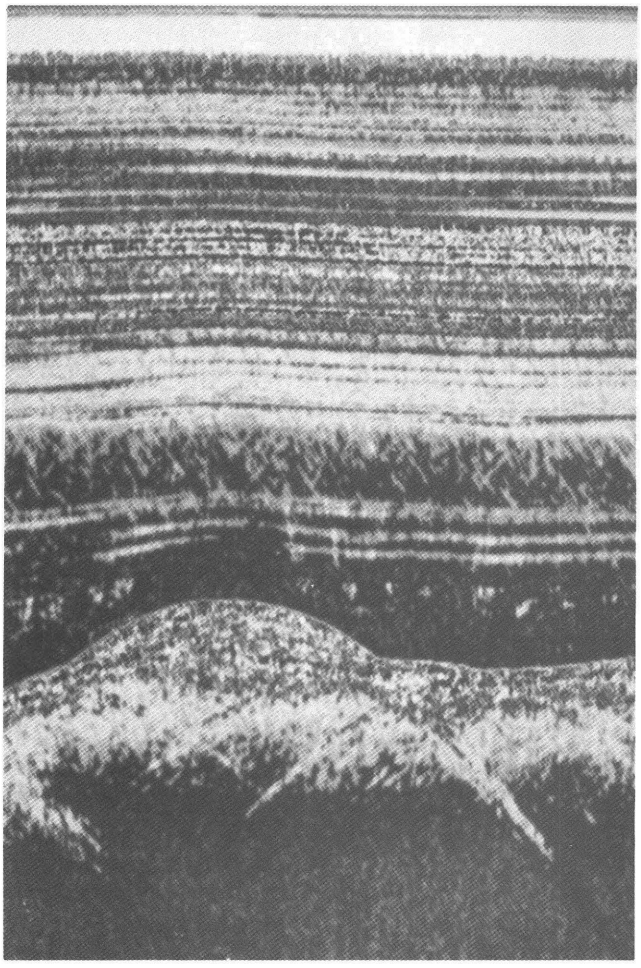

Figure 10. This profile segment is part of a north-south flight line along the more mountainous eastern boundary of grid. Internal layering is visible quite deep in ice and conforms to sub-ice topography. Dot at left-hand side identifies a zone of strong crosshatching thought to be caused by reflections from surface roughness or near-surface crevasses. Slopes of the crosshatching appear to be the same as slopes of return from the cargo pallets in figure 8, as they should be for surface-generated features.

Hodge, 1985). The reflections are particularly dense in the top half and faint or nonexistent in the lower half. It is not clear if this is due to a real change in the electrical properties of the ice at this point in the geologic past (approximately 10,000–20,000 years ago) or to radar system dynamic range limitations. Further investigation is warranted to determine the correct answer to this question.

Figure 9 shows an example of relatively flat bottom topography along a north-south line 12.5 km west of the center of the grid. In general, the topography is flatter in the western part of the grid. Note that internal layering is not visible in the deeper parts of the ice.

In contrast to the previous two examples, figure 10 shows much more mountainous bottom topography. Internal layering is visible quite deep in the ice, and the layers drape over the bottom topography. A zone of crosshatched appearance (marked with a white dot) is thought to be due to reflections produced by roughness of the ice surface caused by wind erosion or by near-surface crevasses. For this interpretation to be correct, the crosshatching should exhibit the same slopes as those produced by the cargo pallet return of figure 8 and would persist to the surface if it were not masked by the internal layering. Figure 10 is a segment of a north-south survey line flown along the mountainous eastern boundary of the grid.

CONCLUSIONS, OTHER APPLICATIONS, AND POSSIBLE IMPROVEMENTS

By designing radar systems tailored to specific applications, both temperate glaciers and cold polar ice have been successfully sounded. Since 1978, the most

significant advances have been made in the area of digital data acquisition, signal averaging, digital recording, and real-time profile display. An order of magnitude saving of time is gained by using real-time digital recording as compared to the previous method of analog recording followed by later digitization. The real-time profiling display also gives the operator an immediate indication of interesting features, anomalous areas, or system problems.

The new data acquisition system incorporates very high speed signal addition and has been very successful. It can record airborne ice sounding radar data having excellent spatial density (10–20 m spacing at LC–130 aircraft speeds in ice 3,000 m thick) while simultaneously adding enough waveforms to achieve significant signal-to-noise improvement (512 waveforms, or 13.5 dB, for uncorrelated noise and a noncoherent radar system such as the TUD radar, or 27 dB for a coherent radar system).

Another significant instrumentation development is navigational control by the global positioning system of satellites (GPS), although the hiatus in the space shuttle program has delayed full implementation of the GPS system. At this writing, only 7 of a planned total of at least 18 satellites are in orbit.

More than 6,000 line-km of ice-sounding radar data over the Greenland ice sheet with good navigational control are now recorded on 9-track computer tape. Maps produced from these data will provide the best topographical information to date of the part of the Greenland ice sheet that was surveyed and will prove invaluable in siting a scientific corehole through the Greenland ice sheet.

Surface and borehole applications of the new DAS will allow more signal addition and therefore increase signal-to-noise enhancement. The system is sufficiently flexible to be used with a number of high repetition rate geophysical radars as proven by the fact that the system was initially designed with no thought of using it with the TUD radar system. The system also may have applications to signal enhancement in other types of active probing, such as ultrasonic scanning, or in any application in which 1–100 MHz signal frequencies and 1–50 kHz repetition rates are required. Use of a higher frequency digitizer or sampling could remove the present 100-MHz upper limit on signal frequencies. Faster static random access memory (SRAM) chips and revised memory architecture would permit the construction of a system that would add signals as fast as they could be digitized. The only limit on signal repetition rate then would be the limits set by the duration of the digitizing window and by data transfer, processing, and display times.

REFERENCES CITED

Brown, C.S., Rasmussen, L.A., and Meier, M.F., 1986, Bed topography inferred from airborne radio-echo sounding of Columbia Glacier, Alaska: U.S. Geological Survey Professional Paper 1258–G, 26 p.

Hammer, C.U., 1980, Acidity of polar ice cores in relation to absolute dating, past volcanism and radio echoes: Journal of Glaciology, v. 25, no. 93, p. 359–372.

Hodge, S.M., 1985, Ice sheet topography and internal characteristics from microwave and radar measurements: International Symposium on Remote Sensing of the Environment, 19th, Ann Arbor, Michigan, October 21–25, 1985, Proceedings, v. 1, p. 237–255.

Millar, D.H.M., 1981, Radio echo layering in polar ice sheets and past volcanic activity: Nature, v. 292, no. 5822, p. 441–443.

National Science Foundation, 1987, FY 1988 geosciences program: Directorate for Geosciences and Directorate for Biological and Social Sciences, Washington, D.C., p. 18–19.

Post, Austin, 1975, Preliminary hydrography and historic terminal changes of Columbia Glacier, Alaska: U.S. Geological Survey Hydrologic Investigations Atlas HA–559, 3 sheets.

Schwartz, Mischa, and Shaw, Leonard, 1975, Signal processing—Discrete spectral analysis, detection, and estimation: New York, McGraw–Hill, 396 p.

Sikonia, W.G., 1982, Finite element glacier dynamics model applied to Columbia Glacier, Alaska: U.S. Geological Survey Professional Paper 1258-B, 74 p.

Skou, N., and Sondergaard, F., 1976, Radioglaciology—A 60 MHz ice sounder system: Electromagnetics Institute, Technical University of Denmark, Lyngby, Rep. R 169, 124 p.

Terry, H., and Radke, L.F., 1986, A new data acquisition and display system for airborne research in Antarctica: Antarctic Journal of the United States, v. 21, no. 3, p. 19–20.

Watts, R.D., and England, A.W., 1976, Radio-echo sounding of temperate glaciers: ice properties and sounder design criteria: Journal of Glaciology, v. 17, no. 75, p. 39–48.

Watts, R.D., and Wright, D.L., 1981, Systems for measuring thickness of temperate and polar ice from the ground or from the air: Journal of Glaciology, v. 27, no. 97, p. 459–469.

Wright, D.L., Bradley, J.A., and Hodge, S.M., 1989, Use of a new high-speed digital data acquisition system in airborne ice-sounding: Institute of Electrical and Electronics Engineers, Transactions on Geoscience and Remote Sensing, v. 27, no. 5, p. 561–567.

SECTION 5: RECENT HARDWARE DEVELOPMENTS

Examples of Two Modern, Integrated Airborne Geophysical Systems

By T.R. Bodger[1]

Abstract

Two modern airborne geophysical systems are described that are being used for mineral-resource surveys in several countries. The first is flown on a fixed-wing aircraft and contains a three-frequency, wing-tip, electromagnetic system, a cesium-vapor magnetometer, and a multichannel radiometrics system. The second system, designed for helicopter use, employs a three-frequency electromagnetic system, a two-frequency very low frequency sensor, and a magnetic gradiometer. These sensors are carried on a sling below the helicopter. The specifications and relative advantages of each system are discussed.

INTRODUCTION

The search for and mapping of subsurface natural resources can be a tedious, costly, and time-consuming project when conducted on the ground. Traverses must be made across mountains, rivers, and swamps and through towns and cultivated areas. In some cases, danger to personnel is involved from disease, animals, insects, and extremes in climate and terrain. If equivalent measurements can be made from the air, great benefits will result in the savings of time and money.

Airborne electromagnetic (AEM) surveying has taken on great importance for base-metal prospecting since the method was first introduced about 1955. In recent years, AEM methods have also been used to make quantitative measurements of the resistivity of near-surface materials such as rocks, overburden, and water. Such measurements can be used to help locate sand and gravel deposits, bauxite, and kimberlite and to assist in ground-water investigations, water-quality analysis, shallow sea bathymetry, sea-ice thickness measurements, and engineering studies such as the selection of suitable sites for radioactive waste disposal and routes for roads and pipelines.

[1]Scintrex Limited, 222 Snidercroft Road, Concord, Ontario L4K 1B5, Canada.

In the past two years, Scintrex Limited has supplied four major airborne systems containing AEM instrumentation to countries throughout the world. Two were helicopter systems and two were fixed-wing systems. To demonstrate the level of sophistication possible in multiparameter aerial geophysical systems in the late 1980's, we will discuss two of these systems, a fixed-wing system sold to the government of India and a helicopter system leased to Suomen Malmi Oy of Finland.

Both systems are multisensor and utilize electronic navigation and digital data acquisition systems. Their instrumentation is both technically advanced and operationally practical, requirements that commonly are conflicting.

THE FIXED-WING SYSTEM

In September 1984, the Indian Ministry of Steel and Mines, acting on behalf of the Geological Survey of India, moved to provide a national capability for airborne geophysical surveying. Scintrex was contracted to provide a deHavilland Twin Otter aircraft integrated with modern airborne geophysical instrumentation (fig. 1), as well as a computer and software for the compilation of maps arising from the airborne surveys. The system was delivered to India in early 1986. At the time this report was prepared, two field survey seasons had been successfully completed, and a third was well underway.

A fixed-wing aircraft has a number of advantages in addition to its low operating costs. First, it has a payload and cabin space larger than a helicopter, and thus can carry more instrumentation and onboard personnel. Second, its operating range is generally three to four times greater than that of a helicopter. Surveys can be flown farther from large population centers, thereby reducing some of the logistical problems of airborne surveying.

Airborne geophysical surveying costs are quite variable (Hood, 1989) (fig. 2). As of the end of 1988, a fixed-wing multisensor (EM, magnetics, and very low

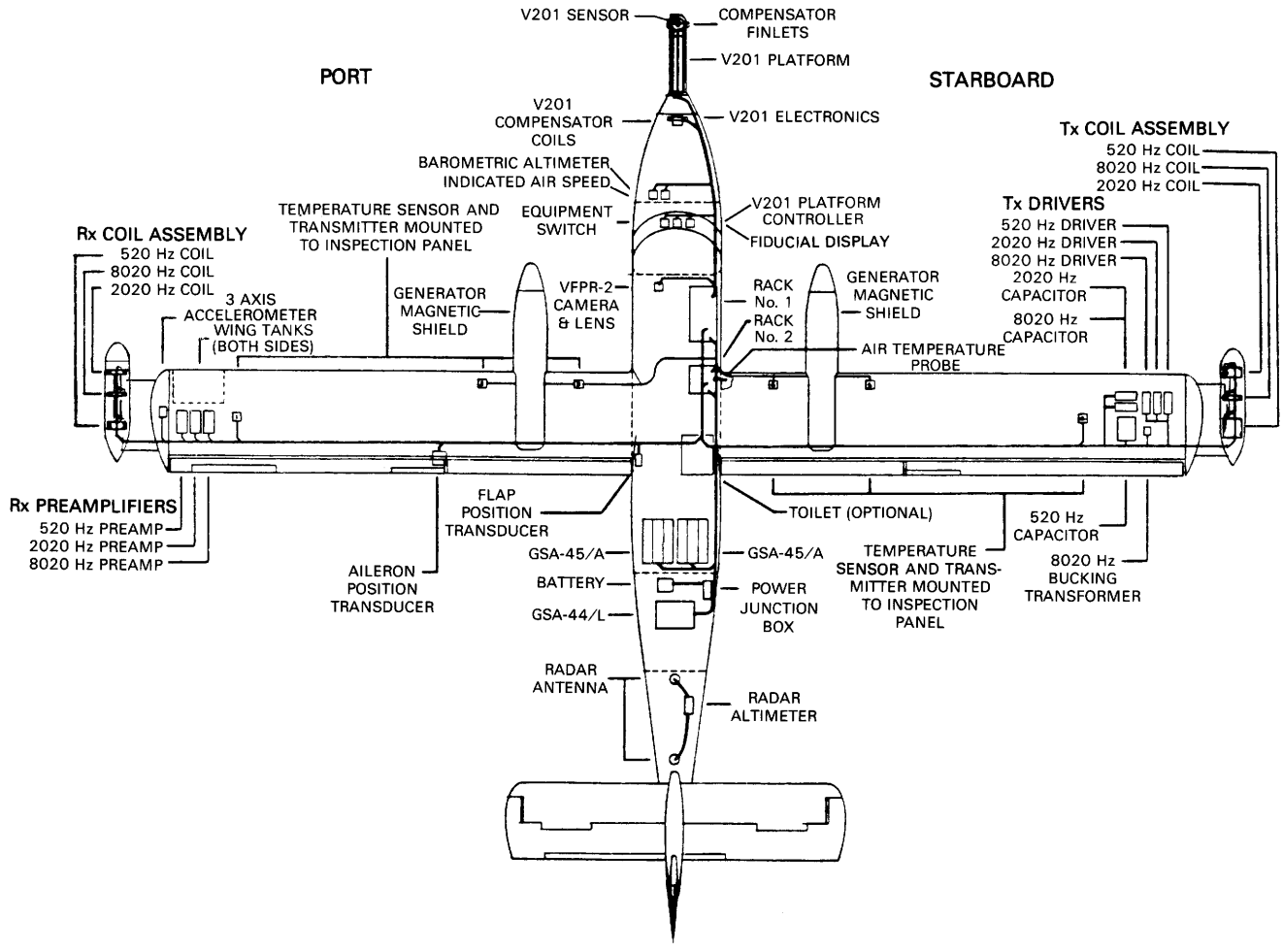

Figure 1. Installation of geophysical, navigational, and ancillary instruments in a Twin Otter aircraft.

frequency (VLF) EM) survey cost about U.S. $35–40/km (U.S. $56–64/mi) to contract. In comparison, a helicopter multisensor survey cost U.S. $60–70/km (U.S. $96–112/mi).

There are several reasons for these differences in prices. A fixed-wing aircraft used for EM surveying generally has an operational range of about 6 hours at an average survey speed of 200 km/hr. Typical production is about 600–650 km per flight, or an average production of about 100 km/hr.

A typical helicopter system has an operational range of about 2.5–3 hours, at an average survey speed of about 100 km/hr. Typical production is about 150–200 km per flight, depending on the length of the survey lines and the terrain over which the survey is flown.

Crew size and costs are about the same for both types of systems. A typical helicopter crew consists a pilot, an operator/navigator, a mechanic, and a geophysicist or dataman. A fixed-wing crew generally also has a copilot/navigator in addition to the other crew members.

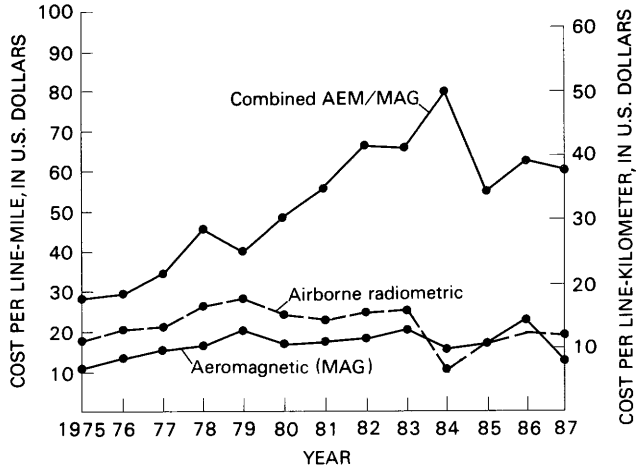

Figure 2. Average yearly worldwide costs per line-kilometer and line-mile for contracted airborne geophysical surveys for the period 1975–1987. Modified from Hood (1989).

Data compilation, mapping, and interpretation costs are similar for both systems.

INSTRUMENTATION IN THE FIXED-WING SYSTEM

Instrumentation in the fixed-wing system includes a three-frequency EM system, a high-sensitivity, optically pumped, cesium-vapor magnetometer with sensor-orienting platform and compensator, and a multichannel radiometrics system. Navigational and positional information is provided by a doppler navigation system. Data outputs from the various geophysical, navigational, and ancillary instruments are recorded by a data acquisition system that includes digital, analog, and video recorders.

The Scintrex Tridem electromagnetic system operates at 520, 2020, and 8020 Hz (Seigel and Pitcher, 1976; Johnson and Seigel, 1986). Transmitter and receiver coils are mounted at the wingtips of the Twin Otter aircraft. The three sets of coils are in vertical coplanar geometry, with a coil separation of 21 m. The Tridem system records the in-phase and quadrature components of the secondary magnetic field as a fraction of the primary field (in parts per million) at the receiver.

The noise level of the system is proportional to the cube of the coil separation. Typically, the Tridem system has dynamic noise levels of better than 20 ppm at a coil separation of 21 m. By comparison, a typical helicopter EM system, with a coil separation of 8 m, has noise levels of 1–2 ppm. If HEM noise levels are extrapolated to a 21-m coil separation, they will be in the same range as Tridem.

This Tridem AEM system includes a number of improvements over earlier versions. The two most significant improvements are the addition of temperature sensors and accelerometers. The principal cause of drift in wing-tip AEM systems is the relative movement of coils as the airframe contracts or expands with changing temperature. Temperature sensors in the wings provide information that can be used to correct the in-phase readings, a technique that may be used to significantly reduce drift. Accelerometers provide information that can be used to eliminate noise caused by aircraft accelerations that distort the airframe and result in changes in relative coil separation and (or) orientation.

The data from the temperature sensors and the accelerometers are not used to make real-time corrections. These data are simply recorded and then used in the postflight processing to make appropriate corrections to the Tridem data.

To calibrate the Tridem system, an accurately measured portion of the transmitter output is fed into the receiver. Because the response of the receiver to this signal is known, calibration of Tridem can be determined.

A Scintrex MAC–4 oriented cesium magnetometer, with a resolution of 0.01 nT, is in an airfoil at the nose of the aircraft. The magnetometer system was specially designed for use in equatorial regions in that its sensor is mounted on an orienting platform and can be remotely and even automatically oriented to its optimum position in the weak fields found in these regions (Hardwick, 1984). In North America, however, an oriented system is not generally required, and, in fact, most cesium magnetometers are operated with their sensors installed in the "strap-down" configuration.

The radiometrics system contains a Scintrex MCA–2 multichannel analyzer capable of providing 256 channels of data from both upward- and downward-directed detector arrays. The terrestrial gamma-ray detector consists of 50 L (3,000 in.^{3}) of sodium iodide. An 8.4-L (500-in.^{3}) detector monitors background atmospheric radiation.

Software in the data acquisition system permits as many as 18 channels of information to be processed. Operations that include windowing and ratioing of the raw radiometrics data are used to correct for Compton scattering and remove the effect of background cosmic rays. The data acquisition system also performs the usual functions of data editing, verification, plotting, and copying.

The navigation system is a Canadian Marconi AN/APN–208(V) doppler navigation system with special survey navigation software. The system derives its heading and attitude information from a Sperry C12 gyroscopic compass and VG14A vertical gyro.

The data acquisition system consists of a Scintrex CDI–7 controller/digital interface with a built-in graphics printer/recorder, two Digi-Data nine-track magnetic tape units, an RMS Instruments GR–33 graphics recorder, a Scintrex NIC–100 navigation interface and ARINC processor, a Scintrex PIC–100 peripheral interface, and a Scintrex VFPR–3 video flight path recover system.

Ancillary instruments such as a power distribution system, radar altimeter, barometric transducer, and rack-mounted test instruments are part of the system.

THE HELICOPTER SYSTEM

The main advantage of a helicopter system is that in most terrains it can fly sufficiently low to the ground to ensure good resolution. Although helicopter cabin space commonly is restricted, modern aerial geophysical instruments can still be installed to make a number of measurements. In helicopter installations, the gamma-ray sensors are carried on board, and the magnetometer and electromagnetic sensors are towed underneath, away from noise sources originating in the helicopter.

The towed sensors are easier to install in a helicopter than in fixed-wing aircraft. Installation in a helicopter can be made very rapidly and, if necessary, can be made in a helicopter very close to the survey area; thus

small-scale surveys can be carried out quite economically using locally available helicopters. Once the survey is finished, the instrumentation can be removed from the helicopter and stored until required. Unlike fixed-wing aircraft, helicopters generally do not need to be heavily modified and need not be dedicated to aerial geophysical surveying for long periods of time. Furthermore, the type of helicopter is less critical than the choice of an aircraft because magnetic and electromagnetic sensors are not mounted on the helicopter but rather are slung below it. Helicopters commonly used for magnetic, electromagnetic, and radiometric surveying include various light- to heavy-duty models produced by Aerospatiale, Bell, Hughes, Sikorsky, and other manufacturers.

Helicopters for geophysical surveys increasingly are being used to fly zones where the utmost detail is required. A fixed-wing aircraft such as the Twin Otter can fly grids with lines spaced from 200 m to as much as 0.5 km apart. Helicopters equipped with appropriate navigation systems regularly fly grids with lines spaced 100 m apart or less at much slower speeds and at lower flight levels than are feasible with the fixed-wing aircraft. As a result, higher resolution is possible.

INSTRUMENTATION IN THE HELICOPTER SYSTEM

The equipment prepared for Finland is perhaps the most sophisticated system ever installed in a helicopter. It includes a three-frequency helicopter electromagnetic (HEM) system, a VLF-electromagnetic system, a vertical aeromagnetic gradiometer, and a multichannel radiometrics system. A radio navigation system is used to provide accurate navigational and positional information. The data are recorded by a data acquisition system in both digital and analog form. As a backup to the radio navigation system, a video flight path recovery system is also used (fig. 3).

The HEM system is a Geotech EMEX–1 three-frequency unit with its receive and transmit coils installed in an 8-m-long Kevlar bird that is towed 45 m beneath the helicopter (fig. 4). The three frequencies used are 900, 7800, and 51,000 Hz. The geometry of the coil-pairs is vertical coplanar for 900 Hz and horizontal coplanar for 7800 and 51,000 Hz. These frequencies were chosen to detect conducting zones and to provide data for resistivity mapping in the high-resistivity environment where the surveys will be flown.

The VLF system is a Herz Totem 2A system,which simultaneously operates at two frequencies in the 15–25 kHz frequency range (Herz, 1986). The parameters measured are the change in total field and the vertical quadrature field. The Totem 2A includes a sensor with three mutually orthogonal iron-cored coils and a preamplifier. The assembly is installed inside an airfoil used as a spreader between the HEM tow cable and the gradiometer tow cable. Data from airborne VLF–EM systems are mainly used for interpreting large-scale geological features such as faults and conducting rock units, although under favorable circumstances, smaller conductors such as sulfide mineralization may be revealed.

The magnetic gradiometer system consists of two Scintrex MAC–3 magnetometers installed in another towed-bird airfoil constructed of Kevlar. The gradiometer is towed beneath the helicopter on a 35-m-long cable. The two sensors are rigidly installed on the bird and are vertically separated by a distance of 3 m. Each of the magnetometers has a resolution of 0.01 nT, and the vertical gradient is measured to a resolution of 0.005 nT/m. The sampling rate is 10 times per second. The nose of the gradiometer bird is attached to the tow cable of the HEM bird (see fig. 4).

The multichannel radiometric system is very similar to that installed in the fixed-wing system, except that the gamma-ray sensor package consists of a single 16.8-L (1,000-in.^{3}) detector installed inside the helicopter cabin.

Navigation information is provided by a Del Norte Trisponder system, which uses dedicated microwave transmitters to provide signals to an onboard digital distance measuring unit. Postflight processing can locate the helicopter with an accuracy of 1–2 m.

A video flight path recorder provides backup flight path recovery capability, and a radar altimeter provides terrain clearance information. The data acquisition system is similar to that used in the fixed-wing system.

This system is large and heavy by helicopter geophysical system standards; therefore, a heavy-duty helicopter is needed as the system platform. The helicopter chosen was an Aerospatiale 360C Dauphine: a large, twin turbined-engine helicopter that has good performance characteristics. The craft is capable of flying 100-m-spaced grid lines. Survey speed is typically 100 km/hr (60 mph) with a nominal altitude of 65 m above the ground.

CONCLUSIONS

Fixed-wing and helicopter aerial geophysical systems are designed for use in very different terrains, although helicopter systems are providing high-resolution surveys in areas traditionally reserved for fixed-wing systems. Fixed-wing installations are more difficult to make than helicopter installations, and once instrumentation is installed it is not advisable to use the aircraft for other purposes. A system should be designed for either fixed-wing or helicopter use to avoid making compromises that might affect system performance; however, many system components can be used in either type of system.

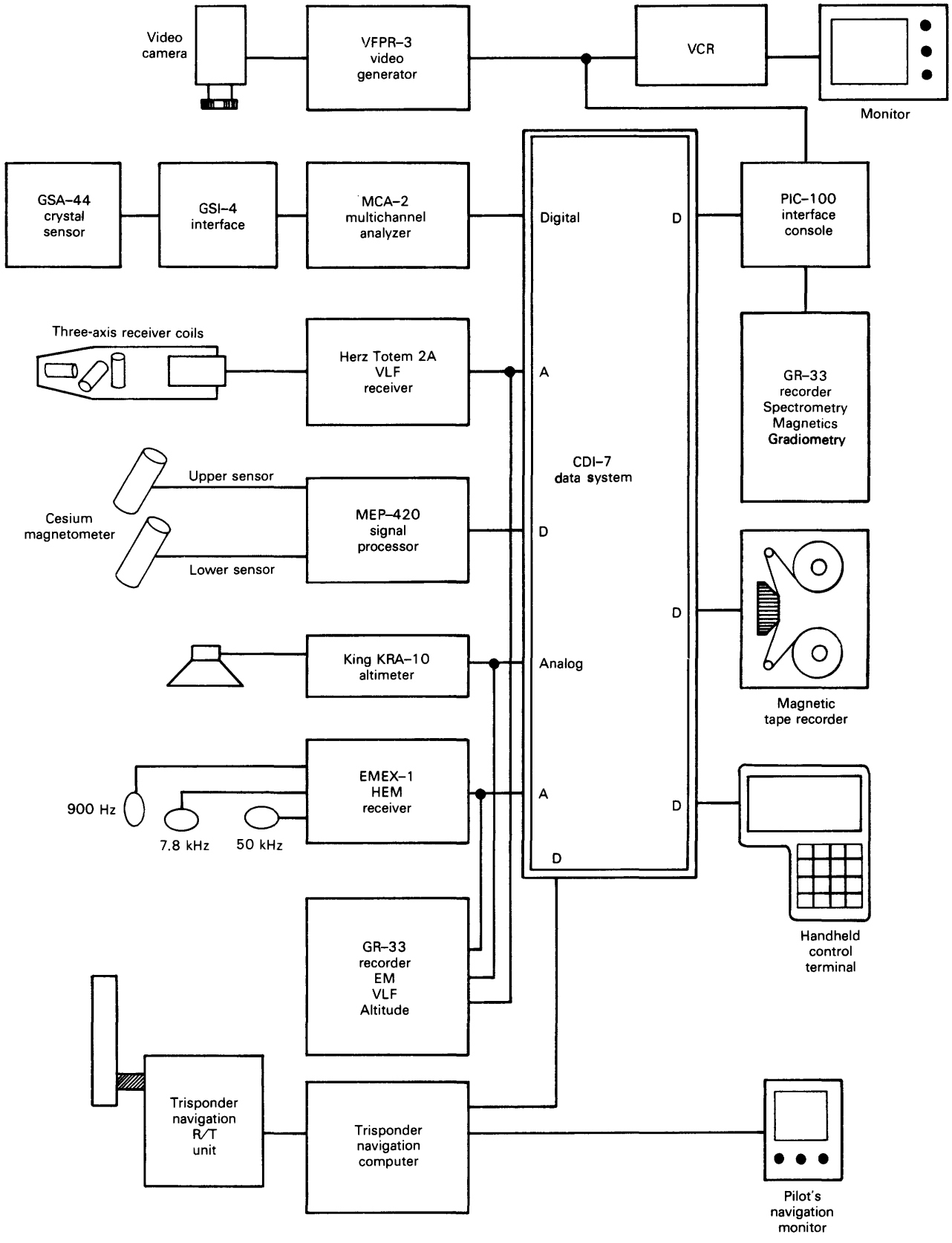

Figure 3. Block diagram of the Scintrex multisensor helicopter geophysical survey system.

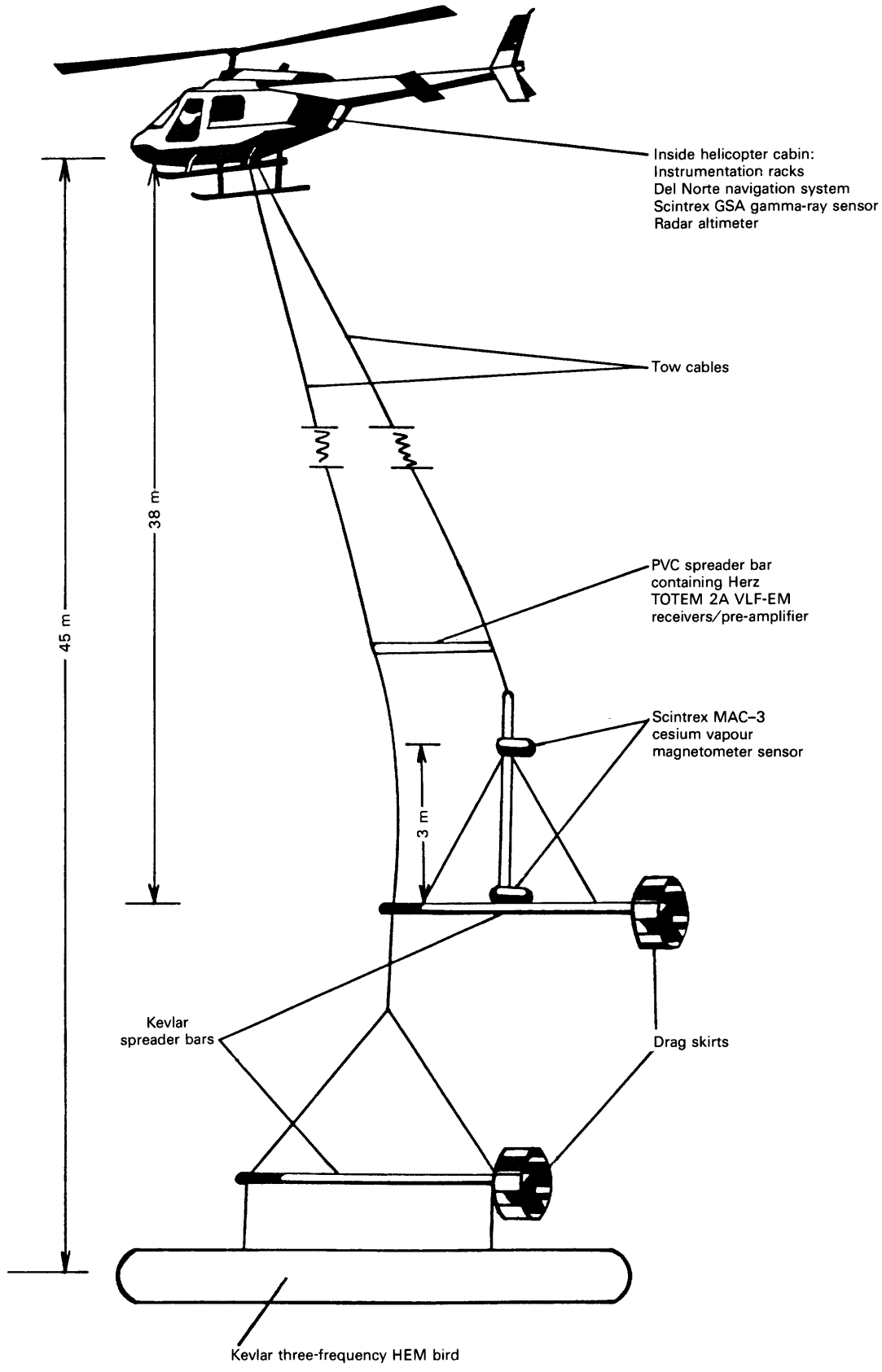

Figure 4. Mounting of sensors on sling used with the Scintrex helicopter geophysical survey system.

REFERENCES CITED

Hardwick, C.D., 1984, Non-oriented cesium sensors for airborne magnetometry and gradiometry: Geophysics, v. 49, p. 2024–2031.

Herz, A., 1986, Airborne EM instruments operating at VLF and higher frequencies, *in* Palacky, G. J., ed., Airborne resistivity mapping: Geological Survey of Canada Paper 86–22, p. 55–61.

Hood, P.J., 1981, Aeromagnetic gradiometry—A superior geological mapping tool for mineral exploration programs, *in* Weinstock H., and Overton, W.C., eds., SQUID applications to geophysics: Society of Exploration Geophysicists, p. 72–77.

_____1989, Mineral exploration trends and developments: Canadian Mining Journal, p. 11–34.

Johnson, I.M., and Seigel, H.O., 1986, Tridem resistivity mapping for natural resources development, *in* Palacky, G.J., ed., Airborne resistivity mapping: Geological Survey of Canada Paper 82–22, p. 125–129.

Seigel, H.O., and Pitcher, D.H., 1976, The tridem airborne electromagnetic system—A multi-purpose natural resource mapping tool: Scintrex Applications Brief 76–3.

Airborne Electromagnetic Mapping Using Powerline Fields

By Victor F. Labson[1]

Abstract

The U.S. Geological Survey has developed a passive airborne magnetic-field receiver for mapping conductive targets using electromagnetic fields generated by powerlines. The low frequency of these fields (60 Hz in the U.S.) allows mapping in areas of thick or conductive overburden. This technique may be useful in highly developed areas where the powerline fields are so strong that they prevent the use of more traditional active electromagnetic techniques.

The prototype receiver consists of a wingtip-mounted three-component magnetic field sensor, a narrow-band N-path synchronous-switched-capacitor filter, and a synchronous detector. It provides very accurate and stable determination of the real and quadrature field strengths in the directions in line, transverse, and vertical to the flight line.

It is unlikely, except in the most unusual case, that the primary powerline field can be determined. The character of the field is controlled both by the location of the many powerlines in an area and their load, which may change with time; thus, relative measurements must be used for interpretation. The most diagnostic parameters from the early field tests are the horizontal polarization parameters of azimuth and ellipticity and the vertical polarization parameters of tilt and ellipticity measured in the azimuthal direction.

The receiver has been tested over several geologic targets both on the ground and in the air. Ground surveys were conducted in the Denver, Colorado, area over steeply dipping faults and contacts. The powerline measurements compare favorably with very low frequency and audio-magnetotelluric resistivity measurements made along the same lines. An airborne test was flown in northern Minnesota in the Precambrian shield area. The receiver functioned well over the entire survey area, even when relatively far from powerlines. Comparison of results with very low frequency and magnetic results obtained on the same flight lines is currently under way.

INTRODUCTION

The use of ambient electromagnetic (EM) signals for airborne mapping of conductive targets is of great value in integrated geophysical surveys. Passive electromagnetic techniques do not generate signals that interfere with devices such as other passive EM receivers or magnetometers. Elimination of a transmitter reduces the weight and size of the EM system; costs are significantly reduced because the system can be used in light fixed-wing aircraft.

The primary example of passive EM systems is the airborne very low frequency (VLF) receiver, which is flown regularly with other geophysical systems. The VLF receiver uses signals from communication transmitters in the 20,000-Hz range and is appropriate for mapping conductivity within the first tens of meters of the surface.

The first passive technique was the audiofrequency magnetic method (AFMAG), which promised much deeper penetration than VLF, in fact deeper penetration than any active system at the time. Using 140- and 510-Hz signals from atmospheric sources, AFMAG showed promise for airborne applications. AFMAG, at least in its original design, was restricted by several limitations including low signal level during winter, particularly in high northern latitudes, and poor reproducibility due to changing source field polarization (Ward and others, 1966). Because of the questionable nature of the results, AFMAG failed to gain widespread acceptance.

The use of powerline electromagnetic fields eliminates the signal strength limitation of AFMAG. The source, although generally indeterminate, is relatively unchanging and measurements can be repeated. The low frequency of the fundamental harmonic (60 Hz in North America) allows much deeper penetration than VLF while retaining the advantages of light weight and passive operation.

Ground electromagnetic surveys using powerline fields have been conducted in at least two cases with success (Strangway and others, 1980; McCollor and others, 1983). Frank Frischknecht of the U.S. Geological Survey (USGS) undertook a program to develop an airborne receiver for profiling using the 60-Hz fundamental frequency of powerline fields, and original design and ground test profiles for that program are summarized by Merkel (1986).

Acknowledgments.—Much of the early development of the powerline receiver was performed by Dave Merkel as part of his Master of Science thesis at the

[1]U.S. Geological Survey, MS964, Box 25046, Denver, Colorado 80225.

Colorado School of Mines. His ground profiles and comparisons to VLF and AMT responses were invaluable in preparing for airborne testing.

A very special acknowledgment must be made to Frank Frischknecht. Before his death, he was responsible for the development of this receiver. Much of the theoretical basis and design for this investigation are his. He closely supervised the entire program including the initial airborne survey. He is sorely missed.

INSTRUMENTATION

The system developed by Frischknecht has been installed in the USGS single-engine turboprop Fairchild Porter aircraft. It consists of a three-component magnetic field sensor and a three-channel phase-sensitive synchronous detector. The system is lightweight and compact and has little impact on aircraft payload or space. A small computer, the HP75C, provides real-time processing of the digital data for quality assurance by the operator. The system requires no operator tuning or other intervention beyond monitoring the real-time output.

The sensor consists of three electrostatically shielded, 25,000-turn, ferrite-cored induction coils that have a natural resonance of approximately 900 Hz. The three coils are tuned capacitively to 60 Hz and have a noise level, with their preamplifiers, on the order of 10^{-5} nT/$\sqrt{\text{Hz}}$. They are shock mounted in a gimballed frame that is self-righting (fig. 1). The mechanical resonance of the sensor is near 5 Hz. A great deal of care was devoted to eliminating resonances near 60 Hz. The sensor is contained in a wingtip pod, and components are oriented in line, transverse, and vertical to the flight line. Low-noise preamplifiers for the induction coils are mounted in the wingtip pod. The preamplifiers include four-pole, Butterworth high-pass filters that have a –3 dB point at 40 Hz to reject motion and vibration noise.

The receiver is a narrow-band, phase-locked, synchronous detector (fig. 2). The signal from each magnetic field component is first low pass filtered to protect against aliasing in the narrow-band N-path filter section (Franks, 1973). The N-path filter is a digitally controlled, sampled data filter that uses previous cycles of the frequency of interest to predict the next. All three channels are controlled by the same crystal to create a bandpass filter at 60 Hz that has a 0.5-Hz bandwidth. Even with this high center frequency to bandwidth ratio the filter is exceptionally stable in amplitude and phase. The filter allows rejection of higher harmonic frequencies of the powerlines as well as noise at frequencies close to the desired primary frequency of the powerlines.

This narrow band signal is amplified by an automatic gain-ranging amplifier controlled by level detection

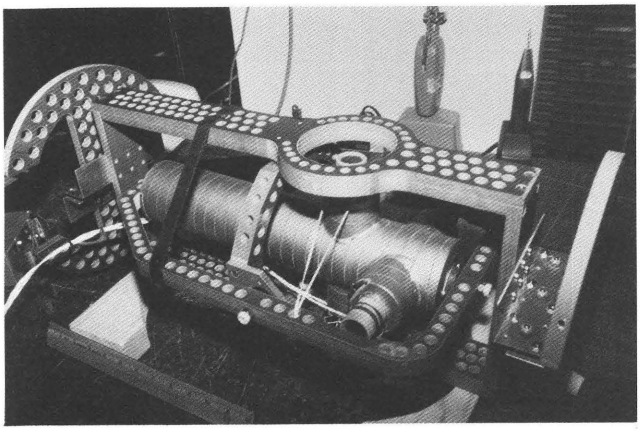

Figure 1. Airborne powerline sensor. One-foot ruler shown for scale.

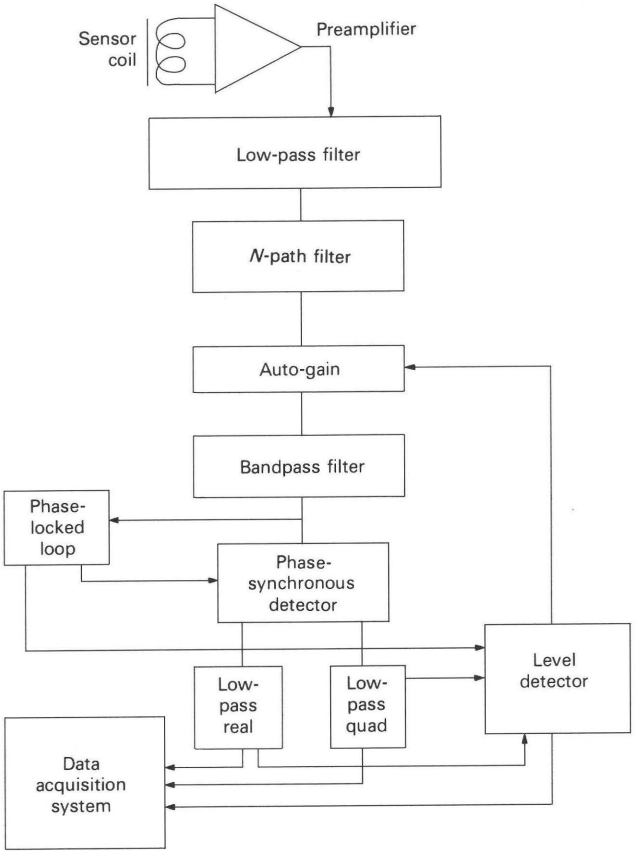

Figure 2. Block diagram of powerline receiver. Modified from Merkel (1986).

of the sum of the synchronous detector outputs of the three magnetic field components. The gain-range selection is stabilized and is only allowed when the data acquisition system is not sampling. The amplified signal is bandpass filtered to remove direct-current offsets and the N-path filter's clock noise in preparation for synchronous detection.

Synchronous detection is achieved by four-quadrant square-wave multiplication of the narrow band signal. In-phase and quadrature amplitudes are separated by use of square waves shifted by one-quarter cycle. The in-phase square wave is generated from the sum of the three narrow-band magnetic field signals by a phase-lock loop. The quadrature square wave is a time delay of the in-phase square wave. By phase locking to the signal, the synchronous detector's center frequency is always the actual powerline frequency.

The in-phase and quadrature outputs of the synchronous detectors are integrated by a low-pass filter that has selectable time constants. These integrated outputs and the gains are digitally recorded by the primary aircraft data acquisition system. They are also acquired for real-time processing by the HP75C computer for monitoring by the operator.

DATA REDUCTION AND INTERPRETATION

It is unlikely that the primary powerline field can be determined because of the unknown locations of the powerlines and the variations in the currents carried by them. In this case of an unknown primary field, all interpretation must be performed on the relations between different components of the magnetic field rather than on the absolute measure of each component.

It is a fair assumption that over the survey area the primary field will be linearly polarized and dominantly vertical; thus, variations of the magnetic field's polarization, particularly the ellipticity, will be indicative of conductive anomalies. The airborne real-time processing system has been programmed to display total field, horizontal azimuth, horizontal ellipticity, and vertical tilt and vertical ellipticity in the azimuthal direction. In flight tests, the polarization quantities were observed to be generally slowly changing with distance except over pipelines and powerlines.

Much refinement is needed in data reduction and interpretation. It is possible that the responses of common geologic targets are smaller than the changes in primary field polarization. If this is so, then some method of normalization, filtering, or possibly estimation of the primary field is required.

TESTING

Prior to flight testing, the powerline EM receiver was tested over several cultural and geologic features (Merkel, 1986), and notable responses due to pipelines, fences, and powerlines were recorded. A survey line in the foothills south of Denver made using 60-Hz, VLF, and audiomagnetotelluric methods (AMT) provides a good example over a geologic target (fig. 3). The response is from a set of steeply dipping sedimentary

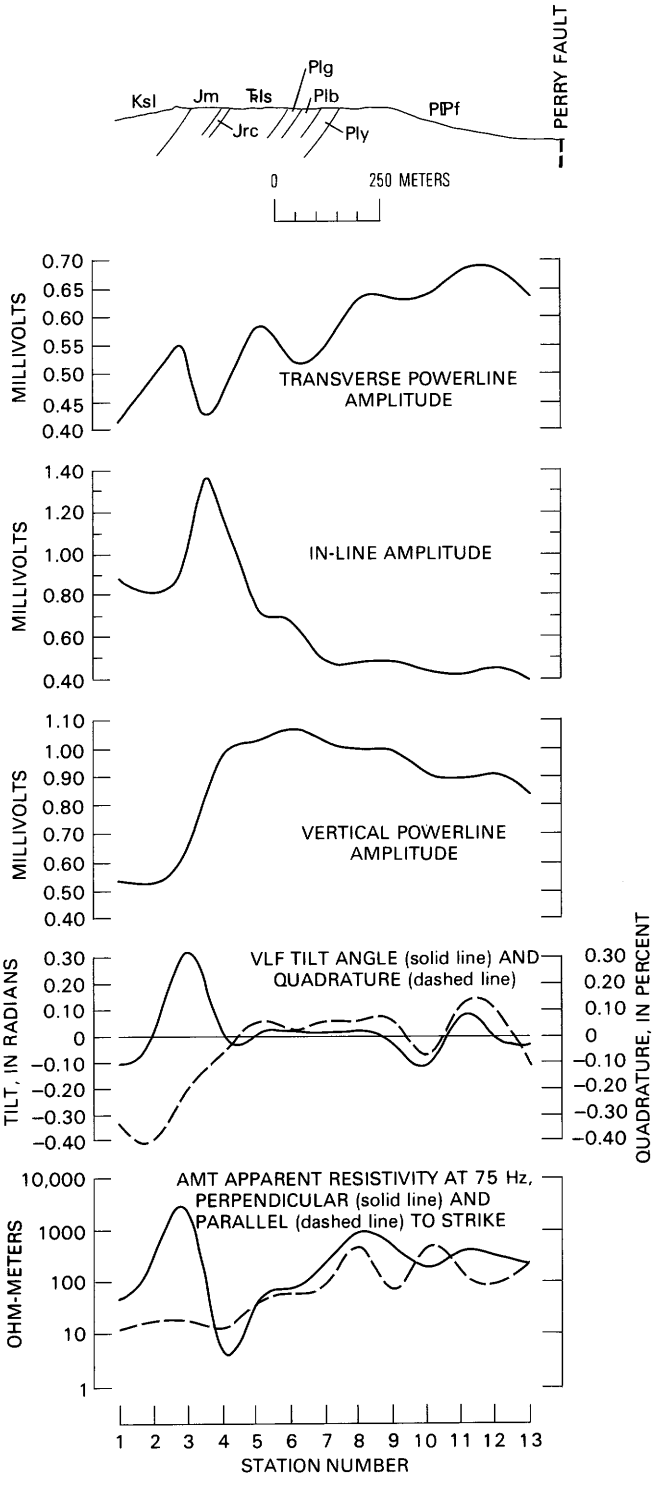

Figure 3. Ground survey in foothills south of Denver, Colo. Geologic units: Ksl, Lytle Formation; Jm, Morrison Formation; Jrc, Ralston Creek Formation; TRls, Lykins Silty Shale; Plg, Lykins Limestone; Plb, Lykins Shale; Ply, Lyons Sandstone. Modified from Merkel (1986).

beds of contrasting resistivity; the most prominent response is at the contact between a moderately resistive Cretaceous sandstone and a more conductive Jurassic silty shale. The AMT profile, oriented perpendicular to strike, shows the resistivity contrast between the sandstone and the shale, and a large VLF anomaly is seen over the contact as well.

The powerline EM response is best shown, in this case, by examination of the amplitudes of the three field components. A crossover in the vertical amplitude is at the same position as a maximum in the in-line component and a minimum in the transverse component. This is the expected response of a conductor whose strike direction differs from the primary field direction. The changing primary field direction along the profile can be seen from the trends in both the in-line and transverse amplitudes. The fact that a sedimentary contact generates a detectable response in an area with a spatially changing primary field orientation prompted airborne testing of the receiver.

The preliminary flight testing of the receiver was carried out in the Denver area over pipelines and isolated powerlines. A number of receiver noise sources were identified. Low-frequency noises were easily dealt with by mechanical damping of the sensor mount and improved high-pass filtering in the preamplifier. A more difficult noise was found to be synchronous to the propeller, a common problem in aircraft that have turboprop engines because of their very constant and limited range of speed. In the USGS Porter, the noise is at 62 or 64 Hz for the two cruise powers. This noise, which is picked up by the sensors, can be larger than the powerline field. The original arrangement of the functional blocks of the receiver allowed the phase-lock loop to lock to this propeller noise. This problem was solved by rearranging the functional blocks of the receiver (fig. 2) and increasing the sensitivity of the system first by reducing the coil damping and by decreasing the bandwidth of the N-path filter. These modifications increased the useful range from a powerline substantially, and the system was deemed ready for an applied field test.

The airborne test area was in the Precambrian shield of northern Minnesota where the glacial overburden is too thick for VLF to penetrate. The powerline data were acquired along 15,600 mi of a routine magnetic survey. Several hundred miles were reflights of VLF profiles. Initial examination of the data suggests that the useful range from the powerlines is only about 10 mi. Within this range the data quality appears to be very good, though no interpretation was attempted to confirm this assumption.

CONCLUSIONS

The powerline EM receiver produced good ground results and appears to have performed satisfactory in an extensive airborne test. From this work, several conclusions were reached. The electronic noise level, and thus sensitivity, of the receiver is adequate. This noise level is far below all other sources of noise. However, the 10-mi range from average powerlines is inadequate. Necessary improvements include reduction of vibration noise in the sensor by further isolation and mechanical damping and increased selectivity by narrowing the receiver's bandwidth, principally by decreasing the bandwidth of the N-path filter. The bandwidth can easily be made half its present width.

Much work remains in data reduction and interpretation. The simple polarization parameters may reflect too much of the primary field's characteristics. A variety of normalization and spatial filtering techniques could be applied to separate primary from secondary fields.

With improvements in instrumentation and completion of a system of data processing and interpretation tools, airborne EM mapping using powerline fields shows great potential for becoming an inexpensive method for locating conductive targets at depths beyond the penetration of other passive EM receivers.

REFERENCES CITED

Franks, L.E., 1973, N-path filter, *in* Temes, G.C., and Mitra, S.K., eds., Modern filter theory and design: New York, John Wiley, p. 465–503.

McCollor, D.C., Watanabe, T., Slawson, W.F., and Shier, R.M., 1983, An EM method for earth resistivity measurements using powerline harmonic fields: Journal of Geomagnetism and Geoelectricity, v. 35, p. 221–244.

Merkel, D.C., 1986, The development and ground testing of the U.S. Geological Survey airborne sixty-hertz reconnaissance system: Golden, Colorado School of Mines, M.S. thesis, 125 p.

Strangway, D.W., Redman, J.D., Holladay, S., and Horne, C., 1980, Audio-frequency magnetotelluric soundings at the Whiteshell Nuclear Research Establishment and Chalk River Nuclear Laboratories: Atomic Energy of Canada, TR–71, 58 p.

Ward, S.H., O'Donnell, J., Rivera, R., Ware, G.H., and Fraser, D.C., 1966, AFMAG; applications and limitations: Geophysics, v. 31, p. 576–605.

Mini Remotely Piloted Vehicle Systems in Mineral Exploration, Earth Sciences, and Environmental Studies

By H. Zafrir[1], G. Steinitz[2], *and* M. Granot[3]

Abstract

The development of mini remotely piloted vehicles (MRPV) provides new opportunities for their use in earth science and environmental studies. MRPV platforms can be used for a wide variety of geophysical and imaging measurements including video photographs, radiometrics, magnetics, electromagnetics, gas analysis, and temperature. Such data collection platforms allow large areas to be quickly surveyed even under adverse ground conditions. Telemetry of data to a ground station permits real-time analysis.

INTRODUCTION

The ability to collect, process, and assess large amounts of data from airborne platforms conducting regional surveys is critical in today's dynamically developing world. Mini remotely piloted vehicle (MRPV) systems, developed and proven as military systems, can be adapted for civilian mapping and monitoring missions. Such systems can provide a means of both real-time data acquisition and online data processing close to the area of interest and thus enable fast, highly professional evaluation and effective response to the critical parameters and targets involved.

In the MRPV system, a small remotely piloted aircraft carrying a scientific payload is piloted from a control station to fly and collect data over any terrain and transmit the data back to the ground control station in real time for online processing.

The scope of operations for which MRPV systems can be used in civilian tasks is very wide. We present a basic concept for the use of such a multidisciplinary and modular system that allows a dual mode of deployment: (1) routine use in civilian surveys, and (2) readiness for use in case of environmental disaster. Such a dual mode of deployment allows optimal use of the system for many tasks, increases the cost effectiveness of the system, and insures a high serviceability of the system and readiness of the operating team, trained in routine daily use of the system, for disaster control.

SUGGESTED MISSIONS AND TASKS

Possible missions in the earth sciences and environmental surveys for the MRPV include:

1. Video photogeologic inspection of the ground for a variety of geologic mapping tasks at flexible and varying scales. Ground targets may be directly viewed, recorded as pictures, or annotated onto maps. This is especially applicable in remote and inaccessible areas.
2. Radiometric airborne surveys of the surface distribution of the naturally occurring radioactive elements (uranium, thorium, potassium). The surveys may be used for geologic mapping and mineral prospecting, as well as for construction of background radiation maps for environmental monitoring.
3. Airborne magnetic and very low frequency (VLF) electromagnetic surveys as a geological and geophysical mapping tool in mineral prospecting.
4. Airborne electromagnetic (EM) surveys, including hydrological surveys and determination of ice thickness in polar regions.
5. Airborne monitoring of gases over volcanic or other geothermal areas and analysis of gases over gas and oil fields, specific crops, and industrial areas.
6. Local monitoring of atmospheric conditions such as surface and air temperature and humidity.
7. Transmission of large volumes of data, in real time, between dispersed geophysical data acquisition systems and large central data processing stations by utilizing the flight and communication capabilities of the MRPV.
8. Control of continental and marine traffic.

Possible environmental disaster control missions of the MRPV include:

1. Damage assessment and direction of relief activity in the event of natural disasters such as earthquakes, floods, hurricanes, volcanic eruptions, and forest fires.

[1]Soreq Nuclear Research Center, Yavne, Israel.
[2]Geological Survey of Israel, Jerusalem, Israel.
[3]Mazlat Ltd., Holon, Israel.

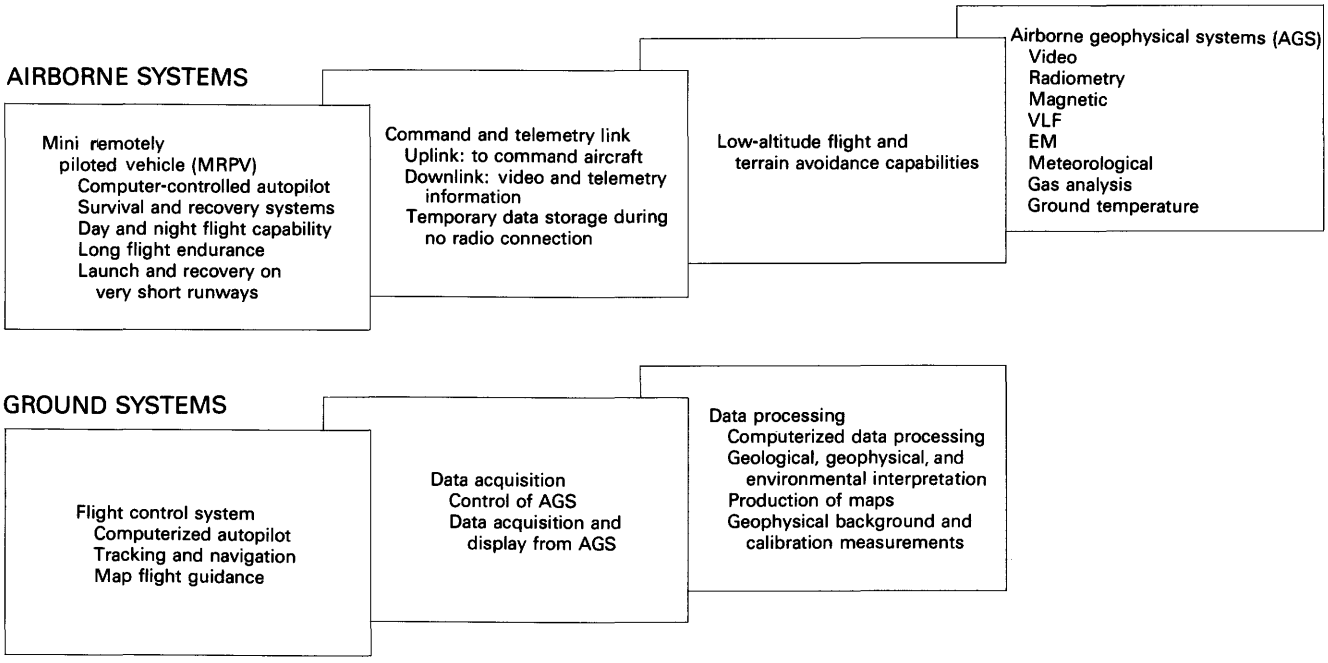

Figure 1. Suggested configuration of mini remotely piloted vehicle (MRPV) for surveys in the earth and environmental sciences.

2. Environmental monitoring of reactor sites and other nuclear installations to determine the distribution of nuclear pollutants in the air and on the ground.

3. Immediate data collection during industrial and environmental accidents, such as release of noxious or toxic substances from chemical and metallurgical installations, to monitor the source and distribution of pollution in the atmosphere, on the surface, or in the sea.

DESCRIPTION OF PROPOSED SYSTEM

The suggested equipment should consist of two subsystems (fig. 1): the airborne subsystem and the ground subsystem. The airborne subsystem can be based on an existing small remotely piloted airplane adapted to carry a modular scientific payload. Such a platform can fly at various altitudes at low speeds, thereby giving long mission durations. The activity of the airplane is governed by an onboard flight computer. Navigation of the airplane is in two modes: radar (distance and direction) tracking system and global positioning satellites (GPS). The flight plan is preprogrammed into the flight computer. A sophisticated radio link serves for the control of the aircraft and for telemetering the data to the ground subsystem.

The ground subsystem, the elements of which control the activity of the airplane and its scientific payload, perform the data acquisition and storage. This allows advanced options of data reduction and processing using existing or special purpose systems.

The following technical specifications for the airborne geophysical system (AGS) are suggested:

1. An existing stabilized television camera to provide a real-time picture of the observed area in the ground control station monitor. The picture is recorded by a video recorder for additional evaluation. The data may also be analyzed by an image-processing system. The camera enables remotely controlled zoom capabilities of 1:15, camera rotation of 360°, pitch scanning range from –105° to +5°, and direction and stabilization control independent of flight direction.

2. A radiometric module for measuring natural gamma-ray radiation that has a sensitivity of 1–2 ppm equivalent uranium at elevations of 60–100 m. The system is miniaturized and based on bismuth germinate crystals. Such a spectrometric unit can measure the natural surface radioactivity of uranium, thorium, and potassium, as well as the distribution of any artificial radioactive isotopes on the surface or in the air. Such a system is well adapted for monitoring radioactive contamination.

3. A magnetic module composed of two highly sensitive, lightweight wingtip magnetometers working as a horizontal gradiometer. Resolution and accuracy of each magnetometer is 0.1–0.5 nT, based on existing instrumentation.

4. A VLF module for measuring the change in the secondary total and vertical quadrature field, due to geological features, as generated by fixed external sources broadcasting in the range of 15–25 kHz. The

specifications of the airborne instrumentation are based on existing systems.

5. Systems for electromagnetic, meteorological, gas analytical, and ground temperature measurement are under consideration.

The following aircraft specifications are suggested for planned missions. Some of these have already been developed for existing military MRPV's. Others will have to be developed. The airplane will be a modular structure built of composite materials. Its overall length will be 4.2 m and its wingspan 5.2 m. Total vehicle weight will be as much as 160 kg, with a scientific payload of as much as 30–40 kg. Flight capabilities will be from altitudes of 100 to as much as 5,000 m at speeds of 110–140 km/hour. Under these conditions, missions of as long as 7 hours are possible.

Flight planning will be done manually or using an expert system. The flight plan will be preprogrammed into the flight computer, and as many as several tens of flight segments will be held in memory. The flight plan can be updated at any stage of the operation. Navigation will be performed using line-of-sight radar or GPS. An operational range of 50–200 km is possible with a navigation precision of at least several tens of meters. A sophisticated wide-band radio link will allow transmission of data and video.

The MRPV can take off from any landing strip (including a dirt road) of less than than 250 m. Alternatively it can be launched by a pneumatic launcher or via rocket-assisted takeoff (RATO). It is recovered using a net or an arresting cable.

The entire system, including aircraft, ground control and processing stations, and other ground support equipment, can be transported by several 4×4 pickup trucks. The MRPV can be disassembled and packed into containers for transport. The ground control and processing systems are housed in small, rugged, air-conditioned shelters. Deployment time is about 2 hours after arrival at a site.

Preparation, launch, and recovery of the aircraft requires one person. Handling of the aircraft and scientific payload requires one or two people, depending upon the complexity of the mission. Data analysis requires from one to four people.

Field servicing of the equipment can be accomplished by two technicians using built-in test equipment and line-replaceable units (LRU).

SUMMARY

Realization of the suggested MRPV system will allow scientific teams to conduct multidisciplinary surveys in the field, while working in optimal environmental conditions using state-of-the-art analytical tools. Payloads may include a wide spectrum of optical, geophysical, and geochemical analytical sensors. The system is modular in design of the instrumental payloads and thus can serve a wide range of disciplines. This modularity also allows easy upgrading once new scientific payloads become operational. In many situations, around the clock operation of the system may be conceived. The mobility of the system allows easy operation over wide areas, as well as easy transportation to remote areas.

APPENDIX

APPENDIX—WORKING GROUP REPORTS, PANEL DISCUSSION, AND NAMES AND ADDRESSES OF PARTICIPANTS

Instrumentation and Data Processing Working Group Report[1]

A. Becker *and* A. P. Annan, *Leaders*

INTRODUCTION

Systematic geological mapping of the continental United States indicates a potential for stimulation of resource exploration through the use of airborne geophysical surveys. Implementation of such a program, now virtually nonexistent, will surely result in much improved access to our economic resources. It will also provide much help in the solution of our environmental problems and, finally, will certainly result in technical improvements to our military posture. Airborne electromagnetics (AEM) is central to such a program. AEM surveys are a particularly cost-effective means of mapping silicate geology. The U.S. Geological Survey (USGS) should be entrusted with the management and coordination of the scientific and technical effort in this discipline. In this, they can secure much help from universities, industry, and other government agencies.

A large working group, composed of some 20 scientists from government, industry and university, met to discuss the state of the art in AEM instrumentation as well as the area of data processing and presentation. Finally, the discussion turned to the role that each of the three partners in progress should play in the application of AEM to the production of superior and cost effective geological maps. Here we speak, of course, of the USGS, the universities, and the airborne geophysical survey industry. Only through careful cooperation can the task before us be accomplished.

CURRENT CAPABILITIES

The general consensus was that existing technology has not been exploited to the fullest extent possible. Specific requirements need to be identified and appropriate funding supplied before any major new system developments are likely. Existing technology has been successfully applied to producing:

1. Mineral exploration maps,
2. Geological maps,
3. Sea-ice thickness and coastal bathymetry maps,
4. Ground-water contamination maps, and
5. Saltwater intrusion maps.

In addition to traditional base-metal exploration, these new application areas place additional demands on the technology and the advances that have and are being made. Significant problem areas requiring attention remain to be addressed. Industry in general is responding to new market opportunities.

PROBLEM AREAS

The following items were identified as problem areas that need to be addressed in future research and technology development:

1. More accurate calibration and reliable zero-levels are needed if systematic data processing that makes use of computerized imaging/inversion is to become widespread. New applications will place demands for systems producing quality data with minimal system artifacts.

2. Data volume is increasing and data archiving standards and technologies to allow rapid retrieval are required.

3. Display methods for multifrequency/multicomponent data sets are evolving; however, more advances are required, particularly in the area of imaging AEM data.

4. Concern was expressed on the subject of civilian access to full global-positioning satellite (GPS) capability. The general consensus was that 1-m horizontal and 10-cm vertical positioning accuracy would be more than satisfactory for the foreseeable future.

5. Concern was expressed that multisensor surveys may result in degraded quality of some of the sensor data. For example, magnetometer operation can be somewhat degraded when operated with a high-power AEM system. In many applications, however, multisensor data acquisition is desirable and occasionally mandatory.

[1]The following people participated in the Instrumentation and Data Processing Working Group: A.P. Annan, A.R. Barringer, A. Becker, T.R. Bodger, D.C. Fraser, A. Herz, R.L.S. Hogg, J.W. Ioup, V.F. Labson, E. Morrison, A. Poikonen, D. Pridmore, S.W. Reford, D. Stanley, M. Steiner, B. Sternberg, C. Vaughan, I.J. Won, and H. Zafrir.

6. The lack of a button-on fixed-wing towed-bird system was identified as a gap in the spectrum of AEM systems currently available.

7. The question as to the cost effectiveness of AEM for geologic mapping was raised. All those attending were painfully aware of this topic and felt that user education is most important.

NEW TECHNOLOGY

Many suggestions were forthcoming in this area, including the following major items:

1. No one system will satisfy all spatial-resolution and exploration-depth requirements. New technology should strive toward general-purpose receiver and sensor technology with applications dictating transmitter, power, and platform requirements.

2. Development of new technology or application of existing technology to monitor system geometry should be part of instrument improvements.

3. The role of passive systems should be expanded and the following topics were discussed: future VLF source reliability; use of natural fields (AFMAG); use of powerline signals (including harmonics); use of Omega transmitters; and use of ELF systems.

4. Extension of system bandwidth is needed as systems are refined and improved to make full use of interpretation capabilities.

5. Airborne radar has been demonstrated in ice-covered areas. Opportunities exist for extension of this technology to other environments.

6. Data archiving procedures compatible with geographic information systems (GIS) must be developed.

7. New systems and processing techniques need to address flight-direction-dependent data problems.

8. More attention needs to be paid to the opportunities presented by RPV's (remotely piloted vehicles).

9. Superconducting transmitters may represent an opportunity in the future.

RESEARCH GOALS

Three areas of research were identified. The first of these is of an applied nature and relates to the USGS responsibility for identifying new, cost-beneficial applications of AEM. The second relates to making AEM data more accessible to the geoscientific community. This indeed must be done if AEM is to be accepted by the scientific and general public. Although no clear path to that goal was indicated, many approaches have yet to be tried. Finally, we arrived at the question of instrumentation. Although this point was not explicitly made in the group discussion, it is obvious that the process of choosing a particular system for a particular application must be scientifically formalized, and procedures for experimental design should be reexamined. The new techniques used in the field of knowledge engineering could be of much help. We see three areas of research opportunity: testing of new applications, new methods of data presentation, and formalization of the experimental design process.

TASK ASSIGNMENT

United States Geological Survey

1. Identify the opportunities for using AEM systems for geological mapping in a variety of different environments.

2. Recognize problems being addressed by other government agencies where AEM surveys can be of help, such as pollution detection and monitoring and bathymetry.

3. Play a leadership role in the application of AEM to new problems by funding and coordinating surveys to demonstrate new technology concept feasibility to the exploration community, particularly to geologists and other government agencies.

4. Fund research of the identified problems.

5. Address data archiving issues raised by the systematic collection of AEM data including data reporting standards and integration of geophysical data into geographical information systems (GIS).

6. Make other government agencies aware of the geoscience community's need for access to full global-positioning system (GPS) resolution data.

Universities

Traditionally, universities have played a role in the advancement of national objectives by evolving and document new knowledge and by training personnel. In this, they seek the cooperation of government agencies so that their research is timely and the skills of the graduates may be put to solving tomorrow's problems as well as those that beset us today.

Industry

Most of the advances in the area of AEM surveying have been made by industry. Not only has industry mastered the operational logistics, but it has also responded to market demands with new and improved instrumentation. The responsibility for the operational aspects of most airborne surveying should be consigned to industry, and the task should be carried under USGS specifications set in consultation with industry (both data consumers and data producers) and universities.

Interpretation Working Group Report[2]

Melvyn E. Best, *Leader*

CURRENT CAPABILITIES IN AIRBORNE ELECTROMAGNETICS

Most current electromagnetic (EM) systems were designed and built for mineral exploration—the search for conductive orebodies. As these systems have become more sophisticated, principally through increased bandwidth, they have been used for resistivity mapping. Apparent resistivity maps can be generated for some systems, and layered-earth inversions have been successful with others.

Current interpretation methods include one-dimensional inversion and model fitting to obviously non-one-dimensional anomalies. For geological mapping purposes, few attempts have been made to combine these approaches because of the expense and complexity of modeling methods for the general inhomogeneous case.

Airborne surveys routinely use free-space plate models for interpreting anomalies. More realistic models, such as conductive sheets and ribbons, arbitrary two-dimensional conductive bodies in layered conductive media, and sphere models, exist and have been used to illustrate response characteristics of particular systems. They are not used, however, for routine interpretation.

For one-dimensional interpretation, equivalent half-space resistivity models have been very useful. Recently, some inversion solutions for an overburden layer, or seawater, over a resistive basement have been developed. Several direct methods have been developed for determining conductivity as a function of depth. In general, EM systems have not been designed for geological mapping applications, and their data are not optimized for one-dimensional interpretation.

Airborne VLF methods are used for geological mapping and are particularly useful for locating contacts, overburden thickness variations, and fault zones. At least one system also measures the horizontal electric field so that apparent resistivities can be determined.

NEW TECHNOLOGY AND FUTURE APPLICATIONS

A major discussion point centered on modeling. Faster, easier to use numerical models are required. New approximations to numerical modeling (for example, a fuzzy model of the earth with no sharp conductivity contrasts), which speed up run times and provide forward models suitable for fast stable inversion schemes, must be developed. The use of parallel processing for the existing numerical programs can speed them up by a factor of 20 or more. A compilation of basic model results that provides a set of interpretation curves over a number of realistic geological situations is needed. In particular, model results should be developed and stored so that the data can be used for a variety of new and existing systems. Perhaps this work should be coordinated by the USGS.

Better methods for detection of nonlayering (lateral inhomogeneities), particularly for geological mapping, are required. Pattern-recognition techniques, when coupled to modeling, can provide the basis for the development of artificial intelligence (AI) applications and expert systems. Interpretation of these nonlayered geological situations can then be accomplished using the stored model results in the basic data base. Another approach to handling areas that are nonlayered would be to use perturbation methods.

Utilizing work stations to display and manipulate the data can provide new methods of interpretation. Real-time processing and display methods coupled to such a work station would allow quick comparison of many models to the data.

Future emphasis will likely focus on interpretation methods that are more directly related to geological sections and maps. Inversion schemes that provide easy to interpret data similar to seismic sections are required. Perhaps interpretation can be enhanced by methods that provide a direct relation to seismic methods so that migration and other seismic techniques can be used. Finally, new dedicated computer hardware, such as the reversed triple-A concept (application, algorithms, and architecture), can be used to solve very large, complex resistivity modeling problems in both the time and frequency domains.

PHILOSOPHY AND RESEARCH GOALS

Although a large-scale general geological mapping program using AEM is not warranted, a limited program involving selected applications is quite important in furthering national interests. These applications include environmental, ground-water, and geological mapping problems. For example, AEM can be used to extend

[2]The following people participated in the Interpretation Working Group: W.L. Anderson, M.E. Best, D.V. Fitterman, M. Goldman, C. Guillozet, G.W. Hohmann, H.F. Morrison, A.K. Sinha, and P. Valla.

geological mapping beneath cover and to map cover thickness, faults, and contaminated zones.

In order to conduct such a program, data processing and interpretation techniques need to be improved and optimized because little of this kind of work has been done in this country. In addition, cultural noise and anomalies will present difficult problems in many areas.

We recommend a test program by the USGS, in cooperation with AEM contractors and universities, to evaluate the applications of AEM to specific problems of importance to the United States. Ground-water mapping in the southwest U.S. and monitoring of saltwater intrusion in coastal areas are examples of such problems. Test surveys in these regions should be flown in many different environments and existing automatic interpretation techniques should be tested using both these field data and synthetic data from realistic physical and numerical models.

More sophisticated automatic interpretation techniques must be developed, tested with synthetic data, and used to interpret data from test surveys. These advanced interpretation techniques might include adjustment of stitched-together one-dimensional inversions along a profile to study the effects of lateral changes. Approximate inversion schemes for two-dimensional resistivity formations are another research area. The new generation of parallel computers, including reverse triple-A machines, may permit sophisticated real-time applications.

Consideration should be given to developing new types of systems or measurements, such as VLF apparent resistivity mapping, tensor AFMAG, and multicomponent towed-bird measurements.

PROBLEM AREAS

A variety of problems presently limit the usefulness of interpretation of AEM data. First, an easily accessible catalog of responses is lacking for geologically realistic models for both numerical and scale-model results for complex (non-one-dimensional) models. Such models could be used both to understand the type of responses to expect and in interpretation.

Second, a systematic assessment of existing AEM systems has never been done using experimental design techniques to evaluate their performance for many geologic targets. Thus it is difficult to specify which system to use for a specific target.

Third, hardware restrictions create interpretational problems. Frequency-domain systems typically suffer from the limited number of frequencies. Time-domain interpretation would be improved by recording multicomponent data. Along these lines, the effect of INPUT window times on data interpretation needs to be analyzed.

Although automatic data interpretation schemes have been developed, more robust methods are needed that can handle several common problems. For example, data should be flagged that do not conform to layered-earth models.

Galvanic effects on data interpretation are not fully appreciated. Likewise, the effects of cultural conductors such as pipes, fences, and powerlines are not understood and need to be identified. This is becoming increasingly important as AEM surveys are used more frequently for environmental problems in developed areas. Model studies of the galvanic and cultural effects should be undertaken.

There is little experience in the United States of geologic interpretation based on interpreted AEM data. Small-scale studies in different geologic settings are needed to assess the utility of different AEM methods.

Resources Working Group Report[3]

George J. Palacky, *Leader*

OBJECTIVE OF SURVEYS

The prime objective of airborne electromagnetic (AEM) surveys is to contribute to the development of geological mapping in three dimensions and to mineral-resource assessment. AEM systems have developed to the stage that conductivity maps can now be routinely obtained. Conductivity is a physical property that is characteristic of many lithologic types and mineral deposits; conductivity of geologic formations now can be determined even in the presence of Quaternary surface cover. Depending on the type of the AEM system used and geologic conditions, penetration is from 100 to 400 m.

Airborne electromagnetic surveys may be flown in conjunction with other airborne geophysical systems, in particular magnetic and gamma-ray sensors. By themselves, AEM systems are cost effective as mapping tools, but their capability is often enhanced by the use of multiple sensors. The use of AEM as an effective tool in geologic mapping and mineral exploration has been demonstrated in Palacky (1988). AEM systems have also been used in geothermal exploration, ground-water prospecting, soil-salinity mapping, permafrost studies, Arctic sea-ice thickness determination, and shallow-ocean bathymetry.

Several countries use AEM methods as part of their national mapping programs (Finland, Norway, Sweden, Thailand, the U.S.S.R., and the Canadian provinces of Ontario and Quebec); the most comprehensive program is in Finland. Between 1959 and 1972, all of Finland was surveyed using a fixed-wing aircraft equipped with magnetic, electromagnetic, and gamma-ray sensors (total flown 800,000 line-km). In 1972, another survey was initiated using more advanced equipment and a tighter line spacing (200 m). By the end of 1985, the Geological Survey of Finland had carried out 676,000 line-km of the second-generation survey (Peltoniemi, 1986). In Quebec between 1969 and 1985, 558,600 line-km of combined AEM and magnetic surveys were flown for the provincial government (Lefebvre and others, 1986). At present, the governments of Austria, Bulgaria, China, Finland, Germany, India, Norway, Sweden, and the U.S.S.R. operate AEM systems (Palacky, 1986).

RECOMMENDED SURVEY SPECIFICATIONS

Meaningful AEM data can be obtained using either fixed-wing or helicopter systems flying at low ground clearance. The mean clearance should not exceed 120 m for the former and 30 m (sensor height) for the latter. The required line spacing is in part determined by the geology and the scale of mapping desired. Working at a scale of 1:50,000, the recommended flight line spacing should not exceed 500 m.

In order to obtain high quality data consistent with state-of-the-art equipment, the following procedures are recommended:

1. Use of electronic navigation for position accuracy and possible infill flying.
2. Use of wide-band or multifrequency, multigeometry AEM systems.
3. Accurate calibration of AEM systems, which is necessary to obtain post-processing output in standard physical units.
4. Standardization of AEM system output (identical digital formats for systems of the same class flown in different surveys).
5. Centralized archiving of all original and processed data.
6. Publication (or other suitable forms of public data release) of conductivity maps at appropriate scales and edited data sets.

PRESENT LIMITATIONS AND PROBLEM AREAS

Before commencing a systematic AEM survey, two problem areas should be investigated:

1. The design of a suitable instrument package for routine surveying. At present, final products of AEM surveys (such as conductivity maps) are not identical if different systems are used in data acquisition (for example, time-domain towed-bird surveys versus multifrequency helicopter surveys). Production of AEM maps unaffected by the survey technique may never be possible because of the fundamental difference of some systems (for example, large versus small coil separations, asymmetry of some systems). If other geophysical sensors such as radiometric spectrometers or magnetic gradiometers are used in conjunction with electromagnetic systems, results may be compromised

[3]The following people participated in the Resources Working Group: J.D. Corbett, C. Guillozet, D.B. Hoover, J. Klein, G.L. Raines, R.J. Smith, and C.M. Swift, Jr.

(particularly serious is the problem of optimum flying height, which presently differs for various geophysical sensors).

2. Constraints on electromagnetic systems due to manmade and natural electromagnetic disturbances. The former could limit the usefulness of AEM surveys in heavily populated areas containing many powerlines and telephone cables. The latter may affect the productivity and hence the cost effectiveness of AEM surveys because optimum flying conditions may not be encountered on many days. Rapid improvements in data acquisition and processing may lessen or even eliminate the problem of atmospheric disturbance (spherics) in the near future.

RESEARCH AREAS

The working group views reliable geological interpretation of conductivity maps as the most critical research area. Intensive field and laboratory studies in mineralized regions of the United States are recommended in order to establish geophysical signatures of a variety of mineral deposit types. Simple testing of geophysical systems over a deposit, as sometimes was done in the past, cannot substitute for systematic studies carried out by integrated teams of geoscientists. Close cooperation between geophysicists and geologists will lead to a greater awareness of the potential of modern AEM techniques among managers of exploration programs.

Further research is needed in the area of integration of airborne geophysical data sets and their meaningful geological interpretation. All available geoscience data should be integrated into a three-dimensional geographic information system (GIS). At present, techniques of displaying large volumes of data are not well developed in airborne geophysics, even though present computer technology makes it feasible.

REFERENCES CITED

Lefebvre, D.L., Dion, D.J., and Keating, P., 1986, La couverture en levé électromagnétique aéroporté de la province de Québec [Airborne electromagnetic coverage of the Province of Quebec], *in* Palacky, G.J., ed., Airborne resistivity mapping: Geological Survey of Canada Paper 86–22, p. 169–173.

Palacky, G.J., 1986, Airborne electromagnetics at crossroads, *in* Palacky, G.J., ed., Airborne resistivity mapping: Geological Survey of Canada Paper 86–22, p. 5–8.

_____ 1988, Resistivity characteristics of geological targets, *in* Nabighian, M.N., ed., Electromagnetic methods in applied geophysics, v. 1, Theory: Society of Exploration Geophysicists, p. 52–129.

Peltoniemi, M., 1986, Systematic airborne electromagnetic surveys in Finland—An overview, *in* Palacky, G.J., ed., Airborne resistivity mapping: Geological Survey of Canada Paper 86–22, p. 159–167.

Bathymetry and Related Uses Working Group Report[4]

Clyde Bergeron, *Leader*

APPLICATIONS OF AEM TO BATHYMETRY AND RELATED PROBLEMS

It is the concensus of this group that coastal bathymetry and sea-ice studies can be categorized as "present" applications. It is our judgment that potential applications include:

1. Studies of coastal-estuarine processes such as monitoring of seasonal and (or) monotonic variations of (a) salinity profiles of salt marshes, coastal bays, and lakes, (b) water depth, and (c) bottom properties.
2. Engineering applications including pre- and post-bathymetric surveys of marine dredging sites, measurement of electrical bottom properties, which may be correlated to mechanical bottom properties, and determination of the conductivity of sea ice, which may be used to infer the age and strength of sea ice.
3. Surficial oceanography utilizing conductivity measured by multifrequency airborne electromagnetic (AEM) measurements. Aircraft based on oceanographic survey ships can be used in implementing and updating the selection of shipborne oceanographic survey areas.
4. Detection of shallow, natural and artificial, sea-floor features.
5. Freshwater-saltwater interface problems including identification of the location and geometry of saltwater wedges in river deltas, freshwater lenses beneath islands and coastal regions, and concentrated brine discharges from shallow offshore and salt marsh oil-production operations.
6. Monitoring temporal changes in the physical properties of fresh and brackish lakes such as lateral salinity distribution, depth, and bottom characteristics.

CURRENTLY AVAILABLE BATHYMETRIC SYSTEMS

Available technology of bathymetric systems includes AEM systems and complementary technologies such as LIDAR (laser radar), passive multispectral scanning, and sonar sounding. The complementary technologies have several weaknesses and strengths vis-á-vis AEM bathymetry. All three have better horizontal resolution than AEM. LIDAR and multispectral scanning, however, fail in turbid waters. Sonar studies give ambiguous results for mushy bottoms and, being ship mounted, are slow and expensive. State-of-the-art AEM systems have a precision of 1 ppm of the primary field in the determination of the secondary field over a frequency range of 35–50,000 Hz for Tx-Rx coil separations of 7–8 m. This implies a depth resolution of 1 percent at one skin depth and 10 percent at two skin depths. For an assumed sea conductivity of 4 S/m and an operating frequency of 45 Hz, the skin depth is approximately 37 m. For bottom conductivities that differ from sea conductivity by less than an order of magnitude, the uncertainty in the determination of the bottom conductivity grows rapidly at depths greater than one skin depth. This implies a significant limitation on the use of present AEM systems in the study of properties of bottom lithologies having small conductivity contrasts. With the above assumed parameters and a frequency high enough that the skin depth of the first layer is less than half the first-layer thickness, the first-layer conductivity and hence salinity can be determined to an accuracy of a few percent.

TECHNICAL DEVELOPMENT REQUIREMENTS

Different applications require different deployment modes. The principal approaches envisaged include:

1. Helicopter with bird.
2. Fixed-wing aircraft with bird.
3. Fixed-wing aircraft with permanently attached sensor requiring an airframe made of nonconducting materials.

Effective use of available sensing hardware requires integration with support systems such as navigational and ancillary instrument outputs. This requirement is necessary for efficient processing and interpretation of data.

Improvements in EM sensor performance are required to realize the full potential of the method. Suggested improvements include:

1. Increasing frequency range and sampling density to fulfill interpretational objectives.
2. Increasing transmitter power to reduce effective averaging time for a given output signal-to-noise ratio, as well as to increase overall signal-to-noise ratio.

[4]The following people participated in the Bathymetry and Related Uses Working Group: C.J. Bergeron, Jr., J.S. Holladay, A. Kovac, E. Mozley, B.D. Smith, R.D.Watts, and D.L. Wright.

3. Improving instrumental platform and ambient signal-to-noise ratios.

4. Developing practical and accurate real-time calibration of complete systems.

5. Reducing the size and weight of the sensor and onboard hardware. The degree to which this is necessary depends on the choice of platforms. Conversely, the degree to which this reduction is achieved may affect the selection of the most appropriate platform.

6. Reducing signal drift to manageable levels. For an intercoil spacing of 7 m, a drift rate of about 10 ppm per hour is probably acceptable, as long as the drift does not vary from linearity by more than 1 ppm.

Full advantage of advances in sensor technology cannot be realized without improvements in digital acquisition and processing. Recommended goals for acquisition and processing methodologies include:

1. Improving system dynamic range and accuracy.

2. Increasing sampling rates, particularly for fixed-wing platforms.

3. Increasing the number of EM data channels required for wide-band systems, perhaps to as many as 100.

4. Utilizing high-capacity, compact storage technology such as optical disk drives to handle the volume of data expected.

RECOMMENDED AREAS OF RESEARCH

Several areas of research are recommended that will hopefully lead to significant advances in the use of AEM for bathymetry and related applications.

1. Laboratory-scale and numerical modeling to give quantitative estimates for the resolving power of AEM systems in the detection and delineation of laterally inhomogeneous layer interfaces. Such inhomogeneities are anticipated in AEM bathymetric surveys.

2. Direct inverse studies and continued extension of analytical and numerical inversion techniques for two- and three-dimensional models.

3. Development of models and inverse algorithms that allow for approximate, but rapid inversion of AEM data. This will permit real-time modification of AEM survey strategies such as redoing a survey line.

4. Field validation work on AEM survey results and laboratory measurements of physical properties extracted from inversion of AEM data.

5. Development of a high-frequency passive system utilizing commercial radio power as the primary source.

RECOMMENDED STRATEGY

We recommend the establishment of closer ties and collaboration between government, academic, and industry AEM research programs as a means of fostering research, disseminating new ideas, and avoiding duplication of effort. Such cooperation should be international in scale. In addition, national programs in the areas of environmental studies and resource assessment should be coordinated; these programs generally are carried out by different agencies and groups. Improved communication will lead to a more coordinated effort. Specifically, we recommend the following actions.

1. Test sites in several coastal areas should be identified for evaluating different AEM bathymetric technologies. AEM techniques should also be compared with LIDAR, multispectral scanning, and conventional acoustic sounding techniques.

2. The test program referred to above should be coordinated by the USGS because of their strong internal resources and expertise in a wide variety of geophysical methods.

3. Based on theoretical, model, and practical survey experience to date, key parameters of AEM systems for different applications should be specified. The optimal AEM system for engineering, ice measurement, and bathymetry-related problems are expected to be substantially different.

Ground-Water and Environmental Applications Working Group Report[5]

Pete Haeni, *Leader*

Summary

Electromagnetic (EM) geophysical techniques have clear applicability to a spectrum of ground-water problems because the techniques respond to electrical properties. We are now in a position to exploit the substantial instrumental and interpretational advances in EM methods of the last decade. Ground-water problems of a very local nature may still be best addressed by ground-based EM studies, but hydrogeologic problems of regional scope are best addressed by airborne EM surveys. Whenever possible, such surveys should include complementary geophysical measurements such as magnetics and radiometrics and should be designed to satisfy multiple users—geologists, engineers, regional planners, developers, and ground-water and environmental specialists. It follows that airborne surveys might best be supported by State or Federal governments. At present, the potential of AEM is not well appreciated by North American ground-water hydrologists. We recommend that selected demonstration AEM surveys be made and widely publicized as case histories. These surveys should address saltwater intrusion into coastal aquifers such as those located at Puget Sound, Cape Cod, Atlantic City, Hilton Head, and the Florida coast.

INTRODUCTION

In ground-water and environmental problems, as in all earth science studies, airborne electromagnetics (AEM) is just one tool among many that must be integrated to complete a successful program. Hydrogeological problems are notable for their complexity, often turning on subtle and local variations in lithology that in turn determine hydraulic properties. Conventional AEM techniques can yield valuable generalized models that need to be refined by further ground and borehole geophysical studies and conventional hydrologic data-gathering methods. In this report, we define AEM to include aircraft-deployed, conventional time- and frequency-domain EM methods in the 100 Hz–100 kHz range but not satellite or aircraft techniques deployed at higher frequencies, such as remote sensing or side-looking airborne radar (SLAR).

Airborne geophysical methods can be effectively used in the following hydrogeologic situations (table A1). In all of these situations, the hydrogeologic units of interest correspond to subsurface zones whose distinct electrical properties are measured by the geophysical method.

1. Saltwater intrusion into freshwater aquifers is a widespread problem along coastal urban corridors and in many inland sections of the country. Identifying, mapping, and monitoring the freshwater-saltwater interface using airborne methods is possible because saltwater is characterized by its high conductivity in contrast to the low conductivity of freshwater.
2. Another geographically widespread problem is the location of fracture zones in consolidated bedrock in order to develop ground-water uses and identify possible flow paths for subsurface contamination. The bedrock fractures are subvertical conductors that can be detected by airborne methods, except in areas where thick conductive overburden is present.
3. Degradation of ground-water quality due to man's activities is an increasing problem. These activities include industrial and municipal waste-disposal, mining, and oil-field operations. When the contaminants are conductive or are associated with conductive fluids, they can be detected and monitored using geophysical methods.
4. Regional mapping of hydrogeologic units such as extensive marine clays, coarse-grained eskers, or gravel deposits and subcrop mapping are needed for qualitative and quantitative aquifer studies. When the hydrogeologic units have electrical properties that differ from those of adjacent units, they can be detected and their areal extent and depth can be mapped.
5. Mapping of geothermal areas and freshwater zones in permafrost areas.

PROBLEMS

The slow acceptance of any geophysical techniques by the hydrologic community is a common problem. This reluctance to fully exploit geophysical possibilities stems from ambiguity of results, oversell by some geophysical groups, high upfront costs, and occasional ignorance on the part of possible users. The role of the USGS in

[5]The following people participated in the Ground-Water and Environmental Applications Working Group: R.B. Barlow, D.L. Campbell, A. Godoy, P. Haeni, P. Hoekstra, J. Kauahikaua, D. Mabey, J.D. McNeill, K.P. Sengpiel, W.D. Stanley, J. Steiger, M. Stewart, and D. Woodward.

Table A1. Suitability of airborne electromagnetic systems to ground-water and environmental applications

Application	Large transmitter loop and towed birds; usually time-domain systems	Rigidly coupled, fixed-wing or helicopter; usually frequency-domain systems	Plane-wave VLF systems	Electric-field VLF systems	Natural field systems
Saltwater intrusion (coastal, inland, islands; moderate to large, two- and three-dimensional targets)	Current systems well suited for deep salinity	Current systems well suited for shallow salinity	Not suitable	Shallow salinity	Not suitable
Fracture zones (long, linear targets)	Spatial resolution probably not adequate for short, conductive fractures	Current systems well suited	Current systems well suited as long as structure is shallow	Not suitable	Well suited for deeper conductive structures
Water quality (oil-well brines, municipal landfills, industrial contamination, mine tailing; small, three-dimensional targets	Spatial resolution probably not adequate	Current systems reasonably well suited but need better spatial and vertical resolution	Not suitable	Current systems moderately well suited for shallow situations	Not suitable
General geological mapping (ground-water aquifers, recharge areas, subcrop)	Spatial resolution suitable for longer targets	Current systems reasonably well suited but need better spatial and vertical resolution	Well suited for complementary information	Current systems moderately well suited for shallow situations	Well suited for complementary information
Geothermal (both deep and shallow; moderately large, two-dimensional targets)	Current systems well suited for moderately deep targets	Current systems well suited for moderately shallow targets	Not suitable	Not suitable	Not suitable
Permafrost (discontinuous zone; small, two- and three-dimensional targets)	Spatial resolution probably not adequate	Current systems reasonably well suited	Not suitable	Not suitable	Not suitable

correcting this imbalance between potential and actual use of geophysics of all kinds is fourfold.

1. Education, including fostering of workshops on specific hydrological problems and how they can be attacked.
2. Performing demonstration studies and developing case histories.
3. Disseminating complete accounts of definitive case histories including clear and simple to understand displays of test results.
4. Fostering or providing test ranges, typical of particular hydrological problem environments for which ground-truth data are available, on which various acquisition and data interpretation schemes can be tested.

NEW TECHNOLOGY AND FUTURE DIRECTIONS

AEM has reached a level of development where the practical application of resistivity mapping has been a useful aid to ground-water problems, particularly in coastal environments. Electromagnetic results acquired on a regional basis can outline regional saline and freshwater boundaries and thus identify optimum sites where further hydrogeology is required.

Considering the present state of the art, the following fields of endeavor need to be addressed.

1. Both spatial and vertical resolution must be improved in order to aid in site-specific problems that involve problems of stratigraphy.
2. The test-range concept can help demonstrate the effectiveness of various techniques and methodology for solving ground-water problems.
3. Hydrogeologists and geophysicists require test ranges that are representative areas for the evaluation, ranking, and integration of techniques and strategies.
4. Data presentation and interpretation (including numerical modeling) need to be improved in order to speed acceptance of AEM methods by nongeophysicists.
5. When applied on a regional scale, AEM techniques must satisfy multidisciplinary needs and general geological mapping requirements. Such multidisciplinary uses will improve the cost effectiveness of the applications.

Panel Discussion

Following the reports of the working groups, a panel discussion was held to summarize conclusions and discuss problem areas. The panel consisted of the following members: Bruce Smith, moderator, U.S. Geological Survey; Roger Barlow, Ontario Geological Survey; Duncan McNeill, Geonics Limited; Frank Morrison, University of California, Berkeley; Ari Poikonen, Geological Survey of Finland; Bob Smith, CRA Exploration Pty. Limited; and Charles Swift, Chevron Resources Co.

Below follows an edited transcript of the panel discussion. The transcript is not complete due to recording difficulties. It starts with comments by Frank Morrison in response to previous discussion about the technical level of geophysics currently used in ground-water applications and what can be done to improve it.

Frank Morrison: I like to reinforce that a little bit and maybe overstate it just a tad in the hope of getting some discussion going. I would like to illustrate my point by referring to the ground geophysics that have been brought to bear on ground-water exploration and ground-water contamination studies. I direct your attention to several publications that come out for the ground-water industry and ground-water hydrology community. There have even been conferences in the application of geophysical techniques. With very few exceptions, my observations have been that the geophysics reported at these meetings and in these journals is about at the level of *Geophysics* in 1950. That whole industry seems, in fact, to be repeating the geophysical history applied to mineral exploration. You find, for example, that Wenner soundings and Schlumberger soundings are routinely applied in nonhomogeneous media where it is quite evident from the results that there is not anything even approaching a layered earth. You begin to get the feeling of déja vu, that some radical thinkers are suggesting that maybe the dipole-dipole array would be something to try in inhomogeneous situations. Thirty years ago the mineral industry went through this wrenching decision to leave Wenner and go to dipole-dipole.

Now the other observation is that there don't seem to be very many familiar names on the papers that report on geophysics applied to ground water. In fact, there don't seem to be very many geophysicists [working on ground-water problems]. So something seems to be happening in the geophysical community that we have grown to know and love. We have somehow dropped the ball, because all this technique development, which we have labored over in the mineral industry, is simply not being brought to bear in ground water-applications. They don't seem to know about our work. Now I have overstated it a little bit. There are some really valiant efforts being made by some contractors that I'm sure most of us know. I won't give them any undo advertising, but there is some excellent work being done in this field by some of the familiar faces that we have known in the mineral business. [However,] there is a real educational effort needed in this ground-water field. I have some ideas for this.

I suppose one thing to consider if we are investigating AEM methods or ground-resistivity methods is to give some thought to publishing in some ground-water journals. Maybe *Geophysics* isn't the place to publish some of this stuff. The other thing we might think about is some sort of workshops where the clientele would be ground-water hydrologists. The theme of the workshop would be applications of geophysics to ground-water hydrology. If we had enough case histories and did a good educational job, a lot of hydrologists would go away from a meeting like that with a different concept of what geophysics could do. I've been talking mostly about the ground-water geophysical methods. The airborne is just a subset of that. If you think the hydrologic community doesn't know about ground resistivity and dipole-dipole, you can imagine what they think about AEM methods and these applications. So I would appreciate anybody who may have some sure thoughts about what we should do about making ourselves more visible in this community.

Duncan McNeill: Frank, the organization about which you speak, the National Water Well Association, is really an amazing group, and Jay Lehr, the guy that heads it, is hellbent on education. He is going to teach the drillers and everybody else how to use more sophisticated techniques. The ball really is in your court. They have seminars, literally dozens and dozens of them every year. They certainly need more information on geophysics, and the university is the place where it should come from. They are ready for you, OK. What's that?

David Campbell: Tarzan's going to go out and teach the apes to read.

Bruce Smith: I think we will have most of the discussion toward the end, but if something spontaneously develops we certainly won't shut it off.

Charles Swift: I am with Chevron Resources. I'm one of the very few in this group that represents the United States resource industry so I might be coming in from

another direction. Somebody was asking me earlier if I was going to be typically cynical. Frankly, I will be. But I was really relieved to hear Dave Campbell talk about the hydrologic and ground-water justification for additional EM. Before we get off on to that, it seemed to me like we had two days of talking to ourselves.

In reviewing the sessions, I kept hearing about the groups renewing their faith. Everybody was advocating more surveys, better equipment, better algorithms, more test areas. You know, we sound like a computer department trying to justify itself concentrating on how good the hardware is and how good the software is. As Frank has pointed out, the real issue is to solve the problems. I know that there is a general USGS justification, which is their mandate to assess the mineral, fuel, and ground-water resources of the country. As such, we are supposed to go out and map it because it is there.

I think we all agree that AEM data are useful. I'm not sure we made the case that it is cost effective. I think we need more demonstration surveys, both in areas where we know what we are going to find and also in areas where we really don't know what we are going to find. We should do some work in areas where the geologists are preparing geological maps and just see what comes up serendipitously. In our working group session yesterday, Bob Smith had an interesting example of an area where in order to obtain an exploration license they volunteered to do an AEM survey, even though they really didn't need it for the problem at hand. With this intensive magnetic and electromagnetic data, some very interesting results came out on the distribution of heavy minerals in ancient river channels in the cover rocks that were totally unpredicted. I think that kind of thing will come out of organized airborne mapping in conjunction with geologic mapping. We really need to get those demonstration surveys out. We know now in the currently fashionable EM survey target of gold that sometimes in detailed surveys areas of low resistivity can be indicative of interesting mineralization. In other areas, high resistivity [indicative of] silicification would also be interesting. When we go to a more regional scale, we don't really have many examples of where AEM coverage would be cost effective. I think we really need to address the cost-effectiveness problem.

I have got a couple of technical comments to make. I will mention just one. In the discussion of the need for careful calibrations and careful positioning of the EM surveys, one reason really hasn't been brought out. The requirement for that kind of accuracy is for doing repeat surveys. If we start monitoring salinity or migration of contaminants by repeat surveys, we want to make sure that variations in response are due to variations in the Earth and not in the equipment or the survey techniques. We found on the ground that repeat surveys can be very useful, but they need to be well controlled. That is particularly true for any airborne surveys.

Bruce Smith: Thank you, Charlie.

Bob Smith: I'm with CRA Exploration, an Australian mining company, so I am representing the resources industry, but not from the U.S. Most of the points I wanted to raise have been mentioned by previous speakers, but I'll just briefly refer to some of them again. I thought several people were rather defensive about geophysics in the last couple of days. I don't think we can collect geophysical data to please some remote being called a "geologist" or "hydrologist" [without] producing what we think is worthwhile. It's passing the buck to produce something someone else wants even though it may not be scientifically useful. And it's irresponsible of us to urge the use of any geophysical method if it is not cost effective to do so. We've got to be objective. I think Charlie referred to this point, too. No one has paid much attention to cost effectiveness. I don't want to discourage development of AEM from a purely selfish viewpoint. We need better systems to cope with the Australian environment so we would love to see the U.S. taxpayers develop better systems.

Nevertheless, I'm not convinced that resistivity mapping with AEM is cost effective when compared to geological mapping, in general. I think Mel Best cast some doubts on this, too. Of course it helps in many areas, but in many other areas a separate layer is either absent or, if it's present, its resistivity can be overprinted by ground water and other factors. For a fraction of the cost of AEM, it's possible to do high-quality magnetic and radiometric surveys from the air, and the results can be much more effective than the AEM. I know that any AEM surveys would be designed to include magnetic or radiometrics, but the point I'm making is if AEM were left off it would be a fraction of the cost. In the examples George Palacky chose to show the advantages of resistivity mapping, the magnetics data are poor or very poorly presented. We can do much better for a modest cost. I think it would be irresponsible to push AEM beyond cost-effective limits. I think Doug Fraser mentioned that the traditional role of AEM anomaly picking for massive sulfides is gone, perhaps forever. This doesn't mean that massive sulfides won't be a target again. When they do become a target, we demand much more than just anomaly picking. And there are some exciting new systems we heard about in this meeting that can give us a lot more than simple anomaly picking. I get nervous when I think of the cost of operating some of these systems. Poikenen mentioned EM means better penetration and discrimination. I would stress the second of these even in the fairly harsh Australian conditions. We frequently can achieve sufficient penetration with existing systems. What we lack is discrimination. If we know

the existence of a conductor, we can usually see it in the data, but we could never pick it out in advance because we can't discriminate. There will be new interpretation games and new processing options developed in the future to help us with discrimination. On the empty targets we haven't thought of that yet. So it's important that we record reliable objective data now so that it can be reused in the future. I think Alex Becker referred to this this morning.

And finally, radar is a tool that is generally considered only suitable in ice, permafrost, and highly resistive areas. It may surprise some of you to know that we use ground-probing radar in Australia in quite conductive areas that only require a few meters of penetration. So far, we have only used it on the ground. We would love to get it in the air if we had the opportunity. I think that radar has an exciting future.

Bruce Smith: Thank you, Bob.

Duncan McNeill: I am from Geonics. Having been involved in the development of the RADIOPHASE and E-PHASE systems for more years than I care to remember, I'm very aware how incredibly difficult it is to follow up an airborne conductivity mapping survey on the ground because of the large amount of really rather coarse data that even the best surveys produce. Incidentally, it was to do followup airborne surveys that we originally designed our ground-conductivity meters because we realized that conventional ground-resistivity techniques were simply too slow by at least an order of magnitude. The sad fact is that ultimately the airborne conductivity surveys never did materialize, and there were two major reasons for this: one, a lack of horizontal resolution, and two, a lack of vertical resolution. These in turn were two shortcomings we could fairly simply rectify on the ground. We have been reasonably successful in getting ground EM techniques used for ground-water contamination mapping and a number of other markets. In the process we have learned that hydrogeologists and geotechnical engineers are indeed a very picky lot. To capture their attention the resolution of AEM systems has to improve rather significantly. There have certainly [been improvements] over the past decade, but it has to keep improving. It is probably still not good enough for a great many applications.

Ari Poikonen: I am Ari Poikonen from the Geological Survey of Finland. I first would like to thank George Palacky for his kind words about the Finnish aerogeophysical program. I see I am the only participant at the workshop from Scandinavia, and there seem only to be a few participants from the whole of Europe. In Scandinavia, especially in Finland, airborne geophysics, and especially airborne EM, has a very important role in mineral exploration and geological mapping. Maybe it could help the USGS to make their plans for the future if I summarized some of the main points of the Finnish way of doing airborne geophysics. First, we have a national program. The Geological Survey of Finland is responsible for it. Actually, we are now on our second national airborne geophysical survey, and progress to get the whole of Finland covered with aeromagnetic airborne EM and radiometric maps measured at low altitude with dense line spacing continues. In recent years, base-metal exploration in Finland has largely been replaced by gold exploration. This meant that airborne geophysics has become more important as an aid in geological mapping. In the case of regional-scale mapping, we have very clearly found that it is more important to do systematic measurements than to argue about modern modifications and some particular method. The second point is that we have quite a straightforward scheme on how to use EM and AEM in geological mapping. Our geologists used to start new mapping projects before the geophysical maps for the particular area were made available. Now our geologists expect to have geophysical maps before they start geologic mapping.

Roger Barlow: I would like to thank the USGS organizers for this very interesting forum. The papers have been solid. The workshop has been an excellent environment. I have some appreciation for the problem of getting programs launched in government, having spent some 15 years in Ontario and being particularly dominated by a lot of geologists in the [Ontario Geological] Survey. I think that one of the things that you require to get this type of program going is just some commonsense strategy and some persistence. The program will sell itself if you try to figure out the key advantages. A point was made about cost effectiveness of AEM. There is no question that AEM is cost effective. In Ontario we can do a survey anywhere in the north country and generate between six and ten times the cost of the survey spent back in exploration in the first year after the maps have been released. This is only handling one particular element of resource mapping. When we get into other areas that we really haven't tapped, we have done some geological mapping. We have pointed out areas where airborne EM can certainly aid the geologist whether he is looking at the stratigraphy as mapped by conductors or whether he is taking a piece of the information and looking at the particular geology on the surface. Other advantages are that you can quickly define good areas for geochemistry [work, particularly] in clay environments. Clay environments aren't very easily done by surface geochemistry. Bedrock environments are the best place to apply geochemistry.

One of the things I think that I have seen in Exploration '87 and also here is that we fail to integrate our ideas with other scientists. When we get the chance to get in a forum where we can talk to other geoscientists, we are apt as geophysicists to stand up and talk about the C-values in Cole-Cole relaxation formulas, which really aren't the point. I think that we are learning that we have a couple of fellows here that are from the hydrogeology area. Certainly we should get a few more. If you look at ground-water mapping in the world it probably is at the same scale as resource mapping. I think we have got a lot to learn about taking apart the Quaternary geology or surface environment for ground water. We can apply airborne EM to coastal aquifers. This has been done fairly well by companies such as Geoterrex in a few places around the world. All we really require is to try to develop the market and get some real customers. I think any instrument manufacturer will tell you that it's a hard battle. All of us have to join in, and all of us have to learn how to communicate better.

Unidentified speaker: In our session yesterday, we talked about the problem facing the USGS in addressing a national program because of the vast differences in geology and hence resistivity structure of the United States; the U.S. is not a 100 percent shield. If we went out and did a conductivity survey in western Kansas, I don't think we would generate intense exploration activity as we would somewhere else. We also have problems in the areas of mineralized shield where 20 years ago Exxon found Crandon, a world-scale mineral deposit. It hasn't been developed yet. There are real differences in economics and in geology. My question really is addressing the geology of the U.S. Should a conductivity mapping program use the same kind of survey design in all parts of the U.S., or should we selectively address the problem, state by state or geologic province by geologic province? I'm sure the interest of the State Geologist of Florida will be significantly different than those of the State Geologists from Arizona or Minnesota. Any comments?

Gary Raines: The comment I just overheard up here at the head table was, "Of course, it will be done on a regional basis." The example I would throw out is the NURE program. It was funded and carried out, and now we've got 6-mi data in the eastern half of the U.S. and 3-mi data in the western half, with a few districts flown with more detail. Indeed, many of us criticize that program, but it wasn't done right or it wasn't done by geologic province. It started flying 6-mi data.

Bruce Smith: As a postscript, certainly the data have turned out to be surprisingly useful. I think that is what Gary was driving at.

Unidentified speaker: Further, to Frank's question earlier today, "Had we convinced the hydrogeologists out there in the NWWA [National Water Well Association] to use geophysics to map geology and specifically to use EM?" Do you feel that the geologists of the USGS are becoming convinced at all that we should use EM or other forms of geophysics for mapping? Is the educational process starting there?

Bruce Smith: Perhaps that should be addressed by someone a little higher in the structure, Gary?

Gary Raines: I think the simplest answer is that we don't have the data to show. Sort of the long-term answer is that where we have gotten the data *and* the geophysicist has worked closely with the geologist from the beginning, we end up getting a convert. That's a very long, slow process and a peculiarity of government. I continually face the argument that a geologic map is cheap to make, but geophysics is expensive. The issue is that everybody in government is measuring in terms of how much money do I have to put out this year. I can send a geologist to the field for very little money. He can do a little bit of work. If I cut the money in half, he does a little less work, but he still does something. In geophysics we always have to get started with a big upfront cost to acquire data. This is what continually scares people away and leads to the erroneous conclusion that geophysics is expensive. If you measure on the back end of the product, it's not expensive. The bottom line is we are not funded that way, so we don't have the data. The geologists don't see it. We have made tremendous inroads in this by simply showing off the data that is coming from the State of Minnesota. They are flying quarter-mile surveys of the entire state. Many people are reacting to it: "Gee, I didn't know that geophysics could do that kind of thing." The feeling is what you can do with geophysics is what we do with 6-mi line space data. There is a tremendous education problem there. I think the only way we are ever going to solve it is to have enough data sets and to have them at the beginning of programs. This is kind of the approach we are trying to develop. That's the theme of the initiative, to have the data there when the programs begin.

So we're trying to make some inroads into education, but it is a very difficult time in budgets. I pick on Tom Hildenbrand all the time. He's got to get more people out there worrying about this educational issue. Maybe I can turn it around a bit. We've made a lot of points by simply putting together a very pretty, colorful book of examples with one-paragraph explanations. I think most of our EM examples are not too flashy. I would emphasize that we need more examples. I consider myself an economic geologist. We need more examples in the Society of Economic Geologists' publication

because the economic geologist doesn't read *Geophysics*. We need to think about that problem; it is just not your problem. The [geological] journals don't necessarily want to publish your papers; that issue can be worked on, too. We need to think about where we put our papers, and who is the real audience. Your buddies in AEM are going to accept it and know it's good stuff, but that's often not your real audience.

Bruce Smith: Perhaps somebody on the spot is the president of a well-known geophysical society who sponsors a very well received publication. Bob, I was wondering if you would care to make a couple of comments about what you think of the relevance of publishing in the geophysical journals to generating better examples of more uses. If it isn't relevant, do you want to see geophysical papers published in Ground Water or Economic Geology?

Bob Smith: [Bob Smith is also president of the Australian Society of Exploration Geophysicists, which publishes *Exploration Geophysics*.] We do tend to publish much more applied sorts of papers, more field data, perhaps less sophisticated than the papers that are published in *Geophysics*. Perhaps as a consequence of this a lot of geologists read our journals. Certainly, exploration geologists frequently join the ASEG [Australian Society of Exploration Geophysicists] and read the journal. *Geophysics* has drifted away from that sort of paper for some reason. I don't quite know why, because I know the editors often request applied papers, but they don't get them. Consequently, I can't imagine too many geologists would read *Geophysics*. The papers tend to be academic and mathematical and quite a distance from the applications. Yes, I think we should try to publish in Economic Geology and ground-water journals. As an example of how to do wrong, I think it was the 75th anniversary volume of Economic Geology, a hardcover book [containing] a number of geophysical papers. There were a number of geological papers describing particular types of deposits, a number of geophysical papers describing particular types of deposits, and a number of geophysical papers describing particular geophysical methods. They were totally separate papers. The description of porphyry copper deposits written by geologists did not mention induced polarization at all. There was a separate chapter on induced polarization in the back of the journal. The geologists read one chapter and the geophysicists read another chapter. That doesn't work. They have to be integrated into one paper, perhaps by co-authorship with geologists and geophysicists.

Unidentified speaker: I wonder if George Palacky might make some comments, having, I believe, organized a successful AEM workshop two years ago and published a very nice book, which I really think is an excellent bit of work. How do you get on with the geologists in the Geological Survey of Canada? Did this publication make an impact on the geologists in the Survey? Are they using airborne EM methods more than they did before or with new awareness? How would you characterize that?

George Palacky: I'm not sure whether the volume ["Airborne Resistivity Mapping," Geological Survey of Canada Paper 86–22] has had much impact on many geologists in the Survey program. Probably my presence in talking to other people during the last two years [has done more]. We have been involved in a new and fairly promising application; that is, Quaternary geology mapping. This is one area where geologists previously had a preconceived idea that if you use geophysics you can only use refraction or possibly shallow-reflection seismic surveys. I have been able to show them that we can achieve the same results using airborne and ground EM. We have flown airborne electromagnetic surveys along several transects in northern Ontario in order to map the lithology and thickness of Quaternary sediments. We have found that conductivity is a very sensible parameter that can be very accurately correlated to Quaternary rock types. In some areas we have also drilled along those transects. In August and September of this year, we drilled about 25 holes. In about half of them, we actually got excellent correlation. The estimate is based on ground EM interpretation and 5-m [deep] drill data. In other areas where we had more complex layering, like repeated sequence of till, sands, or clays, the EM interpretation was breaking down. Because of too many simplifications, we didn't achieve good results.

Going back to the original questions, the most effective way is face to face: to approach people who are working in the same organization, spend time with them, and explain to them what we can do. I agree with the original comment. The key question to everything is education. We spend far too much time giving lectures to known traditional audiences. I went to China to lecture to the Chinese who are more ready to accept some of the ideas I have on lithology mapping using EM than people in the more geophysically established and consolidated countries like Canada and Australia. In Thailand I have been able to convince the government that it would be a very good idea to fly a helicopter EM survey for geological mapping.

Charles Swift: I'll make one specific recommendation and a challenge to this group. There is one well-illustrated magazine journal that comes out, which most American geologists see and actually look through. To get a point across you need short, well-illustrated articles. I think the journal *Geology* that comes out along with the

GSA Bulletin gets read by an incredibly wide audience in the U.S. You can't give a lecture. You have got to get the person motivated enough to go to the lecture. The journal articles in *Geophysics* are sufficiently long that geologists aren't going to read them. We have spectacular illustrations that geologists just love. I'll bet an airborne EM resistivity mapping article in *Geology* would be very well received. Might even make the front cover.

Bruce Smith: Good point, Charlie.

Names and Addresses of Participants

Walter L. Anderson
U.S. Geological Survey
Denver, Colorado

A. Peter Annan
A-Cubed Incorporated
Mississauga, Ontario, Canada

Roger B. Barlow
Ontario Geological Survey
Toronto, Ontario, Canada

Anthony R. Barringer
Barringer Geoservices
Golden, Colorado

Alex Becker
University of California
Berkeley, California

C.J. Bergeron, Jr.
University of New Orleans
New Orleans, Louisiana

Melvyn E. Best
Geological Survey of Canada
Dartmouth, Nova Scotia, Canada

T.R. Bodger
Scintrex Limited
Concord, Ontario, Canada

David L. Campbell
U.S. Geological Survey
Denver, Colorado

Jack D. Corbett
Consulting Geophysicist
Denver, Colorado

Lin Cordell
U.S. Geological Survey
Denver, Colorado

David V. Fitterman
U.S. Geological Survey
Denver, Colorado

Douglas C. Fraser
Dighem Surveys and Processing Inc.
Mississauga, Ontario, Canada

Antonio Godoy
Prospec S.A.
Rio de Janeiro, Brazil

Howard C. Golden
Utah International, Inc.
Salt Lake City, Utah

Mark Goldman
Institute for Petroleum Research and Geophysics
Holon, Israel

Christian Guillozet
COGEM
Velizy-Villacoublay, France

Pete Haeni
U.S. Geological Survey
Hartford, Connecticut

A. Herz
Herz Industries Ltd.
Willowdale, Ontario, Canada

Thomas G. Hildenbrand
U.S. Geological Survey
Denver, Colorado

Steven Hodge
U.S. Geological Survey
Tacoma, Washington

Pieter Hoekstra
The Earth Technology Company
Golden, Colorado

R.L. Scott Hogg
Aerodat Ltd.
Mississauga, Ontario, Canada

Gerald W. Hohmann
University of Utah
Salt Lake City, Utah

J.S. Holladay
Geotech Ltd.
Markham, Ontario, Canada

Donald B. Hoover
U.S. Geological Survey
Denver, Colorado

Robert Horton
U.S. Geological Survey
Denver, Colorado

Juliette W. Ioup
University of New Orleans
New Orleans, Louisiana

James Kauahikaua
U.S. Geological Survey
Hawaii National Park, Hawaii

Jan Klein
Cominco
Richmond, British Columbia, Canada

Austin Kovacs
USCRREL
Hanover, New Hampshire

Victor F. Labson
U.S. Geological Survey
Denver, Colorado

Carl L. Long
U.S. Geological Survey
Denver, Colorado

Don Mabey
Utah Geological and Mineral Survey
Salt Lake City, Utah

J. Duncan McNeill
Geonics Limited
Mississauga, Ontario, Canada

David Morris
Scintrex, Inc.
Salt Lake City, Utah

E. Morrison
Geotech Limited
Markham, Ontario, Canada

H. Frank Morrison
University of California
Berkeley, California

Ed Mozley
NORDA
NSTL, Mississippi

George J. Palacky
Geological Survey of Canada
Ottawa, Ontario, Canada

Ari Poikonen
Geological Survey of Finland
Espoo, Finland

Don Pridmore
Aerodata Holdings
Mississauga, Ontario, Canada

Gary L. Raines
U.S. Geological Survey
Reston, Virginia

S.W. Reford
Paterson, Grant & Watson Ltd.
Toronto, Ontario, Canada

Klaus P. Sengpiel
Bundesanstalt für Geowissenschaften und Rohstoffe
Hannover, Federal Republic of Germany

Ajit K. Sinha
Geological Survey of Canada
Ottawa, Ontario, Canada

Bruce D. Smith
U.S. Geological Survey
Denver, Colorado

R.J. Smith
CRA Exploration Pty. Limited
Norwood, Australia

Dal Stanley
U.S. Geological Survey
Denver, Colorado

Judy Steiger
U.S. Geological Survey
Augusta, Maine

Mario Steiner
Aerodat Ltd.
Mississauga, Ontario, Canada

Ben Sternberg
University of Arizona
Tuscon, Arizona

Mark Stewart
University of South Florida
Tampa, Florida

Charles M. Swift
Chevron Resources Co.
San Francisco, California

Pierre Valla
Bureau de Recherches Géologiques et Minières
Orléans, France

Christopher Vaughan
A-Cubed Incorporated
Mississauga, Ontario, Canada

Raymond D. Watts
U.S. Geological Survey
Reston, Virginia

I.J. Won
Geophex, Ltd.
Raleigh, North Carolina

Dennis Woodward
U.S. Geological Survey
Austin, Texas

David L. Wright
U.S. Geological Survey
Denver, Colorado

Hovav Zafrir
Soreq Nuclear Research Center
Yavne, Israel